

Electrochemical Impedance Spectroscopy and its Applications

Andrzej Lasia

Electrochemical Impedance Spectroscopy and its Applications

 Springer

Andrzej Lasia
Département de chimie
Université de Sherbrooke
Sherbrooke, Québec
Canada

Additional material to this book can be downloaded
from <http://extras.springer.com>

ISBN 978-1-4939-5126-0 ISBN 978-1-4614-8933-7 (eBook)
DOI 10.1007/978-1-4614-8933-7
Springer New York Heidelberg Dordrecht London

© Springer Science+Business Media New York 2014
Softcover reprint of the hardcover 1st edition 2014

This work is subject to copyright. All rights are reserved by the Publisher, whether the whole or part of the material is concerned, specifically the rights of translation, reprinting, reuse of illustrations, recitation, broadcasting, reproduction on microfilms or in any other physical way, and transmission or information storage and retrieval, electronic adaptation, computer software, or by similar or dissimilar methodology now known or hereafter developed. Exempted from this legal reservation are brief excerpts in connection with reviews or scholarly analysis or material supplied specifically for the purpose of being entered and executed on a computer system, for exclusive use by the purchaser of the work. Duplication of this publication or parts thereof is permitted only under the provisions of the Copyright Law of the Publisher's location, in its current version, and permission for use must always be obtained from Springer. Permissions for use may be obtained through RightsLink at the Copyright Clearance Center. Violations are liable to prosecution under the respective Copyright Law.

The use of general descriptive names, registered names, trademarks, service marks, etc. in this publication does not imply, even in the absence of a specific statement, that such names are exempt from the relevant protective laws and regulations and therefore free for general use.

While the advice and information in this book are believed to be true and accurate at the date of publication, neither the authors nor the editors nor the publisher can accept any legal responsibility for any errors or omissions that may be made. The publisher makes no warranty, express or implied, with respect to the material contained herein.

Printed on acid-free paper

Springer is part of Springer Science+Business Media (www.springer.com)

All impedances are complex, but some are more complex than others.

Margaretha Sluyters-Rehbach

Preface

My first practical contact with electrochemical impedance spectroscopy (EIS) was during my postdoctoral training in the laboratory of Prof. Ron W. Fawcett at the University of Guelph, Ontario, Canada, in 1975. At that time I was using ac voltammetry on a dropping mercury electrode. Since then, the technique and equipment have evolved significantly. I was continually using EIS in subsequent years in the kinetics of the reduction of metal cations in nonaqueous solvents to determine the kinetics of hydrogen evolution, adsorption and absorption into metals, impedance of porous electrodes, and electrocatalytic reactions. After a series of seminars on the impedance spectroscopy in the laboratory of Prof. Brian Conway in Ottawa in 1994, he encouraged me to write a review in *Modern Aspects of Electrochemistry*, which was published in 1999. Prof. Conway has also asked me to write a second chapter in *Modern Aspects* on the impedance of hydrogen adsorption, absorption, and evolution (2002). Later, Prof. M. Schlesinger asked me to write yet another chapter on the impedance of porous electrodes (2009). This book originated from my previous reviews and lectures at various universities.

The purpose of this book is to present the concept of impedance, impedance of electrical and electrochemical systems, its limitations, and certain applications. The available books on EIS were written either by physicists or engineers, and I wanted to present it from the chemist's point of view. Some knowledge of electrochemistry is necessary to understand the developments of kinetic equations. I hope that it will be useful to students who are just starting to use this technique and to others already using it in their research. The book contains theory and applications, numerical examples shown in the text, and exercises with full solutions on the Internet.

First, electrical circuits containing resistances only are presented, followed by circuits containing R , C , and L elements in transient and ac conditions. To understand the concept of impedance, the notions of Laplace and Fourier transforms are presented and must be understood thoroughly. In this chapter, impedance plots are also presented, along with several examples for various circuits. Next, methods for determining impedances, including fast Fourier transform-based techniques, are discussed.

Based on that knowledge, the impedance of electrode processes in the presence of diffusion in various geometries and adsorption is mathematically developed. This leads to the general method of determining the impedances of complex mechanisms. As an illustration, the impedance of electrocatalytic reactions involving hydrogen adsorption, absorption, and evolution is presented.

The next two chapters deal with impedance dispersion at solid electrodes and the impedance of porous electrodes in the absence and presence of electroactive species.

It is difficult to present all applications of EIS; some applications (such as those to solid materials and PEM fuel cells, corrosion and passivity, batteries; see Sect. 1.3) may be found in available books. As examples, Mott-Schottky plots obtained for semiconductors, the impedance of coating and paints, and electrocatalysis of hydrogen adsorption, absorption and evolution were presented as they are well known in the electrochemical literature. Additionally, newer and developing applications such as the impedance of self-assembled monolayers, biological bilayers, and biosensors were also shown.

Finally, methods of verification of obtained impedances and the modeling of experimental data are discussed. The last two chapters deal with applications of nonlinear measurements and instrumental limitations.

Besides examples in the text, there are exercises at the end of certain chapters that can be solved using Excel, Maple, or Mathematica and more specialized programs such as ZView and KKtransform, with solutions on the Internet.

This book contains a comprehensive approach to impedance, but there exist more specialized books on impedance that should also be consulted; reading of the research literature cannot be avoided. One hour in the library may save one year of laboratory research.

Sherbrooke, Québec, Canada

Andrzej Lasia

Contents

1	Introduction	1
1.1	Why Impedance?	1
1.2	Short History of Impedance	3
1.3	Publications on Impedance	5
2	Definition of Impedance and Impedance of Electrical Circuits	7
2.1	Introduction	7
2.2	Electrical Circuits Containing Resistances	7
2.2.1	Ohm's Law	7
2.2.2	Kirchhoff's Laws	8
2.3	Capacitance	11
2.4	Inductance	12
2.5	Laplace Transform	13
2.6	Complex Numbers	18
2.7	Fourier Transform	20
2.7.1	Leakage	28
2.7.2	Aliasing	30
2.8	Impedance of Electrical Circuits	32
2.8.1	Application of Laplace Transform to Determination of Impedances	32
2.8.2	Definition of Operational Impedance	33
2.8.3	Application of Fourier Transform to Determination of Impedances	41
2.8.4	Definition of Impedance	44
2.9	Circuit Description Code	47
2.10	Impedance Plots	48
2.10.1	Interpretation of Bode Magnitude Plots	55
2.10.2	Circuits with Two Semicircles	58
2.10.3	Circuits Containing Inductances	62
2.11	Summary	64
2.12	Exercises	64

3	Determination of Impedances	67
3.1	AC Bridges	67
3.2	Lissajous Curves	68
3.3	Phase-Sensitive Detection, Lock-In Amplifiers	69
3.4	Frequency Response Analyzers	70
3.5	AC Voltammetry	72
3.6	Laplace Transform	73
3.7	Methods Based on Fourier Transform	75
3.7.1	Pulse or Step Excitation	75
3.7.2	Noise Perturbation	77
3.7.3	Sum of Sine Wave Excitation Signals	77
3.7.4	Dynamic Electrochemical Impedance Spectroscopy	79
3.8	Perturbation Signal	83
3.9	Conclusions	83
3.10	Exercises	84
4	Impedance of the Faradaic Reactions in the Presence of Mass Transfer	85
4.1	Impedance of an Ideally Polarizable Electrode	85
4.2	Impedance in Presence of Redox Process in Semi-infinite Linear Diffusion: Determination of Parameters	86
4.2.1	General Case	86
4.2.2	DC Reversible Case	92
4.3	Analysis of Impedance in the Case of Semi-infinite Diffusion	97
4.3.1	Randles Analysis	97
4.3.2	De Levie-Husovsky Analysis	99
4.3.3	Analysis of $\cot \varphi$	100
4.3.4	Complex Nonlinear Least-Squares Analysis	102
4.4	Finite-Length Linear Diffusion	102
4.4.1	Transmissive Boundary	103
4.4.2	Reflective Boundary	106
4.5	Generalized Warburg Element	107
4.6	Spherical Diffusion	109
4.6.1	Semi-infinite External Spherical Diffusion	109
4.6.2	Finite-Length Internal Spherical Diffusion	112
4.7	Cylindrical Diffusion	113
4.8	Diffusion to Disk Electrode	116
4.9	Rotating Disk Electrode	117
4.10	Homogeneous Reaction, Gerischer Impedance	121
4.11	Conclusions	124
4.12	Exercises	125
5	Impedance of the Faradaic Reactions in the Presence of Adsorption	127
5.1	Faradaic Reaction Involving One Adsorbed Species, No Desorption	127

5.2	Faradaic Reaction Involving One Adsorbed Species with Subsequent Desorption	131
5.2.1	Determination of Impedance	132
5.2.2	Impedance Plots	137
5.2.3	Distinguishability of the Kinetic Parameters of the Volmer–Heyrovsky Reaction	140
5.3	Faradaic Reaction Involving Two Adsorbed Species	141
5.4	Exercises	145
6	General Method of Obtaining Impedance of Complex Reactions . . .	147
7	Electrocatalytic Reactions Involving Hydrogen	155
7.1	Hydrogen Underpotential Deposition Reaction	155
7.2	Hydrogen Evolution Reaction	159
7.3	Influence of Hydrogen Mass Transfer on HER	163
7.4	Hydrogen Absorption into Metals	166
7.4.1	Hydrogen Adsorption–Absorption Reaction in Presence of Hydrogen Evolution	166
7.4.2	Direct Hydrogen Absorption and Hydrogen Evolution . . .	171
7.4.3	Hydrogen Absorption in Absence of Hydrogen Evolution	172
7.4.4	Hydrogen Absorption in Spherical Particles	174
7.5	Conclusions	175
8	Dispersion of Impedances at Solid Electrodes	177
8.1	Constant Phase Element	177
8.2	Fractal Model	183
8.3	Origin of CPE Dispersion	187
8.3.1	Dispersion of Time Constants	188
8.3.2	Dispersion Due to Surface Adsorption/Diffusion Processes	192
8.4	Determination of Time Constant Distribution Function	196
8.4.1	Regularization Methods	196
8.4.2	Least-Squares Deconvolution Methods	198
8.4.3	Differential Impedance Analysis	198
8.4.4	Summary	200
8.5	Conclusion	201
9	Impedance of Porous Electrodes	203
9.1	Impedance of Ideally Polarizable Porous Electrodes	203
9.1.1	Cylindrical Pore with Ohmic Drop in Solution Only ($i_{dc} = 0$, $r_e = 0$, $r_s \neq 0$)	204
9.1.2	Other Pore Geometry with Ohmic Drop in Solution Only	210
9.1.3	Double or Triple Pore Structure	214
9.1.4	Porous Electrode with Ohmic Drop in Solution and in Electrode Material ($i_{dc} = 0$, $r_s \neq 0$, $r_e \neq 0$)	214

9.2	Porous Electrodes in Presence of Redox Species in Solution . . .	217
9.2.1	Ohmic Drop in Solution Only in Absence of DC Current ($i_{dc} = 0, r_s \neq 0, r_e = 0$)	217
9.2.2	Ohmic Drop in Solution and Electrode Material in Absence of DC Current ($i_{dc} = 0, r_s \neq 0, r_e \neq 0$)	221
9.2.3	Porous Electrodes in Presence of DC Current, Potential Gradient in Pores and No Concentration Gradient, Ideally Conductive Electrode ($i_{dc} \neq 0,$ $dE_{dc}/dx \neq 0, dC_{dc}/dx = 0, r_s \neq 0, r_e = 0$)	222
9.2.4	Porous Electrodes in Presence of DC Current, Concentration Gradient in Pores and No Potential Gradient, Ideally Conductive Electrode ($i_{dc} \neq 0,$ $dC_{dc}/dx \neq 0, dE_{dc}/dx = 0, r_s \neq 0, r_e = 0$)	230
9.2.5	General Case: Potential and Concentration Gradient . . .	241
9.3	Distribution of Pores	244
9.4	Continuous Porous Model	245
9.5	Conclusions	250
9.6	Exercises	250
10	Semiconductors and Mott-Schottky Plots	251
10.1	Semiconductors in Solution	251
10.2	Determination of Flatband Potential	253
11	Coatings and Paints	257
11.1	Electrical Equivalent Models	257
11.2	Water Absorption in Organic Coating	258
11.3	Analysis of Impedances of Organic Coatings	259
11.4	Conclusions	261
12	Self-Assembled Monolayers, Biological Membranes, and Biosensors	263
12.1	Self-Assembled Monolayers	263
12.2	Lipid Bilayers	266
12.3	Biosensors	268
12.4	Conclusions	270
13	Conditions for Obtaining Good Impedances	271
13.1	Kramers-Kronig Relations	271
13.1.1	Polynomial Approximation	273
13.1.2	Checking Kramers-Kronig Compliance by Approximations	275
13.2	Linearity	280
13.3	Stability	281
13.3.1	Drift	281
13.3.2	Dealing with Nonstationary Impedances	282
13.3.3	Stability of Electrochemical Systems	283
13.3.4	Nyquist Stability Criterion	291
13.3.5	Negative Dynamic Resistances and Their Origin	294

13.4	Z-HIT Transform	299
13.5	Summary	300
13.6	Exercises	300
14	Modeling of Experimental Data	301
14.1	Acquisition of “Good” Data	301
14.2	Types of Modeling	302
14.3	Fitting the Experimental Data	310
14.4	Error Classification	311
14.5	Methods for Finding the Best Parameters	311
14.6	Weighting Procedures	312
14.6.1	Statistical Weighting	312
14.6.2	Unit Weighting	313
14.6.3	Modulus Weighting	313
14.6.4	Proportional Weighting	314
14.6.5	Weighting from Measurement Model	314
14.7	Statistical Tests	315
14.7.1	Chi-Square	315
14.7.2	Test F	319
14.7.3	t-test for Importance of Regression Parameters	320
14.8	Conclusion	320
14.9	Exercises	320
15	Nonlinear Impedances (Higher Harmonics)	323
15.1	Simple Electron Transfer Reaction Without Mass Transfer Effects	323
15.2	Other Reaction Mechanism	327
15.3	Conclusions	331
16	Instrumental Limitations	333
16.1	Measurements of High Impedances	333
16.2	Measurements at High Frequencies	334
16.3	Measurements of Low Impedances	336
16.4	Reference Electrode	338
16.5	Conclusions	339
17	Conclusions	341
	Appendix: Laplace Transforms	343
	References	345
	Index	365

Chapter 1

Introduction

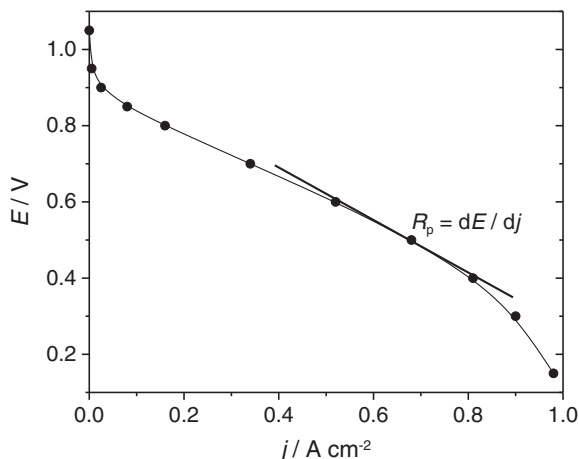
1.1 Why Impedance?

Among the various electrochemical techniques, electrochemical impedance spectroscopy (EIS) holds a special place. The classical electrochemical techniques present measurements of currents, electrical charges or electrode potentials as functions of time (which can also be related to the electrode potential). In contrast, EIS presents the signal as a function of frequency at a constant potential. This often poses some problems in understanding what is happening because electrochemists try to think in terms of time, not frequency. On the other hand, in optical spectroscopy, nobody thinks that light consists of the sinusoidal oscillations of electric and magnetic vectors of various frequencies, phases, and amplitudes. In spectroscopy, we used to think in terms of the frequency domain (wave number, frequency, or some related functions as wavelength) and that what we observed was the Fourier transform of the optical signal.

The issues associated with understanding EIS also relate to the fact that it demands some knowledge of mathematics, Laplace and Fourier transforms, and complex numbers. The concept of complex calculus is especially difficult for students, although it can be avoided using a quite time-consuming approach with trigonometric functions. However, complex numbers simplify our calculations but create a barrier in understanding complex impedance. Nevertheless, these problems are quite trivial and may be easily overcome with a little effort.

The advantages of using EIS are numerous. First of all, it provides a lot of useful information that can be further analyzed. In practical applications of cyclic voltammetry, simple information about peak currents and potentials is measured. These parameters contain very little information about the whole process especially when hardware and software is able sampling the current-potential curve producing thousands of experimental points every fraction of mV. On the other hand, one can use voltammetry with convolution, which delivers information at each potential, although very few people know and use this technique in current research. EIS contains analyzable information at each frequency. This is clearly seen from the examples that follow.

Fig. 1.1 Voltage (E)-current (j) curve for fuel cell. The slope is the polarization resistance (R_p)



Steady-state polarization measurements, that is measurement of the current at constant potential or potential at the constant current provide current-potential curves from which a slope, that is, a polarization resistance, $R_p = dE/dj$, can be determined. An example of such a curve for a fuel cell is displayed in Fig. 1.1.

However, taking the impedance at each potential produces series of data values at different frequencies. Examples of complex plane impedance plots that is imaginary versus real part at various frequencies for different fuel cells are presented in Fig. 1.2. The polarization resistance is the only point corresponding to zero frequency, as indicated in the plots. One may observe that the impedance plots, besides R_p , produce much more information that is not available in steady-state measurements. Impedance plots display complex curves that are rich in information. Such information is contained in every point, not only in one value of R_p . However, one must know how to find this information on the system being studied. This is a more complex problem and can be solved by the proper physicochemical modeling.

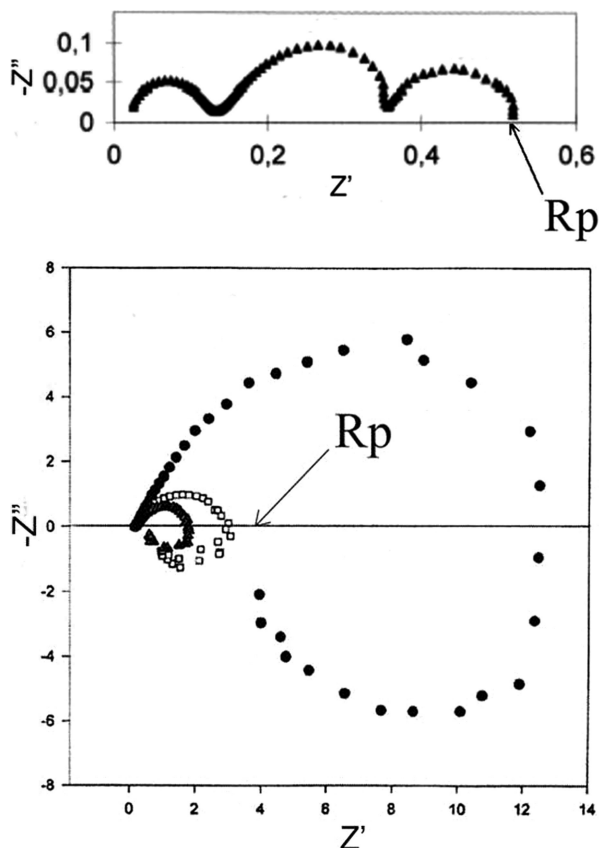
To characterize more complex electrochemical systems other studies of the system: including microscopic, surface morphology, structure, composition, and dc electrochemical characterization, should be carried out and understood thoroughly prior to EIS analysis. Studies may begin with EIS only for the electrical circuits and simple, well understood, systems. Beginning studies of complex systems with EIS is not recommended.

EIS supplies a large amount of information, but it cannot provide all the answers. EIS is usually used for fine-tuning mechanisms and determining the kinetics of processes, resistances, and capacitances, and it allows for the determination of real surface areas in situ. It is a very sensitive technique but must be used with care; it is often abused in the literature.

EIS has numerous applications. It is used in the following types of studies:

1. Interfacial processes: redox reaction at electrodes, adsorption and electrosorption, kinetics of homogeneous reactions in solution combined with redox processes, forced mass transfer

Fig. 1.2 Examples of complex plane impedance plots for fuel cells; *arrows*: polarization resistance also found in steady-state measurements; impedances are in Ω



2. Geometric effects: linear, spherical, cylindrical mass transfer, limited-volume electrodes, determination of solution resistance, porous electrodes
3. Applications in power sources (batteries, fuel cells, supercapacitors, membranes), corrosion, coatings and paints, electrocatalytic reactions (e.g., water electrolysis, Cl_2 evolution), conductive polymers, self-assembled monolayers, biological membranes, sensors, semiconductors, and others.

1.2 Short History of Impedance

EIS uses tools developed in electrical engineering for electrical circuit analysis [1–3]. The mathematical foundations of EIS were laid by Heaviside [4], who developed operational calculus and Laplace transform, introducing differentiation, s , and integration, $1/s$, operators. They made it possible to solve integrodifferential equations appearing in the solutions of electrical circuits (Sect. 2.8) by transforming them into a system of algebraic equations. Heaviside defined impedance,

Table 1.1 Eras in development of EIS [2]

Eras in development of electrochemical impedance spectroscopy
In the beginning (1880–1905)... (O. Heaviside and E. Warburg)
Age of double layer (1930–1965) (D.C. Grahame, R. Payne, J.O'M. Bockris, R. Parsons; C_{dl}/Hg , ac bridges)
Arrival of potentiostat (Hickling, Wenking) and the age of AC polarography (1965–1980) (D.E. Smith, J. H. Sluyters and M. Sluyters-Rehbach)
Age of electrical analogs (1948–present) (J.E.B. Randles, J.R. Macdonald, R. Buck). No unique EEC for a given system!
Age of material characterization (1970–present) (R.A. Huggins, J.R. Macdonald, W. Weppner)
Age of reaction mechanism analysis (1970–present). The real power of EIS! (A.N. Frumkin, R.D. Armstrong, I. Epelboin, M. Keddam, C. Gabrielli, D.D. Macdonald)
Explosion in applications (1985–present)

admittance, reactance, and operational impedance and explained the relation between Laplace and Fourier transforms by introducing a complex operator $s = \sigma + j\omega$. The main advantage of EIS is the fact that it is based on the linear time-invariant system theory, most commonly known as LTI system theory, and the validity of data may be verified using integral transforms (Kramers–Kronig transforms) that are independent of the physical processes involved.

Chemical applications of impedance spectroscopy began with the work of Nernst [5], followed by many others, including those applications to the distribution of relaxation time constants by Cole and Cole [6] and Davidson and Cole [7]. Warburg [8] developed the impedance of mass transfer (the so-called Warburg impedance), which allowed further applications of EIS to redox reactions.

The development of EIS is displayed schematically in Table 1.1. In the subsequent age of the double layer (1930–1965) [1, 2] the structure of a double layer in the absence and in the presence of adsorbed species was studied initially at a dropping mercury electrode and then at solid electrodes using ac bridges. The development of electronic potentiostats has revolutionized electrochemical and impedance measurements. With the presentation of the electrical analog circuit for electrochemical reactions by Dolin and Ershler [9] and Randles [10] the age of electrical analogs [2] began and continues up till now. Electrochemical systems are usually represented by analog circuits containing resistances, capacitances, and inductances, including some distributed elements such as, for example, the Warburg impedance and constant phase element. Commercial software allows for simple modeling of experimental impedance results. However, electrical analog circuits are analogs, not physico-chemical models. Although in simple cases analog circuits can reflect chemistry of the model quite often they either cannot or can lead to the ambiguous circuits. In addition, several different electrical equivalent models can exactly approximate the experimental data because they are not unique. For example, two semicircles on the complex plane plots might be interpreted by a serial or a parallel connection of the circuit elements (see Sect. 9.1.2, Figs. 9.12 and 9.13). In certain cases although approximate electrical analog circuit can be found the physicochemical model may contain elements which cannot be represented by such elements (see Sect. 9.2.3 on

porous electrodes). More discussion is provided in Chap. 14. However, the electrical equivalent circuits are often used in practice.

The age of mechanistic analysis [2] runs in parallel, where starting from chemical/electrochemical equations the impedances are built up, describing the system under study uniquely. These equations may, after some rearrangements, lead to proper electrical equivalent circuits (see, for example, the pioneering work of Epelboin, which was continued by Keddams, Gabrielli, Wiart, and other members of the Paris group [11], and that of D.D. Macdonald). This is the real power of EIS, but it is more difficult to implement. Presently, impedance is used in every area of electrochemistry to study, for example, interfaces, electrochemical reactions, and solid materials (on which more later).

1.3 Publications on Impedance

Electrochemical impedance spectroscopy is usually presented in electrochemistry handbooks [12–22], although such presentations are usually quite brief. There are few books on impedance in English [3, 23–26], one in Russian [27], one on differential impedance analysis [28], and many chapters on specific topics [29–72]. The first book [23] on the topic was edited by Macdonald and centered on solid materials; the second edition [24] by Macdonald and Barsoukov was enlarged by including other applications. Recently, three new books, by Orazem and Tribollet [3], by Yuan et al. [26] on proton exchange membrane fuel cells (PEM FC), and by Lvovich [25], have been published, while that by Stoykov et al. [27] was never translated into English. A third edition of the book by Macdonald and Barsoukov is in preparation. However, not all aspects of EIS are presented, and these books are not complete in the presentation of their applications. Plenty of review articles on different aspects of impedance and its applications have been published; however, they are very specific and can usually be used only by readers who already know the basics of this technique. A Scopus search for “electrochemical impedance spectroscopy” to the end of 2012 comes up with 18,000 papers, most of them since 1996.

Chapter 2

Definition of Impedance and Impedance of Electrical Circuits

2.1 Introduction

To understand the impedance of electrochemical objects, it is necessary to understand the behavior of simple electrical circuits, first in steady state, then in transient conditions. Such circuits contain simple linear electrical elements: resistance, capacitance, and inductance. Then the concept of electrical impedance will be introduced. It demands an understanding of the Laplace and Fourier transforms, which will also be presented. To understand impedance, it is necessary to thoroughly understand the complex plane and Bode plots, which will be presented for a few typical connections of the electrical elements. They can be computed using Excel, Maple, Mathematica, and specialized programs such as ZView. Several examples and exercises will be included.

2.2 Electrical Circuits Containing Resistances

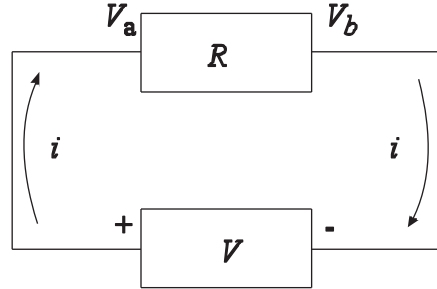
2.2.1 *Ohm's Law*

The total resistance of complex electrical circuits can be determined using two fundamental laws of Ohm and Kirchhoff. Ohm's law relates current passing through resistance i in A, with voltage V in V, and resistance R in Ω :

$$V = Ri. \quad (2.1)$$

It allows one to determine the current if the applied voltage is known or the voltage (ohmic drop) when the current is flowing through the resistance. It also shows that current follows the potential without delay. Additionally, in electrical engineering, by convention, the current is positive when it flows from the positive

Fig. 2.1 Illustration of Ohm's law



to the negative side of the potential source that is the potential drop is related to the direction of the current. This is illustrated in Fig. 2.1. The direction of the current was chosen, and Ohm's law may be written as

$$i = \frac{V_a - V_b}{R} = \frac{V}{R}, \quad (2.2)$$

where $V_a > V_b$ for the chosen direction of the current. From Ohm's law it follows that the equivalent resistance, R_{eq} , of the connection of resistances, R_i , in series equals the sum of the resistances:

$$R_{eq} = \sum_i R_i. \quad (2.3)$$

2.2.2 Kirchhoff's Laws

There are two Kirchhoff laws, one for nodes and one for loops. The first law says that the sum of the currents entering any point is equal to zero:

$$\sum_k i_k = 0, \quad (2.4)$$

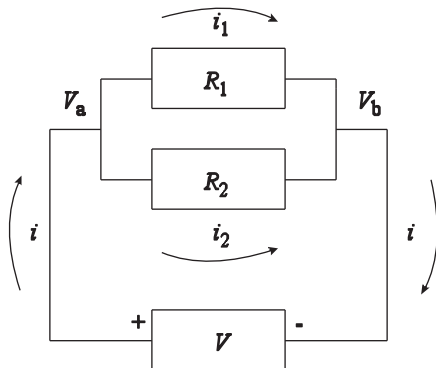
that is, the algebraic sum of currents entering one point is equal to the sum of all currents leaving this point. It simply states that there can be no accumulation of charges in conductors. The second law applies to loops and says that the algebraic sum of voltage drops in a closed loop equals zero:

$$\sum_k V_k = 0. \quad (2.5)$$

These laws allow for resolving any connection of resistances and voltage sources. They will be illustrated in the following examples.

Example 2.1 Find the relation between the total current and voltage and the equivalent resistance of the circuit in Fig. 2.2.

Fig. 2.2 Illustration of Kirchhoff's law for Example 2.1



The total current, i , flows from the positive to the negative connection of the source V . It separates into two currents, i_1 and i_2 , and, according to Kirchhoff's first law,

$$i = i_1 + i_2. \quad (2.6)$$

Using Ohm's law one can write

$$\begin{aligned} i_1 &= \frac{(V_a - V_b)}{R_1} = \frac{V}{R_1}, \\ i_2 &= \frac{V}{R_2}. \end{aligned} \quad (2.7)$$

Combining these equations with Eq. (2.6) gives

$$i = \frac{V}{R_1} + \frac{V}{R_2} = V \left(\frac{1}{R_1} + \frac{1}{R_2} \right) = \frac{V}{R_{eq}}, \quad (2.8)$$

which means that the two resistances can be replaced by one equivalent resistance R_{eq} :

$$R_{eq} = \frac{1}{\frac{1}{R_1} + \frac{1}{R_2}} = \frac{R_1 R_2}{R_1 + R_2} \quad (2.9)$$

or

$$\frac{1}{R_{eq}} = \frac{1}{R_1} + \frac{1}{R_2}.$$

The equivalent resistance is the harmonic mean of two parallel resistances. This formula should always be used for the parallel connection of resistances.

The problem may also be solved using Kirchhoff's second law. It is easy to see that there are three loops in the circuit, one containing the source V and the resistance R_1 , the second containing V and R_2 , and the third containing R_1 and R_2 . For these loops, in the clockwise direction, one can write Kirchhoff's law for loops:

$$\left. \begin{array}{l} i_1 R_1 - V = 0 \\ i_2 R_2 - V = 0 \end{array} \right\} \quad \text{or} \quad i_1 R_1 - i_2 R_2 = 0. \quad (2.10)$$

The negative sign in the first two equations for V appears because the direction of the loop goes from negative to positive voltage. The third equation is equivalent to the Eq. (2.8) and comes from the two first equations; therefore, it is redundant. The solution is, of course, the same as the previous one. Such equations written for any circuit lead to the system of linear equations for which programs were developed in electrical engineering.

Example 2.2 Calculate the currents, voltages, and equivalent resistances for the schema of the circuit in Fig. 2.3.

From Kirchhoff's first law one obtains

$$i = i_1 + i_2 \quad (2.11)$$

and from the second law

$$\left. \begin{array}{l} iR_1 + i_1 R_2 - V = 0 \\ iR_1 + i_2 R_3 - V = 0 \end{array} \right\} \quad \text{or} \quad i_1 R_2 + i_2 R_3 = 0. \quad (2.12)$$

As happened earlier, the third equation arises from the first two previous equations. Elimination of i_2 gives

$$i_1 = i \frac{R_3}{R_2 + R_3}. \quad (2.13)$$

The total voltage drop may be described as

$$\begin{aligned} V &= (V_a - V_b) + (V_b - V_c) = iR_1 + i_1 R_2 = iR_1 + i \frac{R_2 R_3}{R_2 + R_3} \\ &= i \left(R_1 + \frac{1}{\frac{1}{R_2} + \frac{1}{R_3}} \right) = iR_{\text{eq}}. \end{aligned} \quad (2.14)$$

Therefore, all the resistances in the circuit may be substituted by one equivalent resistance, R_{eq} , equal to the sum of R_1 and the parallel connection of resistances R_2 and R_3 .

Fig. 2.3 Circuit for Example 2.2

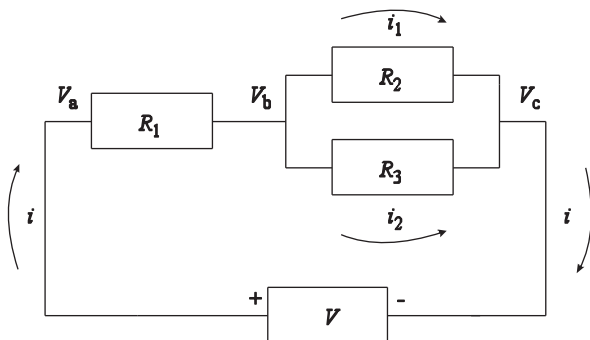
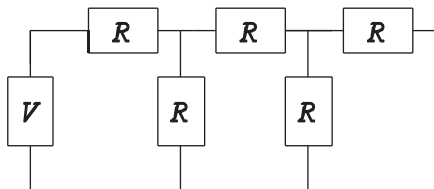


Fig. 2.4 Circuit for Example 2.3



Example 2.3 Find the equivalent resistance in Fig. 2.4.

To determine the total resistance, a circuit can be divided into parts starting from the right. First there are two resistances in parallel, then in series, etc. Answer: $8R/5$.

2.3 Capacitance

Electrical circuits may contain three passive elements: resistors, capacitors, and inductors. The behavior of the capacitance and inductance is different from that of the resistance. A constant current cannot flow through a capacitance, but an electrical charge can accumulate in it, and it is different at each voltage applied. The fundamental relation between charge and voltage is given as

$$V = \frac{Q}{C}, \quad (2.15)$$

where Q is the charge stored in the capacitor in coulombs, C , and C is the capacitance in farads, F. The charge is related to the current flowing in the circuit:

$$Q(t) = \int_0^t i(t) dt. \quad (2.16)$$

Substitution of Eq. (2.16) into (2.15) gives an integral equation:

$$V(t) = \frac{1}{C} \int_0^t i(t) dt. \quad (2.17)$$

If there is a circuit consisting of a resistor and a capacitor in series connected to the voltage source V , the voltage applied to the system is the sum of the potentials on the resistance (ohmic drop) and on the capacitance:

$$E(t) = i(t)R + \frac{1}{C} \int_0^t i(t) dt. \quad (2.18)$$

This constitutes an integral equation where the unknown current is outside and under the integral. The solution of such an equation may be easily accomplished using a Laplace transform. It should be added that in electrochemical systems double layer capacitance is potential dependent and the differential capacitance, $C = dQ/dE$ should be used.

2.4 Inductance

The inductance is usually represented as a coil in which current induces an electromotive force that opposes a change in current. The ideal inductance has a zero resistance and resists changes in the current. The potential difference developed at the inductance is

$$V(t) = L \frac{di(t)}{dt}, \quad (2.19)$$

where L is the inductance in henrys, H. This means that the constant current flows through the inductance without resistance, that is, $V(t) = 0$. In the case of the connections of the resistance and inductance in series the equation describing the system is

$$V = i(t)R + L \frac{di(t)}{dt}. \quad (2.20)$$

To obtain the solution of a transient current, this differential equation must be solved. It can be easily solved using a Laplace transform.

2.5 Laplace Transform

The Laplace transform is a tool that allows for an easy solution of differential or integral equations by changing them into algebraic equations in the Laplace plane. It is also well suited for solving problems in electrical engineering and impedance spectroscopy. The Laplace transform is defined as

$$L[f(t)] = F(s) = \bar{f}(s) = \int_0^{\infty} f(t)e^{-st} dt. \quad (2.21)$$

This is an integral transform that maps the function of time, $f(t)$, into a function called $F(s)$ or $\bar{f}(s)$ of the parameter s , called the frequency, because if t is in s , then s must be in s^{-1} . Of course, integration over the parameter t between 0 and ∞ assures that t will not appear after integration. During the transformation, no information about $f(t)$ is lost and the transform contains the same amount of information, only displayed in the frequency domain. Complex equations are usually much simpler in the Laplace domain. In general, the parameter s can be complex (see Sect. 2.6),

$$s = \sigma + j\omega, \quad (2.22)$$

but usually a real transform is used $s = \sigma$, and for complex s it is a Heaviside transform. Let us first look at the restrictions on the function $f(t)$ because not all functions can be transformed:

- (1) $f(t) \equiv 0$ for $t < 0$, that is, the function must always be zero at $t < 0$.
- (2) $f(t)$ has a finite number of discontinuities.
- (3) $f(t)$ is of exponential order, that is, there are always two constants $\lambda \geq 0$ and $M \geq 0$ for which $|f(t)| < M e^{\lambda t}$ for all values of t . Functions t^n and e^{at} are of exponential order, but the function e^{t^2} is not and cannot be transformed.

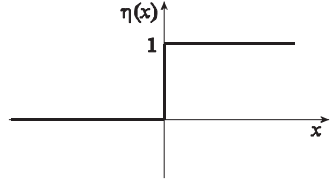
The Laplace transform is linear, that is, the transform of the sum of functions is equal to the sum of transforms:

$$L\{af_1(t) + bf_2(t)\} = a\bar{f}_1(s) + b\bar{f}_2(s). \quad (2.23)$$

To better understand this transform, let us work out a few examples.

Example 2.4 Determine the Laplace transform of the Heaviside step function $\eta(t)$ defined as

Fig. 2.5 Heaviside step function



$$f(t) = \eta(t) = \begin{cases} 0 & t < 0, \\ 1 & t > 0, \end{cases} \quad (2.24)$$

displayed in Fig. 2.5. This function is equal to zero for $t < 0$ (as specified in restriction 1 given earlier) and equal to 1 elsewhere.

Application of the definition given by Eq. (2.21) yields

$$L[\eta(t)] = \int_0^{\infty} 1 e^{-st} dt = -\frac{e^{-st}}{s} \Big|_0^{\infty} = \frac{1}{s}, \quad (2.25)$$

and the transform is simply equal to $1/s$.

Example 2.5 Find the transform of the exponential function $f(t) = \exp(-at)$:

$$L(e^{-at}) = \int_0^{\infty} e^{-at} e^{-st} dt = \int_0^{\infty} e^{-(a+s)t} dt = \frac{e^{-(a+s)t}}{-(a+s)} \Big|_0^{\infty} = \frac{1}{s+a}. \quad (2.26)$$

The exponential function is transformed into a simpler form: $1/(s+a)$.

Example 2.6 Find the transform of the first derivative of the function

$$\begin{aligned} L\{f'(t)\} &= \int_0^{\infty} e^{-st} f'(t) dt = e^{-st} f(t) \Big|_0^{\infty} - \int_0^{\infty} (e^{-st})' f(t) dt \\ &= -f(0^+) + s \int_0^{\infty} e^{-st} f(t) dt = s\bar{f}(s) - f(0^+), \end{aligned} \quad (2.27)$$

where the following formula for integration by parts was used:

$$\int uv' dx = uv - \int u' v dx, \quad (2.28)$$

and $f(0)^+$ is the initial value of the function $f(x)$ at time equal to zero; it is taken as the right-hand-side limit, $\lim_{x \rightarrow 0^+} f(x)$.

Similarly, the transform of the second derivative may be obtained as follows:

$$L[f''(t)] = s^2\bar{f}(s) - sf(0^+) - f'(0^+). \quad (2.29)$$

It can also be shown that the transform of the integral equals

$$L\left\{\int_0^t f(\tau)d\tau\right\} = \frac{1}{s}L\{f(t)\} = \frac{\bar{f}(s)}{s}. \quad (2.30)$$

The preceding examples show that the differentiation is equivalent to the multiplication by the parameter s and the integration is equivalent to the division by s in the Laplace domain. This allows for an easy transformation of differential or integral equations into algebraic equations, solving them in the Laplace domain and then carrying an inverse transformation into the time domain. This is schematically shown below:

$$\text{Time domain} \left\{ \begin{array}{ccc} \text{Differential eqn.} & \xrightarrow{L} & \text{Algebraic eqn.} \\ \text{solution } (t) & \xleftarrow[L^{-1}]{} & \text{solution } (s) \end{array} \right\} \text{Laplace domain} \quad (2.31)$$

To understand this method, let us work out two examples.

Example 2.7 Solve the following differential equation of first-order kinetics:

$$\frac{dy(t)}{dt} = -ky(t) \quad \text{with} \quad y(0) = y_0. \quad (2.32)$$

Application of the Laplace transform to both sides of the equation using Eqs. (2.27) and (2.23) gives

$$s\bar{y}(s) - y_0 = -k\bar{y}(s), \quad (2.33)$$

from which $\bar{y}(s)$ is the solution in the Laplace domain:

$$\bar{y}(s) = y_0 \frac{1}{s+k}. \quad (2.34)$$

The inverse transform using Eq. (2.26) gives the solution in the time domain:

$$y = y_0 e^{-kt}. \quad (2.35)$$

The differential equation was solved only by transformation, which can be done using Laplace transform tables, the solution of an algebraic equation, and the inverse Laplace transform using tables. Tables of Laplace transforms can be easily

found in the literature [73, 74], and several of the most often used ones are shown in the appendix.

Example 2.8 Solve the following differential equation:

$$\frac{d^2 y(t)}{dt^2} - a^2 y(t) + b = 0 \quad (2.36)$$

if the initial values of $y(0)$ and $y'(0)$ are known and a and b are constants.

Transformation into the Laplace domain by applying the formula for the second derivative, Eq. (2.29), and for the constant (2.25) leads to

$$s^2 \bar{y}(s) - sy(0) - y'(0) - a^2 \bar{y}(s) + \frac{b}{s} = 0, \quad (2.37)$$

from which the value of $\bar{y}(s)$ may be isolated:

$$\bar{y}(s) = \frac{-\frac{b}{s} + y'(0) + sy(0)}{s^2 - a^2} = \frac{+s^2 y(0) + sy'(0) - b}{s(s-a)(s+a)}. \quad (2.38)$$

To carry out the inverse Laplace transform, Eq. (2.38) must be separated into simple fractions:

$$\begin{aligned} \bar{y}(s) &= \frac{A}{s+a} + \frac{B}{s-a} + \frac{C}{s} = \frac{A(s^2 - as) + B(s^2 + as) + C(s^2 - a^2)}{s(s^2 - a^2)} \\ &= \frac{s^2(A+B+C) + s(-aA + aB) - Ca^2}{s(s^2 - a^2)}. \end{aligned} \quad (2.39)$$

The constants A , B , and C may be obtained by comparison of the coefficients at s^2 , s , and s^0 between Eqs. (2.38) and (2.39). This gives three equations:

$$\begin{cases} A + B + C = y(0), \\ -aA + aB = y'(0), \\ -Ca^2 = -b, \end{cases} \quad (2.40)$$

from which the following parameters are obtained:

$$\begin{cases} C = \frac{b}{a^2}, \\ A = \frac{y(0)}{2} - \frac{y'(0)}{2a} - \frac{b}{2a^2}, \\ B = \frac{y(0)}{2} + \frac{y'(0)}{2a} - \frac{b}{2a^2}. \end{cases} \quad (2.41)$$

The inverse transform of Eq. (2.39),

$$\bar{y}(s) = \frac{A}{s+a} + \frac{B}{s-b} + \frac{C}{s}, \quad (2.42)$$

leads to the solution in the time domain:

$$y(t) = Ae^{-ax} + Be^{ax} + \frac{b}{a^2}. \quad (2.43)$$

Example 2.9 Solve the differential equation

$$y(t)'' + ky(t) = 0 \quad (2.44)$$

with the following conditions: $y(0) = a$; $y'(0) = b$.

Application of a Laplace transform gives

$$\begin{aligned} s^2\bar{y}(s) - sy(0) - y'(0) + k\bar{y}(s) &= 0, \\ s^2\bar{y}(s) - as - b + k\bar{y}(0) &= 0. \end{aligned} \quad (2.45)$$

The solution in the Laplace domain is

$$\bar{y}(s) = \frac{as+b}{s^2+k} = a\frac{s}{s^2+k} + b\frac{1}{s^2+k}. \quad (2.46)$$

From the Laplace transform tables we have

$$L[\sin(at)] = \frac{a}{s^2+a^2}; \quad L[\cos(at)] = \frac{s}{s^2+a^2}, \quad (2.47)$$

and the solution in the time domain is

$$y(t) = a \cos(\sqrt{k}t) + \frac{b}{\sqrt{k}} \sin(\sqrt{k}t). \quad (2.48)$$

This equation displays the sum of two periodic functions.

The use of the Laplace transform is relatively simple using either Laplace transform tables or programs that make it possible to perform symbolic operations such as Maple or Mathematica. Application of the Laplace transform to solve current-voltage relations in electrical circuits will be illustrated in Sect. 2.8 on the impedance of electrical circuits.

2.6 Complex Numbers

The use of complex numbers is not obligatory, but they greatly simplify mathematical operations.

Let us consider first a vector R rotating with a constant angular frequency $\omega = 2\pi f$, where f is the frequency in s^{-1} or Hz and ω is in radians s^{-1} (Fig. 2.6).

The projection of R on the x - and y -axes, R_x and R_y , can be calculated using simple trigonometry:

$$\begin{aligned} R_x &= |R| \cos(\varphi) = |R| \cos(\omega t), \\ R_y &= |R| \sin(\varphi) = |R| \sin(\omega t), \end{aligned} \quad (2.49)$$

where $|R|$ is the length of the vector and $\varphi = \omega t$. This means that the projections of the rotating vector are periodic cos and sin functions of time. It should be stressed that R_x is the function of the cosine and R_y that of the sine. Of course, using Pythagoras' rule and the trigonometric identity $\sin^2 x + \cos^2 x = 1$ the length of the vector is

$$|R| = \sqrt{R_x^2 + R_y^2}. \quad (2.50)$$

In complex analysis, a projection on the x -axis is called the real part of vector R , and a projection on the y -axis is called the imaginary part. This is a simple way of distinguishing between these two projections, but, as we will see below, it simplifies considerably the calculations. The angle φ can be obtained as

$$\tan(\varphi) = \frac{R_y}{R_x}; \quad \varphi = \text{atan}\left(\frac{R_y}{R_x}\right). \quad (2.51)$$

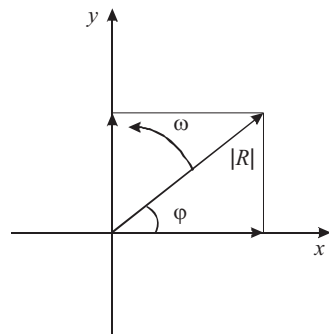
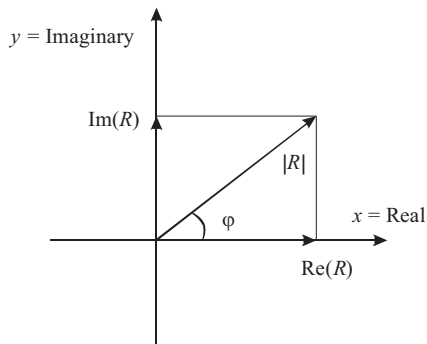


Fig. 2.6 Vector R rotating with constant angular frequency ω

Fig. 2.7 Representation of vector R on complex plane



The imaginary unit is defined as $j^2 = -1$, and the complex plane has two axes, x , which is real, and y , which is imaginary; all the real numbers on the y -axis are multiplied by the imaginary unit j . This means that any point on the complex plane has two parts: a real part on the x -axis and an imaginary part on the y -axis. This is illustrated in Fig. 2.7. Vector R may be written as

$$\hat{R} = \text{Re}(R) + j \text{Im}(R) = R' + jR'', \quad (2.52)$$

where the following definitions were used for the real and imaginary parts of the vector R :

$$\text{Re}(\hat{R}) = R' \text{ and } \text{Im}(R) = R''. \quad (2.53)$$

Of course, the length of the vector $|R|$ is

$$|R| = \sqrt{(R')^2 + (R'')^2}. \quad (2.54)$$

The phase angle of a complex number is called an argument, $\arg(\hat{R})$, and the same point may be described by the angles $\varphi + 2\pi n$, where $n = \pm 1, \pm 2, \dots$. However, we usually need the principal value of the argument denoted by $\text{Arg}(\hat{R})$ which is between 0 and 2π i.e. between 0° and 360° :

$$\varphi = \text{Arg}(\hat{R}) = \text{atan}\left(\frac{R''}{R'}\right). \quad (2.55)$$

Complex numbers can be written in exponential form keeping in mind that

$$e^{j\varphi} = \cos \varphi + j \sin \varphi; \quad (2.56)$$

therefore, each complex number may be written in polar form:

$$R = |R|e^{j\varphi} = |R|(\cos \varphi + j \sin \varphi). \quad (2.57)$$

The length of the vector $|R|$ is found by multiplying R by its complex conjugate R^* :

$$|R| = \sqrt{RR^*} = \sqrt{(R' + jR'')(R' - jR'')} = \sqrt{(R')^2 + (R'')^2}. \quad (2.58)$$

From Eqs. (2.56) and (2.58) it follows that

$$|e^{j\varphi}| = 1. \quad (2.59)$$

It should be kept in mind that addition, multiplication, and division of the complex numbers should be carried out correctly:

$$\begin{aligned} (a + jb) + (c + jd) &= (a + c) + j(b + d), \\ (a + jb)(c + jd) &= (ac - bd) + j(ad + bc), \\ \frac{1}{a + jb} &= \frac{(a - jb)}{(a + jb)(a - jb)} = \left(\frac{a}{a^2 + b^2} \right) - j \left(\frac{b}{a^2 + b^2} \right), \\ \frac{a + jb}{c + jd} &= \frac{(a + jb)(c - jd)}{(c + jd)(c - jd)} = \left(\frac{ac + bd}{c^2 + d^2} \right) + j \left(\frac{bc - ad}{c^2 + d^2} \right). \end{aligned} \quad (2.60)$$

Complex calculations may be carried out in Excel using built-in functions. Further applications of complex calculations will be shown later.

2.7 Fourier Transform

Techniques based on the FT are often used in chemical instrumentation and spectroscopy [e.g., Fourier transform-infrared (FTIR), Fourier transform nuclear magnetic resonance (FT-NMR), FT Raman] and in EIS. They can also be applied to smooth noisy experimental data. To comprehend these methods, a good understanding of the FT technique and its limitations is necessary.

Each periodic function may be presented as an infinite Fourier series composed of sine and cosine functions:

$$f(t) = a_0 + \sum_{k=1}^{\infty} a_k \cos(k\omega_1 t) + b_k \sin(k\omega_1 t), \quad (2.61)$$

where a_0 is a constant and all the parameters a_0 , a_k , and b_k may be found by integration over the function $f(t)$ with cosine and sine functions over one period:

$$a_k = \frac{2}{T} \int_0^T f(t) \cos(k\omega_1 t) dt, \quad (2.62)$$

$$b_k = \frac{2}{T} \int_0^T f(t) \sin(k\omega_1 t) dt. \quad (2.63)$$

The FT of the continuous function $f(t)$ is defined similarly to Eq. (2.21) with the parameter, $s = j\omega$, Eq. (2.22), but with integration from $-\infty$ to ∞ [75–77]:

$$F(\omega) = \int_{-\infty}^{\infty} f(t) e^{-j\omega t} dt. \quad (2.64)$$

It maps the function of time, $f(t)$, into the function of frequency, $F(\omega)$. As with the Laplace transform, no information is lost during this operation. In practice, one uses integration between 0 and T assuming that the function is periodic before and after this time window, which means that this time window is exactly repeated until infinity:

$$F(\omega) = \int_0^T f(t) e^{-j\omega t} dt. \quad (2.65)$$

Taking into account Eq. (2.57) this equation corresponds to two parts of the integral: a real part,

$$F'(\omega) = \int_0^T f(t) \cos(\omega t) dt, \quad (2.66)$$

and an imaginary part,

$$F''(\omega) = j \int_0^T f(t) \sin(\omega t) dt. \quad (2.67)$$

This operation corresponds simply to the integration of our function $f(t)$ with $\cos(\omega t)$ and $\sin(\omega t)$, respectively.

Electrochemistry deals with digitized signals acquired with a constant frequency determined by the analog to digital (A/D) converter, that is, instead of the continuous function we deal with the collection of N points every Δt during the time period T . The points i are numbered from 0 to $N - 1$, but only the point number is indicated and the corresponding time must be calculated from the sampling rate:

Function of time	Point number	
$f[0]$	$f(0)$	
$f[\Delta t]$	$f(1)$	
$f[2\Delta t]$	$f(2)$	
\dots	\dots	
$f[(N - 2)\Delta t]$	$f(N - 2)$	
$f[(N - 1)\Delta t]$	$f(N - 1)$	(2.68)

The acquired series of points may be integrated using Eq. (2.65), rewritten for the discretized function (the integral is written as a sum):

$$F(u) = \frac{1}{N} \sum_{i=0}^{N-1} f(i) \exp(-j\omega_u t_i), \quad (2.69)$$

where ω_u is a series of harmonic frequencies and u is a whole number between 0 and $N - 1$,

$$\omega_u = u\omega_1, \quad (2.70)$$

and the fundamental angular frequency ω_1 is related to the fundamental frequency ν_1 determined by the data acquisition time:

$$\omega_1 = 2\pi\nu_1 = \frac{2\pi}{T} = \frac{2\pi}{N\Delta t}. \quad (2.71)$$

Taking into account that

$$t_i = i\Delta t \quad (2.72)$$

and substituting these values into Eq. (2.69), the following equation is obtained:

$$F(u) = \frac{1}{N} \sum_{i=0}^{N-1} f(i) \exp\left(-\frac{j2\pi ui}{N}\right). \quad (2.73)$$

This equation represents the so-called discrete Fourier transform (DFT) and shows how the series of points $f(i)$ in the time domain is transformed into a series of points in the frequency domain $F(u)$. The exponent depends only on the numbers u (point number in frequency domain), i (point number in the time domain), and the

total number of points N . It should be noticed that Δt cancels and does not appear in the equation. This operation can be shown in a schema, where the parameters i and u change from 0 to $N - 1$:

Time domain	Frequency domain	
$f(0)$	$F(0)$	
$f(1)$	$F(1)$	
$f(2)$	$F(2)$	
\dots	\dots	
$f(i)$	$F(u)$	
\dots	\dots	
$f(N - 1)$	$F(N - 1)$	(2.74)

However, the highest frequency for which information can be obtained corresponds to the point $N/2$. This is the so-called *Nyquist frequency* and it expresses the fact that in order to obtain information about a periodic function (sine or cosine), this function must be sampled at least two times per period. The Nyquist frequency is

$$v_{\max} = \frac{Nv_1}{2} = \frac{N}{2T} = \frac{N}{2(N\Delta t)} = \frac{1}{2\Delta t}. \quad (2.75)$$

Although N points in the frequency domain are obtained, the information about the frequency is contained for u from 0 (constant) up to $N/2$. After this point the values are repeated, and no new information is found. Nevertheless, to carry out the inverse FT, all N points must be used (for u from $u = 0$ to $N - 1$):

$$f(i) = \sum_{u=0}^{N-1} F(u) \exp\left(\frac{j2\pi ui}{N}\right). \quad (2.76)$$

The frequencies at each point are calculated using the equation

$$v_u = \frac{u}{N\Delta t} \text{ for } u = 0 \dots N/2. \quad (2.77)$$

The DFT is numerically inefficient and demands many multiplications/divisions. Cooley and Tukey have developed a more efficient algorithm that reduces the number of calculations for N^2 to $N \log_2 N$. This is the so-called fast Fourier transform (FFT) [75], which is implemented in many programs including Microsoft Excel. However, it requires that the number of data points be a power of 2, that is, $N = 2^k$, where k is an integer number, e.g., 4, 8, 16, 32, 64, 128, ... Although manual calculation of the FT is possible for a few points, it is always done by computer. To better understand this transform, let us look at a few examples. They can be completed using Excel. In Exercise 2.1, the function $E(t) = \cos(2\pi t_i/0.32)$ is generated for 64 points and its FT is computed in Excel. Plots of the functions are

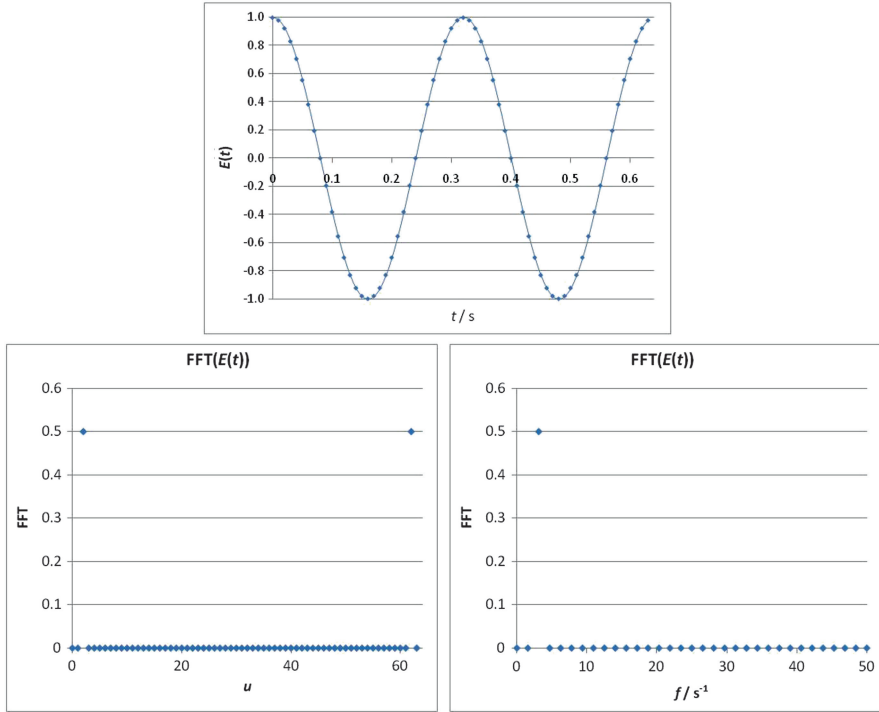


Fig. 2.8 Assumed function $E(t) = \cos(2\pi t/0.32)$ (64 points) and its FT in Excel plotted versus u and versus frequency

displayed in Fig. 2.8. The FT displays only one point at the frequency $\nu = 1/0.32 \text{ s}^{-1} = 3.125 \text{ s}^{-1}$, with the real part 0.5 and the imaginary part 0. This indicates that the function transformed was the cosine without a phase shift. The phase angle is calculated using Eq. (2.78):

$$\varphi = \text{Arg}\left(\frac{0}{0.5}\right) = 0. \quad (2.78)$$

The value of 0.5 is simply the FT of the cosine function with an amplitude of one:

$$\frac{1}{T} \int_0^T \cos(2\pi t/T) e^{-j(2\pi/T)t} dt = 0.5 \quad (2.79)$$

for $\nu = 3.125 \text{ s}^{-1}$. It should be stressed that the FT of the cosine function is always real.

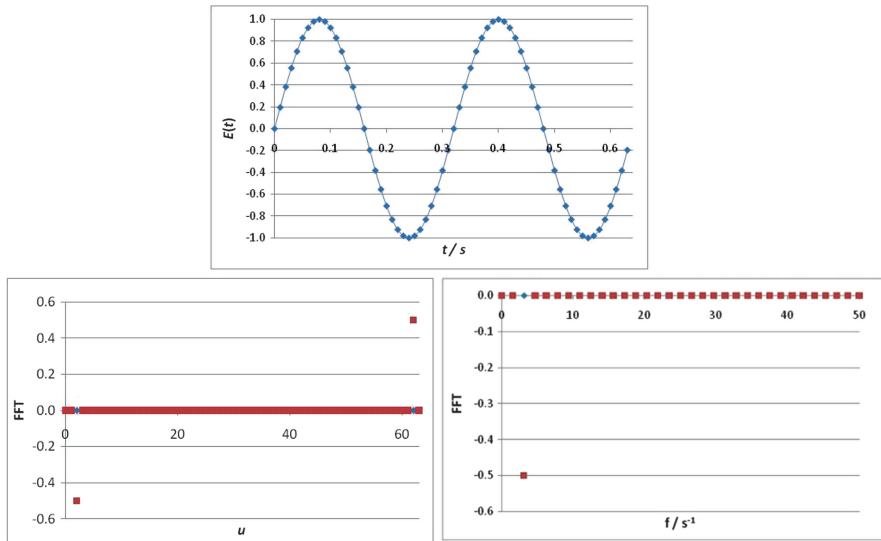


Fig. 2.9 Assumed function $\sin(2\pi t_i / 0.32)$ (64 points) and its FT (imaginary part) in Excel plotted versus u and versus frequency up to Nyquist frequency

The FT of the sinus function $E(t) = \sin(2\pi t / T_a)$ is studied in Exercise 2.2. It is simply the cosine function studied in Exercise 2.1 but shifted in phase by $-\pi/2 = -90^\circ$:

$$\sin\left(\frac{2\pi t}{T_a}\right) = \cos\left(\frac{2\pi t}{T_a} - \frac{\pi}{2}\right) \quad (2.80)$$

The assumed function and its FT are presented in Fig. 2.9.

The FT of this function shows that all the real values are equal to 0. The FT displays two imaginary values: $-0.5j$ for $u = 2$ and $0.5j$ for $u = 62$. The frequency of the function is 3.125 s^{-1} . The phase angle is

$$\varphi = \text{Arg}\left(\frac{-0.5}{0}\right) = -\frac{\pi}{2}, \quad (2.81)$$

that is, -90° . FT is characterized by three parameters: the real (0) and imaginary (-0.5) parts and the frequency 3.125 s^{-1} . The equivalent representation is by the modulus 0.5, the phase angle $-\pi/2$, and the frequency 3.125 s^{-1} .

Let us consider now what happens if the cosine function is shifted by the phase angle φ . This is also illustrated in Exercise 2.3, where the function $E(t) = \cos(2\pi t / T + \pi / 3)$ is transformed. The function and its FT are displayed in Fig. 2.10.

In this case the FT versus u presents values different from 0 for $u = 2$ and 62 ; they are both complex, the real part is the same, and the imaginary is just of the

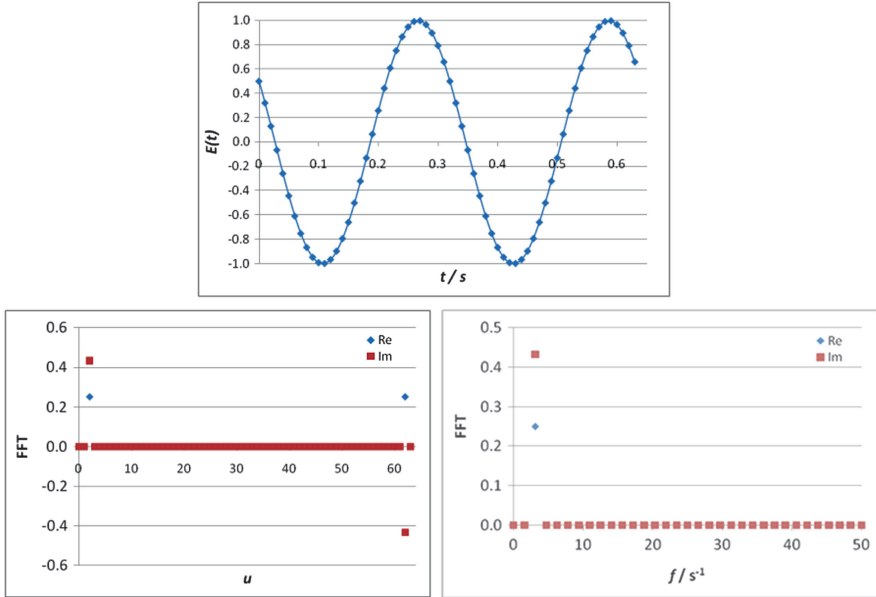


Fig. 2.10 Assumed function $E(t) = \cos(2\pi t/0.32 + \pi/3)$ (64 points) and its FT (real and imaginary parts) in Excel plotted versus u and versus frequency, f

opposite sign. The plot versus frequency displays real and imaginary values different from zero for one frequency $f = 3.125 \text{ s}^{-1}$. The phase angle is

$$\varphi = \text{Arg}\left(\frac{\text{Im}}{\text{Re}}\right) = \frac{\pi}{3} = 60^\circ. \quad (2.82)$$

From these values one can write that the original function is $\cos(2\pi \cdot 3.125 t + \pi/3)$. The modulus of the FT is $\sqrt{0.25^2 + 0.43301^2} = 0.5$, and it is the same as in Exercises 2.1 and 2.2. In all these exercises the amplitude of the periodic functions was assumed to be one.

In general, the cosine function (without the phase shift) always produces real values and the sine only imaginary values. A cosine function shifted in phase produces the real and imaginary parts from which the phase shift can be determined.

In the next example we will examine the FT of an intrinsically nonperiodic function. This is also illustrated in Exercise 2.4, in which the function $E(t) = \exp(-3t_i)$ for 32 points is transformed. This function and its FT are displayed in Fig. 2.11. It is evident that nonzero values of the FT are obtained at all frequencies; with the exception of $u = 0$ and 16, they are all complex. The first constant value for $f = 0$ is simply the average value of all the experimental points. Note that from $u > N/2$ that is from $u = 17$ the real values are repeated in inverse order, that is, $\text{Re}_{17} = \text{Re}_{15}$, $\text{Re}_{18} = \text{Re}_{14}$, etc., while the imaginary parts change sign: $\text{Im}_{17} = -\text{Im}_{15}$, $\text{Im}_{18} = -\text{Im}_{14}$, etc., around the central value for $u = N/2 = 16$. It must be

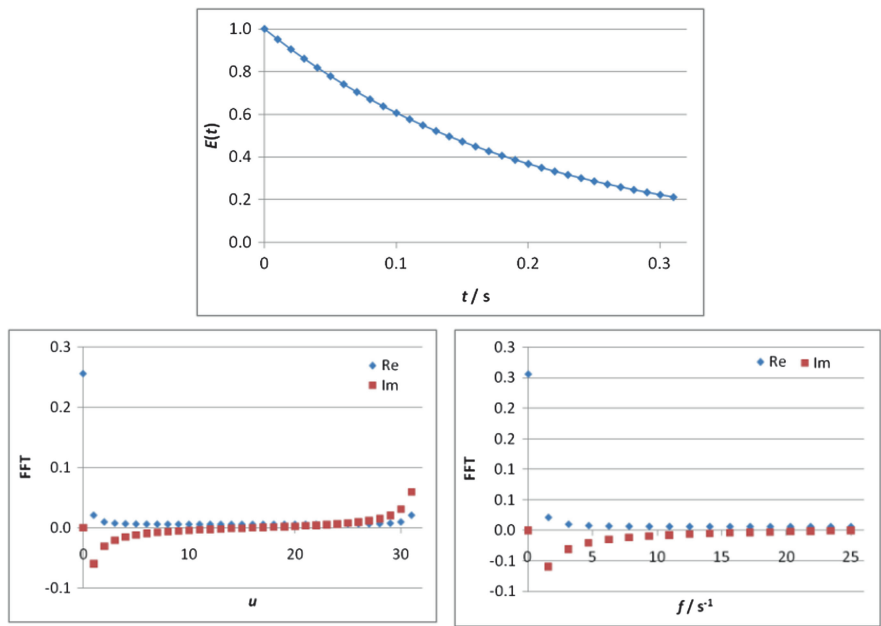


Fig. 2.11 Assumed function $E(t) = \exp(-3t)$ (32 points) and its FT (real and imaginary parts) in Excel plotted versus u and versus frequency

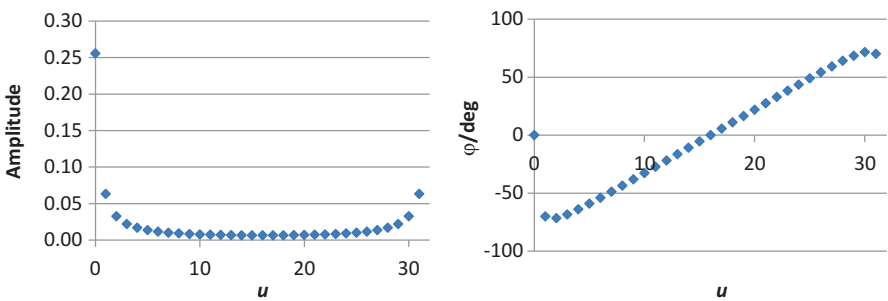


Fig. 2.12 Amplitude and phase angle of FT of exponential function in Fig. 2.11

stressed that all the frequencies are necessary to approximate the experimental points. The experimental points of the exponential function are approximated by a sum of the cosine functions with different amplitudes and different phase angles. The amplitude (modulus) at each frequency and the phase angle are displayed in Fig. 2.12. The same information is contained in the real and imaginary values at each frequency as in the amplitude and the phase angle. It should be stressed that FT gives an exact approximation of the experimental function at each point by the sum of the periodic functions. Of course, one cannot use the sum of the obtained periodic functions to interpolate it between the experimental points.

Fig. 2.13 *Top: curve a* containing whole number of periods (here one); *curve b* containing 1.5 periods. *Bottom: FT assumes that this element is periodically repeated producing discontinuities for curve b*

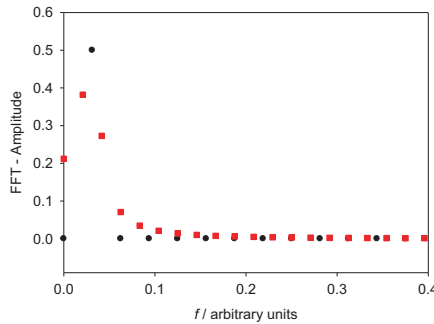
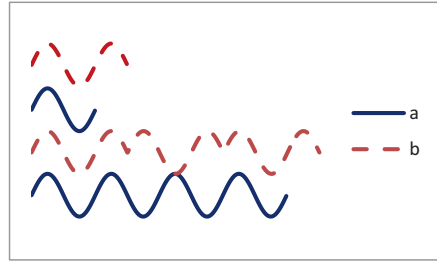


Fig. 2.14 Fourier transform (amplitude) of function in Fig. 2.13a, bottom, containing whole number (one) of periods (●) and Fig. 2.13b, bottom, containing three blocks of 1.5 periods each (■) during data acquisition time

2.7.1 Leakage

There are some limitations of the FT technique connected with so-called leakage. The FFT works well if there is a whole number of periods of the function $f(t)$ in the total acquisition time, T . As was mentioned at the beginning, the FT is an integral from $-\infty$ to ∞ , and the transform assumes that what is observed in the total data acquisition time is repeated before and after our time window from 0 to T . This is illustrated in Fig. 2.13; curve a, containing a whole number of periods (here one), produces a smooth curve (without discontinuities) when it is repeated before and after the time window. However, when the number of periods is not a whole or integer number, curve b (in this example 1.5 periods), repetition of this curve produces discontinuities, as at the end of the period the curve is decreasing and at the beginning of a new block it is increasing. The FT of curve a, Fig. 2.14, produces one point in the frequency domain corresponding to the frequency of the wave. However, in the case of curve b, in the list of frequencies calculated using Eq. (2.77), there is no frequency corresponding to the natural frequency of that sine function (there are others around this number; see Fig. 2.14), and a dispersion of frequencies appears. This problem is called leakage and always appears when there are no whole numbers of periods in the data acquisition time T , that is, the

Fig. 2.15 Plot of a complex function composed of the sum of seven simple periodic functions

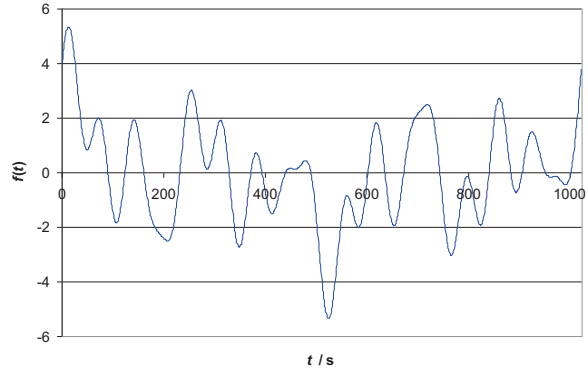
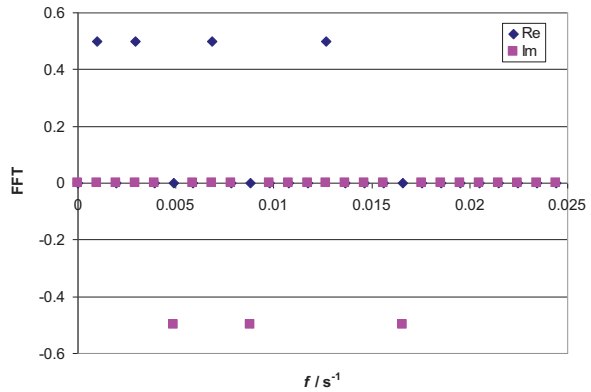


Fig. 2.16 Fourier transform of function displayed in Fig. 2.15



ratio of T/T_a , where T_a is the period of the studied function, is not a whole number. An example of leakage is illustrated in Exercise 2.5.

The main conclusion of this part is that to avoid leakage, one always should keep a whole number of periods in the total acquisition time. The problem of leakage may be minimized (but not completely eliminated) when the total time and number of periods of the function increase, which means that more frequencies are added to the list and their separation becomes smaller (Exercise 2.5). Some authors have proposed that using a digital filter that decreases the importance of the initial and final points decreases the effect of leakage.

Therefore, when using a sum of frequencies in impedance (Chap. 3.7.3) one must also ensure that the number of periods of each function during the data acquisition time is a whole number.

The advantage of the FFT is that this analysis allows one to determine the response of each periodic function when their sum is applied. It should be stressed, however, that the frequency information is for f between $f_{\min} = 1/T$ and the Nyquist frequency $f_{\max} = 1/2\Delta t$. For example, the FT of the curve displayed in Fig. 2.15 shows that it is composed of four cosine (only real values in the Fourier domain) and three sine functions (only imaginary values in the Fourier domain) (Fig. 2.16).

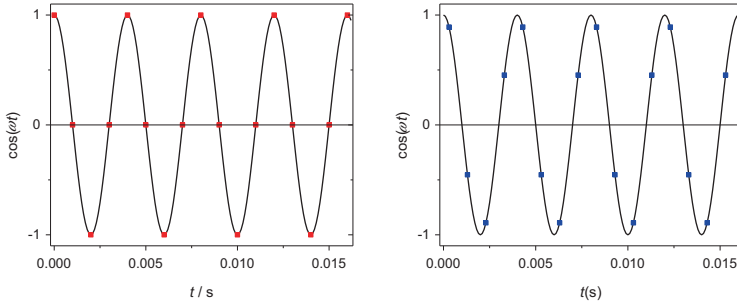


Fig. 2.17 Examples of sampling wave of frequency 250 Hz at rate of 1,000 Hz. The wave is sampled four times per period, which can be at different places (phases) of the wave

Although the shape of the function $f(t)$ seems quite complex, the FT analysis reveals all the underlying functions and their frequencies. Details are presented in Exercise 2.6.

2.7.2 Aliasing

Another problem with the FFT is related to the Nyquist sampling theorem. As was shown earlier, the highest frequency for which information can be found from the FFT is given by Eq. (2.75); this is the so-called Nyquist frequency, ν_{\max} . If the experimental frequency is larger than this value, it cannot be found with the FFT. Instead, new frequencies lower than ν_{\max} appear. This can be illustrated in the following example. Let us suppose that the sampling frequency is 1 kHz, that is, samples are measured every 1 ms. This means that the Nyquist frequency is $f_{\max} = 1/(2 \times 0.001 \text{ s}) = 500 \text{ Hz}$. When a cosine wave of frequency 250 Hz is applied, the FT is able to find it because the periodic wave is sampled four times per period. This is illustrated in Fig. 2.17. When the wave frequency is 500 Hz (Nyquist frequency), the wave is sampled two times per period. This is a minimum sampling rate necessary to determine the frequency (Fig. 2.18). While sampling with the Nyquist frequency one can find, by accident, that all the sampled values are zero or very small. In the second case, the measurements might not be precise enough (noisy), although theoretically the FFT should give correct values (Fig. 2.18). In such a case, the waveform should be resampled. In practice, sampling with the Nyquist frequency might be less reliable and should be repeated.

Finally, when the wave frequency is 625 Hz, which is larger than the Nyquist frequency (500 Hz), the FT cannot find it. Instead, it finds a different frequency, lower than the Nyquist frequency, in this case 375 Hz. This frequency does not exist in the system but is reconstructed by the FT. It is illustrated in Fig. 2.19. This example indicates that when performing FFT one should ensure that the sampling rate is sufficiently large, larger than the Nyquist frequency. It could be verified by doubling the sampling frequency; no changes in the frequencies found should appear. Sometimes, it is advantageous to use a low-pass filter to cut off all

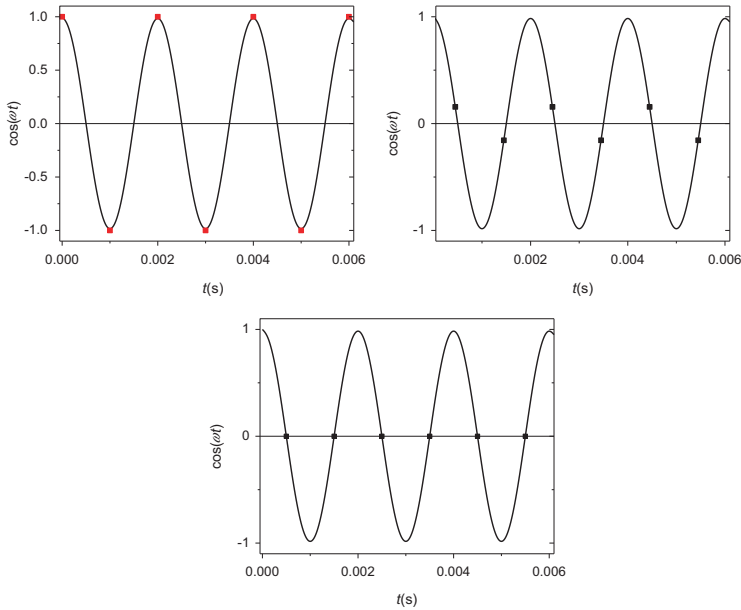


Fig. 2.18 Sampling of wave of frequency 500 Hz with Nyquist frequency of 1,000 Hz. It may appear in some cases that the measured signal is either zero or very small; in such cases, the wave should be resampled

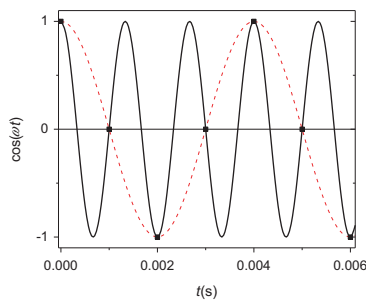


Fig. 2.19 Example of wave of 750 Hz (*continuous line*) being sampled with frequency of 1,000 Hz. The Nyquist frequency is 500 Hz. The Fourier transform finds a “phantom” frequency of 250 Hz (*dashed line*) that does not exist in the system

frequencies larger than the Nyquist frequency. A problem with leakage is presented in Exercise 2.5.

In summary, the sampled waveform should contain a whole number of periods to avoid leakage and the sampling should be with at least the Nyquist frequency or faster to avoid aliasing. In EIS practice, a waveform containing a predetermined number of frequencies and whole number of periods of waveforms is used and sampling is synchronized (Chap. 3.7).

2.8 Impedance of Electrical Circuits

Knowledge of the Laplace and Fourier transforms allows us to determine the system impedance and to solve the equations $i(t) = f[E(t)]$ for an arbitrary perturbation.

2.8.1 Application of Laplace Transform to Determination of Impedances

Let us assume that an arbitrary potential function $E(t)$ is applied to a simple connection of the resistance R and capacitance C in series. Such a circuit is described by Eq. (2.18):

$$E(t) = i(t)R + \frac{1}{C} \int_0^t i(t) dt. \quad (2.18)$$

To solve the problem, which is an integral equation, we could use the Laplace transform:

$$\bar{E}(s) = R\bar{i}(s) + \frac{1}{Cs} \bar{i}(s), \quad (2.83)$$

where an integral equation in the time domain was transformed into an algebraic equation in the frequency domain s . From this equation one can easily find $\bar{i}(s)$:

$$\bar{i}(s) = \frac{1}{R + \frac{1}{sC}} \bar{E}(s). \quad (2.84)$$

Similarly, one can solve differential Eq. (2.20) describing the connection of the resistance, R , and inductance, L , in series:

$$E(t) = i(t)R + L \frac{di(t)}{dt}. \quad (2.20)$$

Applying the Laplace transform to this equation and keeping in mind Eq. (2.27) for the transform of the first derivative the following form is obtained:

$$\bar{E}(s) = \bar{i}(s)R + \bar{i}(s)sL, \quad (2.85)$$

Table 2.1 Operational impedance of linear electrical elements

Element	Impedance
R	R
C	$\frac{1}{sC}$
L	sL

from which a current in the Laplace domain may be easily obtained:

$$i(s) = \frac{E(s)}{R + sL}. \quad (2.86)$$

To obtain a current as a function of time, the form of the potential program must be known. In the case of a simple resistance in the circuit, the solution is obvious:

$$i(t) = \frac{E(t)}{R} \text{ and } \bar{i}(s) = \frac{\bar{E}(s)}{R}. \quad (2.87)$$

2.8.2 Definition of Operational Impedance

Analysis of Eqs. (2.84), (2.86), and (2.87) reveals that the relation between current and potential in the presence of resistance, capacitance, and inductance may be represented in a general form:

$$\hat{Z}(s) = \frac{L[E(t)]}{L[i(t)]} = \frac{\bar{E}(s)}{\bar{i}(s)}, \quad (2.88)$$

where $\hat{Z}(s)$ is called the operational impedance and has units of the resistance, Ω , and for each electrical element one can write the corresponding impedance (Table 2.1) and calculate the total impedance using Ohm's and Kirchhoff's laws.

The *operational impedance* is the ratio of the Laplace transform of the potential to the Laplace transform of the current (Eq. 2.88). It is usually used for an arbitrary perturbation signal. For the periodic signal it is equivalent to the definition using Fourier transformation. What follows are examples of the application of the Laplace technique to the determination of the current–potential relations and the impedances.

Example 2.10 Determine the current after application of the potential step $E_0\eta(t)$ [see Fig. 2.5 for a definition of the Heaviside function $\eta(t)$ and its transform] to the connection of the resistance, R , and capacitance, C , in series.

The system is described by Eq. (2.84). The transform of the potential step $E_0\eta(t)$ is

$$L[E_0\eta(t)] = E_0L[\eta(t)] = \frac{E_0}{s}, \quad (2.89)$$

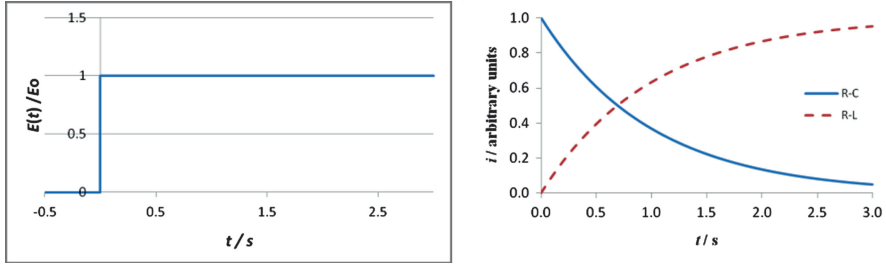


Fig. 2.20 Current–time transients due to application of step function to connection R - C and R - L in series; the time constant in both cases is 1 s

where Eq. (2.25) was used for the transform of the $\eta(t)$ function. The operational impedance corresponds to the connection of the impedances of the R and C elements in series. Using the impedances from Table 2.1 the total impedance is

$$\hat{Z}(s) = R + \frac{1}{Cs}, \quad (2.90)$$

and from Eq. (2.88)

$$\bar{i}(s) = \frac{\bar{E}(s)}{\hat{Z}(s)} = \frac{E_0}{s} \frac{1}{R + \frac{1}{Cs}} = \frac{E_0}{R} \frac{1}{s + 1/RC}. \quad (2.91)$$

An inverse Laplace transform using Eq. (2.26) gives the solution in the time domain:

$$i(t) = \frac{E_0}{R} \exp\left(-\frac{t}{RC}\right) = \frac{E_0}{R} \exp\left(-\frac{t}{\tau}\right). \quad (2.92)$$

The current starts at $i = E_0/R$ at $t = 0$ then decreases exponentially with time to zero as the capacitor is charged from 0 to E_0 ; the constant current cannot flow through the capacitance. The potential step and the response of the system are displayed in Fig. 2.20. The rate at which the current decreases with time depends on RC , which is called the system time constant $\tau = RC$; if the time constant is smaller (smaller resistance or capacitance), then the current decay is faster.

Let us consider an application of the same potential step function to the R - L connection in series.

Example 2.11 Determine the current after application of the potential step $E_0 \eta(t)$ to the connection of the resistance, R , and inductance, L , in series.

The proposed system is described by the differential Eq. (2.20). The impedance of the system is

$$\hat{Z}(s) = R + Ls. \quad (2.93)$$

Substitution into the expression for the current gives

$$\bar{i}(s) = \frac{\bar{E}(s)}{\bar{Z}(s)} = \frac{E_0}{s(R + sL)} = \frac{E_0}{L} \frac{1}{s(s + R/L)} = \frac{E_0}{R} \left(\frac{1}{s} - \frac{1}{s + R/L} \right). \quad (2.94)$$

The inverse transform gives

$$i(t) = \frac{E_0}{R} \left[1 - \exp\left(-\frac{Rt}{L}\right) \right]. \quad (2.95)$$

A plot of current versus time is given in Fig. 2.20. At time $t = 0$ the exponential term is equal to 1 and the current is zero. This corresponds to the properties of a coil that resists fast changes in a current. Then the current increases to the limiting value E_0/R as the coil does not oppose the passage of the constant current [$L di(t)/dt = 0$ in Eq. (2.20)]. The characteristic time constant of the system is $\tau = L/R$.

Let us consider a more difficult example.

Example 2.12 Determine the current after application of the potential step $E_0\eta(t)$ to the connection of the resistance, R , capacitance, C , and inductance, L , in series.

The operator impedance of the circuit is simply a connection of the three elements in series:

$$\hat{Z}(s) = R + \frac{1}{Cs} + Ls. \quad (2.96)$$

Substitution into the equation for the current gives

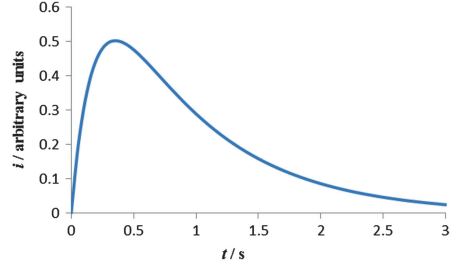
$$\bar{i}(s) = \frac{E_0}{s(R + \frac{1}{Cs} + Ls)} = \frac{E_0}{L} \frac{1}{(s^2 + \frac{R}{L}s + \frac{1}{RL})}. \quad (2.97)$$

To be able to carry out the inverse transform, the second-order expression for s must be separated into simple fractions:

$$s^2 + \frac{R}{L}s + \frac{1}{RL} = (s - s_1)(s - s_2), \quad (2.98)$$

$$\begin{aligned} s_1 &= \frac{R}{2L} \left(-1 - \sqrt{1 - \frac{4L}{R^2C}} \right) = \frac{1}{2\tau_1} \left(-1 - \sqrt{1 - \frac{4\tau_1}{\tau_2}} \right), \\ s_2 &= \frac{R}{2L} \left(-1 + \sqrt{1 - \frac{4L}{R^2C}} \right) = \frac{1}{2\tau_1} \left(-1 + \sqrt{1 - \frac{4\tau_1}{\tau_2}} \right), \end{aligned} \quad (2.99)$$

Fig. 2.21 Current–time transients due to application of step function to connection R - C - L in series; $\tau_1 = 0.15$ s, $\tau_2 = 3$ s



assuming that $\Delta > 0$, that is, $1 - 4\tau_1 / \tau_2 > 0$

$$\frac{1}{s^2 + \frac{R}{L}s + \frac{1}{RL}} = \frac{1}{(s - s_1)(s - s_2)} = \frac{A}{s - s_1} + \frac{B}{s - s_2} = \frac{s(A + B) - As_2 - Bs_1}{(s - s_1)(s - s_2)},$$

$$A = -B = -\frac{2L}{R\sqrt{1 - \frac{4L}{R^2C}}} = -\frac{2}{\tau_1\sqrt{1 - \frac{4\tau_1}{\tau_2}}}.$$
(2.100)

After substitution into the expression for the Laplace transform of the current,

$$\bar{i}(s) = \frac{E_0}{R\sqrt{1 - \frac{4\tau_1}{\tau_2}}} \left(\frac{1}{s - s_2} - \frac{1}{s - s_1} \right),$$
(2.101)

the inverse transform is

$$i(t) = \frac{E_0}{R\sqrt{1 - \frac{4L}{R^2C}}} (e^{s_2 t} - e^{s_1 t})$$

$$= \frac{E_0}{R\sqrt{1 - \frac{4\tau_1}{\tau_2}}} \left[e^{-\frac{1}{2\tau_1} \left(1 - \sqrt{1 - \frac{4\tau_1}{\tau_2}} \right) t} - e^{-\frac{1}{2\tau_1} \left(1 + \sqrt{1 - \frac{4\tau_1}{\tau_2}} \right) t} \right].$$
(2.102)

The current relaxation is controlled by two time constants, $\tau_1 = L/R$ and $\tau_2 = RC$, which correspond to the relaxation of the system corresponding to R - L and R - C connections. A plot of the current versus time is presented in Fig. 2.21. At $t = 0$ the current is zero, and then it increases as in the case of the connection R - L . Then it starts to decrease to zero as with the connection R - C .

The method of the Laplace transform may also be used to determine the $i(t)$ relation in the case where the ac signal is applied. This is illustrated in Example 2.13.

Example 2.13 Determine the current after application of the periodic function $E(t) = E_0 \sin(\omega t)$ to the connection of the resistance, R , and capacitance, C , in series.

As in Example 2.10, the relation between current and potential in the Laplace domain is described as

$$\bar{i}(s) = \frac{\bar{E}(s)}{\bar{Z}(s)} = \frac{E(s)}{R + \frac{1}{Cs}} \quad (2.103)$$

The Laplace transform of the sine function is found in Appendix 1:

$$L[\sin(\omega t)] = \frac{\omega}{s^2 + \omega^2}. \quad (2.104)$$

Substitution into Eq. (2.103) gives, after rearrangements,

$$\begin{aligned} \bar{i}(s) &= E_0 \frac{\omega}{s^2 + \omega^2} \frac{1}{R + \frac{1}{Cs}} = E_0 \frac{\omega}{(s^2 + \omega^2)} \frac{s}{R \left(s + \frac{1}{RC} \right)} = \\ &= \frac{E_0 \omega}{R} \frac{s}{(s^2 + \omega^2) \left(s + \frac{1}{RC} \right)}. \end{aligned} \quad (2.105)$$

The last term in Eq. (2.105) must be separated into simple fractions:

$$\begin{aligned} \bar{i}(s) &= \frac{As + B}{s^2 + \omega^2} + \frac{D}{s + \frac{1}{RC}} = \\ &= \frac{s^2(A + D) + s \left(B + \frac{A}{RC} \right) + \left(\frac{B}{RC} + D\omega^2 \right)}{(s^2 + \omega^2) \left(s + \frac{1}{RC} \right)}. \end{aligned} \quad (2.106)$$

Comparison of Eqs. (2.106) and (2.105) allows for the determination of the parameters A , B , and D :

$$\begin{aligned}
 A + D = 0 \quad B + \frac{A}{RC} = 1 \quad \frac{B}{RC} + D\omega^2 = 0, \\
 A = -D = \frac{RC}{1 + (\omega RC)^2} \quad B = \frac{(\omega RC)^2}{1 + (\omega RC)^2}.
 \end{aligned} \tag{2.107}$$

Substitution of these parameters into Eq. (2.106) leads to

$$\bar{i}(s) = \frac{E_0\omega}{R} \left[\frac{\frac{RC}{1 + (\omega RC)^2} \frac{s}{(s^2 + \omega^2)} + \frac{(\omega RC)^2}{1 + (\omega RC)^2} \frac{1}{(s^2 + \omega^2)}}{\frac{RC}{1 + (\omega RC)^2} \frac{1}{s + \frac{1}{RC}}} \right] = \tag{2.108}$$

$$\begin{aligned}
 &= \frac{E_0\omega}{R(\omega RC)^2 \left(1 + \frac{1}{(\omega RC)^2}\right)} \left[RC \frac{s}{(s^2 + \omega^2)} + (\omega RC)^2 \frac{1}{(s^2 + \omega^2)} \right] = \\
 &= \frac{E_0}{R} \frac{1}{\left[1 + \frac{1}{(\omega RC)^2}\right]} \left[\frac{1}{\omega RC} \frac{s}{(s^2 + \omega^2)} + \frac{\omega}{(s^2 + \omega^2)} \right],
 \end{aligned} \tag{2.109}$$

where the third term displaying a transient exponential relaxation was neglected because it disappears in the steady state. This equation can be transformed into the time domain keeping in mind that

$$L[\cos(\omega t)] = \frac{s}{s^2 + \omega^2}, \tag{2.110}$$

and the following expression is obtained:

$$i(t) = \frac{E_0}{R} \frac{1}{1 + \frac{1}{(\omega RC)^2}} \left[\frac{1}{\omega RC} \cos(\omega t) + \sin(\omega t) \right]. \tag{2.111}$$

Note that any real number can be represented as $\tan(x)$; in our case we can use

$$\tan \varphi = \frac{1}{\omega RC}. \tag{2.112}$$

Substitution of Eq. (2.112) into (2.111) gives

$$\begin{aligned} i(t) &= \frac{E_0}{R} \frac{1}{1 + \frac{1}{(\omega RC)^2}} [\tan(\varphi) \cos(\omega t) + \sin(\omega t)] \\ &= \frac{E_0}{R} \frac{1}{1 + \frac{1}{(\omega RC)^2}} [\cos(\omega t) \sin(\varphi) + \sin(\omega t) \cos(\varphi)] \end{aligned} \quad (2.113)$$

Using the trigonometric identities

$$\begin{aligned} \cos(\varphi) &= \sqrt{\frac{1}{1 + \tan^2(\varphi)}} = \sqrt{\frac{1}{1 + \frac{1}{(\omega RC)^2}}} \\ \cos(\omega t) \sin(\varphi) + \sin(\omega t) \cos(\varphi) &= \sin(\omega t + \varphi) \end{aligned} \quad (2.114)$$

one obtains the final form:

$$i(t) = \frac{E_0}{\sqrt{R^2 + \frac{1}{(\omega C)^2}}} \sin(\omega t + \varphi) = \frac{E_0}{|Z|} \sin(\omega t + \varphi). \quad (2.115)$$

Comparison of the applied voltage and obtained current reveals that the current oscillates with the same frequency as the potential but is shifted in phase by the angle φ depending on the frequency, according to Eq. (2.112). The term $|Z|$ is the modulus of the impedance:

$$|Z| = \sqrt{R^2 + \frac{1}{(\omega C)^2}} \quad (2.116)$$

is a sum of two perpendicular vectors, R and $1/\omega C$. We will find later that the same answer will be obtained using FT.

An exercise where the sine function is replaced by the cosine is presented in Example 2.14.

Example 2.14 Determine the current following application of the periodic function $E(t) = E_0 \cos(\omega t)$ to the connection of the resistance, R , and capacitance, C , in series.

This example is analogous to Example 2.13, with the exception of the periodic function, which is now the cosine. Using the Laplace transform of the cosine function the transformed current is obtained and must be separated into simple fractions:

$$\begin{aligned}
\bar{i}(s) &= E_0 \frac{s}{(s^2 + \omega^2) \left(R + \frac{1}{sC} \right)} = \frac{E_0}{R} \frac{s^2}{(s^2 + \omega^2) \left(s + \frac{1}{RC} \right)} \\
&= \frac{E_0}{R \left(1 + (\omega RC)^2 \right)} \left[(\omega RC)^2 \frac{s}{(s^2 + \omega^2)} - \omega RC \frac{\omega}{(s^2 + \omega^2)} + \frac{1}{\left(s + \frac{1}{RC} \right)} \right] \\
&= \frac{E_0}{R} \frac{(\omega RC)^2}{1 + (\omega RC)^2} \left[\frac{s}{(s^2 + \omega^2)} - \frac{1}{\omega RC} \frac{\omega}{(s^2 + \omega^2)} \right] \\
&= \frac{E_0}{R} \frac{1}{1 + \frac{1}{(\omega RC)^2}} \left[\frac{s}{(s^2 + \omega^2)} - \frac{1}{\omega RC} \frac{\omega}{(s^2 + \omega^2)} \right].
\end{aligned} \tag{2.117}$$

As before, the transient term was neglected. The inverse Laplace transform may be rearranged as before:

$$\begin{aligned}
i(t) &= \frac{E_0}{R} \frac{1}{1 + \frac{1}{(\omega RC)^2}} [\cos(\omega t) - \tan(\varphi) \sin(\omega t)] \\
&= \frac{E_0}{R} \frac{1}{1 + \frac{1}{(\omega RC)^2}} \left[\frac{\cos(\omega t) \cos(\omega t) - \sin(\varphi) \sin(\omega t)}{\cos(\omega)} \right],
\end{aligned} \tag{2.118}$$

and using the trigonometric identity, Eq. (2.114), and

$$\cos(\omega t) \cos(\omega t) - \sin(\varphi) \sin(\omega t) = \cos(\omega t + \varphi) \tag{2.119}$$

the final expression is obtained:

$$\begin{aligned}
i(t) &= \frac{E_0}{R} \cos^2(\varphi) \frac{\cos(\omega t + \varphi)}{\cos(\varphi)} = \frac{E_0}{R} \frac{1}{\sqrt{1 + \frac{1}{(\omega RC)^2}}} \cos(\omega t + \varphi) \\
i(t) &= \frac{E_0}{\sqrt{R^2 + \frac{1}{(\omega C)^2}}} \cos(\omega t + \varphi) = \frac{E_0}{|Z|} \cos(\omega t + \varphi).
\end{aligned} \tag{2.120}$$

As in Example 2.13, the current is shifted in phase by angle φ and the modulus of the impedance is the same. Such an exercise is mathematically simple but time consuming. It should be added that the program Maple, which allows for symbolic calculations, allows for automatic separation of expressions into simple fractions using the function `convert(f, parfrac, s)`, in which function f of the parameter s is transformed into simple fractions, for example:

$$\begin{aligned}
 &> f := s^2/(s^2 + a^2)/(s + b); \\
 &f := \frac{s^2}{(s^2 + a^2)(s + b)} \\
 &> yy := \text{convert}(f, \text{parfrac}, s); \\
 &yy := -\frac{a^2(b - s)}{(b^2 + a^2)(s^2 + a^2)} + \frac{b^2}{(b^2 + a^2)(s + b)}.
 \end{aligned} \tag{2.121}$$

2.8.3 Application of Fourier Transform to Determination of Impedances

In the Laplace transform above, we assumed a real transform with $s = \sigma$. As in the impedance technique, we usually apply a periodic cosine perturbation, and in such a case it is simpler to use the FT with $s = j\omega$. In general, a periodic potential perturbation, ΔE , applied to a circuit may be written as a complex analog of the simple periodic perturbation, see Eq. (2.56):

$$\Delta E = E_0 \exp(j\omega t) \tag{2.122}$$

or, in a more general form, assuming that there is an initial phase shift at $t = 0$:

$$\Delta E = E_0 \exp[j(\omega t + \phi_1)] = E_0 \exp(j\phi_1) \exp(j\omega t) = \tilde{E} \exp(j\omega t). \tag{2.123}$$

Equation (2.123) represents a vector of length E_0 rotating with a constant frequency ω and with the initial phase shift ϕ_1 , and projections of this vector on the x - and y -axes are called real and imaginary parts, respectively. The value of ΔE oscillates between $\pm E_0$. This is represented schematically in Fig. 2.22. Vector \tilde{E} can be written as a product of the amplitude and exponential:

$$\tilde{E} = E_0 \exp(j\phi_1), \tag{2.124}$$

which represents a vector of lengths E_0 shifted by the angle ϕ_1 and the term $\exp(j\omega t)$, which is responsible for the rotation of the vector \tilde{E} at a constant rate ω . The parameter \tilde{E} is called a *phasor* and represents an immobile vector shifted by the angle ϕ_1 . Similarly, for the vector corresponding to the current we can write

Fig. 2.22 Representation of rotating vectors ΔE , Eq. (2.124), and ΔI on complex plane. They both rotate with a constant angular frequency ω , but there is a constant phase difference between them, $\phi_1 - \phi_2$

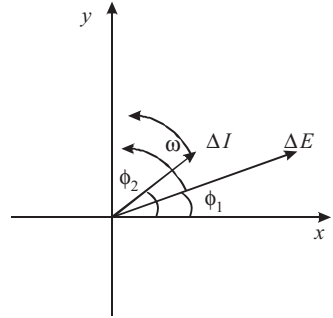
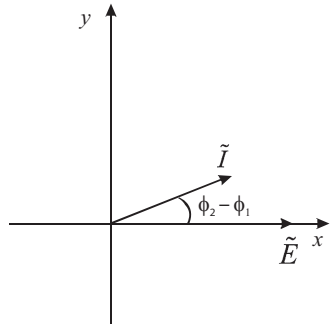


Fig. 2.23 Representation of phasors of \tilde{E} and \tilde{I} on complex plane plot. These vectors are immobile and there is a constant phase difference, $\phi_2 - \phi_1 = \phi$, between them. The initial phase angle for the potential \tilde{E} was chosen as zero



$$\Delta I = I_0 \exp[j(\omega t + \phi_2)] = I_0 \exp(j\phi_2) \exp(j\omega t) = \tilde{I} \exp(j\omega t), \quad (2.125)$$

where \tilde{I} is the phasor of the current. The rotating vectors of $E(t)$ and $I(t)$ are shown in Fig. 2.22 and the corresponding phasors in Fig. 2.23. The initial phase shift for \tilde{E} is usually assumed to be zero because it is the signal of reference created by the signal generator and all other signals are referred to it. The *ac impedance of the system is defined as the ratio of phasors \tilde{E} and \tilde{I}* :

$$\hat{Z}(j\omega) = \frac{\Delta E}{\Delta I} = \frac{\tilde{E}}{\tilde{I}}. \quad (2.126)$$

In other words, the impedance is the ratio of the FTs of the potential and current, which is equal to the ratio of the corresponding phasors:

$$\hat{Z}(j\omega) = \frac{F[E(t)]}{F[I(t)]} = \frac{\tilde{E}}{\tilde{I}}. \quad (2.127)$$

To better understand how the impedance is determined, let us suppose that the applied ac voltage and measured current are described by the following equations: $E(t) = E_0 \cos(\omega t)$ and $I(t) = I_0 \cos(\omega t + \pi/3)$, where $E_0 = 0.01$ V, $I_0 = 0.002$ A, $\omega = 2\pi f = 2\pi/T_a$, $T_a = 0.32$ s. The calculations are carried out in Exercise 2.7.

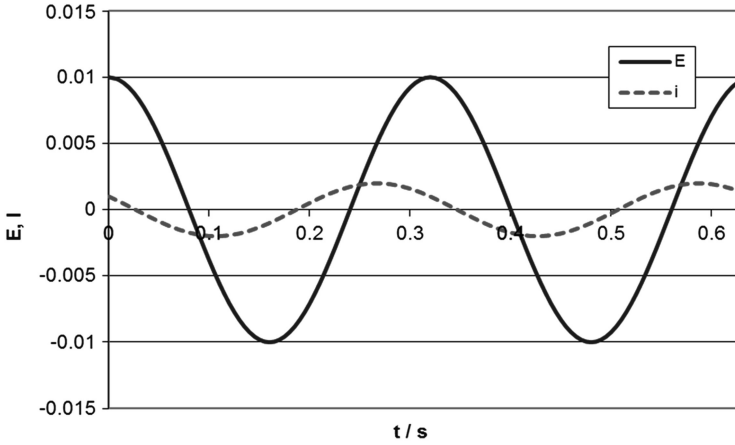


Fig. 2.24 Potential and current functions for calculation of impedance using following data: $E(t) = E_0 \cos(\omega t)$ and $I(t) = I_0 \cos(\omega t + \pi / 3)$, where $E_0 = 0.01$ V, $I_0 = 0.002$ A, $\omega = 2\pi f = 2\pi/T_a$, $T_a = 0.32$ s (Exercise 2.7)

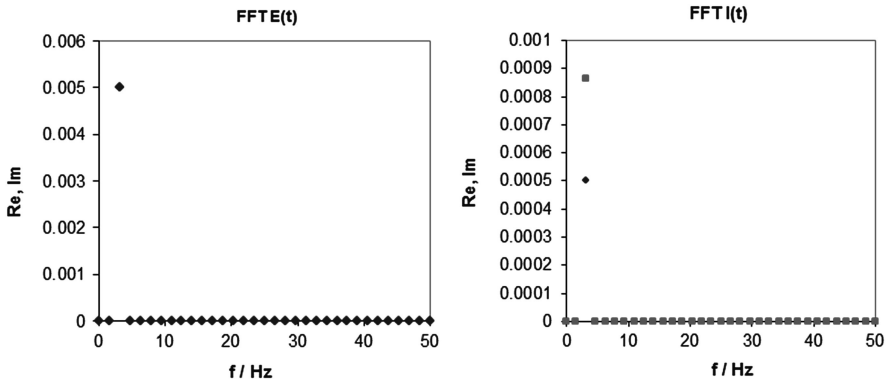


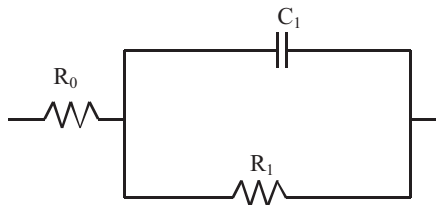
Fig. 2.25 Fast Fourier transform of potential and current functions in: real part – diamonds, imaginary – squares of functions in Fig. 2.24

The potential and current functions are displayed in Fig. 2.24 and their FTs in Fig. 2.25. Using complex calculations in Excel the ratio of the FT of the potential and the current gives the total impedance:

$$\begin{aligned}\tilde{E} &= 0.005 \text{ V}, & \tilde{I} &= 3.20 \times 10^{-2} + 5.54256 \times 10^{-2}j \text{ A}, \\ \hat{Z} = \tilde{E}/\tilde{I} &= 2.5 - 4.33013j \text{ } \Omega, \\ \phi &= -60^\circ, |Z| = 5 \text{ } \Omega \text{ at } f = 3.125 \text{ Hz.}\end{aligned}$$

Modern impedance measuring equipment is able to extract the impedance from the experimentally measured potential and current.

Fig. 2.26 Circuit for Example 2.15



2.8.4 Definition of Impedance

From the preceding section we can write a general definition of impedance. The general operational definition of impedance is described by Eq. (2.88):

$$\hat{Z}(s) = \frac{L[E(t)]}{L[i(t)]} = \frac{\bar{E}(s)}{\bar{i}(s)}, \quad (2.88)$$

where the symbol L denotes the Laplace transform, Eq. (2.21). As was mentioned earlier, the parameter s , called the frequency, may be complex: $s = \sigma + j\omega$. In the classical Laplace transform the parameter s is real: $s = \sigma$. To obtain the impedance of electrical circuits, the impedance of the elements R , C , and L are defined in Table 2.1 and the impedance of the total circuit is written using Ohm's and Kirchhoff's laws. The following examples illustrate this method.

Example 2.15 Write the impedance of the circuit in Fig. 2.26.

Applying the laws for the connections of impedances in series and in parallel, and substituting the impedance of the elements from Table 2.1, the total impedance of this circuit may be written as

$$\hat{Z}(s) = R_0 + \frac{1}{sC_1 + \frac{1}{R_1}}. \quad (2.128)$$

Example 2.16 Write the impedance of the circuit in Fig. 2.27.

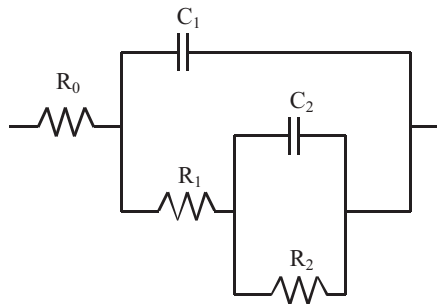
The impedance of this circuit may be written as

$$\hat{Z}(s) = R_0 + \frac{1}{sC_1 + \frac{1}{R_1 + \frac{1}{sC_2 + \frac{1}{R_2}}}}. \quad (2.129)$$

From the preceding examples one can see that writing the impedance of the circuits is straightforward.

The foregoing examples are valid for any potential perturbation. In the particular case of ac impedance, that is, when the applied potential perturbation is sinusoidal, one uses the FT (Eq. 2.127):

Fig. 2.27 Circuit for Example 2.16



$$\hat{Z}(j\omega) = \frac{F[E(t)]}{F[I(t)]} = \frac{\tilde{E}(j\omega)}{\tilde{I}(j\omega)}, \quad (2.127)$$

where the parameter s is imaginary: $s = j\omega$. It should be stressed that all the definitions presented above are equivalent for periodic signal perturbation while the operator impedance applies better to any perturbation. Besides *impedance* other terms are also used; the inverse of impedance is *admittance*:

$$\hat{Y}(s) = \frac{1}{\hat{Z}(s)}. \quad (2.130)$$

Both impedance and admittance are called *immittances*. Between other related functions, *complex dielectric constant* should also be mentioned [78]. It is used in the analysis of dielectric relaxation and is obtained from the measured admittance (impedance) of a cell with a given dielectric (liquid or solid):

$$\hat{\epsilon} = \frac{\hat{Y}}{j\omega C_c}, \quad (2.131)$$

where \hat{Y} is the admittance of the cell $\hat{Y} = j\omega\hat{C}$, and

$$\hat{C} = \frac{\hat{\epsilon} \epsilon_0 A_c}{d} \quad (2.132)$$

is the capacitance of the studied material, $\hat{\epsilon}$ is the complex dielectric constant (function of the frequency), $\epsilon_0 = 9.8542 \times 10^{-14}$ F/cm is the dielectric permittivity of a vacuum, d is the distance between electrodes, A_c is their surface area, and C_c is the capacity of the empty cell (containing air or in vacuum) $C_c = \epsilon_0 A_c / d$. Another function used in dielectric research is the modulus, $\hat{M} = 1/\hat{\epsilon}$.

To obtain the ac impedance of circuits represented by Eqs. (2.128) and (2.129) substitution of s must be done, and the appropriate equations become

$$\hat{Z}(j\omega) = R_0 + \frac{1}{j\omega C_1 + \frac{1}{R_1}}, \quad (2.133)$$

Table 2.2 Operational and ac impedance of linear electrical elements

Element	Operational impedance	Ac impedance
R	R	R
C	$\frac{1}{sC}$	$\frac{1}{j\omega C}$
L	sL	$j\omega L$

$$\hat{Z}(j\omega) = R_0 + \frac{1}{j\omega C_1 + \frac{1}{R_1 + \frac{1}{j\omega C_2 + \frac{1}{R_2}}}}. \quad (2.134)$$

Therefore, in general, the impedance of the electrical elements used is displayed in Table 2.2.

Equations (2.133) and (2.134) can be further rearranged using the complex calculus. For example, Eq. (2.133) may be rearranged into

$$\begin{aligned} \hat{Z}(j\omega) &= R_0 + \frac{R_1}{1 + j\omega R_1 C_1} = R_0 + \frac{R_1(1 - j\omega R_1 C_1)}{1 + (\omega R_1 C_1)^2} = \\ &= R_0 + \frac{R_1}{1 + (\omega R_1 C_1)^2} - j \frac{\omega R_1 C_1}{1 + (\omega R_1 C_1)^2} \end{aligned} \quad (2.135)$$

and the impedance consists of two parts, one real and positive and one imaginary and negative:

$$\begin{aligned} \text{Re}[\hat{Z}(j\omega)] &= R_0 + \frac{R_1}{1 + (\omega R_1 C_1)^2}, \\ \text{Im}[\hat{Z}(j\omega)] &= - \frac{\omega R_1 C_1}{1 + (\omega R_1 C_1)^2}, \end{aligned} \quad (2.136)$$

and both parts are frequency dependent. Similarly, Eq. (2.134) may be rearranged into

$$\hat{Z}(j\omega) = R_0 + \frac{R_1 + R_2 + j\omega R_1 R_2 C_2}{1 - \omega^2 R_1 R_2 C_1 C_2 + j\omega[R_2 C_2 + C_1(R_1 + R_2)]}, \quad (2.137)$$

and multiplying by the conjugated form of the denominator yields

$$\begin{aligned} \text{Re}[\hat{Z}(j\omega)] &= R_0 \frac{(R_1 + R_2)(1 - \omega^2 R_1 R_2 C_1 C_2) + \omega^2 R_1 R_2 C_2 [R_2 C_2 + C_1(R_1 + R_2)]}{(1 - \omega^2 R_1 R_2 C_1 C_2)^2 + \omega^2 [R_2 C_2 + C_1(R_1 + R_2)]^2}, \\ \text{Im}[\hat{Z}(j\omega)] &= \frac{\omega R_1 R_2 C_2 (1 - \omega^2 R_1 R_2 C_1 C_2) - \omega(R_1 + R_2)[R_2 C_2 + C_1(R_1 + R_2)]}{(1 - \omega^2 R_1 R_2 C_1 C_2)^2 + \omega^2 [R_2 C_2 + C_1(R_1 + R_2)]^2}. \end{aligned} \quad (2.138)$$

The calculations are simple but time consuming and may be carried out easily using Maple (see below):

```
>Z:= 1/(I * om * C1 + 1/(R1 + 1/(I * om * C2 + 1/R2))) ;
```

$$Z := \frac{1}{I \, om \, C1 + \frac{1}{R1 + \frac{1}{I \, om \, C2 + \frac{1}{R2}}}}$$

```
> Z1:= simplify (Z) ;
```

$$Z1 := -\frac{I \, R1 \, om \, C2 \, R2 + R1 + R2}{om^2 \, C1 \, R1 \, C2 \, R2 - I \, om \, C1 \, R1 - I \, om \, C1 \, R2 - I \, om \, C2 \, R2 - 1}$$

```
> evalc (Re (Z1)) ;
```

$$-\frac{(R1 + R2)(om^2 \, C1 \, R1 \, C2 \, R2 - 1)}{(om^2 \, C1 \, R1 \, C2 \, R2 - 1)^2 + (-om \, C1 \, R1 - om \, C1 \, R2 - om \, C2 \, R2)^2} \\ -\frac{R1 \, om \, C2 \, R2(-om \, C1 \, R1 - om \, C1 \, R2 - om \, C2 \, R2)}{(om^2 \, C1 \, R1 \, C2 \, R2 - 1)^2 + (-om \, C1 \, R1 - om \, C1 \, R2 - om \, C2 \, R2)^2}$$

```
>evalc (Im (Z1)) ;
```

$$-\frac{R1 \, om \, C2 \, R2 (om^2 \, C1 \, R1 \, C2 \, R2 - 1)}{(om^2 \, C1 \, R1 \, C2 \, R2 - 1)^2 + (-om \, C1 \, R1 - om \, C1 \, R2 - om \, C2 \, R2)^2} \\ +\frac{(R1 + R2)(-om \, C1 \, R1 - om \, C1 \, R2 - om \, C2 \, R2)}{(om^2 \, C1 \, R1 \, C2 \, R2 - 1)^2 + (-om \, C1 \, R1 - om \, C1 \, R2 - om \, C2 \, R2)^2}.$$

The obtained results might be visualized using impedance plots.

2.9 Circuit Description Code

Boukamp [79] has proposed a simple notation for the connection of various electrical elements. It can be used instead of circuit schematics.

A simple connection of the elements in series, for example R , L , and C in series, is RLC . The use of parentheses means a change from a connection in series to a connection in parallel. That is, the connection of R and C in parallel (Fig. 2.33) is (RC) , and the connection of R , L , and C parameters in parallel is (RLC) . The connection of R_s with a parallel connection of R and C becomes (Fig. 2.34) $R_s(RC)$.

The next parentheses indicate a subsequent change from parallel to series connection. Inserting the capacitance in series with the resistance in a nested circuit (Fig. 2.35) is described as $R_s(C_{dl}(R_{ct}C_p))$, that is, R_s in series with the parallel connection of C_{dl} and a series connection of R_{ct} and C_p .

Fig. 2.28 Example of a more complex circuit from ref. [79] with permission of author

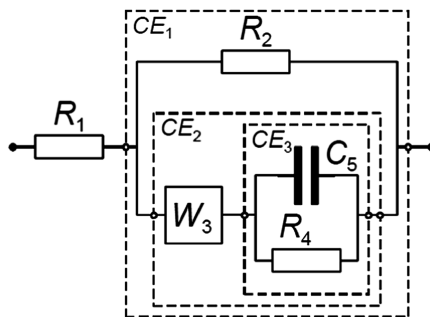
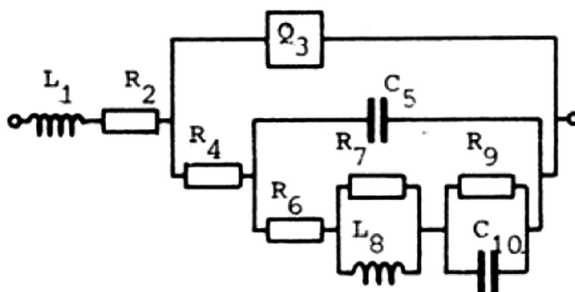


Fig. 2.29 Example of a more complex circuit from ref. [79] with permission of author



The two circuits in Fig. 2.37 in series and nested are described by $R_0(C_1R_1)(R_2C_2)$ and $R_0(C_1(R_1(C_2R_2)))$. Other distributed circuit elements can also be used: Q represents a constant phase element, CPE , W a semi-infinite Warburg element, W_s a finite length transmissive element, W_o a finite length reflecting element, and so forth. In the case of distributed elements, it is preferable to define them specifically.

Let us look at a more complex example (Fig. 2.28). It can be represented as $R_1(R_2(W_3(C_5R_4)))$. In this example, R_1 is in series with the circuit CE_1 , which is R_2 in parallel with CE_2 , which is W_3 in series with CE_3 , that is, a parallel connection of C_5 and R_4 .

Another, more complex, example is shown in Fig. 2.29. It is described using Boukamp's notation as follows: $L_1R_2(Q_3(R_4(C_5(R_6(R_7L_8)(R_9C_{10}))))))$.

In this way, almost any arbitrary circuit may be simply represented.

2.10 Impedance Plots

Impedance measurements produce numerical results, usually as real Z' and imaginary Z'' impedances or modulus $|Z|$ and phase angle φ as functions of frequency. Visual (graphical) inspection of the obtained results usually makes it possible to identify the electrical equivalent circuit containing R , C , and L elements.

However, this inspection is insufficient, and mathematical modeling involving fit to the circuit or equation should be carried out (Chap. 14). In the case of real electrochemical systems, the situation is more complex because the studied objects are not electrical circuits but systems involving interfaces, electrochemical reactions, transport of species, etc. Nevertheless, graphical inspection usually helps in deciding whether the experiments are proceeding correctly and in making a first assessment of data.

There are two fundamental types of graph:

1. Complex plane plots, also called Argand diagrams (or, less correctly, Nyquist plots). They are plots of imaginary versus real impedance. In these plots $-Z''$ is plotted versus Z' as the imaginary impedances of the electrochemical systems are usually negative. It should be added that, although the name Nyquist plot is often used in the electrochemical literature, it is not precise because Nyquist plots are used for assessing the stability of a system with feedback.
2. Bode plots. There are two types of Bode plot:
 - (a) $\log |Z|$ (magnitude) versus $\log f$ (frequency)
 - (b) phase angle φ versus $\log f$

It should be stressed that in complex plane plots, the unit length of real and imaginary parts should be the same; otherwise, deformation of the plots is observed. Moreover, these plots do not contain all the information about frequency, and some frequencies are often added in these plots to better visualize the frequency domain. They are preferred by electrochemists because a model can be more easily found from them (especially by inexperienced researchers). On the other hand, two Bode plots contain all the necessary information. From a practical point of view, typical data acquisition and analysis programs display both plots. It is strongly recommended that both types of plots be used, especially when comparing experimental data with the fit to the appropriate model. In some cases other plots are also presented, for example, complex admittance plots, complex capacitance plots, and tridimensional impedance plots. Admittance plots can be useful when dealing with blocking systems, where very small and very large impedances are present (Fig. 2.30).

An example of a tridimensional plot, Z'' , Z' , $\log f$, created automatically in ZView, is displayed in Fig. 2.31.

Several examples of impedance plots are presented in Exercises 2.8 and 2.10.

First, let us look at the complex plane and Bode plots obtained for an R - C connection in series, RC in Boukamp's notation, with $R = 150 \, \Omega$, $C = 40 \, \mu\text{F}$, Exercise 2.8. The impedance of such a circuit is described as

$$\hat{Z}(j\omega) = R + \frac{1}{j\omega C} = R - j\frac{1}{\omega C}. \quad (2.139)$$

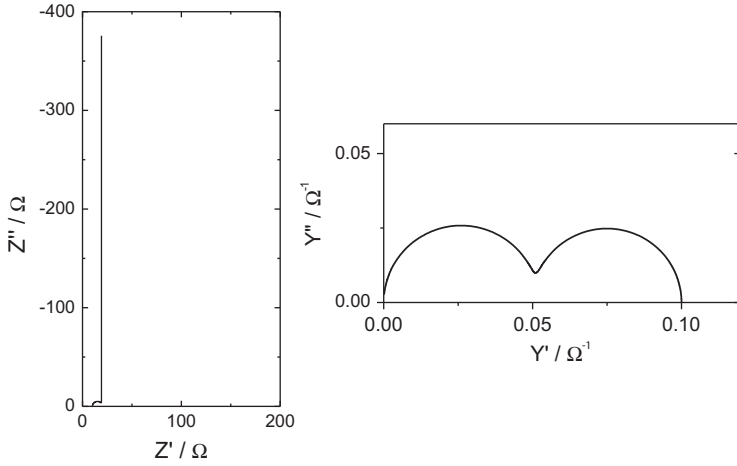


Fig. 2.30 Complex plane impedance, Z' vs. Z'' , Eq. (2.139), and admittance, Y' vs. Y'' , Eq. (2.141), plots for circuit $R_s(C_{dl}(R_p C_p))$ with $R_s = 10 \Omega$, $C_{dl} = 4 \times 10^{-5} \text{ F}$, $R_p = 10 \Omega$, $C_p = 0.001 \text{ F}$

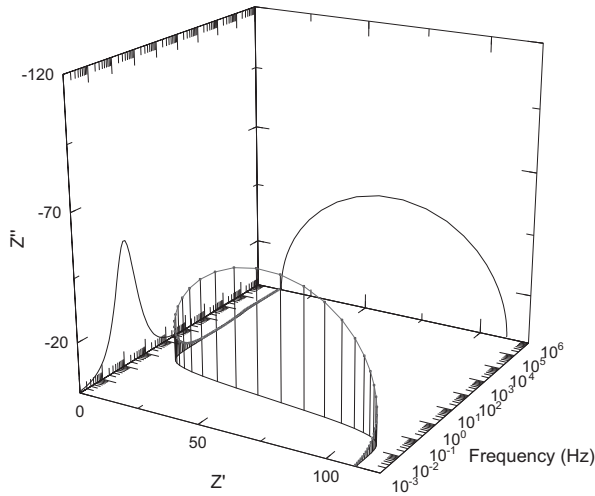


Fig. 2.31 Example of tridimensional impedance (in Ω) plot generated by ZView

The modulus and the phase angle are

$$|Z| = \sqrt{R^2 + \frac{1}{(\omega C)^2}}$$

$$\varphi = \text{atan}\left(\frac{Z''}{Z'}\right) = \text{atan}\left(-\frac{1}{\omega RC}\right) = \text{atan}\left(\frac{1}{\omega RC}\right), \quad (2.140)$$

and the admittance is

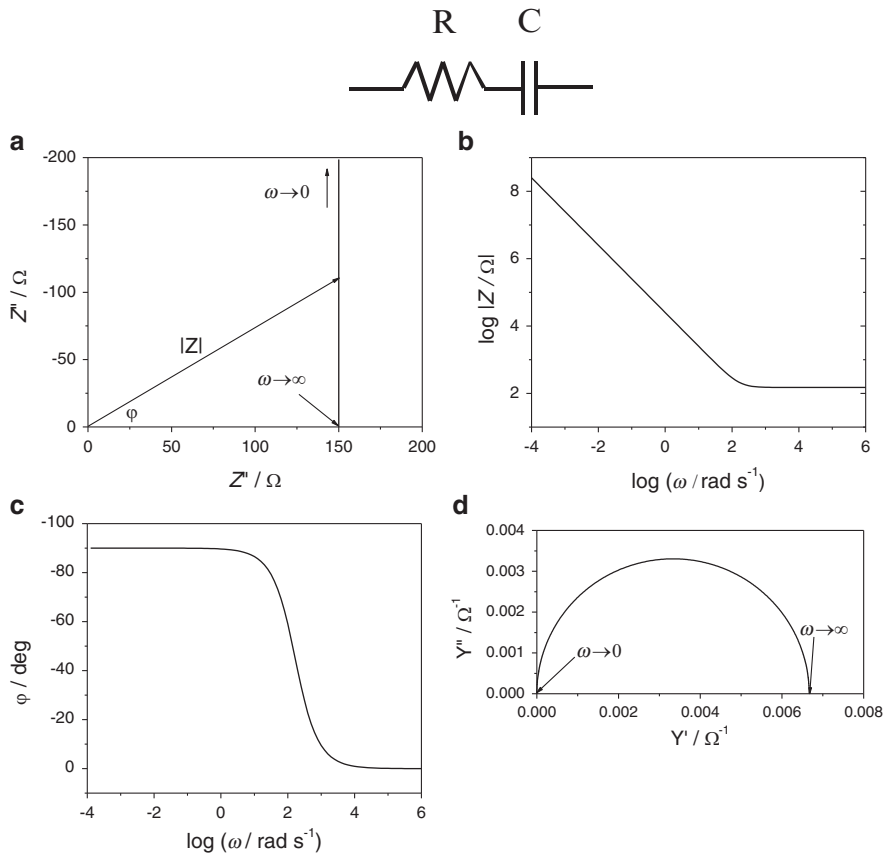


Fig. 2.32 Complex plane (a), Bode magnitude (b), Bode phase angle (c), and complex admittance (d) plots for R - C connection in series; $R = 150 \, \Omega$, $C = 40 \, \mu\text{F}$

$$\hat{Y}(j\omega) = \frac{1}{\hat{Z}(j\omega)} = \frac{1}{R - j\frac{1}{\omega C}} = \frac{R}{R^2 + \frac{1}{\omega^2 C^2}} + j \frac{1}{\omega C \left(R^2 + \frac{1}{\omega^2 C^2} \right)}. \quad (2.141)$$

Equation (2.140) should be compared with Eq. (2.115); it is evident that the same equation describing impedance was obtained from Eq. (2.139) using complex algebra. The plots are displayed in Fig. 2.32.

In a complex plane plot, the real part is always constant, $Z' = R$, and the imaginary part, $Z'' = -1/\omega C$, changes from zero at infinite frequency to infinity at zero frequency. A dc current cannot circulate through such a circuit because $|Z|$ also goes to infinity as f goes to zero.

The Bode magnitude contains two elements: R and $1/\omega C$. The plot presents a constant value $\log |Z| = \log R$ at high frequencies and a straight line with a slope -1 :

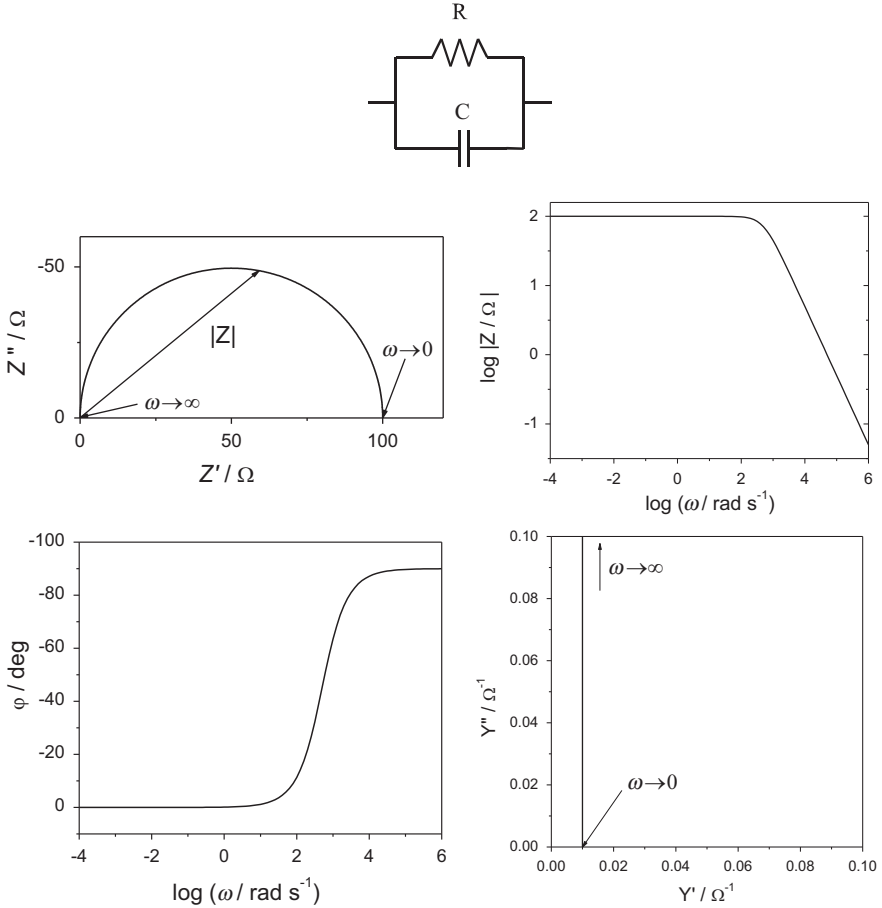


Fig. 2.33 Complex plane impedance, Bode, and complex plane admittance plots for a connection of R and C in parallel (RC), $R = 100 \Omega$, $C = 20 \mu\text{F}$

$\log |Z| = -\log \omega - \log C$ at low frequencies. There is an inflection point where these two elements are identical, giving the break-point frequency $\omega = 1/RC$. The Bode phase angle plot represents two bend points and changes between angle zero at high frequencies and 90° at very low frequencies.

The admittance presents a semicircle (Eq. 2.141); at very low frequencies the admittance is zero (impedance infinite), and at high frequencies it is equal to $1/R$ because the impedance of the capacitance is zero. The maximum of admittance is at $\omega = 1/RC$.

Let us now look at the R - C connection in parallel, i.e., the circuit (RC) using Boukamp's notation (Exercise 2.10). The impedance of the system is

$$Z = \frac{1}{\frac{1}{R} + j\omega C} = \frac{R}{1 + j\omega RC} = \frac{R}{1 + (\omega RC)^2} - j \frac{\omega R^2 C}{1 + (\omega RC)^2}, \quad (2.142)$$

$$|Z| = \frac{\sqrt{R^2 + (\omega R^2 C)^2}}{1 + (\omega RC)^2} \quad \varphi = \text{atan}(-\omega RC) = -\text{atan}(\omega RC), \quad (2.143)$$

and the admittance is

$$\hat{Y} = \frac{1}{R} + j\omega C. \quad (2.144)$$

The impedance presents a semicircle; when the frequency goes to infinity, the impedance goes to zero because the impedance of the capacitor becomes zero and when the frequency goes to zero the impedance becomes real $Z = R$ because a constant dc current can flow through the circuit. The maximum of the imaginary part is observed at the frequency $\omega = 1/RC$, and RC is called the time constant of the system. As in the preceding example, the imaginary part of the impedance is always negative.

There are two linear parts of the Bode magnitude plot; when the frequency is very low, Eq. (2.142) reduces to $|Z| = R$, and when the frequency is very large, the real part becomes small and $|Z| = 1/\omega C$. There is one break-point frequency on a Bode magnitude plot, when $R = 1/\omega C$, and the break-point frequency corresponds to the system time constant:

$$\omega = \frac{1}{\tau} = \frac{1}{RC}. \quad (2.145)$$

The admittance plot for (RC) connections is similar in shape to the impedance plot for an R - C connection in series. The difference is that for circuits containing capacitances the imaginary part of the impedance is negative and that of the admittance positive.

Next, let us consider R_s in series with a parallel connection of R and C , that is, circuit $R_s(CR)$ (Exercise 2.11 and Fig. 2.34).

The total impedance of the system is

$$\begin{aligned} \hat{Z} &= R_s + \frac{1}{\frac{1}{R} + j\omega C} = R_s + \frac{R}{1 + j\omega RC} \\ &= R_s + \frac{R}{1 + (\omega RC)^2} - j \frac{\omega R^2 C}{1 + (\omega RC)^2}, \end{aligned} \quad (2.146)$$

and the complex plane plots are displayed in Fig. 2.34.

A complex plane plot represents a semicircle shifted to higher values by a constant resistance R_s . The high-frequency current flows through the capacitance C and the total impedance is real and equal to R_s . The dc current ($\omega = 0$) flows through R_s and R and the impedance is real and here equal to $R_s + R$.

The phase angle is

$$\varphi = \text{atan}\left(\frac{Z''}{Z'}\right) = -\text{atan}\left[\frac{\omega R^2 C}{R_s + R + R_s(\omega RC)^2}\right], \quad (2.147)$$

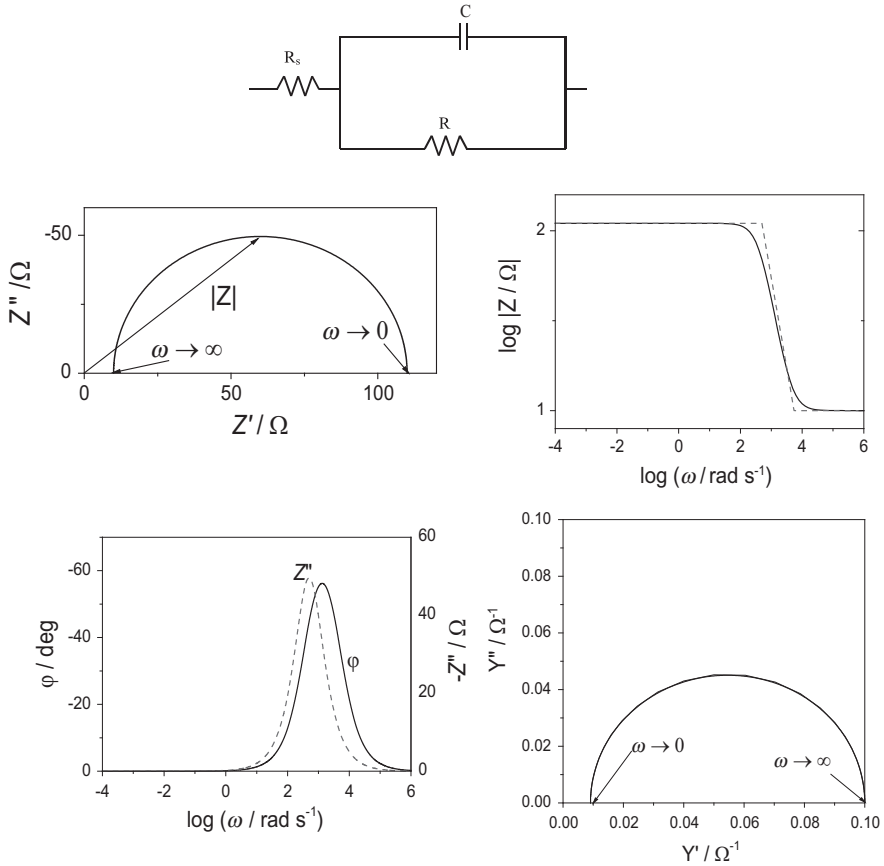


Fig. 2.34 Complex plane impedance, Bode, and complex plane admittance plots for resistance R_s with connection of R and C in parallel, $R_s = 10 \, \Omega$, $R = 100 \, \Omega$, $C = 20 \, \mu\text{F}$

and the maximum of the phase angle is observed at the frequency

$$\omega_{\max} = \frac{1}{RC} \sqrt{\frac{R_s}{R} + 1}, \quad (2.148)$$

which in this example appears at $\omega_{\max} = 1658 \, \text{rad s}^{-1}$. One notices that the maximum of the phase angle appears at a frequency higher than the maximum of the imaginary part of the semicircle, which is at $\omega_{\max, \text{Im}} = 1/RC = 500 \, \text{rad s}^{-1}$, as in the simple (RC) parallel circuit. This is schematically displayed in Fig. 2.34, Bode phase angle. The value of ω_{\max} approaches that of $\omega_{\max, \text{Im}}$ when $R_s / R \ll 1$, that is, when the series resistance R_s is very small.

2.10.1 Interpretation of Bode Magnitude Plots

The total impedance of the circuit in Fig. 2.34 can be rewritten as

$$\begin{aligned}\hat{Z} &= R_s + \frac{1}{1 + j\omega RC} = \frac{R_s + R + j\omega R_s RC}{1 + j\omega RC} = (R_s + R) \frac{1 + j\omega \left(\frac{R_s R}{R_s + R} C \right)}{1 + j\omega(RC)} \quad (2.149) \\ &= (R_s + R) \frac{1 + j\omega\tau_2}{1 + j\omega\tau_1},\end{aligned}$$

where τ_1 and τ_2 are the two characteristic time constants of the circuit in Fig. 2.34; these time constants are $\tau_1 = 2$ ms and $\tau_2 = 0.1818$ ms, corresponding to two break-point frequencies, $\omega_1 = 500$ rad s⁻¹ and $\omega_2 = 5500$ rad s⁻¹. From Eq. (2.149) the Bode magnitude plot can be evaluated:

$$\log|Z| = \log(R_s + R) + \log(|1 + j\omega\tau_2|) - \log(|1 + j\omega\tau_1|). \quad (2.150)$$

Depending on the frequencies, the logarithmic terms $\log(|1 + j\omega\tau|)$ may take two different values; when $\omega\tau \ll 1$, $\log(|1 + j\omega\tau|) = 0$, and when $\omega\tau \gg 1$, $\log(|1 + j\omega\tau|) = \log \omega + \log \tau$, which gives a line with a slope of one. From this equation three asymptotes can be constructed. When $\omega\tau \ll 1$ $\log|Z| = \log(R_s + R)$, in the intermediate frequency zone, taking into account that $\tau_2 < \tau_1$, $\log|Z| = \log(R_s + R) + \log \omega + \log \tau_2$, and at high frequencies the third term in Eq. (2.150) must also be taken into account, and the impedance becomes $\log|Z| = \log(R_s + R) + \log \omega + \log \tau_2 - \log \omega - \log \tau_1 = \log R_s$. This produces three straight lines and two break-point frequencies on the Bode magnitude plot. This is schematically shown in Fig. 2.34 (Bode magnitude) as a dashed line. The method presented above allows for a quick visualization of Bode magnitude plots.

Let us look now at the circuit in Fig. 2.35, denoted as $R_s(C_{dl}(R_{ct}C_p))$; it is described in detail in Exercise 2.12. The impedance of the system is easily written as

$$\hat{Z} = R_s + \frac{1}{j\omega C_{dl} + \frac{1}{R_{ct} + \frac{1}{j\omega C_p}}}. \quad (2.151)$$

The total impedance can be separated into real and imaginary parts, although the calculations are laborious and it is easy to make a mistake. It can be done easily in Maple (Exercise 2.12), and the obtained impedances are

$$Z' = \frac{R_s(C_{dl}^2 + 2C_{dl}C_p) + C_p^2(R_s + R_{ct}) + (R_s R_{ct} C_{dl} C_p \omega)^2}{(C_{dl} + C_p)^2 + (R_{ct} C_{dl} C_p \omega^2)^2}, \quad (2.152)$$

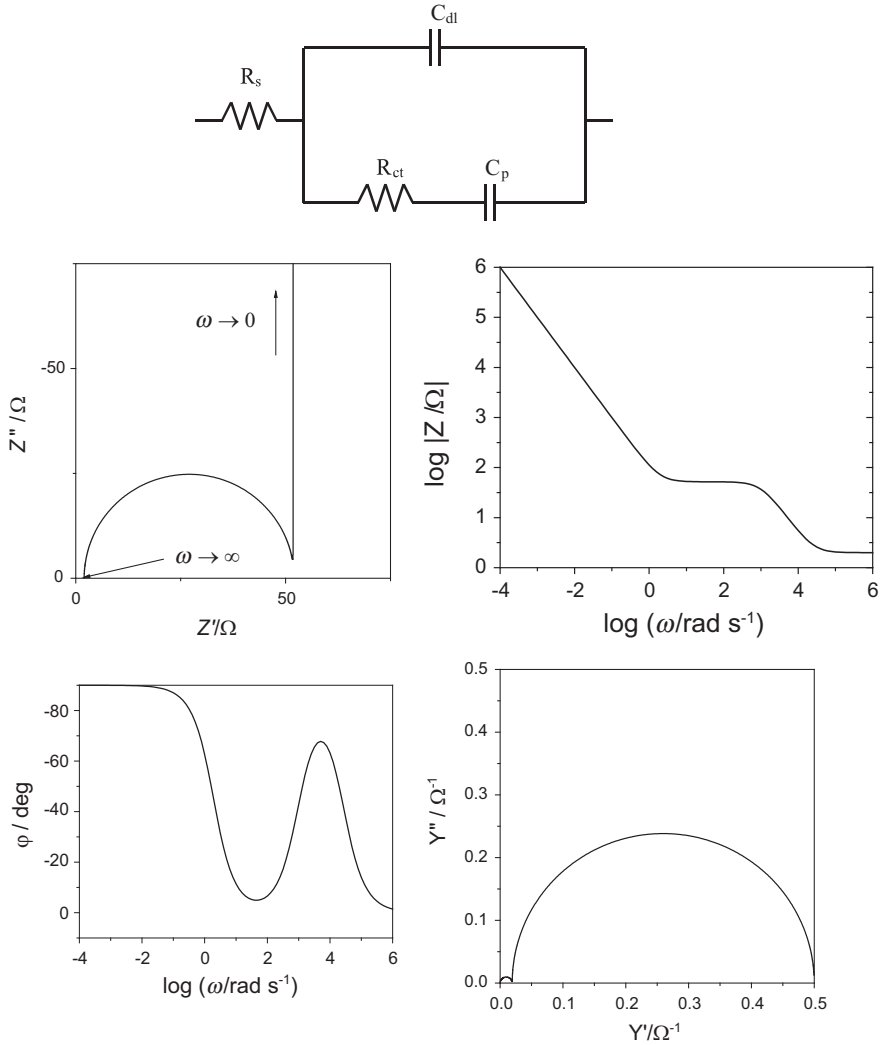
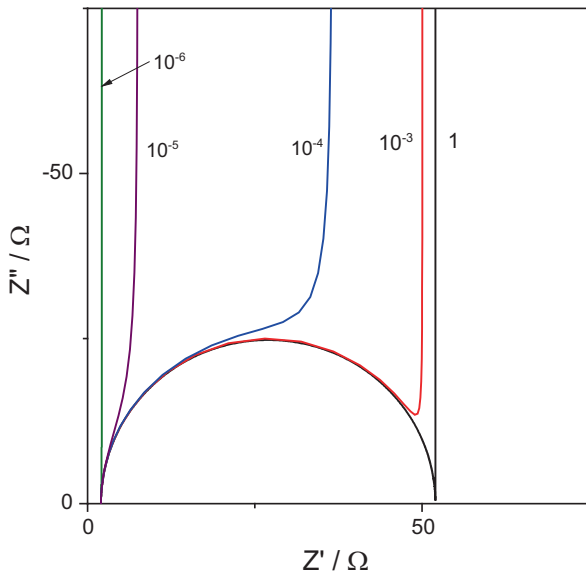


Fig. 2.35 Complex plane impedance, Bode, and complex plane admittance plots for circuit $R_s(C_{dl}(R_{ct}C_p))$; $R_s = 2 \Omega$, $R_{ct} = 50 \Omega$, $C_{dl} = 20 \mu\text{F}$, $C_p = 0.01 \text{ F}$

$$Z'' = - \frac{C_{dl} + C_p + C_{dl}(R_{ct}C_p\omega)^2}{\left[(C_{dl} + C_p)^2 + (R_{ct}C_{dl}C_p\omega^2)^2 \right] \omega}. \quad (2.153)$$

To calculate the impedances, either the preceding equations may be used or they can be calculated stepwise in Excel starting from \hat{Z}_f :

Fig. 2.36 Complex plane plots for circuit in Fig. 2.35 and different values of parameter C_p indicated in figure in farads



$$\begin{aligned}
 \hat{Z}_f &= R_{ct} + \frac{1}{j\omega C_p} = R_{ct} - j\frac{1}{\omega C_p}, \\
 \hat{Y}_f &= \frac{1}{\hat{Z}_f}, \\
 \hat{Y}_{el} &= \hat{Y}_f + j\omega C_{dl}, \\
 \hat{Z}_{el} &= \frac{1}{\hat{Y}_{el}}, \\
 \hat{Z} &= R_s + \hat{Z}_{el}.
 \end{aligned} \tag{2.154}$$

The complex plane and the Bode plots are displayed in Fig. 2.35.

Looking at the circuit, it is evident that a dc current cannot flow through it because the two parallel branches are blocked by capacitances. This means that the low-frequency imaginary impedance part must go to negative infinity. On the other hand, at very high frequencies the capacitances do not obstruct current flow (impedance of the capacitance goes to zero), and the total ac current flows through R_s and the upper branch; therefore, the impedance is R_s . In the medium frequencies, the coupling of R_{ct} and C_{dl} produces a semicircle with the time constant $\tau = R_{ct}C_{dl} = 1$ ms. On Bode plots a semicircle produces an S-shaped wave followed by a straight line with a slope of -1 . The phase angle plots show a peak at higher frequencies, corresponding to the semicircle, and then the phase angle goes to -90° as the imaginary part of the impedance goes to $-\infty$. On the complex admittance at high frequencies the admittance is $1/2 \Omega = 0.5 \Omega^{-1}$, at low frequencies it goes to

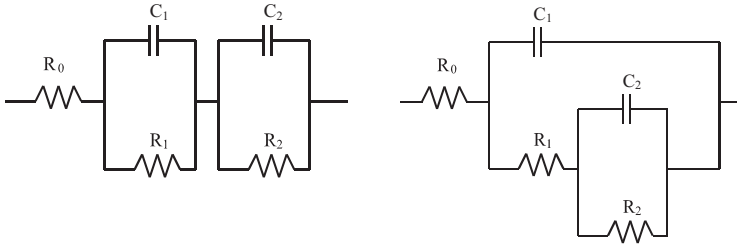


Fig. 2.37 Examples of two circuits producing two semicircles on complex plane plots: left series $R_0(R_1C_1)(R_2C_2)$ and right nested $R_0(C_1(R_1(R_2C_2)))$

zero as the impedance goes to $-\infty$. Two semicircles are observed on the complex admittance plots. The radius of the small low-frequency semicircle corresponds to $1/(R_s + R_{ct}) = 1/52 \text{ } \Omega^{-1}$, which is the total low-frequency real resistance in the complex impedance plots.

It is interesting to note that the shape of complex plane plots depends on the relative ratio of both capacitances. Figure 2.36 shows a series of plots for different values of C_p and the same values of all other parameters as previously. When C_p is very large ($C_p \gg C_{dl}$), a full semicircle touching the real part is formed. With a decrease of C_p , a smaller part of the semicircle is produced. Finally, when $C_{dl} \gg C_p$, the current flows not through the branch R_p - C_p but through R_s - C_{dl} , which produces a straight line on the complex plane plots, as in Fig. 2.32.

2.10.2 Circuits with Two Semicircles

Let us consider two circuits leading to the formation of two semicircles on complex plane plots, one consisting of two parallel (RC) circuits in series and another a nested circuit (Fig. 2.37), i.e., $R_0(R_1C_1)(R_2C_2)$ and $R_0(C_1(R_1(R_2C_2)))$. In the simulations, the following parameters were used: $R_0 = 10 \text{ } \Omega$, $R_1 = R_2 = 100 \text{ } \Omega$, $C_1 = 20 \text{ } \mu\text{F}$, and different values of $C_2 = 0.1, 10^{-3}, 10^{-4}, 2 \times 10^{-5}$, and 10^{-5} F . This circuit contains two time constants: $\tau_1 = R_1C_1 = 2 \text{ ms}$ and $\tau_2 = R_2C_2 = 10, 0.1, 0.01, 0.001$, and 0.002 s . The results of simulations of the complex plane and Bode plots are displayed in Fig. 2.38. The numerical values recopied from ZView can be found in files (Exercise 2.13). When the two time constants are very different, two well-separated semicircles are formed on the complex plane plots. At the same time, two steps are observed on the Bode magnitude plots and two peaks on the Bode phase angle plots. When the two time constants merge, separation of the two semicircles becomes less obvious, a large semicircle is formed, $\tau_2 = 0.01 \text{ s}$, and later it is difficult to decide just by looking at the plots that there still are two semicircles, $\tau_2 = 0.001 \text{ s}$. In this case, only an analysis of the impedances (i.e., fit to the appropriate circuit) may determine whether there is one or two semicircles. Finally, when the time constants of the two circuit elements

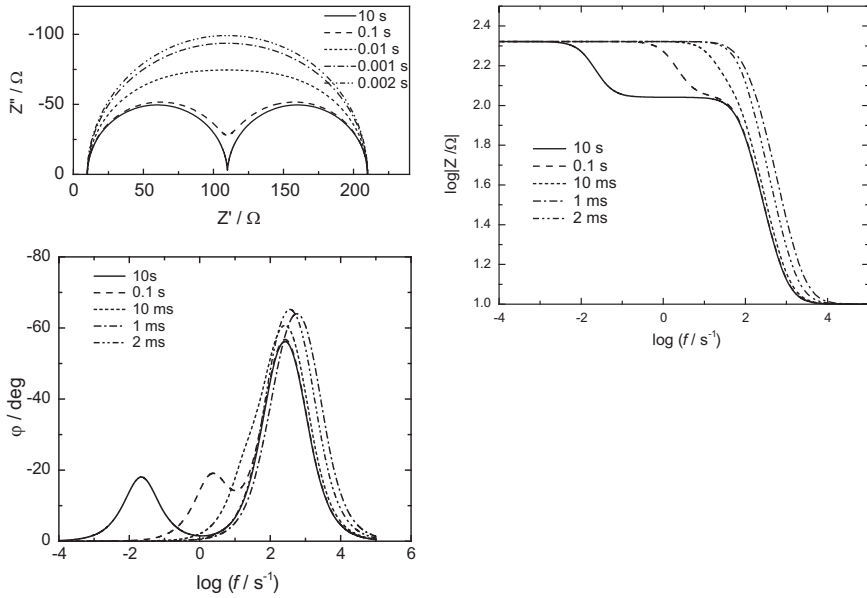


Fig. 2.38 Complex plane and Bode plots for a series circuit in Fig. 2.37, $R_0(R_1C_1)(R_2C_2)$, using following parameters: $R_0 = 10 \, \Omega$, $R_1 = R_2 = 100 \, \Omega$, $C_1 = 20 \, \mu\text{F}$, and different values of $C_2 = 0.1, 10^{-3}, 10^{-4}, 2 \times 10^{-5}$, and 10^{-5} F. Values of τ_2 are indicated on plots

are identical, one semicircle appears in the complex plane plots. This effect is confirmed by the equation

$$\begin{aligned}
 Z &= R_0 + \frac{1}{\frac{1}{R_1} + j\omega C_1} + \frac{1}{\frac{1}{R_2} + j\omega C_2} = R_0 + \frac{1}{\frac{1}{R_1} + j\omega C_1} + \frac{1}{\frac{1}{R_1} + j\omega C_1} = \\
 &= R_0 + \frac{2}{\frac{1}{R_1} + j\omega C_1} = R_0 + \frac{1}{\frac{1}{(2R_1)} + j\omega \left(\frac{C_1}{2}\right)}. \quad (2.155)
 \end{aligned}$$

In such a case, one semicircle on the complex plane plots has a diameter of $2R_1 = 200 \, \Omega$ and a capacitance of $C_1/2 = 10 \, \mu\text{F}$. In this case, analysis of the circuit reveals only one time constant, although two identical parallel (RC) elements were used in simulations.

Let us look now at the impedance plots for a nested circuit using the same parameters as for a circuit in series. The results are presented in Fig. 2.39.

Note that, using the same set of parameters R_1, C_1, R_2 , and C_2 , different plots are obtained for both circuits. Nevertheless, exactly the same plots as in the case of a nested circuit can be obtained using a circuit in series but with different parameters.

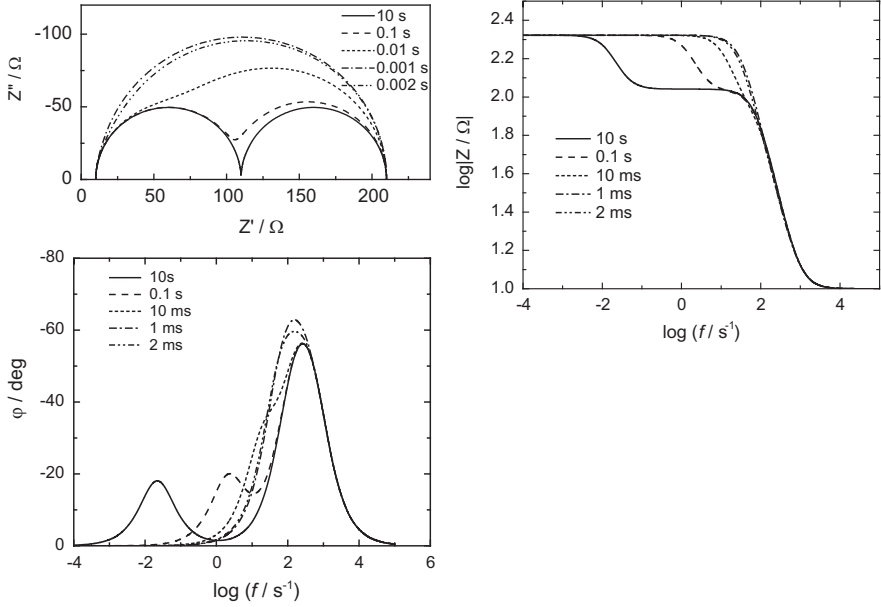


Fig. 2.39 Complex plane and Bode plots for a nested circuit in Fig. 2.37, $R_0(C_1(R_1(R_2C_2)))$, using parameters as in Fig. 2.38. Values of τ_2 are indicated on plots

Table 2.3 Results of fit of impedances in Fig. 2.39 to circuit containing two parallel (RC) elements in series. The parameters of the nested circuit are as follows: $R_0 = 10 \Omega$, $R_1 = R_2 = 100 \Omega$, $C_1 = 20 \mu\text{F}$, and different assumed values of C_2 indicated below; the parameters found using fit to the series circuit are indicated

C_2 assumed / F	R_1 found / Ω	C_1 found / F	R_2 found / Ω	C_2 found / F
0.100	99.96	2.00×10^{-5}	100.0	1.53×10^{-6}
1.00×10^{-3}	96.00	2.04×10^{-5}	104.0	1.35×10^{-8}
1.00×10^{-4}	62.86	2.57×10^{-5}	137.1	1.54×10^{-9}
2.00×10^{-5}	10.56	7.24×10^{-5}	189.4	3.02×10^{-10}
1.00×10^{-5}	2.99	1.47×10^{-4}	197.0	1.57×10^{-10}

In fact, plots for the nested circuit can be obtained using the circuit in series and the parameters shown in Table 2.3, where the resistance R_0 is always the same, $R_0 = 10 \Omega$, and other parameters are different. It should be stressed that the fit is exact, which means that the two circuits give exactly the same values of impedances.

This effect arises from the fact that impedances of circuits in series and nested circuits (Fig. 2.37) can be represented by the same equation:

$$\hat{Z} = R_0 \frac{(s - z_1)(s - z_2)}{(s - p_1)(s - p_2)}, \quad (2.156)$$

where $s = j\omega$. This equation comes from the expressions for the impedances of both circuits:

$$\hat{Z} = R_0 + \frac{1}{\frac{1}{R_1} + sC_1} + \frac{1}{\frac{1}{R_2} + sC_2}, \quad (2.157)$$

$$\hat{Z} = R_0 + \frac{1}{sC_1 + \frac{1}{R_1 + \frac{1}{\frac{1}{R_2} + sC_2}}}. \quad (2.158)$$

The values of the zeros z_i and poles p_i of the equation are

$$z_{1,2} = \frac{\frac{1}{R_1 C_1} + \frac{1}{R_2 C_2} + \frac{1}{R_0 C_1} + \frac{1}{R_0 C_2}}{2} \left[-1 \pm \sqrt{1 - \frac{\frac{4}{C_1 C_2} \left(\frac{1}{R_1 R_2} + \frac{1}{R_0 R_1} + \frac{1}{R_0 R_2} \right)}{\left(\frac{1}{R_1 C_1} + \frac{1}{R_2 C_2} + \frac{1}{R_0 C_1} + \frac{1}{R_0 C_2} \right)^2}} \right]$$

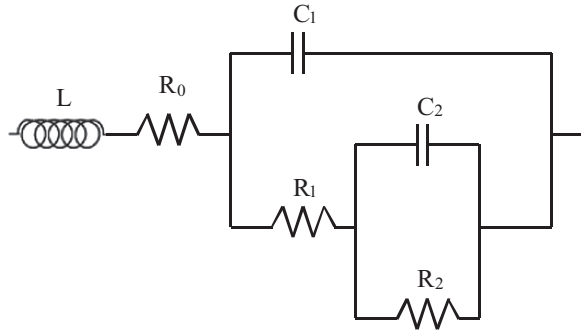
$$p_1 = -\frac{1}{R_1 C_1}, \quad p_2 = -\frac{1}{R_2 C_2} \quad (2.159)$$

for the circuit in series and

$$z_{1,2} = \frac{1}{2} \left(\frac{1}{R_1 C_1} + \frac{1}{R_0 C_1} + \frac{1}{R_1 C_2} + \frac{1}{R_2 C_2} \right) \times \left[-1 \pm \sqrt{1 - \frac{4 \left(\frac{1}{R_1 C_1 R_2 C_2} + \frac{1}{R_0 R_2 C_1 C_2} + \frac{1}{R_0 R_1 C_1 C_2} \right)}{\left(\frac{1}{R_1 C_1} + \frac{1}{R_0 C_1} + \frac{1}{R_1 C_2} + \frac{1}{R_2 C_2} \right)^2}} \right]$$

$$p_{1,2} = \frac{1}{2} \left(\frac{1}{R_1 C_1} + \frac{1}{R_1 C_2} + \frac{1}{R_2 C_2} \right) \left[-1 \pm \sqrt{1 - \frac{4 \left(\frac{1}{R_1 C_1 R_2 C_2} \right)}{\left(\frac{1}{R_1 C_1} + \frac{1}{R_1 C_2} + \frac{1}{R_2 C_2} \right)^2}} \right] \quad (2.160)$$

Fig. 2.40 Nested circuit with inductance L in series; $L = 2 \times 10^{-4}$ H, $C_2 = 0.1$ F; other parameters as in Fig. 2.39



for the nested circuit. From the preceding equations it is obvious that the impedances for both circuits have exactly the same general form with different formulas for zeros and poles. These are only two out of three possible circuits that will be discussed in Example 14.2.

2.10.3 Circuits Containing Inductances

Until now, only circuits containing resistances and capacitances have been discussed. Inductive effects in electrical circuits appear when alternative electrical current flow creates a magnetic field interacting with the flowing current; of course, in a straight wire the inductance is very small, but in looped wires or a coil it becomes larger. The inductive effects always lead to positive imaginary impedances, as will be shown in what follows. Let us first consider the circuit in Fig. 2.40, which contains inductance L in series with resistance R_0 and a nested connection of two (RC) circuits, i.e., $LR_0(C_1(R_1(R_2C_2)))$. The complex plane and Bode plots for this circuit without inductance were presented in Fig. 2.39.

From the impedance plots it follows that the presence of inductance in series does not affect low-frequency data. At high frequencies a positive imaginary straight line appears on the complex plane plots and the phase angle changes sign from negative to positive, while the modulus of the frequency displays a minimum at $R_0 = 10 \Omega$. This positive imaginary impedance is characteristic of the presence of inductance.

Finally, let us consider a simple circuit containing an RLC connection in series. The impedance of such a circuit is

$$\hat{Z} = R + j\omega L - j\frac{1}{\omega C} = R + j\left(\omega L - \frac{1}{\omega C}\right). \quad (2.161)$$

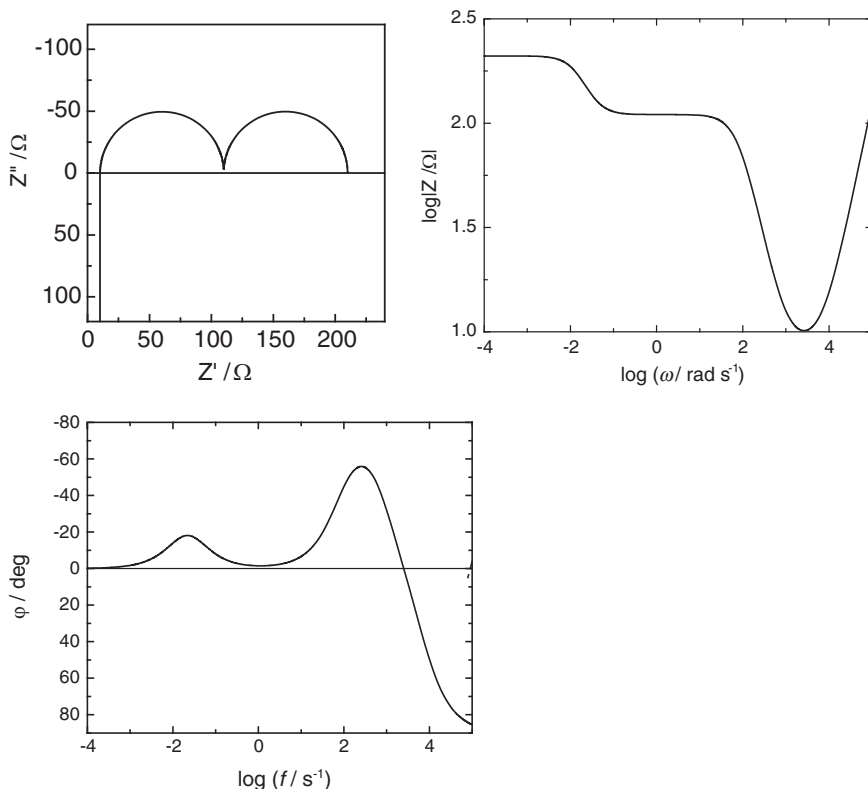


Fig. 2.41 Complex plane and Bode plots for circuit in Fig. 2.40

The real part of the impedance is constant and equal to R , while the imaginary impedance may be positive at high frequencies or negative at low frequencies. The imaginary impedance becomes zero when $\omega_{\text{rez}} = 1/\sqrt{LC}$; this is the so-called resonant frequency. An example of the complex plane and Bode plots for such a circuit is presented in Fig. 2.42. A complex plane plot is a straight line perpendicular to the real axis. The upper negative part corresponds to low frequencies and is identical to an RC connection in series. The lower positive part corresponds to an RL connection in series. The Bode magnitude plot shows two lines at 45° corresponding to the capacitive (negative slope) and inductive (positive slope) parts. The phase angle plot passes through $Z'' = 0$ at the resonant frequency and goes to -90° or 90° at very low or very high frequencies, respectively.

These results are shown in Exercise 2.14.

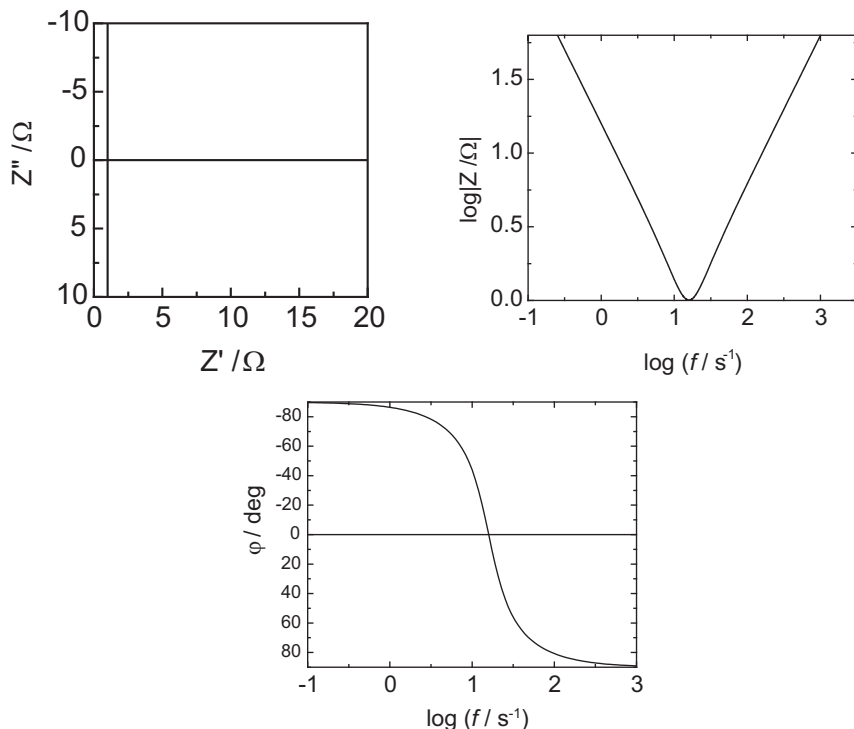


Fig. 2.42 Complex plane and Bode plots for RLC connection in series; $R = 1\ \Omega$, $C = 0.01\ \text{F}$, $L = 0.01\ \text{H}$

2.11 Summary

Impedance of an electrical circuit containing linear electrical elements R , C , and L can be calculated using the impedance of these elements and Ohm's and Kirchhoff's laws. The complex plane and Bode plots can be easily produced using programming in Excel, Zplot, Maple, Mathematica, etc., which are readily available. It should be stressed that these electrical elements are linear, that is, their impedance is independent of the applied ac amplitude. In subsequent chapters, we will see how the impedance of electrochemical systems can be described.

2.12 Exercises

Exercise 2.1 Generate a digitalized function $E(t) = \cos(2\pi t/T_a)$ containing 64 points from 0 to 63 for the sampling time 0.01 s and wave period $T_a = 0.32\ \text{s}$

for 0.63 s. Then use Excel to carry out a FFT. Show the plots of the function and its FT. What information can be obtained from it?

Exercise 2.2 Generate a digitalized function $E(t) = \sin(2\pi t/T_a)$ containing 64 points from 0 to 63 for the sampling time 0.01 s and for wave period $T_a = 0.32$ s for 0.63 s. Then use Excel to carry out a FFT. Show the plots of the function and its FT. What information can be obtained from it?

Exercise 2.3 Generate a digitalized function $E(t) = \cos(2\pi t/T_a + \pi/3)$ containing 64 points from 0 to 63 for the sampling time 0.01 s and for $T_a = 0.32$ s for 0.63 s. Then use Excel to carry out a FFT. Show the plots of the function and its FT. What information can be obtained from it?

Exercise 2.4 Generate a digitalized function $E(t) = \exp(-3t_i)$ containing 32 points for the sampling time 0.01 s. Use Excel to carry out a FFT. What information can be obtained from it?

Exercise 2.5 Generate a digitalized function $E(t) = \sin(2\pi t/T_a)$ containing 256 points for the sampling time 0.2 s and $T_a = 34$ s. Use Excel to carry out a FFT. What information can be obtained from it? Is it possible to obtain the studied function frequency from FT analysis?

Exercise 2.6 Simulate the sum of frequencies curve consisting of the following functions: $\cos(k \cdot 2\pi t/1024)$ for $k = 1, 3, 7$, and 13 and $\sin(k \cdot 2\pi t/1024)$ for $k = 5, 9$, and 17, and t from 0 to 1023. Perform a FFT, determine the frequencies, and compare with the frequencies of assumed individual functions.

Exercise 2.7 To determine the impedance of a system, data of the applied voltage and circulating current were measured for 0.64 s every 0.01 s. To calculate the impedance, generate “experimental” data (normally they would be presented as series of numbers) using the following equations: $E(t) = E_0 \cos(\omega t)$ and $I(t) = I_0 \cos(\omega t + \pi/3)$, where $E_0 = 0.01$ V, $I_0 = 0.002$ A, $\omega = 2\pi f = 2\pi/T_a$, $T_a = 0.32$ s.

Exercise 2.8 Determine impedance using data obtained from D/A data acquisition of voltage and current. These data, containing time, potential, and current: t , $E(t)$, $I(t)$ in s, V, and A, respectively, can be found in the file Ex2_8.txt. What is the frequency of these functions?

Exercise 2.9 Make complex plane, Bode, and complex admittance plots of an RC connection in series; $R = 150 \Omega$, $C = 40 \mu\text{F}$.

Exercise 2.10 Make complex plane, Bode, and complex admittance plots of an (RC) connection in parallel; $R = 100 \Omega$, $C = 20 \mu\text{F}$.

Exercise 2.11 Make complex plane, Bode, and complex admittance plots of R_s in series with the parallel connection of (RC) , $R_s(RC)$; $R_s = 10 \Omega$, $R = 100 \Omega$, $C = 20 \mu\text{F}$.

Exercise 2.12 Make complex plane and Bode plots for the circuit $R_s(C_{dl}(R_{ct}C_p))$ with the following elements: $R_s = 2 \ \Omega$, $R_{ct} = 50 \ \Omega$, $C_{dl} = 2 \times 10^{-5} \text{ F}$, and $C_p = 0.01 \text{ F}$.

Exercise 2.13 Simulate using ZView the impedance of the two models displayed in Fig. 2.37, in series $R_0(R_1C_1)(R_2C_2)$ and nested $R_0(C_1(R_1(R_2C_2)))$, using the following parameters: $R_s = 10 \ \Omega$, $R_1 = 100 \ \Omega$, $C_1 = 2 \times 10^{-5} \text{ F}$, $R_2 = 100 \ \Omega$, $C_2 = 10^{-1}, 10^{-3}, 10^{-4}, 2 \times 10^{-5}, 10^{-5} \text{ F}$. Make the approximations of the impedances of the nested circuit using those in series. Compare with the results in Ch2. xlsx, Worksheets Ex2.13 serial, Ex2.13 nested, and Ex2.13 approx.

Exercise 2.14 Simulate impedances for the circuit RCL in series for $R = 1 \ \Omega$, $C = 0.01 \text{ F}$, and $L = 0.01 \text{ H}$. Make simulations using ZView and Excel. Make complex plane and Bode plots.

Chapter 3

Determination of Impedances

Modern potentiostats are able to apply various potential programs to a working electrode. In EIS measurements, a small sinusoidal perturbation of a controlled amplitude and frequency must be applied together with the dc electrical program. The system impedance may be measured using various techniques:

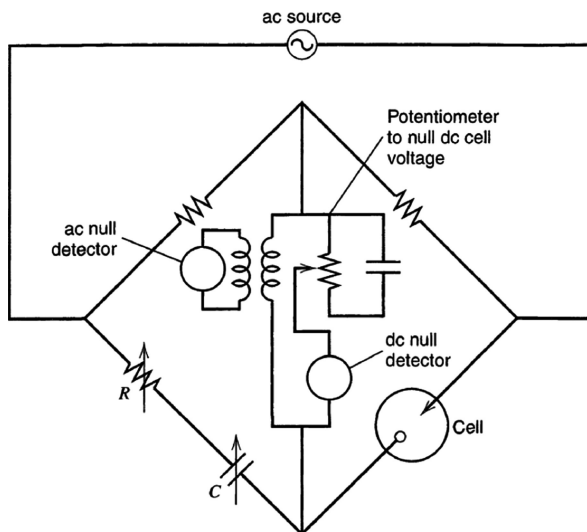
1. Ac bridges
2. Lissajous curves
3. Phase-sensitive detection (PSD)
4. Frequency response analyzers (FRA)
5. Fast Fourier transform (FFT)
6. Laplace transform of applied signal

3.1 AC Bridges

Ac bridges were used before modern electronic apparatus were developed. Such bridges provided a very precise but very laborious and time-consuming method of measurement. A schema of an ac bridge is presented in Fig. 3.1.

The ac bridge is based on a classical Wheatstone (or Wien for ac measurements) bridge in which one part is replaced by an electrochemical cell and the other compensating part by a variable, R or C . The dc potential is supplied by a potentiometer in the center and ac by the external source. The double layer capacitance measurements were initially carried out on a dropping mercury electrode (DME), and the bridge compensation had to be carried out always at the same surface area of the DME, that is, after exactly the same time from the beginning of

Fig. 3.1 Ac bridge for electrochemical impedance measurements (From Ref. [17] with permission from Wiley)

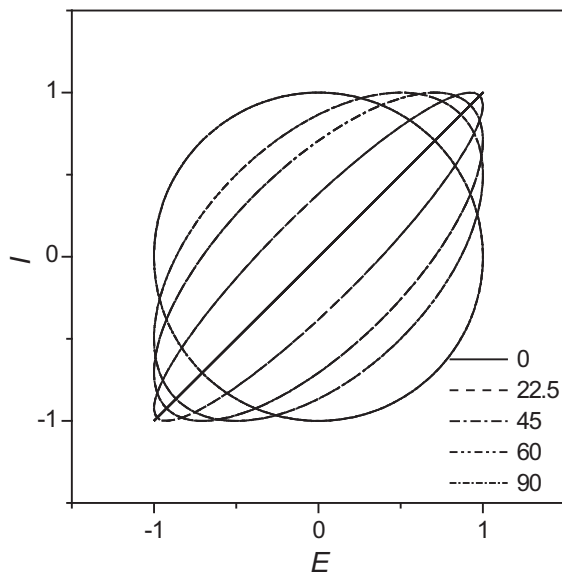


the drop fall [80]. Early papers were reviewed by Delahay [81] and Mohilner [82]. By now, ac bridges have been replaced by frequency analyzers or lock-in amplifiers.

3.2 Lissajous Curves

In general, after application of an ac potential perturbation to an electrochemical system, $E(t) = E_0 \cos(\omega t)$, the obtained current is shifted in phase with respect to the voltage: $i(t) = i_0 \cos(\omega t + \varphi)$. By applying the voltage to the x -axis and the current (transformed into the corresponding voltage) to the y -axis of the oscilloscope one obtains so-called Lissajous curves [3, 24]. When the phase angle difference φ is zero, a straight line at 45° is obtained, and when the phase difference is 90° , a semicircle is obtained; for intermediate phase shifts, ellipses at different angles are obtained. Examples of Lissajous curves for different values of the phase angle φ are displayed in Fig. 3.2. The ratio of the amplitudes of both signals gives the modulus of the impedance, $|Z|$, and the phase angle φ is determined from the inclination of the ellipse. From $|Z|$ and φ the real and imaginary parts of the impedance are determined. Such an analysis must be carried out at all frequencies studied. Nonlinearity causes the formation of asymmetric curves [3, 126]. However, this method is time consuming and is rarely used nowadays.

Fig. 3.2 Lissajous curves for various phase differences; the values of φ in degrees are shown in the legend



3.3 Phase-Sensitive Detection, Lock-In Amplifiers

Two additional methods use a potentiostat with a device permitting automatic determination of the impedance. Phase-sensitive detection (PSD) is used in lock-in amplifiers [83]. The most popular commercial equipment of this type was used by EG&G Princeton Applied Research. In this technique, the measured ac signal, which is the potential or current, $E_1 = E_0 \sin(\omega t + \varphi_1)$, is multiplied by a square wave signal of the same frequency ω . The square wave signal of unit amplitude can be represented by an infinite Fourier series:

$$E_2 = \frac{4}{\pi} \sum_{n=0}^{\infty} \frac{1}{2n+1} \sin [(2n+1)(\omega t + \varphi_2)] \quad (3.1)$$

which is a sum of the sin functions of odd harmonics of the fundamental frequency ω , and its amplitude was taken as unity. In general, both signals may contain different phases φ_1 and φ_2 , respectively. In practice, as both the potential and current signals are multiplied by the same square signal, its initial phase shift might be considered zero. Usually the same generator inside the lock-in amplifier is used to produce the square wave and the ac signal used in the impedance analysis. The operation of multiplying $E_1 \times E_2$ gives

$$\begin{aligned}
E_1 E_2 &= \frac{4E_0}{\pi} \sum_{n=0}^{\infty} \frac{1}{(2n+1)} \sin(\omega t + \varphi_1) \sin[(2n+1)(\omega t + \varphi_2)] \\
&= \frac{2E_0}{\pi} \sum_{n=0}^{\infty} \frac{1}{(2n+1)} \left\{ \begin{array}{l} \cos[-2n\omega t + \varphi_1 - (2n+1)\varphi_2] \\ -\cos[(2n+2)\omega t + \varphi_1 + (2n+1)\varphi_2] \end{array} \right\} \\
&= \frac{2E_0}{\pi} \left\{ \begin{array}{l} \cos(\varphi_1 - \varphi_2) - \cos(2\omega t + \varphi_1 + \varphi_2) \\ +\frac{1}{3}\cos(-2\omega t + \varphi_1 - 3\varphi_2) - \frac{1}{3}\cos(4\omega t + \varphi_1 + 3\varphi_2) \\ +\frac{1}{5}\cos(-4\omega t + \varphi_1 - 5\varphi_2) - \frac{1}{5}\cos(6\omega t + \varphi_1 + 5\varphi_2) + \dots \end{array} \right\} \quad (3.2)
\end{aligned}$$

The result of this operation contains a series consisting of the constant element $(2E_0/\pi) \cos(\varphi_1 - \varphi_2)$ and harmonics of the fundamental signal. The constant element is proportional to the amplitude of the measured signal and contains information on the phase of the measured signal. The average value of a periodic signal is, of course, zero, and this signal is sent to the low-pass filter, which passes only the constant term (integrating the signal):

$$\text{Average}(E_1 \times E_2) = \frac{1}{T} \int_0^T E_1 E_2 dt = \frac{2E_0}{\pi} \cos(\varphi_1 - \varphi_2) \quad (3.3)$$

In practice, the measured signal is usually mixed with two signals, with $\varphi_2 = 0$ and $\varphi = 90^\circ$ extracting the real and imaginary parts, respectively, of the measured signal: $(2E_0/\pi)\cos(\varphi_1)$ and $(2E_0/\pi)\sin(\varphi_1)$. The schema of the two-phase lock-in amplifier is presented in Fig. 3.3. Note that if harmonic signals are present in the measured signal, then they are attenuated by 1/3, 1/5, 1/7, etc. Lock-in amplifiers operate in a frequency range of 0.5–10 Hz the lower limit, depending on the manufacturer, to approximately $\sim 10^5$ Hz, with a precision of 0.1–0.2 %. Modern lock-in amplifiers are controlled by a microprocessor and permit automated measurements.

3.4 Frequency Response Analyzers

The system impedance at different frequencies may also be measured using frequency response analyzers. Frequency response analyzers operate on the basis of the correlation of the studied signal with the reference signal [84]. The measured signal, $E = E_0 \cos(\omega t + \varphi)$, is multiplied by a cosine and sine signal of the same frequency, and the product is integrated during one or more wave periods. Integrating over n periods gives

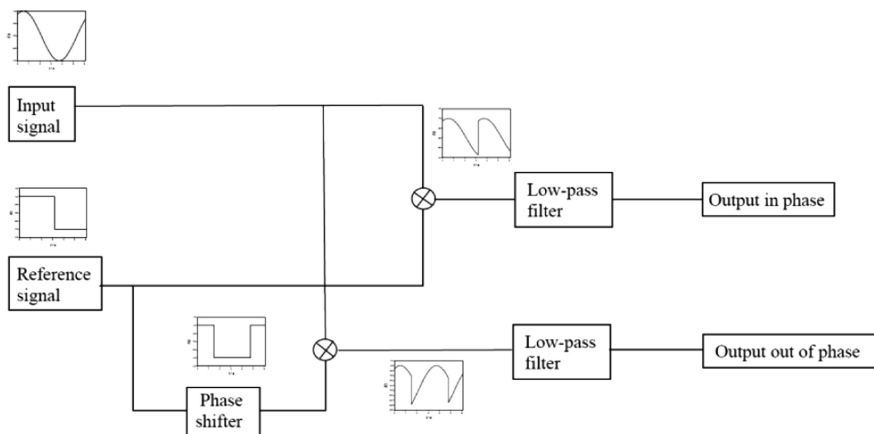


Fig. 3.3 Schema of two-phase lock-in amplifier. The input signal is mixed with the simple square wave signal and the square wave signal shifted by 90° . After filtering the periodic functions, in-phase (*real*) and out-of-phase (*imaginary*) parts of the signal are obtained

$$\text{Re}(E_1) = \frac{1}{nT} \int_0^{nT} E_0 \cos(\omega t + \varphi) \cos(\omega t) dt = \frac{E_0}{2} \cos(\varphi) \quad (3.4)$$

and

$$\text{Im}(E_1) = \frac{1}{nT} \int_0^{nT} E_0 \cos(\omega t + \varphi) \sin(\omega t) dt = \frac{E_0}{2} \sin(\varphi) \quad (3.5)$$

Note that Eqs. (3.4) and (3.5) correspond to the Fourier transform (FT) of the function E , Eqs. (2.66) and (2.67). This operation produces real and imaginary parts of the measured signal. Such an operation is carried out for the potential and current signal, and the impedance of the system is calculated as the ratio of the FTs, Eq. (2.127). The functioning of a frequency response analyzer is displayed in Fig. 3.4.

Frequency response analyzers were popularized in electrochemistry by Solartron, but presently other companies are using them more frequently (e.g., PAR – AMETEK, Oak Ridge, Tennessee, Metrohm Autolab, Utrecht, The Netherlands, ZAHNER, Kronach, Germany, Scribner Associates, Southern Pines, North Carolina, Zive Zcon, Seoul, Korea). It can also be shown that all the harmonics, if presented in the input signal, are strictly rejected, that is, the correlation of $\sin(k\omega t + \varphi)$ with $\sin(\omega t)$ or with $\cos(\omega t)$ is equal to zero for $k > 1$. The advantage of the correlation process is also a reduction in noise (of arbitrary frequency), its influence decreasing with increases in the integration time. Figure 3.5 shows the attenuation of an output signal as a function

Fig. 3.4 Scheme of frequency response analyzer

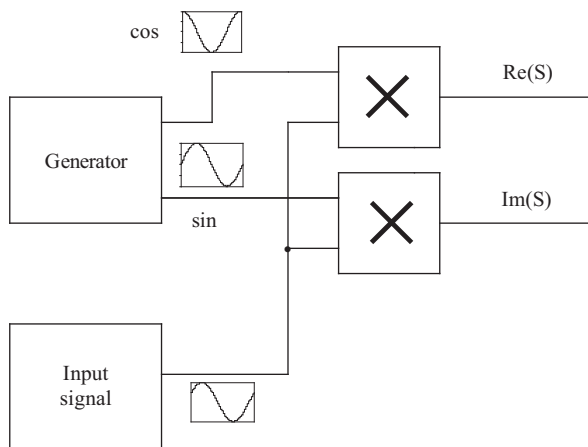
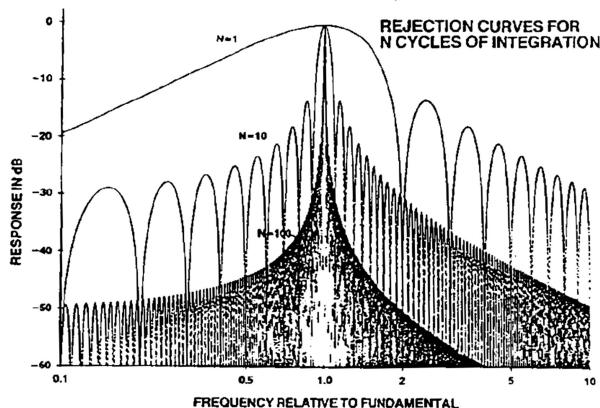


Fig. 3.5 Frequency response of a FRA averaging filter for different numbers of integration cycles (From Ref. [84] with permission from Solartron)



of frequency and the number of integration cycles N . Modern frequency response analyzers carry out all computations digitally. Frequency response analyzers have a wide frequency range (12 decades) and high precision.

A comparison of PSD and FRA was presented by Evans [85] and is shown in Table 3.1.

3.5 AC Voltammetry

Using either a lock-in amplifier or frequency response analyzer it is possible to study impedance during cyclic voltammetric dc potential cycling. During a slow voltammetric sweep, an ac signal can be superimposed and the ac response measured at one frequency at a time as a function of potential. If such an experiment is repeated at various frequencies, a complete impedance curve can be acquired, although for individual sweeps complex admittance is usually registered.

Table 3.1 Comparison of lock-in amplifiers and frequency response analyzers [85]

Lock-in amplifier	FRA
<i>Advantages</i>	<i>Advantages</i>
Very sensitive	Faster analysis
Effectively removes noise	Wide frequency range
Reduces harmonic distortion	Removes harmonic distortion
Suppresses dc noise	Direct output to external device
Relatively low cost	Easy standalone measurements
<i>Disadvantages</i>	<i>Disadvantages</i>
Limited frequency range	Higher cost
Slower	Limited noise removal
Standalone readings difficult	Limited sensitivity

This technique was applied, for example, to Pt oxidation [86], electrocatalysis of methanol [87], formic acid oxidation [88], or hydrogen adsorption [89]. There is a limitation on the smallest frequency at a given sweep rate, v ; during the ac cycle the electrode potential cannot change too much [86]:

$$\frac{RT}{F} v \ll \omega \quad (3.6)$$

For example, a sweep rate of 10 mV s^{-1} and minimum frequency of 2 Hz were used in such studies [86]. The main problem in this technique is that it takes a long time to carry out potential sweeps at many frequencies, and the measured system should not evolve with time.

3.6 Laplace Transform

As was mentioned in Sects. 2.8.1 and 2.8.2, application of the Laplace transform to the transient potential and current permits determination of the operational impedance. Such a method was initially introduced by Pilla [90–93] and applied to studies using mercury electrodes. Using a fast potentiostat a small potential step was applied, and both voltage and current transients were measured. Of course, because of the nonideal potentiostat response, the potential increase was not a rectangular step but occurred more slowly. Examples of the measured potential and current transients are shown in Fig. 3.6. Such data acquisition was extended to longer times and then extrapolated as the integration had to be continued to infinity.

This method was later critically reviewed and modified by Barsoukov et al. [94]. They showed that the weakness of the direct Laplace transform lies in its large sensitivity to noise. Instead of direct numerical integration, Eq. (2.21), they proposed instead to fit first the time-domain data to a “carrier function,” which could then be directly transformed. The operator impedance of stable systems is

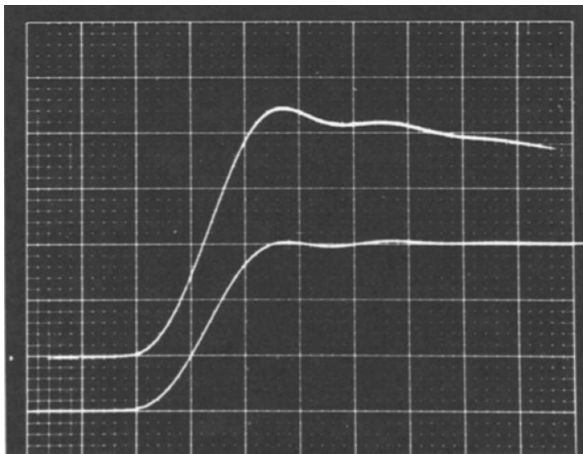


Fig. 3.6 Current (*upper curve*) and potential (*lower curve*) transients due to potential step of 6 mV applied to electrical equivalent circuit $R(C(R(CR)))$; current scale is 7 mA and potential scale is 2 mV per major division. The time scale is 50 ns per major horizontal division (From Ref. [90]; reproduced by permission of Electrochemical Society)

described as a ratio of two polynomials with negative poles that, in the case of first-order poles, may be represented as simple fractions (see also Sect. 13.3.3):

$$z(s) = \frac{K \prod_{m=1}^M (s - \mu_m)}{\prod_{q=1}^Q (s - \lambda_q)} = \sum_{q=1}^Q \frac{A_q}{s - \lambda_q} \quad (3.7)$$

In the case of the galvanostatic step, the observed potential transient is described by

$$V(t) = A_0 + \sum_{q=1}^Q A_q e^{\lambda_q t} \quad (3.8)$$

where all values $\lambda_q < 0$. In such a case, the experimental voltage transient must be fitted to Eq. (3.8). If $V(t)$ and $I(t)$ are known, the impedance can be easily obtained, but in this case, instead of numerical integration, a direct transformation of the approximating voltage function, Eq. (3.8), and current step $I(s) = I/s$ is performed. Barsoukov et al. [94] found that this method works well when logarithmically distributed time samples are used. They also studied in detail error propagation during such experiments. As in the case of the fast Fourier transform (FFT) (Sect. 3.7), the frequency information is obtained between $f_{\max} = 1/(2\Delta t)$ and $f_{\min} = 1/T$, where Δt is the sampling time and T the total data acquisition time. This method was applied to study the charge state of lithium batteries. It requires equipment that is much simpler than a frequency response analyzer or a lock-in amplifier and is faster than sequential frequency sweep. It can be compared to the

multisine fast Fourier-based techniques because it requires a similar experiment time. However, its implementation is simpler because only current (or potential) steps are necessary.

3.7 Methods Based on Fourier Transform

The FT method makes it possible to study system response to a series of different frequencies. Taking the FT of the perturbation signal and that of the resulting signal allows one to determine the transfer function, e.g., impedance, of the measured system, Eq. (2.127). The FFT provides a fast and efficient algorithm for computing the FT [95]; however, the number of points acquired must be equal to 2^k , where k is an integer. However, discrete Fourier transform, DFT, which does not have this limitation, can also be used as the power of computers has increased tremendously since the invention of the FFT algorithm. In principle, any form of the excitation signal might be used, but in practice, few types of excitation are applied [96–98]: (1) pulse or step, (2) noise, and (3) sum of sine waves. It should be kept in mind the total signal applied to the system should be small enough to keep the system in the linear zone.

3.7.1 Pulse or Step Excitation

The FT of an infinite short pulse, $h(t) = K\delta(t)$, where $\delta(t)$ is Dirac's delta function, equals $H(j\omega) = K$, that is, it contains all frequencies with the same amplitude K . Such a method is used in FFT nuclear magnetic resonance. An ideal pulse function cannot be realized in practice because of the limitations of the electronics, and in practice it must be substituted by a pulse of a short duration Δt . However, such a function does not have a uniform response in the Fourier (i.e., frequency) domain. The applied pulse function is defined as $h(t) = 1$ for $t = 0$ to Δt and $h(t) = 0$ elsewhere. Its FT is

$$H(j\omega) = \int_0^{\infty} h(t)e^{-j\omega t} dt = \int_0^{\Delta t} e^{-j\omega t} dt = \frac{1 - e^{-j\omega\Delta t}}{j\omega} \quad (3.9)$$

The amplitude of this function equals

$$|H(j\omega)| = \frac{\sqrt{2}\Delta t}{\omega\Delta t} \sqrt{1 - \cos(\omega\Delta t)} \quad (3.10)$$

It is presented in Fig. 3.7. Clearly, at $\omega < 1/\Delta t$, all the frequencies are presented in the excitation function, but their amplitude decreases quickly at higher frequencies. By decreasing Δt , a wider frequency window is obtained. However, in

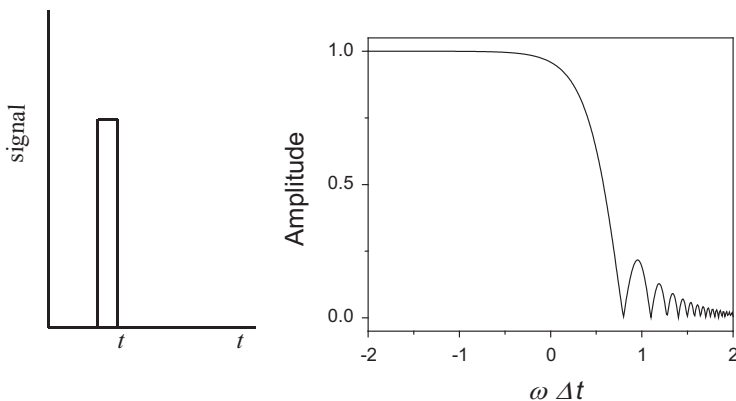


Fig. 3.7 Pulse signal, $h(t)$, and its frequency spectrum $|H(j\omega)|$, Eq. (3.10), as a function of frequency

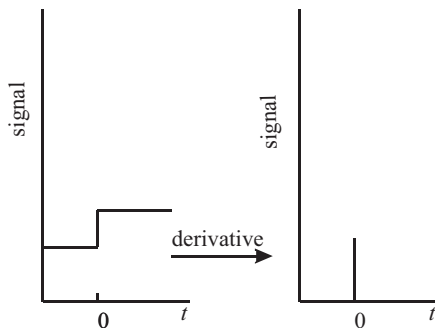


Fig. 3.8 Step function and its derivative

practice, we are limited by the response of the potentiostat, which has a limited response time.

Because it is difficult to apply a very short pulse function, there is another way of obtaining this effect; one can apply a step function and take its derivative, which is Dirac's delta function, $\delta(t)$ (Fig. 3.8).

Such a method was used in the literature for the determination of impedances [99–101], and a commercial apparatus [102] applying a current step was described. Taking the FT of the derivative of the potential and current versus time gives the impedance as a function of frequency. However, some authors [100, 101] tried to extrapolate the obtained results to low frequencies beyond the experimental values. If the data are acquired during time $T = N\Delta t$, the information in the measured signal is obtained for frequencies from $1/T$ up to the Nyquist frequency $1/2\Delta t$, where Δt is the sampling time. It has been shown [103] that extrapolating impedances to frequencies lower than $1/T$ introduces artifacts. In addition, the measured

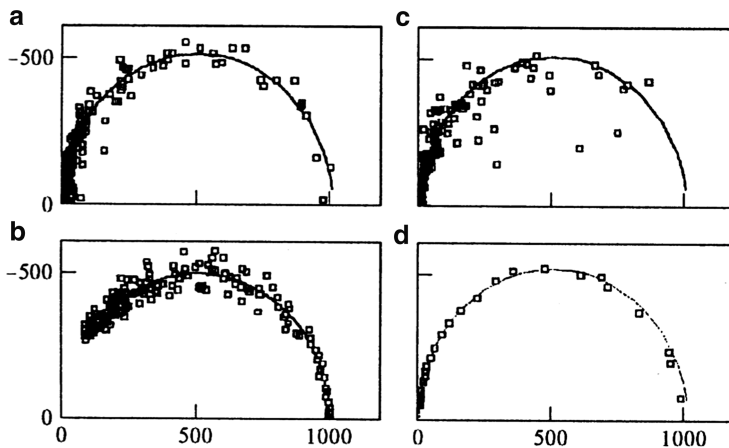


Fig. 3.9 Complex plane plots of numerically simulated impedances, in Ω , for different perturbation waveforms with 1 % noise added; (a) rectangular pulse, (b) exponentially decaying perturbation, (c) quasi-random noise, (d) sum of sine waves with constant amplitudes and zero phases (From Ref. [105] with permission of editorial board)

response signals decay fast with time, and at longer times the signals are hidden in noise [99, 101, 104].

Although the methods using pulse or step excitation are correct from a mathematical point of view, their FT contains all frequencies between $f_{\text{low}} = 1/T = 1/N\Delta t$ and $f_{\text{high}} = 1/2\Delta t$, and the amplitude for each frequency is quite weak. This causes large sensitivity to noise (Fig. 3.9a). In addition, the measured response signals decay fast with time, and at longer times the signals are hidden in noise.

Popkirov and Schindler [105] also attempted to use exponentially decaying voltage pulse perturbation. It presents a relatively noisy response (Fig. 3.9b).

3.7.2 Noise Perturbation

White noise is a signal that contains a continuous spectrum of frequencies with flat amplitudes [99, 104, 105]. However, single-frequency components have quite low amplitudes, and the response to individual frequencies is also weak. Impedance calculated using a white noise perturbation signal with small 1 % noise added is displayed in Fig. 3.9c. It is obvious that very noisy results are generated, and such an excitation is not recommended for acquiring impedance spectra.

3.7.3 Sum of Sine Wave Excitation Signals

It seems that the best way to obtain a response to multiple frequencies is to apply a sum of odd harmonic sine waves, $\sum \sin(2\pi f_i t)$, where f_i are $f, 3f, 5f, \dots, (2n + 1)f$,

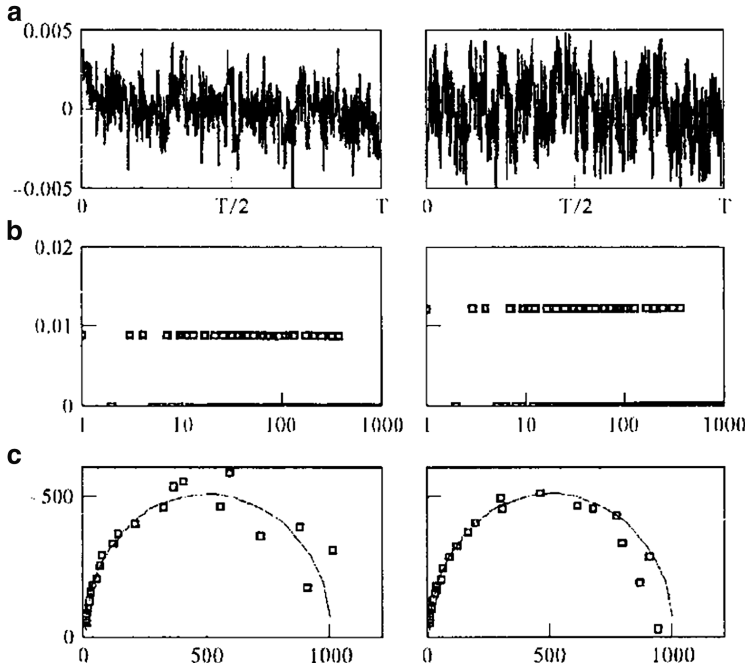


Fig. 3.10 Sum of 25 sine waves with equal amplitudes: *left* – no phase optimization, *right* – optimization of phases; (a) perturbation voltage, (b) Fourier transform of perturbation signal, (c) complex plane plots obtained by adding 5 % noise to current response; *solid lines*: ideal response without noise. Impedances are in Ω . (From Ref. [105] with permission of editorial board)

where f is the fundamental frequency [99, 105–109]. The theoretical formulation of this test was discussed by Diard et al. [110]. To avoid problems with leakage, a whole number of periods should be included in the total measurement time T . The lowest frequency is $f = 1/T$ and the highest $1/(2\Delta t)$, where Δt is the sampling time. However, from a practical point of view, sampling two times per period, although theoretically justifiable, is not practical, and at least four samples per period should be taken [107]. Moreover, averaging several sine periods improves the signal-to-noise ratio. Because of the proprieties of the FFT, the number of points must be a power of two, $N = 2^k$. The ac perturbation signal is described as

$$E(t) = \sum_{i=1}^m a_i \sin(2\pi f_i t + \phi_i) \quad (3.11)$$

where a_i are the amplitudes, f_i frequencies, and ϕ_i the initial phases of the sine functions applied. An example of such a signal consisting of 25 sine waves is presented in Fig. 3.10a. It was suggested that by randomizing the phases ϕ_i one could increase the amplitude of each sine function without exceeding the total amplitude of 5 mV. This is shown in Fig. 3.10, right, where one can see that after randomization the amplitudes are larger (Fig. 3.10b), and the noise of the

impedances is smaller. Popkirov and Schindler [105, 106] presented the values of phases one could use in programming perturbation functions. Carrying out phase optimization, one can have even larger amplitudes [111].

It can be seen from Fig. 3.10 that noise is always larger at low frequencies. This means that in order to obtain “good” data one should use larger amplitudes at low frequencies, while they could be lower at higher frequencies. Such a method was suggested by Popkirov and Schindler [105, 106]. They used the first impedance measurement as a test and adjusted amplitudes of all the sine waves, a_j as proportional to the impedance modulus:

$$a_j = K \sqrt{(z')^2 + (z'')^2} \quad (3.12)$$

where K is a coefficient determined by the condition that the total signal amplitude must be within the linearity limits (usually 5 mV), and then a second measurement is performed with both adjusted amplitudes and phases. An example of such optimization is shown in Fig. 3.11.

It is evident that amplitude optimization reduces noise significantly, by a factor of about 4–5. Garland et al. [107] proposed to decrease the amplitude by a factor of two per decade of frequencies. This avoids the necessity of repetition of measurements. The authors also proposed to use a chirp-z transform to carry out a discrete Fourier transform in the case where the number of points is $N \neq 2^k$.

3.7.4 Dynamic Electrochemical Impedance Spectroscopy

EIS is usually used in stationary conditions at a constant potential or current. However, there is an interest in studying systems that change with time or during potential cycling in cyclic voltammetry. In such cases, so-called dynamic electrochemical impedance spectroscopy (DEIS) is used. It is also called by some authors potentiodynamic EIS, PDEIS, or time-resolved impedance spectroscopy. Typically, the sum of odd harmonic signals is applied during slow cycling of electrodes. In such a case, the relation expressed by Eq. (3.6) between the sweep rate and the lowest frequency must be observed. The FFT is applied to time windows where the system can be considered pseudostationary. In each window the impedance is measured at different frequencies. Such a procedure leads to a series of impedances measured in regular time intervals. This method has been used by several research groups [112–132].

Sacci and Harrington [133] recently developed hardware and software for DEIS. They typically used 34 frequency numbers: 1, 3, 5, 7, 9, 11, 13, 17, 21, 25, 31, 37, 44, 52, 64, 75, 90, 100, 110, 130, 170, 210, 250, 310, 370, 440, 520, 640, 750, 900, 1000, 1100, 1300, and 1700, that is, the smallest frequency chosen was multiplied by these numbers to obtain real frequencies. The data were sampled continually during the potential sweep, and the FFT was performed on blocks of 4,096 (or 2,024) points. A schema of a DEIS system, based on the Keithley KUSB3116

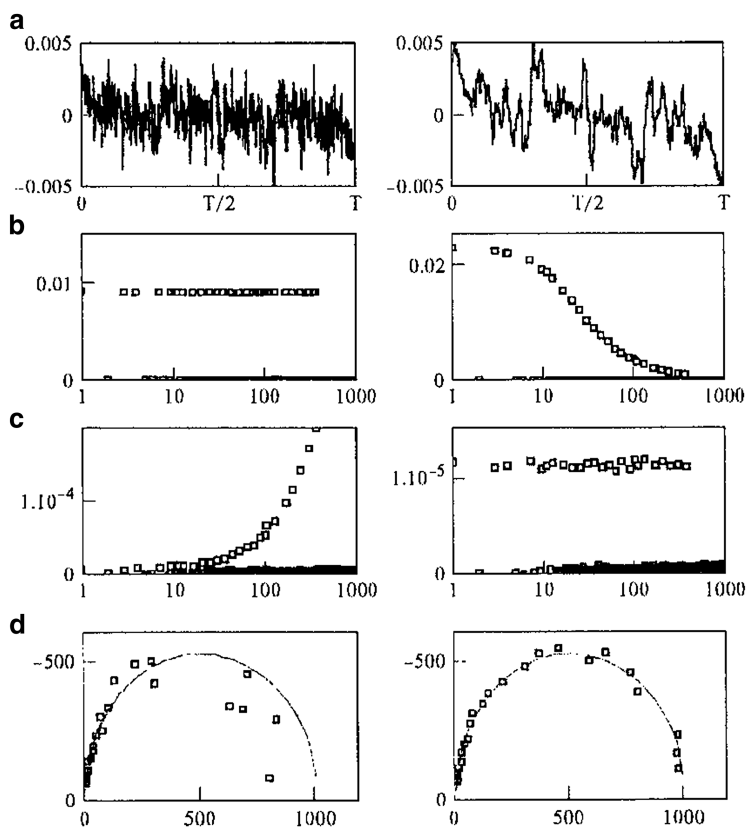


Fig. 3.11 Sum of 25 sine waves: *left* – no amplitude optimization, *right* – optimization of amplitudes according to Eq. (3.12); (a) perturbation voltage in time domain, (b) Fourier transform of perturbation signal, (c) complex plane plots obtained by adding 10 % noise to current response presented in frequency domain, (d) complex plane plots with 10 % noise added to current response; *solid lines*: ideal response without noise. Impedances are in Ω . (From Ref. [105] with permission of editorial board)

Data Acquisition Module, is shown in Fig. 3.12. The digital-to-analog converter generates the sum of sine waves with a total amplitude of, for example, ± 2.5 V, which is divided electronically by 500 to obtain a signal of 5 mV amplitude. This ac signal is added to the dc signal from the linear sweep generator and applied to the potentiostat. Three signals are measured by analog-to-digital (A/D) converters: ac current (directly from the potentiostat or as a potential drop on a standard resistor, amplified using an analog amplifier), ac potential from the potential output from the potentiostat after subtracting the dc component and amplification, and dc potential. Because the potential and current are sampled sequentially (not simultaneously), a phase correction must be made. If they are sampled at equal intervals δt , an apparent phase shift of $\varphi = 2\pi f \delta t$ radians is introduced. Since this is known for each frequency, it can be corrected for by multiplying the calculated impedance at that frequency by

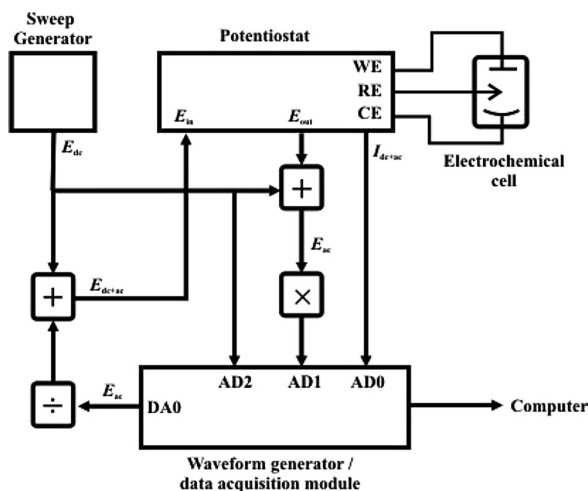
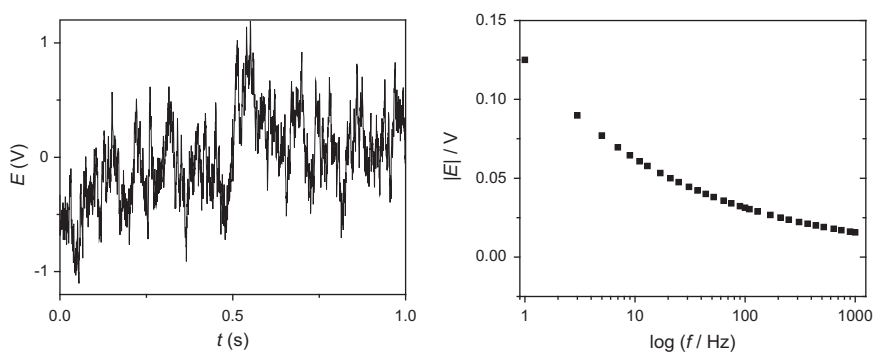


Fig. 3.12 Schema of dynamic electrochemical impedance spectroscopy system (From Ref. [133]. Reproduced by permission of Electrochemical Society)



$\exp(-j\varphi)$. A detailed schema of the electronics was recently developed by D. Auger and published in the Ph.D. thesis of M. Martin [134]. The applied ac signal and the FT of its amplitude are displayed in Fig. 3.13; see also Exercise 3.1.

FT-EIS allows for measurements of nonstationary systems evolving slowly with time or during a potential sweep. In addition, it allows for detecting and quantifying the presence of time variance and nonlinear distortions in experimental data [123–127, 135]. In these experiments, a series of odd harmonics was applied from which every third or fourth frequency was removed. They were 1, 3, 9, 11, 15, 17, 21... or 3, 5, 7, 11, 15, 17, 19, 21, 25... This method was applied to study organic coatings on Al [125]. The signal contained frequencies between 0.1 Hz and

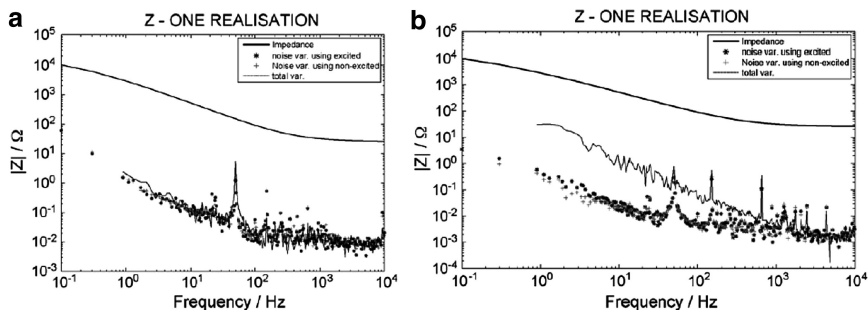


Fig. 3.14 Impedance modulus for Aluzinc in 0.1 M Na₂SO₄ after 14 days of immersion measured with two total amplitudes (a) 8 mV and (b) 48 mV; *continuous line* – $|Z|$, * – noise estimated from excited frequencies, + noise from nonexcited frequencies, — – total variance of impedance (Reprinted from Ref. [125], Copyright (2010), with permission from Elsevier)

approximately 10^4 Hz with a total amplitude of 10 mV rms (root mean square), amplitudes a_i decreasing proportionally to $1/\sqrt{N}$, where N denotes the frequency number, and randomized phases (see Sect. 3.7.3). Such measurements allowed the determination of the noise level at the excited frequencies, the noise at the nonexcited frequencies, and the total variance of the impedance, which includes the noise and nonlinear distortions. Comparison of the amplitude of the impedance with the noise at nonexcited frequencies allowed for the estimation of the signal-to-noise ratio while information about the linearity was assessed comparing the total variance with the noise level at the nonexcited frequencies [123–125]. When these values are similar the system is linear. An example of the application of this method is illustrated in Fig. 3.14. For lower amplitude the system behaves as linear but for larger amplitude it behaves as nonlinear. Although larger amplitude improves signal-to-noise ratio it introduces nonlinearities. Comparison of the noise at excited frequencies with that at the nonexcited frequencies shows that both are similar therefore the system is stationary after 14 days of immersion. Similar measurements after 11 days of immersion revealed that the system is nonstationary [125].

In classical implementations of the FFT analysis of impedances to avoid leakage problems, the data acquisition must be synchronized with the wave periods, and in the data acquisition window there must always be an integer number of periods of each wave. Darowicki and coworkers [136–141] proposed a so-called short time FT (STFT). It was later extended to large-amplitude analysis [142]. It is similar to the FFT-based method discussed previously, but a time window of the applied sum of frequencies was selected by applying a moving Gaussian window centered in the middle of the window. The size of the cutout fragment depends on the Gaussian distribution parameter. In practice, the signal is multiplied by the Gauss window and the product is Fourier transformed. Because of the leakage problem and lower power spectrum, the authors recently modified this technique [143]. They analyze a time period containing a whole number of periods of all functions, but because they do not acquire exactly 2^k points, they use the discrete Fourier transform (DFT).

FT-based measurements allow for faster measurements because all the frequencies are applied at the same time, and to carry out impedance measurements during the potential sweep, it is assumed that the changes during the data block used for transformation are negligible (pseudostationary). FT-based measurements also permit one to determine time variance and nonlinear distortions in the data. However, the cost of this convenience is a lower amplitude for each frequency compared to classical EIS. This produces a weaker signal and larger noise. The interest in this method is constantly increasing.

3.8 Perturbation Signal

In EIS one can use potential or current sinusoidal perturbations. In practice, the potential perturbation of 10 mV peak to peak or a 5 mV amplitude is usually used because EIS is based on the linearization of nonlinear electrochemical equations. This also means that as the sum of sine waves is applied, its total amplitude cannot exceed 5 mV. In practice amplitude of 5 mV rms is usually used for diffusion and adsorption limited processes, see Sect. 13.2, but in certain cases of surface processes where sharp voltammetric peaks appear the amplitude should be much lower. The linearity can be simply checked by decreasing amplitude and comparing the obtained results, Sect. 13.2. It should be kept in mind that the apparatus used in electrochemistry displays the root-mean-squared (rms) amplitude, which is the effective amplitude measured by an ac voltmeter. This rms amplitude is equal to the real amplitude divided by $\sqrt{2}$:

$$E_{\text{rms}} = \frac{E_{\text{ampl}}}{\sqrt{2}} \quad (3.13)$$

This means that to have an amplitude of 5 mV, the rms value should be set to $E_{\text{rms}} = 5/\sqrt{2} \sim 3.5$ mV.

It is also possible to apply a current sinusoidal perturbation and measure the oscillating voltage generated in the system. This galvanostatic mode is usually used in studies of power sources: fuel cells, batteries, and supercapacitors. Further determination of impedances from alternating the voltage and current is the same as for the potential perturbation. However, in the latter, care must be taken to verify whether the amplitude of the alternating voltage is not larger than 5 mV, which can be easily checked using an oscilloscope.

3.9 Conclusions

Nowadays it is possible to carry out automatic impedance measurements with modern equipment that uses frequency analyzers, lock-in amplifiers, and FT techniques. This equipment comes with its own software for data acquisition and analysis. Usually, ten frequencies per decade are acquired and one must use the appropriate ac amplitude.

Equipment dedicated to simultaneous FT analysis at a constant potential or during ac sweep is still less common. More details on how to choose the ac amplitude and to assure that good impedances will be obtained will be discussed in Sect. 13.2.

3.10 Exercises

Exercise 3.1 Simulate the sum of odd harmonic functions $\sum A_i \cos(2\pi\nu_i t + \pi b_i)$ for:

Frequencies, ν_i/Hz

1	3	5	7	9	11	13	17	21	25	31	37
44	52	64	75	90	100	110	130	170	210	250	310
370	440	520	640	750	900	1,000					

Relative amplitudes, A_i :

0.25	0.1796024	0.154003	0.1391682	0.1290281	0.1214646
0.1155073	0.1065462	0.09997981	0.09486765	0.08891917	0.08430711
0.08002237	0.0760977	0.07148676	0.06815384	0.06451406	0.0625
0.06073228	0.05775367	0.0532731	0.04998991	0.04743382	0.04445958
0.04215356	0.04001119	0.03804884	0.03574338	0.03407692	0.03225703
0.03125					

Relative phases, b_i , $\varphi = \pi * b_i$

0.7055475	0.533424	0.5795186	0.2895625	0.301948	0.7747401
0.01401764	0.7607236	0.81449	0.7090379	0.04535276	0.4140327
0.8626193	0.79048	0.3735362	0.9619532	0.8714458	0.05623686
0.9495566	0.3640187	0.5248684	0.7671117	0.05350453	0.5924582
0.4687001					

Perform simulations for the total time of 1 s for $N = 2,048$ points, that is, for $\Delta t = 1/2048$ s. Calculate the FT of this function and its amplitude (modulus) versus frequency up to the Nyquist frequency. The results are in the file Ch3.xlsx.

Chapter 4

Impedance of the Faradaic Reactions in the Presence of Mass Transfer

In Chap. 2 we saw the responses of electrical circuits containing the elements R , C , and L . Because these are linear elements, their impedance is independent of the ac amplitude used. However, in electrochemical systems, we do not have such elements; we have solution–electrode interfaces, redox species, adsorption, etc. In this and the following chapters, we will learn how to express the electrochemical interfaces and reactions in terms of equations that, in particular cases, can be represented by the electrical equivalent circuits. Of course, such circuits are only the electrical representations of physicochemical phenomena, and electrical elements such as resistance, capacitance, or inductance do not exist physically in cells. However, such a presentation is useful and helps in our understanding of the physicochemical phenomena taking place in electrochemical cells. Before presenting the case of electrochemical reactions, the case of an ideally polarizable electrode will be presented.

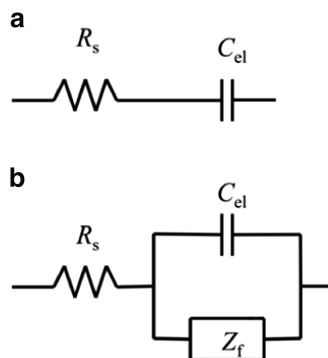
4.1 Impedance of an Ideally Polarizable Electrode

An ideally polarizable electrode also called blocking electrode, is an electrode at which there is no charge transfer between electrode and solution [17]. Such an electrode immersed in a solution containing supporting electrolyte can be represented as a connection of the solution resistance and electrode capacitance in series (Fig. 4.1a), and its impedance is described as

$$\hat{Z} = R_s + \frac{1}{j\omega C_{el}}, \quad (4.1)$$

where, when the impedance is measured in a three-electrode setup [working electrode (WE), counter electrode (CE), and reference electrode (RE)] with a potentiostat, R_s represents the solution resistance, that is, the resistance between the electrode surface and the tip of the reference electrode (or Luggin capillary), and C_{el} represents the capacitance of the electrode surface equal to

Fig. 4.1 Equivalent electrical circuits of (a) an ideally polarized electrode, (b) electrode in the presence of redox reaction



$$C_{el} = S_r C_{dl}, \quad (4.2)$$

where S_r is the real surface area and C_{dl} is the specific double layer capacitance of the electrode. Examples of ideally polarized electrodes are mercury electrodes in a supporting electrolyte between mercury dissolution and reduction of the cations of the supporting electrolyte in a rather large potential range (up to 2 V), Pt in aqueous solutions between hydrogen underpotential deposition (UPD) and Pt oxidation (relatively narrow potential zone of ~ 0.4 V), Au electrode with a rather large potential zone between the reduction of the supporting electrolyte and Au oxidation, and glassy carbon in a more anodic zone.

It must be added that if the impedance is measured in a two-electrode cell, then C_{el} represents the sum of the capacitance of the working and counter electrodes,

$$\frac{1}{C_{el}} = \frac{1}{C_{WE}} + \frac{1}{C_{CE}}, \quad (4.3)$$

and R_s is the solution resistance between these electrodes. When we are interested in the impedance of the working electrode only, the surface area and, consequently, capacitance of the CE must be much larger than that of the WE because its capacitance in Eq. (4.3) must be negligible.

4.2 Impedance in Presence of Redox Process in Semi-infinite Linear Diffusion: Determination of Parameters

4.2.1 General Case

In the presence of redox species in solution, an electrochemical process involving the transfer of electrons between the electrode and species in solution may take place at some potentials. The electrical equivalent circuit in such a case contains the

faradaic impedance, Z_f , in parallel with the electrode capacitance, Fig. 4.1b. The electrochemical reaction taking place at the electrode surface is



The dc current in such a case is described by the current-potential equation [17]

$$i = nF[k_b C_R(0) - k_f C_O(0)], \quad (4.5)$$

where i is the current density, n is the number of electrons exchanged in the process, $C_O(0)$ and $C_R(0)$ are the surface concentrations of the Ox and Red species, respectively, and k_f and k_b are the potential dependent heterogeneous rate constants of the forward (reduction) and backward (oxidation) processes:

$$k_f = k^0 \exp[-\alpha n f (E - E^0)], \quad (4.6)$$

$$k_b = k^0 \exp[(1 - \alpha) n f (E - E^0)]. \quad (4.7)$$

E^0 is the standard potential of the redox process, α is the transfer coefficient, k^0 is the heterogeneous rate constant at the standard potential in centimeters per second, $f = F/RT$, F is the Faraday constant, R is the gas constant, and T is the absolute temperature in Kelvin. In Eq. (4.5) the oxidation current was taken as positive. To solve problems involving diffusion, one should solve Fick's second law for Ox and Red species. This equation contains partial derivatives versus time, t , and distance from the electrode surface, x . In the case of linear semi-infinite diffusion it is [144]

$$\frac{\partial C_i(x, t)}{\partial t} = D_i \frac{\partial^2 C_i(x, t)}{\partial x^2} \quad (4.8)$$

as the concentrations are functions of the distance from the electrode surface, x , and time, t .

Let us suppose that a small alternating voltage perturbation is applied to the working electrode around a constant dc potential, E_{dc} :

$$E = E_{dc} + \Delta E = E_{dc} + E_0 \cos(\omega t), \quad (4.9)$$

where E_0 is the amplitude of the ac signal. To simplify the mathematical development, we will suppose that ΔE is expressed as a rotating vector of length E_0 as in Eq. (2.123), assuming that the initial phase shift is zero:

$$E = E_{dc} + \Delta E = E_{dc} + \tilde{E} \exp(j\omega t) = E_{dc} + E_0 \exp(j\omega t). \quad (4.10)$$

Such a perturbation causes oscillation of the current and concentrations:

$$i = i_{dc} + \Delta i, \quad (4.11)$$

$$C_O = C_{O,dc} + \Delta C_O \text{ and } C_R = C_{R,dc} + \Delta C_R, \quad (4.12)$$

and

$$\begin{aligned} \Delta E &= \tilde{E} \exp(j\omega t), \\ \Delta i &= \tilde{i} \exp(j\omega t), \\ \Delta C_O &= \tilde{C}_O \exp(j\omega t), \\ \Delta C_R &= \tilde{C}_R \exp(j\omega t), \end{aligned} \quad (4.13)$$

where \tilde{E} , \tilde{i} , \tilde{C}_O , and \tilde{C}_R are the phasors of the ac potential, current, and concentrations containing a complex phase shift, Eq. (2.124):

$$\begin{aligned} \tilde{E} &= E_0 \exp(j\phi_E), \\ \tilde{i} &= i_0 \exp(j\phi_i), \\ \tilde{C}_O &= C_{O,0} \exp(j\phi_{C_{O,0}}), \\ \tilde{C}_R &= C_{R,0} \exp(j\phi_{C_{R,0}}), \end{aligned} \quad (4.14)$$

where the index 0 indicates the amplitude of the oscillating parameter and ϕ_k is a phase shift of parameter k . In practice, the initial phase shift of the potential perturbation is set to zero, $\phi_E = 0$, and all other phase shifts are calculated with respect to the applied voltage. Because the current in Eq. (4.5) is a function of the potential and concentration, it can be represented as an infinite Maclaren series:

$$\begin{aligned} \Delta i &= \left(\frac{\partial i}{\partial E} \right) \Delta E + \left(\frac{\partial i}{\partial C_O} \right) \Delta C_O + \left(\frac{\partial i}{\partial C_R} \right) \Delta C_R \\ &+ \frac{1}{2} \left(\frac{\partial^2 i}{\partial E^2} \right) (\Delta E)^2 + \frac{1}{2} \left(\frac{\partial^2 i}{\partial C_O^2} \right) (\Delta C_O)^2 + \frac{1}{2} \left(\frac{\partial^2 i}{\partial C_R^2} \right) (\Delta C_R)^2 \\ &+ \left(\frac{\partial^2 i}{\partial E \partial C_O} \right) \Delta E \Delta C_O + \left(\frac{\partial^2 i}{\partial E \partial C_R} \right) \Delta E \Delta C_R + \left(\frac{\partial^2 i}{\partial C_O \partial C_R} \right) \Delta C_O \Delta C_R + \dots \end{aligned} \quad (4.15)$$

The partial derivatives can be calculated from Eq. (4.5). It is obvious that this equation is linear with respect to concentrations because all second and higher derivatives with respect to concentration are equal to zero. It should be stressed that the dependence of a current on the potential is strongly nonlinear; however, it can be linearized for very small potential perturbations. In such a case, only linear terms might be kept, and Eq. (4.15) becomes

$$\Delta i = \left(\frac{\partial i}{\partial E} \right) \Delta E + \left(\frac{\partial i}{\partial C_O} \right) \Delta C_O + \left(\frac{\partial i}{\partial C_R} \right) \Delta C_R. \quad (4.16)$$

This linearization is the fundamental property of EIS, and small amplitudes $\leq 8/n$ mV peak-to-peak [32] should be used; otherwise, higher harmonics will appear in the response. In the present and following chapters, a linear impedance approach will be presented. A discussion of higher harmonics will take place in Chap. 15. In practice, an amplitude of ~ 5 mV is used. It should be stressed that impedance programs usually display root-mean-square (rms) values, that is, the absolute amplitude is divided by $\sqrt{2}$. This means that to obtain an amplitude of 5 mV, one should configure the data acquisition program to 3.5 mV rms. Setting the rms amplitude to 5 mV indicates that the absolute amplitude is $5\sqrt{2} = 7.1$ mV or 14.2 mV peak to peak.

The simplest approach to diffusion/kinetics problems is to solve Fick's equation for oscillating variables only. First, the stationary conditions must be solved, that is, the derivatives in Eq. (4.16) must be evaluated in the steady state:

$$\frac{\partial i}{\partial E} = n^2 F f [\alpha k_f C_O(0) + (1 - \alpha) k_b C_R(0)], \quad (4.17)$$

$$\frac{\partial i}{\partial C_O} = -n F k_f \text{ and } \frac{\partial i}{\partial C_R} = n F k_b. \quad (4.18)$$

Now, Fick's equation must be written for ΔC_i :

$$\frac{\partial \Delta C_O}{\partial t} = D_O \frac{\partial^2 \Delta C_O}{\partial x^2} \text{ and } \frac{\partial \Delta C_R}{\partial t} = D_R \frac{\partial^2 \Delta C_R}{\partial x^2}. \quad (4.19)$$

Substituting ΔC_i from Eq. (4.13) one obtains

$$\frac{\partial \Delta C_O}{\partial t} = j\omega \tilde{C}_O \exp(j\omega t), \quad (4.20)$$

$$j\omega \tilde{C}_O \exp(j\omega t) = D_O \frac{\partial^2 \tilde{C}_O}{\partial x^2} \exp(j\omega t). \quad (4.21)$$

Simplification leads to a system of ordinary differential equations for phasors:

$$j\omega \tilde{C}_O = D_O \frac{d^2 \tilde{C}_O}{dx^2} \text{ and } j\omega \tilde{C}_R = \frac{d^2 \tilde{C}_R}{dx^2}, \quad (4.22)$$

with the following boundary conditions:

$$x = 0 \quad \frac{d\tilde{C}_O}{dx} = -\frac{\tilde{i}}{nFD_O} \text{ and } \frac{d\tilde{C}_R}{dx} = \frac{\tilde{i}}{nFD_R}, \quad (4.23)$$

$$D_O \frac{d\tilde{C}_O}{dx} + D_R \frac{d\tilde{C}_R}{dx} = 0, \quad (4.24)$$

$$x \rightarrow \infty \quad \tilde{C}_O \rightarrow 0 \text{ and } \tilde{C}_R \rightarrow 0. \quad (4.25)$$

The first condition at the surface relates the concentration gradients to the current. This is the continuity of fluxes at the electrode surface, and it states that Ox is changed to Red according to Eq. (4.24), which is the law of conservation of matter. Far from the electrode at $x \rightarrow \infty$ there are no oscillations of concentrations of redox species and the phasors become zero.

Equation (4.22) may be rearranged into simpler forms:

$$\frac{d^2\tilde{C}_O}{dx^2} = \left(\frac{j\omega}{D_O}\right)\tilde{C}_O = s_O^2\tilde{C}_O \text{ and } \frac{d^2\tilde{C}_R}{dx^2} = \left(\frac{j\omega}{D_R}\right)\tilde{C}_R = s_R^2\tilde{C}_R, \quad (4.26)$$

where

$$s_O = \sqrt{\frac{j\omega}{D_O}} \text{ and } s_R = \sqrt{\frac{j\omega}{D_R}}. \quad (4.27)$$

Equation (4.26) has general solutions

$$\begin{aligned} \tilde{C}_O(x) &= A \exp(-s_O x) + B \exp(s_O x) \\ \text{and } \tilde{C}_R(x) &= A' \exp(-s_R x) + B' \exp(s_R x). \end{aligned} \quad (4.28)$$

For semi-infinite linear diffusion parameters B and B' are equal to zero from the conditions expressed by Eq. (4.25). The other two constants, A and A' , can be determined from the conditions at the electrode surface:

$$\frac{d\tilde{C}_O}{dx} = -s_O A = -\frac{\tilde{i}}{nFD_O} \text{ and } \frac{d\tilde{C}_R}{dx} = -s_R A' = \frac{\tilde{i}}{nFD_R}, \quad (4.29)$$

and together with condition Eq. (4.24) these parameters are determined:

$$A = \tilde{C}_O(0) = \frac{\tilde{i}}{nF\sqrt{j\omega D_O}} \text{ and } A' = \tilde{C}_R(0) = -\frac{\tilde{i}}{nF\sqrt{j\omega D_R}}, \quad (4.30)$$

and the solutions of Eq. (4.28) are

$$\tilde{C}_O(x) = \frac{\tilde{i}}{nF\sqrt{j\omega D_O}} \exp(-s_O x) \quad \text{and} \quad \tilde{C}_R(x) = -\frac{\tilde{i}}{nF\sqrt{j\omega D_R}} \exp(-s_R x). \quad (4.31)$$

Finally, substitution into Eq. (4.16) using Eqs. (4.17) and (4.18) gives the relation between the current and the potential phasors:

$$\tilde{i} = \frac{n^2 F^2}{RT} [\alpha k_f C_O(0) + (1 - \alpha) k_b C_R(0)] \tilde{E} - \frac{\tilde{i} k_f}{\sqrt{j\omega D_O}} - \frac{\tilde{i} k_b}{\sqrt{j\omega D_R}}, \quad (4.32)$$

from which the faradaic impedance, $\hat{Z}_f = \tilde{E}/\tilde{i}$, may be calculated:

$$\begin{aligned} \hat{Z}_f = & \frac{RT}{n^2 F^2} \frac{1}{\alpha k_f C_O(0) + (1 - \alpha) k_b C_R(0)} \\ & + \frac{RT}{n^2 F^2} \frac{\frac{k_f}{\sqrt{j\omega D_O}} + \frac{k_b}{\sqrt{j\omega D_R}}}{\alpha k_f C_O(0) + (1 - \alpha) k_b C_R(0)}. \end{aligned} \quad (4.33)$$

The faradaic impedance consists of one real part arising from the derivative Eq. (4.17) and is called the charge transfer resistance, R_{ct} , and the second part containing $j^{-1/2}$ is called the mass transfer impedance, \hat{Z}_w , which, in the case of semi-infinite linear diffusion, is called the Warburg impedance and is composed of two parts: $\hat{Z}_{w,O}$ and $\hat{Z}_{w,R}$, [8, 30, 145]

$$\hat{Z}_f = R_{ct} + \hat{Z}_w = R_{ct} + \hat{Z}_{w,O} + \hat{Z}_{w,R}, \quad (4.34)$$

where

$$R_{ct} = \frac{RT}{n^2 F^2} \frac{1}{\alpha k_f C_O(0) + (1 - \alpha) k_b C_R(0)}, \quad (4.35)$$

$$\begin{aligned} \hat{Z}_{w,O} = & \frac{RT}{n^2 F^2} \frac{k_f}{\sqrt{j\omega D_O} [\alpha k_f C_O(0) + (1 - \alpha) k_b C_R(0)]} \\ = & \frac{RT}{n^2 F^2} \frac{1}{\sqrt{j\omega D_O} \{ \alpha C_O(0) + (1 - \alpha) C_R(0) \exp[nf(E - E^0)] \}}, \end{aligned} \quad (4.36)$$

$$\hat{Z}_{w,R} = \frac{RT}{n^2 F^2} \frac{\exp[nf(E - E^0)]}{\sqrt{j\omega D_R} \{ \alpha C_O(0) + (1 - \alpha) C_R(0) \exp[nf(E - E^0)] \}}. \quad (4.37)$$

It is obvious that the charge transfer resistance depends on the reaction kinetics; it is inversely proportional to the heterogeneous rate constants, and the mass transfer impedance is independent of the kinetics. From Eq. (2.57) both $1/j = \exp(-j\pi/2)$ and

$$\frac{1}{\sqrt{j}} = \exp\left(-\frac{j\pi}{4}\right) = \cos\left(\frac{\pi}{4}\right) - j \sin\left(\frac{\pi}{4}\right) = \frac{1}{\sqrt{2}}(1 - j), \quad (4.38)$$

and it follows that the mass transfer impedance contains two parts: one real and one imaginary of the same magnitude. To determine the faradaic impedance, the surface concentrations must be known. The simplest case is when one is working with known bulk concentrations C_O^* and C_R^* at the equilibrium potential (dc current equal to zero), where $C_O(0) = C_O^*$ and $C_R(0) = C_R^*$. In the presence of a dc current the surface concentrations can be estimated from the dc current [17]:

$$C_O(0) = 1 - \frac{i}{i_{\text{lim}}} \text{ and } C_R(0) = \frac{i}{i_{\text{lim}}}. \quad (4.39)$$

4.2.2 DC Reversible Case

Equations of the faradaic impedance can be simplified assuming that the surface concentrations follow the Nernst law that is they correspond to the electro-chemical equilibrium after staying at a constant potential for a certain time while the ac concentrations corresponding to higher frequencies or shorter times are out of equilibrium. Using the Nernst equation:

$$\frac{C_O(0)}{C_R(0)} = \exp[nf(E - E^0)] \quad (4.40)$$

Equations (4.35), (4.36) and (4.37) can be simplified. The Warburg impedance becomes

$$\begin{aligned} \hat{Z}_W &= \hat{Z}_{W,O} + \hat{Z}_{W,R} = \frac{RT}{n^2 F^2 \sqrt{j\omega}} \left(\frac{1}{\sqrt{D_O C_O(0)}} + \frac{1}{\sqrt{D_R C_R(0)}} \right) \\ &= \frac{\sigma'}{\sqrt{j\omega}} = \frac{\sqrt{2}}{\sqrt{j}} \frac{\sigma}{\sqrt{\omega}} = \frac{\sigma}{\sqrt{\omega}} (1 - j), \end{aligned} \quad (4.41)$$

where $\sigma' = \sqrt{2}\sigma$ is the mass transfer coefficient equal to the sum of the contributions of the Ox and Red forms:

$$\sigma' = \sigma'_O + \sigma'_R = \frac{RT}{n^2 F^2} \left[\frac{1}{\sqrt{D_O} C_O(0)} + \frac{1}{\sqrt{D_R} C_R(0)} \right]. \quad (4.42)$$

In the particular case where initially only Ox species are present in the solution with bulk concentration C_O^* , the surface concentrations may be calculated as functions of the electrode potential [17]:

$$C_O(0) = C_O^* \frac{\xi \theta}{1 + \xi \theta} \text{ and } C_R(0) = C_O^* \frac{\xi}{1 + \xi \theta}, \quad (4.43)$$

where

$$\begin{aligned} \xi &= (D_O/D_R)^{1/2}, \theta = \exp \left[nf(E - E^{0'}) \right], \\ \text{and } \theta \xi &= \exp \left[nf(E - E_{1/2}) \right], \end{aligned} \quad (4.44)$$

and $E_{1/2}$ is the reversible half-wave potential [17]:

$$E_{1/2} = E^{0'} + \frac{RT}{nF} \ln \sqrt{\frac{D_R}{D_O}}. \quad (4.45)$$

Then, the mass transfer coefficient becomes

$$\sigma' = \frac{RT}{n^2 F^2 C_O^* \sqrt{D_O}} \frac{[1 + \exp[nf(E - E_{1/2})]]^2}{\exp[nf(E - E_{1/2})]} \quad (4.46)$$

or, introducing the function $\cosh(x)$,

$$\cosh(x) = \frac{e^x + e^{-x}}{2} \quad (4.47)$$

one obtains

$$\sigma' = \frac{4RT}{n^2 F^2 C_O^* \sqrt{D_O}} \cosh^2 \left[\frac{nf(E - E_{1/2})}{2} \right] \quad (4.48)$$

and the Warburg impedance

$$\hat{Z}_w = \frac{\sigma'}{\sqrt{j\omega}} = \frac{\sigma}{\sqrt{\omega}} - j \frac{\sigma}{\sqrt{\omega}} = \frac{4RT}{n^2 F^2 C_O^* \sqrt{j\omega D_O}} \cosh^2 \left[\frac{nf(E - E_{1/2})}{2} \right], \quad (4.49)$$

with

$$\sigma = \frac{4RT}{n^2 F^2 C_O^* \sqrt{2D_O}} \cosh^2 \left[\frac{nf(E - E_{1/2})}{2} \right]. \quad (4.50)$$

The Warburg impedance is a function of $\omega^{-1/2}$ and cannot be represented as a simple function of R , C , and L parameters. It contains real and imaginary parts of the same value, with the real part positive and the imaginary negative. Its phase angle is $\varphi = \text{atan}(Z''/Z') = \text{atan}(-1) = -\pi/2 = -45^\circ$. It is inversely proportional to the bulk concentration and depends on the electrode potential, but it is independent of any kinetic parameters. It can be shown that \hat{Z}_w has a minimum at $E = E_{1/2}$.

Similarly, under the same conditions of initial concentrations, the charge transfer resistance can also be presented:

$$\begin{aligned} R_{ct} &= \frac{RT}{n^2 F^2 k_b C_O^*} \frac{1 + \exp[nf(E - E_{1/2})]}{\xi} = \\ &= \frac{RT}{n^2 F^2 k^0 C_O^*} \frac{1 + \exp[nf(E - E_{1/2})]}{\xi^\alpha \exp[(1 - \alpha)nf(E - E_{1/2})]}, \end{aligned} \quad (4.51)$$

and it has a minimum at

$$E_s = E_{1/2} + \frac{RT}{nF} \ln \frac{1 - \alpha}{\alpha} \quad (4.52)$$

and only when $\alpha = 0.5$ $E_s = E_{1/2}$. The charge transfer resistance is inversely proportional to the bulk concentration and the rate constant.

The corresponding electrical equivalent circuit, a so-called Randles circuit, is shown in Fig. 4.2. The same figure shows plots of the Warburg impedance, Eq. (4.34), dotted line, and the total impedance including solution resistance and double layer capacitance. The mass transfer impedance starts at R_{ct} and continues as a straight line at 45° . The total impedance displays a semicircle due to coupling of the charge transfer resistance with the double layer capacitance at high frequencies and a straight line due to \hat{Z}_w at low frequencies. The Bode magnitude plot displays a step from R_s at the highest frequencies to $R_s + R_{ct}$ at intermediate frequencies (corresponding to the semicircle on the complex plane plot) and a straight line at 45° at low frequencies. The Bode phase angle plot shows a peak corresponding to the semicircle at higher frequencies and a line going asymptotically to 45° at low frequencies. It is important to note that the kinetic effect appears at higher frequencies and mass transfer effects at low frequencies. The semicircle, which is well visible in Fig. 4.2, is not always clearly visible. It depends on the relative values of the kinetic and mass transfer parameters. The effect of the concentration is

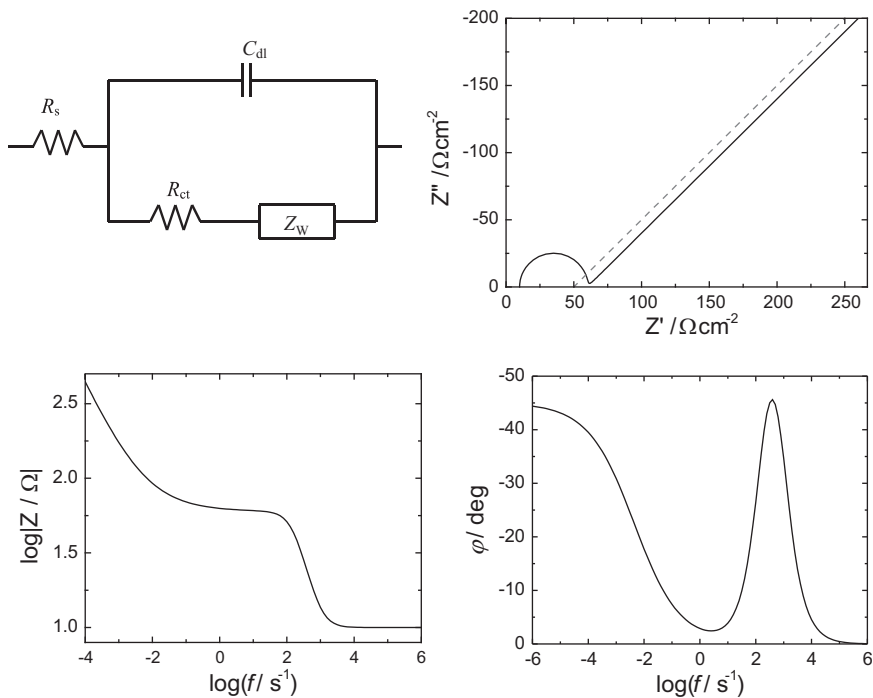


Fig. 4.2 Complex plane and Bode plots for redox system with diffusion; $R_s = 10 \Omega$, $C_{dl} = 25 \mu F$, $R_{ct} = 50 \Omega$, $\sigma' = 10 \Omega s^{-1/2}$; dotted line – Warburg impedance

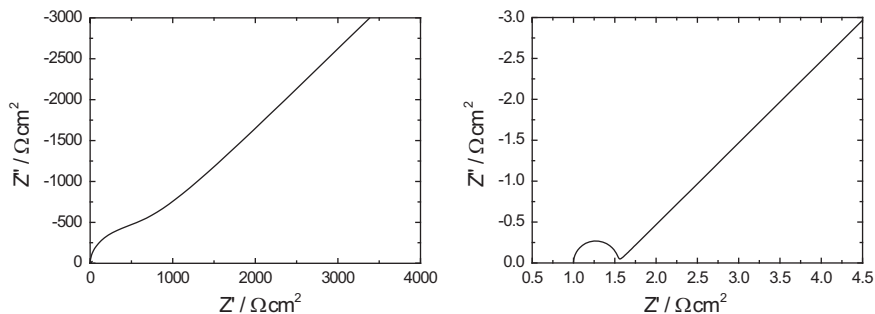
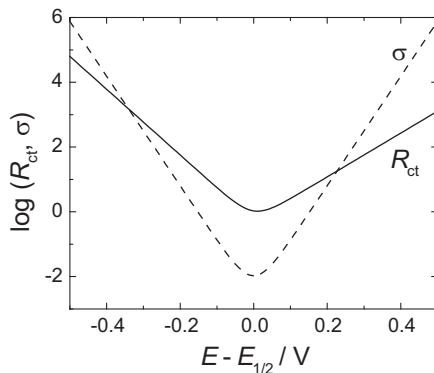


Fig. 4.3 Complex plane plots for redox system with diffusion; $k^0 = 0.01 \text{ cm s}^{-1}$, $D_o = 10^{-5} \text{ cm}^2 \text{ s}^{-1}$, $R_s = 1 \Omega$, at $E = E_{1/2}$, concentrations C_o^* : left 10^{-4} M , right 0.1 M

displayed in Fig. 4.3 for the same kinetics of the electrode process. From Eqs. (4.49) and (4.51) it is obvious that both \hat{Z}_W and R_{ct} depend on the concentration of electroactive species. At low concentrations the semicircle overlaps with the diffusion while at higher concentrations both processes are well separated.

Fig. 4.4 Dependence of parameters R_{ct} and σ on potential for $C_O^* = 0.1$ M, $k^0 = 0.01$ cm s⁻¹, $\alpha = 0.4$, and $D_O = 10^{-5}$ cm² s⁻¹



However, complex nonlinear least-squares (CNLS) approximation can recover both kinetic and mass transfer parameters in this case. For faster processes this might be difficult [146].

The dependence of the kinetic parameter R_{ct} and mass transfer coefficient σ on the potential is shown in Fig. 4.4. The logarithm of the mass transfer coefficient is symmetrical around and has a minimum exactly at $E_{1/2}$, and the slopes are $dE/d\ln\sigma = \pm RT/nF$. The minimum of the charge transfer resistance is at the potential described by Eq. (4.52). If the process is not symmetrical, then the slopes of the cathodic and anodic branches of $\log R_{ct}$ are different: $dE/d\ln R_{ct} = -RT/\alpha nF$ and $dE/d\ln R_{ct} = RT/(1-\alpha)nF$.

VanderNoot [147] studied the case of poorly separated kinetic and diffusional phenomena. He found that the kinetic information could be extracted from the experimental impedances when the ratio of the kinetic, $\tau_k = R_{ct}C_{dl}$, and diffusional, $\tau_d = R_{ct}^2/(2\sigma)^2$ time constants, $\tau_k/\tau_d = 2\sigma^2 C_{dl}/R_{ct}$, was lower than 30.

The general kinetic-diffusional model has two limiting cases:

1. Diffusional mass transfer can be neglected; this is the case with large concentrations of redox species and low currents;
2. Kinetics may be neglected; this is observed for very fast electrode processes, i.e., very small R_{ct} .

Examples of these two cases are displayed in Fig. 4.5. Reduction of Hg_2^{2+} is a very fast reaction, with R_{ct} very small, and only a straight line at 45° is visible in the whole frequency range. On the other hand, the couple $Zn^{2+}/Zn(Hg)$ is quite slow and almost a full semicircle is observed, only at the lowest frequencies is the beginning of the mass transfer impedance visible.

The time dependence of impedances measured at a constant potential was also studied [29, 30, 149].

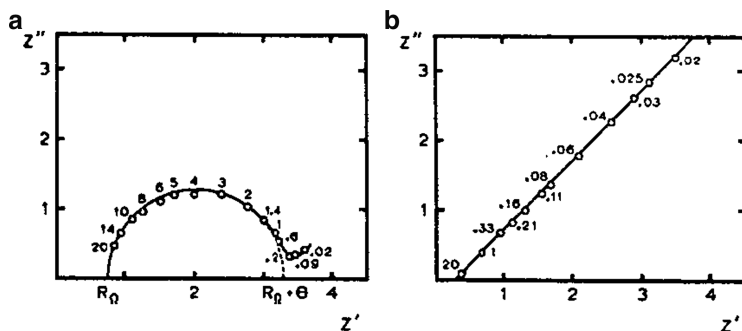


Fig. 4.5 Complex plane plots for (a) $\text{Zn}^{2+}/\text{Zn}(\text{Hg})$ and (b) $\text{Hg}_2^{2+}/\text{Hg}$ illustrating very slow and very fast electrodes (impedances are in Ω , Z'' should be negative) (From Ref. [148], Copyright Wiley-VCH Verlag GmbH & Co. KGaA. Reproduced with permission)

4.3 Analysis of Impedance in the Case of Semi-infinite Diffusion

The impedances acquired in the case of processes controlled by diffusion and kinetics of the electrode process is described by the Randles circuit (Fig. 4.2). They were analyzed by several different methods.

4.3.1 Randles Analysis

Historically, impedances were measured on dropping mercury or amalgam electrodes using an ac bridge [9, 10, 24, 30, 39] and registered as functions of the electrode potential. Information on the electrode process was included in the faradaic impedance. It may be obtained by subtracting the solution resistance and double layer capacitance from the total impedance, \hat{Z}_t :

$$\frac{1}{\hat{Z}_f} = \hat{Y}_f = \frac{1}{\hat{Z}_t - R_s} - j\omega C_{dl}. \quad (4.53)$$

R_s and C_{dl} can be obtained from the measurement in the presence of the supporting electrolyte only if the distance between the Luggin capillary and the working electrode is the same. One can also determine these parameters in the presence of the electroactive species: R_s at high frequencies and C_{dl} by interpolation of the \hat{Y}_t plot versus the potential before and after the faradaic peak. An example of such an interpolation is shown in Fig. 4.6, where the in-phase (real part) ac current proportional to the real part of the total admittance is displayed for Cd^{2+} reduction in dimethylsulfoxide (DMSO) [150]. Similar measurements of the out-of-phase (imaginary) part make it possible to determine the double layer capacitance in the presence of the redox reaction.

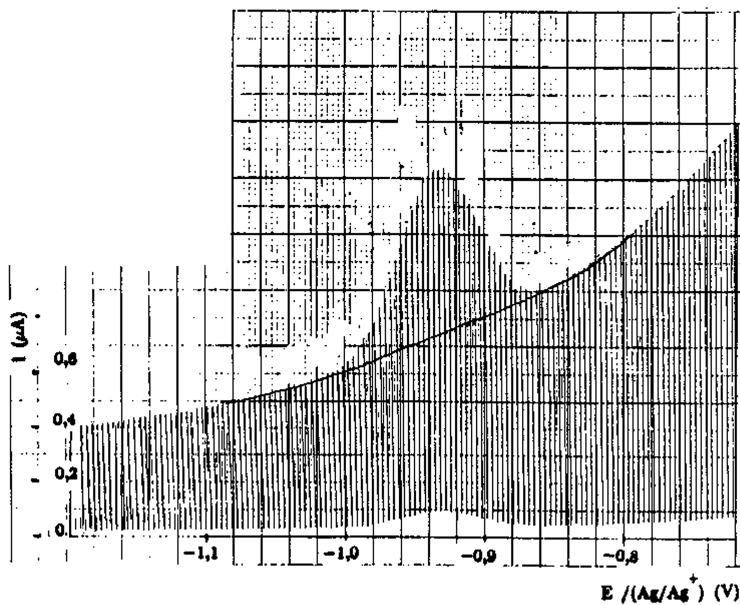


Fig. 4.6 Dependence of in-phase current, proportional to real part of total electrode admittance for Cd^{2+} reduction at Hg dropping electrode in dimethyl-sulfoxide (From Ref. [150] with permission of author)

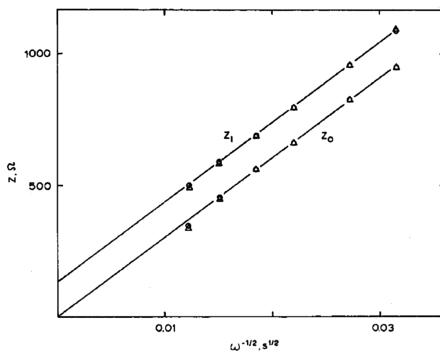


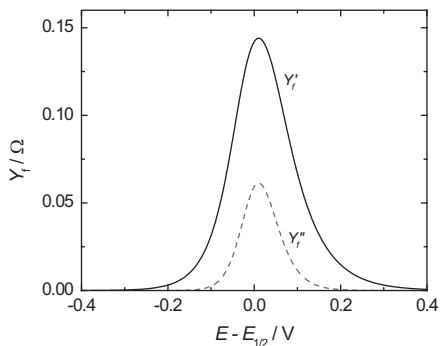
Fig. 4.7 Randles plot of faradaic impedance for reduction of nitromesitylene in dimethyl-formamide on a dropping mercury electrode, Z_0 – out-of-phase (imaginary), Z_1 in-phase (real) impedance (Reprinted with permission Ref. [151]. Copyright 1978 American Chemical Society)

The faradaic impedance

$$\hat{Z}_f = \left(R_{ct} + \frac{\sigma}{\sqrt{\omega}} \right) - j \left(\frac{\sigma}{\sqrt{\omega}} \right) \quad (4.54)$$

contains real and imaginary parts. The plot of the real and imaginary parts versus $\omega^{-1/2}$ presents straight lines with the same slopes, and the origin of the real part

Fig. 4.8 Dependence of real and imaginary faradaic admittances on electrode potential for $\alpha = 0.4$



gives R_{ct} . An example of such plots is shown in Fig. 4.7. Such an analysis must be performed at different potentials and R_{ct} and σ plotted as functions of the potential. Kinetic information is contained in R_{ct} , Eq. (4.51). Concentration of the electroactive species and the electrode surface area may be eliminated if the ratio of σ/R_{ct} is calculated:

$$\frac{\sigma}{R_{ct}} \frac{\exp[nf[E - E_{1/2}]]}{1 + \exp[nf[E - E_{1/2}]]} = \frac{\xi k_b}{\sqrt{2D_0}}. \quad (4.55)$$

Moreover, at the reversible half-wave potential this ratio becomes

$$\left(\frac{\sigma}{R_{ct}} \right)_{E_{1/2}} = \frac{2\xi^\alpha}{\sqrt{2D_0}} k^0; \quad (4.56)$$

taking into account the relation between k_b and $E_{1/2}$:

$$k_b = k^0 e^{(1-\alpha)nf(E-E_{1/2})} \xi^{\alpha-1}, \quad (4.57)$$

which allows for a quick assessment of k^0 .

4.3.2 De Levie-Husovsky Analysis

De Levie and Husovsky [152] proposed another method based on the analysis of faradaic admittances:

$$\hat{Y}_f = \frac{1}{\hat{Z}_t - R_s} - j\omega C_{dl}. \quad (4.58)$$

An example of the dependence of the real and imaginary faradaic admittances on the electrode potential is displayed in Fig. 4.8.

The ratio of the imaginary to real faradaic admittance is determined as follows:

$$\frac{Y''_f}{Y'_f} = \frac{\xi}{1 + \xi}, \quad (4.59)$$

where

$$\begin{aligned} \xi &= \frac{Y''_f}{Y'_f - Y''_f} = \frac{\sigma}{\sqrt{2\omega R_{ct}}} = \frac{k_f}{\sqrt{2\omega D_O}} + \frac{k_b}{\sqrt{2\omega D_R}} \\ &= \frac{k_f}{\sqrt{2\omega D_O}} (1 + \exp[nf(E - E_{1/2})]). \end{aligned} \quad (4.60)$$

The plot of $\log [\zeta / \{1 + \exp [nf(E - E_{1/2})]\}] = \log (k_f / \sqrt{2\omega D_O})$ versus the potential allows for the determination of the rate constant.

4.3.3 Analysis of $\cot \varphi$

Another type of analysis is based on the determination of the phase angle, φ , of the faradaic impedance. From Eq. (4.54) the cotangent of the phase angle,

$$\cot \varphi = \frac{Z'_f}{Z''_f} = 1 + \frac{R_{ct}}{\sigma} \omega^{1/2}, \quad (4.61)$$

is a linear function of $\omega^{1/2}$ with an origin of one. After substitution the definitions of R_{ct} and σ , Eq. (4.61), become

$$\cot \varphi = 1 + \frac{\sqrt{2} D_O^{(1-\alpha)/2} D_R^{\alpha/2}}{k^0 \exp[(1-\alpha)f(E - E_{1/2})] \{1 + \exp[-nf(E - E_{1/2})]\}} \omega^{1/2}. \quad (4.62)$$

An example of the dependence of $\cot \varphi$ on the potential and frequency is shown in Fig. 4.9. Further, at each potential a plot of $\cot \varphi$ versus $\omega^{1/2}$ is constructed (Fig. 4.10). The maximum of the phase angle is described as

$$[\cot \varphi]_{\max} = 1 + \frac{(2 D_O^{1-\alpha} D_R^{\alpha})^{1/2}}{k^0 \left[\left(\frac{\alpha}{\beta} \right)^{-\alpha} + \left(\frac{\alpha}{\beta} \right)^{\beta} \right]} \omega^{1/2} \quad (4.63)$$

Fig. 4.9 Dependence of $\cot \varphi$ on potential for reduction of TiCl_4 in solution containing $\text{H}_2\text{C}_2\text{O}_4$ measured at different frequencies (Reprinted with permission from Ref. [153]. Copyright 1963 American Chemical Society)

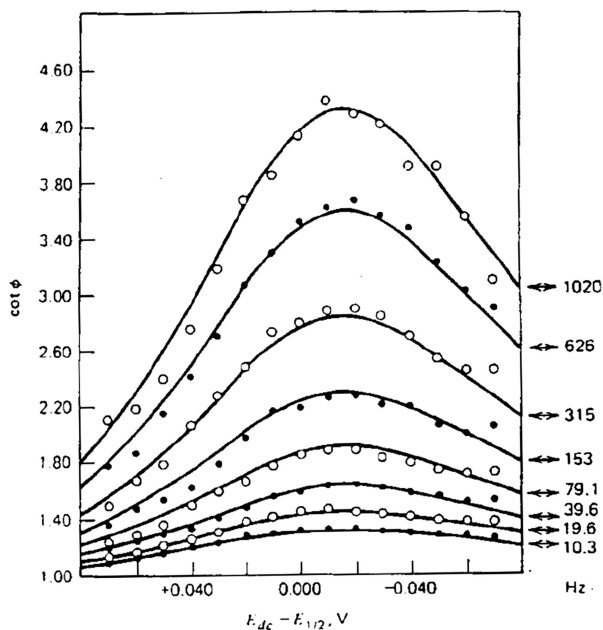
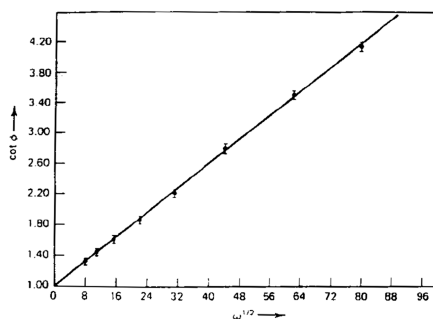


Fig. 4.10 Dependence of $\cot \varphi$ versus $\omega^{1/2}$ for TiCl_4 reduction in $\text{H}_2\text{C}_2\text{O}_4$ (Reprinted with permission from Ref. [153]. Copyright 1963 American Chemical Society)



or, at the half-wave potential,

$$[\cot \varphi]_{E_{1/2}} = 1 + \left(\frac{D_O^{1-\alpha} D_R^\alpha}{2} \right)^{1/2} \frac{\omega^{1/2}}{k^0}. \quad (4.64)$$

Such an analysis gives easy access to the kinetics of the electrode process.

4.3.4 Complex Nonlinear Least-Squares Analysis

Presently, the most often used analysis is based on the complex nonlinear least-squares approximation of the impedance data acquired at a constant potential. The total impedance may be separated into the real and imaginary parts and fitted to the Randles model:

$$\begin{aligned}\hat{Z}_t &= R_s + \frac{1}{\frac{1}{R_{ct}} + j\omega C_{dl}} = \\ &= R_s + \frac{R_{ct} + \sigma\omega^{-1/2}}{(\sigma\omega^{1/2}C_{dl} + 1)^2 + \omega^2 C_{dl}^2 (R_{ct} + \sigma\omega^{-1/2})^2} + \\ &\quad -j \frac{\omega C_{dl} (R_{ct} + \sigma\omega^{-1/2})^2 + \sigma^2 C_{dl} + \sigma\omega^{-1/2}}{(\sigma\omega^{1/2}C_{dl} + 1)^2 + \omega^2 C_{dl}^2 (R_{ct} + \sigma\omega^{-1/2})^2}.\end{aligned}\quad (4.65)$$

Of course, using higher-level languages such as Fortran or Maple/Mathematica it is not necessary to separate \hat{Z}_t into real and imaginary parts because this is automatically calculated in the program. The use of approximation packages such as ZView allows one to carry out the fitting by constructing an appropriate model and avoiding the mathematical complexities. Exercises present a construction of such models in ZView and Maple.

4.4 Finite-Length Linear Diffusion

In practical applications, very often diffusion is not semi-infinite. Such finite-length linear diffusion is observed, for example, for internal diffusion into mercury film deposited on a planar electrode, in deposited conducting polymers, for hydrogen diffusion into thin films or membranes of Pd or other hydrogen absorbing materials, or for a rotating disk electrode where the diffusion layer corresponds to the layer thickness. There are two cases of finite-length diffusion displayed Fig. 4.11:

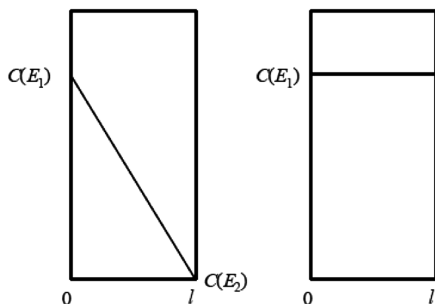


Fig. 4.11 Concentration profiles in two cases of finite-length linear diffusion: *left* – transmissive boundary, *right* – reflective boundary

- a. If species penetrate the layer at $x = 0$ and leave at the other end at $x = l$, this is a case of a transmissive boundary. Such a case is observed when hydrogen ions are reduced at the entry plane and hydrogen is oxidized and leaves the membrane at the exit plane. In this case, a steady-state concentration gradient exists in the membrane.
- b. When no charge transfer is possible at $x = l$, this plane is impermeable, and it is called a reflective boundary. Such a case is observed for conductive polymers deposited on metallic surfaces or for hydrogen absorption in Pd deposited on metallic surface (Au, Pt), where further adsorption into the base metal is impossible.

4.4.1 Transmissive Boundary

The problem to be solved is described by a system of two differential equations, Eq. (4.26), with the general solution described by Eq. (4.28). Let us assume that the concentration at the exit plane is equal to zero. Four constants (A, A', B, B') must be obtained from the boundary conditions for the transmissive boundary:

$$\begin{aligned}
 x = 0 \quad \frac{d\tilde{C}_O}{dx} &= -s_O A + s_O B = -\frac{\tilde{i}}{nFD_O}, \\
 \frac{d\tilde{C}_R}{dx} &= s_R A' + s_R B' = \frac{\tilde{i}}{nFD_R}, \\
 x = l \quad \tilde{C}_O &= A \exp(-s_O l) + B \exp(s_O l) = 0, \\
 \tilde{C}_R &= A' \exp(-s_R l) + B' \exp(s_R l) = 0.
 \end{aligned} \tag{4.66}$$

These give the following constants:

$$\begin{aligned}
 A &= \frac{\tilde{i}}{nF\sqrt{j\omega D_O}} \frac{\exp(s_O l)}{\exp(s_O l) + \exp(-s_O l)}, \\
 B &= -\frac{\tilde{i}}{nF\sqrt{j\omega D_O}} \frac{\exp(-s_O l)}{\exp(s_O l) + \exp(-s_O l)}, \\
 A' &= \frac{\tilde{i}}{nF\sqrt{j\omega D_R}} \frac{\exp(s_R l)}{\exp(s_R l) + \exp(-s_R l)}, \\
 B' &= -\frac{\tilde{i}}{nF\sqrt{j\omega D_R}} \frac{\exp(s_R l)}{\exp(s_R l) + \exp(-s_R l)},
 \end{aligned} \tag{4.67}$$

from which the surface concentrations are as follows:

$$\begin{aligned}\tilde{C}_O(0) &= \frac{\tilde{i}}{nF\sqrt{j\omega D_O}} \tanh\left(\sqrt{\frac{j\omega}{D_O}}l\right), \\ \tilde{C}_R(0) &= -\frac{\tilde{i}}{nF\sqrt{j\omega D_R}} \tanh\left(\sqrt{\frac{j\omega}{D_R}}l\right).\end{aligned}\quad (4.68)$$

The Warburg impedance may be obtained, for the reversible case, from

$$\hat{Z}_w = \frac{dE}{di} = \sum_{i=O,R} \frac{dE}{dC_i} \frac{\tilde{C}_i(0)}{\tilde{i}}, \quad (4.69)$$

and the derivatives dE/dC_i are obtained from the Nernst equation:

$$\frac{dE}{dC_O} = \frac{RT}{nFC_O(0)} \quad \text{and} \quad \frac{dE}{dC_R} = -\frac{RT}{nFC_R(0)}. \quad (4.70)$$

Using these relations the mass transfer impedance is obtained:

$$\begin{aligned}\hat{Z}_w &= \frac{RT}{n^2F^2C_O(0)\sqrt{j\omega D_O}} \tanh\left(\sqrt{\frac{j\omega}{D_O}}l\right) \\ &\quad + \frac{RT}{n^2F^2C_R(0)\sqrt{j\omega D_R}} \tanh\left(\sqrt{\frac{j\omega}{D_R}}l\right).\end{aligned}\quad (4.71)$$

Assuming that the diffusion coefficients of Ox and Red are the same, \hat{Z}_w becomes

$$\hat{Z}_w = \frac{\sigma'}{\sqrt{j\omega}} \tanh\left(\sqrt{\frac{j\omega}{D}}l\right) = \frac{\sigma}{\sqrt{\omega}} \tanh\left(\sqrt{\frac{j\omega}{D}}l\right) (1-j), \quad (4.72)$$

where

$$\tanh(x) = \frac{\sinh(x)}{\cosh(x)} = \frac{e^x - e^{-x}}{e^x + e^{-x}}. \quad (4.73)$$

The complex plane plots obtained in this case are shown in Fig. 4.12. The faradaic impedance displays a straight line at 45° at high frequencies where the ac diffusion, that is, the oscillations of the concentration, are limited to the zone around the electrode and diffusion behaves in a semi-infinite linear manner. At higher frequencies oscillations of the concentrations arrive at the back wall and a

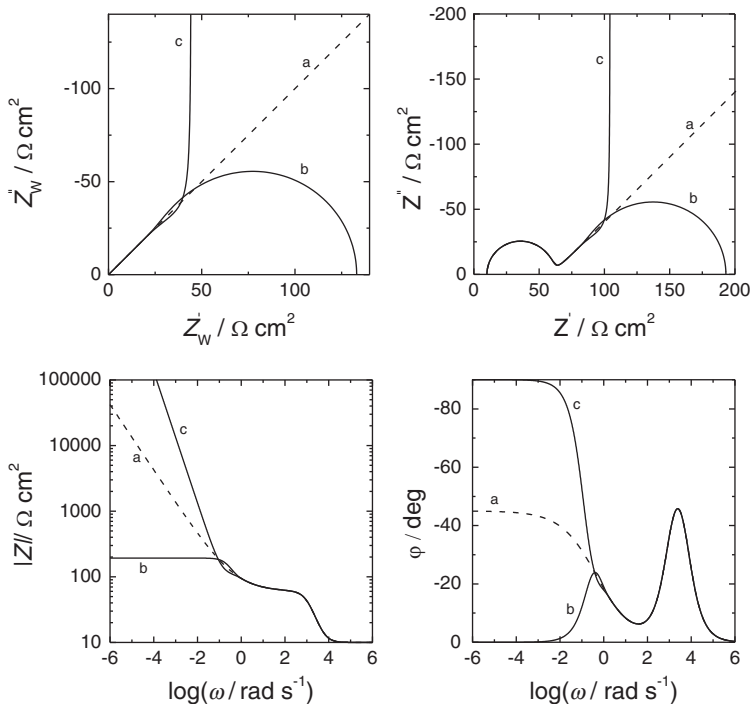


Fig. 4.12 Complex plane and Bode plots of mass transfer and total impedances for (a) semi-infinite linear, (b) transmissive, and (c) reflective boundary; $l = 0.01$ cm, other parameters used: $R_s = 10 \Omega \text{ cm}^2$, $R_{ct} = 50 \Omega \text{ cm}^2$, $C_{dl} = 20 \mu\text{F cm}^{-2}$, $C_i^* = 2 \text{ mM}$, $D_i = 10^{-5} \text{ cm}^2 \text{ s}^{-1}$

semicircle is obtained because at $\omega \rightarrow \infty$ a dc current can flow. For low values of the argument,

$$\lim_{x \rightarrow 0} \left[\frac{\tanh(x)}{x} \right] = 1, \quad (4.74)$$

it is possible to obtain the limiting value of the mass transfer impedance at zero frequency:

$$\lim_{\omega \rightarrow 0} (\hat{Z}_w) = \frac{\sigma' l}{\sqrt{D_0}} \quad (4.75)$$

and the limit of the total frequency:

$$\lim_{\omega \rightarrow 0} (\hat{Z}_t) = R_s + R_{ct} \frac{\sigma' l}{\sqrt{D_0}}. \quad (4.76)$$

Equation (4.72) is often written as

$$\hat{Z}_w = R_D \frac{\tanh \sqrt{j\omega T_D}}{\sqrt{j\omega T_D}}, \quad (4.77)$$

where

$$R_D = \frac{\sigma' l}{\sqrt{D}} \quad \text{and} \quad T_D = \frac{l^2}{D}. \quad (4.78)$$

4.4.2 Reflective Boundary

In this case, one boundary condition in Eq. (4.66) at $x = l$ must be changed:

$$x = l \quad \frac{dC_O}{dx} = 0 \quad \text{and} \quad \frac{dC_R}{dx} = 0 \quad (4.79)$$

or

$$\begin{aligned} \frac{d\tilde{C}_O}{dx} &= -s_O A \exp(-s_O l) + s_O B \exp(s_O l) = 0, \\ \frac{d\tilde{C}_R}{dx} &= -s_R A' \exp(-s_R l) + s_R B' \exp(s_R l) = 0, \end{aligned} \quad (4.80)$$

as the Ox and Red forms cannot penetrate this boundary. Determination of the constants and substitution into Eq. (4.28) gives the surface concentration phasors:

$$\begin{aligned} \tilde{C}_O(0) &= \frac{\tilde{i}}{nF\sqrt{j\omega D_O}} \coth \left(\sqrt{\frac{j\omega}{D_O}} l \right), \\ \tilde{C}_R(0) &= -\frac{\tilde{i}}{nF\sqrt{j\omega D_R}} \coth \left(\sqrt{\frac{j\omega}{D_R}} l \right). \end{aligned} \quad (4.81)$$

Then, using Eq. (4.69) the mass transfer impedance is

$$\begin{aligned} \hat{Z}_w &= \frac{RT}{n^2 F^2 C_O(0) \sqrt{j\omega D_O}} \coth \left(\sqrt{\frac{j\omega}{D_O}} l \right) \\ &\quad + \frac{RT}{n^2 F^2 C_R(0) \sqrt{j\omega D_R}} \coth \left(\sqrt{\frac{j\omega}{D_R}} l \right) \end{aligned} \quad (4.82)$$

or assuming equal diffusion coefficients:

$$\hat{Z}_W = \frac{\sigma'}{\sqrt{j\omega}} \coth \left(\sqrt{\frac{j\omega}{D}} l \right). \quad (4.83)$$

The impedance plots are shown in Fig. 4.12. The mass transfer impedance displays a straight line at 45° at high frequencies because the penetration length of the ac signal is smaller than the layer thickness and at low frequencies the imaginary part goes to infinity as the constant current cannot flow in the system. At very thin layers or low frequencies a capacitive behavior is observed. In fact, because

$$\left. \frac{\coth(x)}{x} \right|_{x \rightarrow 0} \approx \frac{1}{3} + \frac{1}{x^2} + \dots, \quad (4.84)$$

the low-frequency impedance becomes

$$\hat{Z}_W(\omega \rightarrow 0) = \frac{\sigma' l}{3\sqrt{D}} - j \frac{\sqrt{D}\sigma'}{\omega l} = R_W - j \frac{1}{\omega C_W} \quad (4.85)$$

and represents the connection between the resistance, R_W , and the pseudocapacitance, C_W , in series, where

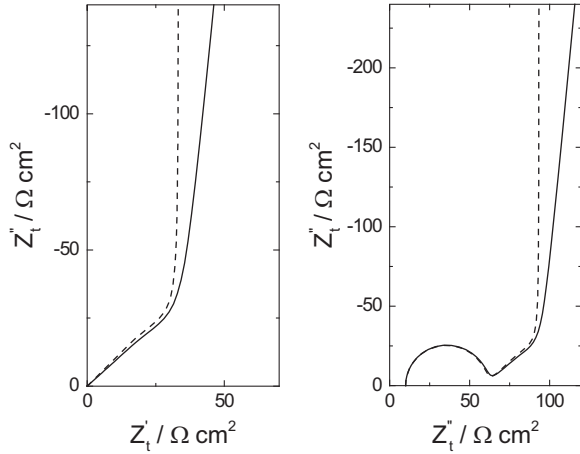
$$R_W = \frac{\sigma' l}{3\sqrt{D}} \quad \text{and} \quad C_W = \frac{l}{\sqrt{D}\sigma'}. \quad (4.86)$$

The finite-length transmissive impedance may be found in ZView as Warburg Element (short) W_s and the finite-length reflective impedance as Warburg Element (open) W_o . Examples of simulations in Mathematica are shown in files in the exercises.

4.5 Generalized Warburg Element

In practical applications of EIS it is often found that the experimental data for the finite-length diffusion cannot be approximated by Eq. (4.72) or Eq. (4.83). For example, in the case of hydrogen absorption in Pd the low-frequency reflective impedance is not strictly capacitive, or in the transmissive case the complex plane plot is slightly depressed [154–156]. In such cases one should use a so-called generalized finite-length Warburg element for transmissive

Fig. 4.13 Complex plane plots for reflective finite-length diffusion; *left* – Warburg impedance, *right* – total impedance; *dashed line* – ideal case, *continuous line* – generalized Warburg with $\phi_w = 0.94$



$$\hat{Z}_W = \frac{\sigma' l}{\sqrt{D} \left(\sqrt{\frac{j\omega}{D}} l \right)^{\phi_w}} \tanh \left(\sqrt{\frac{j\omega}{D}} l \right)^{\phi_w} \quad (4.87)$$

or for reflective

$$\hat{Z}_W = \frac{\sigma' l}{\sqrt{D} \left(\sqrt{\frac{j\omega}{D}} l \right)^{\phi_w}} \coth \left(\sqrt{\frac{j\omega}{D}} l \right)^{\phi_w} \quad (4.88)$$

geometry [24], where ϕ_w is the experimental parameter, always ≤ 1 . The physical interpretation is related to the nonuniform diffusion or multiple paths existing in the system [24, 155–157] and corresponds to the application of the constant phase element (CPE) model (Chap. 8) to diffusion. An example of the finite-length reflective diffusion mode is illustrated in Fig. 4.13, where mass transfer and total impedances are shown for the ideal case, $\phi_w = 1$ and for $\phi_w = 0.94$. Deviation starts already at high frequencies but is clearly visible at low frequencies. In such a case, the low-frequency behavior is changed from the $R_W - C_W$ connection in series to an $R_W - CPE_W$ connection, where the impedance of the CPE element is given as

$$\hat{Z}_W = \frac{\sigma' l}{3\sqrt{D}} + \frac{\sigma' D^{\phi_w-0.5}}{(j\omega)^{\phi_w} l^{2\phi_w-1}} = R_W + \frac{1}{(j\omega)^{\phi_w} T_W}, \quad (4.89)$$

where

$$T_W = \frac{l^{2\phi_w-1}}{\sigma' D^{\phi_w-0.5}}. \quad (4.90)$$

Macdonald and coworkers [158–164] obtained an exact solution of the finite-length diffusion impedance in unsupported conditions where the Nernst–Planck and continuity equations for both negative and positive mobile charges were solved and involved full satisfaction of Poisson’s equation. One can expect such conditions in diluted electrolytic solutions and in poorly conductive solids.

4.6 Spherical Diffusion

In the case of spherical diffusion, there is an additional term in the differential equation indicating an increase of the mass transfer to a sphere [144]. These equations may be written for the concentration phasors as

$$\frac{\partial \tilde{C}_O}{\partial t} = D_O \left(\frac{\partial^2 \tilde{C}_O}{\partial r^2} + \frac{2}{r} \frac{\partial \tilde{C}_O}{\partial r} \right) \quad \text{and} \quad \frac{\partial \tilde{C}_R}{\partial t} = D_R \left(\frac{\partial^2 \tilde{C}_R}{\partial r^2} + \frac{2}{r} \frac{\partial \tilde{C}_R}{\partial r} \right) \quad (4.91)$$

and transformed into a simpler form, similar to that of Eq. (4.26), by a standard substitution introducing two auxiliary variables \tilde{u} and \tilde{v} :

$$\tilde{u} = r\tilde{C}_O \quad \text{and} \quad \tilde{v} = r\tilde{C}_R. \quad (4.92)$$

Then Eq. (4.91) become

$$\frac{d^2 \tilde{u}}{dx^2} = s_O^2 \tilde{u} \quad \text{and} \quad \frac{d^2 \tilde{v}}{dx^2} = s_R^2 \tilde{v}. \quad (4.93)$$

These equations can be solved for semi-infinite external diffusion, where both Red and Ox forms are in the solution outside the sphere (diffusion to a spherical or hemispherical hanging mercury electrode, metallic solid spherical electrode), or they may diffuse inside the sphere (amalgam formation at mercury electrode, intercalation of Li into particles, hydrogen absorption into spherical hydrogen-absorbing particles).

4.6.1 Semi-infinite External Spherical Diffusion

In this case, the boundary and initial conditions are as follows:

$$x = r_0 \quad \frac{d\tilde{C}_O}{dx} = -\frac{\tilde{i}}{nFD_O} \quad \text{and} \quad \frac{d\tilde{C}_R}{dx} = \frac{\tilde{i}}{nFD_R},$$

$$D_O \frac{d\tilde{C}_O}{dx} + D_R \frac{d\tilde{C}_R}{dx} = 0,$$

$$x \rightarrow \infty \quad \tilde{C}_O \rightarrow 0 \text{ and } \tilde{C}_R \rightarrow 0, \quad (4.94)$$

where r_0 is the sphere radius. Keeping in mind that

$$\frac{d\tilde{u}}{dr} = \tilde{C}_O + r \frac{d\tilde{C}_O}{dr} \text{ and } \frac{d\tilde{v}}{dr} = \tilde{C}_R + r \frac{d\tilde{C}_R}{dr} \quad (4.95)$$

and using the condition at the electrode surface, the solution for the auxiliary variables is

$$\tilde{u} = A \exp\left(-\sqrt{\frac{j\omega}{D_O}} r\right) \text{ and } \tilde{v} = A' \exp\left(-\sqrt{\frac{j\omega}{D_R}} r\right), \quad (4.96)$$

and returning to the initial variables:

$$\tilde{C}_O(0) = \frac{\tilde{i}}{nF\sqrt{D_O}\left(\sqrt{j\omega} + \frac{\sqrt{D_O}}{r_0}\right)},$$

$$\tilde{C}_R(0) = -\frac{\tilde{i}}{nF\sqrt{D_R}\left(\sqrt{j\omega} + \frac{\sqrt{D_R}}{r_0}\right)}. \quad (4.97)$$

A comparison of Eqs. (4.97) and (4.30) indicates that an additional real term, D_i/r_0 , appeared in the denominator under the square root. The Warburg impedance, using Eq. (4.69), becomes

$$\hat{Z}_w = \sum_{i=O,R} \frac{RT}{n^2 F^2 \sqrt{D_i} C_i(0)} \frac{1}{\left(\sqrt{j\omega} + \frac{\sqrt{D_i}}{r_0}\right)} = \sum_{i=O,R} \frac{\sigma'_i}{\sqrt{j\omega}} \frac{1}{\left(1 + \frac{\sqrt{D_i}}{r_0 \sqrt{j\omega}}\right)} \quad (4.98)$$

$$= \sum_{i=O,R} \frac{\sigma'_i r_0}{\sqrt{D_i}} \frac{1}{\sqrt{\frac{j\omega}{D_i} r_0^2 + 1}},$$

and the total impedance is described by Eq. (4.34). From Eq. (4.98) it is evident that spherical diffusion introduces a constant term in the denominator. This means that, contrary to the semi-infinite linear diffusion where the Warburg impedance $\hat{Z}_w \rightarrow \infty$ as $\omega \rightarrow 0$, in the case of spherical diffusion the impedance goes to a real

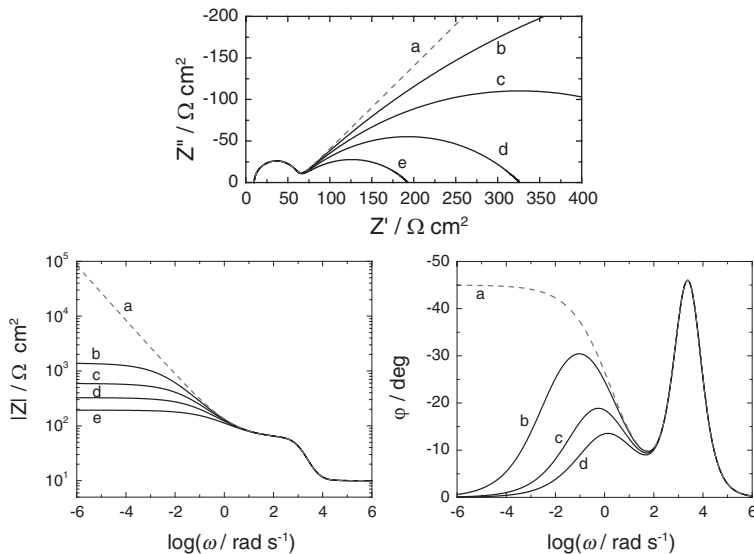


Fig. 4.14 Complex plane and Bode plots for semi-infinite external spherical diffusion; r_0 : (a) ∞ semi-infinite linear diffusion, (b) 0.005, (c) 0.01, (d) 0.02, (e) 0.05 cm; other parameters as in Fig. 4.12

constant as $\omega \rightarrow 0$. This is analogous to chronoamperometry, where for semi-infinite linear diffusion the current always decreases as $t^{-1/2}$ and never reaches zero, and for spherical diffusion the current becomes constant at very long times. The fact that the *faradaic impedance becomes real at $\omega = 0$* indicates that a *dc current may circulate in a circuit*. Such effects are easily observed at ultramicroelectrodes. Examination of Eq. (4.98) reveals that the mass transfer impedance can be written as

$$\hat{Z}_w = \frac{1}{\sqrt{j\omega}T + \frac{1}{R_D}} \quad (4.99)$$

corresponding to the connection of the resistance $R_D = \sigma' r_0 / \sqrt{D}$ and the CPE element with the value of $\phi = 0.5$ and $T = 1/\sigma'$ in parallel.

Impedance plots are modified at spherical electrodes. Examples of such plots, using an equivalent circuit in Fig. 4.1, are shown in Fig. 4.14. The high-frequency semicircle is related to the coupling of R_{ct} and C_{dl} , while the low-frequency, depressed semicircle is related to spherical diffusion.

4.6.2 Finite-Length Internal Spherical Diffusion

Let us consider now diffusion inside a sphere neglecting the diffusion gradient outside the sphere. Such a case might be observed for hydrogen absorption or Li intercalation into spherical particles. Diffusion inside the sphere can go only to the sphere center and is called finite-length internal spherical diffusion. In the steady state in which the impedance measurements are carried out, dc concentration inside the sphere is uniform, and no dc current is flowing. Ac perturbation causes oscillations of concentration at the sphere surface, which diffuse inside the sphere. In such a case, two boundary conditions in Eq. (4.94) are changed:

$$\begin{aligned} r = r_0 \quad \frac{d\tilde{C}_R}{dx} &= -\frac{\tilde{i}}{nFD_R}, \\ r = 0 \quad \tilde{C}_R &= 0. \end{aligned} \quad (4.100)$$

Using the standard substitution, Eq. (4.92), and using the condition at $r = 0$ one obtains

$$\tilde{C}_R = \frac{2A}{r} \sinh(s_R r), \quad (4.101)$$

and applying the first condition the constant is found:

$$A = -\frac{\tilde{i}}{2nF\sqrt{D_R} \left[\sqrt{j\omega} r_0 \cosh(s_R r_0) - \frac{\sqrt{D_R}}{r_0} \sinh(s_R r_0) \right]}, \quad (4.102)$$

where

$$\sinh(x) = \frac{e^x - e^{-x}}{2} \quad \text{and} \quad \cosh(x) = \frac{e^x + e^{-x}}{2}. \quad (4.103)$$

The final solution for the concentration is

$$\tilde{C}_R = -\frac{\tilde{i} \sinh(s_R r)}{nF\sqrt{D_R} \left[\sqrt{j\omega} \cosh(s_R r_0) - \frac{\sqrt{D_R}}{r_0} \sinh(s_R r_0) \right]}, \quad (4.104)$$

and at the electrode surface:

$$\tilde{C}_R(0) = \frac{\tilde{i}}{nF\sqrt{D_R} \left[\sqrt{j\omega} \coth(s_R r_0) - \frac{\sqrt{D_R}}{r_0} \right]}. \quad (4.105)$$

This equation can be compared with Eq. (4.97) to see that for internal spherical diffusion the first term in brackets is multiplied by \coth , and there is a change in sign in one term. Using Eq. (4.69) the mass transfer impedance is obtained:

$$\begin{aligned}
 \hat{Z}_W &= \frac{RT}{n^2 F^2 \sqrt{D_R} C_R(0)} \frac{1}{\sqrt{j\omega} \coth\left(\sqrt{\frac{j\omega}{D_R}} r_0\right) - \frac{\sqrt{D_R}}{r_0}} \\
 &= \frac{\sigma'}{j\omega} \frac{1}{\coth\left(\sqrt{\frac{j\omega}{D_R}} r_0\right) - \frac{\sqrt{D_R}}{r_0 \sqrt{j\omega}}} \\
 &= \frac{\sigma' r_0}{\sqrt{D_R}} \frac{1}{\left(\sqrt{\frac{j\omega}{D_R}} r_0\right) \coth\left(\sqrt{\frac{j\omega}{D_R}} r_0\right) - 1}.
 \end{aligned} \tag{4.106}$$

The difference between Eqs. (4.106) and (4.98) is that one is replaced by \coth in the denominator. It should be added that the difference in the denominator is always positive.

For large values of r_0 or high frequencies $\coth(x) \approx 1$ and both equations become similar. On the other hand for low values of x , that is for small r_0 and low frequencies, $1/[x \coth(x) - 1] = 1/5 + 3/x^2$ and this equation simplifies to:

$$\hat{Z}_W = \frac{\sigma' r_0}{5\sqrt{D_R}} + \frac{3\sigma' \sqrt{D_R}}{j\omega r_0} = R_W + \frac{1}{j\omega C_W} \tag{4.107}$$

that is to the connection of R_W and C_W in series (not a mistake in Ref. [61]). The complex plane plots of the mass transfer and the total impedance are shown in Fig. 4.15. The mass transfer impedance displays a straight line at 45° at high frequencies followed by a vertical line at low frequencies. The high frequency part corresponds to the semi-infinite diffusion where the diffusion layer thickness is much smaller than the sphere radius that is the electrode behaves as flat (compare with the case of $r_0 \rightarrow \infty$) while the low frequency part corresponds to the diffusion layer thickness much larger than the sphere radius. In such a case diffusion arrives at the very center of the electrode and cannot proceed any further and no dc current can flow.

4.7 Cylindrical Diffusion

Cylindrical diffusion is observed, for example, during diffusion to a thin metallic wire or a carbon fiber electrode. Impedance of cylindrical electrodes was studied by Fleischmann et al. [165, 166] and Jacobsen and West [167]. The partial differential equation describing diffusion to a cylinder, written for the oscillation concentration of an Ox form, is [144]

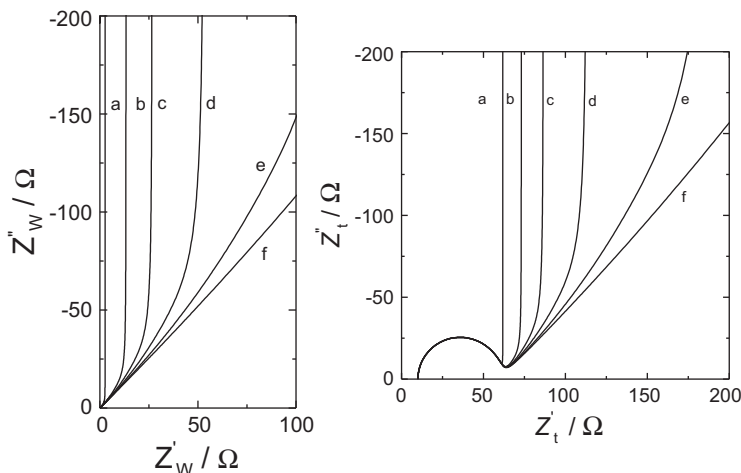


Fig. 4.15 Complex plane plots of mass transfer and total impedances at spherical electrodes assuming internal diffusion; sphere radius r_0 (a) 0.001, (b) 0.005, (c) 0.01, (d) 0.02, (e) 0.05, (f) 0.2 cm; other parameters as in Fig. 4.12

$$\frac{\partial \Delta C_O}{\partial t} = D_O \left(\frac{\partial^2 \Delta C_O}{\partial r^2} + \frac{1}{r} \frac{\partial \Delta C_O}{\partial r} \right), \quad (4.108)$$

and introducing concentration phasor it is reduced to

$$\frac{d^2 \tilde{C}_O}{dr^2} + \frac{1}{r} \frac{d\tilde{C}_O}{dr} - \left(\frac{j\omega}{D_O} \right) \tilde{C}_O = 0. \quad (4.109)$$

The only difference between equations for the cylindrical, Eq. (4.108), and spherical, Eq. (4.91), is a constant factor (one instead of two), but this has a quite important effect on the solution; Eq. (4.108) cannot be reduced to a simple form by substitution. A standard substitution used for cylindrical geometry is $z = r(j\omega/D_O)^{1/2}$, and Eq. (4.109) simplifies to

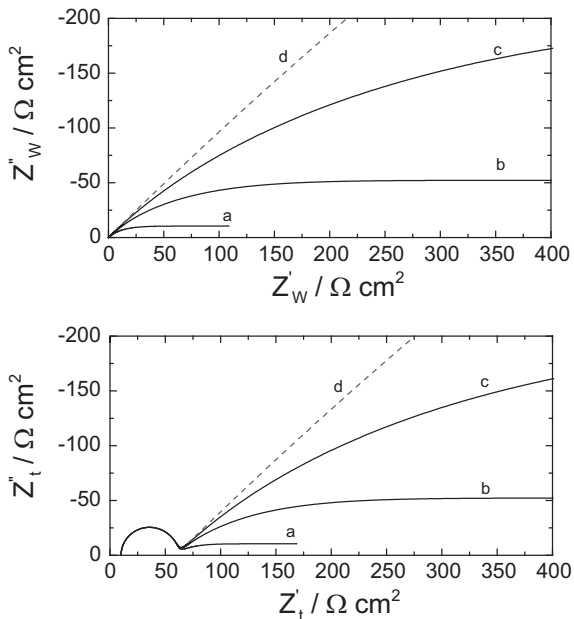
$$\frac{d^2 \tilde{C}_O}{dz^2} + \frac{1}{z} \frac{d\tilde{C}_O}{dz} - \tilde{C}_O = 0. \quad (4.110)$$

This is a modified Bessel equation of zero order that has a solution

$$\tilde{C}_O = A I_0(z) + B K_0(z), \quad (4.111)$$

where A and B are the constants to be found from the initial and boundary conditions, Eq. (4.94), and I_0 and K_0 are zero-order modified Bessel functions. Taking into account the condition at $z \rightarrow \infty$ ($r \rightarrow \infty$), $A = 0$ is obtained.

Fig. 4.16 Complex plane plots of mass transfer, \hat{Z}_w , and total, \hat{Z}_t , impedances for cylindrical external diffusion, r_0 : (a) 0.001, (b) 0.005, (c) 0.02 (d) ∞ cm; other parameters as in Fig. 4.12



The derivative at the electrode surface $r = r_0$ or $z = z_0$, taking into account that $dK_0(z)/dz = -K_1(z)$, is

$$\frac{d\tilde{C}_O}{dr} = -\sqrt{\frac{j\omega}{D_O}}BK_1(z_0) = -\frac{\tilde{i}}{nFD_O}, \quad (4.112)$$

from which the constant B is

$$B = \frac{\tilde{i}}{nF\sqrt{j\omega D_O}K_1(z_0)} \quad (4.113)$$

and

$$\tilde{C}_O = -\frac{\tilde{i}K_0(z)}{nF\sqrt{j\omega D_O}K_1(z_0)}. \quad (4.114)$$

Using Eq. (4.69) the mass transfer impedance is

$$\hat{Z}_w = \frac{RT}{n^2F^2\sqrt{D_O}C_O(0)} \frac{K_0(z_0)}{\sqrt{j\omega}K_1(z_0)} = \frac{\sigma'}{\sqrt{j\omega}} \frac{K_0(z_0)}{K_1(z_0)}. \quad (4.115)$$

The complex plane plots of the mass transfer and total impedances are displayed in Fig. 4.16.

In the case of cylindrical diffusion at low frequencies, impedance becomes parallel to the real axis and never approaches the real axis. This is related to the fact that in chronoamperometry the current never goes to zero. Jacobsen and West [167] also considered a case of finite-length cylindrical diffusion.

4.8 Diffusion to Disk Electrode

Disk electrodes are very often used as metallic or carbon disks embedded in an insulator. They are also used as ultramicroelectrodes. Fleischmann et al. [165, 166, 168] presented the impedance of such electrodes. Diffusion to a disk is more complex because it includes normal and radial directions, i.e., it is 2D diffusion described as

$$\frac{\partial C_O}{\partial t} = D \left(\frac{\partial^2 C_O}{\partial r^2} + \frac{1}{r} \frac{\partial C_O}{\partial r} + \frac{\partial^2 C_O}{\partial z^2} \right), \quad (4.116)$$

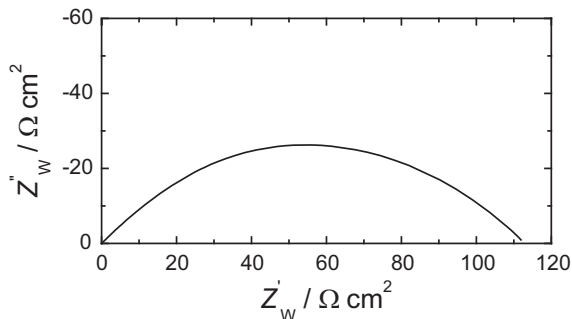
where r and z are the radial and normal directions, and assuming that the Ox form only is initially present in the solution, the following initial and boundary conditions describe the system:

$$\begin{aligned} t = 0 \quad 0 < r < \infty, \quad 0 < z < \infty, \quad C_O &= C_O^*, \\ t > 0 \quad r \rightarrow \infty, \quad z \rightarrow \infty, \quad C_O &\rightarrow C_O^*, \\ 0 < r < r_0, \quad z = 0, \quad D_O \frac{\partial C_O}{\partial z} + D_R \frac{\partial C_R}{\partial z} &= 0, \\ r_0 < r < \infty, \quad z = 0, \quad D_O \frac{\partial C_O}{\partial z} &= D_R \frac{\partial C_R}{\partial z} = 0. \end{aligned} \quad (4.117)$$

The solution of the problem is [166]

$$\begin{aligned} Z'_w &= \frac{4RT}{n^2 F^2 \pi D_O^{1/2} r_0^2 \omega^{1/2} C_O^*} \int_0^\infty \left[J_1 \left(\beta \frac{r_0}{l} \right) \right]^2 \frac{\cos(\Theta/2) d\beta}{\beta(1 + \beta^4)^{1/4}} = \\ &= \frac{4RT}{n^2 F^2 \pi D_O^{1/2} r_0^2 \omega^{1/2} C_O^*} \Phi_4 \left(\frac{r_0^2 \omega}{D_O} \right) \\ Z''_w &= \frac{4RT}{n^2 F^2 \pi D_O^{1/2} r_0^2 \omega^{1/2} C_O^*} \int_0^\infty \left[J_1 \left(\beta \frac{r_0}{l} \right) \right]^2 \frac{\sin(\Theta/2) d\beta}{\beta(1 + \beta^4)^{1/4}} = \\ &= - \frac{4RT}{n^2 F^2 \pi D_O^{1/2} r_0^2 \omega^{1/2} C_O^*} \Phi_5 \left(\frac{r_0^2 \omega}{D_O} \right), \end{aligned} \quad (4.118)$$

Fig. 4.17 Complex plane plot of mass transfer impedance at a disk electrode, $r_0 = 0.005$ cm; other parameters as in Fig. 4.12



where J_1 is the Bessel function of the first kind and first order, $l^2 = D/\omega$, and $\tan\Theta = 1/\beta^2$. The functions Φ_4 and Φ_5 were tabulated [166] and can be used to construct impedance plots (note a mistake in Ref. [165] where a different definition was used and the values of Φ_i were multiplied by $2/\sqrt{r_0^2\omega/D_0}$). The complex plane plots are displayed in Fig. 4.17. It should be noticed that at low frequencies impedances tend to a real value and the plots for small disks resemble those for microspherical electrodes, while at high frequencies a slope at 45° corresponding to semi-infinite linear diffusion is observed. However, the mass transfer impedance for a disk electrode cannot be fitted to a spherical electrode model. It could be fitted to the model described by Eq. (4.99):

$$\hat{Z}_w = R_1 + \frac{1}{(j\omega)^\phi T + \frac{1}{R_D}}, \quad (4.119)$$

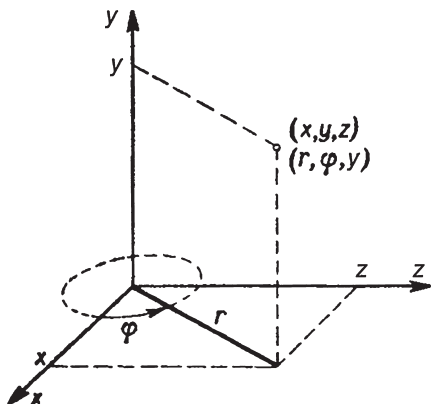
with $\phi \sim 0.55$, although the approximation is not perfect.

Recently, Michel et al. [169] carried out a numerical computation of the faradaic impedance of inlaid microdisk electrodes using a finite-element method and discussed the limitations of the Fleischmann and Pons [168] approach. Calculation of the functions Φ_4 and Φ_5 is shown in Exercise 4.8.

4.9 Rotating Disk Electrode

Impedance may also be studied in the case of forced diffusion. The most important example of such a technique is a rotating disk electrode (RDE). In a RDE conditions a steady state is obtained and the observed current is time independent, leading to the Levich equation [17]. The general diffusion-convection equation written in cylindrical coordinates y , r , and φ is [17]

Fig. 4.18 Definition of cylindrical coordinates



$$\frac{\partial C_i}{\partial t} + v_r \frac{\partial C_i}{\partial r} + v_\varphi \frac{\partial C_i}{\partial \varphi} + v_y \frac{\partial C_i}{\partial y} = D_i \left[\frac{\partial^2 C_i}{\partial y^2} + \frac{\partial^2 C_i}{\partial r^2} + \frac{1}{r} \frac{\partial C_i}{\partial r} + \frac{1}{r^2} \frac{\partial^2 C_i}{\partial \varphi^2} \right], \quad (4.120)$$

where y is a normal distance from the disk surface, r is the radial distance from the disk axis, and φ is the angle (Fig. 4.18).

It is obvious that because of the cylindrical symmetry derivatives $\partial C_i / \partial \varphi = 0$ and because $C_i(0)$ is independent of the coordinate r , Eq. (4.120) reduces to

$$\frac{\partial C_i}{\partial t} + v_y \frac{\partial C_i}{\partial y} = D_i \frac{\partial^2 C_i}{\partial y^2}. \quad (4.121)$$

To solve this equation, the velocity of the solution flowing toward the electrode must be known. This is a hydrodynamic problem involving a Navier–Stokes equation solved by von Karman and Cochran assuming laminar flow [170]:

$$v_y = \sqrt{\nu \Omega} H(\zeta) = \sqrt{\nu \Omega} \left(-a\zeta^2 + \frac{1}{3}\zeta^3 + \frac{b}{6}\zeta^4 + \dots \right), \quad (4.122)$$

where ν is the kinematic viscosity of the solution, Ω is the angular rotation velocity, $\Omega = 2\pi f$, f is the rotation frequency in s^{-1} , parameters a and b are constants, $a = 0.51023$, $b = -0.6159$, ζ is the dimensionless distance normal to disk surface, and $\zeta = y\sqrt{\Omega/\nu}$. Assuming a steady-state solution, $\partial C_i / \partial t = 0$, and keeping only the first term in v_y leads to the well-known Levich equation. This simplification of v_y is valid for large Schmidt numbers ($\rightarrow \infty$), $\text{Sc} = \nu/D$. For diluted aqueous solutions $\nu \approx 0.01 \text{ cm}^2 \text{ s}^{-1}$, and for $D = 10^{-5} \text{ cm}^2 \text{ s}^{-1}$ $\text{Sc} = 1,000$.

The simplest solution may be obtained assuming that the diffusion takes place inside the stationary Nernst diffusion layer of thickness [obtained taking only the first term in Eq. (4.122)]

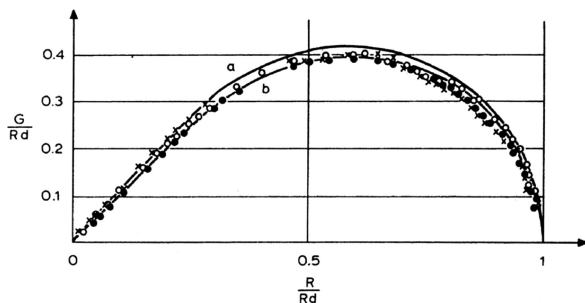


Fig. 4.19 Normalized complex plane plots obtained at RDE for reduction of 1 mM $\text{Fe}(\text{CN})_6^{3-}$ at Pt electrode at potentials corresponding to $1/4$ (\times), $1/2$ (\bullet), and $3/4$ (\times) of limiting current; (a) approximation of Nernst diffusion layer, (b) numerical solution [171] (From Ref. [177], Copyright (1970), with permission from Elsevier)

$$\delta_N = 1.612D^{1/3}\Omega^{-1/2}\nu^{1/6}. \quad (4.123)$$

In such a case the diffusion layer thickness l is replaced by δ_N in the finite-length transmissive diffusion impedance, Eq. (4.72):

$$\hat{Z}_w = \frac{\sigma'}{\sqrt{j\omega}} \tanh\left(\sqrt{\frac{j\omega}{D}}\delta_N\right) = R_D \frac{\tanh\left(\sqrt{\frac{j\omega}{D}}\delta_N\right)}{\left(\sqrt{\frac{j\omega}{D}}\delta_N\right)}, \quad (4.124)$$

and its complex plane plot is as in Fig. 4.12b. This solution simply corresponds to an infinite value of the Schmidt number. However, this is an approximate solution sometimes leading to large errors.

A more precise solution may be found by linearizing Eq. (4.121),

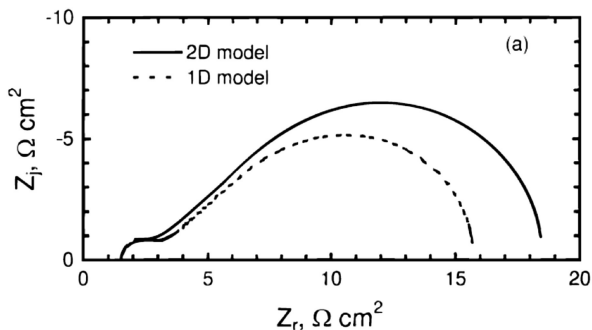
$$j\omega\tilde{C}_i + \nu_y \frac{\partial\tilde{C}_i}{\partial y} = D_i \frac{\partial^2\tilde{C}_i}{\partial y^2}, \quad (4.125)$$

with the following conditions:

$$\begin{aligned} y = 0 & \quad \tilde{C}_i = \tilde{C}_i(0), \\ y \rightarrow \infty & \quad \tilde{C}_i \rightarrow 0. \end{aligned} \quad (4.126)$$

Many attempts have been made in the literature to solve this equation numerically [171] or analytically in the form of series [172, 173] or Airy function [174] and keeping only the first term in Eq. (4.122), which is valid for large Sc numbers. Other authors have used more terms in Eq. (4.122) [175, 176].

Fig. 4.20 Simulated complex plane plots at RDE using 1D and 2D models (From Ref. [179]. Reproduced by permission of Electrochemical Society)



A comparison of the experimental data with the solution based on the diffusion layer theory and the numerical solution presented by Coueignoux and Schuhmann [171] was made by Deslouis et al. [177]. Figure 4.19 presents the normalized complex plane plots for ferricyanide obtained at different potentials corresponding to 1/4, 1/2, and 3/4 of the limiting currents. It is obvious that the approximation using the simplified Nernst diffusion layer theory, curve (a), goes above the experimental points while the numerical solution, curve (b), is much better.

Later, it was shown that in the case of ferricyanide, time-dependent impedance was observed due to surface film formation [178].

Radial nonuniformity in current distribution was taken into account in later models. This effect leads to the 2D models (i.e., containing a concentration distribution in the y - and r -directions) [179]. In such a case the radial term was added to Eqs. (4.121), (4.122), (4.123), (4.124) and (4.125) leading to

$$j\omega\tilde{C}_i + v_y \frac{\partial \tilde{C}_i}{\partial y} + v_r \frac{\partial \tilde{C}_i}{\partial r} = D_i \frac{\partial^2 \tilde{C}_i}{\partial y^2}. \quad (4.127)$$

It was found that neglecting this term may lead to serious errors, especially for fast kinetics. A comparison of the 1D and 2D solutions is displayed in Fig. 4.20.

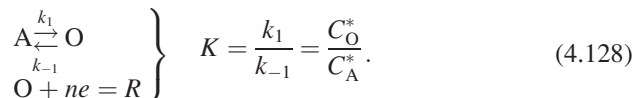
In summary, diffusion to a RDE is a complex problem for which numerical solutions exist; one can use either tables in publications or perform calculations following descriptions in papers. Under conditions where a 2D current distribution exists, the 1D model may provide an adequate fit to the experimental data, but the physical parameters obtained by regression will be incorrect [179].

However, this is an important issue in the determination of a diffusion coefficient from experimental data. It seems that the charge transfer resistance, necessary to determine the reaction kinetics, is less affected by a 2D current distribution, and so a simpler model might be used in the kinetic studies. Even simple models based on the Nernst diffusion layer are often used in kinetic studies [180] because of their simplicity.

4.10 Homogeneous Reaction, Gerischer Impedance

Homogeneous chemical reactions proceeding or following the electrochemical process affect the process impedance [15, 29, 30, 39]. The theory of the impedance of the preceding CE [15, 29, 30, 39, 181–183], following first-order [15, 39, 184–186], dimerization [187], ECE mechanism [15, 188, 189], disproportionation [190], catalytic [191], and other reactions [192–195], has been studied in the literature where E denotes electrochemical and C chemical reactions. Below, an example of the impedance of a CE process will be presented. Readers can find details for other reactions in the cited literature.

A CE process is described by the following reactions:



These chemical equations are described by the following system of diffusion-kinetic equations assuming that the diffusion coefficients of all species are identical:

$$\begin{aligned} \frac{\partial C_A}{\partial t} &= D \frac{\partial^2 C_A}{\partial x^2} - k_1 C_A + k_{-1} C_O, \\ \frac{\partial C_O}{\partial t} &= D \frac{\partial^2 C_O}{\partial x^2} + k_1 C_A - k_{-1} C_O, \\ \frac{\partial C_R}{\partial t} &= D \frac{\partial^2 C_R}{\partial x^2}, \end{aligned} \quad (4.129)$$

with the following conditions:

$$\begin{aligned} t &= 0 \text{ or } t > 0, x \rightarrow \infty, \\ C_A^* + C_O^* &= C^0, \\ C_R^* &= 0, \\ K &= \frac{C_O^*}{C_A^*}, \\ t > 0, x &= 0, \\ D \frac{\partial C_O}{\partial x} &= -D \frac{\partial C_R}{\partial x} = \frac{i}{nF}, \\ D \frac{\partial C_A}{\partial x} &= 0. \end{aligned} \quad (4.130)$$

To solve these equations, the following substitutions may be used:

$$C_T = C_A + C_O \text{ and } C_S = C_A - \frac{C_O}{K}, \quad (4.131)$$

which give the following equations:

$$\frac{\partial C_T}{\partial t} = D \frac{\partial^2 C_T}{\partial x^2} \quad \text{and} \quad \frac{\partial C_S}{\partial t} = D \frac{\partial^2 C_S}{\partial x^2} - k C_S, \quad (4.132)$$

with $k = k_1 + k_{-1}$. The equation for C_R does not change. For these equations the following conditions exist:

$$\begin{aligned} t = 0 \text{ and } t > 0, x \rightarrow \infty, \\ C_T = C^0, C_S = 0, C_R = 0, \\ t > 0, x = 0, \\ D \frac{\partial C_T}{\partial x} &= -\frac{i}{nF}, \\ D \frac{\partial C_S}{\partial x} &= -\frac{i}{nFK}, \\ D \frac{\partial C_R}{\partial x} &= -\frac{i}{nF}. \end{aligned} \quad (4.133)$$

Solution for phasors is necessary to obtain impedance:

$$\begin{aligned} j\omega \tilde{C}_T &= D \frac{\partial \tilde{C}_T}{\partial x}, \\ j\omega \tilde{C}_S &= D \frac{\partial \tilde{C}_S}{\partial x} - k \tilde{C}_S, \\ j\omega \tilde{C}_R &= D \frac{\partial \tilde{C}_R}{\partial x}. \end{aligned} \quad (4.134)$$

Following the standard solution procedure and using the initial and boundary conditions the resulting equations are

$$\begin{aligned} \tilde{C}_T &= A_1 \exp\left(-\sqrt{\frac{j\omega}{D}}x\right), \\ \tilde{C}_R &= A_2 \exp\left(-\sqrt{\frac{j\omega}{D}}x\right), \\ \tilde{C}_S &= A_3 \exp\left(-\sqrt{\frac{j\omega}{D} + \frac{k}{D}}x\right), \end{aligned} \quad (4.135)$$

and using the boundary condition at $x = 0$ the parameters A_i are obtained:

$$\begin{aligned} A_1 = \tilde{C}_O &= \frac{\tilde{i}}{nFD^{1/2}\sqrt{j\omega}}, \\ A_2 &= -\frac{\tilde{i}}{nFD^{1/2}\sqrt{j\omega}}, \\ A_3 &= -\frac{\tilde{i}}{nFD^{1/2}\sqrt{j\omega + k}}, \end{aligned} \quad (4.136)$$

from which phasors of the surface concentrations are

$$\begin{aligned} \tilde{C}_O(0) &= \frac{\tilde{i}}{nFD^{1/2}} \frac{K}{K+1} \left(\frac{1}{\sqrt{j\omega}} + \frac{1}{K\sqrt{j\omega + k}} \right), \\ \tilde{C}_R(0) &= -\frac{\tilde{i}}{nFD^{1/2}\sqrt{j\omega}}. \end{aligned} \quad (4.137)$$

Finally, the mass transfer impedance may be obtained from the equation

$$\hat{Z}_w = \frac{dE}{di} = \sum_{i=O,R} \frac{dE}{dC_i} \frac{\tilde{C}_i}{\tilde{i}}, \quad (4.138)$$

where dE/dC_i is calculated from the Nernst equation:

$$dE/dC_O = RT/nFC_O(0) \text{ and } dE/dC_R = -RT/nFC_R(0), \quad (4.139)$$

which gives [30]

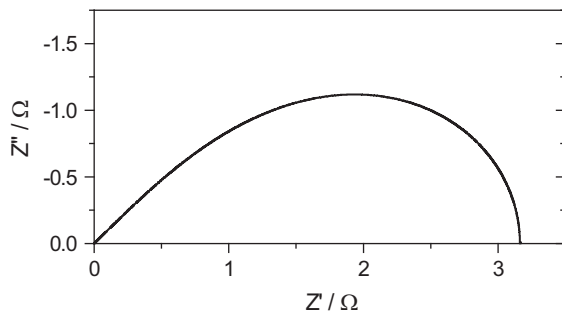
$$\hat{Z}_w = \sigma_O \left(\frac{K}{K+1} \frac{1}{\sqrt{j\omega}} + \frac{1}{K+1} \frac{1}{\sqrt{j\omega + k}} \right) + \sigma_R \frac{1}{\sqrt{j\omega}}. \quad (4.140)$$

A complex plane plot obtained is displayed in Fig. 4.21. This impedance presents a skewed semicircle. Under conditions specified in the legend the total impedance can be reduced to a simpler form:

$$\hat{Z} = \frac{Z_0}{\sqrt{j\omega + k}}. \quad (4.141)$$

This term was first obtained by Gerischer [196] and is called the Gerischer impedance. Such a behavior was observed in solid oxide fuel cells [197–199] and interpreted as a competition between surface [200] and bulk diffusion coupled

Fig. 4.21 Complex plane plot for EC mechanism, Eq. (4.140), for $K = 10^5$, $k = 0.1 \text{ s}^{-1}$, and for simplification $\sigma_O = \sigma_R = 1 \text{ } \Omega \text{ s}^{-1/2}$



through the surface oxygen exchange process or slow adsorption coupled with surface diffusion [201]. Boukamp [197–199] also introduced a so-called finite-length Gerischer impedance:

$$\hat{Z} = \frac{Z_0}{\sqrt{(j\omega + k)D}} \tanh \left[\sqrt{(j\omega + k)/D} l \right], \quad (4.142)$$

where l is the diffusion layer thickness. This equation reduces to Eq. (4.141) for large values of l . Boukamp [197, 199] later modified Eq. (4.142), introducing a so-called double fractal model:

$$\hat{Z} = \frac{Z_0}{\sqrt{[(j\omega)^\alpha + k]^\beta D}} \tanh \left[[(j\omega)^\alpha + k]^\beta l \right], \quad (4.143)$$

which reduces for large l to

$$\hat{Z} = \frac{Z_0}{\sqrt{[(j\omega)^\alpha + k]^\beta D}}. \quad (4.144)$$

These equation approximate better the experimental impedances for anodes in the solid oxide fuel cells (SOFC). It might be noticed that Eq. (4.144) is formally identical to the empirical Havriliak–Negami dielectric response function [202].

4.11 Conclusions

EIS response is very sensitive to the geometry of mass transfer. Data analysis permits us to determine the characteristic parameters describing mass and electron transfer. In most cases, analytical solutions exist; however, in the case of disk diffusion and RDEs (forced mass transfer), numerical solutions must be used.

4.12 Exercises

Exercise 4.1 Write a program in Maple or Mathematica for the Randles model and create the corresponding complex plane and Bode plots.

Exercise 4.2 Construct a model of a Randles circuit in ZView and perform a simulation using data in Fig. 4.2 (book) $R_s(C_{dl}(R_{ct}Z_W))$: $R_s = 10\ \Omega$, $C_{dl} = 25\ \mu\text{F}$, $R_{ct} = 50\ \Omega$, $\sigma' = 10\ \Omega\ \text{s}^{-1/2}$. Repeat the simulations in Maple or Mathematica.

Exercise 4.3 Write a Maple/Mathematica program to simulate spherical internal diffusion and create the corresponding complex plane and Bode plots using the following parameters: $R_s = 10\ \Omega$, $C_{dl} = 2 \times 10^{-5}\ \text{F}$, $D_O = 10^{-5}\ \text{cm}^2\ \text{s}^{-1}$, $R_{ct} = 50\ \Omega$, $C_O = 2 \times 10^{-6}\ \text{mol cm}^{-3}$, $r_0 = 10^{-3}\ \text{cm}$.

Exercise 4.4 Write a program in Maple or Mathematica to simulate semi-infinite spherical fusion (external) diffusion and create the corresponding complex plane and Bode plots. The parameters are as in Exercise 4.3, except $r_0 = 0.01\ \text{cm}$.

Exercise 4.5 Write a program in Maple/Mathematica to simulate transmissive impedance and create the corresponding complex plane and Bode plots. The parameters are as in Exercise 4.3, with $l = 0.01\ \text{cm}$.

Exercise 4.6 Write a program in Maple/Mathematica to simulate reflective mass transfer impedance and create the corresponding complex plane and Bode graphs. Use data from Exercise 4.5.

Exercise 4.7 Write a Maple/Mathematica program to simulate cylindrical diffusion and create the corresponding complex plane and Bode plots. Use parameters from Exercise 4.5 and $r_0 = 0.01\ \text{cm}$.

Exercise 4.8 Write a program to calculate Φ_4 and Φ_5 for diffusion to a disk electrode.

Chapter 5

Impedance of the Faradaic Reactions in the Presence of Adsorption

In Chap. 4, the faradaic reaction involving the diffusion of redox species was presented. In this chapter reactions involving adsorption without diffusion will be presented, starting with simple electrosorption as in underpotential deposition, followed by adsorption/desorption involving one, two, or more adsorbed species.

5.1 Faradaic Reaction Involving One Adsorbed Species, No Desorption

Let us suppose the simplest adsorption reaction involving one species that stays adsorbed, that is, there is no desorption:



where \vec{k} and \overleftarrow{k} are the potential dependent forward and backward rate constants. The rate of this process (in units of flux, $\text{mol cm}^{-2} \text{s}^{-1}$) is expressed, assuming the Langmuir adsorption isotherm, as Eq. (5.2):

$$\begin{aligned} v = & k_1^0 \exp[-\beta f(E - E^0)] (\Gamma_\infty - \Gamma_B) C_A(0) \\ & - k_{-1}^0 \exp[(1 - \beta) f(E - E^0)] \Gamma_B \end{aligned} \quad (5.2)$$

or introducing the surface coverage, $\theta_B = \Gamma_B/\Gamma_\infty$:

$$\begin{aligned} v = & k_1^0 \Gamma_\infty \exp[-\beta f(E - E^0)] (1 - \theta_B) C_A(0) \\ & - k_{-1}^0 \Gamma_\infty \exp[(1 - \beta) f(E - E^0)] \theta_B, \end{aligned} \quad (5.3)$$

where k_1^0 are the standard heterogeneous rate constants (at standard potential), k_1^0 is in $\text{cm}^3 \text{s}^{-1} \text{mol}^{-1}$ and k_{-1}^0 in s^{-1} , Γ_∞ is the total surface concentration of active sites,

and Γ_B is the surface concentration (in mol cm^{-2}) of the adsorbed form B. Note that for this reaction the dc current and reaction rate are always null and the surface concentration is equal to that in bulk $C_A(0) = C_A^*$. Introducing the equilibrium potential, that is, when $v_1 = 0$,

$$E_{\text{eq}} = E^0 + \frac{RT}{F} \ln \left[\frac{k_1^0}{k_{-1}^0} C_A^* \frac{(1 - \theta_B^*)}{\theta_B^*} \right], \quad (5.4)$$

where * denotes the equilibrium values. Taking as the reference potential E_p at $\theta = 0.5$ and defining $\eta = E - E_p$ yields

$$E_p = E^0 + \frac{RT}{F} \ln \left[\frac{k_1^0}{k_{-1}^0} C_A^* \right]. \quad (5.5)$$

Equation (5.3) becomes

$$\begin{aligned} v &= \left(k_1^{0(1-\beta)} k_{-1}^{0\beta} \Gamma_\infty C_A^{*1-\beta} \right) (1 - \theta_B) e^{-\beta f \eta} \\ &\quad - \left(k_1^{0(1-\beta)} k_{-1}^{0\beta} \Gamma_\infty C_A^{*1-\beta} \right) \theta_B e^{(1-\beta) f \eta} \\ &= \vec{k} (1 - \theta_B) - \overleftarrow{k} \theta_B, \end{aligned} \quad (5.6)$$

where \vec{k} and \overleftarrow{k} are the potential dependent heterogeneous rate constants of the surface reactions

$$\begin{aligned} \vec{k} &= k^0 \exp[-\beta f \eta]; \quad \overleftarrow{k} = k^0 \exp[(1 - \beta) f \eta]; \\ k^0 &= (k_1^0)^{(1-\beta)} (k_{-1}^0)^\beta \Gamma_\infty (C_A^*)^{(1-\beta)} \end{aligned} \quad (5.7)$$

The current is related to the change in the surface coverage:

$$i = \frac{dQ}{dt} = -(F \Gamma_\infty) \frac{d\theta_B}{dt} = -F v = -F \left[\vec{k} (1 - \theta_B) - \overleftarrow{k} \theta_B \right], \quad (5.8)$$

where $Q = F \Gamma_\infty \theta_B$ is the amount of adsorbed B expressed as the electrical charge. Equation (5.8) describes the dc behavior of our system. From the condition that the dc current is zero in steady-state conditions, one obtains the adsorption isotherm and the surface coverage:

$$\frac{\theta_B}{1 - \theta_B} = e^{-f \eta} \quad \text{or} \quad \theta_B = \frac{1}{1 + \exp(f \eta)}. \quad (5.9)$$

Next, the ac solution must be developed for Δi , $\Delta \eta$, and $\Delta \theta_B$:

$$\Delta i = -F \Delta v = -F \left[\left(\frac{\partial v}{\partial \eta} \right) \Delta \eta + \left(\frac{\partial v}{\partial \theta_B} \right) \Delta \theta_B \right] \quad (5.10)$$

and

$$\begin{aligned} (F\Gamma_\infty) \frac{\partial \Delta\theta_B}{\partial t} &= j\omega(F\Gamma_\infty)\Delta\theta_B = j\omega\sigma_1\Delta\theta_B \\ &= F \left[\left(\frac{\partial v}{\partial \eta} \right) \Delta\eta + \left(\frac{\partial v}{\partial \theta_B} \right) \Delta\theta_B \right], \end{aligned} \quad (5.11)$$

where $\sigma_1 = F\Gamma_\infty$ is the charge necessary for the complete coverage of the surface by B. After division of both sides by $\exp(j\omega t)$, the following equations are obtained:

$$\tilde{i} = -F \left[\left(\frac{\partial v}{\partial \eta} \right) \tilde{\eta} + \left(\frac{\partial v}{\partial \theta_B} \right) \tilde{\theta}_B \right], \quad (5.12)$$

$$j\omega\sigma_1\tilde{\theta}_B = F \left[\left(\frac{\partial v}{\partial \eta} \right) \tilde{\eta} + \left(\frac{\partial v}{\partial \theta_B} \right) \tilde{\theta}_B \right]. \quad (5.13)$$

Equations (5.12) and (5.13) may be rearranged and written in matrix form:

$$\begin{bmatrix} -\frac{\partial v_1}{\partial \eta} \\ -\frac{\partial v_1}{\partial \eta} \end{bmatrix} = \begin{bmatrix} \frac{1}{F} & \frac{\partial v_1}{\partial \theta_B} \\ 0 & \frac{\partial v_1}{\partial \theta_B} - j\omega \frac{\sigma_1}{F} \end{bmatrix} \begin{bmatrix} \tilde{i} \\ \tilde{\eta} \\ \tilde{\theta}_B \\ \tilde{\eta} \end{bmatrix} \quad (5.14)$$

with the solution

$$\tilde{Y}_f = \frac{\tilde{i}}{\tilde{\eta}}, \quad (5.15)$$

$$\hat{Y}_f = -F \left(\frac{\partial v}{\partial \eta} \right) - \frac{\left[-F \left(\frac{\partial v}{\partial \eta} \right) \right] \left[-\frac{F}{\sigma_1} \left(\frac{\partial v}{\partial \theta_B} \right) \right]}{j\omega + \left[-\frac{F}{\sigma_1} \left(\frac{\partial v_1}{\partial \theta_B} \right) \right]} = A - \frac{AC}{j\omega + C}, \quad (5.16)$$

where

$$\begin{aligned} A &= -F \left(\frac{\partial v}{\partial \eta} \right) = F \left[\beta f \vec{k} (1 - \theta_B) + (1 - \beta) f \overleftarrow{k} \theta_B \right], \\ C &= -\frac{F}{\sigma_1} \left(\frac{\partial v}{\partial \theta_B} \right) = \frac{F}{\sigma_1} \left(\vec{k} + \overleftarrow{k} \right), \end{aligned} \quad (5.17)$$

or, introducing values of θ_B and rearranging,

$$\begin{aligned}
A &= \frac{Ffk^0}{2} \frac{1}{\cosh(0.5f\eta)}, \\
C &= \frac{2Fk^0}{\sigma_1} \cosh(0.5f\eta).
\end{aligned}
\tag{5.18}$$

The faradaic impedance is obtained as

$$\hat{Z}_f = \frac{1}{\hat{Y}_f} = \frac{1}{A} + \frac{1}{j\omega(A/C)} = R_{ct} + \frac{1}{j\omega C_p}, \tag{5.19}$$

with

$$R_{ct} = \frac{1}{A} \text{ and } C_p = \frac{A}{C}, \tag{5.20}$$

and it corresponds to the connection between the resistance of the charge transfer, R_{ct} , and the pseudocapacitance, C_p , in series. For $\beta = 0.5$, the parameter R_{ct} may be rearranged to

$$R_{ct} = \frac{2RT}{F^2 k^0} \cosh(0.5f\eta). \tag{5.21}$$

This kinetic parameter is inversely proportional to the rate constant of the electrode process of adsorption. On the other hand, the adsorption pseudocapacitance reduces to

$$C_p = \frac{F\sigma_1}{4RT} \frac{1}{\cosh^2(0.5f\eta)} \tag{5.22}$$

and contains no kinetic parameters. Of course, integration of C_p gives the total adsorption charge:

$$\int_{-\infty}^{\infty} C_p d\eta = \sigma_1. \tag{5.23}$$

To obtain the total impedance, the faradaic impedance, Eq. (5.19), must be inserted into the total impedance (Fig. 4.1b). The complex plane and Bode plots of the total impedance are as in Fig. 2.35. The circuit parameters R_{ct} and C_p depend on the potential, as illustrated in Fig. 5.1. The charge transfer resistance displays a minimum at E_p and its logarithm is linear with the potential further from the minimum, while the pseudocapacitance displays a maximum. These values at the potential E_p are

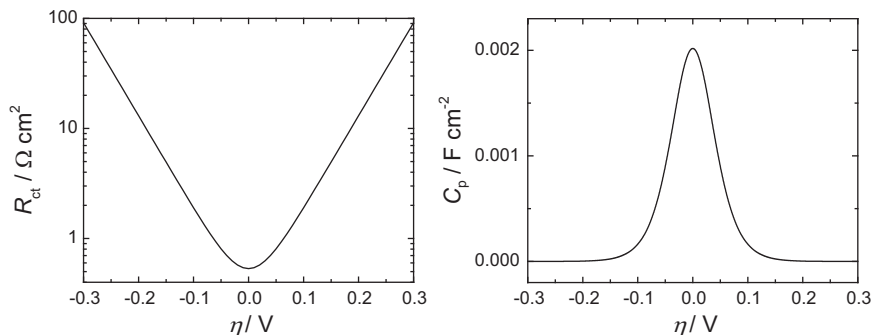


Fig. 5.1 Dependence of charge transfer resistance and pseudocapacitance on potential assuming $k^0 = 10^{-6} \text{ mol cm}^{-2} \text{ s}^{-1}$, $\beta = 0.5$, and $\sigma_1 = 210 \text{ } \mu\text{F cm}^{-2}$.

$$R_{\text{ct}} = \frac{2RT}{F^2 k^0} = \frac{5.38 \times 10^{-7}}{k^0} \Omega \text{cm}^2 \quad \text{and} \quad C_p = \frac{F\sigma_1}{4RT} = 2.04 \text{ mF cm}^{-2} \quad (5.24)$$

for the parameters in Fig. 5.1.

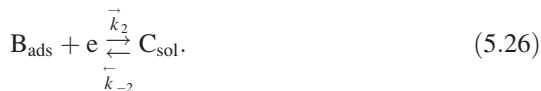
This type of reaction is observed for the underpotential deposition of hydrogen or metals. Unfortunately, the Langmuir isotherm is rarely found in practice, but for more complex isotherms the same impedance plots are observed; only the potential dependence of the reaction parameters R_{ct} and C_p is different. In the presence of the Frumkin adsorption isotherm with a negative interaction parameter, discontinuous impedances might be observed [203, 204].

The theory of the process where both Red and Ox species are adsorbed at the electrode surface was analyzed by Laviron [205] and Los and Laviron [206]. Recently, such a case was studied experimentally for the redox couple azobenzene/hydrazobenzene at a mercury electrode by Prieto et al. [207] and the rate constants of the sequential protonation–electron transfer reactions were determined. The total impedance in this case is described by the circuit displayed in Fig. 2.35, but the rate constant is a more complex function of the electrode potential because the process involves two protonation and two electron transfer processes.

5.2 Faradaic Reaction Involving One Adsorbed Species with Subsequent Desorption

Let us consider now a more complex reaction where adsorbed species are electrochemically desorbed in the second reaction:





This is a so-called Volmer–Heyrovsky type of mechanism, although it was originally found for the hydrogen evolution reaction.

5.2.1 Determination of Impedance

As before, the steady-state behavior must be described first. The rates of these reactions, assuming a Langmuir adsorption isotherm, are

$$\begin{aligned} v_1 &= k_1^0 \Gamma_{\infty} C_A(0) (1 - \theta_B) \exp[-\beta_1 f(E - E_1^0)] \\ &\quad - k_{-1}^0 \Gamma_{\infty} \theta_B \exp[(1 - \beta_1) f(E - E_1^0)], \end{aligned} \quad (5.27)$$

$$\begin{aligned} v_2 &= k_2^0 \Gamma_{\infty} \theta_B \exp[-\beta_2 f(E - E_2^0)] \\ &\quad - k_{-2}^0 \Gamma_{\infty} C_C(0) (1 - \theta_B) \exp[(1 - \beta_2) f(E - E_2^0)]. \end{aligned} \quad (5.28)$$

Next, the equilibrium potential and the overpotential will be introduced. At the equilibrium potential the rates of both reactions are zero, from which the following equations are obtained:

$$\exp[f(E_{\text{eq}} - E_1^0)] = \frac{k_1^0}{k_{-1}^0} C_A^* \frac{1 - \theta_B^*}{\theta_B^*}, \quad (5.29)$$

$$\exp[f(E_{\text{eq}} - E_2^0)] = \frac{k_2^0}{k_{-2}^0} \frac{1}{C_C^*} \frac{\theta_B^*}{1 - \theta_B^*}, \quad (5.30)$$

where θ_B^* is the surface coverage at the equilibrium potential and C_i^* are the bulk concentrations. Now the potential difference may be expressed as the overpotential $E - E_i^0 = E - E_{\text{eq}} + E_{\text{eq}} - E_i^0 = \eta + E_{\text{eq}} - E_i^0$:

$$\begin{aligned} v_1 &= \left\{ k_1^{0(1-\beta_1)} k_{-1}^0 \beta_1 \Gamma_{\infty} C_A^{*- \beta_1} \left(\frac{\theta_B^*}{1 - \theta_B^*} \right)^{\beta_1} C_A(0) \right\} (1 - \theta_B) \exp(-\beta_1 f \eta) \\ &\quad - \left\{ k_1^{0(1-\beta_1)} k_{-1}^0 \beta_1 \Gamma_{\infty} C_A^{*(1-\beta_1)} \left(\frac{1 - \theta_B^*}{\theta_B^*} \right)^{1-\beta_1} \right\} \theta_B \exp[(1 - \beta_1) f \eta] \\ &= k_1 (1 - \theta_B) \exp(-\beta_1 f \eta) - k_{-1} \theta_B \exp[(1 - \beta_1) f \eta] \\ &= \vec{k}_1 (1 - \theta_B) - \overset{\leftarrow}{k}_{-1} \theta_B, \end{aligned} \quad (5.31)$$

$$\begin{aligned}
v_2 &= \left\{ k_2^{0(1-\beta_2)} k_{-2}^0 \beta_2 \Gamma_\infty C_C^{*\beta_2} \left(\frac{1-\theta_B^*}{\theta_B^*} \right)^{\beta_2} \right\} \theta_B \exp(-\beta_2 f \eta) \\
&\quad - \left\{ k_2^{0(1-\beta_2)} k_{-2}^0 \beta_2 \Gamma_\infty C_C^{*(-1+\beta_2)} \left(\frac{\theta_B^*}{1-\theta_B^*} \right)^{1-\beta_2} C_C(0) \right\} (1-\theta_B) \exp[(1-\beta_2) f \eta] \\
&= k_2 \theta_B \exp(-\beta_2 f \eta) - k_{-2} (1-\theta_B) \exp[(1-\beta_2) f \eta] \\
&= \overrightarrow{k_2} \theta_B - \overleftarrow{k_{-2}} (1-\theta_B),
\end{aligned} \tag{5.32}$$

where

$$k_1 = k_1^{0(1-\beta_1)} k_{-1}^0 \beta_1 \Gamma_\infty C_A^{*1-\beta_1} \left(\frac{\theta_B^*}{1-\theta_B^*} \right)^{\beta_1} C_A(0), \tag{5.33}$$

$$k_{-1} = k_1^{0(1-\beta_1)} k_{-1}^0 \beta_1 \Gamma_\infty C_A^{*1-\beta_1} \left(\frac{1-\theta_B^*}{\theta_B^*} \right)^{1-\beta_1}, \tag{5.34}$$

$$k_2 = k_2^{0(1-\beta_2)} k_{-2}^0 \beta_2 \Gamma_\infty C_C^{*\beta_2} \left(\frac{1-\theta_B^*}{\theta_B^*} \right)^{\beta_2}, \tag{5.35}$$

$$k_{-2} = k_2^{0(1-\beta_2)} k_{-2}^0 \beta_2 \Gamma_\infty C_C^{*(-1+\beta_2)} \left(\frac{\theta_B^*}{1-\theta_B^*} \right)^{1-\beta_2} C_C(0). \tag{5.36}$$

Assuming there is no concentration gradient and the surface and bulk concentrations are the same one obtains

$$k_1 = k_1^{0(1-\beta_1)} k_{-1}^0 \beta_1 \Gamma_\infty C_A^{*1-\beta_1} \left(\frac{\theta_B^*}{1-\theta_B^*} \right)^{\beta_1}, \tag{5.37}$$

$$k_{-2} = k_2^{0(1-\beta_2)} k_{-2}^0 \beta_2 \Gamma_\infty C_C^{*\beta_2} \left(\frac{\theta_B^*}{1-\theta_B^*} \right)^{1-\beta_2}. \tag{5.38}$$

It should be stressed that this condition may be met only when the concentrations of A and C are large and the currents are small. Such conditions are met, for example, for water electrolysis or chlorine evolution from concentrated electrolytes. One should add the condition at the equilibrium potential, which leads to

$$\frac{k_1 k_2}{k_{-1} k_{-2}} = 1, \tag{5.39}$$

which indicates that only three rate constants are independent and the fourth may be calculated from Eq. (5.39). Assuming there are four rate constants leads to an overdetermined system and errors [208, 209]. In fact, substituting the rate constants

Eqs. (5.34), (5.35), (5.37), and (5.38) into (5.39) also confirms this identity. Equations (5.31) and (5.32) can be rearranged into other useful forms:

$$v_1 = v_1^0 \left[\left(\frac{1 - \theta_B}{1 - \theta_B^*} \right) \left(\frac{C_A(0)}{C_A^*} \right) \exp(-\beta_1 f \eta) - \left(\frac{\theta_B}{\theta_B^*} \right) \exp[(1 - \beta_1) f \eta] \right], \quad (5.40)$$

$$v_2 = v_2^0 \left[\left(\frac{\theta_B}{\theta_B^*} \right) \exp(-\beta_2 f \eta) - \left(\frac{1 - \theta_B}{1 - \theta_B^*} \right) \left(\frac{C_C(0)}{C_C^*} \right) \exp[(1 - \beta_1) f \eta] \right], \quad (5.41)$$

and the corresponding exchange current densities for reactions (5.25) and (5.26) are

$$i_1^0 = F v_1^0 \quad \text{and} \quad i_2^0 = F v_2^0. \quad (5.42)$$

To find the kinetic parameters of these reactions, one must find either three (out of four) rate constants or two exchange current densities and θ_B^* and, of course, two transfer coefficients.

The total current is the sum of two reactions,

$$i = -F(v_1 + v_2) = -F r_0, \quad (5.43)$$

and the change in the surface coverage by species B,

$$\frac{d\Gamma_B}{dt} = \Gamma_\infty \frac{d\theta_B}{dt} = \frac{\sigma_1}{F} \frac{d\theta_B}{dt} = r_1 = v_1 - v_2 = 0, \quad (5.44)$$

which, in the steady state, is equal to zero, where $\sigma_1 = F\Gamma_\infty$ is the charge necessary for the total coverage of the electrode surface.

To calculate the impedance, equations for the total current and the changes in the surface coverage must be linearized:

$$\Delta i = - \left(\frac{\partial i}{\partial \eta} \right)_\theta \Delta \eta - \left(\frac{\partial i}{\partial \theta} \right)_\eta \Delta \theta_B = -F \left[\left(\frac{\partial r_0}{\partial \eta} \right)_\theta \Delta \eta + \left(\frac{\partial r_0}{\partial \theta_B} \right)_\eta \Delta \theta_B \right], \quad (5.45)$$

$$\frac{\sigma_1}{F} \frac{d\Delta \theta_B}{dt} = \Delta r_1 = \left(\frac{\partial r_1}{\partial \eta} \right)_{\theta_B} \Delta \eta + \left(\frac{\partial r_1}{\partial \theta_B} \right)_\eta \Delta \theta_B. \quad (5.46)$$

Taking into account the definitions of Δ :

$$\begin{aligned} \Delta i &= \tilde{i} \exp(j\omega t), \quad \Delta r_i = \tilde{r}_i \exp(j\omega t), \\ \Delta \eta &= \tilde{\eta} \exp(j\omega t), \quad \text{and} \quad \Delta \theta_B = \tilde{\theta}_B \exp(j\omega t), \end{aligned} \quad (5.47)$$

the following equations are obtained:

$$-\frac{\tilde{i}}{F} = \tilde{r}_0 = \left(\frac{\partial r_0}{\partial \eta} \right)_{\theta_B} \tilde{\eta} + \left(\frac{\partial r_0}{\partial \theta_B} \right)_{\eta} \tilde{\theta}_B, \quad (5.48)$$

$$\frac{\sigma_1}{F} j\omega \tilde{\theta}_B = \left(\frac{\partial r_1}{\partial \eta} \right)_{\theta_B} \tilde{\eta} + \left(\frac{\partial r_1}{\partial \theta_B} \right)_{\eta} \tilde{\theta}_B. \quad (5.49)$$

As before, division by $\tilde{\eta}$ and rearrangement leads to

$$\begin{bmatrix} -\frac{\partial r_0}{\partial \eta} \\ -\frac{\partial r_1}{\partial \eta} \end{bmatrix} = \begin{bmatrix} \frac{1}{F} & \frac{\partial r_0}{\partial \theta_B} \\ 0 & \frac{\partial r_1}{\partial \theta_B} - j\omega \frac{\sigma_1}{F} \end{bmatrix} \begin{bmatrix} \frac{\tilde{i}}{\tilde{\eta}} \\ \frac{\tilde{\theta}_B}{\tilde{\eta}} \end{bmatrix}. \quad (5.50)$$

The solution of this equation gives the faradaic admittance, Eq. (5.15):

$$\hat{Y}_f = \frac{\tilde{i}}{\tilde{\eta}} = -F \left(\frac{\partial r_0}{\partial \eta} \right)_{\theta_B} - \frac{\frac{F^2}{\sigma_1} \left(\frac{\partial r_0}{\partial \theta_B} \right)_{\eta} \left(\frac{\partial r_1}{\partial \eta} \right)_{\theta_B}}{j\omega - \frac{F}{\sigma_1} \left(\frac{\partial r_1}{\partial \theta_B} \right)_{\eta}} = A + \frac{B}{j\omega + C}, \quad (5.51)$$

where

$$A = -F \left(\frac{\partial r_0}{\partial \eta} \right)_{\theta_B}, B = -\frac{F^2}{\sigma_1} \left(\frac{\partial r_0}{\partial \theta_B} \right)_{\eta} \left(\frac{\partial r_1}{\partial \eta} \right)_{\theta_B}, \text{ and } C = -\frac{F}{\sigma_1} \left(\frac{\partial r_1}{\partial \theta_B} \right)_{\eta}, \quad (5.52)$$

and, rearranging into impedance,

$$\hat{Z}_f = \frac{1}{A} - \frac{B}{j\omega A^2 + AB} = \frac{1}{A} + \frac{1}{-j\omega \frac{A^2}{B} - \frac{A^2 C}{B} - A} \quad (5.53)$$

or

$$\hat{Z}_f = R_{ct} + \frac{1}{j\omega C_p + \frac{1}{R_p}}, \quad (5.54)$$

where

$$R_{ct} = \frac{1}{A}, \quad C_p = -\frac{A^2}{B}, \text{ and } R_p = -\frac{1}{\frac{A^2 C}{B} + A}, \quad (5.55)$$

that is, the faradaic impedance consists of the charge transfer resistance in series with the parallel connection between the resistance R_p and pseudocapacitance C_p . The total impedance is

$$\hat{Z}_t = R_s + \frac{1}{j\omega C_{dl} + \frac{1}{R_{ct} + \frac{1}{\frac{1}{R_p} + j\omega C_p}}} \quad (5.56)$$

and is the same as shown earlier in Eq. (2.158) for the nested circuit in Fig. 2.37, right. The meaning of the parameters in this circuit may be better understood following their calculation:

$$A = Ff \left[\beta_1 \vec{k}_1 (1 - \theta_B) + (1 - \beta_1) \overleftarrow{k}_{-1} \theta_B + \beta_2 \vec{k}_2 \theta_B + (1 - \beta_2) \overleftarrow{k}_{-2} (1 - \theta_B) \right], \quad (5.57)$$

$$B = \frac{F^2 f}{\sigma_1} \left(-\vec{k}_1 - \overleftarrow{k}_{-1} + \vec{k}_2 + \overleftarrow{k}_{-2} \right) \times \left[\beta_1 \vec{k}_1 (1 - \theta_B) + (1 - \beta_1) \overleftarrow{k}_{-1} \theta_B - \beta_2 \vec{k}_2 \theta_B - (1 - \beta_2) \overleftarrow{k}_{-2} (1 - \theta_B) \right], \quad (5.58)$$

and

$$C = \frac{F}{\sigma_1} \left(\vec{k}_1 + \overleftarrow{k}_{-1} + \vec{k}_2 + \overleftarrow{k}_{-2} \right), \quad (5.59)$$

from which it is evident that parameters A and C are always positive but B might be positive or negative, which will influence the impedance plots. The faradaic polarization resistance, R_{pol} , that is, the impedance at $\omega = 0$ is $R_{pol} = R_{ct} + R_p$.

The steady-state surface coverage, θ_B , is calculated from the rate constants using the steady-state condition $v_1 = v_2$:

$$\theta_B = \frac{\vec{k}_1 + \overleftarrow{k}_{-2}}{\vec{k}_1 + \overleftarrow{k}_{-1} + \vec{k}_2 + \overleftarrow{k}_{-2}}. \quad (5.60)$$

Note that, assuming no concentration polarization and $\beta_1 = \beta_2$, this parameter becomes potential independent and changes from:

$$\theta_B = \frac{\vec{k}_1}{\vec{k}_1 + \vec{k}_2} = \frac{k_1}{k_1 + k_2} \quad (5.61)$$

at very negative overpotentials to:

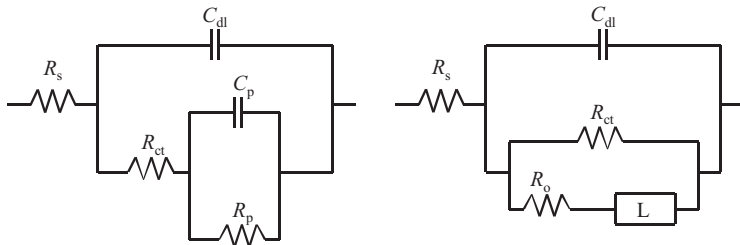


Fig. 5.2 Electrical equivalent circuits describing electrochemical reaction with one adsorbed species, Eq. (5.53), *left* for $B < 0$, *right* for $B > 0$

$$\theta_B = \frac{k_1}{k_1 + k_{-1}} = \frac{k_{-2}}{k_{-1} + k_{-2}} \quad (5.62)$$

at zero overpotential, and

$$\theta_B = \frac{k_{-2}}{k_{-1} + k_{-2}} \quad (5.63)$$

at very positive potentials [210].

5.2.2 Impedance Plots

Impedance plots corresponding to the general Eq. (5.53) depend on the sign of parameter B and relative values of the capacitances in the circuit.

1. $B < 0$

(a) $R_p > 0$

When $B < 0$, the faradaic impedance is described by Eq. (5.54). It describes resistance R_{ct} in series with a parallel connection between C_p and R_p (Fig. 5.2, left). The complex plane plots in this case display two semicircles (Fig. 5.3a).

(b) $R_p = \infty$

In this case, the impedance becomes simply a connection between R_{ct} and C_p in series:

$$\hat{Z}_f = R_{ct} + \frac{1}{j\omega C_p}, \quad (5.64)$$

and the complex plane plots are presented in Fig. 5.3b.

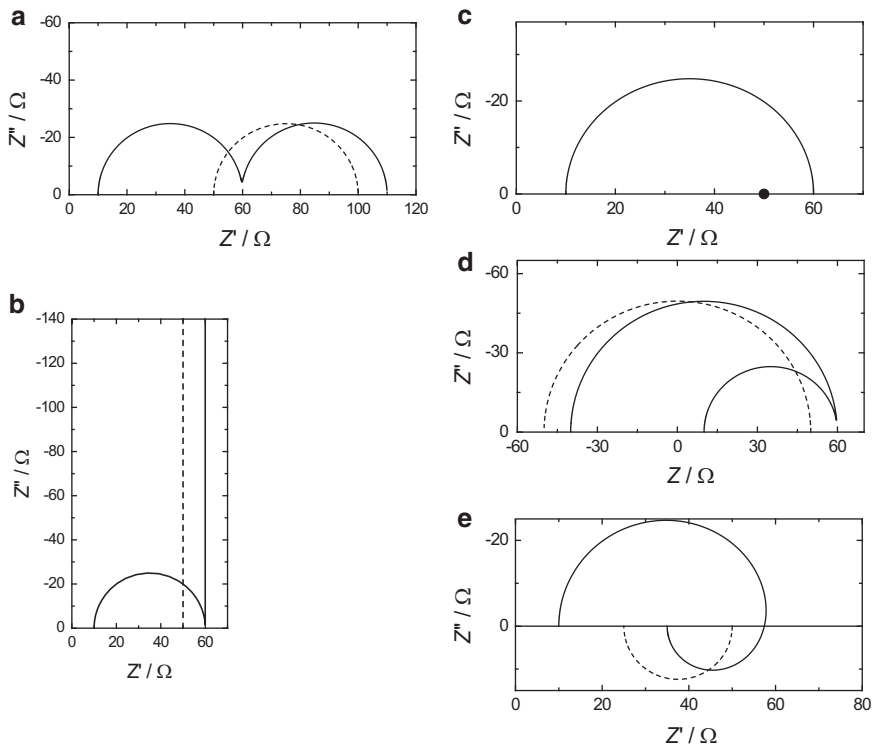


Fig. 5.3 Complex plane plots of faradaic (*dashed lines*) and total (*continuous lines*) impedances obtained using Eq. (5.54) (a–d) or (5.65) to calculate faradaic impedance; $R_s = 10 \Omega$, $R_{ct} = 50 \Omega$, $C_{dl} = 20 \mu\text{F}$. (a) $B < 0$, $R_p = 50 \Omega$, $C_p = 0.1 \text{ F}$; (b) $B < 0$, $R_p = \infty$; (c) $B < 0$, $R_p = 0$, or $B = 0$; (d) $B < 0$, $R_p = -100 \Omega$, $C_p = 0.1 \text{ F}$; (e) $B > 0$, $R_o = 50 \Omega$, $L = 0.1 \text{ H}$

(c) $R_p = 0$

In this case, the faradaic impedance equals R_{ct} and the complex plane plot of the faradaic impedance is a point while the total impedance displays one semicircle on the complex plane plots (Fig. 5.3c).

(d) $R_p < 0$

Three cases are possible: $R_{ct} < -R_p$, $R_{ct} = -R_p$, and $R_{ct} > -R_p$. In such cases, the faradaic impedance plot displays a semicircle going from $\lim_{\omega \rightarrow \infty} \hat{Z}_f = R_{ct}$ at high frequencies to $\lim_{\omega \rightarrow 0} \hat{Z}_f = R_{ct} + R_p$ at low frequencies. Examples of complex plane plots in the case where $R_{ct} < -R_p$ are presented in Fig. 5.3d.

2. $B = 0$

This case is identical with $B < 0$ and $R_p = 0$. In general, the faradaic impedance equals R_{ct} when $A \gg |B|/C$. An example of such a plot is shown in Fig. 5.3b.

3. $B > 0$

In this case, the impedance equation may be rearranged into

$$\hat{Z}_f = \frac{1}{A + \frac{1}{\frac{1}{B}j\omega + \frac{C}{B}}} = \frac{1}{\frac{1}{R_{ct}} + \frac{1}{j\omega L + R_o}}, \quad (5.65)$$

where

$$R_{ct} = \frac{1}{A}, R_o = \frac{C}{B}, L = \frac{1}{B}, \quad (5.66)$$

representing the connection between R_{ct} and L - R_o in parallel (Fig. 5.2, right), with all the parameters positive. Of course, these are only electrical representations of the general equation, and there are relations between the parameters of both circuits:

$$L = -R_{ct}^2 C_p \text{ and } R_o = -\frac{R_{ct}(R_{ct} + R_p)}{R_p}. \quad (5.67)$$

The circuit in Eq. (5.65) can be represented by that in Eq. (5.54) assuming that $C_p < 0$, $R_p < 0$ and $R_{ct} > -R_p$. The complex plane plots are displayed in Fig. 5.3e. Note that the faradaic impedance is always positive and the total impedance displays a plot with capacitive and inductive loops.

In addition, the impedance for $B < 0$ can also be represented by the circuit in Fig. 5.2b, but with both R_o and L negative [211]. In this case, the time constant of the circuit is positive and the circuit is stable (see Sect. 13.3). Of course, there are no physical (simple electrical) elements representing negative parameters, but this is only an electric representation of Eq. (5.51), which might be useful but is not necessary as long as we have an equation describing the system.

As can be seen from Fig. 5.3 and the preceding discussion, one simple Eq. (5.51) describing the faradaic admittance in the presence of one adsorbed species, in combination with the double-layer capacitance, can produce many different complex plane plots and electrical equivalent circuits. It should be stressed that the kinetic equations with physically possible rate parameters in Eqs. (5.25) and (5.26) may not give all the behaviors, i.e. impedance plots, found by arbitrarily allocating values to the circuit elements.

It is interesting to discover when inductive loops may be observed. First of all, let us consider the case of large overpotentials where the process becomes irreversible, i.e., the backward rates are negligible. In this case, the faradaic impedance simplifies to

$$\hat{Z}_f = \frac{1}{Ff} \frac{\vec{k}_1 + \vec{k}_2}{\vec{k}_1 \vec{k}_2} \frac{1}{\left[\beta_1 + \beta_2 + \frac{\frac{F^2 f}{\sigma_1} (\vec{k}_2 - \vec{k}_1) (\beta_1 - \beta_2)}{j\omega + \frac{F}{\sigma_1} (\vec{k}_1 + \vec{k}_2)} \right]}. \quad (5.68)$$

This equation was presented by Gabrielli [11] and indicates that when $\beta_1 = \beta_2$, the faradaic impedance is real and one semicircle must be obtained on the total

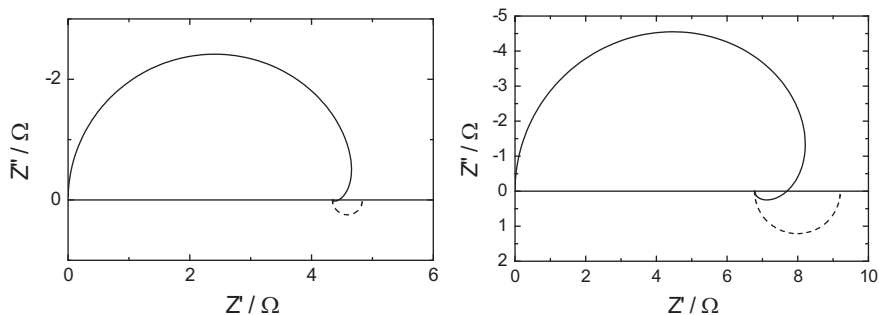


Fig. 5.4 Complex plane plots of faradaic (*dashed lines*) and total (*continuous lines*) impedances where $B > 0$, $C_{dl} = 25 \mu\text{F}$; *left*: $\eta = -0.095 \text{ V}$, $\beta_1 = \beta_2 = 0.5$, $k_1 = 10^{-6.65}$, $k_{-1} = 10^{-9.2}$, $k_2 = 10^{-8.05} \text{ mol cm}^{-2} \text{ s}^{-1}$, $R_{ct} = 4.835 \Omega$, $R_0 = 42.76 \Omega$, $L = 0.0471 \text{ H}$; *right*: $\eta = -0.14 \text{ V}$, $\beta_1 = 0.7$, $\beta_2 = 0.3$, $k_1 = 10^{-9.2}$, $k_{-1} = 10^{-8.05}$, $k_2 = 10^{-6.35} \text{ mol cm}^{-2} \text{ s}^{-1}$, $R_{ct} = 9.2 \Omega$, $R_0 = 25.7 \Omega$, $L = 0.0241 \text{ H}$

impedance complex plane plots. Gabrielli obtained an inductive loop assuming $\beta_1 = 0.925$ and $\beta_2 = 0.257$. It must be stressed that the value of β_1 is quite extreme. The same values of transfer coefficients were also chosen by Orazem and Tribollet in their book [3] using different rate constants to obtain an inductive loop, and quite different values of transfer coefficients, 0.2 and 0.6, were chosen by Diard et al. [212].

For the general mechanism involving all four rate constants and assuming that the transfer coefficients are both 0.5 and the rate constants are between 10^{-5} and $10^{-15} \text{ mol cm}^{-2} \text{ s}^{-1}$ one can find that the ratio of R_0/R_{ct} is never lower than 8 and the inductive loop is hardly visible taking into account that the value of L must be sufficiently large. On the other hand, when the transfer coefficients are different, e.g., $\beta_1 = 0.7$ and $\beta_2 = 0.3$, the ratio $R_0/R_{ct} \geq 2.5$ and an inductive loop may be observed. Examples of complex plane plots obtained in these two cases are displayed in Fig. 5.4.

5.2.3 Distinguishability of the Kinetic Parameters of the Volmer–Heyrovsky Reaction

It has been found [213] that the kinetic parameters of the Volmer–Heyrovsky type of mechanism cannot be unambiguously determined. In fact, two sets of kinetic parameters can describe the experimental parameters of current and impedance, and formally these two solutions are indistinguishable and arise from the permutation of the parameters of the Volmer and Heyrovsky reactions:

$$k_1 \leftrightarrow k_2, \quad k_{-1} \leftrightarrow k_{-2}, \quad \beta_1 \leftrightarrow \beta_2. \quad (5.69)$$

The only difference obtained is that the value of θ_B for one set is replaced by $1 - \theta_B$ for the other set of parameters, that is, the surface coverage increases or decreases with the overpotential [213]. However, this parameter is not directly measurable and is calculated from the rate constants, Eq. (5.60). This problem was subsequently discussed in detail in the literature [214–217] and extended to other mechanisms. Other measurements, for example electrogravimetric ones, are necessary to distinguish between the two sets of parameters. In a series of papers, Diard et al. [218–221] studied possible graphs obtained for such a reaction and the general conditions when an inductive loop might be observed [220].

The preceding equations were written assuming the Langmuir adsorption isotherm for both species. In the case of the Frumkin adsorption isotherm with negative interaction terms the situation is more complex and multi-steady-state curves can be obtained. Such a situation was discussed by Berthier et al. [222].

5.3 Faradaic Reaction Involving Two Adsorbed Species

Electrocatalytic and corrosion reactions often involve two or more adsorbed species. A mechanism involving two adsorbed species and the exchange of two electrons is presented below:



where reaction (5.72) is a simple chemical (potential independent) desorption reaction. These reactions are described by the following kinetic equations:

$$v_1 = \vec{k}_1(1 - \theta_B - \theta_C) - \overleftarrow{k}_{-1}\theta_B, \quad (5.73)$$

$$v_2 = \vec{k}_2\theta_B - \overleftarrow{k}_{-2}\theta_C, \quad (5.74)$$

$$v_3 = k_3\theta_C - k_{-3}(1 - \theta_B - \theta_C), \quad (5.75)$$

and the current equals

$$i = -F(v_1 + v_2) = -Fr_0 \quad (5.76)$$

as the electrons are changed only in the first and second steps. From the equilibrium condition $v_1 = v_2 = v_3 = 0$ one can obtain an additional condition for the rate constants:

$$\frac{k_1 k_2 k_3}{k_{-1} k_{-2} k_{-3}} = 1, \quad (5.77)$$

which is an analogous condition to Eq. (5.39). In addition, two equations describe changes in the surface coverage:

$$\frac{\sigma_1}{F} \frac{d\theta_B}{dt} = v_1 - v_2 = r_1, \quad (5.78)$$

$$\frac{\sigma_2}{F} \frac{d\theta_C}{dt} = v_2 - v_3 = r_2, \quad (5.79)$$

where σ_i are the charges necessary for a full coverage of the electrode surface by B and C , respectively. Equations (5.76), (5.78), and (5.79) describe the electrochemical behavior of the system. To describe the system impedance, these equations should be rewritten for the phasors:

$$\tilde{i} = -F \left[\left(\frac{\partial r_0}{\partial \eta} \right)_{\theta_B, \theta_C} \tilde{\eta} + \left(\frac{\partial r_0}{\partial \theta_B} \right)_{\eta, \theta_C} \tilde{\theta}_B + \left(\frac{\partial r_0}{\partial \theta_C} \right)_{\eta, \theta_B} \tilde{\theta}_C \right], \quad (5.80)$$

$$j\omega \frac{\sigma_1}{F} \tilde{\theta}_B = \left(\frac{\partial r_1}{\partial \eta} \right)_{\theta_B, \theta_C} \tilde{\eta} + \left(\frac{\partial r_1}{\partial \theta_B} \right)_{\eta, \theta_C} \tilde{\theta}_B + \left(\frac{\partial r_1}{\partial \theta_C} \right)_{\eta, \theta_B} \tilde{\theta}_C, \quad (5.81)$$

$$j\omega \frac{\sigma_2}{F} \tilde{\theta}_C = \left(\frac{\partial r_2}{\partial \eta} \right)_{\theta_B, \theta_C} \tilde{\eta} + \left(\frac{\partial r_2}{\partial \theta_B} \right)_{\eta, \theta_C} \tilde{\theta}_B + \left(\frac{\partial r_2}{\partial \theta_C} \right)_{\eta, \theta_B} \tilde{\theta}_C, \quad (5.82)$$

from which the faradaic admittance, $\hat{Y}_f = \tilde{i}/\tilde{\eta}$, can be determined:

$$\hat{Y}_f = \frac{1}{\hat{Z}_f} = \frac{\tilde{i}}{\tilde{\eta}} = A + \frac{B + j\omega C}{j\omega D - \omega^2 + E}, \quad (5.83)$$

where

$$A = \frac{1}{R_{ct}} = -F \left(\frac{\partial r_0}{\partial \eta} \right)_{\theta_B, \theta_C}, \quad (5.84)$$

$$B = -\frac{F^3}{\sigma_1 \sigma_2} \left\{ \begin{aligned} & - \left(\frac{\partial r_0}{\partial \theta_B} \right) \left(\frac{\partial r_1}{\partial \eta} \right) \left(\frac{\partial r_2}{\partial \theta_C} \right) + \left(\frac{\partial r_0}{\partial \theta_B} \right) \left(\frac{\partial r_1}{\partial \theta_C} \right) \left(\frac{\partial r_2}{\partial \eta} \right) \\ & - \left(\frac{\partial r_0}{\partial \theta_C} \right) \left(\frac{\partial r_1}{\partial \theta_B} \right) \left(\frac{\partial r_2}{\partial \eta} \right) + \left(\frac{\partial r_0}{\partial \theta_C} \right) \left(\frac{\partial r_1}{\partial \eta} \right) \left(\frac{\partial r_2}{\partial \theta_B} \right) \end{aligned} \right\}, \quad (5.85)$$

$$C = -F^2 \left[\frac{1}{\sigma_1} \left(\frac{\partial r_0}{\partial \theta_B} \right) \left(\frac{\partial r_1}{\partial \eta} \right) + \frac{1}{\sigma_2} \left(\frac{\partial r_0}{\partial \theta_C} \right) \left(\frac{\partial r_2}{\partial \eta} \right) \right], \quad (5.86)$$

$$D = -F \left[\frac{1}{\sigma_1} \left(\frac{\partial r_1}{\partial \theta_B} \right) + \frac{1}{\sigma_2} \left(\frac{\partial r_2}{\partial \theta_C} \right) \right], \quad (5.87)$$

$$E = \frac{F^2}{\sigma_1 \sigma_2} \left[\left(\frac{\partial r_1}{\partial \theta_B} \right) \left(\frac{\partial r_2}{\partial \theta_C} \right) - \left(\frac{\partial r_1}{\partial \theta_C} \right) \left(\frac{\partial r_2}{\partial \theta_B} \right) \right], \quad (5.88)$$

where parameters A , C , and D are always positive and B and E can be either positive or negative. From Eq. (5.83) the faradaic impedance is

$$\hat{Z}_f = R_{ct} + \frac{B + j\omega C}{A^2[(D + B/A) + j\omega(E + C/A) - \omega^2]} \quad (5.89)$$

and the polarization resistance

$$R_{pol} = R_{ct} + \frac{B}{A^2(D + \frac{B}{A})}. \quad (5.90)$$

Equation (5.89) represents a second-order impedance [223], and its denominator can be expressed in the form [222]

$$1 + j\omega \frac{2\zeta}{\omega_n} - \left(\frac{\omega}{\omega_n} \right)^2 = 1 + s \frac{2\zeta}{\omega_n} + s^2 \frac{1}{\omega_n^2}, \quad (5.91)$$

where ω_n is called the undamped natural frequency and ζ is the damping ratio of the system [224] expressed as

$$\omega_n = \sqrt{D + \frac{B}{A}} \text{ and } \zeta = \frac{1}{2} \frac{E + \frac{C}{A}}{\sqrt{D + \frac{B}{A}}} = \frac{1}{2} \frac{E + \frac{C}{A}}{\omega_n}. \quad (5.92)$$

The roots of Eq. (5.91) are

$$s_{1,2} = \frac{-\zeta \pm \sqrt{\zeta^2 - 1}}{\omega_n}. \quad (5.93)$$

Depending on the value of ζ , the roots of the denominator may be real or complex. Taking into account possible combinations of the values and the nature of the roots and poles, there are at least 54 theoretically different cases [221]. However, not all the cases are experimentally possible. An example of a circuit

Fig. 5.5 Example of electrical equivalent circuit obtained in case of two adsorbed species

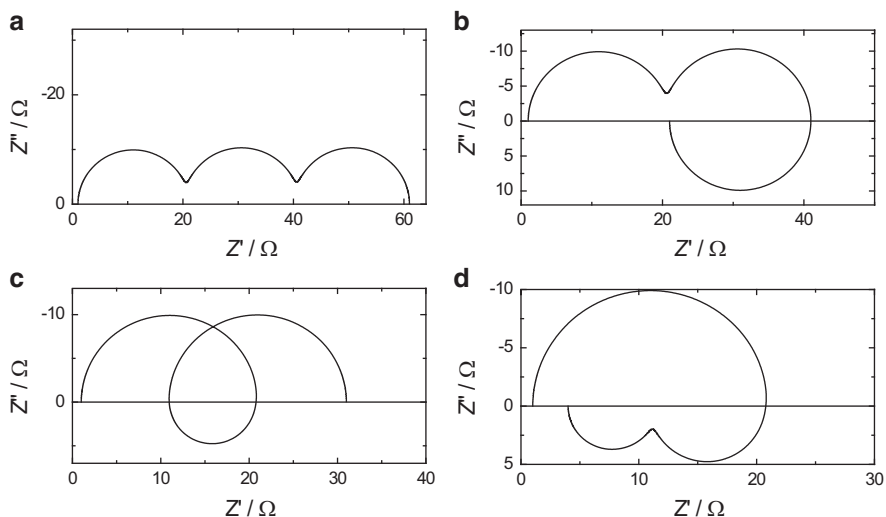
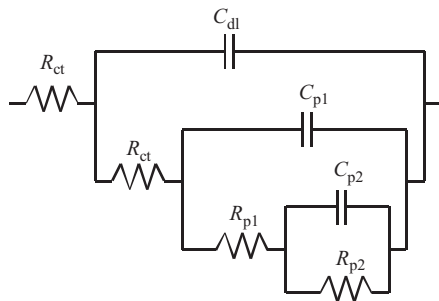


Fig. 5.6 Examples of complex plane plots obtained in presence of two adsorbed species assuming the following parameters: $R_s = 1 \Omega$, $C_{dl} = 20 \mu\text{F}$, $R_{ct} = 20 \Omega$; (a) $R_{p1} = R_{p2} = 20 \Omega$, $C_{p1} = 0.02 \text{ F}$, $C_{p2} = 2 \text{ F}$; (b) $R_{p1} = 20 \Omega$, $R_{p2} = -20 \Omega$, $C_{p1} = 0.02 \text{ F}$, $C_{p2} = -2 \text{ F}$; (c) $R_{p1} = -10 \Omega$, $R_{p2} = 20 \Omega$, $C_{p1} = -0.02 \text{ F}$, $C_{p2} = 2 \text{ F}$; (d) $R_{p1} = -10 \Omega$, $R_{p2} = -7 \Omega$, $C_{p1} = -0.02 \text{ F}$, $C_{p2} = -2 \text{ F}$

representing the total impedance, which could be obtained using the faradaic impedance, Eq. (5.89), is displayed in Fig. 5.5. Of course, this is not a unique circuit, and, depending on the signs and values of parameters A – E , other representations are possible.

A few examples of the complex plane plots that can be obtained in such a case are shown in Fig. 5.6. Many other possible plots are discussed in Ref. [225]. In a similar way, impedance equations for three [11, 57, 226] or more adsorbed species can be obtained [227]. Macdonald et al. [1, 227] studied Al corrosion in KOH and considered three adsorbed species of aluminum and adsorbed hydrogen. They considered six possible mechanisms and found one that explained well changes of the impedance with the electrode potential. Examples of the experimental

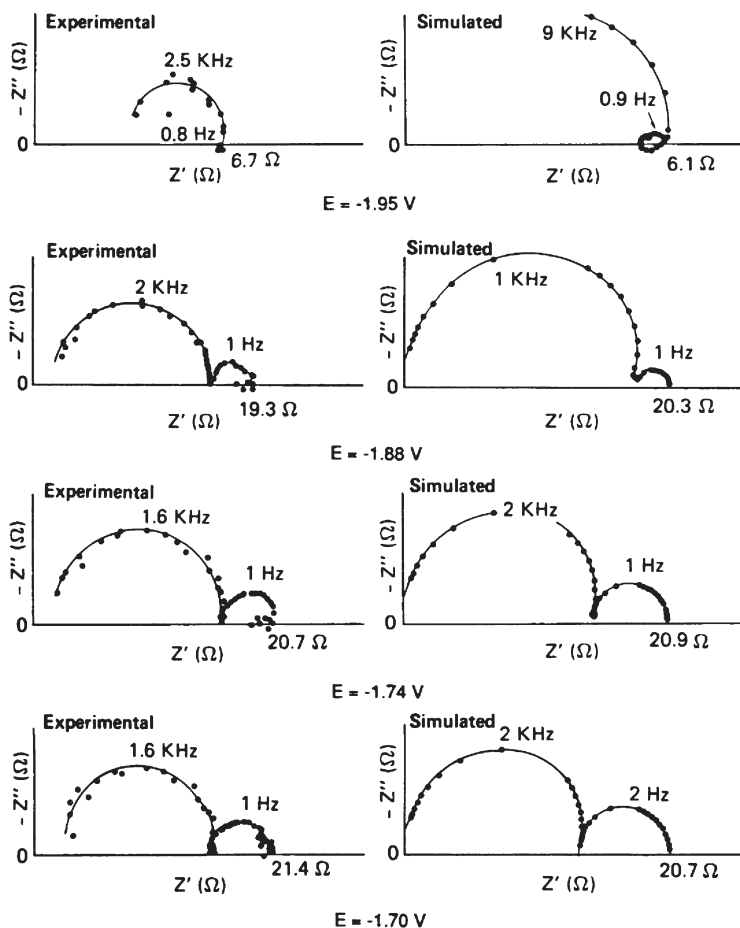


Fig. 5.7 Experimental and simulated impedance spectra for Al in 4 M KOH at 25 °C as a function of applied potential (From Ref. [227]. Reproduced by permission of Electrochemical Society)

impedances and their fit to the assumed mechanism are displayed in Fig. 5.7. More complex cases involving the Frumkin isotherm and second-order mixed terms were studied for methanol oxidation [228].

Using the general method explained in this chapter other mechanisms can be simply described and their impedances found. However, to distinguish between different possible models, measurements should be carried out under different conditions by changing, for example, the electrode potential or concentration.

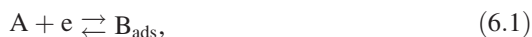
5.4 Exercises

Exercise 5.1 Simulate in ZView the plots in Fig. 5.6.

Chapter 6

General Method of Obtaining Impedance of Complex Reactions

It is possible to write the impedance for each electrochemical mechanism which is described by a series of chemical/electrochemical reactions. In this chapter a general method will be presented using matrix notation, which simplifies the task. An example of a reaction mechanism containing two diffusing, A and C, and one adsorbed species B, described by Eq. (6.1), will be presented:



It involves the diffusion of A toward an electrode, a surface adsorption reaction at an area that is not already occupied by B, desorption of B, and diffusion of C from the electrode. First of all, the system *dc behavior* must be described by appropriate equations. Because the reactions proceed by an exchange of electrons, the rate constants of forward and backward reactions are potential dependent:

$$v_1 = k_1 \exp[-\beta_1 f \eta] (\Gamma_\infty - \Gamma_B) C_A(0) - k_{-1} \exp[(1 - \beta_1) f \eta] \Gamma_B, \quad (6.3)$$

$$v_2 = k_2 \exp[-\beta_2 f \eta] \Gamma_B - k_{-2} \exp[(1 - \beta_2) f \eta] (\Gamma_\infty - \Gamma_B) C_C(0), \quad (6.4)$$

where v_i are the rates of reaction in the units of flux, $\text{mol cm}^{-2} \text{ s}^{-1}$, k_i and k_{-i} are the heterogeneous rate constants of the forward and backward reactions, respectively, β_i are the symmetry coefficients of the electrode processes, $\eta = E - E_{\text{eq}}$ is the overpotential, E_{eq} is the equilibrium potential, Γ_∞ is the surface concentration of all available free sites in the absence of adsorption, Γ_B is the surface concentration of B (in mol cm^{-2}), and $C_i(0)$ are the surface concentrations. By introduction of the surface coverage, θ_b , which is the portion of the surface occupied by adsorbed B species,

$$\theta_B = \frac{\Gamma_B}{\Gamma_\infty}, \quad (6.5)$$

a simpler form may be written:

$$v_1 = \vec{k}_1(1 - \theta_B)C_A(0) - \overleftarrow{k}_{-1}\theta_B, \quad (6.6)$$

$$v_2 = \vec{k}_2\theta_B - \overleftarrow{k}_{-2}(1 - \theta_B)C_C(0), \quad (6.7)$$

where

$$\vec{k}_i = k_i \exp(-\beta_i f \eta) \text{ and } \overleftarrow{k}_{-i} = k_{-i} \exp[(1 - \beta_i) f \eta] \quad (6.8)$$

are the potential-dependent rate constants. Considering the condition at the equilibrium potential

$$v_1 = v_2 = 0 \quad (6.9)$$

leads to the relation

$$\frac{k_1 k_2}{k_{-1} k_{-2}} \frac{C_A^*}{C_C^*} = 1, \quad (6.10)$$

where C_i^* are the bulk concentrations. This relation indicates that there are only three out of four independent rate constants in the system. Such a condition should be checked for each mechanism involving adsorption to avoid further problems with the determination of the kinetic parameters (overdetermined system). More details on such conditions will be presented in Chap. 5.

Next, solving the problem in the steady state, it is necessary to write the following items:

1. Current as a function of the rates of reactions (6.6) and (6.7)
2. Current as function of fluxes of diffusing species
3. Mass balance relations for adsorbed species

The current is described as

$$i = -F(v_1 + v_2) = -Fr_0, \quad (6.11)$$

where $r_0 = v_1 + v_2$ and the negative sign must be added because the reduction current is negative and that of oxidation is positive. Relations between the current and fluxes are

$$i = -2FD_A \left(\frac{\partial C_A}{\partial x} \right)_{x=0} = 2FD_C \left(\frac{\partial C_C}{\partial x} \right)_{x=0} \quad (6.12)$$

and the change in the surface coverage is

$$\Gamma_{\infty} \frac{d\theta_B}{dt} = v_1 - v_2 = r_1, \quad (6.13)$$

where $r_1 = v_1 - v_2$. Equations (6.11), (6.12) and (6.13) describe the dc behavior of our system. Next, equations must be written for the oscillating current, concentrations, and surface coverage, Eq. (4.13), using a linearization procedure, Eq. (4.16). The linearization of Eq. (6.11) (neglecting the higher-order terms) gives

$$\Delta i = -F \left[\left(\frac{\partial r_0}{\partial \eta} \right) \Delta \eta + \left(\frac{\partial r_0}{\partial \theta_B} \right) \Delta \theta_B + \left(\frac{\partial r_0}{\partial C_A} \right) \Delta C_A(0) + \left(\frac{\partial r_0}{\partial C_C} \right) \Delta C_C(0) \right], \quad (6.14)$$

which may be simplified by dividing both sides by $\exp(j\omega t)$:

$$\tilde{i} = -F \left[\left(\frac{\partial r_0}{\partial \eta} \right) \tilde{\eta} + \left(\frac{\partial r_0}{\partial \theta_B} \right) \tilde{\theta}_B + \left(\frac{\partial r_0}{\partial C_A} \right) \tilde{C}_A(0) + \left(\frac{\partial r_0}{\partial C_C} \right) \tilde{C}_C(0) \right]. \quad (6.15)$$

Solution of a semi-infinite linear diffusion Fick's equations (4.19) and (4.22) leads to the expression of Eq. (6.12) in terms of phasors, that is and expressing Eq. (4.30) at the electrode surface, $x = 0$, leads to

$$\begin{aligned} \tilde{i} &= 2F\sqrt{j\omega D_A} \tilde{C}_A(0), \\ \tilde{i} &= -2F\sqrt{j\omega D_C} \tilde{C}_C(0). \end{aligned} \quad (6.16)$$

Finally, linearization of Eq. (6.13) gives the following equation:

$$\begin{aligned} \Gamma_{\infty} \frac{d\Delta\theta_B}{dt} = \Delta r_1 &= \left(\frac{\partial r_1}{\partial \eta} \right) \Delta \eta + \left(\frac{\partial r_1}{\partial \theta_B} \right) \Delta \theta_B \\ &+ \left(\frac{\partial r_1}{\partial C_A} \right) \Delta C_A(0) + \left(\frac{\partial r_1}{\partial C_C} \right) \Delta C_C(0), \end{aligned} \quad (6.17)$$

which gives, after division of both sides by $\exp(j\omega t)$,

$$\Gamma_{\infty} j\omega \tilde{\theta}_B = \left(\frac{\partial r_1}{\partial \eta} \right) \tilde{\eta} + \left(\frac{\partial r_1}{\partial \theta_B} \right) \tilde{\theta}_B + \left(\frac{\partial r_1}{\partial C_A} \right) \tilde{C}_A(0) + \left(\frac{\partial r_1}{\partial C_C} \right) \tilde{C}_C(0). \quad (6.18)$$

We have obtained four equations, (6.15), (6.16), and (6.18), which can be rearranged by dividing all by $\tilde{\eta}$ and keeping constant terms on one side:

$$\begin{aligned}
-\left(\frac{\partial r_0}{\partial \eta}\right) &= \frac{1}{F} \frac{\tilde{i}}{\tilde{\eta}} - \left(\frac{\partial r_0}{\partial \theta_B}\right) \frac{\tilde{\theta}_B}{\tilde{\eta}} - \left(\frac{\partial r_0}{\partial C_A}\right) \frac{\tilde{C}_A(0)}{\tilde{\eta}} - \left(\frac{\partial r_0}{\partial C_C}\right) \frac{\tilde{C}_C(0)}{\tilde{\eta}}, \\
0 &= -\frac{1}{2F} \frac{\tilde{i}}{\tilde{\eta}} + \sqrt{j\omega D_A} \frac{\tilde{C}_A(0)}{\tilde{\eta}}, \\
0 &= \frac{1}{2F} \frac{\tilde{i}}{\tilde{\eta}} + \sqrt{j\omega D_C} \frac{\tilde{C}_C(0)}{\tilde{\eta}}, \\
-\left(\frac{\partial r_1}{\partial \eta}\right) &= -\Gamma_\infty j\omega \frac{\tilde{\theta}_B}{\tilde{\eta}} + \left(\frac{\partial r_1}{\partial \theta_B}\right) \frac{\tilde{\theta}_B}{\tilde{\eta}} + \left(\frac{\partial r_1}{\partial C_A}\right) \frac{\tilde{C}_A(0)}{\tilde{\eta}} + \left(\frac{\partial r_1}{\partial C_C}\right) \frac{\tilde{C}_C(0)}{\tilde{\eta}}.
\end{aligned} \tag{6.19}$$

It is evident that the ratio $\tilde{i}/\tilde{\eta}$ is the faradaic admittance; therefore, this term should be calculated from the system of Eq. (6.19). To simplify the procedure, they may be written in the matrix form $\mathbf{Y} = \mathbf{A}\mathbf{X}$:

$$\begin{bmatrix} -\frac{\partial r_0}{\partial \eta} \\ 0 \\ 0 \\ -\frac{\partial r_1}{\partial \eta} \end{bmatrix} = \begin{bmatrix} \frac{1}{F} & -\frac{\partial r_0}{\partial \theta_B} & -\frac{\partial r_0}{\partial C_A} & -\frac{\partial r_0}{\partial C_C} \\ -\frac{1}{2F} & 0 & \sqrt{j\omega D_A} & 0 \\ \frac{1}{2F} & 0 & 0 & \sqrt{j\omega D_C} \\ 0 & \frac{\partial r_1}{\partial \theta_B} - \Gamma_\infty j\omega & \frac{\partial r_1}{\partial C_A} & \frac{\partial r_1}{\partial C_C} \end{bmatrix} \begin{bmatrix} \frac{\tilde{i}}{\tilde{\eta}} \\ \frac{\tilde{\theta}_B}{\tilde{\eta}} \\ \frac{\tilde{C}_C(0)}{\tilde{\eta}} \\ \frac{\tilde{C}_A(0)}{\tilde{\eta}} \end{bmatrix}. \tag{6.20}$$

The faradaic admittance $\tilde{Y} = \tilde{i}/\tilde{\eta}$ may be calculated using Cramer's rule as $\tilde{Y}_f = T/A$, where $A = \det(\mathbf{A})$, $T = \det(\mathbf{T})$, and determinant T is obtained by replacing the first column in A by Y :

$$A = \begin{vmatrix} \frac{1}{F} & -\frac{\partial r_0}{\partial \theta_B} & -\frac{\partial r_0}{\partial C_A} & -\frac{\partial r_0}{\partial C_C} \\ -\frac{1}{2F} & 0 & \sqrt{j\omega D_A} & 0 \\ \frac{1}{2F} & 0 & 0 & \sqrt{j\omega D_C} \\ 0 & \frac{\partial r_1}{\partial \theta_B} - \Gamma_\infty j\omega & \frac{\partial r_1}{\partial C_A} & \frac{\partial r_1}{\partial C_C} \end{vmatrix}, \tag{6.21}$$

$$T = \begin{vmatrix} -\frac{\partial r_0}{\partial \eta} & -\frac{\partial r_0}{\partial \theta_B} & -\frac{\partial r_0}{\partial C_A} & -\frac{\partial r_0}{\partial C_C} \\ 0 & 0 & \sqrt{j\omega D_A} & 0 \\ 0 & 0 & 0 & \sqrt{j\omega D_C} \\ -\frac{\partial r_1}{\partial \eta} & \frac{\partial r_1}{\partial \theta_B} - \Gamma_\infty j\omega & \frac{\partial r_1}{\partial C_A} & \frac{\partial r_1}{\partial C_C} \end{vmatrix}, \quad (6.22)$$

and after calculation of the determinants

$$T = \sqrt{D_A D_C} \left[\Gamma_\infty \frac{\partial r_0}{\partial \eta} (j\omega)^2 + \left(-\frac{\partial r_0}{\partial \eta} \frac{\partial r_1}{\partial \theta_B} - \frac{\partial r_0}{\partial \theta_B} \frac{\partial r_1}{\partial \eta} \right) (j\omega) \right] \quad (6.23)$$

$$= a_4(j\omega)^2 + a_2(j\omega),$$

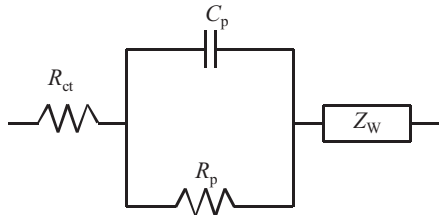
$$A = \frac{1}{2F} \left[\begin{aligned} & -2\sqrt{D_A D_C} \Gamma_\infty (j\omega)^2 \\ & + \Gamma_\infty \left(\sqrt{D_C} \frac{\partial r_0}{\partial C_A} - \sqrt{D_A} \frac{\partial r_0}{\partial C_C} \right) (j\omega)^{3/2} \\ & 2\sqrt{D_A D_C} \frac{\partial r_1}{\partial \theta_B} (j\omega) \\ & + \left(\sqrt{D_C} \frac{\partial r_0}{\partial C_A} \frac{\partial r_1}{\partial \theta_B} + \sqrt{D_A} \frac{\partial r_0}{\partial C_C} \frac{\partial r_1}{\partial \theta_B} \right) \\ & + \left(-\sqrt{D_C} \frac{\partial r_0}{\partial \theta_B} \frac{\partial r_1}{\partial C_A} - \sqrt{D_A} \frac{\partial r_0}{\partial \theta_B} \frac{\partial r_1}{\partial C_C} \right) (j\omega)^{1/2} \end{aligned} \right] \quad (6.24)$$

$$= \frac{1}{2F} \left[b_4(j\omega)^2 + b_3(j\omega)^{3/2} + b_2(j\omega) + b_1(j\omega)^{1/2} \right],$$

and the faradaic admittance:

$$\begin{aligned} \hat{Y}_f &= 2F \frac{a_4(j\omega)^2 + a_2(j\omega)}{b_4(j\omega)^2 + b_3(j\omega)^{3/2} + b_2(j\omega) + b_1(j\omega)^{1/2}} \\ &= 2F \frac{a_4(j\omega)^{3/2} + a_2(j\omega)^{1/2}}{b_4(j\omega)^{3/2} + b_3(j\omega) + b_2(j\omega)^{1/2} + b_1} \\ &= 2F \left\{ \frac{a_4}{b_4} - \frac{a_4}{b_4} \left[\frac{\frac{b_3}{b_4}(j\omega) + \left(\frac{b_2}{b_4} - \frac{a_2}{a_4} \right) (j\omega)^{1/2} + \frac{b_1}{b_4}}{(j\omega)^{3/2} + \frac{b_3}{b_4}(j\omega) + \frac{b_2}{b_4}(j\omega)^{1/2} + \frac{b_1}{b_4}} \right] \right\}, \end{aligned} \quad (6.25)$$

Fig. 6.1 Electrical equivalent model of faradaic impedance described by Eqs. (6.28) and (6.26)



or, for the faradaic impedance,

$$\hat{Z}_f = \frac{1}{2F} \frac{b_4(j\omega)^{3/2} + b_3(j\omega) + b_2(j\omega)^{1/2} + b_1}{a_4(j\omega)^{3/2} + a_2(j\omega)^{1/2}}. \quad (6.26)$$

This can be rearranged into

$$\begin{aligned} \hat{Z}_f &= \frac{1}{2F} \frac{b_4}{a_4} + \frac{1}{2F} \frac{b_4}{a_4} \left[\frac{\frac{b_3}{b_4}j\omega + \left(-\frac{a_2}{a_4} + \frac{b_2}{b_4}\right)(j\omega)^{1/2} + \frac{b_1}{b_4}}{(j\omega)^{1/2} \left[j\omega + \frac{a_2}{a_4}\right]} \right] \\ &= R_{ct} + \frac{1}{2F} \left[\frac{\frac{b_3}{a_2}j\omega + \left(-\frac{b_4}{a_4} + \frac{b_2}{a_2}\right)(j\omega)^{1/2} + \frac{b_1}{a_2}}{(j\omega)^{1/2} \left[j\omega + \frac{a_4}{a_2} + 1\right]} \right], \end{aligned} \quad (6.27)$$

where R_{ct} is the charge transfer resistance. It is evident that the denominator of the last expression has two poles corresponding to one diffusive, $(j\omega)^{-1/2}$, and one capacitive, $(j\omega)^{-1}$, term, which should appear in the equivalent electrical circuit. It can be shown that this equation similar to a general model (Fig. 6.1). In fact, the impedance of this model may be expressed as

$$\begin{aligned} \hat{Z}_f &= R_{ct} + \frac{1}{j\omega C_p + \frac{1}{R_p}} + Z_w = R_{ct} + \frac{1}{j\omega C_p + \frac{1}{R_p}} + \frac{\sigma}{\sqrt{j\omega}} \\ &= R_{ct} + \frac{(j\omega)\sigma + (j\omega)^{1/2} \frac{1}{C_p} + \frac{\sigma}{R_p C_p}}{(j\omega)^{1/2} \left[j\omega + \frac{1}{R_p C_p}\right]}, \end{aligned} \quad (6.28)$$

Fig. 6.2 Complex plane plot for circuit in Fig. 6.1.

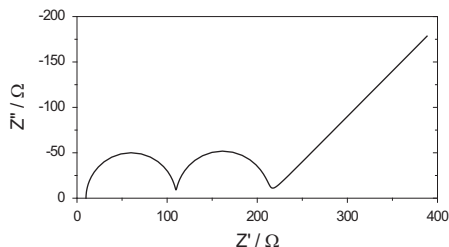
Parameters: $R_s = 10 \Omega$,

$R_{ct} = R_p = 100 \Omega$,

$C_{dl} = 2 \times 10^{-5} \text{ F}$,

$C_p = 0.01 \text{ F}$,

$\sigma' = 0.5 \Omega \text{ s}^{-1/2}$



which has a form similar to Eq. (6.27). However, Eq. (6.27) contains five independent parameters and Eq. (6.28) only four, therefore exact equivalence of the parameters of both equations cannot be established unless there is a relation between the parameters of Eq. (6.27). If such a relation exists one can get a plot displaying two semicircles followed by a straight line at 45° on the complex plane plots, Fig. 6.2. General plot of Eq. (6.27) might be more complex.

Comparison of the parameters in Eqs. (6.27) and (6.28) leads to the physical meaning of the parameters found:

$$R_{ct} = \frac{1}{2F} \frac{b_4}{a_4}; \quad C_p = 2F \frac{a_4}{b_4} \frac{1}{\left(\frac{b_2}{b_4} - \frac{a_2}{a_4}\right)}; \quad R_p = \frac{1}{2F} \frac{b_4}{a_2} \left(\frac{b_2}{b_4} - \frac{a_2}{a_4}\right); \quad (6.29)$$

$$\sigma = \frac{1}{2F} \frac{b_3}{a_4}; \quad b_1 = \frac{a_2 b_3}{a_4}$$

Of course, Eq. (6.27) might also have other equivalent circuit representations.

The method presented above can be applied to any mechanism. In a later chapter it will be used for the calculation of impedances of other mechanisms. In general, in the faradaic impedance, inverse of resistances are proportional to rate constants and capacitances depend on the surface coverages (which contain the ratios of the rate constants that is depend on the equilibrium constants), although some lengthy rearrangements might be required to prove this.

Harrington et al. [229–235] proposed a more general method based on a general model for chemical reactions [236] and linear algebra, making it possible to predict the number and nature of parameters and the equivalent circuit for mechanisms involving diffusion and adsorption. Practical information about the stability and complexity of impedance plots and the relation between the reaction mechanism and equivalent circuit may be deduced. For example, the model predicts that inductive loops cannot be observed at equilibrium. However, a detailed presentation of this method is beyond the scope of this book.

Chapter 7

Electrocatalytic Reactions Involving Hydrogen

Many reactions of industrial importance are electrocatalytic, i.e., they involve the specific adsorption of intermediates, for example hydrogen, chlorine, and oxygen evolution, oxygen reduction, and methanol or ethanol oxidation in fuel cells. Many different electrochemical techniques were used to study these reactions, and EIS is one of them, providing interesting kinetic and surface information. Certain model reactions will be presented in what follows with a detailed method of relating impedance parameters with mechanistic and kinetic equations.

7.1 Hydrogen Underpotential Deposition Reaction

On several noble metals (Pt, Rh, Ru, Ir, and Pd) hydrogen adsorption takes place at the potentials positive to the equilibrium potential for the hydrogen evolution reaction. This is a so-called hydrogen underpotential deposition reaction (HUPD) and indicates a strong adsorptive interaction between atomic hydrogen and the surface metal atoms. Similar UPD processes are observed for the deposition of metals on metals [237]. Certain reactions, like Cu UPD at Pt, Ru, or Rh, are used as diagnostic tools to determine the real surface area of electrocatalytic materials.

Although the adsorption isotherms are usually complex [238], the simplest Langmuir isotherm will be presented first and later the Frumkin isotherm will be shown. The following development is similar to that in Sect. 5.1. The HUPD reaction in acid and alkaline solutions may be written as



or



The kinetic equations in acid solution are

$$i = -Fv_1 = \frac{dQ}{dt} = -F \frac{d\Gamma_{\text{H}}}{dt} = -\sigma_1 \frac{d\theta_{\text{H}}}{dt}, \quad (7.3)$$

$$\begin{aligned} v_1 &= k_1^0 C_{\text{H}^+}(0)(\Gamma_{\infty} - \Gamma_{\text{H}})e^{-\beta f(E-E_1^0)} - k_{-1}^0 \Gamma_{\text{H}} e^{(1-\beta)f(E-E_1^0)} \\ &= \Gamma_{\infty} \left[k_1^0 C_{\text{H}^+}(0)(1 - \theta_{\text{H}})e^{-\beta f(E-E_1^0)} - k_{-1}^0 \theta_{\text{H}} e^{(1-\beta)f(E-E_1^0)} \right], \end{aligned} \quad (7.4)$$

where Q is the charge corresponding to the adsorption of H (C cm^{-2}), v_1 is the reaction rate ($\text{mol cm}^{-2} \text{s}^{-1}$), $\sigma_1 = F \Gamma_{\text{H}}$ is the charge necessary for one monolayer coverage by adsorbed H (C cm^{-2}), k_1^0 is the standard rate constant of hydrogen adsorption ($\text{cm}^3 \text{mol}^{-1} \text{s}^{-1}$), k_{-1}^0 is the standard rate constant of desorption (s^{-1}), $C_{\text{H}^+}(0)$ is the surface concentration of hydrogen ions, Γ_{∞} is the total surface concentration of adsorption sites (mol cm^{-2}), Γ_{H} is the surface concentration of adsorbed H, E_1^0 is the standard potential of reaction (7.1), θ_{H} is the fractional surface coverage by adsorbed hydrogen, and $\theta_{\text{H}} = \Gamma_{\text{H}}/\Gamma_{\infty}$. It is evident that the current can flow only when there is a change in surface coverage and in the steady state the current is zero. The equilibrium and peak potential for the HUPD reaction are described by (5.4) and (5.5).

Assuming that the bulk and surface concentrations are the same (i.e., the hydrogen surface concentration is not affected by the passing current) the following equation is obtained:

$$\begin{aligned} v_1 &= \Gamma_{\infty} (k_1^0)^{1-\beta} (k_{-1}^0)^{\beta} (C_{\text{H}^+}^*)^{1-\beta} (1 - \theta_{\text{H}}) e^{-\beta f(E-E_p)} \\ &\quad - \Gamma_{\infty} (k_1^0)^{1-\beta} (k_{-1}^0)^{\beta} (C_{\text{H}^+}^*)^{1-\beta} \theta_{\text{H}} e^{(1-\beta)f(E-E_p)} \\ &= k^0 e^{-\beta f(E-E_p)} (1 - \theta_{\text{H}}) - k^0 e^{(1-\beta)f(E-E_p)} \theta_{\text{H}} \\ &= \overrightarrow{k}_1 (1 - \theta_{\text{H}}) - \overleftarrow{k}_1 \theta_{\text{H}}, \end{aligned} \quad (7.5)$$

where $k^0 = \Gamma_{\infty} (k_1^0)^{1-\beta} (k_{-1}^0)^{\beta} (C_{\text{H}^+}^*)^{1-\beta}$ is the concentration-dependent rate constant, and the potential-dependent rate constants are $\overrightarrow{k}_1 = k^0 \exp[-\beta f(E - E_p)]$ and $\overleftarrow{k}_1 = k^0 \exp[(1-\beta)f(E - E_p)]$. For simplicity let us introduce the overpotential $\eta = E - E_p$, see Eq. (5.5). The further development is identical to that described in Sect. 5.1 [61, 211]. The faradaic impedance is described in Eq. (5.19) and the dependence of the parameters R_{ct} and C_p on the potential is shown in Fig. 5.1. At the current peak potential the charge transfer resistance is at a minimum and the pseudocapacitance at a maximum. It is interesting to note that for the Langmuir

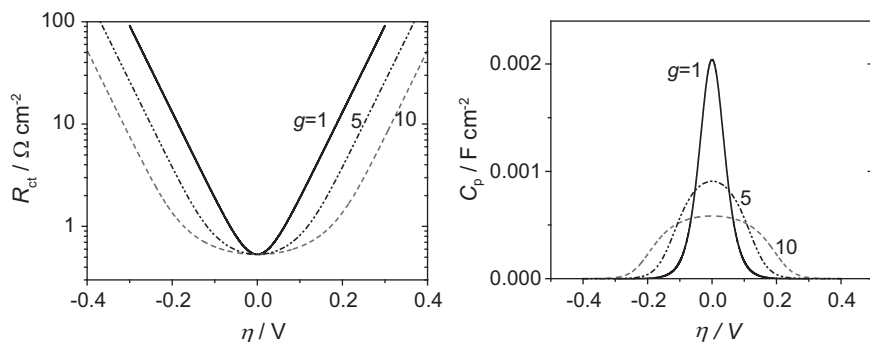


Fig. 7.1 Comparison of parameters R_{ct} and C_p for HUPD reaction, continuous line Langmuir isotherm, $g = 1$, dash-dotted and dashed lines: Frumkin isotherm with $g = 5$ and 10 , $k^0 = 10^{-6} \text{ mol cm}^{-2} \text{ s}^{-1}$

adsorption isotherm the maximum value of the pseudocapacitance, C_p , depends only on the total hydrogen adsorption charge, $\sigma_1 = 210 \mu\text{C cm}^{-2}$ [239], and equals 2.04 mF cm^{-2} .

In the case of the Frumkin adsorption isotherm, which includes lateral interactions between adsorbed hydrogen atoms, the reaction rate is described by [240]

$$\begin{aligned} v_1 &= k^0 \exp(-\beta f \eta) \exp[-\lambda g(\theta_H - 0.5)](1 - \theta_H) \\ &\quad - k^0 \exp[(1 - \beta)f \eta] \exp[(1 - \lambda)g(\theta_H - 0.5)]\theta_H \\ &= \vec{k}_1 \exp[-\lambda g(\theta_H - 0.5)](1 - \theta_H) - \overleftarrow{k}_1 \exp[(1 - \lambda)g(\theta_H - 0.5)]\theta_H, \end{aligned} \quad (7.6)$$

where g is the interaction parameter, positive for repulsions and negative for interactions [17], and λ is the adsorption symmetry factor between 0 and 1, typically ~ 0.5 [240]. In the steady state, the current is equal to zero and the following relation is obtained:

$$\frac{\theta_H}{1 - \theta_H} e^{g(\theta_H - 0.5)} = e^{-f \eta}, \quad (7.7)$$

which is the definition of the Frumkin isotherm. Continuing the development, the same expression for the impedance is obtained, Eq. (5.19), but with different values of the derivatives $\partial v_1 / \partial \eta$ and $\partial v_1 / \partial \theta_H$. The influence of the parameter g on the parameters R_{ct} and C_p is illustrated in Fig. 7.1.

It is evident that an increase in the repulsion between H atoms causes a flattening of both curves and a decrease in the maximum of the pseudocapacitance. It can be added that the Frumkin isotherm was found to describe HUPD at Pt(100) in HClO_4 , Pt(110) in H_2SO_4 , and Pt(111) in both acids [241]. The value of the parameter g at Pt(111) was approximately 12. Unfortunately, the isotherms at other surfaces or metals are much more complicated. The HUPD kinetics was studied on different polycrystalline metals. It was found that the kinetics at Pt [242] was about three orders of magnitude faster than that at Ru [243], Pd [244, 245], or Rh [246] electrodes, while that at Ir was intermediate between those groups [247] (on the

Fig. 7.2 Complex plane plots for HUPD reaction at polycrystalline Pt electrode in 0.1 M H_2SO_4 ; potentials versus reversible hydrogen electrode indicated in graph. Points – experimental, lines – fit (From Ref. [242], copyright (2012), with permission from Elsevier)

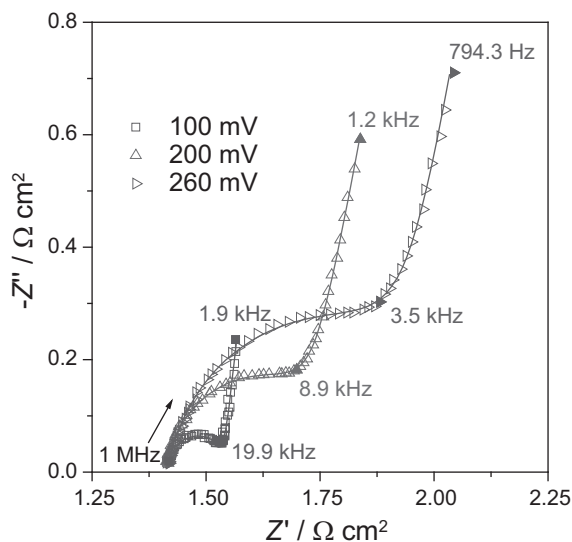
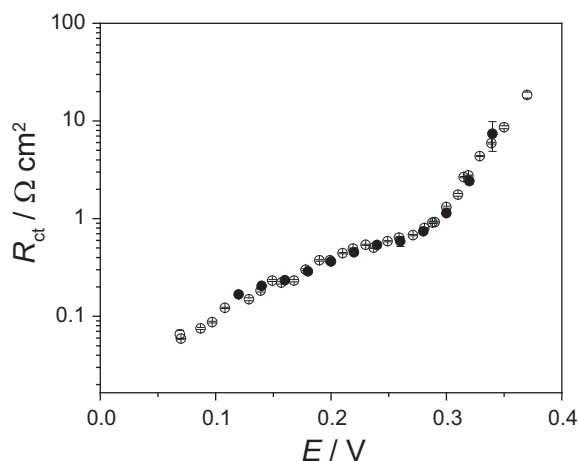


Fig. 7.3 Dependence of charge transfer resistance (per real surface area) on potential for HUPD reaction at polycrystalline Pt in 0.1 M H_2SO_4 (From Ref. [242], copyright (2012), with permission from Elsevier)

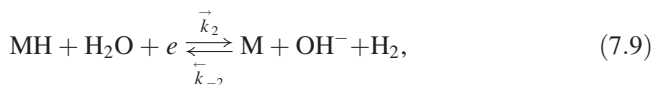
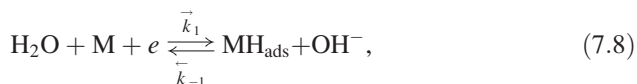


logarithmic scale). An example of the complex plane plots obtained at polycrystalline Pt in H_2SO_4 is presented in Fig. 7.2. To approximate the experimental curves, it was necessary to replace C_{dl} and C_p by the constant phase elements, CPE, see Chap. 8. The dependence of the charge transfer resistance on the potential is shown in Fig. 7.3.

It is evident that R_{ct} decreases with a decrease in the electrode potential in the entire range. At the lowest potentials there is an influence of the overpotentially deposited hydrogen (HOPD), which is related to the classical hydrogen evolution, and dissolved hydrogen formation at the solution around the electrode. The kinetics is very fast and was measured without a potentiostat [242]. Because the adsorption isotherm is rather complex [248] no rate constants were determined. It should be added that in earlier studies, at monocrystalline Pt, it was found that R_{ct} was potential independent [249], which may be connected with equipment artifacts.

7.2 Hydrogen Evolution Reaction

The hydrogen evolution reaction (HER) is one of the most important and most studied electrocatalytic processes [61, 211, 239, 250, 251]. It is well accepted that the first step is the Volmer reaction, (7.8), followed by Heyrovsky, (7.9), or Tafel, (7.10), steps. Because the process is usually carried out in alkaline solutions these steps are written as follows:



It might be noticed that the Volmer and Heyrovsky reactions are electrochemical while the Tafel reaction is chemical, without an exchange of electrons. Assuming a Langmuir adsorption isotherm for H, the rates, v_i , are written as

$$v_1 = k_1^0 \Gamma_\infty a_{\text{H}_2\text{O}} (1 - \theta_{\text{H}}) e^{-\beta_1 f (E - E_1^0)} - k_{-1}^0 \Gamma_\infty a_{\text{OH}^-} \theta_{\text{H}} e^{(1 - \beta_1) f (E - E_1^0)}, \quad (7.11)$$

$$v_2 = k_2^0 \Gamma_\infty a_{\text{H}_2\text{O}} \theta_{\text{H}} e^{-\beta_2 f (E - E_2^0)} - k_{-2}^0 \Gamma_\infty a_{\text{H}_2} a_{\text{OH}^-} (1 - \theta_{\text{H}}) e^{(1 - \beta_2) f (E - E_2^0)}, \quad (7.12)$$

$$v_3 = (k_3^0 \Gamma_\infty^2) \theta_{\text{H}}^2 - (k_{-3}^0 \Gamma_\infty^2) (1 - \theta_{\text{H}})^2 a_{\text{H}_2}. \quad (7.13)$$

For simplicity the surface concentrations of OH^- , H_2O , and H_2 are written as dimensionless $a_i = C_i(0)/C^*$, where the superscripted asterisk denotes bulk or equilibrium values. In general, the standard potentials of the Volmer and Heyrovsky steps are different. Proceeding in a way similar to that described in Sect. 5.2.1 the following equations are obtained:

$$v_1 = \left\{ (k_1^0)^{(1 - \beta_1)} (k_{-1}^0)^{\beta_1} \Gamma_\infty \left(\frac{a_{\text{OH}^-}^* \theta_{\text{H}}^*}{a_{\text{H}_2\text{O}}^* (1 - \theta_{\text{H}}^*)} \right)^{\beta_1} \right\} a_{\text{H}_2\text{O}} (1 - \theta_{\text{H}}) \exp(-\beta_1 f \eta) - \left\{ (k_1^0)^{(1 - \beta_1)} (k_{-1}^0)^{\beta_1} \Gamma_\infty \left(\frac{a_{\text{H}_2\text{O}}^* (1 - \theta_{\text{H}}^*)}{a_{\text{OH}^-}^* \theta_{\text{H}}^*} \right)^{1 - \beta_1} \right\} a_{\text{OH}^-} \theta_{\text{H}} \exp[(1 - \beta_1) f \eta], \quad (7.14)$$

$$\begin{aligned}
v_2 = & \left\{ (k_2^0)^{(1-\beta_2)} (k_{-2}^0)^{\beta_2} \Gamma_\infty \left(\frac{a_{\text{H}_2}^* a_{\text{OH}^-}^*}{a_{\text{H}_2\text{O}}^*} \frac{1 - \theta_{\text{H}}^*}{\theta_{\text{H}}^*} \right)^{\beta_2} \right\} a_{\text{H}_2\text{O}} \theta_{\text{H}} \exp(-\beta_2 f \eta) \\
& - \left\{ (k_2^0)^{(1-\beta_2)} (k_{-2}^0)^{\beta_2} \Gamma_\infty \left(\frac{a_{\text{H}_2\text{O}}^*}{a_{\text{H}_2}^* a_{\text{OH}^-}^*} \frac{\theta_{\text{H}}^*}{1 - \theta_{\text{H}}^*} \right)^{1-\beta_2} \right\} a_{\text{H}_2} a_{\text{OH}^-} (1 - \theta_{\text{H}}) \exp[(1 - \beta_2) f \eta].
\end{aligned} \tag{7.15}$$

Assuming that the surface and bulk concentrations are the same one obtains

$$v_1 = k_1(1 - \theta_{\text{H}})e^{-\beta_1 f \eta} - k_{-1}\theta_{\text{H}}e^{(1-\beta_1)f \eta} = \vec{k}_1(1 - \theta_{\text{H}}) - \overleftarrow{k}_{-1}\theta_{\text{H}}, \tag{7.16}$$

$$v_2 = k_2\theta_{\text{H}}e^{-\beta_2 f \eta} - k_{-2}(1 - \theta_{\text{H}})e^{(1-\beta_2)f \eta} = \vec{k}_2\theta_{\text{H}} - \overleftarrow{k}_{-2}(1 - \theta_{\text{H}}), \tag{7.17}$$

$$v_3 = k_3\theta_{\text{H}}^2 - k_{-3}(1 - \theta_{\text{H}})^2, \tag{7.18}$$

where

$$k_1 = (k_1^0)^{(1-\beta_1)} (k_{-1}^0)^{\beta_1} \Gamma_\infty \left(\frac{a_{\text{OH}^-}^*}{a_{\text{H}_2\text{O}}^*} \frac{\theta_{\text{H}}^*}{1 - \theta_{\text{H}}^*} \right)^{\beta_1}, \tag{7.19}$$

$$k_{-1} = (k_1^0)^{(1-\beta_1)} (k_{-1}^0)^{\beta_1} \Gamma_\infty \left(\frac{a_{\text{H}_2\text{O}}^*}{a_{\text{OH}^-}^*} \frac{1 - \theta_{\text{H}}^*}{\theta_{\text{H}}^*} \right)^{1-\beta_1},$$

$$k_2 = (k_2^0)^{(1-\beta_2)} (k_{-2}^0)^{\beta_2} \Gamma_\infty \left(\frac{a_{\text{H}_2}^* a_{\text{OH}^-}^*}{a_{\text{H}_2\text{O}}^*} \frac{1 - \theta_{\text{H}}^*}{\theta_{\text{H}}^*} \right)^{\beta_2}, \tag{7.20}$$

$$k_{-2} = (k_2^0)^{(1-\beta_2)} (k_{-2}^0)^{\beta_2} \Gamma_\infty \left(\frac{a_{\text{H}_2\text{O}}^*}{a_{\text{H}_2}^* a_{\text{OH}^-}^*} \frac{\theta_{\text{H}}^*}{1 - \theta_{\text{H}}^*} \right)^{1-\beta_2},$$

$$k^3 = k_3^0 \Gamma_\infty^2, \tag{7.21}$$

$$k_{-3} = k_{-3}^0 \Gamma_\infty^2 a_{\text{H}_2}^*.$$

Equations (7.16), (7.17), and (7.18) can also be presented in another form:

$$v_1 = v_1^0 \left[\left(\frac{1 - \theta_{\text{H}}}{1 - \theta_{\text{H}}^*} \right) \left(\frac{a_{\text{H}_2\text{O}}}{a_{\text{H}_2\text{O}}^*} \right) \exp(-\beta_1 f \eta) - \left(\frac{\theta_{\text{H}}}{\theta_{\text{H}}^*} \right) \left(\frac{a_{\text{OH}^-}}{a_{\text{OH}^-}^*} \right) \exp[(1 - \beta_1) f \eta] \right], \tag{7.22}$$

$$v_2 = v_2^0 \left[\begin{aligned} &\left(\frac{\theta_H}{\theta_H^0} \right) \left(\frac{a_{H_2O}}{a_{H_2O}^*} \right) \exp(-\beta_2 f \eta) \\ &- \left(\frac{1 - \theta_H}{1 - \theta_H^0} \right) \left(\frac{a_{H_2}}{a_{H_2}^*} \right) \left(\frac{a_{OH^-}}{a_{OH^-}^*} \right) \exp[(1 - \beta_2) f \eta] \end{aligned} \right], \quad (7.23)$$

$$v_3 = v_3^0 \left[\left(\frac{\theta_H}{\theta_H^*} \right)^2 - \left(\frac{1 - \theta_H}{1 - \theta_H^*} \right)^2 \left(\frac{a_{H_2}}{a_{H_2}^*} \right) \right], \quad (7.24)$$

where

$$v_1^0 = (k_1^0)^{(1-\beta_1)} (k_{-1}^0)^{\beta_1} \Gamma_\infty (a_{OH^-}^*)^{\beta_1} (a_{H_2O}^*)^{1-\beta_1} (\theta_H^*)^{\beta_1} (1 - \theta_H^*)^{1-\beta_1}, \quad (7.25)$$

$$v_2^0 = (k_2^0)^{(1-\beta_2)} (k_{-2}^0)^{\beta_2} \Gamma_\infty (a_{H_2}^* a_{OH^-}^*)^{\beta_2} (a_{H_2O}^*)^{1-\beta_2} (\theta_H^*)^{1-\beta_2} (1 - \theta_H^*)^{\beta_2}, \quad (7.26)$$

$$v_3^0 = \frac{k_3 k_{-3} \Gamma_\infty a_{H_2}^*}{(\sqrt{k_3} + \sqrt{k_{-3} a_{H_2}^*})}. \quad (7.27)$$

It is important to remember that all rate constants, Eqs. (7.19), (7.20), and (7.21), and the standard rates, Eqs. (7.25), (7.26), and (7.27), are concentration dependent, and the experimenter should ensure that they stay constant at various current densities. It is also possible to redefine all the equations introducing the real surface concentrations, which should be known from the experiments. Then the current flowing in the system is described by

$$i = -F(v_1 + v_2) = -F r_0. \quad (7.28)$$

At the equilibrium potential, the rates of all reactions are zero,

$$v_1 = v_2 = v_3 = 0, \quad (7.29)$$

and the following relation between the rate constants is obtained [217]:

$$\frac{k_1 k_2}{k_{-1} k_{-2}} = \frac{k_1^2 k_3}{k_{-1}^2 k_{-3}} = \frac{k_2^2 k_3}{k_{-2}^2 k_{-3}} = 1. \quad (7.30)$$

As a consequence, two equivalent solutions exist (see also Sect. 5.2.3) giving the same values of the physically measured currents and impedances [213–217] in which the appropriate rate constants can be exchanged:

$$k_1 \leftrightarrow k_2 \quad k_{-1} \leftrightarrow k_{-2} \quad k_3 \leftrightarrow k_{-3}. \quad (7.31)$$

The only difference is that the values of θ_H are replaced by $1-\theta_H$, that is, the surface coverage decreases or increases with the negative overpotential. This makes the rate constants indistinguishable, and other experiments must be used to decide which solution is correct.

At the steady state, the surface coverage by adsorbed hydrogen may be obtained from the condition that the rates of hydrogen adsorption and desorption are equal:

$$\frac{d\Gamma_H}{dt} = \frac{\sigma_1}{F} \frac{d\theta_H}{dt} = r_1 = v_1 - v_2 - 2v_3 = 0, \quad (7.32)$$

which leads to a second-order equation [217, 252, 253]. In the case where the Tafel reaction is neglected, a simpler equation is obtained:

$$\theta_H = \frac{\vec{k}_1 + \overset{\leftarrow}{k}_{-2}}{\vec{k}_1 + \overset{\leftarrow}{k}_{-1} + \vec{k}_2 + \overset{\leftarrow}{k}_{-2}}, \quad (7.33)$$

which, at negative overpotentials, reaches a constant value lower than unity (in contrast to the HUPD reaction):

$$\theta_H = \frac{k_1}{k_1 + k_2}, \quad (7.34)$$

Having described the HER in dc conditions the impedance of this process is described by the linearization of the changes in the surface coverage and the current:

$$\Delta i = \left(\frac{\partial i}{\partial \eta} \right)_{\theta_H} \Delta \eta + \left(\frac{\partial i}{\partial \theta_H} \right)_{\eta} \Delta \theta_H = F \left[\left(\frac{\partial r_0}{\partial \eta} \right)_{\theta_H} \Delta \eta + \left(\frac{\partial r_0}{\partial \theta_H} \right)_{\eta} \Delta \theta_H \right], \quad (7.35)$$

$$\frac{\sigma_1}{F} \frac{d\Delta \theta_H}{dt} = \Delta r_1 = \left(\frac{\partial r_1}{\partial \eta} \right)_{\theta_H} \Delta \eta + \left(\frac{\partial r_1}{\partial \theta_H} \right)_{\eta} \Delta \theta_H. \quad (7.36)$$

Following the procedure described in Sect. 5.2 the faradaic impedance described by Eq. (5.54) is obtained. The kinetics of the HER has been studied often using EIS, but the rate constants were rarely determined, e.g., at Ni [213, 254], Pt [255–258], alloys [259–262], or composite [263–269] electrodes. The best method for determining the rate constant is the simultaneous approximation of the impedance parameters and the dc current [213, 254, 263].

7.3 Influence of Hydrogen Mass Transfer on HER

During the HER, hydrogen is produced at the electrode surface, Eqs. (7.9), and (7.10), and diffuses toward the bulk of the solution. At the electrode surface at the rotating disk electrode (RDE), oversaturation may appear without bubble formation [180, 270, 271]. In such cases, reactions (7.12) and (7.13) should be rearranged to

$$v_2 = \vec{k}_2 \theta_H - \overleftarrow{k}_{-2} (1 - \theta_H) a_{H_2}, \quad (7.37)$$

$$v_3 = k_3 \theta_H^2 - k_{-3} (1 - \theta_H)^2 a_{H_2}, \quad (7.38)$$

where the definitions of k_2 , k_{-2} , and k_{-3} must be modified to exclude the dimensionless surface concentration of hydrogen, a_{H_2} . Besides Eqs. (7.28), (7.29), (7.30), (7.31), and (7.32) another equation involving dissolved hydrogen flux, J_{H_2} , must be added:

$$J_{H_2} = -D_{H_2} C^0 \frac{da_{H_2}}{dx} = v_2 + v_3 = r_2. \quad (7.39)$$

For the RDE one can write a simplified equation, $J_{H_2} = D_{H_2} C^0 (a_{H_2} - a_{H_2}^*) / \delta$, where $\delta = 1.612 D_{H_2}^{1/3} \nu^{1/6} \Omega^{-1/2}$ and C^0 is the surface concentration of hydrogen (see also Sect. 4.9). Writing the equation for the flux phasor in finite-length transmissive mass transfer, Eq. (4.68), leads to

$$\tilde{J}_{H_2} = \tilde{a}_{H_2} \left[C^0 \sqrt{j\omega D_{H_2}} \coth \left(\sqrt{\frac{j\omega}{D_{H_2}}} \delta \right) \right] = J' \tilde{a}_{H_2}. \quad (7.40)$$

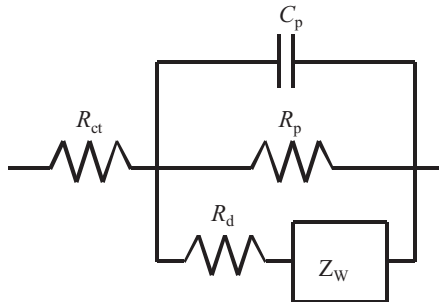
The linearized equations describing the system are

$$\tilde{i} = -F \left[\left(\frac{\partial r_0}{\partial \eta} \right) \tilde{\eta} + \left(\frac{\partial r_0}{\partial \theta_H} \right) \tilde{\theta}_H \right], \quad (7.41)$$

$$j\omega \frac{\sigma_1}{F} \tilde{\theta}_H = \left(\frac{\partial r_1}{\partial \eta} \right) \tilde{\eta} + \left(\frac{\partial r_1}{\partial \theta_H} \right) \tilde{\theta}_H + \left(\frac{\partial r_1}{\partial a_{H_2}} \right) \tilde{a}_{H_2}, \quad (7.42)$$

$$J' \tilde{a}_{H_2} = \left(\frac{\partial r_2}{\partial \theta_H} \right) \tilde{\theta}_H + \left(\frac{\partial r_2}{\partial a_{H_2}} \right) \tilde{a}_{H_2}. \quad (7.43)$$

Fig. 7.4 Electrical equivalent circuit of faradaic impedance corresponding to HER with hydrogen diffusion, Eq. (7.48)



They may be written in matrix form:

$$\begin{bmatrix} -\frac{\partial r_0}{\partial \eta} \\ -\frac{\partial r_1}{\partial \eta} \\ 0 \end{bmatrix} = \begin{bmatrix} \frac{1}{F} & \frac{\partial r_0}{\partial \theta_H} & 0 \\ 0 & \frac{\partial r_1}{\partial \theta_H} - j\omega \frac{\sigma_1}{F} & \frac{\partial r_1}{\partial a_{H_2}} \\ 0 & \frac{\partial r_2}{\partial \theta_H} & \frac{\partial r_2}{\partial a_{H_2}} - J' \end{bmatrix} \begin{bmatrix} \frac{\tilde{i}}{\tilde{\eta}} \\ \frac{\tilde{\theta}_H}{\tilde{\eta}} \\ \frac{\tilde{a}_{H_2}}{\tilde{\eta}} \end{bmatrix}. \quad (7.44)$$

The faradaic admittance is

$$\hat{Y}_f = \frac{\tilde{i}}{\tilde{\eta}} = A + \frac{B}{j\omega + C + \frac{D}{E - J'}}, \quad (7.45)$$

where parameters A , B , and C are as defined in Eq. (5.52) and

$$D = \frac{F}{\sigma_1} \left(\frac{\partial r_1}{\partial a_{H_2}} \right) \left(\frac{\partial r_2}{\partial \theta_H} \right) \text{ and } E = \left(\frac{\partial r_2}{\partial a_{H_2}} \right). \quad (7.46)$$

The faradaic admittance may be rearranged into impedance:

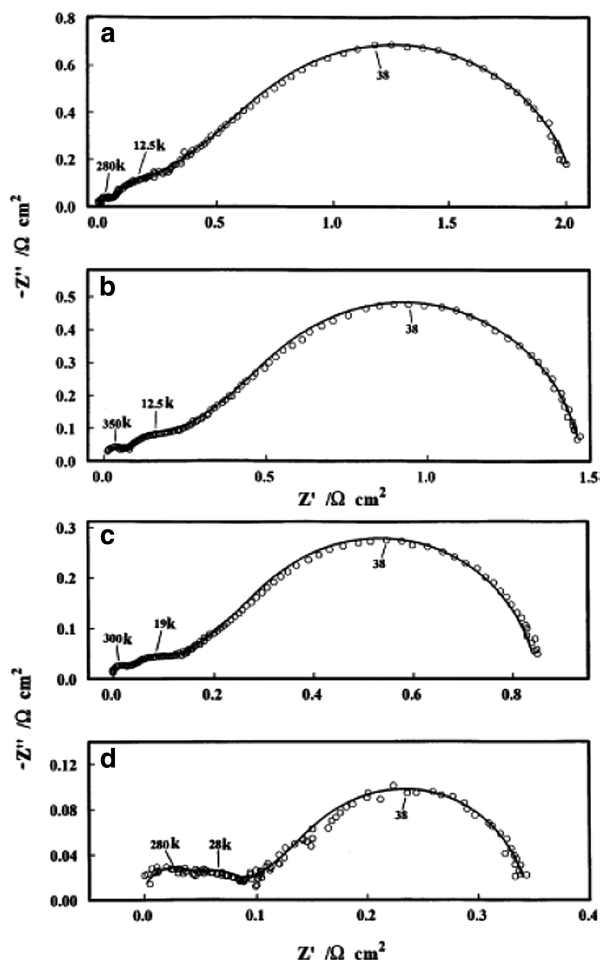
$$\hat{Z}_f = R_{ct} + \frac{1}{j\omega C_p + \frac{1}{R_p} + \frac{1}{R_d + \hat{Z}_w}}, \quad (7.47)$$

where

$$R_d = -\frac{BE}{A^2 D}, \quad \hat{Z}_w = \frac{B}{A^2 D} C^0 \sqrt{j\omega D_{H_2}} \coth \left(\sqrt{\frac{j\omega}{D_{H_2}}} \delta \right). \quad (7.48)$$

The electrical equivalent circuit corresponding to Eq. (7.48) is presented in Fig. 7.4.

Fig. 7.5 Complex plane plots for Pt(511) at η (a) -7.3 mV; (b) -14 mV; (c) -30 mV; (d) -40 mV, in 0.5 M H_2SO_4 at RDE $3,500$ rpm (From Ref. [180], copyright (1998), with permission from Elsevier)



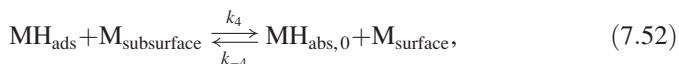
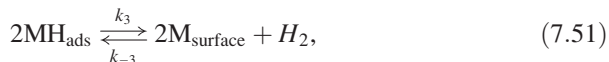
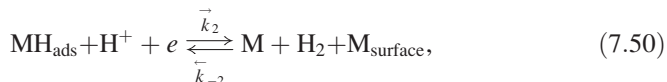
Comparing this circuit with that for a simple hydrogen evolution without mass transfer effects, Fig. 5.1 left, it is evident that a new branch in parallel consisting of the resistance R_d in series with the finite-length mass transfer impedance, Z_w , was added to the circuit. Studies of the HER at various monocrystalline Pt surfaces displayed one or two semicircles followed by a finite-length diffusion impedance on the complex plane plots [180]. Examples of the impedance plots obtained at the rotating disk at the Pt(511) electrode are displayed in Fig. 7.5. The equations developed earlier might also be used to describe a hydrogen oxidation reaction.

7.4 Hydrogen Absorption into Metals

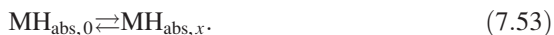
Besides hydrogen adsorption and evolution, hydrogen absorption into metals might occur. It is observed in Pd and certain alloys of the type AB_5 (e.g., $LaNi_5$) or AB_2 and is used in metal hydride batteries. The theory developed here is also applicable to other reactions, e.g., Li intercalation in Li-ion batteries. Let us consider first the simplest adsorption–absorption reaction [272].

7.4.1 Hydrogen Adsorption–Absorption Reaction in Presence of Hydrogen Evolution

In this case, the hydrogen adsorption reaction, (7.49), is followed by hydrogen evolution, (7.50) and (7.51), in parallel with hydrogen absorption, (7.52), during which a hydrogen atom at the surface goes to a subsurface site at a distance $x = 0$ [273–275]:



where M_{surface} and $M_{\text{subsurface}}$ are the empty surface and subsurface sites. The absorbed hydrogen diffuses into the bulk [276]:



The rate of reaction (7.49) is described by Eq. (7.5) and that of reaction (7.52) by

$$v_4 = k_4 \theta_H (1 - X_0) - k_{-4} (1 - \theta_H) X_0, \quad (7.54)$$

where X is the dimensionless bulk hydrogen concentration, the surface concentration is $X_0 = C_{H,0}/C_{H,\text{max}}$, and $C_{H,\text{max}}$ is the saturation concentration under given experimental conditions. A thus defined X takes values between 0 and 1. Under steady-state conditions, when $v_4 = 0$, Eq. (7.54) becomes

$$X_0 = \frac{k_4\theta_H}{k_4\theta_H + k_{-4}(1 - \theta_H)} = \frac{K_4\theta_H}{K_4\theta_H + (1 - \theta_H)}, \quad (7.55)$$

which defines the absorption isotherm and $K_4 = k_4/k_{-4}$ is the absorption equilibrium constant. The diffusion of hydrogen into metal is described by Fick's equation:

$$\frac{\partial X}{\partial t} = D_H \frac{\partial^2 X}{\partial x^2}, \quad (7.56)$$

and the surface hydrogen flux equals the absorption rate:

$$J_H = -D_H \frac{\sigma_X}{F} \left(\frac{\partial X}{\partial x} \right)_{x=0} = v_4, \quad (7.57)$$

where $\sigma_X = FC_{H,\max}$ is the charge corresponding to the saturation of metal with hydrogen.

Diffusion Eq. (7.56) must be solved for the oscillating dimensionless concentration of hydrogen: $\Delta X = \tilde{X} \exp(j\omega t)$, and an equation analogous to (4.22) is obtained:

$$j\omega \tilde{X} = D_H \frac{d^2 \tilde{X}}{dx^2}, \quad (7.58)$$

and, assuming finite-length linear diffusion with the impermeable conditions at $x = l$,

$$\begin{aligned} x = 0 \quad & -D_H \frac{\sigma_X}{F} \frac{d\tilde{X}}{dx} = \tilde{J}_H, \\ x = l \quad & \frac{d\tilde{X}}{dx} = 0. \end{aligned} \quad (7.59)$$

The solution of Eq. (7.58) is

$$\tilde{X} = Ae^{-sx} + Be^{sx}, \quad (7.60)$$

where $s = \sqrt{j\omega/D_H}$. Taking into account the boundary conditions, the solution for \tilde{X} is

$$\tilde{X} = \frac{F}{\sigma_X} \frac{\tilde{J}_H}{\sqrt{j\omega D_H}} \frac{\cosh[s(l-x)]}{\sinh[sl]}, \quad (7.61)$$

and at the electrode surface

$$\tilde{X}_0 = \frac{F}{\sigma_X} \frac{\tilde{J}_H}{\sqrt{j\omega D_H}} \coth\left(\sqrt{\frac{j\omega}{D_H}} l\right). \quad (7.62)$$

From Eq. (7.62) the hydrogen flux is

$$\tilde{J}_H = \frac{\sigma_X}{F} \tilde{X}_0 \sqrt{j\omega D_H} \tanh\left(\sqrt{\frac{j\omega}{D_H}} l\right) = J'_H \tilde{X}_0 = \left(\frac{\partial v_4}{\partial \theta_B}\right) \tilde{\theta}_B + \left(\frac{\partial v_4}{\partial X_0}\right) \tilde{X}_0, \quad (7.63)$$

where

$$J'_H = \frac{\sigma_X}{F} \sqrt{j\omega D_H} \tanh\left(\sqrt{\frac{j\omega}{D_H}} l\right). \quad (7.64)$$

The current is given by

$$-\frac{\Delta i}{F} = \Delta r_0 = \Delta v_1 + \Delta v_2 \quad (7.65)$$

and its phasor by

$$\tilde{r}_0 = -\frac{\tilde{i}}{F} = \left(\frac{\partial r_0}{\partial \eta}\right) \tilde{\eta} + \left(\frac{\partial r_0}{\partial \theta_H}\right) \tilde{\theta}_H. \quad (7.66)$$

A similar linearization must be applied to the surface coverage by adsorbed hydrogen:

$$\begin{aligned} \frac{\sigma_1}{F} \frac{d\tilde{\theta}_H}{dt} &= \frac{\sigma_1}{F} j\omega \tilde{\theta}_H = \tilde{v}_1 - \tilde{v}_2 - 2\tilde{v}_3 - \tilde{v}_4 = \tilde{r}_1 - \tilde{v}_4 \\ &= \left(\frac{\partial r_1}{\partial \theta_H}\right) \tilde{\theta}_H + \left(\frac{\partial r_1}{\partial \eta}\right) \tilde{\eta} - \left(\frac{\partial r_4}{\partial \theta_H}\right) \tilde{\theta}_H - \left(\frac{\partial r_4}{\partial X_0}\right) \tilde{X}_0. \end{aligned} \quad (7.67)$$

This equation is simplified because $\partial r_1/\partial X_0 = \partial v_4/\partial \eta = 0$. Equations (7.63), (7.66), and (7.67) can be written in matrix form:

$$\begin{bmatrix} -\frac{\partial r_0}{\partial \eta} \\ -\frac{\partial r_1}{\partial \eta} \\ 0 \end{bmatrix} = \begin{bmatrix} -\frac{1}{F} & \frac{\partial r_0}{\partial \theta_H} & 0 \\ 0 & \frac{\partial r_1}{\partial \theta_H} - \frac{\partial v_4}{\partial \theta_H} - j\omega \frac{\sigma_1}{F} & -\frac{\partial v_4}{\partial X_0} \\ 0 & \frac{\partial v_4}{\partial \theta_H} & \frac{\partial v_4}{\partial X_0} - J'_H \end{bmatrix} \begin{bmatrix} \tilde{i} \\ \tilde{\eta} \\ \tilde{\theta}_H \\ \tilde{\eta} \\ \tilde{X}_0 \\ \tilde{\eta} \end{bmatrix}. \quad (7.68)$$

The solution obtained using Cramer's rule is $\tilde{i}_f/\tilde{\eta} = T_1/B$:

$$T_1 = \begin{vmatrix} -\frac{\partial r_0}{\partial \eta} & \frac{\partial r_0}{\partial \theta_H} & 0 \\ -\frac{\partial r_1}{\partial \eta} & \frac{\partial r_1}{\partial \theta_H} - \frac{\partial v_4}{\partial \theta_H} - j\omega \frac{\sigma_1}{F} & -\frac{\partial v_4}{\partial X_0} \\ 0 & \frac{\partial v_4}{\partial \theta_H} & \frac{\partial v_4}{\partial X_0} - J'_H \end{vmatrix} \quad (7.69)$$

and

$$B = \begin{vmatrix} -\frac{1}{F} & \frac{\partial \partial r_0}{\partial \theta_H} & 0 \\ 0 & \frac{\partial r_1}{\partial \theta_H} - \frac{\partial v_4}{\partial \theta_H} - j\omega \frac{\sigma_1}{F} & -\frac{\partial v_4}{\partial X_0} \\ 0 & \frac{\partial v_4}{\partial \theta_H} & \frac{\partial v_4}{\partial X_0} - J'_H \end{vmatrix}, \quad (7.70)$$

from which the faradaic admittance is

$$\hat{Y}_f = -\frac{\tilde{i}}{\tilde{\eta}} = -F \left(\frac{\partial r_0}{\partial \eta} \right) - \frac{\frac{F^2}{\sigma_1} \left(\frac{\partial r_0}{\partial \theta_H} \right) \left(\frac{\partial r_1}{\partial \eta} \right)}{j\omega - \frac{F}{\sigma_1} \left(\frac{\partial r_1}{\partial \theta_H} \right) + \frac{\frac{F}{\sigma_1} \left(\frac{\partial v_4}{\partial \theta_H} \right)}{1 - \frac{\left(\frac{\partial v_4}{\partial X_0} \right)}{J'_H}}}, \quad (7.71)$$

which may be written in a form similar to Eq. (5.51) for an electrocatalytic reaction with one adsorbed species and to that for the HER:

$$\tilde{Y}_f = A + \frac{B}{j\omega + C + \frac{D}{1 + \frac{E}{\sqrt{j\omega D_H \tanh\left(\sqrt{\frac{j\omega}{D_H}} l\right)}}}}, \quad (7.72)$$

where the parameters A , B , and C are as defined earlier, Eq. (5.52), and D and E are defined as

$$D = \frac{F}{\sigma_1} \left(\frac{\partial v_4}{\partial \theta_H} \right)_{X_0} \quad \text{and} \quad E = -\frac{F}{\sigma_X} \left(\frac{\partial v_4}{\partial X_0} \right)_{\theta_H}. \quad (7.73)$$

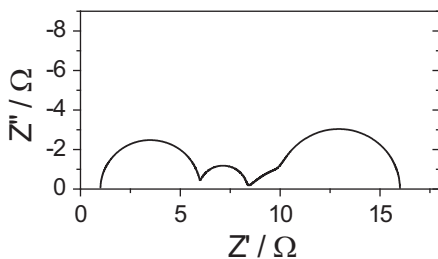


Fig. 7.6 Complex plane plot corresponding to hydrogen evolution and adsorption in finite-length reflective conditions; $R_s = 1 \, \Omega$, $C_{dl} = 20 \, \mu\text{F}$, $C_p = 0.01 \, \text{F}$, $R_{ct} = 5 \, \Omega$, $R_p = 10 \, \Omega$, $R_{ab} = 3 \, \Omega$, $R_D = 10 \, \Omega$, $T_D = 1,000 \, \text{s}$, see Eq. (4.77) for definition of latter two parameters

The difference between Eqs. (5.51) and (7.72) is the presence of the additional term in the denominator. The faradaic impedance is

$$\begin{aligned}
 \hat{Z}_f &= \frac{1}{\hat{Y}_f} \\
 &= \frac{1}{A} - \frac{1}{j\omega \left(\frac{A^2}{B} \right) + \left(\frac{A^2 C}{B} + A \right) + \frac{1}{\left(\frac{B}{A^2 D} \right) + \left(\frac{BE}{A^2 D} \right) \frac{\coth \left(\sqrt{\frac{j\omega}{D_H}} l \right)}{\sqrt{j\omega D_H}}} = \\
 &= R_{ct} + \frac{1}{j\omega C_p + \frac{1}{R_p} + \frac{1}{R_{ab} + \hat{Z}_w}},
 \end{aligned} \tag{7.74}$$

where R_{ct} , R_p , and C_p are as defined in Eq. (5.55) and the new parameters are

$$\begin{aligned}
 R_{ab} &= -\frac{B}{A^2 D} = \frac{1}{C_p} \frac{1}{D}; & \sigma' &= -\frac{BE}{A^2 D} = \frac{1}{C_p} \frac{E}{D}; \\
 \hat{Z}_w &= \frac{\sigma'}{\sqrt{j\omega D_H}} \coth \left(\sqrt{\frac{j\omega}{D_H}} l \right).
 \end{aligned} \tag{7.75}$$

This equation corresponds to a circuit similar to that in Fig. 7.4 (where R_{ab} replaces R_d). The complex plane plot corresponding to the total circuit including the solution resistance and the double-layer capacitance is shown in Fig. 7.6. Three semicircles are observed corresponding to the coupling $R_{ct} - C_{dl}$, $R_{ab} - C_p$, and

$R_p - C_p$ and a part of the mass transfer impedance. In this case, the low-frequency impedance is real because a constant current flows through $R_s - R_{ct} - R_p$.

A case of finite diffusion length with transmissive boundary conditions has also been considered in the literature [277, 278]. It corresponds to the case where hydrogen diffuses across a membrane and is oxidized on the other side. The same Eq. (7.74) is obtained but with \tanh replacing \coth in Eq. (7.75).

7.4.2 Direct Hydrogen Absorption and Hydrogen Evolution

Most authors assumed the foregoing indirect adsorption–absorption mechanism; however, others proposed a direct absorption mechanism [279–281]:



with the rate

$$v_5 = \vec{k}_5(1 - X_0) - \overleftarrow{k}_{-5}X_0, \quad (7.77)$$

from which the subsurface hydrogen concentration is

$$X_0 = \frac{\overline{K}_5}{1 + \overline{K}_5} \text{ and } \overline{K}_5 = \frac{\vec{k}_5}{\overleftarrow{k}_{-5}} = \frac{k_5^0}{k_{-5}^0} e^{-f\eta}. \quad (7.78)$$

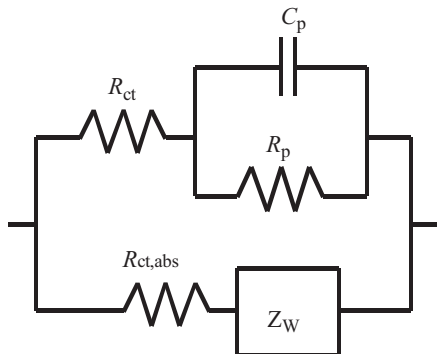
This reaction leads to an impedance, \hat{Z}_{abs} , consisting of the charge transfer resistance and mass transfer impedance:

$$\hat{Z}_{\text{abs}} = R_{\text{ct,abs}} + \hat{Z}_w, \quad (7.79)$$

where

$$\begin{aligned} \frac{1}{R_{\text{ct,abs}}} &= A = -F \left(\frac{\partial v_5}{\partial \eta} \right)_{X_0}, \\ \hat{Z}_w &= \frac{\sigma'}{\sqrt{j\omega D_H}} \coth \left(\sqrt{\frac{j\omega}{D_H}} l \right), \\ \sigma' &= \frac{E}{A}, E = -\frac{F}{\sigma_X} \left(\frac{\partial v_6}{\partial X_0} \right), \end{aligned} \quad (7.80)$$

Fig. 7.7 Electrical equivalent circuit for faradaic impedance of direct hydrogen absorption in presence of hydrogen adsorption–evolution



and the mass transfer impedance was written for the finite-length reflecting conditions. Of course, besides the hydrogen direct absorption, hydrogen adsorption and evolution might take place. The total electrical equivalent circuit for the faradaic impedance is displayed in Fig. 7.7, where the upper branch corresponds to hydrogen adsorption and evolution and the lower branch corresponds to direct hydrogen absorption.

Besides hydrogen evolution and absorption, there might also be a HUPD reaction adding another $R_{\text{UPD}}\text{--}C_{\text{UPD}}$ branch in parallel [272, 282]. From a structural point of view circuits for indirect and direct hydrogen absorption are indistinguishable. Studies of hydrogen absorption in palladium suggest that direct hydrogen absorption is faster than the indirect path [283, 284].

7.4.3 Hydrogen Absorption in Absence of Hydrogen Evolution

Very often hydrogen absorption is studied at potentials before hydrogen evolution, especially in the HUPD zone [282–285]. In such cases, the circuit becomes simplified because $R_p = \infty$ and parameter $B = -AC$. The faradaic impedance in the case of indirect adsorption–absorption mechanism becomes

$$\hat{Z}_f = R_{ct} + \frac{1}{j\omega C_p + \frac{1}{R_{ab} + \hat{Z}_W}}, \quad (7.81)$$

where

$$\begin{aligned} C_p &= \frac{A}{C} = f\sigma_1 \frac{\bar{K}_1}{(\bar{K}_1 + 1)^2}; R_{ab} = \frac{1}{C_p D}; \\ \sigma' &= \frac{E}{C_p D} = \frac{1}{f\sigma_X} \frac{(\bar{K}_1 K_4 + 1)^2}{\bar{K}_1 K_4}, \end{aligned} \quad (7.82)$$

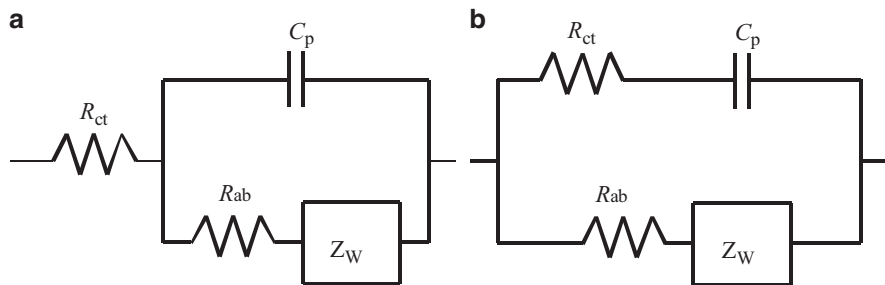
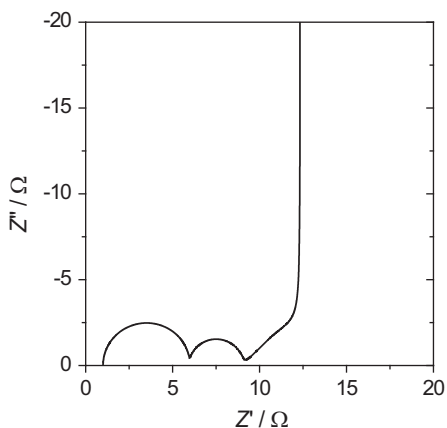


Fig. 7.8 Electrical equivalent circuits of faradaic impedance corresponding to (a) indirect, Eq. (7.81), and (b) direct, Eq. (7.83), hydrogen absorption reaction with finite-length linear diffusion of hydrogen

Fig. 7.9 Complex plane plot corresponding to indirect hydrogen absorption reaction, Eq. (7.81), in presence of finite-length reflective linear diffusion.
Parameters: $R_s = 1 \Omega$, $C_{dl} = 20 \mu\text{F}$, $R_{ct} = 5 \Omega$, $R_{ab} = 3 \Omega$, $C_p = 0.01 \text{ F}$, $R_D = 10 \Omega$, $T_D = 1,000 \text{ s}$



and for the direct absorption mechanism

$$\hat{Z}_f = \frac{1}{\frac{1}{R_{ct} + \frac{1}{j\omega C_p}} + \frac{1}{R_{ab} + \hat{Z}_W}}. \quad (7.83)$$

The electrical equivalent circuits of the faradaic impedance corresponding to the indirect, Eq. (7.81), and direct, Eq. (7.83), hydrogen absorption reaction with finite-length linear diffusion are displayed in Fig. 7.8.

The total impedance complex plane plot for indirect hydrogen absorption without hydrogen evolution, including solution resistance and double-layer capacitance, is displayed in Fig. 7.9. It shows two semicircles due to the $R_{ct} - C_{dl}$ and $R_{ab} - C_p$ coupling followed by the finite-length reflective linear diffusion displaying a line at 45° followed by a capacitive line at 90° .

In practice, the hydrogen absorption resistance is usually very small, and one semicircle is observed on the complex plane plots. Examples of the complex plane

Fig. 7.10 Complex plane plots obtained on Pd foil (50 μm) in 0.1 M H_2SO_4 at $E = 0.12$ V versus reversible hydrogen electrode, RHE (From Ref. [286] with permission of author)

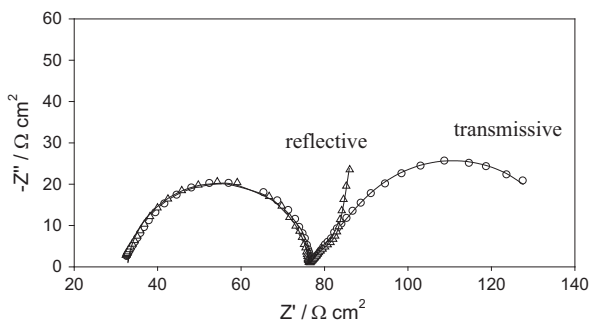
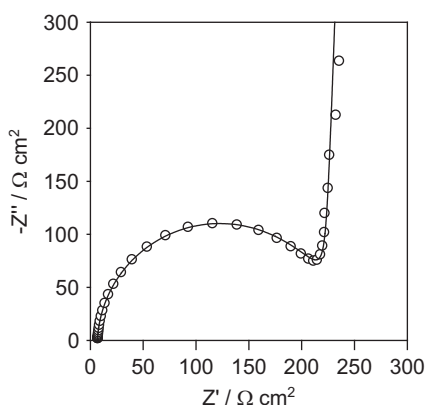


Fig. 7.11 Complex plane plots obtained on 10 ML of Pd on Au(111), in 0.1 M H_2SO_4 at $E = 0.15$ V versus RHE (From Ref. [286] with permission of author)



plots obtained for hydrogen absorption at Pd membrane in the transmissive and reflective conditions [155] are displayed in Fig. 7.10. The high-frequency part corresponding to the coupling $R_{\text{ct}} - C_{\text{dl}}$ is identical, and parts of the transmissive and reflective mass transfer impedances are visible (compare with Fig. 4.12).

For thin absorbing layers the mass transfer impedance in reflective conditions reduces to an $R_{\text{W}} - C_{\text{W}}$ connection in series, Eq. (4.85). The observed impedance for the hydrogen absorption reaction in 10 monolayers (ML) of Pd on Au(111) [155] is shown in Fig. 7.11, where a high-frequency semicircle is followed directly by a low-frequency vertical capacitive line (corresponding to the penetration of the ac signal to the bottom of the layer).

7.4.4 Hydrogen Absorption in Spherical Particles

Very often H absorption is studied in practical powdered materials (e.g., in NiMH batteries) that consist of spherical particles for which a finite-length spherical diffusion treatment must be used [287–289]. In this case the diffusion Eq. (7.56) must be written for the spherical diffusion, as in Eq. (4.91):

$$\frac{\partial X}{\partial t} = D_H \left[\frac{\partial^2 X}{\partial r^2} + \frac{2}{r} \frac{\partial X}{\partial r} \right]. \quad (7.84)$$

Proceeding as in Sect. 4.6.2, the mass transfer impedance is described as

$$\hat{Z}_w = \frac{\sigma' r_0}{D_H} \frac{1}{\left[\left(\sqrt{\frac{j\omega}{D_H}} r_0 \right) \coth \left(\sqrt{\frac{j\omega}{D_H}} r_0 \right) - 1 \right]}, \quad (7.85)$$

and the impedance is as in Fig. 4.15. At low frequencies a capacitive behavior, Eq. (4.107), is observed as the hydrogen can diffuse only to the sphere center. This equation was used in modeling the hydrogen absorbing materials [287, 288, 290]. The influence of self-stress on hydrogen absorption has also been studied [291–294].

The preceding theory may be extended to other intercalation reactions, e.g., in lithium batteries. It has also been extended to bilayers [295, 296].

7.5 Conclusions

Hydrogen adsorption, evolution, and absorption reactions were presented as examples of electrocatalytic reactions, i.e., involving adsorption at the electrode surface. The general rules of development of impedance equations involving first the dc description followed by linearization of the equations were used. The electrode processes involved adsorption and mass transfer either in solution or inside the electrode material. In a similar way, other electrocatalytic reaction mechanisms such as, for example, oxygen reduction or evolution, chlorine evolution, and lithium intercalation, might be discussed. The transfer mechanisms of hydrogen through membranes might also be studied using transfer functions other than impedance and admittance; see, e.g., Ref. [61].

Chapter 8

Dispersion of Impedances at Solid Electrodes

8.1 Constant Phase Element

The impedance of ideally polarizable liquid electrodes (e.g., mercury, amalgams, indium-gallium) may be modeled by an R - C circuit (Fig. 4.1a). However, most impedance studies are now carried out at solid electrodes. At these electrodes the double-layer capacitance is not purely capacitive and often displays a certain frequency dispersion. Such behavior cannot be modeled by a simple circuit consisting of R , L , and C elements. To explain such behavior, a constant phase element (CPE) is usually used.

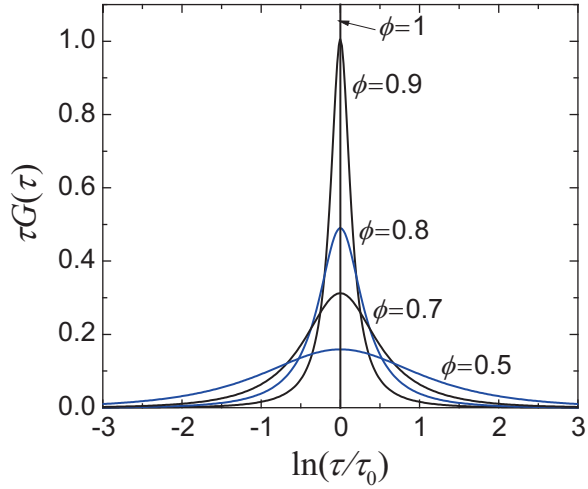
In general, bulk dielectric dispersion in solids and liquids is well known and described in the literature [24, 297, 298]. In this chapter, the dispersion of capacitances at electrode surfaces in solutions will be discussed. The complex dielectric constant is described as

$$\frac{\varepsilon(\omega) - \varepsilon_{\infty}}{\varepsilon_S - \varepsilon_{\infty}} = \int_0^{\infty} \frac{G(\tau)}{1 + j\omega\tau} d\tau, \quad (8.1)$$

where ε_{∞} and ε_S are the dielectric constants at frequencies $\omega \rightarrow \infty$ and $\omega \rightarrow 0$ and $G(\tau)$ is the function describing the distribution of time constants. If there is no distribution of time constants, i.e., the dielectric constant may be described by one time constant, the function $G(\tau)$ is simply Dirac's δ function, $G(\tau) = \delta(\tau - \tau_0)$, and integration in Eq. (8.1) gives

$$\frac{\varepsilon(\omega) - \varepsilon_{\infty}}{\varepsilon_S - \varepsilon_{\infty}} = \frac{1}{1 + j\omega\tau_0}. \quad (8.2)$$

Fig. 8.1 Dependence of time constant distribution function, $\tau G(\tau)$, Eq. (8.5), on $\ln(\tau/\tau_0)$



Cole and Cole [297] described the observed dispersion by the function

$$\frac{\varepsilon(\omega) - \varepsilon_\infty}{\varepsilon_S - \varepsilon_\infty} = \frac{1}{1 + (j\omega\tau_0)^\phi}, \quad (8.3)$$

where ϕ is the dimensionless parameter and $\phi \leq 1$. By analogy, the dispersion of impedances may be described by

$$\frac{\hat{Z}(\omega) - Z_\infty}{Z_0 - Z_\infty} = \int_0^\infty \frac{\tau G(\tau)}{1 + j\omega\tau} d\ln \tau. \quad (8.4)$$

The distribution function is described by [297]

$$G(\tau) = \frac{1}{2\pi\tau} \frac{\sin[(1-\phi)\pi]}{\cosh[\phi \ln(\tau/\tau_0)] - \cos[(1-\phi)\pi]}, \quad (8.5)$$

and the plot of $\tau G(\tau)$ versus $\ln(\tau/\tau_0)$ is shown in Fig. 8.1. When $\phi = 1$, the distribution function reduces to Dirac's delta function, and with its decrease the distribution becomes wider around $\tau = \tau_0$.

In such a case, the impedance of the ideal capacitor, $1/(j\omega C)$, must be replaced by the impedance of a CPE:

$$\hat{Z}_{\text{CPE}} = \frac{1}{T(j\omega)^\phi}, \quad (8.6)$$

where T is the parameter related to the electrode capacitance ($\text{F s}^{\phi-1} \text{ cm}^{-2}$), and ϕ is the constant phase exponent ($0 < \phi < 1$) related to the deviation of the straight

capacitive line from 90° by an angle $\alpha = 90^\circ(1 - \phi)$. The units of T can also be rearranged [299] to $\Omega^{-1} \text{ s}^\phi \text{ cm}^{-2}$; however, as it becomes purely capacitive for $\phi = 1$, it seems more logical to use farads instead of ohms. Taking into account the properties of the complex numbers, $j^\phi = \cos(\phi\pi/2) - j \sin(\phi\pi/2)$ is a complex number and Eq. (8.6) may be expressed as

$$\hat{Z}_{\text{CPE}} = \left[\frac{\cos(\phi\pi/2)}{T\omega^\phi} \right] - j \left[\frac{\sin(\phi\pi/2)}{T\omega^\phi} \right], \quad (8.7)$$

which means that the impedance of this element is no longer purely imaginary and always contains both real and imaginary components. Therefore, the CPE represents a nonideal or “leaking capacitor” and causes energy dissipation because of the presence of the impedance real part [299–301]. In fact, the inverse transform of the CPE element into the time domain shows that after the potential step the current decreases proportionally to $t^{-\phi}$, that is, it never reaches zero [302], which means the electrode charge goes to infinity! Such an electrode cannot be called ideally polarizable [301] and it physically cannot exist. This means that somewhere beyond the measured low-frequency range it must become ideally polarizable. The name *constant phase element* originates from its behavior displayed on the complex plane and Bode plots in Fig. 8.2. The complex plane plots deviate from the ideal capacitor case by 9° for $\phi = 0.9$ and by 18° for $\phi = 0.8$. The Bode phase angle is always constant and equal to $90^\circ\phi$, and the slope of the logarithmic Bode magnitude plots equals ϕ . In the absence of redox species in solution, the electrical equivalent circuit consists of a $R_s - \text{CPE}_{\text{dl}}$ connection in series. The corresponding complex plane and Bode plots are displayed in Fig. 8.3. The slopes in the complex plane plots are the same as in Fig. 8.2, and the Bode plots approach those for the CPE only at lower frequencies.

To more easily identify the presence of the CPE, Orazem et al. [303] proposed using Bode plots of impedances corrected for the solution resistance, $\log|Z''|$ versus $\log f$, and effective capacitance plots T_{eff} versus $\log f$:

$$T_{\text{eff}} = -\sin\left(\frac{\phi\pi}{2}\right) \frac{1}{Z''(2\pi f)^\phi}. \quad (8.8)$$

Such plots will be presented below (Fig. 8.5).

In the presence of a redox reaction without diffusion limitations, the system impedance is described by the electrical equivalent circuit $R_s(C_{\text{dl}}R_{\text{ct}})$ displayed in Fig. 2.34. Replacing the double-layer capacitance with the CPE produces complex plane and Bode plots (Fig. 8.4) corresponding to the equation for the impedance of such a system:

$$Z = R_s + \frac{1}{(j\omega)^\phi T + \frac{1}{R_{\text{ct}}}}. \quad (8.9)$$

The complex plane plots represent “sunken” or rotated semicircles with their center located below the real axis [304]. There are also changes in the Bode plots.

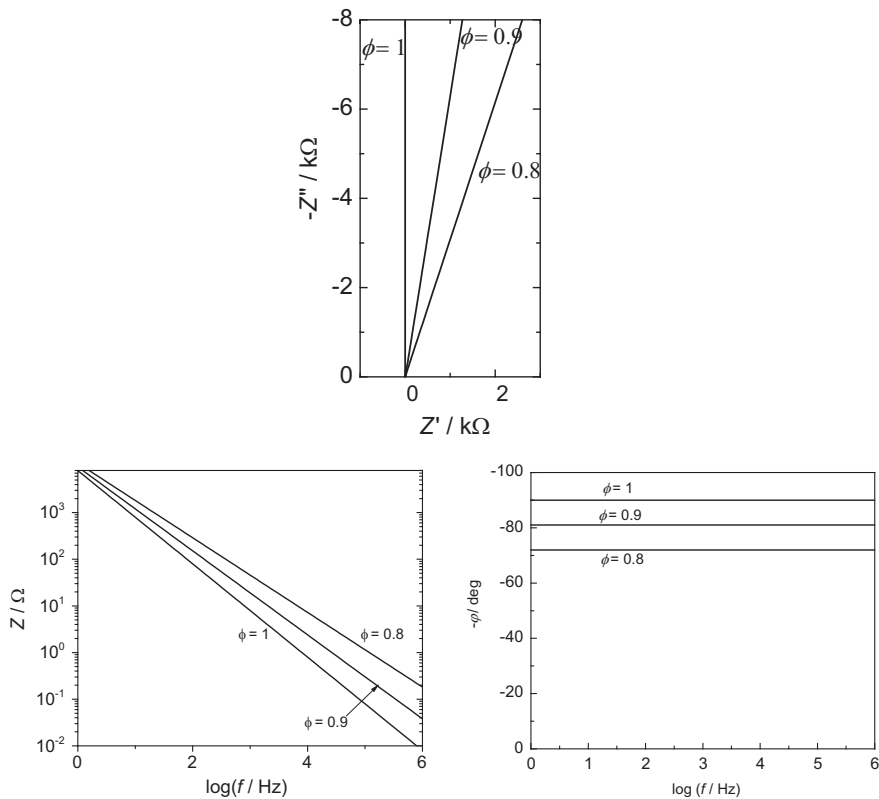


Fig. 8.2 Complex plane and Bode plots of CPE element, Eq. (8.6), for $T = 20 \mu\text{F cm}^{-2} \text{ s}^{\phi-1}$

The plots of $\log|Z''|$ versus $\log f$ and the effective capacitance plot of T_{eff} versus $\log f$ are displayed in Fig. 8.5. Note that such plots are very sensitive to variations in the CPE exponent, which is determined experimentally. Such a procedure could be used when the equivalent circuit describing the system is not known.

Brug et al. [305] proposed a simple model that allows estimation of an average double-layer capacitance, \overline{C}_{dl} , for the CPE behavior. The model consists of the solution resistance, R_s , and the CPE in series, R_s -CPE, i.e., electrode-supporting electrolyte interface. Assuming dispersion of the time constants, $\tau = R_s C_{\text{dl}}$, around an average value, $\tau_0 = R_s \overline{C}_{\text{dl}}$, and the Cole-Cole formula, Eq. (8.3), the researchers obtained

$$\hat{Z} = R_s + \frac{1}{(j\omega)^\phi T} = R_s \left[1 + \frac{1}{(j\omega)^\phi (R_s T)} \right] = R_s \left[1 + \frac{1}{(j\omega \tau_0)^\phi} \right]. \quad (8.10)$$

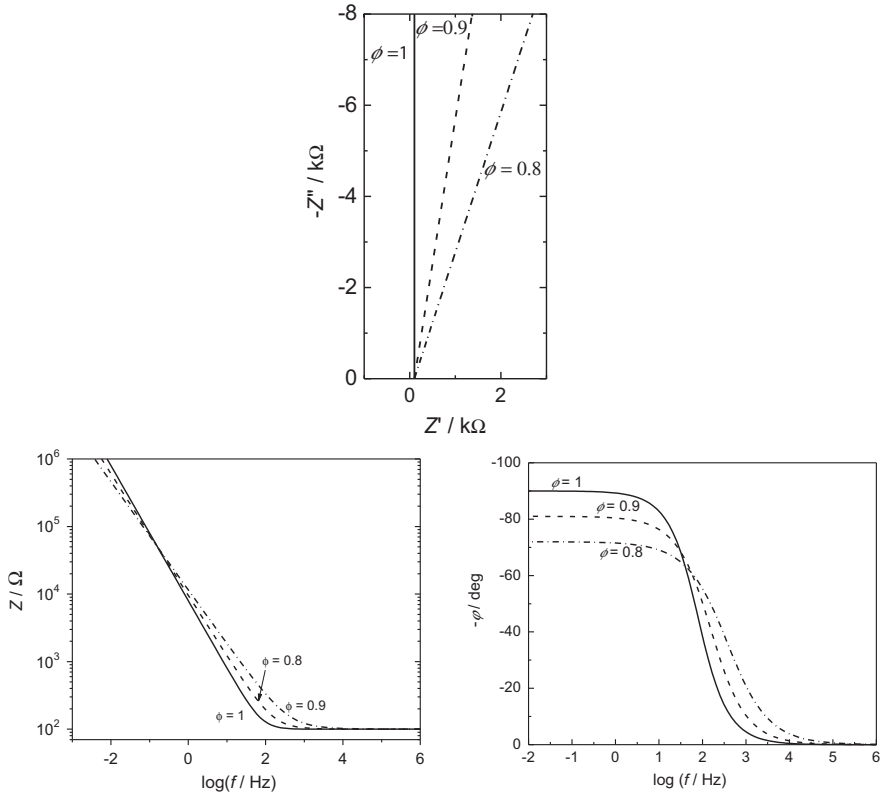


Fig. 8.3 Complex plane and Bode plots for the R -CPE circuit in series, $R = 100 \, \Omega$, $T = 20 \, \mu\text{F cm}^{-2} \text{s}^{\phi-1}$

Comparison of the terms in parentheses leads to

$$T = \overline{C}_{\text{dl}}^{\phi} R_{\text{s}}^{-(1-\phi)} \text{ or } C_{\text{dl}} = T^{1/\phi} \left(\frac{1}{R_{\text{s}}} \right)^{1-\frac{1}{\phi}}, \quad (8.11)$$

from which \overline{C}_{dl} is obtained. In a similar way, for the circuit $R_{\text{s}}(CPE_{\text{dl}}R_{\text{ct}})$ (as in Fig. 2.34) they obtained

$$T = \overline{C}_{\text{dl}}^{\phi} [R_{\text{s}}^{-1} + R_{\text{ct}}^{-1}]^{1-\phi}. \quad (8.12)$$

Hsu and Mansfeld [306] proposed another formula that is applicable to cases where a semicircle is observed on complex plane plots:

$$\overline{C}_{\text{dl}} = T(\omega_{\text{c}})^{\phi-1}, \quad (8.13)$$

where ω_{c} is the frequency corresponding to the maximum of the imaginary part (corresponding to the maximum of the semicircle). This frequency may be calculated from [307]

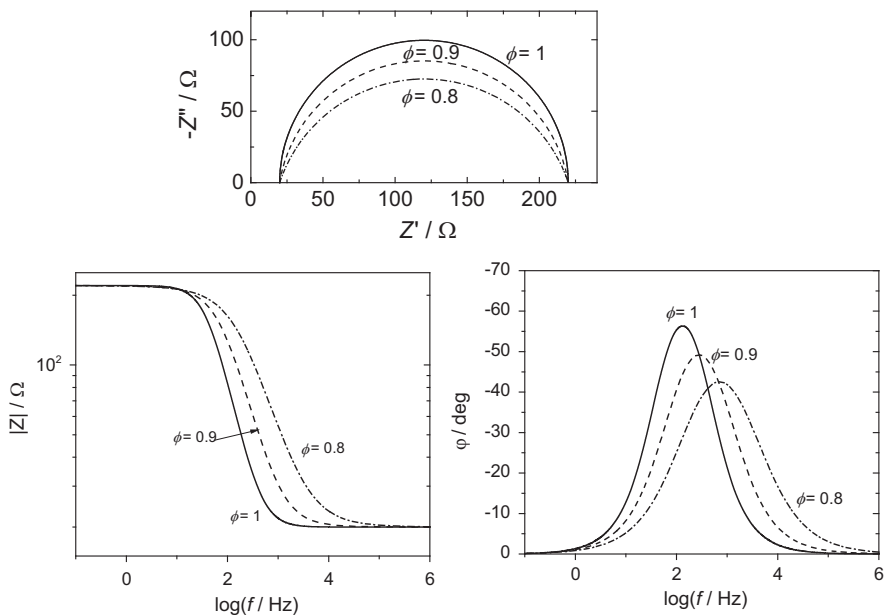


Fig. 8.4 Complex plane and Bode plots for circuit consisting of solution resistance in series with parallel connection of CPE and resistance R_{ct} . Parameters: $R_s = 10 \, \Omega$, $T = 20 \, \mu\text{F cm}^{-2} \text{ s}^{\phi-1}$, $R_{ct} = 200 \, \Omega$

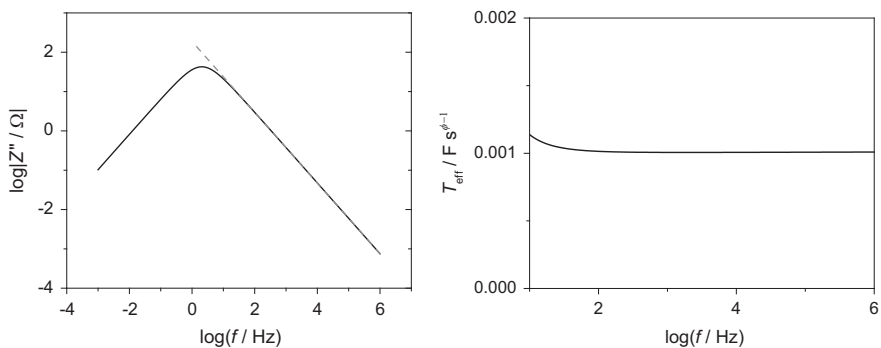


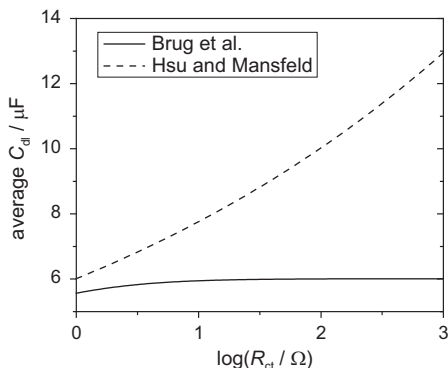
Fig. 8.5 Plots of $\log|Z''|$ versus $\log f$ and T_{eff} versus $\log f$ for $R_s(R_{ct}CPE)$ circuit with $R_s = 10 \, \Omega$, $R_{ct} = 100 \, \Omega$, $T = 0.001 \, \text{F s}^{\phi-1}$, and $\phi = 0.9$

$$\omega_c = \left(\frac{1}{R_{ct}T} \right)^{1/\phi}, \quad (8.14)$$

which leads to

$$\bar{C}_{dl} = T^{1/\phi} \left(\frac{1}{R_{ct}} \right)^{1-\frac{1}{\phi}}, \quad (8.15)$$

Fig. 8.6 Comparison of average values of interfacial capacitance, \overline{C}_{dl} , using Brug et al. [305] and Hsu and Mansfeld [306], Eqs. (8.15) and (8.16), as functions of charge transfer resistance, R_{ct} . Parameters: $R_s = 10 \Omega$, $T_{dl} = 20 \mu F$, $s^{\phi-1}$, $\phi = 0.9$



and it can be compared with Brug et al.'s [305] formula:

$$\overline{C}_{dl} = T^{1/\phi} \left(\frac{1}{R_s} + \frac{1}{R_{ct}} \right)^{1-\frac{1}{\phi}}. \quad (8.16)$$

The difference between these two equations is related to the presence of an additional term $1/R_s$ in Brug et al.'s formula. In fact, they merge when $R_s \gg R_{ct}$. A comparison of the estimation of \overline{C}_{dl} using Eqs. (8.15) and (8.16) is shown in Fig. 8.6. It is evident that the value obtained from the Hsu and Mansfeld model is very sensitive to the value of R_{ct} , and deviations between the \overline{C}_{dl} values obtained increases with increases in R_{ct} . Several authors have indicated that Brug et al.'s formula seems to work better [307–311]. It should also be mentioned that it is often experimentally observed that when the parameter ϕ decreases, the value of T increases [213, 312, 313]. In such cases, Brug et al.'s formula produces smoother \overline{C}_{dl} data because they are proportional to $T^{1/\phi}$.

8.2 Fractal Model

Real polycrystalline solid surfaces contain surface defects, scratches, irregularities, and pores, and their detailed geometry is usually unknown and cannot be exactly described. To describe such cases, a fractal model was proposed [314]. Fractal models describe self-similar surfaces in which further magnification reveals a self-similarity in which further magnification always shows a similar structure. Such a description could also be used to model random surface inhomogeneities. To better understand fractal scaling, let us look at a comparison of the fractal and classical magnifications shown in Fig. 8.7 [315]. Using a simple three times magnification ($a \rightarrow b$), each element of the length l is increased three times in length, to $3l$. However, fractal magnification of each element ($a \rightarrow c$) shows that it consists of additional similar elements. In the case presented in Fig. 8.7, each element l is

Fig. 8.7 Comparison of classical (a) and fractal (b) magnification; fractal dimension $D_H = 1.2619$ (From Ref. [315], copyright (1990), with permission from Elsevier)

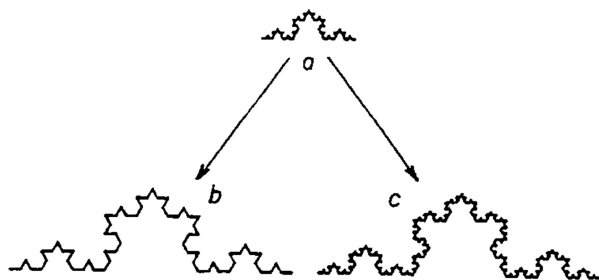
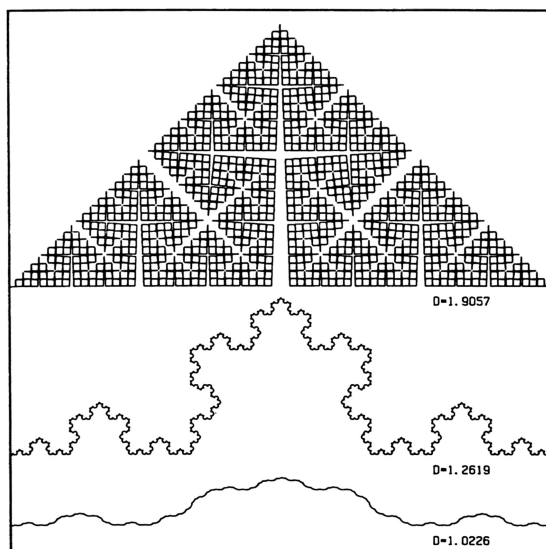


Fig. 8.8 Examples of von Koch curves for three different fractal dimensions (From ref. [317], copyright (1985), with permission from Elsevier)



increased four times in length, to $4l$. This leads to the fractal Hausdorff dimension [316], $D_H = \ln 4 / \ln 3 = 1.2619$ [315, 317]. This dimension is larger than that of a simple magnification, which corresponds to a linear dimension of 1. This means that this simple fractal line has a dimension of 1.2619. A line consisting of self-similar segments scaled fractally is called a von Koch line [318]. This line has an infinite length as each magnification increases its length and is nowhere differentiable. A fractal structure is a mathematical model, but in nature, magnification is limited by the atomic structure and is limited to dimensions between 10 nm and 0.1 mm [315]. Examples of von Koch curves for three different fractal dimensions are shown in Fig. 8.8. The fractal dimension of a line may be between $1 \leq D_h < 2$ and for the surfaces $2 \leq D_h < 3$. As the fractal dimensions increase, the complexity of the line increases.

The concept of fractals was introduced for electrochemical impedance by Le Méhauté and coworkers [319, 320] and later developed by Nyikos and Pajkossy [317, 321–328]. They showed that the fractal geometry of a blocking interface leads to constant phase element behavior, Eq. (8.6).

Fractal theory was subsequently extended to irregular or quasi-random surfaces lacking well-defined self-similarity [323, 326, 329–331]. Pajkossy and Nyikos [332] carried out simulations of blocking electrodes with a self-similar spatial capacitance distribution and found that the calculated impedances exhibited CPE behavior.

It was found subsequently that, although fractal geometry produces CPE behavior, in practice there is no relation between the CPE exponent and fractal dimensions [333, 334]. Qualitatively, however, higher fractal dimensions lead to smaller values of ϕ . This is related to the different type of fractals like Cantor bars [335–338] or Sierpiński carpets [339–341], for which different relations hold. This means that the impedance technique does not allow for the determination of the surface fractal dimension. Such information can be obtained by the analysis of current-time curves in the presence of diffusion to the surface [323, 324, 342–344].

Fractal theory has also been applied to systems with faradaic reactions [315, 323, 324, 345, 346]. De Levie [315, 345] showed that the impedance of a fractal electrode in the presence of a simple faradaic reaction but in the absence of dc current is

$$\hat{Z} = R_s + \frac{1}{b} \left(\frac{1}{\frac{1}{R_{ct}} + j\omega C_{dl}} \right)^\phi, \quad (8.17)$$

where the parameter b is [317, 345]

$$b = f_g \rho_s^{\phi-1}, \quad (8.18)$$

ρ_s is the solution resistivity, and f_g is a geometric factor depending on the fractal surface geometry. De Levie [345] specified that this factor reflects the fact that a fractal description ignores details of the surface morphology, focusing only on the global response, and different surface geometries can have the same fractal dimension but different geometric factors f_g . Of course, for flat surfaces $\phi = 1$, $f_g = 1$, $b = 1$. Equation (8.17) is formally identical with that postulated by Davidson and Cole [298] for dielectric studies.

Although the CPE and fractal systems give the same impedance in the absence of redox reactions, a comparison of Eq. (8.9) for the CPE model with Eq. (8.17) for a fractal system in the presence of a redox reaction shows that they are structurally different. In fact, they produce different complex plane and Bode plots. This is clearly visible from Fig. (8.9), which can be compared with Fig. 8.4 for the CPE model. With a decrease in the value of ϕ , an asymmetry on the complex plane plot occurs that is also visible on the phase angle Bode plots. This is related to the different topology of the equivalent circuits; they are compared in Fig. 8.10. In the CPE model, only the impedance of the double-layer capacitance is taken to the power ϕ , while in the fractal model the whole electrode impedance is taken to the power ϕ . The asymmetry of the complex plane and Bode plots for fractal systems arises from the asymmetric distribution function of time constants in Eq. (8.4) according to the equation [298, 347]

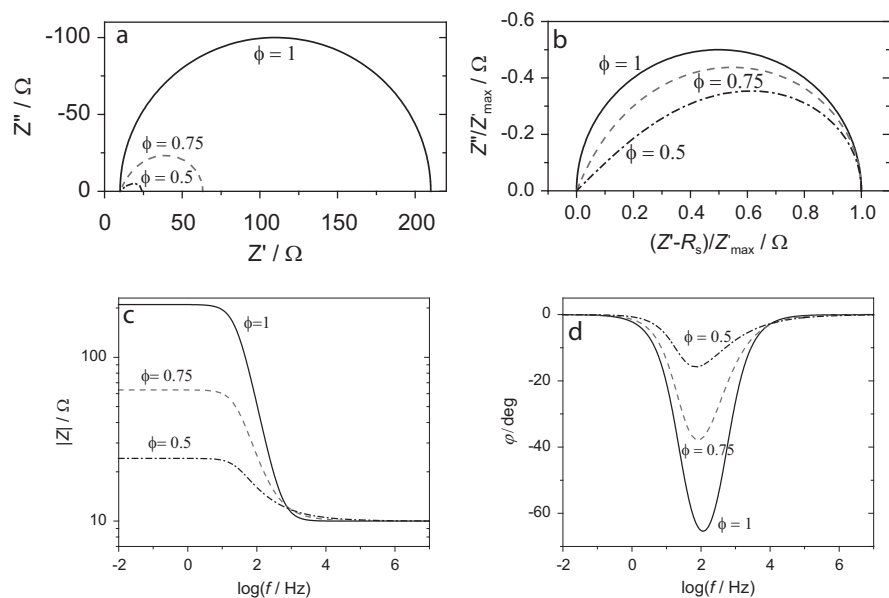


Fig. 8.9 Complex plane (a), normalized complex plane (b), and Bode plots (c, d) for fractal model with redox reaction, Eq. (8.17), assuming the following parameters: $R_s = 10 \Omega$, $R_{ct} = 200 \Omega$, $C_{dl} = 20 \mu F$, $b = 1$, and various values of ϕ

Fig. 8.10 Comparison of CPE and fractal models for systems with faradaic reaction

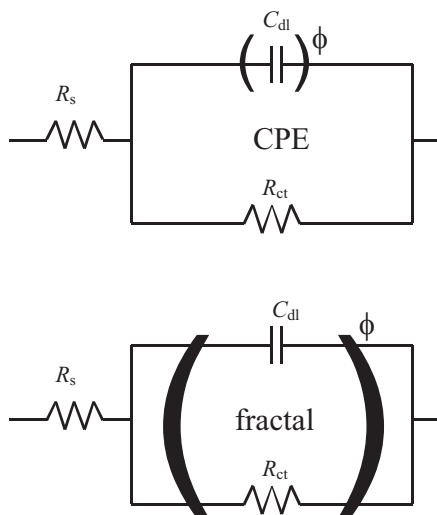
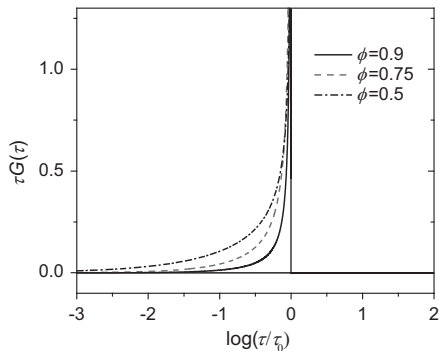


Fig. 8.11 Time constant distribution function for fractal model for different values of ϕ



$$\tau G(\tau) = \begin{cases} \frac{\sin(\phi\pi)}{\pi} \left(\frac{\tau}{\tau_0 - \tau} \right)^\phi & \text{for } \tau < \tau_0, \\ 0 & \text{for } \tau > \tau_0, \end{cases} \quad (8.19)$$

which means that the time constants are dispersed only up to the maximal value τ_0 . The plot of this function is shown in Fig. 8.11. It is evident that the distribution function is asymmetric.

Because of the presence of the unknown parameter f_g in Eq. (8.18), it is impossible to determine the value of the factor b , and the values of the charge transfer resistance and double-layer capacitance remain unknown. From the experiment it is possible to determine only these parameters multiplied or divided by the factor $b^{1/\phi}$:

$$C_{dl,exp} = C_{dl} b^{1/\phi} \text{ and } R_{ct,exp} = \frac{R_{ct}}{b^{1/\phi}}. \quad (8.20)$$

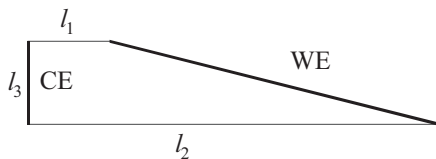
8.3 Origin of CPE Dispersion

The presence of the CPE in experimentally measured impedances generated a lot of discussion and confusion in the literature [334]. Of course, the fractal model described earlier also leads to CPE behavior for blocking electrodes; however, in the presence of faradaic reactions it leads to skewed semicircles instead of a decrease in the center of the semicircle below the real axis, without the further deformation typically observed in experimental conditions (CPE behavior).

In general, the appearance of CPE-like behavior can be attributed to two phenomena:

1. Dispersion of time constants, $\tau = R_s C_{dl}$;
2. Dispersion due to surface adsorption/diffusion processes (the so-called kinetic dispersion effect).

Fig. 8.12 Schematic representation of Hull cell used in simulations. *CE*, counter electrode, *WE*, working electrode



8.3.1 Dispersion of Time Constants

Schelder [348] attributed CPE dispersion to the microscopic surface roughness through bulk electrolyte conductivity; however, his branched R - C model does not seem to reflect correctly the actual current distribution [334]. Initially, CPE dispersion continued to be considered a consequence of surface microscopic roughness or porosity. However, surface porosity gives quite different effects (Chap. 9). Moreover, several authors [313, 334, 349, 350] demonstrated experimentally that an increase in the microroughness of a Pt electrode causes a decrease in the deviation from the ideal capacitive behavior, that is, the parameter ϕ becomes close to one for an electrochemically roughened surface. Even a very porous Pt powder microcavity electrode prepared by ball milling with a dispersing agent displays almost ideal low-frequency behavior with $\phi = 0.992$ [351]. In addition, for very porous gold-based electrodes, after the initial line at 45° a vertical line showing only a small deviation from the ideal behavior is observed on complex plane plots [352]. Simple estimation shows that the microscopic roughness of macroscopically flat electrodes could show the dispersion of the time constants in a very high (kHz to MHz) frequency range, contrary to the experimental observations of dispersion in a very wide frequency range [353].

In general, the distribution of the time constants $\tau = R_s C_{dl}$ can arise from

- i. The distribution of solution resistances, R_s
- ii. The distribution of double-layer capacitances, C_{dl}

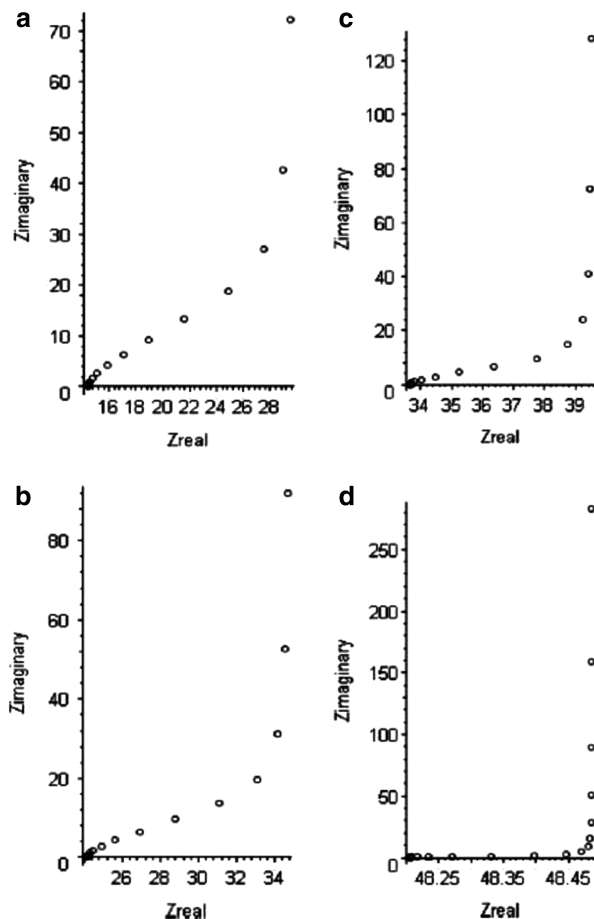
The distribution of solution resistances is observed in the Hull cell [354] displayed in Fig. 8.12, where the distance between the working and the counter electrode changes between l_1 and l_2 .

A simulation of impedances for different values of l_1 is shown in Fig. 8.13. When $l_1 < l_2$, dispersion of the impedances is observed displaying a CPE-like behavior but only in a limited frequency range. Adding a charge transfer resistance in parallel with the double-layer capacitance leads to a skewed semicircle with a radius lower than the assumed R_{ct} . When the two electrodes are parallel, no dispersion is observed and a correct result is obtained. Simulations of impedances in the presence of the redox reaction represented by R_{ct} is displayed in Fig. 8.14, where distorted semicircles are obtained.

It should be added that in the foregoing cases, the current lines are not parallel as the current is looking for a path of least resistance.

Fig. 8.13 Complex plane plots for ideally polarizable working electrode in Hull cells with different geometry; parameters:

$\rho_s = 10 \Omega \text{ cm}$,
 $C_{dl} = 20 \mu\text{F cm}^{-2}$,
 $l_2 = 5 \text{ cm}$, $l_3 = 1 \text{ cm}$, $l_1 =$
 (a) 1 cm, (b) 2 cm, (c) 3 cm,
 (d) 5 cm; see Fig. 8.12 for
 definitions of geometric
 parameters, (impedances
 are in Ω , imaginary part is
 negative) (From Ref. [354],
 copyright (2007), with
 permission from Elsevier)



Newman found that at disk electrodes current distribution is nonuniform in the radial direction (known as the primary [355] and secondary [356] current distributions), which leads to impedance dispersion [357]. Recently, Huang et al. [310, 358, 359] continued these studies in more detail using a local impedance approach. Global admittance corresponds to the integration of the local admittances over the total disk area. Impedance can also be defined (and experimentally measured) locally as a function of the position on the electrode surface. In the case of the disk geometry, it changes radially from the disk center, $r = 0$, to the disk radius, $r = r_0$. The authors distinguished two types of distribution of time constants:

- 2D distribution arising from surface heterogeneities and geometry-induced nonuniform current and potential distribution.
- 3D distribution arising from variations in properties normal to the electrode surface, for example, changes in the conductivity of oxide layers with the distance from the electrode surface.

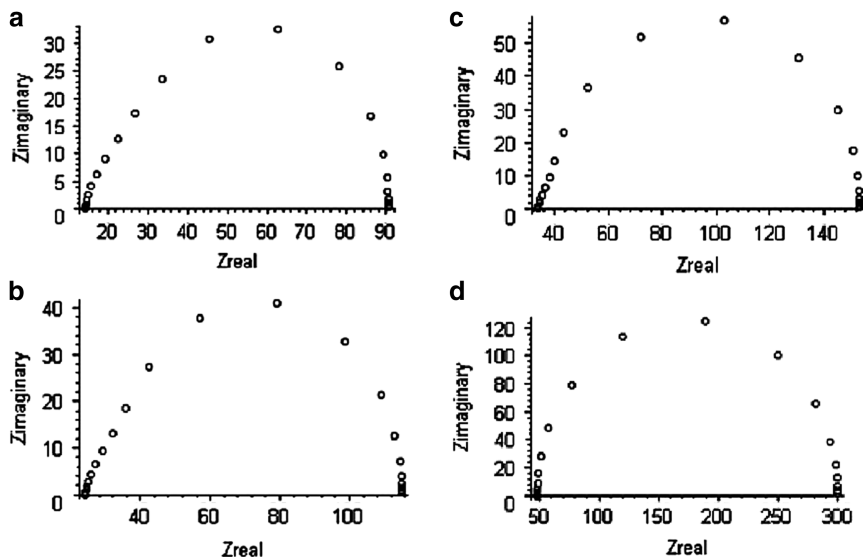


Fig. 8.14 Complex plane plots for faradaic reaction with $R_{ct} = 250 \, \Omega \, \text{cm}^2$ in various Hull cells; cell parameters as in Fig. 8.13, (impedances are in Ω , imaginary part is negative) (From Ref. [354], copyright (2007), with permission from Elsevier)

The local impedance, $z(r)$, consists of two contributions: the local interfacial impedance, $z_0(r)$, and the local ohmic solution impedance, $z_e(r)$:

$$z(r) = z_0(r) + z_e(r), \quad (8.21)$$

and the global impedance, Z , is obtained by integration of the admittances:

$$Z = \left(2\pi \int_0^{r_0} \frac{1}{z(r)} r \, dr \right)^{-1}, \quad (8.22)$$

where $z_0(r)$ is measured between the electrode surface and a point just outside the diffuse double layer, and $z_e(r)$ is measured in solution between the point outside the diffuse layer and the reference electrode at infinity. The behavior of the total electrode impedance for an ideally polarizable electrode obtained at a disk electrode is shown in Fig. 8.15. This behavior depends on the dimensionless frequency factor, K , defined as

$$K = \frac{\omega C_{dl} r_0}{\kappa}, \quad (8.23)$$

where C_{dl} is the specific double-layer capacitance and κ is the solution-specific conductivity. At frequencies corresponding to $K < 1$ the electrode behaves as an ideal capacitance, whereas for $K > 1$ deviations are observed (in accordance with

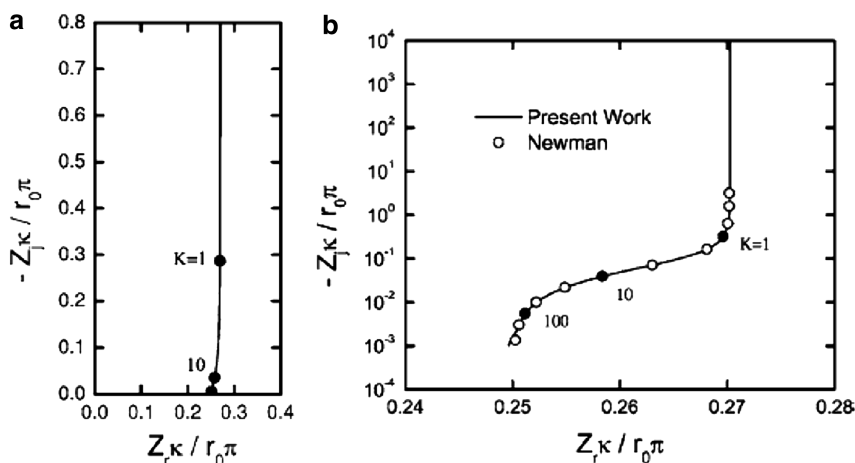


Fig. 8.15 Simulated complex plane plots of impedance response for ideally polarized disk electrode: (a) linear plot showing effect of dispersion at frequencies $K > 1$ as deviation from vertical line; (b) plot in logarithmic scale for imaginary impedances (From Ref. [358]. Reproduced with permission of Electrochemical Society)

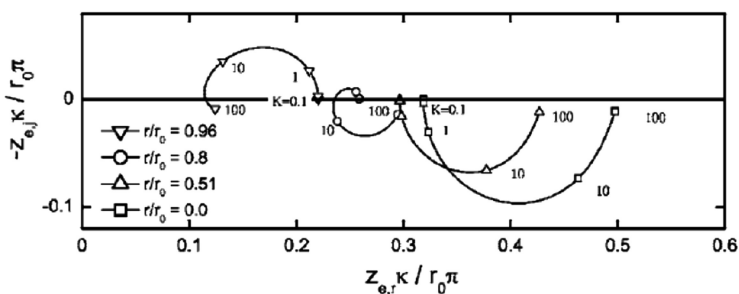


Fig. 8.16 Complex plane plots of normalized local ohmic impedance for different positions at disk surface, r/r_0 (From Ref. [358]. Reproduced with permission of Electrochemical Society)

Newman's predictions [357]). These deviations are more clearly visible on the logarithmic plot. It is interesting to note that the local interfacial impedance corresponds to an ideal capacitance, while the local ohmic impedance displays a more complicated behavior showing capacitive or inductive effects, see Ref. [359].

This means that the deviations from the ideal capacitive behavior observed for global impedance at high frequencies originate from the behavior of the local ohmic solution impedance (Fig. 8.16) caused by a nonlinear current and potential distribution at disk electrodes [360]. Similar effects were observed in the presence of faradaic reactions [310, 361, 362]. Theory discussed above was experimentally verified for corroding materials [359, 360, 363] or film thickness [311, 364, 365]. It is important to note that the Brug et al. formula, Eqs. (8.15) and (8.16), seems to work much better than that of Hsu and Florian, Eq. (8.15) [310]. Moreover, the recessed disk electrodes for which the current distribution is uniform do not show such impedance dispersion and behave ideally [366].

Another possible source of dispersion of time constants is the dispersion of capacitances arising from atomic-scale surface inhomogeneities such as grain boundaries, crystal faces on a polycrystalline electrode, or other variations in surface properties [313, 334, 350, 358]. However, experimental studies do not confirm this hypothesis. In fact, an increase in surface roughness, that is, of surface inhomogeneities, does not decrease the CPE parameter ϕ but increases it and such a surface becomes more similar to the ideal capacitance [313, 334, 350].

8.3.2 Dispersion Due to Surface Adsorption/Diffusion Processes

Dispersion due to surface adsorption/diffusion processes, or the so-called kinetic dispersion effect, is related to slow, i.e., kinetically limited, adsorption of ions or neutral molecules (often impurities) at the electrode surface. It has also been observed for surface reconstruction and changes in the adsorption layer where sharp deviations from ideal behavior and drop of the CPE exponent appeared. It has been found that in very clean solutions at monocrystalline electrodes the CPE parameter ϕ is very close to unity, e.g., at Au(111) in 0.1 M HClO₄ it is 0.997 [367], which indicates a practically ideal capacitive behavior. However, in the presence of specifically adsorbed anions, this value is always smaller. This behavior could be explained by assuming diffusion-kinetics-controlled ionic adsorption [367–375] and is described by the Frumkin and Melik-Gaykazyan model [376, 377]. The rate of an ionic adsorption reaction, v , is described by the following equation [367]:

$$v = \frac{d\Gamma}{dt} = v_{\text{ad}} - v_{\text{d}}, \quad (8.24)$$

where subscripts ad and d denote adsorption and desorption, respectively, and Γ is the surface excess of adsorbed ions. The current related to this reaction is

$$j = F \frac{d\Gamma}{dt} = \frac{dq^{\text{M}}}{dt} = -\gamma F v, \quad (8.25)$$

where γ is the electrosorption valency that is the charge transferred between the electrode and the adsorbed ion in reaction: $\text{A}^- + \lambda e = \text{A}_{\text{ads}}^{-1+\lambda}$, and q^{M} is the excess charge density in a metal electrode. Applying the standard linearization procedure the reaction impedance is obtained:

$$\hat{Z}_{\text{f}} = R_{\text{ad}} + \frac{1}{j\omega C_{\text{ad}}} + \hat{Z}_{\text{w,ad}}, \quad (8.26)$$

where R_{ad} and C_{ad} are the adsorption capacitance and resistance, respectively, and $\hat{Z}_{\text{w,ad}}$ is the mass transfer impedance. The electrical impedance model is displayed in Fig. 8.17 and its elements are defined as

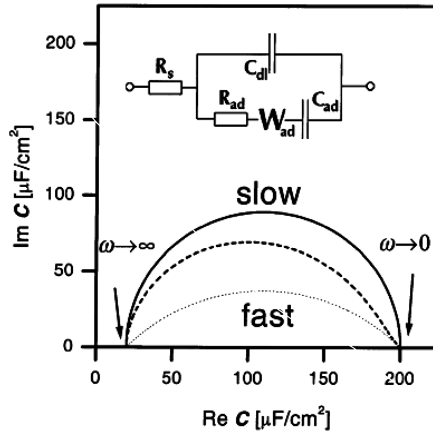


Fig. 8.17 Complex plane plots of complex capacitance, \hat{C} , defined using Eq. (8.28) for limiting cases of slow (*continuous line*), fast (diffusion limited, *dotted line*), and intermediate (*dashed line*) adsorption. Insert: equivalent electrical model for this process (From Ref. [367], copyright (2002), with permission from Elsevier)

$$C_{ad} = \gamma F \frac{\left(\frac{\partial v}{\partial E} \right)}{\left(\frac{\partial v}{\partial \Gamma} \right)}; \quad R_{ad} = - \frac{1}{\gamma F \left(\frac{\partial v}{\partial E} \right)}; \quad (8.27)$$

$$\hat{Z}_{W,ad} = \frac{\sigma_{ad}}{\sqrt{j\omega}} = - \frac{1}{\gamma F \sqrt{j\omega D}} \frac{\left(\frac{\partial v}{\partial C} \right)}{\left(\frac{\partial v}{\partial E} \right)},$$

where C is the bulk concentration of adsorbed ions, D their diffusion coefficient, and σ_{ad} the Warburg coefficient. Because complex plane plots are quite featureless, the analysis was carried out by transforming the impedances into complex capacitances:

$$\hat{C} = \frac{1}{j\omega(\hat{Z}_{tot} - R_s)} = C_{dl} + \frac{1}{\frac{1}{C_{ad}} \sigma_{ad} \sqrt{j\omega} + R_{ad}}. \quad (8.28)$$

Examples of complex capacitances simulated for kinetically slow, fast (i.e., diffusion limited), and intermediate adsorption rates are shown in Fig. 8.17. For the kinetically controlled reaction a perfect semicircle is observed and it becomes

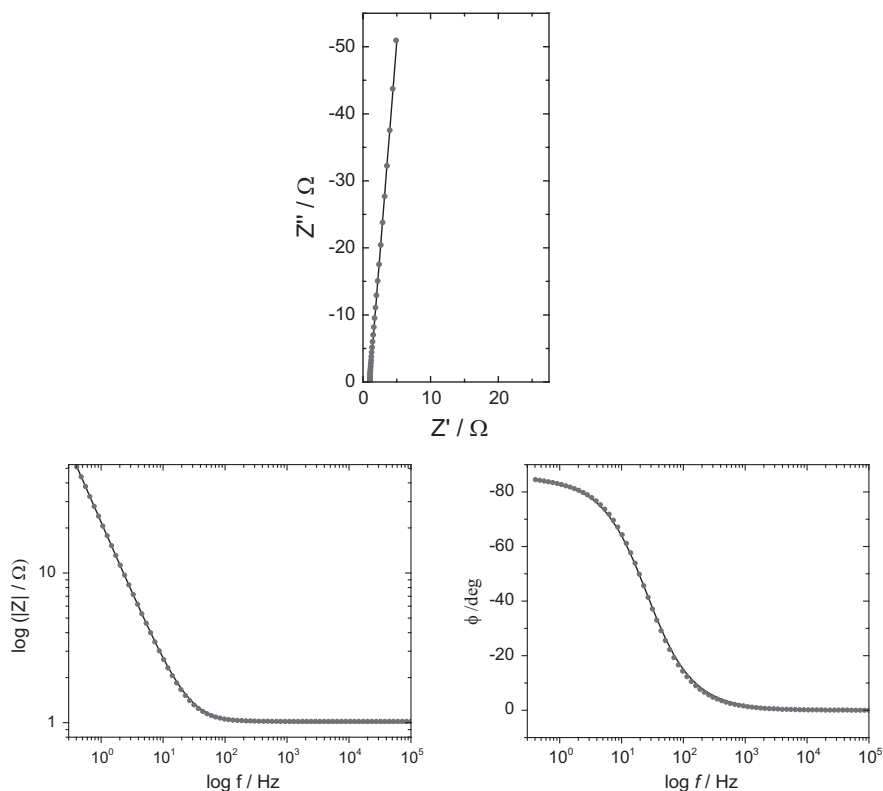


Fig. 8.18 Approximation of impedances simulated using CPE model with $T = 8 \text{ mF s}^{-0.05}$, $\phi = 0.95$, and $R_s = 1 \Omega$ (points) by kinetic Frumkin-Melik-Gayakazan model (lines)

distorted in the presence of mixed kinetic-diffusion control. Such an analysis was applied to study anionic adsorption on several well-defined metallic surfaces [367–375].

Experimental studies confirm that the CPE is often related to the adsorption of impurities. Studies performed on a polycrystalline Au electrode in the double-layer zone [352] in 1 M H_2SO_4 display almost ideal capacitive behavior with $\phi \sim 0.99$, while in the same cell on the same electrode in 1 M NaNO_3 a larger CPE deviation with $\phi \sim 0.93$ was observed because sodium nitrate is not as pure as sulfuric acid. Moreover, at well-polished and annealed polycrystalline Pt (roughness factor $R_f = 1.4$) the parameter ϕ is between 0.97 and 0.977 in the double-layer zone in 0.1 M H_2SO_4 [352]. However, after electrochemical roughening ($R_f = 5.1$) ϕ increases to >0.99 . This can only be explained by the fact that the surface (ionic) impurities become distributed over a larger surface area and their coverage becomes smaller.

Although the CPE and the kinetic Frumkin and Melik-Gayakazan models are intrinsically different, they lead to the same impedance behavior in a certain frequency range.

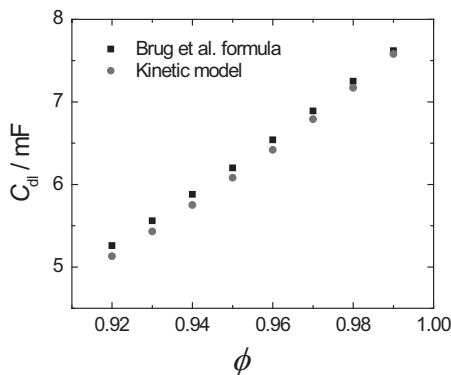


Fig. 8.19 Dependence of double-layer capacitance, \overline{C}_{dl} , determined using Brug et al. CPE model, Eq. (8.11), (■), and C_{dl} estimated from kinetic model, (●), Eq. (8.26) (with $R_{ad} = 0$) determined from impedances simulated using CPE data: $T = 8 \text{ mF s}^{\phi-1}$, $R_s = 1 \Omega$ versus CPE exponent ϕ

Figure 8.18 shows complex plane plots simulated with the CPE model assuming $T_{dl} = 8 \text{ mF s}^{-0.05}$ and $\phi = 0.95$. These data could be very well approximated [313] using the kinetic model with $C_{dl} = 6.08 (0.02) \text{ mF}$, $\sigma = 0.0053 (0.0001) \Omega \text{ s}^{-1/2}$, $C_p = 2.83 (0.01) \text{ mF}$, and $R_{ad} = 0$, where the numbers in parentheses denote the standard deviations of the parameters. The fit was carried out in the frequency range 100 kHz to 0.4 Hz and the goodness-of-fit parameter is $\chi^2 = 7.5 \times 10^{-4}$. At lower frequencies deviations appear. The obtained results indicate that both models might be indistinguishable in practice, although the CPE model contains fewer adjustable parameters.

If the experimental data arise from the kinetic model, the use of Brug's et al.'s formula cannot be justified. In fact, this formula leads, for the foregoing example, to an average value of $\overline{C}_{dl} = 7 \text{ mF}$, while the true C_{dl} is 6.1 mF and $C_p = 2.8 \text{ mF}$. Surprisingly, both values are relatively close to each other. However, the influence of the solution and charge transfer resistances in Brug et al.'s formula is relatively small because they are taken to the power $(1-\phi)/\phi$.

Data simulated using the CPE model and $T = 8 \text{ mF s}^{\phi-1}$, values of ϕ between 0.90 and 0.99, and $R_s = 1 \Omega$ could be approximated using the kinetic Frumkin-Melik-Gayakazan model, Eq. (8.26). Comparison of the values of C_{dl} from the kinetic model and \overline{C}_{dl} obtained using Brug et al.'s formula, Eq. (8.11), is displayed in Fig. 8.19. The values obtained using the Brug et al.'s CPE model are close to those obtained using the kinetic model with a relative error from 2 % at $\phi = 0.9$ % to 0.5 % at $\phi = 0.99$. Similar approximations were obtained for lower values of the parameter T (corresponding to those obtained in the double-layer zone) but at frequencies higher than 4 Hz.

It should be stressed again that in the kinetic model the CPE-like behavior appears in a limited frequency range only.

8.4 Determination of Time Constant Distribution Function

As was shown earlier, the presence of the CPE of fractal impedance produces a distribution of the time constants. In addition, other elements such as the Warburg (semi-infinite or finite-length) linear or nonlinear diffusion, porous electrodes, and others also produce a dispersion of time constants. Knowledge about the nature of such dispersion is important in the characterization of electrode processes and electrode materials. Such information can be obtained even without fitting the experimental impedances to the corresponding models, which might be still unknown. Several methods allow for the determination of the distribution of time constants [378, 379], and they will be briefly presented below.

8.4.1 Regularization Methods

Equation (8.4), defining the time constant distribution function, is known as the Fredholm integral equation of the first kind:

$$g(\omega) = \int_0^{\infty} K(\tau, \omega) f(\tau) d\tau, \quad (8.29)$$

where the left-hand side is a known function:

$$g(\omega) = \frac{\hat{Z}(\omega) - Z_{\infty}}{Z_0 - Z_{\infty}}, \quad (8.30)$$

$K(\omega, \tau)$ is a known kernel:

$$K(\omega, \tau) = \frac{1}{1 + j\omega\tau}, \quad (8.31)$$

and

$$f(\tau) = \tau G(\tau) \quad (8.32)$$

is the unknown time constant distribution function [248, 380–382]. Equation (8.29) can be solved numerically by its transformation into a system of linear equations:

$$\mathbf{g} = g(\omega) = \sum_{j=1}^N w_i K_{i,j} f_i = \mathbf{KWg} = \mathbf{Af}, \quad (8.33)$$

where w_i are the coefficients corresponding to the quadrature used for integration, $K_{ij} = K(\tau_i, \omega_j)$, $f_i = f(\tau_i)$, and bold letters denote vectors or matrices. For example, for a simple trapezoidal integration rule the weights are $w_1 = w_N = 0.5$ and the

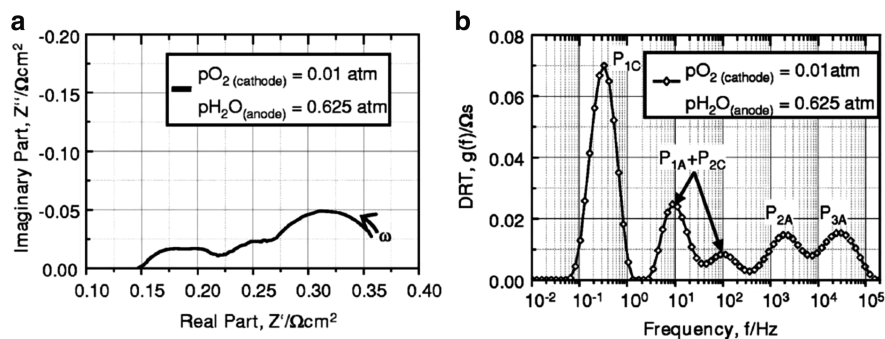


Fig. 8.20 Impedance spectrum and distribution of relaxation time function for solid oxide fuel cell (From Ref. [385]. Reproduced with permission of Electrochemical Society)

other $w_i = 1$. The linear system of equations $\mathbf{g} = \mathbf{A}\mathbf{f}$ can be solved by minimizing the residuals using a least-squares method: minimize $\|\mathbf{A}\mathbf{f} - \mathbf{g}\|^2$ with respect to \mathbf{f} . This leads to a known solution: $\mathbf{f} = (\mathbf{A}^T \mathbf{A})^{-1} \mathbf{A}^T \mathbf{g}$, where the index T denotes a transposed matrix. However, this procedure is an ill-posed problem involving the inversion of large matrices, and its solution leads to strong oscillations of $f(\tau)$ due to experimental errors of the measured impedance. To stabilize the solution, regularization techniques must be used depending on the value of the regularization parameter λ , which smooths function \mathbf{f} . The biggest problem is how to choose the optimal value of λ because too small values of λ allow oscillations and too large values distort the function (too much damping). There are, however, several methods of regularization and determination of the optimal values of the regularization parameter [383]. It was found using data simulated for the CPE or fractal models that correct distribution functions were obtained [381, 382]. However, the results were sensitive to experimental errors, and for a more complicated model involving a finite-length porous model the distribution function obtained contained some oscillations around the large peak [382]. When these oscillations were damped, the data recalculated from the distribution function differed from the assumed values. This indicated that the regularization method was not reliable for determining the time constant distribution function.

Ivers-Tiffé and coworkers proposed a modification of the solution of Eq. (8.4) using a Fourier transform [384]. They applied their method to determine the time constant distribution in solid electrolytes and batteries [384–387]. An example of the application of this technique to solid oxide fuel cells (SOFCs) is shown in Fig. 8.20. The complex plane plot shows several poorly separated semicircles, while the time constant distribution function displays five peaks; the authors assigned these time constants to different processes.

8.4.2 Least-Squares Deconvolution Methods

The kernel in Eq. (8.31) corresponds to one element of a Voigt circuit, and the time constant distribution function, Eq. (8.32), is continuous. However, the integral in Eq. (8.4) can be substituted by a sum of discrete functions [378, 379]:

$$\frac{\hat{Z}(\omega) - Z_\infty}{Z_0 - Z_\infty} = \int_0^\infty \frac{G(\tau)}{1 + j\omega\tau} d\tau = \sum_{m=1}^M \frac{g_m}{1 + j\omega\tau_m}, \quad (8.34)$$

where the continuous function $G(\tau)$ was replaced by a sum of discrete values g_m . For a series of fixed time constants uniformly distributed on a logarithmic scale, τ_m , the values of g_m might be determined by a complex nonlinear least-squares method. This method was implemented in J. Ross Macdonald's program LEVM (distributed at no cost on the Internet) [388]. Macdonald and Tuncer [378, 379] applied this method to study the dispersion of dielectric permittivities.

A modification of this procedure was proposed in the literature [389] and applied to determine the time constant distribution function [379]. This method is based on the predistribution of time constants uniformly on the logarithmic scale, and to improve the quality of the analysis, a Monte Carlo technique was used to increase the number of analyzed time constants. Approximation was carried out using a constrained least-squares method and led to a continuous distribution function. This procedure converted the nonlinear problem to a linear one from which g_m versus τ_m were obtained and produced positive values of the distribution function. The procedure was also applied to the distribution of the dielectric constants [379, 389].

8.4.3 Differential Impedance Analysis

Stoynov and coworkers [28, 390–398] proposed another method for the determination of the distribution of parameters called differential impedance analysis (DIA). It is based on the application of a simple three parameter $R_1(R_2C)$ model [a so-called local operating model (LOM)] to the impedance spectra. At each frequency three parameters Z' , Z'' , and ω are known but they are not sufficient to determine the parameters R_1 , R_2 , and C . Therefore, two more parameters are added: $dZ'/d \log \omega$ and $dZ''/d \log \omega$. This LOM is swept across the experimental impedance data producing series of the parameters at each frequency. The impedance of the LOM is

$$\hat{Z}_{\text{LOM}} = R_1 + \frac{R_2}{1 + \omega^2 \tau^2} - j \frac{R_2}{1 + \omega^2 \tau^2} = R_{\text{eff}}(\omega) + j\omega L_{\text{eff}}(\omega) \quad (8.35)$$

where the model containing two frequency dependent parameters, R_{eff} and L_{eff} was introduced. Time constant may be found as $\tau = R_2 C = (dL_{\text{eff}}/d \log \omega)/(dR_{\text{eff}}/d \log \omega)$ and then all the parameters using Eq. (8.35). To avoid oscillations, the

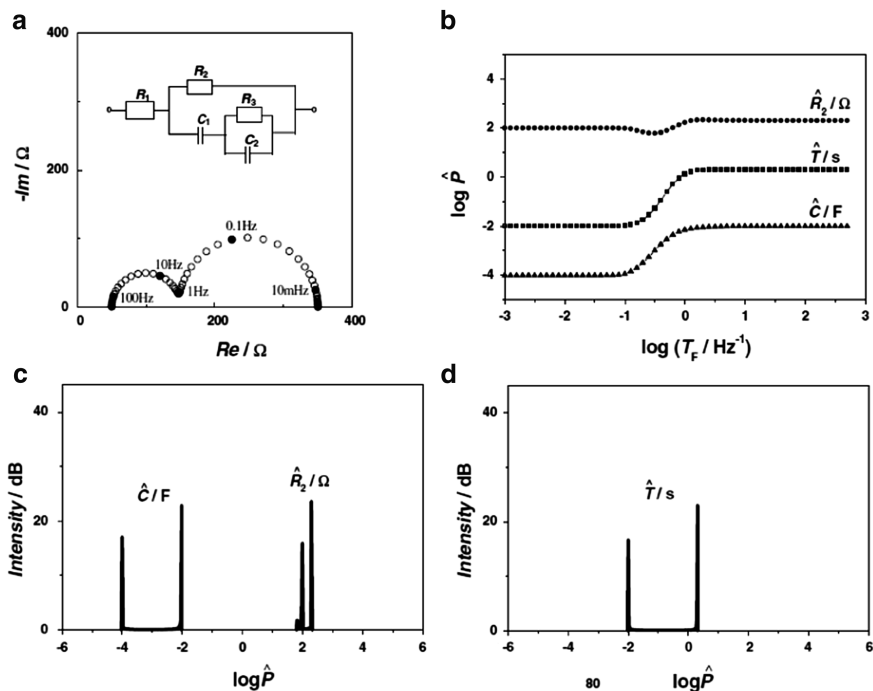


Fig. 8.21 Application of DIA to impedance data simulated using electrical equivalent model containing two time constants; (a) electrical equivalent model and impedance complex plane plot; (b) log of obtained parameters R_2 , C , and time constant $\tau = T$ as functions of log of inverse frequency $\log T_F = -\log f_F$; (c) and (d) cumulative spectral line's intensity plots as functions of log of values of parameters (From Ref. [392], copyright (2004), with permission from Elsevier)

experimental data might be smoothed using splines. Let us look at the application of this method to the impedance data shown in Fig. 8.21a. Values of the parameters, \hat{P} , obtained as a function of the logarithm of frequency are displayed in Fig. 8.21b. It is obvious that there are two values of R_2 , C , and the time constant $\tau = T$. Figure 8.21c, d shows the cumulative spectral line's intensity plots as functions of the logarithm of the parameter values. Now it is obvious that there are two time constants (d) and two values of the resistance and capacitance, in agreement with the model (a). To deal with the distributed elements as the CPE, the authors proposed a secondary DIA. The complex plane impedance plot for the CPE is shown in Fig. 8.22a, and the plot of the values of the parameters versus $\log T_f = -\log f$ are shown in panel b. There is a linear relation between the log of these parameters and $\log f$. Then one can determine the derivatives of these lines:

$$\delta_{P_i} = \frac{d \log P_i}{d \log \omega}, \quad (8.36)$$

which, according to the definition of the CPE, are $\delta_R = \alpha$, $\delta_C = 1 - \alpha$ and $\delta_T = 1$. These derivatives are shown in Fig. 8.22c as functions of $\log T_f$; they are constant,

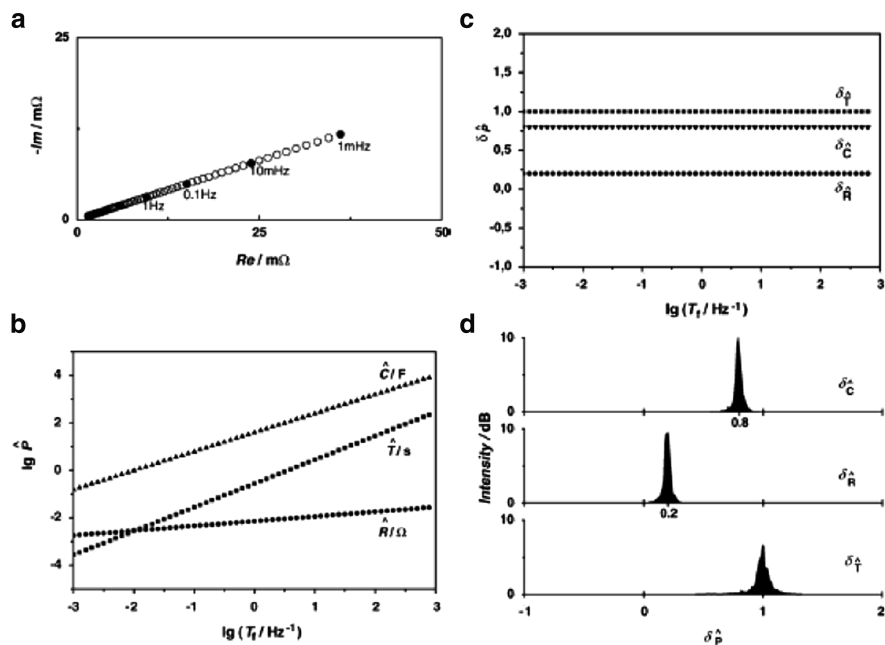


Fig. 8.22 DIA of CPE with $\phi = 0.8$ simulated in frequency range 10^3 – 10^{-3} Hz: (a) impedance diagram; (b) plot of CPE parameters versus $T_f = -\log f$; (c) differential temporal plots of parameters versus $\log T_f$; (d) differential spectral plots versus values of these derivatives (From Ref. [395], copyright (2006), with permission from Elsevier)

in agreement with the theory. Finally, the cumulative spectral line's intensity plots as functions of the logarithm of the parameter values are shown in panel d. The original value of the parameter ϕ is recovered. The DIA behavior of other distributed elements was shown in Ref. [28]. It should be added that DIA does not give directly the dispersion of the time constants but rather the dispersion of parameters that arises from the distribution of the time constants.

An example of the application of DIA to the impedance analysis of SOFCs is shown in Fig. 8.23.

8.4.4 Summary

Determination of the time constant distribution function is still carried out quite rarely. Several methods make it possible to determine this distribution function. Such procedures can be carried out without prior knowledge of the impedance model. Studies of the changes in the values and nature of time constants as functions of temperature or partial pressure of gases in SOFCs make it possible to assign these time constants to particular processes and to better understand the process mechanisms. The biggest drawback of this procedure is the lack of commercial programs allowing such an analysis. Mathematically, the simplest methods

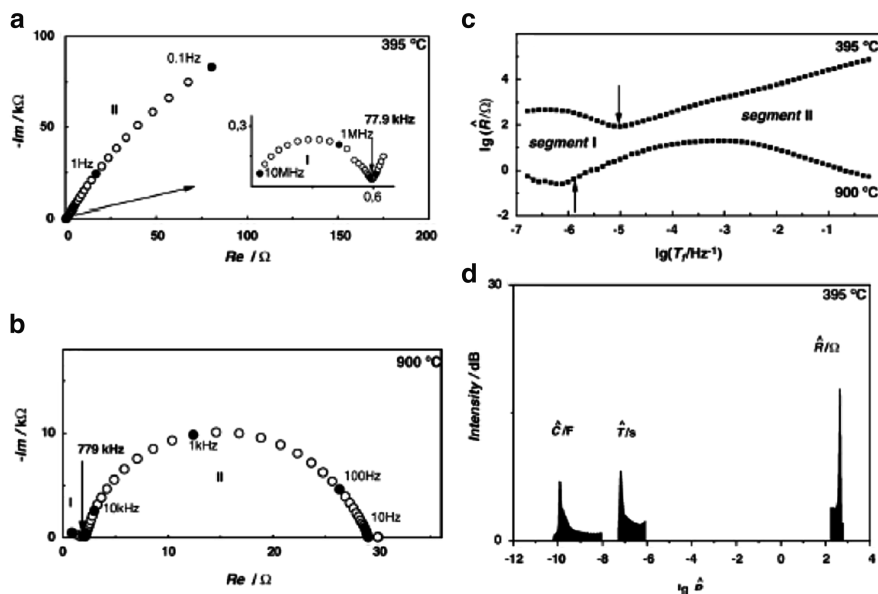


Fig. 8.23 Complex plane plots of YSZ single crystal in (a) 395 °C and (b) 900 °C; (c) plot of parameters versus $-\log f$; (d) spectral plot of determined parameters (From Ref. [395], copyright (2006), with permission from Elsevier)

are the least-squares deconvolution method (implemented in LEVM program) and the DIA, although some authors (Tuncer, program in Matlab [379]) intend to provide their programs.

8.5 Conclusion

The problem of impedance dispersion at solid electrodes is still a subject of heated discussion. The CPE model that is usually used in practice makes it possible to fit experimental data; however, from a physical point of view it cannot be valid in the whole frequency range. The main sources of dispersion are the distribution of solution resistances (e.g., Hull cells, disk geometry) and the adsorption of ionic impurities. It must be stressed that both processes contribute to dispersion in a limited frequency range; however, in many cases it is impossible to go to sufficiently low frequencies to notice this effect. Of course, it is difficult to carry out detailed studies of the origin of the observed CPE in each experimental case, and the CPE might be used in the modeling of experimental impedances. The use of the Brug et al. formulas (8.11) and (8.16) to estimate the average double-layer capacitance seems to be an acceptable compromise, although, fundamentally, they are not correct. However, in kinetic studies, it was noticed that the presence of the CPE did not affect the charge transfer resistances. In fact, studies of the kinetics of the HUPD at a polycrystalline Pt carried out in two different geometric arrangements produced quite different CPE ϕ exponents, but the determined charge transfer resistances were identical [399].

Chapter 9

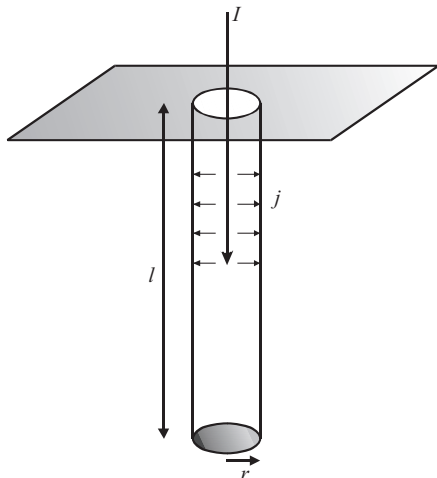
Impedance of Porous Electrodes

In the industrial applications of electrochemistry, the use of smooth surfaces is impractical and the electrodes must possess a large real surface area in order to increase the total current per unit of geometric surface area. For that reason porous electrodes are usually used, for example, in industrial electrolysis, fuel cells, batteries, and supercapacitors [400]. Porous surfaces are different from rough surfaces in the depth, l , and diameter, r , of pores; for porous electrodes the ratio l/r is very important. Characterization of porous electrodes can supply information about their real surface area and electrochemical utilization. These factors are important in their design, and it makes no sense to design pores that are too long and that are impenetrable by a current. Impedance studies provide simple tools to characterize such materials. Initially, an electrode model was developed by several authors for dc response of porous electrodes [401–406]. Such solutions must be known first to be able to develop the ac response. In what follows, porous electrode response for ideally polarizable electrodes will be presented, followed by a response in the presence of redox processes. Finally, more elaborate models involving pore size distribution and continuous porous models will be presented.

9.1 Impedance of Ideally Polarizable Porous Electrodes

Pore geometry influences the shape of impedance plots. In what follows, various pore geometries will be presented. First, the ohmic drop in solution only will be taken into account, and later the ohmic drop in solution and in the electrode material will be considered [407].

Fig. 9.1 Model of a cylindrical pore; gray area is not conductive. I axial current flowing to pore, j local current flowing to pore walls



9.1.1 Cylindrical Pore with Ohmic Drop in Solution

Only ($i_{dc} = 0$, $r_e = 0$, $r_s \neq 0$)

The simplest model involves a cylindrical pore with length l and radius r filled with electrolytic solution (Fig. 9.1). It is assumed that only the pore walls are conducting and behave as ideally polarizable. There is no dc current, but the ac current will flow charging the double layer of pore walls through the solution resistance.

The ac current I enters the pore and flows to the walls. Because of the ohmic drop in the solution, inside the pore it decreases with the penetration depth and its amplitude decreases as it flows to the walls as j . An equation for the impedance of the cylindrical pore was developed by de Levie [408]. The following assumptions were made:

- The pore is cylindrical.
- Only the pore side walls are conducting; the resistance of the electrode material is zero ($\rho_e = 0$).
- The pore is filled with supporting electrolyte characterized by the resistivity, ρ_s (Ω cm).
- The ac potential gradient exists in the axial direction only, i.e., there is no radial potential gradient.

The specific impedance of the pore walls is $\hat{Z}_{el} = 1/j\omega C_{dl}$ (in Ω cm²), where C_{dl} is the specific capacitance (F cm⁻²) of the pore walls. The ac potential phasor, \tilde{E} , that enters the pore decreases from the initial value at the pore orifice, \tilde{E}_0 , because of the ohmic drop in solution, and the ac charging current phasor, \tilde{I} , decreases with

the pore depth as it flows to the pore walls from its initial value \tilde{I}_0 at the pore orifice. This problem can be described by a system of two differential equations describing the current and potential drop along the pore:

$$\frac{d\tilde{I}}{dx} = \frac{\tilde{E}}{\hat{z}}, \quad (9.1)$$

$$\frac{d\tilde{E}}{dx} = -r_s \tilde{I}, \quad (9.2)$$

where the parameter x changes from zero at the pore orifice to l at the pore bottom, \hat{z} is the impedance unit pore length (Ω cm); for ideally polarized electrodes $\hat{z} = \hat{Z}_s l = 1/(j\omega c_{dl})$, where $\hat{Z}_s = 1/(j\omega c_{dl} 2\pi r l)$ is the total impedance of the pore wall (Ω), c_{dl} is the double-layer capacitance per unit of pore length (F cm⁻¹), and \hat{z} can also be written as $\hat{z} = \hat{Z}_{el}/s = 1/(j\omega C_{dl} 2\pi r)$, C_{dl} is the specific double layer capacitance in F cm⁻², $s = 2\pi r l$ is the total surface area of the pore wall, r_s is the solution resistance in the pore per unit length, $r_s = R_{\Omega,p}/l = (\rho_s l/\pi r^2)/l = \rho_s/\pi r^2$ (Ω cm⁻¹), and $R_{\Omega,p}$ is the total resistance of the pore filled with solution, $R_{\Omega,p} = \rho_s l/\pi r^2$ (Ω). The second derivative of \tilde{E} , Eq. (9.2), versus x equals

$$\frac{d^2\tilde{E}}{dx^2} = -r_s \frac{d\tilde{I}}{dx} = \frac{r_s}{\hat{z}} \tilde{E}, \quad (9.3)$$

with the following conditions:

$$\begin{aligned} x = 0 & & \tilde{E} = \tilde{E}_0, \\ x = l & & d\tilde{E}/dx = 0. \end{aligned}$$

The solution of Eq. (9.3) is

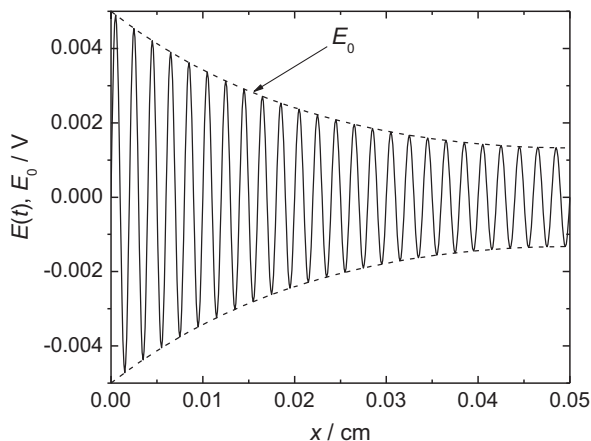
$$\tilde{E} = \tilde{E}_0 \frac{\cosh[\sqrt{\frac{r_s}{\hat{z}}}(l-x)]}{\cosh[\sqrt{\frac{r_s}{\hat{z}}}l]}. \quad (9.4)$$

This equation predicts that the amplitude of the ac signal, which penetrates into the pore, decreases with the distance in the pore x . An example of such a relation is shown in Fig. 9.2.

The amplitude of the ac signal decreases with x and reaches a constant value at $x = l$. Of course, such a graph is different at different frequencies. To determine the total impedance, the ratio of the phasors of the potential and current at the pore orifice must be calculated. The potential gradient at the pore orifice is

$$\left. \frac{d\tilde{E}}{dx} \right|_{x=0} = -\tilde{E}_0 \sqrt{\frac{r_s}{\hat{z}}} \tanh\left(\sqrt{\frac{r_s}{\hat{z}}}l\right) = -\tilde{I}_0 r_s, \quad (9.5)$$

Fig. 9.2 Dependence of ac voltage $E(t)$, and its amplitude, E_0 , on distance in the pore according to Eq. (9.4); $E_0 = 0.005$ V, $l = 0.05$ cm



and the pore impedance (Ω) is

$$\hat{Z}_{\text{pore}} = \frac{\tilde{E}_0}{\tilde{I}_0} = \sqrt{r_s \hat{z}} \coth \left(\sqrt{\frac{r_s}{\hat{z}}} l \right). \quad (9.6)$$

This equation may be rearranged into another useful form [409]:

$$\hat{Z}_{\text{pore}} = \frac{R_{\Omega,p}}{\Lambda^{1/2}} \coth(\Lambda^{1/2}) \quad (9.7)$$

where

$$\Lambda = \frac{r_s l^2}{\hat{z}} = \frac{2\rho_s l^2}{r \hat{Z}_{\text{el}}} = \frac{2\rho_s l^2 j \omega C_{\text{dl}}}{r} \quad (9.8)$$

is the dimensionless admittance of the porous electrode. For n identical pores and when the solution resistance outside pores is R_{sol} , the total impedance is

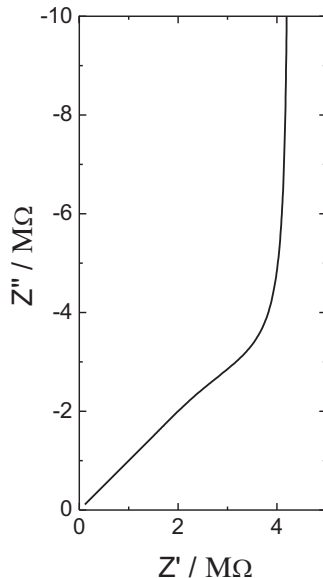
$$\hat{Z} = R_{\text{sol}} + \frac{\hat{Z}_{\text{pore}}}{n}. \quad (9.9)$$

The complex plane plot of the impedance of a single pore is displayed in Fig. 9.3. Very large values of the impedance are related to the very low pore surface area. This plot reveals a straight line at 45° at high frequencies followed by a vertical line at low frequencies. These features originate from the properties of Eq. (9.7). At very high frequencies Λ is large, $\coth(\Lambda^{1/2}) \rightarrow 1$, and it simplifies to

$$\hat{Z}_{\text{pore}} = \sqrt{r_s \hat{z}} = \frac{R_{\Omega,p}}{\Lambda^{1/2}} = \frac{\rho_s^{1/2}}{\sqrt{2\pi r^{3/2}}} \sqrt{\hat{Z}_{\text{el}}} = \frac{\rho_s^{1/2}}{2\pi r^{3/2} \omega^{1/2} C_{\text{dl}}^{1/2}} (1 - j) \quad (9.10)$$

Fig. 9.3 Complex plane plot of impedance of single pore; parameters:

$\rho_s = 10 \Omega \text{ cm}$, $l = 0.05 \text{ cm}$,
 $r = 10^{-4} \text{ cm}$,
 $C_{dl} = 20 \mu\text{F cm}^{-2}$



taking into account that $1/\sqrt{j} = (1-j)/\sqrt{2}$. Equation (9.10) indicates that the real and imaginary parts of the impedance are identical, $Z' = -Z''$, which leads to a straight line at 45° on the complex plane plots. Note that the pore length does not appear in this equation.

At low frequencies $\coth(\Lambda^{1/2})/\Lambda^{1/2} \approx 1/3 + 1/\Lambda$ and Eq. (9.7) becomes

$$\hat{Z}_{\text{pore}} = \frac{R_{\Omega,p}}{3} + \frac{R_{\Omega,p}}{\Lambda} = \frac{\rho_s l}{3\pi r^2} + \frac{1}{j\omega C_{dl}(2\pi r l)} = R_{\text{pore}} + \frac{1}{j\omega C_{\text{pore}}} \quad (9.11)$$

corresponding to a $R_{\text{pore}} - C_{\text{pore}}$ connection in series and it displays a straight capacitive line with resistance $R_{\text{pore}} = R_{\Omega,p}/3$ and capacitance equal to the total capacitance of the pore wall (specific capacitance C_{dl} times the surface area $s = 2\pi r l$, $C_{\text{pore}} = C_{dl} 2\pi r l$). This means that from low-frequency measurements it is possible to determine the total electrode surface area, which allows for the determination of the *real surface area* (if the specific double-layer capacitance of the electrode material is known) and the *solution resistance in pores*, $R_{\Omega,p}$.

The observed complex plane plots may be explained in terms of the penetration length of the ac signal into pores, $\sqrt{\Lambda} = l/\lambda$ or $\lambda = l/\sqrt{\Lambda} = (r\hat{Z}_{el}/2\rho_s)^{1/2}$. At high frequencies, $\hat{Z}_s \rightarrow 0$, $\Lambda \rightarrow \infty$, $\lambda \ll l$, and the ac signal cannot penetrate to the bottom of the pore, i.e., the pore behaves as a semi-infinite-length pore. On the other hand, at low frequencies, $\lambda \gg l$, and the ac signal can penetrate to the bottom of the pore and the porous system can be represented by an $R - C_{\text{pore}}$ connection in series. The dependence of λ on the frequency is presented in Fig. 9.5; the dashed line corresponds to the pore length. At $\omega = 10^2 \text{ rad s}^{-1}$ the penetration length is

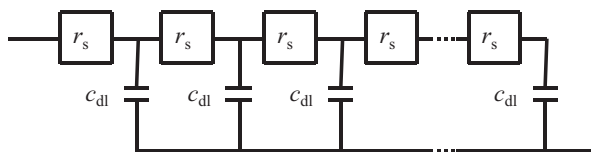


Fig. 9.4 Uniform transmission line representing impedance of flooded ideally polarized porous electrode; r_s and c_{dl} are the solution resistance and double-layer capacitance, respectively, of a small element of the pore length

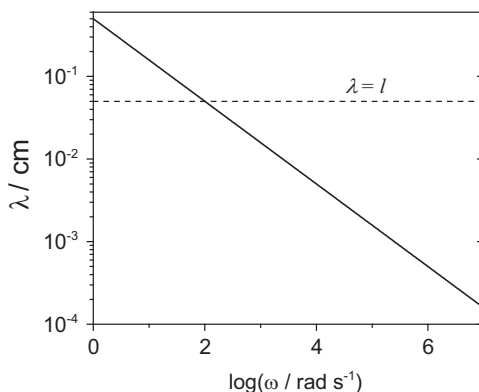


Fig. 9.5 Dependence of ac signal penetration length on frequency; parameters as in Fig. 9.3; *dashed line*: pore length

equal to the pore length. At much lower frequencies, $\lambda \gg l$, the ac signal can penetrate to the bottom of the pore, and the measured capacitance corresponds to the total capacitance of the pore walls. At much higher frequencies, $\lambda \ll l$, and the ac signal cannot enter deeply into the pore because of the IR drop and a very low impedance of the pore walls.

The porous electrode model described in Eq. (9.7) cannot be represented by a simple connection of R , L , and C elements. However, it can be represented by a semi-infinite series of R - C elements called a transmission line [410, 411], shown in Fig. 9.4. Of course, this representation is equivalent to Eq. (9.7). Some authors tried to use a transmission line to approximate experimental data using a sufficient number of RC elements and verifying whether the number of these parameters was sufficient. This procedure can approximate, then, experimental impedances, but the use of Eq. (9.7) is more appropriate because it allows for the direct estimation of certain parameters and their standard deviations. This model is included in the recent version of the ZView program.

The model presented above is valid for the isolated pore. However, such pores are usually present in an electrode material, and the capacitance of the top flat layer must be taken into account and added to the total electrode impedance [352]. In such a case the total impedance consists of the impedance of the porous part, \hat{Z}_{pore} , and that of a

Fig. 9.6 Equivalent electrical circuit of electrode containing porous and external flat part

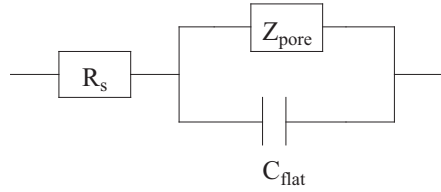
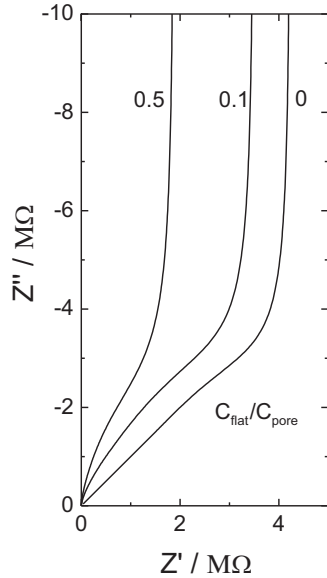


Fig. 9.7 Complex plane plots for ideally polarizable porous electrode containing contribution from external flat surface for different ratios of flat external and porous internal capacitances



flat part of the electrode, $\hat{Z}_{\text{flat}} = 1/j\omega C_{\text{flat}}$. The corresponding electrical equivalent circuit is displayed in Fig. 9.6.

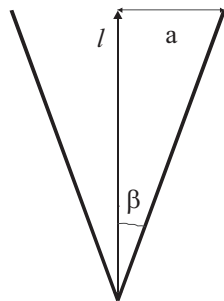
Its impedance is

$$\hat{Z} = R_s + \frac{1}{j\omega C_{\text{flat}} + \frac{1}{\hat{Z}_{\text{pore}}}}. \quad (9.12)$$

The complex plane plots for different ratios of $C_{\text{flat}}/C_{\text{pore}}$, where $C_{\text{pore}} = C_{\text{dl}}$, are presented in Fig. 9.7. With the increase of the importance of the external flat surface there is a decrease in the low-frequency resistance, and the low-frequency capacitance is the total capacitance of the porous and flat surface:

$$R_{\text{pore}} = \frac{R_{\Omega,p}}{3} \frac{1}{\left(1 + \frac{C_{\text{flat}}}{C_{\text{pore}}}\right)^2} C_{LF} = C_{\text{pore}} + C_{\text{flat}}. \quad (9.13)$$

Fig. 9.8 Cross section of groove electrode



The preceding model was tested for different ideally polarizable gold-based electrodes [352, 412]. The model porous electrodes were gold brush electrodes consisting of 140 Au wires 1 cm in length and 0.25 mm in diameter fixed in a Teflon sleeve and gold wire 0.1 mm in diameter in a glass capillary with 0.45 mm of internal diameter. Calculated (taking into account the particular geometry of pores) and experimental values of $R_{\Omega,p}$ were very similar, as was the real surface area. In addition, for other porous gold electrodes obtained by thermal decomposition of Au_2O_3 , AuCl, or amalgamated gold (after dissolution of mercury) the ratio of the porous to flat surface area was obtained by the CNLS fit of the experimental impedance to the model in Fig. 9.6. The obtained ratios of capacitance of the porous to flat areas were between 0.46 and approximately 500.

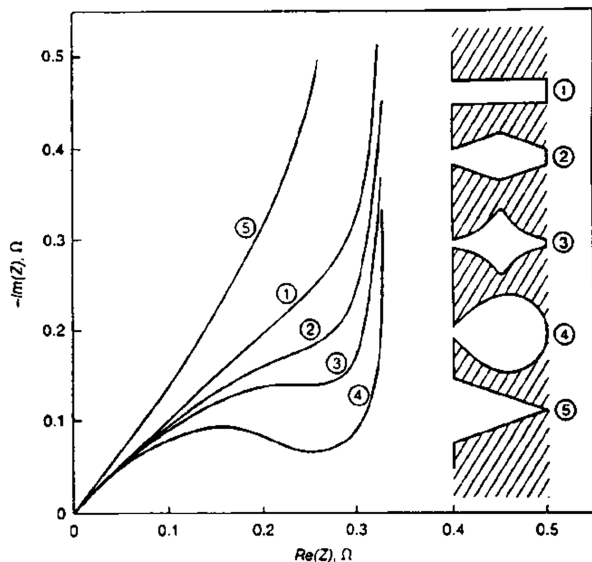
Working in conditions of ideal polarizability allows for the easiest characterization of porous electrodes. This can be achieved in the absence of a faradaic reaction by changing the electrode potential or solution composition or by using nitrogen as a feed gas in fuel cells. However, in many cases, such a characterization cannot be performed because of the redox reactions. In subsequent sections it will be shown that such a characterization is also possible in the presence of redox reactions.

9.1.2 Other Pore Geometry with Ohmic Drop in Solution Only

The cylindrical pore model is an idealization of a real porous electrode. Other pore geometries were also studied. De Levie [413] obtained an analytical solution for the impedance of V-grooved pores. Such pores might be obtained, for example, by scratching the electrode surface. A cross section of such a groove is displayed in Fig. 9.8. Its impedance per unit of groove length is

$$\tilde{Z} = \frac{\rho_s}{\tan \beta} \frac{I_0(\lambda)}{\lambda I_1(\lambda)}, \quad (9.14)$$

Fig. 9.9 Impedance curves obtained for ideally polarized porous electrodes of different pore shapes (From Ref. [415], copyright (1976), with permission from Elsevier)



where β is the angle between the groove wall and the normal to the surface, I_0 and I_1 are the modified Bessel functions of zero and first order, the dimensionless parameter λ is

$$\lambda = 2 \sqrt{\frac{\rho_s l}{\hat{Z}_{el} \sin \beta}}, \quad (9.15)$$

l is the groove depth (normal to the surface), and \hat{Z}_{el} is the double-layer impedance per unit of the true surface area. Equation (9.14) reduces to the impedance of a perfectly flat surface for $\beta = 90^\circ$ and to the impedance of cylindrical porous electrode for $\beta = 0^\circ$. Gunning [414] obtained an exact solution of the de Levie grooved surface not restricted to a pseudo-one-dimensional problem in the form of an infinite series. Comparison with de Levie's equation (9.14) shows that the deviations arise at higher frequencies or, more precisely, at high values of the dimensionless parameter $\Omega = \omega C_{dl} a / \rho_s$, where a is half of the distance of the groove opening, $a = l \tan \beta$ (Fig. 9.8).

The impedance of porous electrodes having different pore shapes (Fig. 9.9) was studied by Keiser et al. [415]. The complex plane plots obtained at high frequencies depend on the pore shape's changing from a straight line at more than 45° for the groove shape to a semicircle for pear-shaped pores. These features are due to geometric effects, are related to the coupling of the double-layer capacitance and the solution resistance in pores, and appear at high frequencies. Because all the electrodes are ideally polarizable at low frequencies, they display a vertical line corresponding to the complete penetration of the ac signal into pores.

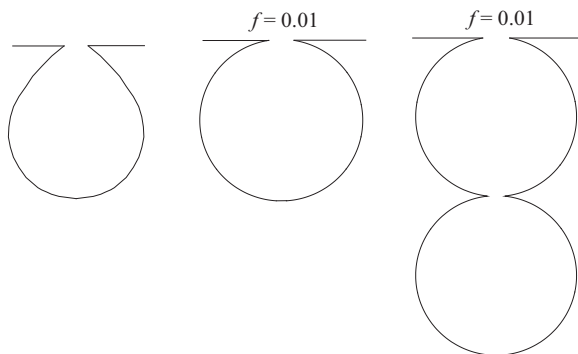


Fig. 9.10 Pore shapes used in simulation of impedances; f is a fraction of the sphere radius at which the pore was cut out for the opening (From Ref. [416], copyright (2001), with permission from Elsevier)

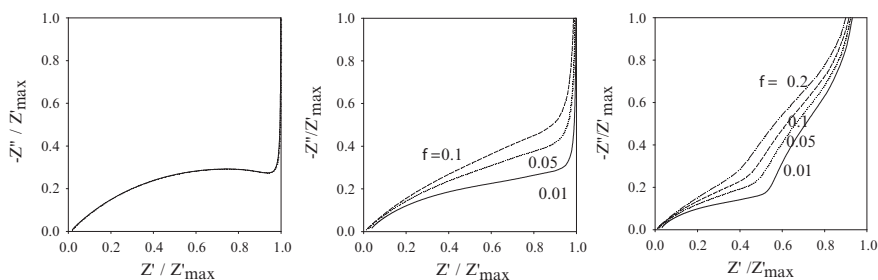
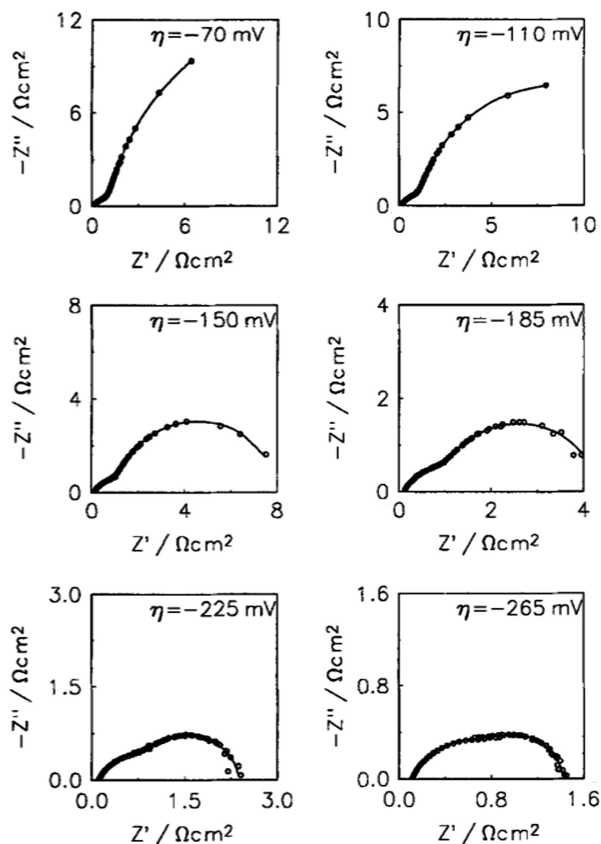


Fig. 9.11 Reduced impedance curves obtained for three pore shapes displayed in Fig. 9.10 for different values of parameter f (From Ref. [416], copyright (2001), with permission from Elsevier)

Similar simulations were later continued for the pear-shaped and spherical or bispherical pores presented in Fig. 9.10, and the obtained impedances are displayed in Fig. 9.11 [416]. The shape of the impedance curves depends on the pore geometry and on the size of the opening. It is characterized by a ratio, f , of the distance from the surface where the sphere was cut out to the sphere radius. In the case of bispherical pores, the effects of each sphere can be observed at different frequencies; at high frequencies, the ac signal penetrates only to the first sphere, and at lower frequencies it penetrates up to the second (deeper) sphere displaying two overlapping semicircles. Impedance of other arbitrary noncylindrical pores was also simulated using division into small cylinders and matrix calculations [417, 418].

The pear-shaped pores predict the formation of a semicircle on the complex plane plots that might be confused with a semicircle related to the coupling of the charge transfer resistance and double-layer capacitance. Such effects were observed experimentally for hydrogen evolution on porous electrodes [415, 416, 419, 420]. This suggests that at some electrodes, pores of a pearlike shape are present

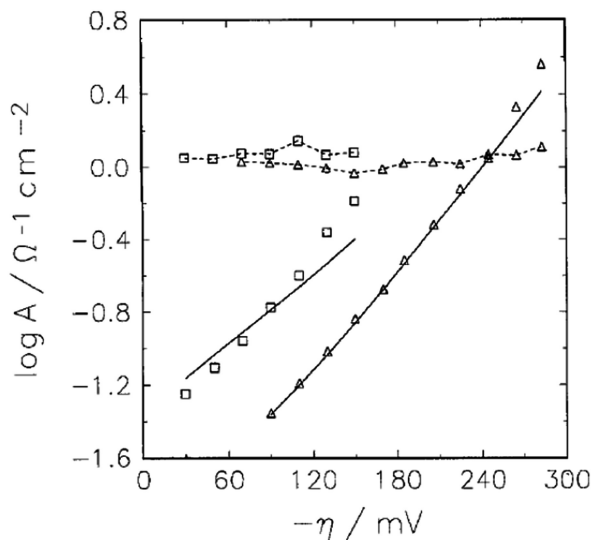
Fig. 9.12 Complex plane plots obtained on Ni (Al) pressed powder porous electrodes (after leaching out Al) during hydrogen evolution reaction in 1 M NaOH at different overpotentials (From Ref. [420]. Reproduced with permission of Electrochemical Society)



during the continuous gas evolution reaction. An example of such complex plane curves registered during hydrogen evolution on porous Ni electrodes, obtained by pressing Ni and Al or Zn powders and subsequent leaching out Al or Zn in alkaline solution, is shown in Fig. 9.12. These impedances were modeled using a so-called two-CPE model, $R(R \text{ CPE})(R \text{ CPE})$, consisting of a solution resistance and a connection between two parallel $R\text{-CPE}$ elements in series; the high-frequency $R\text{-CPE}$ element is related to the porosity, while the low-frequency element is related to the kinetics of the hydrogen evolution reaction [416, 419–422].

In general, the formation of two semicircles on complex plane plots may be of kinetic origin (see the case of one adsorbed species, Chap. 5, Sect. 5.1), or the first semicircle might be of geometric and the second of kinetic origin. To distinguish between these models, experimental tests were developed [416, 419, 420, 422]. If the first semicircle (or deformed semicircle) is of geometric origin, it should depend less on the temperature (through the solution resistance), be independent of the applied potential, and be insensitive to poisons. The dependence of the radius of the first and second semicircles on the overpotential for the electrodes in Fig. 9.12 is shown in Fig. 9.13. It is clear that the first semicircle is independent of the

Fig. 9.13 Dependence of logarithm of parameter $\log A = -\log R_{ct}$ on overpotential for hydrogen evolution reaction, at two different Ni(Al) electrodes; conditions as in Fig. 9.12; *dashed lines*: results for first semicircle; *continuous lines*: those for second semicircle (From Ref. [420]. Reproduced with permission of Electrochemical Society)



overpotential and is geometric in nature, while the second one depends on the potential, as predicted for a kinetically limited process. These tests are easy to carry out and furnish definitive answers.

9.1.3 Double or Triple Pore Structure

For a simple pore structure a straight line at 45° is predicted at high frequencies on complex plane plots. In such a case, Eq. (9.26) predicts a linear relation of $\log |Z'|$ versus $\log f$ with a slope of 0.5. In the case of more complex coatings, secondary pores might appear from the primary pores, making a branched pore structure [423–425]. In such a geometry, secondary pores perpendicular to the walls of the primary pores [423] or fractal pores [424, 425] are formed. In such a case, complex plane plots may display an angle of 22.5° [423, 425] at high frequencies ($d \log |Z''|/d \log f = -0.25$) on the complex plane plots for double pores and even 11.25° [425] ($d \log |Z''|/d \log f = -0.125$) for branched triple pores. By changing the frequency, transitions between different slopes is possible.

9.1.4 Porous Electrode with Ohmic Drop in Solution and in Electrode Material ($i_{dc} = 0$, $r_s \neq 0$, $r_e \neq 0$)

Earlier it was assumed that the electrode material was well conducting and its resistance negligible. However, when the resistivity of the electrode material cannot be neglected, i.e., it becomes comparable to or larger than that of the solution, a

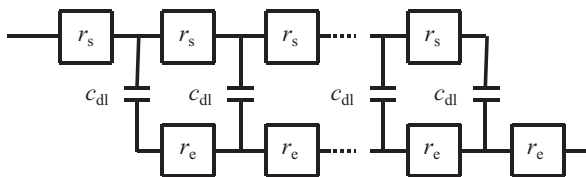


Fig. 9.14 Transmission representing impedance of ideally polarizable porous electrode in presence of solution and electrode resistance; r_s and r_e are resistances of small sections of solution and electrode, respectively, and c_{dl} is the double-layer capacitance of such a section

more complex equation should be used. Such effects are observed for certain conducting polymers, batteries, lithium intercalation compounds, semiconductors, oxides, etc. The theory of such electrode materials was first developed by Paasch et al. [426] and then discussed in detail by Bisquert et al. [427–429]. These authors assumed ionic conduction by the solution in pores and electronic conduction in solids. It should be stressed that the same result is obtained either assuming a cylindrical pore or using an effective macrohomogeneous description of two closely mixed phases [427]. In such cases the system can be described by a transmission line in which the ohmic drop appears in two branches. This model is shown in Fig. 9.14.

Assuming that the electrode impedance does not depend on the position in a pore (macrohomogeneous material), an analytical equation describing this circuit was developed [426–429]:

$$\hat{Z}_{\text{pore}} = \frac{r_s r_e}{r_s + r_e} \left[l + \frac{2\lambda}{\sinh\left(\frac{l}{\lambda}\right)} \right] + \lambda \frac{r_s^2 + r_e^2}{r_s + r_e} \coth\left(\frac{l}{\lambda}\right), \quad (9.16)$$

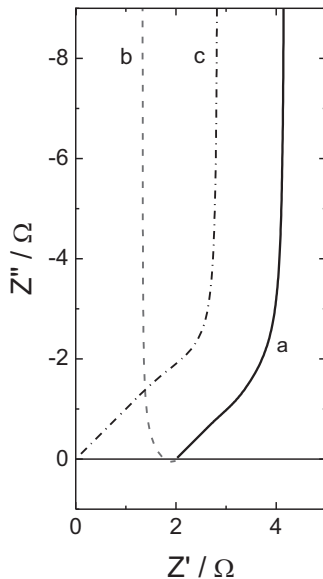
where r_s and r_e are the resistances per unit pore length ($\Omega \text{ cm}^{-1}$) of the electrolytic solution and electrode material, λ is the ac signal penetration length,

$$\lambda \sqrt{\frac{\hat{Z}}{r_s + r_e}}, \quad (9.17)$$

and $\hat{z} = (j\omega c_{dl})^{-1}$ is the electrode interfacial impedance pore length ($\Omega \text{ cm}^{-1}$) and is the capacitance per unit length (in F cm^{-1}). Láng et al. [430] proposed to rearrange this equation in another form:

$$\hat{Z}_{\text{pore}} = \frac{r_s r_e}{r_s + r_e} l + \frac{(r_s + r_e)\lambda}{2} \coth\left(\frac{l}{2\lambda}\right) + \frac{(r_s - r_e)^2 \lambda}{2(r_s + r_e)} \tanh\left(\frac{l}{2\lambda}\right). \quad (9.18)$$

Fig. 9.15 Complex plane plots for porous electrode according to Eq. (9.19); *a* – total impedance, Eq. (9.19), *b* – impedance of first term, *c* – impedance of second term; parameters:
 $r_e = 200 \, \Omega \, \text{cm}^{-1}$
 $r_s = 50 \, \Omega \, \text{cm}^{-1}$,
 $\hat{z} = 1/j\omega c_{dl}$,
 $c_{dl} = 0.001 \, \text{F cm}^{-1}$,
 $l = 0.05 \, \text{cm}$



Equation (9.16) can also be written in a form similar to that in Eq. (9.7):

$$\hat{z}_{\text{pore}} = \bar{R}_{\Omega,p} \left[1 + \frac{2}{\Lambda^{1/2} \sinh \Lambda^{1/2}} \right] + \frac{R_{\Omega,p}}{\Lambda^{1/2}} \coth \Lambda^{1/2}, \quad (9.19)$$

where

$$\begin{aligned} \bar{R}_{\Omega,p} &= \frac{r_s r_e}{r_s + r_e} l, \quad R_{\Omega,p} = \frac{r_s^2 r_e^2}{r_s + r_e} l, \\ \Lambda^{1/2} &= \frac{l}{\hat{z}} = 1 \sqrt{\frac{(r_s + r_e)}{\hat{z}}} = l \sqrt{(r_s + r_e) j \omega c_{dl}}. \end{aligned} \quad (9.20)$$

Equation (9.19) differs from de Levie's equation, Eq. (9.7), by the presence of one additional term. It should be noted that when $r_e = 0$, Eq. (9.19) reduces to Eq. (9.6) or (9.7). When the frequency $\omega \rightarrow \infty$, $\Lambda \rightarrow \infty$, the second term in Eq. (9.19) goes to zero and the first term becomes $\bar{R}_{\Omega,p}$, which corresponds to the average harmonic resistance of the solution and the electrode. When $\omega \rightarrow 0$, the real part of the first term in parentheses goes to $2/3$ and the first term becomes $2\bar{R}_{\Omega,p}/3$, while the real part of the second term goes to $\bar{R}_{\Omega,p}/3$. This means that the low-frequency impedance is real and equal to $2\bar{R}_{\Omega,p}/3 + \bar{R}_{\Omega,p}/3$. At low frequencies the imaginary parts of both terms go to infinity and the electrode displays its capacitive behavior. The complex plane plots of the total impedance, as well as those of the first and second terms, are compared in Fig. 9.15. The second term in Eq. (9.19), Fig. 9.15c, shows a complex plane plot that is similar to that in the absence of the electrode resistance (de Levie's solution). The first term shows a

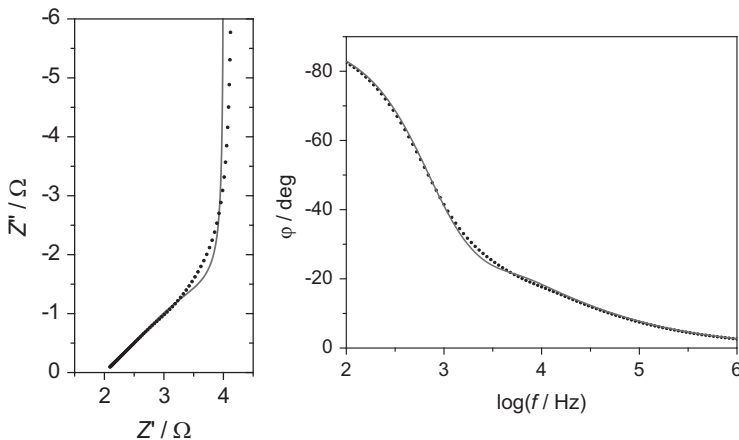


Fig. 9.16 Comparison of complex plane and Bode phase angle plots simulated using Eq. (9.16), symbols, and their approximation by de Levie's model, Eq. (9.7), lines

more complicated behavior passing through the positive imaginary part at high frequencies and displays capacitive behavior at lower frequencies.

It is interesting to note that impedances simulated using Eq. (9.19) may in practice be approximated by Eq. (9.7), which means that without separate knowledge of r_s and r_e one cannot obtain any new information from the experimental impedances. This behavior is illustrated in Fig. 9.16. Although some deviations are visible in the experimental conditions, noise could hide such deviations. These deviations are smaller when the specific resistances of the electrode material and the solution are similar.

9.2 Porous Electrodes in Presence of Redox Species in Solution

First, let us consider a case where redox species are present in solution but there is no dc current flowing, that is, the system is at the equilibrium potential. Later on, cases in the presence of a dc current will be considered, in the absence and in the presence of the concentration gradient in pores.

9.2.1 Ohmic Drop in Solution Only in Absence of DC Current ($i_{dc} = 0$, $r_s \neq 0$, $r_e = 0$)

In the absence of a dc current, there is no dc potential or dc concentration drop in the pore; therefore, the faradaic impedance is constant along the pore. However, the ac current will flow and the ac potential drop will appear. Such a case was solved by de

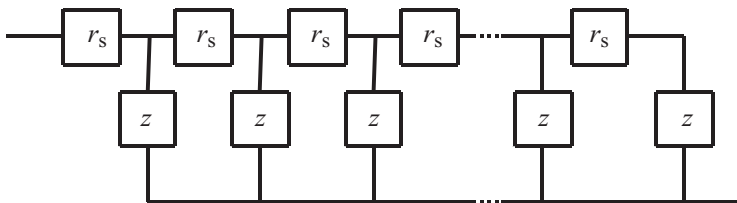


Fig. 9.17 Transmission line representing impedance of porous electrode in presence of redox reaction; r_s and z are resistances and impedances of small sections of electrode

Levie [408], who assumed that the electrode was a perfect conductor. The problem is formally identical to that described in Sect. 9.1.1, and the equations describing the system, (9.1) and (9.2), are solved assuming that the impedance unit pore length contains a faradaic reaction represented as the charge transfer resistance:

$$\hat{z} = \frac{1}{\frac{1}{r_{ct}} + j\omega c_{dl}} = \frac{1}{2\pi r \left(\frac{1}{R_{ct}} + j\omega C_{dl} \right)}, \quad (9.21)$$

where r_{ct} is the charge transfer resistance pore length, c_{dl} is the pore wall capacitance per unit pore length, and R_{ct} and C_{dl} are the specific parameters in $\Omega \text{ cm}^2$ and F cm^{-2} , respectively. The equation describing impedance of the pore has the same form as in the absence of redox species, Eqs. (9.6) and (9.7), but the impedance of the pore walls contains a charge transfer resistance and double-layer capacitance in parallel:

$$\hat{Z}_{el} = \frac{1}{\frac{1}{R_{ct}} + j\omega C_{dl}}, \quad (9.22)$$

and the parameter Λ is

$$\Lambda = \frac{r_s l^2}{\hat{z}} = \frac{2\rho_s l^2}{r} \frac{1}{\hat{Z}_{el}} = \frac{2\rho_s l^2}{r} \left(\frac{1}{R_{ct}} + j\omega C_{dl} \right). \quad (9.23)$$

Impedance in this case can be represented as a transmission line, shown in Fig. 9.17, and is described by Eq. (9.7).

The impedance plots observed for such a system depend on the penetration length of the ac signal into the pore. Three cases can be distinguished, as follows [431].

1. General case, intermediate pores

In this case, the impedance of the porous electrode is described by Eq. (9.7). The complex plane plot is presented in Fig. 9.18a. It represents a straight line at 45°

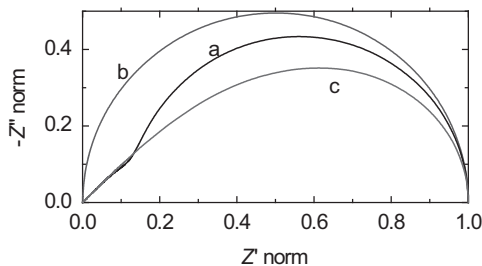


Fig. 9.18 Normalized (Z/Z'_{\max}) complex plane plots for a porous electrode in presence of redox system in solution and in absence of dc current; (a) general case, ac signal penetration length comparable with the pore length, $\lambda \sim l$; (b) shallow pores, $\lambda \gg l$; (c) semi-infinite-length pores, $\lambda \ll l$, ac signal cannot penetrate bottom of pore

at high frequencies followed by a semicircle at lower frequencies. At $\omega \rightarrow 0$ the impedance becomes real value; which is a so-called polarization resistance R_p :

$$\hat{Z}_{\text{pore}}(\omega = 0) = R_p = \sqrt{\frac{\rho_s R_{\text{ct}}}{2\pi^2 r^3}} \coth\left(\sqrt{\frac{2\rho_s l}{r R_{\text{ct}}}}\right). \quad (9.24)$$

The high-frequency section is similar to that observed for ideally polarizable porous electrodes (Fig. 9.3), which corresponds to the coupling of the solution resistance and double-layer capacitance in pores and does not contain information about the redox reaction.

2. Shallow pores

When pores are shallow and wide, the ac signal penetration length $\lambda \gg l$, and the signal can always penetrate to the bottom of the pore at all frequencies, and the pore behaves as a flat surface. In this case, $\Lambda = (l/\lambda)^2 \rightarrow 0$, $\coth(\Lambda^{1/2}) \rightarrow \Lambda^{-1/2}$, and Eq. (9.7) becomes

$$\hat{Z}_{\text{pore}} = \frac{R_{\Omega, \text{p}}}{\Lambda} = \frac{1}{2\pi r l} \hat{Z}_{\text{el}} = \frac{1}{2\pi r l} \frac{1}{\frac{1}{R_{\text{ct}}} + j\omega C_{\text{dl}}}. \quad (9.25)$$

In this case, the impedance of the pore equals to the impedance of a flat electrode of the surface area is $s = 2\pi r l$ because it is assumed that only pore walls are electrochemically active. It represents the impedance described by Eq. (9.25), that is, a perfect semicircle (Fig. 9.18b). Of course, if the pores are too wide, the assumption that the ac potential gradient is one-dimensional fails and the equation cannot be used.

3. Semi-infinite-length pores

When pores are very deep and narrow, i.e., l^2/r very large, the ac signal penetration length may be smaller than the pore length, $\lambda \ll l$, the general equation can be simplified, $\Lambda \rightarrow \infty$, $\coth(\Lambda^{1/2}) \rightarrow 1$, and the impedance becomes

$$\hat{Z}_{\text{pore}} = \frac{R_{\Omega, \text{p}}}{\Lambda^{1/2}} = \left(\frac{\rho}{2n^2 \pi^2 r^2} \right)^{1/2} \hat{Z}_{\text{el}}^{1/2}, \quad (9.26)$$

and the pore impedance is proportional to the square root of the pore wall impedance and the pore length disappears from the equation. The corresponding complex plane plot is shown in Fig. 9.18c and displays a straight line at 45° at high frequencies followed by a skewed semicircle. Such a case is indistinguishable from the fractal model, Eq. (8.17), for $\phi = 0.5$.

The skewed semicircle in Fig. 9.18c contains the square root of the impedance. De Levie [408] showed a plot of the square of the impedances according to the following equation:

$$\begin{aligned} Z_{\text{re}} &= |z|^2 \cos(2\varphi) & Z_{\text{im}} &= |z|^2 \sin(2\varphi), \\ \text{where} & & & \\ \varphi &= \text{atan}(-Z''/Z') & |Z| &= \sqrt{Z'^2 + Z''^2} \end{aligned} \quad (9.27)$$

produces an ideal semicircle on the complex plane plots.

For semi-infinite-length pores the double-layer capacitance and the charge transfer resistance cannot be determined because the accessible surface area changes with the frequency [422]. However, Eq. (9.26) can be rearranged into

$$\hat{Z}_{\text{pore}} = \left[\frac{\rho_s}{2n^2 \pi^2 r^3} \frac{1}{\frac{1}{R_{\text{ct}}} + \frac{1}{j\omega C_{\text{dl}}}} \right]^{1/2} = \left[\frac{1}{uR_{\text{ct}}} + \frac{j\omega C_{\text{dl}}}{u} \right]^{-1/2}, \quad (9.28)$$

where $u = \rho_s / (2n^2 \pi^2 r^3)$, which is usually unknown because the exact geometry and number of pores are not known for actual porous electrodes. The only parameters that can be experimentally determined are uR_{ct} and C_{dl}/u . However, the product of the experimentally accessible parameters

$$uR_{\text{ct}} \frac{C_{\text{dl}}}{u} = R_{\text{ct}} C_{\text{dl}} \quad (9.29)$$

equals the product of the specific charge transfer resistance and double-layer capacitance. Because the specific double-layer capacitance of metallic electrodes is usually in the range of $20\text{--}25 \mu\text{F cm}^{-2}$, the kinetics of the reaction might be estimated. Such studies were carried out for Ni and Raney Ni and Ni-Mo electrodes, and it was found that, although they displayed very high apparent activity toward hydrogen evolution, their intrinsic activities were not larger than those of polycrystalline Ni electrodes, and the

Fig. 9.19 Transmission line representing porous electrode in presence of redox species and resistance of solution, r_s , and electrode, r_e

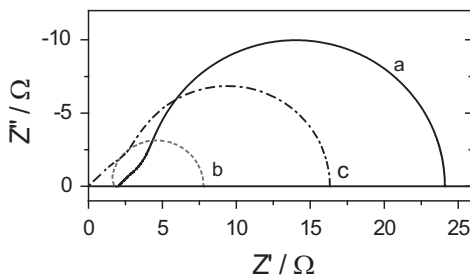
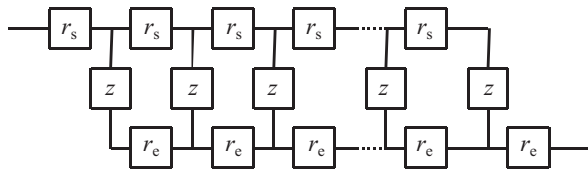


Fig. 9.20 Complex plane plots for porous electrode in presence of redox species at equilibrium potential according to Eq. (9.19); a – total impedance, Eq. (9.19); b – impedance of first term; c – impedance of second term; $r_{ct} = 1 \Omega \text{ cm}$; other parameters as in Fig. 9.15

observed activity came from the increase in the real surface area [422]. It was found experimentally that by changing the electrode potential or solution viscosity the observed impedance model changed from a finite-length to a semi-infinite-length pore model [416].

9.2.2 Ohmic Drop in Solution and Electrode Material in Absence of DC Current ($i_{dc} = 0$, $r_s \neq 0$, $r_e \neq 0$)

In the presence of redox species and for porous electrodes containing a contribution of the resistance of the solution and the electrode material the equations describing the impedance are identical to those in the absence of redox species, Eqs. (9.16) and (9.19), with exception of the impedance of the pore walls, which contains the charge transfer resistance, Eq. (9.21). In this case the parameter $\Lambda^{1/2}$ is defined as

$$\Lambda^{1/2} = l \sqrt{(r_s + r_e) \left(\frac{1}{r_{ct}} + j\omega c_{dl} \right)}. \quad (9.30)$$

This model corresponds to the transmission line depicted in Fig. 9.19. The complex plane plots of the total impedance, Eq. (9.19), as well as the first and second terms of this equation, are displayed in Fig. 9.20. The total impedance starts at high frequencies at $\bar{R}_{\Omega, p}$ and initially displays a straight line at 45° followed by a semicircle (Fig. 9.20a). The first term in Eq. (9.19) shows a small inductive loop at high frequencies, followed by a semicircle, Fig. 9.20b, while the second term is similar to that of the porous electrode with solution resistance only, Fig. 9.20c.

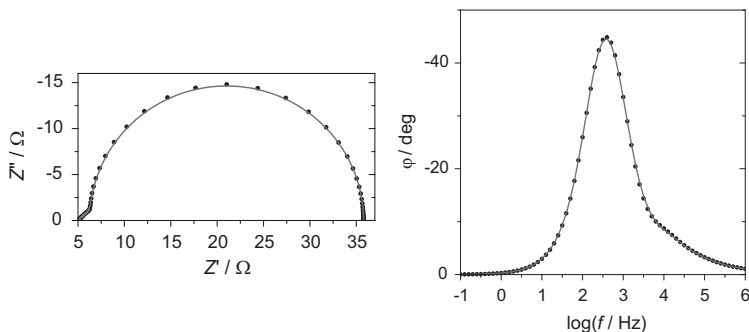


Fig. 9.21 Comparison of complex plane and Bode phase angle plots simulated using Eqs. (9.16) and (9.30), symbols, and their approximation by de Levie's model, Eq. (9.7), lines

Similarly as in the case of the ideally polarized electrode, the total impedance simulated using Eq. (9.19) may be well fitted by the simple de Levie model involving the resistance of the solution, only with $r_e = 0$. This is shown in Fig. 9.21.

The results obtained there show again that without a priori knowledge of the solution and electrode resistivities, the full Eq. (9.19) cannot be used because the system may be well approximated by a simpler model involving the solution resistance only, Eq. (9.7).

9.2.3 Porous Electrodes in Presence of DC Current, Potential Gradient in Pores and No Concentration Gradient, Ideally Conductive Electrode ($i_{dc} \neq 0$, $dE_{dc}/dx \neq 0$, $dC_{dc}/dx = 0$, $r_s \neq 0$, $r_e = 0$)

9.2.3.1 DC Solution

When a system containing redox species is no longer at the equilibrium potential, a dc current must circulate. The presence of a dc current causes a potential and concentration drop in the pores. First, let us consider the case where the dc concentration gradient is negligible and only a dc potential drop is observed. Such cases are observed at high concentrations of redox species in solutions or for gas evolution reactions from concentrated solutions (hydrogen, oxygen, chlorine evolution). Under such conditions the dc current circulates into the pore flowing to the pore walls. The current flows through the solution resistance, and the ohmic dc potential drop develops inside the pore. To solve this problem, two

equations (for dc conditions) must be solved. The first is a dc analog of Eq. (9.2) describing Ohm's law:

$$\frac{d\eta}{dx} = -r_s I, \quad (9.31)$$

where η is the overpotential. The second equation describes a decrease in the axially flowing current I with the distance in pores. Its decrease, $-dI$, is related to the faradaic current, j , flowing to each section dx of the pole walls:

$$-dI = (2\pi r dx)j, \quad (9.32)$$

where $2\pi r dx$ is the surface area of the pore section and the faradaic current density is defined by the Butler-Volmer relation [17]:

$$j = j_0 \left[e^{(1-\alpha)nf\eta} - e^{-anf\eta} \right]. \quad (9.33)$$

From Eq. (9.32) one obtains after division by dx

$$\frac{dI}{dx} = -\frac{(2\pi r dx)j}{dx} = -2\pi r j, \quad (9.34)$$

and Eqs. (9.31) and (9.34) are dc analogs of Eqs. (9.1) and (9.2). Taking the second derivative of Eq. (9.31) leads to

$$\frac{d^2\eta}{dx^2} = r_s \frac{dI}{dx} = 2\pi r r_s j = \frac{2\rho_s j_0}{r} \left[e^{(1-\alpha)nf\eta} - e^{-anf\eta} \right]. \quad (9.35)$$

To obtain the potential distribution in the pore, Eq. (9.35) must be solved using the following boundary conditions:

$$\begin{aligned} x = 0, & \quad \eta = \eta_0, \\ x = l, & \quad d\eta/dx = 0, \end{aligned} \quad (9.36)$$

where η_0 is the potential at the pore orifice. This equation was solved in the literature in terms of special functions [400, 403–405, 432] or assuming certain simplifications [406, 433, 434]. The first integration of Eq. (9.35) gives

$$\frac{d\eta}{dx} = \left\{ \left(\frac{4\rho_s j_0}{r} \right) \left[\frac{\exp(\alpha f \eta)}{\alpha f} + \frac{\exp[-(1-\alpha)f\eta]}{(1-\alpha)f} \right] \right\}^{1/2}, \quad (9.37)$$

where $\eta_l = \eta(l)$ is the potential at the bottom of the pore. This equation does not have an analytical solution and it cannot be directly integrated because the value of η_l is not known a priori. It was solved analytically using elliptic integrals for $\alpha = 1/2, 1/3$, and $2/3$ [405] and numerically searching for values of η_l satisfying the condition $d\eta/dx = 0$ at $x = l$ [435]. It could also be solved by initially finding η_l by numerically solving the equation

$$\int_{\eta_0}^{\eta_l} \frac{d\eta}{\left[\frac{\exp(\alpha f \eta)}{\alpha f} + \frac{\exp[-(1-\alpha)f\eta]}{(1-\alpha)f} - \frac{\exp(\alpha f \eta_l)}{\alpha f} - \frac{\exp[-(1-\alpha)f\eta_l]}{(1-\alpha)f} \right]^{1/2}} \quad (9.38)$$

$$= -\sqrt{\frac{4\rho_s j_0}{r}} l$$

and then numerically solving Eq. (9.37). Equation (9.35) may be simplified, assuming $a = 0.5$, to

$$\frac{d^2\eta}{dx^2} = \frac{4\rho_s j_0}{r} \sinh(0.5nf\eta) = \frac{4\rho_s j_0}{r} \sinh(b\eta) \quad (9.39)$$

and after the first integration

$$\frac{d\eta}{dx} = -\sqrt{\frac{8\rho_s j_0}{rb}} \sqrt{\cosh(b\eta) - \cosh(b\eta_1)}, \quad (9.40)$$

where $b = 0.5f$, solved using elliptic integrals by determining the value of x for a given value of η_0 and η_l .

For the semi-infinite-length pore, i.e., when $\eta_l = 0$, $\cosh(b\eta_l) = 1$, this expression can be rearranged to

$$\frac{d\eta}{dx} = -4\sqrt{\frac{\rho_s j_0}{rb}} \sinh\left(\frac{b\eta}{2}\right), \quad (9.41)$$

and the analytical solution is

$$\tanh\left(\frac{b\eta}{4}\right) = \tanh\left(\frac{b\eta_0}{4}\right) \exp\left(-2\sqrt{\frac{\rho_s j_0 b}{r}} x\right). \quad (9.42)$$

Note that this equation is formally identical with that obtained for the potential distribution in the Guy-Chapman theory of double layers [17].

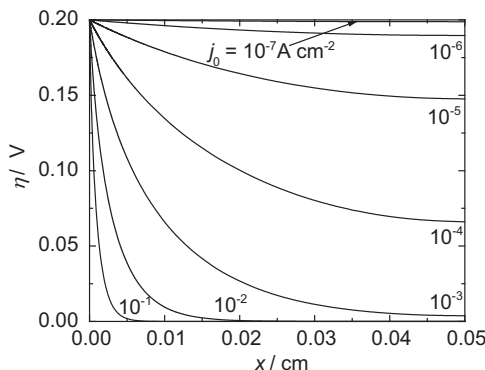


Fig. 9.22 Dependence of overpotential in pore as a function of distance from pore orifice for different exchange current densities and constant overpotential; parameters: $\eta = 0.2$ V, $\alpha = 0.5$, $l = 0.05$ cm, $r = 10^{-4}$ cm, $\rho_s = 10$ Ω cm; the values of j_0 are displayed in the figure (From Ref. [72] with kind permission from Springer Science and Business Media)

Current entering the pore (at $x = 0$), I_0 , can be calculated using Eqs. (9.31) and (9.41):

$$I_0 = 4\pi r \sqrt{\frac{rj_0}{b\rho_s}} \sinh\left(\frac{b\eta_0}{2}\right). \quad (9.43)$$

This equation for the semi-infinite-length pore can be compared with the classical Butler-Volmer formula for flat surfaces $I = sj_0 \sinh(b\eta)$. It is evident that the classical logarithmic Tafel slope from the Butler-Volmer equation $\ln(10)/(b) = \ln(10)/(0.5f) = 118.3$ mV dec^{-1} at 25° is replaced by $\ln(10)/(b/2) = \ln(10)/(0.25f) = 236.6$ mV dec^{-1} for the semi-infinite-length porous electrode, that is, the Tafel slope is doubled.

The numerical solution of Eq. (9.37) [435] shows the dependence of the potential and current in the pore. Examples of such plots are shown in Figs. 9.22 and 9.23. At very low current densities there is practically no potential gradient (negligible IR drop), and as a consequence, the current decreases linearly with distance. For higher j_0 a potential drop in pores appears and decreases to a constant value, $\eta(l) > 0$, at $x = l$, while the current decreases nonlinearly. For faster kinetics, $j_0 > 10^{-3}$ A cm^{-2} , the potential and current drop to zero inside the pore, that is, some part of the pore is not used for the redox reaction.

Tafel curves at porous electrodes are shown in Fig. 9.24. Note that for low exchange current densities, $j_0 < 10^{-3}$ A cm^{-2} , and at lower overpotentials the Tafel slope is 0.118 V dec^{-1} , but it doubles to 0.2366 V dec^{-1} at higher exchange currents and higher overpotentials. This higher slope is an indication of the fact that the electrical current and potential cannot penetrate to the bottom of the pore. At higher j_0 the slope always remains doubled in the linear Tafel zone.

Fig. 9.23 Current distribution in pores, expressed as ratio of current I at distance x to total current entering pore, I_0 , as a function of distance x , for different j_0 ; other parameters as in Fig. 9.22 (From Ref. [72] with kind permission from Springer Science and Business Media)

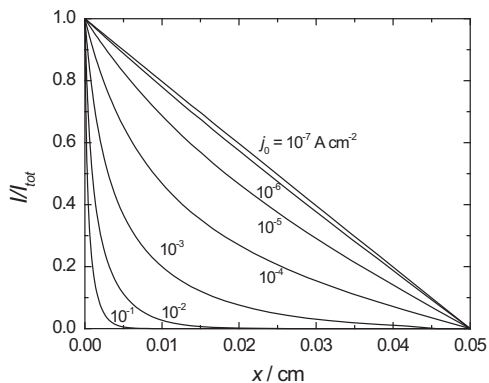
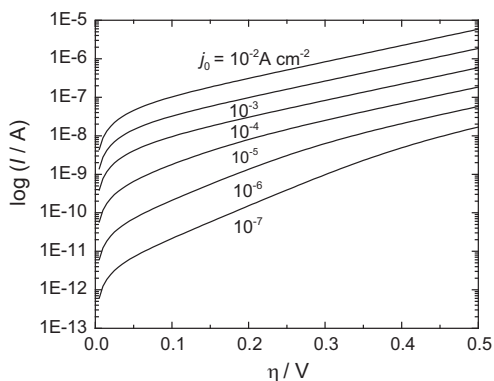


Fig. 9.24 Tafel curves at porous electrodes in absence of concentration gradient; parameters as in Fig. 9.22 (From Ref. [72] with kind permission from Springer Science and Business Media)

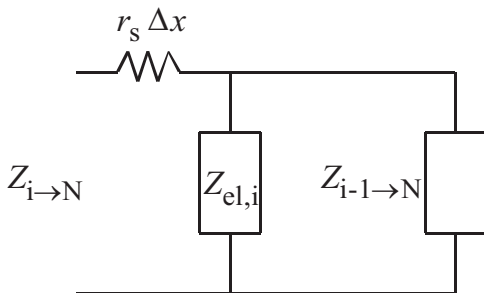


9.2.3.2 AC Solution

Knowledge of the potential inside pores makes it possible to calculate the impedances. In this case only a numerical solution exists. The impedance can be obtained by summing the electrode admittances of N small sections, Δx ($N = 1,000$ to $5,000$ elements), of the pore starting from the bottom at $x = l$ [435]. For each segment the electrode impedance consists of the solution resistance and the impedance of the pore wall:

$$\begin{aligned}\hat{Z}_i &= r_s \Delta x + \hat{Z}_{\text{el},i} = r_s \Delta x + \frac{\hat{Z}_{\text{el},i,\text{spec}}}{2\pi r \Delta x} \\ &= \left(\frac{\rho_s}{\pi r^2}\right) \Delta x + \frac{1}{2\pi r \Delta x \left(\frac{1}{R_{\text{ct}}} + j\omega C_{\text{dl}}\right)},\end{aligned}\quad (9.44)$$

Fig. 9.25 Electrical equivalent circuit representing determination of impedance of porous electrode



where $\hat{Z}_{el,i,spec}$ is the specific impedance of pore walls ($\Omega \text{ cm}^{-2}$) and

$$\frac{1}{\hat{Z}_f} = \frac{1}{R_{ct}} = \frac{dj}{d\eta} = j_0 n f \left[\alpha e^{-\alpha n f \eta} + (1 - \alpha) e^{(1-\alpha) n f \eta} \right]. \quad (9.45)$$

The pore impedance from the bottom to element i , $\hat{Z}_{i \rightarrow N}$, is a sum:

$$\hat{Z}_{i \rightarrow N} = \left(\frac{\rho_s}{\pi r^2} \right) \Delta x + \frac{1}{\frac{1}{\hat{Z}_{el,i}} + \frac{1}{\hat{Z}_{i-1 \rightarrow N}}}, \quad (9.46)$$

where $\hat{Z}_{i-1 \rightarrow N}$ is the impedance of the section of the pore from the bottom to element $i-1$. This process corresponds to the calculation of the impedances in Fig. 9.25. As the summation progresses, the faradaic impedance, \hat{Z}_f , changes while the solution resistance stays the same.

Impedances computed using Eq. (9.46) are displayed in Figs. 9.26 and 9.27 and compared with de Levie's solution, which assumes that the faradaic impedance is independent of the distance in the pore, i.e., the potential in the pores is constant and equal to η_0 . With the increase in the exchange current density, i.e., the electrode activity, and of the overpotential, the pores behave as semi-infinite length. A semicircle corresponding to the penetration of the ac signal to the bottom of the pore corresponds to that of a semi-infinite-length and the complex plane plot is as predicted in Fig. 9.18c. It is obvious that de Levie's solution underestimates the impedance because, in a real case, the impedance inside the pore increases with x as the overpotential decreases. Note that for a semi-infinite-length pore the ratio of the impedances obtained at $\omega \rightarrow 0$ using the full model and that of de Levie is equal to $\sqrt{2}$.

Because the correct numerical solution for a porous electrode in the presence of a potential gradient in pores demands knowledge of the pore parameters and more complex mathematics, in practice, a simplified de Levie equation (9.7) is used in approximations, which means that the experimentally measured impedances are fitted to Eq. (9.7). As was shown earlier, for the same pore and kinetic parameters, de Levie's equation underestimates low-frequency impedances by up to 100%, which might not be that important for very porous electrodes characterized by a very large surface area.

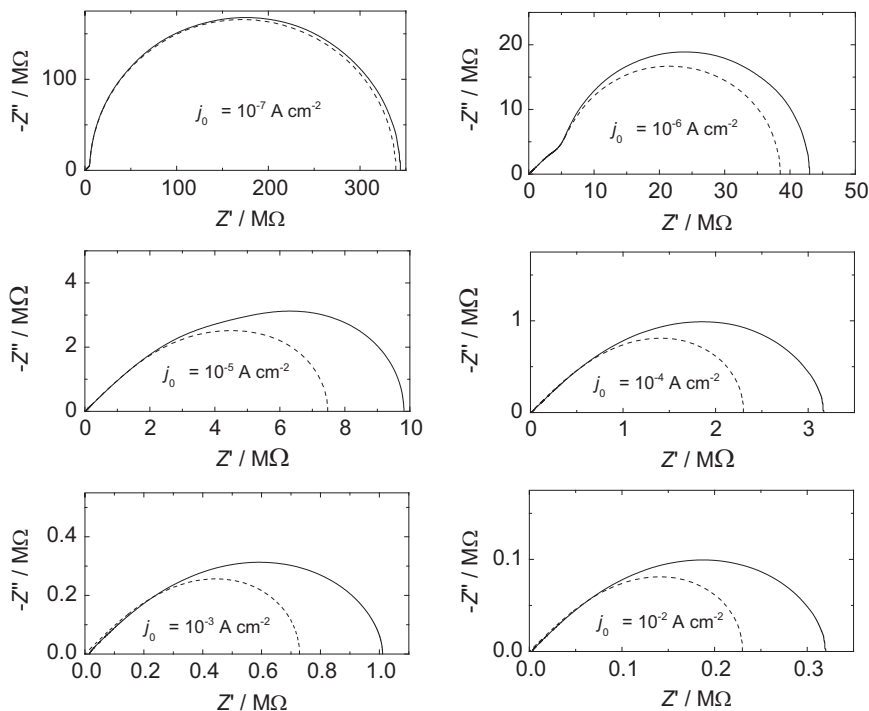


Fig. 9.26 Complex plane plots at porous electrode in presence of redox process at constant overpotential $\eta_0 = 0.2$ V and different exchange current densities; *continuous lines* – simulations, Eq. (9.46), *dashed line* – according to de Levie's equation (9.7); $C_{dl} = 20 \mu\text{F cm}^{-2}$, other pore parameters as in Fig. 9.22 (From Ref. [72] with kind permission from Springer Science and Business Media)

The potential profile in pores depends on the transfer coefficient through Eq. (9.37) and influences impedances through Eq. (9.45) [435]. Examples of the complex plane plots for three different values of transfer coefficients are displayed in Fig. 9.28, which shows the importance of knowing α .

As was mentioned earlier, the square of the semi-infinite-length pore impedance, Eq. (9.27), produces a perfect semicircle; however, simulated impedances in the presence of a constant current lead to somewhat distorted semicircles [407]. This fact is clear from the CNLS approximations of the simulated impedances by de Levie's equation [435]. Such a fit is displayed in Fig. 9.29. However, when the CPE was used in Λ in Eq. (9.23),

$$\Lambda = \frac{2\rho_s l^2}{r} \left[\frac{1}{R_{ct}} + (j\omega)^\phi T_{dl} \right], \quad (9.47)$$

the approximation was very good (Fig. 9.29), with $\phi = 0.92$, depending on the pore parameters. Small deviations, which are visible in Fig. 9.29, would be indistinguishable

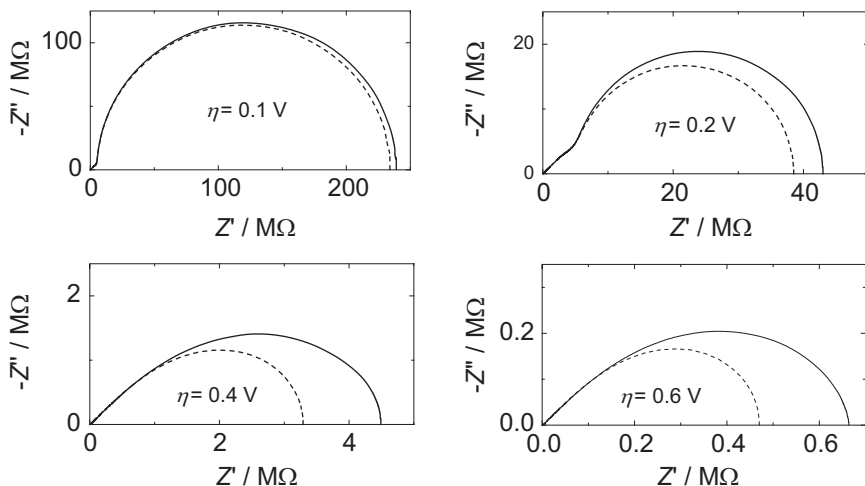


Fig. 9.27 Complex plane plots at porous electrode at constant exchange current density $j_0 = 10 \text{ A cm}^{-2}$ and different overpotentials; *continuous lines* – simulations, Eq. (9.46), *dashed line* – according to de Levie's equation (9.7); other parameters as in Figs. 9.22 and 9.26 (From Ref. [72] with kind permission from Springer Science and Business Media)

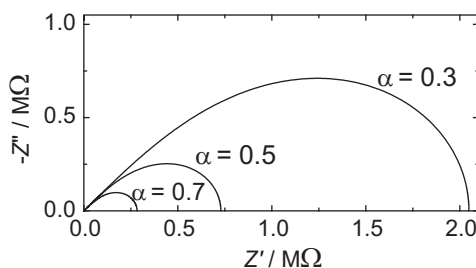


Fig. 9.28 Complex plane plots obtained on porous electrode at different values of transfer coefficient, $\eta_0 = 0.2 \text{ V}$, $j_0 = 10^{-3} \text{ A cm}^{-2}$, other parameters as in Fig. 9.26 (From Ref. [72] with kind permission from Springer Science and Business Media)

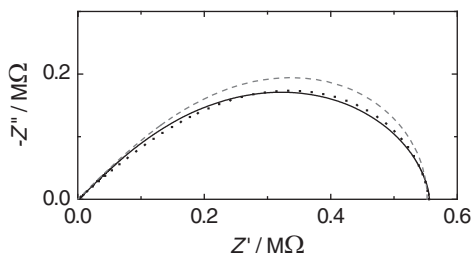


Fig. 9.29 Complex plane plot of the impedance simulated for the semi-infinite pore length using Eq. (9.44), *continuous line*, its CNLS approximations by de Levie's model, Eq. (9.7), *dashed line*, and fit to de Levie's model with CPE, *dotted line*; for $\eta_0 = 0.5 \text{ V}$, $j_0 = 10^{-5} \text{ A cm}^{-2}$, pore parameters as in Fig. 9.26 (From Ref. [72] with kind permission from Springer Science and Business Media)

in the presence of experimental noise. However, such a fit leads to higher double-layer capacitances [435].

In summary, the presence of a dc current generates a potential gradient in pores (the concentration gradient was neglected here). This gradient causes an increase in the observed charge transfer resistance as the overpotential decreases and R_{ct} increases in the pore, and a certain deformation of the complex plane plots was especially visible for semi-infinite-length pores. With an increase in the kinetics of the redox reaction or pore parameter l^2/r , the finite-length porous model becomes a semi-infinite-length model. The obtained impedance cannot be well approximated by de Levie's equation, but it can be approximated by introducing a CPE. However, such an approximation produces higher double-layer capacitances. Nevertheless, for simplicity, de Levie's equation is used in practical applications, although it can overestimate the real surface area by a factor of up to ~ 2.7 [435]. For example, for hydrogen evolution on porous Ni electrodes good approximations by de Levie's equation were found with ϕ between 1 and 0.88 [431].

9.2.4 Porous Electrodes in Presence of DC Current, Concentration Gradient in Pores and No Potential Gradient, Ideally Conductive Electrode ($i_{dc} \neq 0$, $dC_{dc}/dx \neq 0$, $dE_{dc}/dx = 0$, $r_s \neq 0$, $r_e = 0$)

Another limiting case is a porous electrode in the presence of redox species and a concentration gradient in pores, $dC/dx \neq 0$, but in the absence of a potential gradient, $dE/dx = 0$. In what follows, the case of an ideally conductive electrode and a resistive solution in pores will be considered.

9.2.4.1 DC Solution

During a redox reaction in a porous electrode the concentrations of the redox species change with depth x . This problem was studied by several authors [411, 433, 436–443]. In this case, an analytical solution for the concentration gradient and the impedance [443] might be obtained.

Let us assume the redox process



which is described by the current density-potential relation in the pore:

$$j(x, t) = nF \left[C_O(x, t) \vec{k}_f - C_R(x, t) \overset{\leftarrow}{k}_b \right], \quad (9.49)$$

where $C_O(x)$ and $C_R(x)$ are the concentrations of the oxidized and reduced forms in the pore at a distance x from the pore orifice, $\vec{k}_f = k_s \exp[-\alpha n f (E - E^0)]$ and $\overleftarrow{k}_b = k^s \exp[(1 - \alpha) n f (E - E^0)]$ are potential-dependent rate constants, k_s is the standard rate constant, α the cathodic transfer coefficient, and E^0 the standard potential. Let us assume that at the bulk of the solution $C_O = C_O^*$ and $C_R = 0$. Then Eq. (9.49) may be rearranged to

$$j(x, t) = n F C_O^* \left[a(x, t) \left(\vec{k}_f + \overleftarrow{k}_b \right) - \overleftarrow{k}_b \right], \quad (9.50)$$

where $a = C_O/C_O^*$ assuming that the diffusion coefficients of both forms are equal and, as a consequence, $C_O(x, t) + C_R(x, t) = C_O^*$. The current density flowing to the pore walls between the distance x and $x + dx$ may also be described as

$$j(x) = -\frac{nF}{2\pi r dx} \frac{dN_O(x)}{dt}, \quad (9.51)$$

where N is the number of moles of the oxidized substance being reduced. It can be rearranged by the introduction of concentrations in a small section dx of the pore,

$$C_O(x, t) = \frac{N_O(x, t)}{\pi r^2 dx}, \quad (9.52)$$

to

$$\begin{aligned} j(x, t) &= \frac{nF}{2\pi r dx} (\pi r^2 dx) \frac{d}{dt} \left(\frac{N_O(x, t)}{\pi r^2 dx} \right) = -\frac{nFr}{2} \frac{dC_O(x, t)}{dt} \\ &= -\frac{nFrC_O^*}{2} \frac{da(x, t)}{dt}, \end{aligned} \quad (9.53)$$

which yields

$$\frac{da(x, t)}{dt} = -\frac{2}{nFrC_O^*} j(x, t). \quad (9.54)$$

Fick's equation in the pore, taking into account the current flowing to the pore walls, contains a diffusion term and the loss of the electroactive substance due to electroreduction:

$$\frac{\partial a(x, t)}{\partial t} = D \frac{\partial^2 a(x, t)}{\partial x^2} - \frac{2}{nFrC_O^*} j(x, t), \quad (9.55)$$

or, introducing the dimensionless distance $z = x/l$,

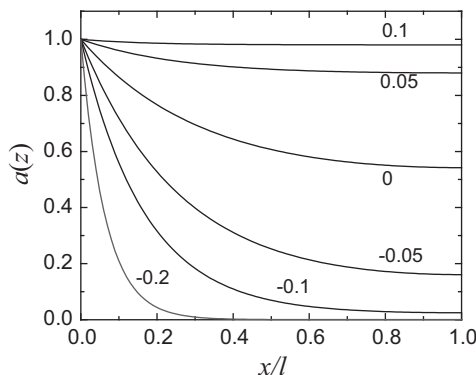


Fig. 9.30 Dependence of dimensionless concentration in pores as function of distance, $z = x/l$, from pore orifice at different potentials $E - E^0$ indicated in graph (V); parameters: $l = 0.05$ cm, $r = 10^{-4}$ cm, $k^0 = 10^6$ cm s $^{-1}$, $D_0 = 10^{-5}$ cm 2 s $^{-1}$ (From Ref. [72] with kind permission from Springer Science and Business Media)

$$\frac{\partial a(z, t)}{\partial t} = \left(\frac{D}{l^2}\right) \frac{\partial^2 a(z, t)}{\partial z^2} - \left(\frac{2}{nFrC_O^*}\right) j(z, t). \quad (9.56)$$

To obtain the concentration distribution in pores, we need to know the steady-state solution, when $da(z)/dt = 0$. This condition means that the flux of O entering the pore equals the flux of R leaving the pore and that the concentration outside the pore is uniform. Equation (9.56) is then simplified to

$$\frac{d^2 a(z)}{dz^2} = \frac{2l^2}{nFrDC_O^*} j(z) \quad \text{with} \quad \begin{cases} a(0) = 1, \\ \frac{da(1)}{dz} = 0. \end{cases} \quad (9.57)$$

An analytical solution of Eq. (9.57) is [443]

$$a(z) = \frac{1}{1+P} \left\{ P + \frac{\cosh[\sqrt{B}(1-z)]}{\cosh[\sqrt{B}]} \right\}, \quad (9.58)$$

where

$$B = \left(\frac{2k_s l^2}{rD} \right) (p^{-\alpha} + p^{1-\alpha}) = 2\Phi_0^2 (P^{-\alpha} + P^{1-\alpha}), \quad (9.59)$$

$$\Phi_0^2 = \frac{2k^0 l^2}{rD} \quad P = e^{nf(E-E^0)}.$$

The concentration in pores depends on the electrode potential, and parameter B relates to the normalized Thiele modulus Φ_0 [444], which characterizes the mass transfer in pores. Examples of concentration gradients obtained at different potentials $E - E^0$ are presented in Fig. 9.30. As the potential becomes more negative,

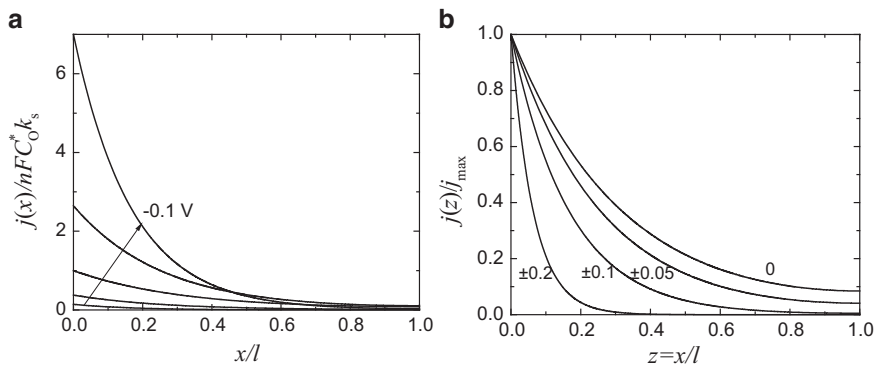


Fig. 9.31 Dependence of dimensionless current as function of distance in pore for potentials from 0.1 V to -0.1 V, every 0.05 V (arrow: direction of increase in negative potential) and dependence of current in pore divided by maximal current flowing at pore orifice on dimensionless distance (From Ref. [72] with kind permission from Springer Science and Business Media)

the concentrations of the oxidized species decrease (and those of the reduced species increase). At some potentials the concentration drops to zero inside the pore (for $E - E^0 < -0.1$ V) and a part of the pore is not used for the electrochemical reaction; for example, at $E - E^0 = -0.2$ V only approximately 30 % of the pore is electrochemically active.

The current flowing to the pore walls increases with increases in the negative potential (Fig. 9.31); however, the current divided by the maximal current flowing at the pore orifice $j_{\max} = j(z = 0)$ behaves differently; the largest value is observed for $E - E^0 = 0$ and identical values are obtained for the positive and negative potentials, i.e., $j(x)/j_{\max}(E - E^0) = j(x)/j_{\max}(E - E^0)$ (Fig. 9.31).

From the current flowing to the pore walls at any distance the total current entering the pore can be calculated by integration [443]:

$$I = 2\pi r l \int_0^1 j(z) dz = nF(2\pi r l)C_O^* \vec{k}_f \frac{\tanh \sqrt{B}}{\sqrt{B}}. \quad (9.60)$$

This equation has two limiting cases:

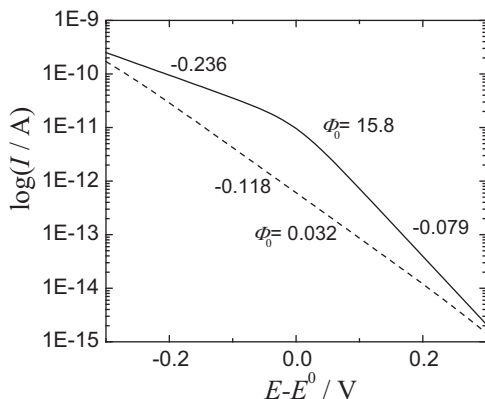
- For shallow (short and wide) pores, l^2/r is small and $B \ll 1$. In this case, $\tanh \sqrt{B}/\sqrt{B} \rightarrow 1$, and Eq. (9.60) reduces to

$$I = nF(2\pi r l)C_O^* \vec{k}_f, \quad (9.61)$$

and a normal Tafelian behavior is observed with the slope $-\ln 10 / \alpha n f = -118 \text{ mV dec}^{-1}$ for $\alpha = 0.5$ at 25°C .

- In the case of long and narrow pores $B \gg 1$, $\tanh \sqrt{B} \rightarrow 1$, and Eq. (9.60) reduces to

Fig. 9.32 Tafel plots on porous electrode;
continuous line: long pores,
 $l = 0.5$ cm, $\Phi_0 = 15.8$;
dashed line: shallow pores,
 $l = 0.001$ cm, $\Phi_0 = 0.032$;
 other parameters as in
 Fig. 9.30 (From Ref. [72]
 with kind permission from
 Springer Science and
 Business Media)



$$I = nF(2\pi rl)C_O^* k_f \frac{1}{\sqrt{B}} = \frac{nF\pi\sqrt{2r^3k^0DC_O^*}}{\sqrt{P^\alpha + P^{1+\alpha}}}, \quad (9.62)$$

and two slopes are observed on the Tafel plots, $-\ln 10 / \{[(1 + \alpha)/2]nf\} = -78.9/n$ mV at more positive potentials and $-\ln 10 / [(\alpha/2)nf] = -237/n$ mV dec⁻¹ at more negative potentials, assuming $\alpha = 0.5$ at 25 °C. The slope observed at more negative potentials corresponds to a doubling of the typical kinetic Tafel plot observed on flat electrodes. The Tafel plots corresponding to these two cases are displayed in Fig. 9.32.

9.2.4.2 AC Solution

To obtain the expression for the impedance, the expression for current must be linearized [407, 441, 443]:

$$\Delta j = \left(\frac{\partial j}{\partial E} \right)_a \Delta E + \left(\frac{\partial j}{\partial a} \right)_E \Delta a, \quad (9.63)$$

where $\Delta j = \tilde{j} \exp(j\omega t)$, $\Delta E = \tilde{E} \exp(j\omega t)$, $\Delta a = \tilde{a} \exp(j\omega t)$, and the symbols \tilde{j} , \tilde{E} , and \tilde{a} are the phasors [407]. The faradaic impedance, \hat{Z}_f , and admittance, \hat{Y}_f are

$$\frac{1}{\hat{Z}_f} = \hat{Y}_f = -\frac{\tilde{j}}{\tilde{E}} = -\left(\frac{\partial j}{\partial E} \right) - \left(\frac{\partial j}{\partial a} \right) \frac{\tilde{a}}{\tilde{E}}, \quad (9.64)$$

where the negative sign appears because the reduction current was defined as positive. To calculate the impedance, it is necessary to determine \tilde{a}/\tilde{E} , while the derivatives in parentheses are easily calculated from Eq. (9.50). Therefore, Eq. (9.56), which

describes the diffusion of the redox species in the pore, must be solved for Δa . Substitution of Δa followed by division by $\exp(j\omega t)$ gives

$$j\omega\tilde{a} = D \frac{d^2\tilde{a}}{dz^2} - \frac{2l^2}{nFrC_O^*} \left[\left(\frac{\partial j}{\partial a} \right) \tilde{a} + \left(\frac{\partial j}{\partial E} \right) \tilde{E} \right], \quad (9.65)$$

or, expressing the solution in terms of the parameter \tilde{a}/\tilde{E} necessary in Eq. (9.64),

$$\frac{d^2(\tilde{a}/\tilde{E})}{dz^2} = \left(\frac{\tilde{a}}{\tilde{E}} \right) \left[\frac{j\omega l^2}{D} + \frac{2l^2}{nFrDC_O^*} \left(\frac{\partial j}{\partial a} \right) \right] + \left[\frac{2l^2}{nFrDC_O^*} \left(\frac{\partial j}{\partial E} \right) \right] = \left(\frac{\tilde{a}}{\tilde{E}} \right) \hat{K} + L, \quad (9.66)$$

where

$$\hat{K} = \frac{j\omega l^2}{D} + \frac{2l^2}{nFrDC_O^*} \left(\frac{\partial j}{\partial a} \right) = \frac{j\omega l^2}{D} + B; \quad L = \frac{2l^2}{nFrDC_O^*} \left(\frac{\partial j}{\partial E} \right), \quad (9.67)$$

with the following boundary conditions:

$$\begin{cases} z = 0 & \tilde{a} = 0, \\ z = 1 & d\tilde{a}/dz = 0. \end{cases}$$

The solution of Eq. (9.66) is

$$\frac{\tilde{a}}{\tilde{E}} = \frac{L}{\hat{K}} \left\{ -1 + \frac{\cosh[\sqrt{\hat{K}}(1-z)]}{\cosh(\sqrt{\hat{K}})} \right\}. \quad (9.68)$$

The total impedance of the pore walls consists of the faradaic and the double-layer impedances. They are connected in parallel, Eq. (9.22); therefore, the faradaic admittance, $\hat{Y}_{f,\text{tot}}$, and double-layer admittance, \hat{Y}_{dl} , must be added in series:

$$\hat{Y}_{\text{tot}} = \hat{Y}_{f,\text{tot}} + \hat{Y}_{\text{dl}} = \hat{Y}_{f,\text{tot}} + j\omega C_{\text{dl}}(2\pi r l) \quad (9.69)$$

and

$$\hat{Y}_{f,\text{tot}} = \int_0^1 \hat{Y}_f dz. \quad (9.70)$$

Substitution of Eqs. (9.64) and (9.68) into Eq. (9.70) and assuming $\alpha = 0.5$ gives the analytical solution

$$\begin{aligned}
\hat{Y}_{f,\text{tot}} = & u \left(\frac{P}{1+P} \right) \left(1 - \frac{B}{\hat{K}} \right) + u \left[\frac{\alpha - (1-\alpha)P}{1+P} \right] \left(1 - \frac{B}{\hat{K}} \right) \frac{\tanh\sqrt{B}}{\sqrt{B}} \\
& + u \left(\frac{P}{1+P} \right) \frac{B \tanh\sqrt{\hat{K}}}{\hat{K} \sqrt{\hat{K}}} \\
& + u \left[\frac{\alpha - (1-\alpha)P}{1+P} \right] \frac{B \sqrt{\hat{K}} \cosh\sqrt{\hat{K}} - \sqrt{B} \cosh\sqrt{B}}{\hat{K} - B},
\end{aligned} \tag{9.71}$$

where $u = n^2 F f C_O^* \vec{k}_f$. This is a different form but equivalent to that shown earlier [407, 443]. It simplifies at low and high frequencies. At very low frequencies, $\omega \rightarrow 0$, $B/\hat{K} \rightarrow 1$, and Eq. (9.71) simplifies to

$$\begin{aligned}
\hat{Y}_{f,\text{tot}}(\omega \rightarrow 0) = & \frac{1}{R_p} = u \frac{P}{1+P} \frac{\tanh\sqrt{B}}{\sqrt{B}} \\
& + u \left[\frac{\alpha - (1-\alpha)P}{1+P} \right] \left[\frac{1}{2} + \frac{\tanh\sqrt{B}}{2\sqrt{B}} - \frac{1}{2} \tanh^2\sqrt{B} \right],
\end{aligned} \tag{9.72}$$

where R_p is the polarization resistance. At very high frequencies, $\omega \rightarrow \infty$, $B/\hat{K} \rightarrow 0$, $1 - B/\hat{K} \rightarrow 1$, and the admittance becomes

$$\hat{Y}_{f,\text{tot}}(\omega \rightarrow \infty) = \frac{1}{R_t} = u \frac{P}{1+P} u \left[\frac{\alpha - (1-\alpha)P}{1+P} \right] \frac{\tanh\sqrt{B}}{\sqrt{B}}. \tag{9.73}$$

When $\hat{Y}_{f,\text{tot}}(\omega \rightarrow 0)$ is different from $\hat{Y}_{f,\text{tot}}(\omega \rightarrow \infty)$, that is, at porous electrodes in the presence of a concentration gradient, the faradaic impedance forms a semicircle on the complex plane plots. This means that the total impedance exhibits two semicircles for a simple redox reaction, which, on a flat electrode, exhibits only one semicircle. The difference between the high- and low-frequency admittance equals

$$\begin{aligned}
\hat{Y}_{f,\text{tot}}(\omega \rightarrow \infty) - \hat{Y}_{f,\text{tot}}(\omega \rightarrow 0) = \\
u \frac{P}{1+P} \left(1 - \frac{\tanh\sqrt{B}}{\sqrt{B}} \right) + u \left[\frac{\alpha - (1-\alpha)P}{1+P} \right] \left[\frac{\tanh\sqrt{B}}{2\sqrt{B}} - \frac{1}{2} + \frac{1}{2} \tanh^2\sqrt{B} \right].
\end{aligned} \tag{9.74}$$

For flat electrodes $B \rightarrow 0$, $\tanh\sqrt{B} \rightarrow 0$, $\tanh\sqrt{B}/\sqrt{B} \rightarrow 1$, and Eq. (9.74) becomes

$$\hat{Y}_{f,\text{tot}}(\omega \rightarrow \infty) - \hat{Y}_{f,\text{tot}}(\omega \rightarrow 0) = 0. \quad (9.75)$$

and

$$\hat{Y}_{f,\text{tot}} = u \frac{P}{1+P} + \frac{u}{2} \left(\frac{1-P}{1+P} \right) = 0.5u. \quad (9.76)$$

In this case, the high- and low-frequency impedances are the same as for flat electrodes, and only one semicircle is observed on the complex plane plots.

For long pores, $B \rightarrow \infty$, and at very negative potentials these admittances are

$$\begin{aligned} \hat{Y}_{f,\text{tot}}(\omega \rightarrow \infty) &= \frac{u}{2} \frac{1}{\sqrt{B}}, \\ \hat{Y}_{f,\text{tot}}(\omega \rightarrow 0) &= \frac{u}{4} \frac{1}{\sqrt{B}}, \end{aligned} \quad (9.77)$$

and their ratio becomes constant equal to two:

$$\frac{\hat{Y}_{f,\text{tot}}(\omega \rightarrow \infty)}{\hat{Y}_{f,\text{tot}}(\omega \rightarrow 0)} = \frac{R_p}{R_t} = 2. \quad (9.78)$$

In this case, the faradaic impedance is represented as a semicircle starting at $2\sqrt{B}/u$ and ending at $4\sqrt{B}/u$. When combined with the double-layer capacitance, the electrode impedance displays two semicircles of the same radius on the complex plane plots. Examples of complex plane plots at different concentrations of the active species and the same potential are displayed in Fig. 9.33. In this case, the ratio of the highest to the lowest faradaic impedance is constant; however, at low concentrations, the double-layer capacitance causes poor visibility of the first semicircle. Two distinct semicircles are well formed at higher concentrations of the electroactive species.

The influence of the electrode potential, $E - E^0$, on the complex plane plots is shown in Fig. 9.34. With an increase in the negative potential the faradaic impedance changes and tends to the condition in Eq. (9.78). The total impedance always displays two semicircles; however, their separation is most visible at around $E - E^0 = 0$.

The influence of the electrode porosity is displayed in Fig. 9.35. At very low porosities, i.e., for very shallow pores ($l = 0.005$ cm), the electrode behaves practically as flat, and one semicircle is observed on the complex plane plots. With an increase in the pore length, two semicircles are observed ($l = 0.05$ cm), and with further increases, one semicircle is observed identical to the faradaic impedance and the influence of the double-layer capacitance disappears.

To better acquaint ourselves with this problem, let us solve the same problem in the case where both forms, Ox and Red, are present in solution.

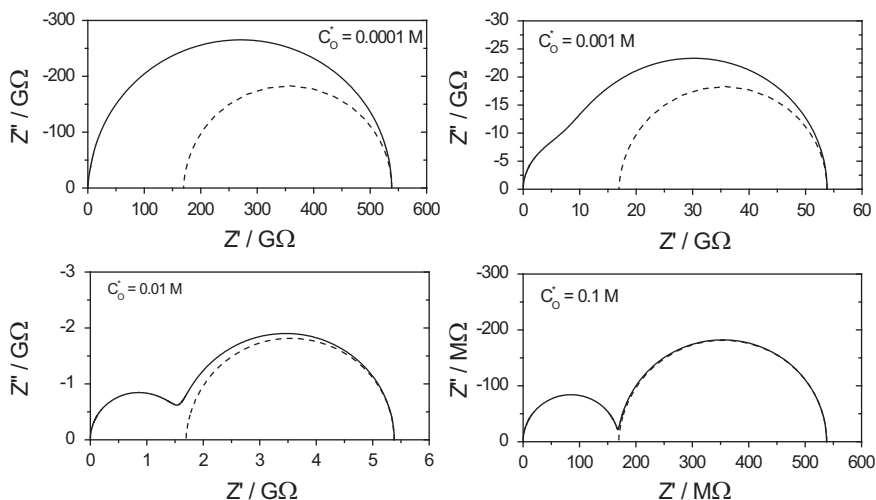


Fig. 9.33 Complex plane plots on porous electrode at various concentrations of oxidized species in absence of potential gradient in pores; parameters: $E - E^0 = 0$ V, $l = 0.05$ cm, $r = 10^{-4}$ cm, $D = 10^{-5}$ cm² s⁻¹, $k^0 = 10^{-6}$ cm s⁻¹, $\Phi_0 = 1.58$; concentrations indicated in graph; *continuous line*: total impedance, *dashed lines*: faradaic impedances

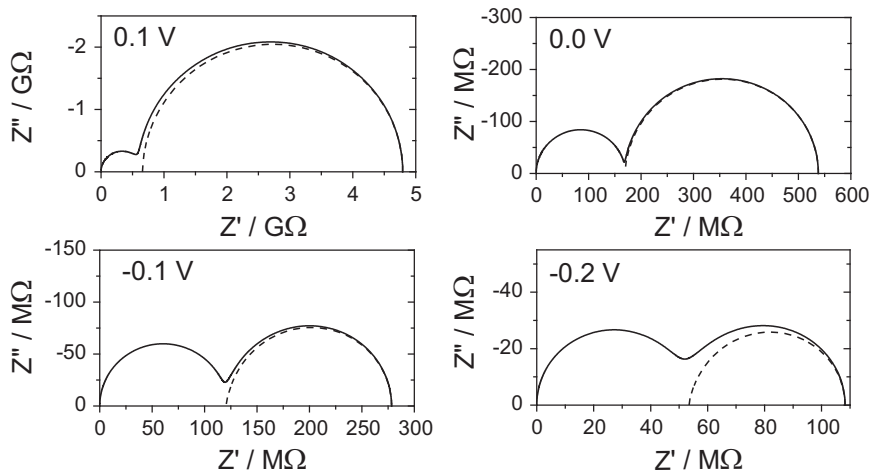


Fig. 9.34 Influence of electrode potential, $E - E^0$, on complex plane plots for porous electrode in absence of potential gradient, $C_O^* = 0.1$ M; other parameters as in Fig. 9.33; *continuous line*: total impedances, *dashed lines*: faradaic impedances

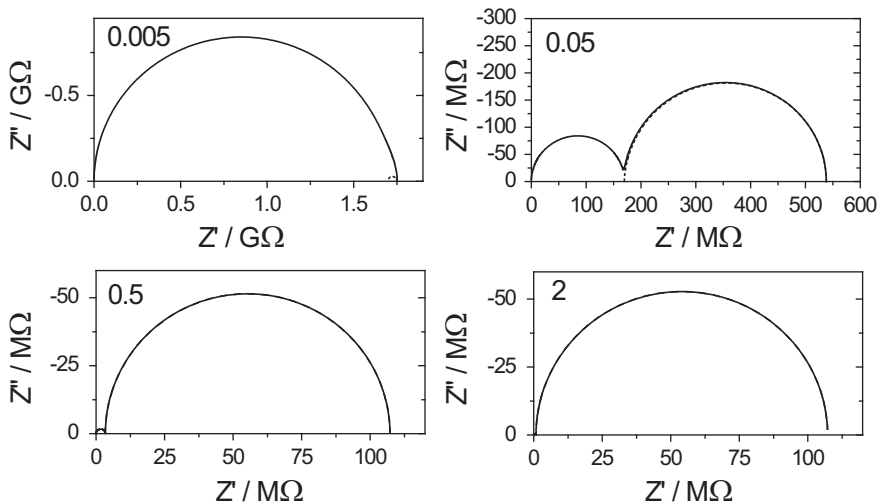


Fig. 9.35 Influence of electrode porosity parameter on impedance plots, characterized by different pore lengths, indicated in figures in centimeters, $r = 10^{-4}$ cm; other parameters as in Fig. 9.34, at a constant potential $E - E^0 = 0$ V; *continuous line*: total impedance, *dashed lines*: faradaic impedances

Example 9.1 Determine the concentration gradient and impedance of a porous electrode in the presence of solution with both R and O forms present in solution; their concentrations are C_O^* and C_R^* .

In this case the current is described by the current-overpotential equation:

$$j(x) = j_0 \left(\frac{C_O(x)}{C_O^*} e^{-anf\eta} - \frac{C_R(x)}{C_R^*} e^{(1-\alpha)nf\eta} \right). \quad (9.79)$$

Assuming that the diffusion coefficients of both forms are identical one can write the mass conservation equation in the pore:

$$C_O^* + C_R^* = C_O(x) + C_R(x). \quad (9.80)$$

Equation (9.79) can be rearranged introducing dimensionless concentrations:

$$a(x) = \frac{C_O(x)}{C_O^*} \quad \text{and} \quad m = \frac{C_R^*}{C_O^*}, \quad (9.81)$$

$$\begin{aligned} j(x) &= j_0 \left[a(x) \left(e^{-anf\eta} + m e^{(1-\alpha)nf\eta} - (m+1) e^{(1-\alpha)nf\eta} \right) \right] = \\ &= j_0 \left[a(x) \left(P^{-\alpha} + m P^{1-\alpha} - (m+1) P^{1-\alpha} \right) \right]. \end{aligned} \quad (9.82)$$

The steady-state concentration in the pore, Eq. (9.57), becomes

$$\begin{aligned}\frac{d^2 a(z)}{dz^2} &= \frac{2l^2}{nFrDC_O^*} j(z) \\ &= \frac{2l^2 j_0 (P^{-\alpha} + mP^{1-\alpha})}{nFrDC_O^*} a(z) - \frac{2l^2 j_0 (1+m)P^{1-\alpha}}{nFrDC_O^*} \\ &= Ba(z) - A.\end{aligned}\quad (9.83)$$

The solution of this equation is

$$a(z) = \frac{(1+m)P}{1+mP} + \frac{1-P}{1+mP} \frac{\cosh[\sqrt{B}(1-z)]}{\cosh[\sqrt{B}]}. \quad (9.84)$$

It can be shown that at very negative potentials, the parameter a reaches zero and at very positive potentials $(1+m)/m$. Substitution into Eqs. (9.68) and (9.64) and assuming $n = 1$ leads to the faradaic admittance at a distance z from the orifice:

$$\begin{aligned}Y_f(z) &= u_2 \left(1 - \frac{B}{\hat{K}}\right) + u_3 \left(1 - \frac{B}{\hat{K}}\right) \frac{\cosh[\sqrt{B}(1-z)]}{\cosh[\sqrt{B}]} + u_2 \frac{B}{\hat{K}} \frac{\cosh[\sqrt{\hat{K}}(1-z)]}{\cosh[\sqrt{\hat{K}}]} \\ &\quad + u_3 \frac{B}{\hat{K}} \frac{\cosh[\sqrt{B}(1-z)]}{\cosh[\sqrt{B}]} \frac{\cosh[\sqrt{\hat{K}}(1-z)]}{\cosh[\sqrt{\hat{K}}]},\end{aligned}\quad (9.85)$$

where

$$u_2 = j_0 f P^{1-\alpha} \frac{(1+m)}{1+mP} \text{ and } u_3 = j_0 f P^{-\alpha} \frac{[\alpha - m(1-\alpha)P]}{1+mP} (1-P). \quad (9.86)$$

Integration of the faradaic admittance, Eq. (9.70), gives the total faradaic impedance:

$$\begin{aligned}Y_{f,\text{tot}} &= u_2 \left(1 - \frac{B}{\hat{K}}\right) + u_3 \left(1 - \frac{B}{\hat{K}}\right) \frac{\tanh[\sqrt{B}]}{\sqrt{B}} + u_2 \frac{B}{\hat{K}} \frac{\tanh[\sqrt{\hat{K}}]}{\sqrt{\hat{K}}} + \\ &\quad + u_3 \frac{B}{\hat{K}} \frac{\tanh[\sqrt{B}] - \tanh[\sqrt{\hat{K}}]}{\hat{K} - B}.\end{aligned}\quad (9.87)$$

In summary, in the case of a concentration gradient in pores and in the absence of a potential gradient, the faradaic impedance becomes a semicircle instead of a

constant value. This translates into the formation of two semicircles of the total impedance on complex plane plots. The formation of two semicircles was observed experimentally on porous gold electrodes [412].

9.2.5 General Case: Potential and Concentration Gradient

9.2.5.1 DC Solution

In the general case, the potential and concentration gradients appear in pores simultaneously [433, 436–441, 445]. It is assumed that the concentrations of the redox species outside the pores are C_O^* and C_R^* and the current may be expressed in terms of the overpotential as in Eqs. (9.79) and (9.82). To solve for the concentration and potential gradient, Eqs. (9.1) and (9.2) must be solved simultaneously:

$$\frac{dI(x)}{dx} = -2\pi r j(x) \text{ and } \frac{d\eta(x)}{dx} = -\left(\frac{\rho_s}{\pi r^2}\right)I(x). \quad (9.88)$$

Taking the second derivative of the overpotential and substitution of the current gradient gives

$$\frac{d^2\eta(x)}{dx^2} = \frac{2\rho_s}{r}j(x), \quad (9.89)$$

or, in dimensionless form,

$$\frac{d^2\eta(z)}{dz^2} = \frac{2\rho_s l^2}{r}j(z). \quad (9.90)$$

This equation must be solved together with Eq. (9.57). They both represent second-order differential equations for $\eta(x)$ and $a(x)$ with the following conditions:

$$\begin{aligned} z = 0 \quad a = 1, \quad \eta = \eta_0, \\ z = 1, \quad da/dz = d\eta/dz = 0. \end{aligned} \quad (9.91)$$

Combination of these two equations gives

$$\frac{d^2\eta(z)}{dz^2} = (nFDC_O^*\rho_s) \frac{d^2a(z)}{dz^2} = \nu \frac{d^2a(z)}{dz^2}, \quad (9.92)$$

where $\nu = nFDC_O^*\rho_s$. Equation (9.92) has an analytical solution:

$$\eta_0 - \eta(z) = \nu[1 - a(z)]. \quad (9.93)$$

This solution means that there is a linear relation between the potential and concentration in the pores. There are two limiting cases:

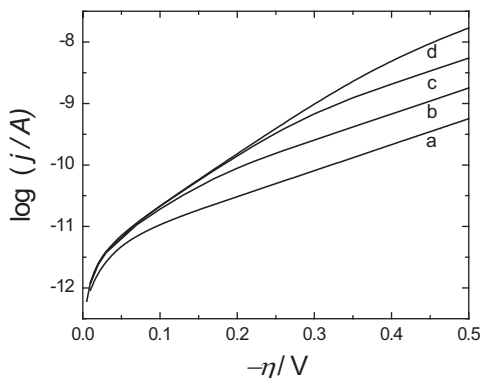


Fig. 9.36 Tafel plots on porous electrode at different concentrations of active species. Concentrations: (a) 0.01, (b) 0.1, (c) 1 M, (d) limit at infinite concentration (no concentration gradient); pore parameters: $l = 0.05$ cm, $r = 10^{-4}$ cm, $\rho_s = 10 \Omega$ cm, $D = 10^{-5}$ cm² s⁻¹, $m = 1$, $j_0 = 10^{-7}$ A cm⁻² (From Ref. [72] with kind permission from Springer Science and Business Media)

- When $\nu \ll 1$ V, $\eta_0 - \eta(z) \approx 0$, the overpotential is practically constant in the pores and the system is determined by the concentration gradient; this case corresponds to that described in Sect. 9.2.4.
- When $\nu \gg 1$ V, the potential gradient in the pores is important, while the concentration gradient is negligible; this case corresponds to that described in Sect. 9.2.3.

The value of the parameter ν for typical experimental conditions, $n = 1$, $D = 10^{-5}$ cm² s⁻¹, $\rho_s = 10 \Omega$ cm, and concentrations, C_0^* , 1 and 10 mM, equals $\nu \sim 10^{-5}$ and 10^{-4} V, respectively. This means that for typical concentrations the process is limited by the concentration gradient in the pores. Only in the case of very large concentrations of electroactive species or solvent reduction/oxidation (water electrolysis, chlorine evolution in concentrated solutions) might the potential gradient be important.

Substitution of Eq. (9.93) into Eqs. (9.57) and (9.90) gives the following two equations:

$$\frac{d^2 a}{dz^2} = \left(\frac{2j_0 l^2}{nFrDC_0^*} \right) \left[a(e^{-b(\eta_0 - \nu) + bva} + me^{b(\eta_0 - \nu) - bva}) - (m+1)e^{b(\eta_0 - \nu) - bva} \right], \quad (9.94)$$

$$\frac{d^2 \eta}{dz^2} = \left(\frac{2\rho j_0 l^2}{r} \right) \left[\left(1 - \frac{\eta_0}{\nu} + \frac{\eta}{\nu} \right) (e^{-b\eta} + me^{b\eta}) - (m+1)e^{b\eta} \right]. \quad (9.95)$$

It is sufficient to solve only one of these equations because the parameters $a(z)$ and $\eta(z)$ are related by Eq. (9.93). The first integration can be carried out analytically, but the second one must be carried out numerically, searching for the values of $a(1)$ or $\eta(1)$ at $z = 1$ (i.e., $x = l$) satisfying the conditions $da/dz = d\eta/dz = 0$ [441]. These computations usually demand higher computing precision (quadruple precision in FORTRAN using a procedure for stiff differential equations).

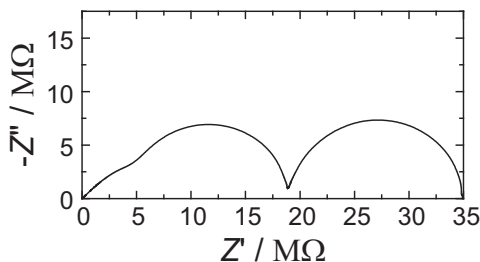


Fig. 9.37 Complex plane plot on porous electrode in presence of potential and concentration gradients; $j_0 = 10^{-5} \text{ A cm}^{-2}$, $C_0^* = 1 \text{ M}$, $\eta = -0.2 \text{ V}$; other pore parameters as in Fig. 9.36 (From Ref. [72] with kind permission from Springer Science and Business Media)

Examples of the Tafel plots obtained at porous electrodes are shown in Fig. 9.36. At lower concentrations of the electroactive species the electroreduction process is controlled by the concentration gradient, and the Tafel slope at 25°C is $2\ln(10)/\alpha f = 237 \text{ mV dec}^{-1}$ for $\alpha = 0.5$. At higher concentrations and lower overpotentials, the Tafel slope becomes $\ln(10)/\alpha f = 118 \text{ mV dec}^{-1}$ because the concentration gradient is negligible; however, at higher overpotentials and, subsequently, higher currents, the slope increases as the concentration and potential gradients appear again.

9.2.5.2 AC Solution

To obtain the ac solution, one must solve Eq. (9.63), which leads to the solution, Eq. (9.68), for the local impedance in the pore [441]. To calculate the total impedance, one must use the concentration and potential distribution in pores and carry out numerical addition of impedances using Eq. (9.44), similarly to the case of the potential gradient only [435] but using the full expression for the current, Eq. (9.82), where both $a(x)$ and $\eta(x)$ are distance dependent. An example of the complex plane impedance plot obtained in the case of the potential and concentration gradients in pores is shown in Fig. 9.37. It is evident that there are two semicircles related to the concentration gradient at lower frequencies (Fig. 9.34) and a straight line at 45° corresponding to the potential drop in pores at high frequencies (Fig. 9.27).

An influence of the concentration on the impedance spectra is illustrated in Fig. 9.38. At high frequencies, a short straight line at 45° is observed due to the potential gradient. At lower frequencies, two semicircles appear, and their diameter decreases with an increase in the concentration. In the case where there is no concentration gradient ($C_0^* \rightarrow \infty$), impedance due to the potential gradient only is observed (Fig. 9.38(4)).

The complex plane plots obtained in the general case involve concentration and potential gradients. They display characteristic features corresponding to a concentration gradient, i.e., two semicircles, and potential gradient, i.e., a straight line at

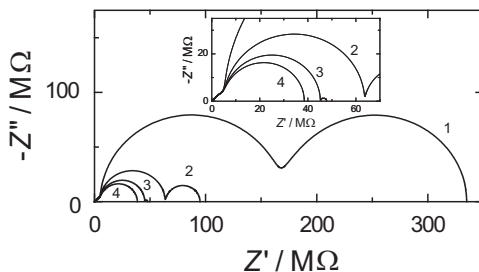


Fig. 9.38 Influence of concentration of electroactive species on impedance spectra. Concentrations: (1) 10^{-4} , (2) 10^{-3} , (3) 10^{-2} mol cm^{-3} , (4) limit at infinite concentration (potential gradient only); $\eta = 0.2$ V, $j_0 = 10^{-6}$ A cm^{-2} ; other parameters as in Fig. 9.36 (From Ref. [72] with kind permission from Springer Science and Business Media)

45° at high frequencies. This theory was also applied to the dissolved hydrogen concentration buildup in pores during the hydrogen evolution reaction where its concentration increased inside the pore with the distance from the pore orifice [441].

9.3 Distribution of Pores

All the simulations presented previously were carried out assuming the presence of one or multiple uniform pores of the same geometry. However, in real systems, there are many different pores of different geometry.

The simplest method of taking into account the distribution of pores of different sizes is to use the transmission line ladder network (Fig. 9.4, 9.14, 9.17, or 9.19) and use different values for the parameters r_i , r_e , and c_i or interfacial impedances z_i and calculate the total admittance by the addition of the admittances of the small pore elements. Such a method was used, for example, by Macdonald et al. [446, 447] and Pyun et al. [448]. Although such a model can be used to simulate impedance spectra assuming changes in parameters with the position in the pore, it is difficult to obtain the pore parameters from the experimental spectra.

Another method is to assume a certain distribution of pore parameters. Song et al. [449–452], in a series of papers, considered the distribution of pore parameters for electrodes in the absence of electroactive species, i.e., for purely capacitive electrodes. De Levie's equation (9.7) is applicable to individual pores, but for different pores different values of the parameter Λ are obtained. The dimensionless penetrability parameter, α , was defined as

$$\alpha = \frac{\lambda}{l} = \left(\frac{1}{2l} \sqrt{\frac{r}{C_{dl}\rho_s}} \right) \omega^{-1/2} = \alpha_0 \omega^{-1/2}, \quad (9.96)$$

where α_0 is the so-called penetrability coefficient, in $s^{-1/2}$, directly proportional to \sqrt{r}/l . The authors used different distribution functions of α_0 : normal, lognormal, Lorentzian, and log Lorentzian. The total impedance of the porous electrode was calculated by integration over all pores:

$$\frac{1}{Z_{\text{tot}}} = \int_{-\infty}^{\infty} \frac{1}{Z_p(\alpha_0)} f(\alpha_0, \mu, \sigma) d\alpha_0, \quad (9.97)$$

where $Z_p(\alpha_0)$ is the impedance of a single pore characterized by the parameter α_0 and $f(\alpha_0, \mu, \sigma)$ is the continuous pore size distribution function of the parameter α_0 with mean value μ and standard deviation σ . The integration was carried out over all values of α_0 . In the case of the lognormal distribution function at low frequencies, the impedances displayed a quasi-CPE behavior. Later, these authors proposed so-called electrochemical porosimetry in an attempt to determine the pore size distribution function from impedance measurements [451, 452].

Recently, Musiani et al. [453] critically reviewed the aforementioned papers and found that Song et al.'s calculation did not correspond to a lognormal pore radius distribution because, in spite of a constant μ value, the median of the cumulative distribution function depends on the standard deviation σ . Since the number of pores is also affected by the σ value (at constant pore volumes), Song et al.'s calculations correspond to allowing both n and median r_μ to change when σ changes. The new simulations were carried out [453] using the classical lognormal distribution function for pore radiuses:

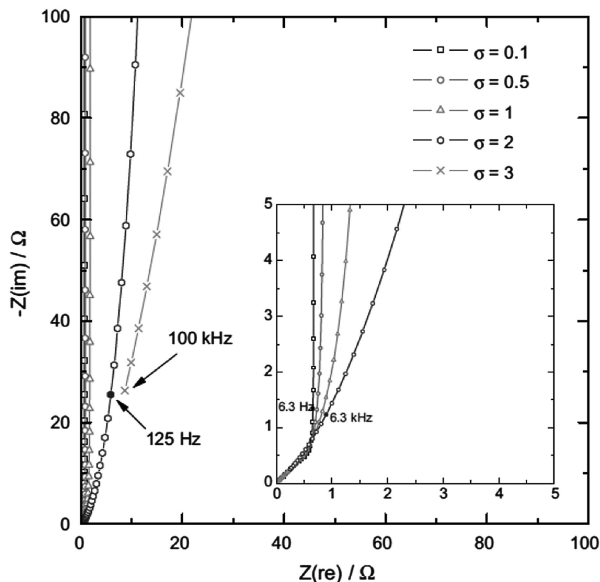
$$f(r) = \frac{1}{r\sqrt{2\pi\sigma}} \exp \left[-\frac{1}{2} \left(\frac{\ln(r) - \ln(r_\mu)}{\sigma} \right)^2 \right]. \quad (9.98)$$

Under such conditions, a constant median of the pore radius, r_μ , and adjusted number of pores, n , made it possible to keep the total volume constant. Examples of complex plane plots for such systems are presented in Fig. 9.39. The phase angle changes from 45° at high frequencies to 90° at very low frequencies when the ac signal can penetrate to the bottom of the pore. In the medium frequency range, the impedance resembles CPE behavior. However, the surface area calculated using Brug et al.'s equation (8.11) leads to a right order of magnitude but fails to yield the correct value as the physical model used in Brug et al.'s equation is inappropriate here.

9.4 Continuous Porous Model

In the preceding sections the impedance of a single pore or the distribution of simple pores of known geometry was treated. However, in real cases of porous electrodes used in, for example, lithium or hydrogen storage batteries or fuel cells, one does not

Fig. 9.39 Complex plane plots for lognormally distributed pores with ideally polarizable walls for constant pore volume and various standard deviations σ (From Ref. [453], copyright (2011), with permission from Elsevier)



know the exact geometry of the electrode and the pores; they display a random structure. Real porous electrodes often consist of particles of an electronic conductor, sometimes containing a nonconducting material, and the pores are filled with solution containing electroactive species, for example, Li^+ ions in the case of lithium batteries and H_2 or O_2 in fuel cells. A continuous theory of porous electrodes in dc conditions was presented by Newman [454]. Such a model is schematically shown in Fig. 9.40, where the ionic current, i_2 , is flowing from the solution into a porous electrode. It gradually decreases in the porous electrode while the electronic current, i_1 , increases as it is transferred from the solution to the solid matrix.

At the interface solution-electrode at $x = 0$ there is only an ionic current, and the total current $I = i_2$, the electronic current $i_1 = 0$, and the potential in solution $\Phi_2 = 0$ (by definition). On the other hand, at the electrode-solid contact interface at $x = l$ there is only an electronic current, $I = i_1$, ionic current, $i_2 = 0$, and the potential in the electrode is $\Phi_1(l)$. As x increases from zero to l , the ionic current decreases and the electronic current increases, and inside the porous electrode $i_1 + i_2 = I$. In this model, a continuous variation of the potential Φ_1 in the solid and Φ_2 in the solution is assumed.

Ohm's law in the solid matrix and in solution may be written as

$$\frac{\partial \Phi_1}{\partial x} = -\frac{i_1}{\sigma} \quad \frac{\partial \Phi_2}{\partial x} = -\frac{i_2}{\kappa}, \quad (9.99)$$

where σ and κ are the conductivities of the solid phase and the solution, respectively. The faradaic current that flows between the matrix and solution may be

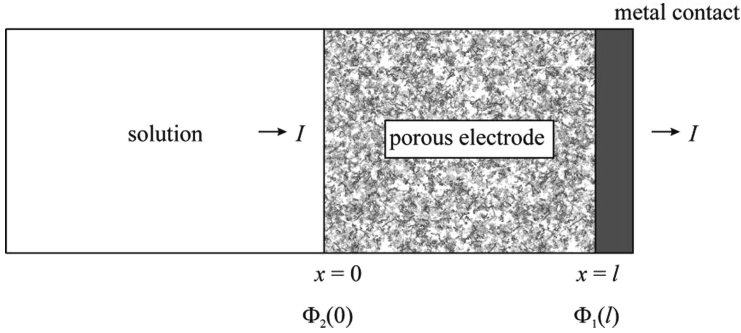


Fig. 9.40 Schematic representation of continuous porous electrode (From Ref. [72] with kind permission from Springer Science and Business Media)

described by the Butler-Volmer equation if the concentration polarization is neglected:

$$i_f = ai_0[\exp(\alpha_a f \eta_s) - \exp(-\alpha_c f \eta_s)], \quad (9.100)$$

where a is the specific interfacial area of the pore walls per unit volume of the electrode (cm^{-1}), i_0 is the exchange current density, the indices a and c indicate anodic and cathodic processes, respectively, the overpotential is $\eta_s = \Phi_1 - \Phi_2 - E_{\text{eq}}$, and E_{eq} is the open circuit (equilibrium) potential. In the case of concentration polarization, the current-overpotential equation should be used:

$$i_f = ai_0 \left[\frac{C_{\text{ox}}}{C_{\text{ox}}^*} \exp(\alpha_a f \eta_s) - \frac{C_{\text{red}}}{C_{\text{red}}^*} \exp(-\alpha_c f \eta_s) \right]. \quad (9.101)$$

The diffusion equation in pores is given by an analog of Eq. (9.55) [454, 455]:

$$\varepsilon \frac{\partial C}{\partial t} = \varepsilon D \frac{\partial^2 C}{\partial x^2} - \frac{a}{F} i_f, \quad (9.102)$$

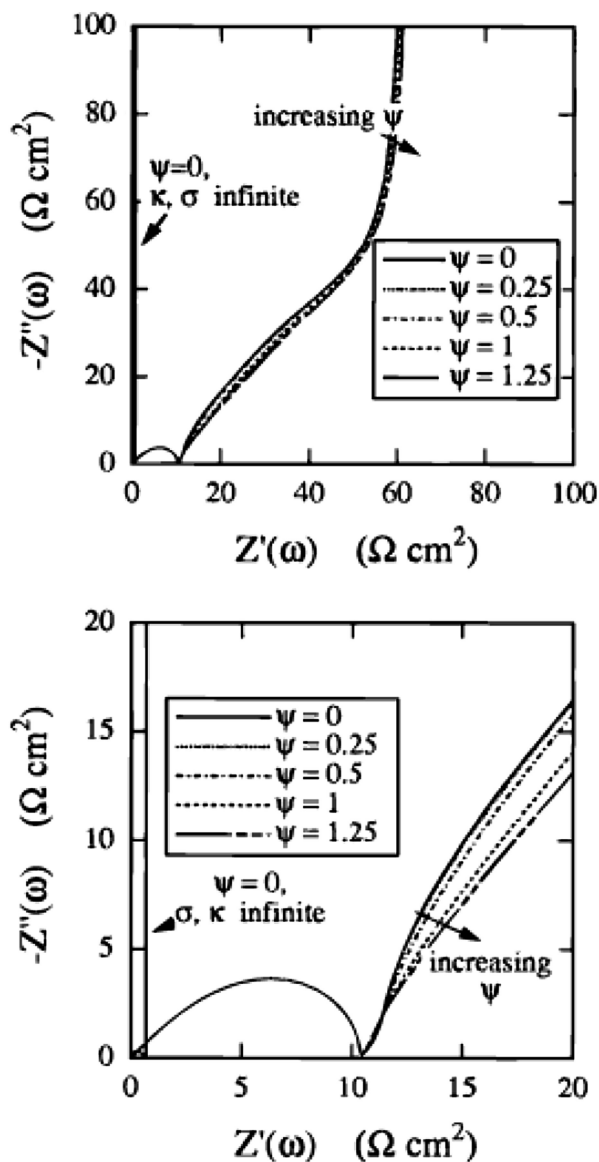
where ε is the electrode porosity. In the preceding equations, the parameters D , κ , and σ are the effective values, which are different from the values outside of pores [454, 455]:

$$D = \varepsilon^{0.5} D_0; \quad \kappa = \varepsilon^{1.5} \kappa_0; \quad \sigma = (1 - \varepsilon)^{1.5} \sigma_0, \quad (9.103)$$

where the index 0 denotes values outside pores.

The impedances may be evaluated by applying a small ac perturbation that generates a small perturbations of the parameters around their dc values, adding the charging current [456, 457],

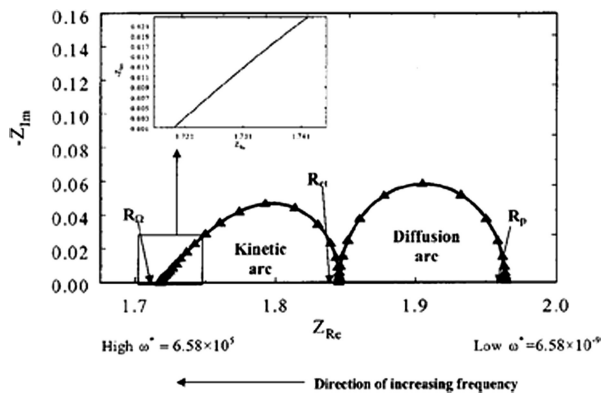
Fig. 9.41 Complex plane plots simulated for porous electrodes with various particle size distributions, ψ ; $\psi = 0$ corresponds to uniform particle size. The lower figure is an expanded view at high frequencies (From Ref. [457]. Reproduced with permission of Electrochemical Society)



$$i_{dl} = C_{dl} \frac{\partial(\Phi_1 - \Phi_2)}{\partial t}, \quad (9.104)$$

and solving the equations numerically. Such calculations were carried out by Meyers et al. [457] for lithium intercalation in spherical particles, assuming a lognormal distribution of particle dimensions. Examples of the complex plane plots obtained on such electrodes are displayed in Fig. 9.41. At high frequencies,

Fig. 9.42 Complex plane plot of porous electrode: *continuous line*: analytical solution, *triangles*: numerical solution; *inset*: high-frequency part of plot (impedances are in Ω) (From Ref. [455]. Reproduced with permission of Electrochemical Society)



a skewed semicircle is observed, similar to those presented for a semi-infinite-length porous electrode (Fig. 9.26), while the low-frequency part represents the finite-length diffusion (Fig. 9.3).

This theory was later extended to rechargeable lithium batteries, including a concentrated solution theory of binary electrolytes and assuming that transference numbers were constant [456]. Devan et al. [455] developed an analytical solution for the impedance of porous electrodes using the concentrated solution theory and a linear electrode kinetics that was a linear form of the Butler-Volmer equation: $i_f = i_0 f(\alpha_a + \alpha_c) \eta$. Such a solution (although formally rather complex) permitted study of the influence of different parameters on impedance plots and the limiting cases of the impedance parameters. An example plot is displayed in Fig. 9.42. It represents two semicircles, the high-frequency kinetic skewed arc and the low-frequency semicircle due to diffusion in pores. These plots might be compared with the plots for single-pore impedance in the absence of a potential drop (Fig. 9.3) or a general case of a single pore in the presence of potential and concentration gradients (Fig. 9.37).

This method was also applied by other authors to hydrogen absorption in a porous electrode consisting of spherical particles of AB₅-type material [458] to describe a whole polymer electrolyte fuel cell with gas diffusion in pores [459], alkaline fuel cells [460], and intercalation electrodes [461]. Several authors attempted to fit the experimental impedances to their models [456–461].

It is evident that a single-pore theory cannot describe more complex cases of real porous electrodes containing particles of different sizes that are randomly distributed. Nevertheless, numerical simulations demand some additional information about the electrode, particle size distribution, possible heterogeneity of the material, conductivity of different phases, etc., and the electrode studied should be composed of a uniform packing of the particles with their size being much smaller than the electrode thickness.

9.5 Conclusions

The impedance of porous electrodes is now relatively well understood. It depends strongly on pore geometry and the presence and concentration of redox species. In some cases involving the resistance of electrode and solution, it might be difficult to obtain characteristic parameters from the experimental curves because often they might be well approximated by a simpler model involving the solution resistance only. Detailed knowledge of the porous material parameters permits simulations of the impedance using continuous models, although obtaining certain parameters from the experiment might be more difficult. Porosity effects usually appear at high frequencies as a small line or a semicircle, and they are often confused with faradaic reaction effects. However, some simple tests allow one to distinguish between these two cases.

9.6 Exercises

Exercise 9.1 Using Maple or Mathematica simulate the impedance described by Eq. (9.18) using data from Fig. 9.15.

Exercise 9.2 Simulate the impedances defined in Eq. (9.16) using ZView and then approximate them using de Levie's classical model. This model might be found in the new version of ZView only. Use the following parameters: $r_e = 200 \, \Omega \, \text{cm}^{-1}$, $r_s = 50 \, \Omega \, \text{cm}^{-1}$, $c_{dl} = 0.001 \, \text{F cm}^{-1}$, $l = 0.05 \, \text{cm}$.

Exercise 9.3 Using Maple or Mathematica simulate the impedance described by Eqs. (9.16) and (9.30) using data from Fig. 9.20.

Exercise 9.4 Simulate the impedance of a porous electrode in the presence of solution and electrode resistance and a redox system using ZView. Use the parameters from Fig. 9.20. Fit the obtained data to the simple de Levie model.

Chapter 10

Semiconductors and Mott-Schottky Plots

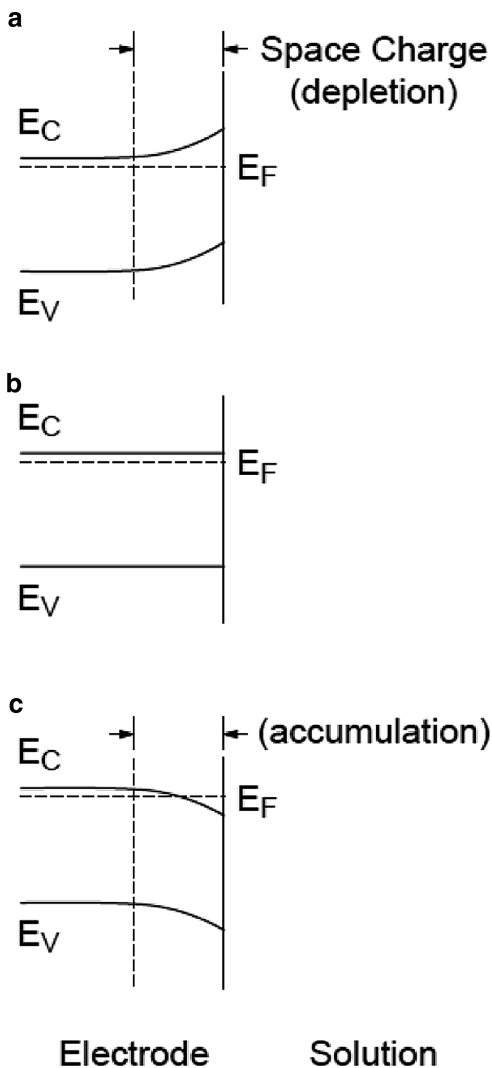
10.1 Semiconductors in Solution

When a conductive electrode (e.g., metallic or glassy carbon) is in contact with an electrolytic solution, the excess electronic charge is accumulated at the electrode surface and charge distribution occurs in the solution only. This is related to the fact that as the number of charged species increases, the space in which the redistribution of charges occurs shrinks. At a metallic electrode–solution interface, the charge redistribution in solution depends on the applied potential and is described by the Guy-Chapman-Stern theory. The characteristic thickness of the diffuse layer in nonadsorbing electrolytes varies from 0.3 nm in 1 M to 3 nm in 0.01 M aqueous electrolyte, while the thickness of the Helmholtz layer is much smaller [17].

In the case of semiconductor electrodes, the concentration of conductive species (electrons or holes) is much smaller than that in solution. This creates a redistribution of the space charge in the semiconductor electrode at distances much larger than that in solutions, 10–100 nm [462, 463]. This leads to much smaller capacitances of the semiconductor electrodes. Passive films formed on metallic surfaces behave as semiconductors, and their properties are important in studies of corrosion protection.

Because of the charge redistribution in the conduction and valence band, potential bending appears at the surface. This effect is illustrated in Fig. 10.1. For the *n*-type semiconductor electrode at an open circuit, the Fermi level is usually higher than the redox potential of the electrolyte, and the electrons are transferred from the electrode to the solution, producing a positive charge associated with the space charge region, causing an upward bending of the band edges. The opposite effect, that is, a downward bending of the band edges, is observed for *p*-type semiconductors [3, 17, 462, 463]. The magnitude and direction of bending depends on the applied potential, as seen in Fig. 10.1. At a certain applied potential, no bending is observed, and this potential is called a flatband potential, E_{fb} . The value of this potential may be determined electrochemically using Mott-Schottky plots [464–466].

Fig. 10.1 Effect of applied potential, E , on band edges in interior of n -type semiconductor; (a) $E > E_{fb}$, (b) $E = E_{fb}$, (c) $E < E_{fb}$



Under depletion conditions there is a relation between $1/C_{SC}^2$ and the potential, where C_{SC} is the semiconductor electrode capacitance. For n -type semiconductors the following relation is found:

$$\frac{1}{C_{SC}^2} = \frac{2}{\epsilon \epsilon_0 e N_D} \left(E - E_{fb} - \frac{kT}{e} \right), \quad (10.1)$$

where ϵ is the dielectric constant of the semiconductor, ϵ_0 is the dielectric permittivity of the vacuum, e is the elementary electric charge, k is the

Boltzmann constant, N_D is the donor density, and $kT/e = 0.0257$ V at 25°C . A similar expression exists for p -type semiconductors:

$$\frac{1}{C_{sc}^2} = \frac{-2}{\epsilon\epsilon_0 e N_A} \left(E - E_{fb} + \frac{kT}{e} \right), \quad (10.2)$$

where N_A is the acceptor density.

10.2 Determination of Flatband Potential

Capacitance measurements are usually carried out at one frequency, and the measured capacitance is determined as

$$C = \frac{-1}{\omega Z''}, \quad (10.3)$$

where C is the measured electrode capacitance. In general, it consists of the connection between the space charge capacitance, C_{sc} , and the double-layer capacitance, C_{dl} , in series:

$$\frac{1}{C} = \frac{1}{C_{sc}} + \frac{1}{C_{dl}}, \quad (10.4)$$

but usually $C_{sc} \ll C_{dl}$ and $C \approx C_{sc}$. Examples of Mott-Schottky plots are presented in Fig. 10.2.

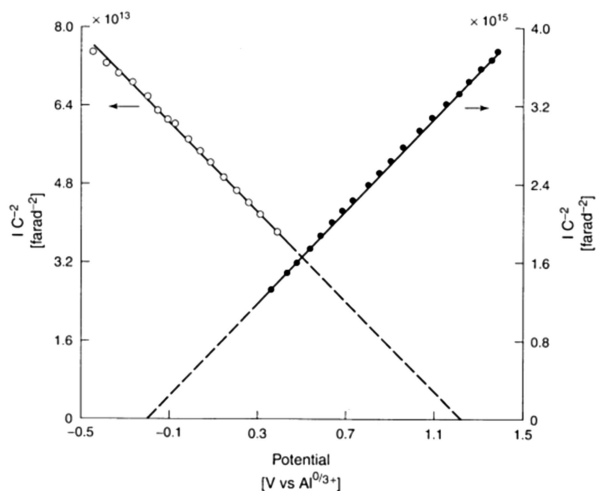
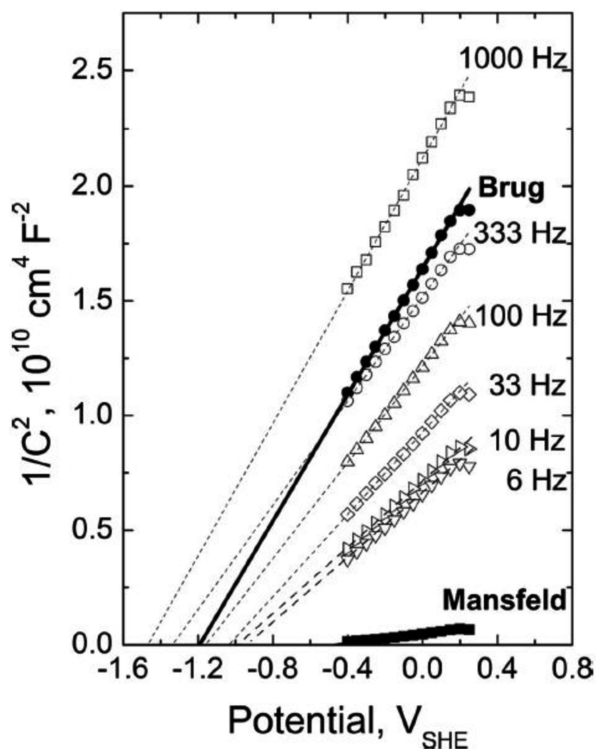


Fig. 10.2 Mott-Schottky plots obtained on n -GaAs (filled circles) and p -GaAs (open circles) electrodes in 2:1 AlCl_3 – n -butylpyridinium chloride molten salt electrolyte; the frequency was 2 kHz (From Ref. [467], copyright (1983), with permission from Elsevier)

Fig. 10.3 Mott-Schottky plots at Cr electrode using capacitance measured at one frequency (indicated), Eq. (10.3), and using Brug et al. [305] and Hsu and Mansfeld [306] models (From Ref. [468]. Reproduced with permission of Electrochemical Society)



The intercept of these plots provides the value of the flatband potential, E_{fb} , and the slope gives the donor or acceptor density. In agreement with Eqs. (10.1) and (10.2), the slope for n -type semiconductor is positive and that for p -type semiconductors is negative.

The use of Eq. (10.3) assumes that the semiconductor-electrolyte interface is ideally capacitive and can be represented by the solution resistance, R_s , and the interface capacitance, C , in series. However, such an interface is almost never purely capacitive and must be represented by the CPE. This leads to different slopes at different frequencies and sometimes different values of the flatband potential. An example of such a behavior is shown in Fig. 10.3. It is evident that measurements at different frequencies display different intercepts and slopes, and, as a consequence, different E_{fb} and N_D .

In general, behavior described by R_s CPE or $R_s(R_p$ CPE) circuits is observed, that is, displaying impedances as in Figs. 8.3 and 8.4. Harrington and Devine [468] and Rodriguez and Carranza [469] proposed to determine the average double-layer capacitance from the CPE model using Brug et al. [305] and Hsu and Mansfeld [306] models (Sect. 8.1). They found that the Hsu and Mansfeld model leads to incorrect data, while that of Brug et al. gives correct results.

A comparison of the results obtained from these two models is shown in Fig. 10.3. Of course, in such cases, at each potential the complete impedance spectrum must be obtained, which leads to longer experiments and possible changes in the surface layer with time.

Impedance of semiconductors in the presence of electron transfer through surface states is much more complex; see, e.g., Ref. [470–472].

Chapter 11

Coatings and Paints

Electrochemical impedance spectroscopy is very well suited to study paints and coatings used to prevent corrosion. There are even ISO norms developed for such tests [675] and technical notes from the equipment manufacturers [676, 681]. This topic has also been reviewed in several books [473–475].

11.1 Electrical Equivalent Models

The ideal coating is a pure capacitor (Fig. 11.1a), where R_s is the solution resistance and C_c the coating capacitance. However, real coatings in solutions rarely behave in an ideal manner; they have defects and regions of low cross linking. An electrical equivalent circuit for such coatings is displayed in Fig. 11.1b, in which the coating capacitance is in parallel with the coating resistance, R_{po} , and in series with the capacitance of the diffuse layer at the coating (containing ions [474])/metal interface, C_d^0 [474]. The index 0 indicates that the geometric and real surface areas are identical as the coating is adhering well to the metal surface. Because of the low dielectric constant of the coating, this value is small, approximately $0.05 \mu\text{F cm}^{-2}$. The capacitance of the coating, C_c , is usually one to two orders of magnitude lower than C_d^0 .

During further exposure of the coating to solution corrosion starts under the pinholes and can spread around, but in general it is localized. This produces a double-layer capacitance of the metal/solution interface under coating, C_d , greater than that of metal/coating, $C_d > C_d^0$. The faradaic corrosion reaction is represented by the resistance, R_c (Fig. 11.1c). When disbonding of the coating continues, the solution can penetrate under the coating (Fig. 11.2). In such a case, the impedance can be modeled as a transmission line (Fig. 11.1d). When the ohmic resistance under the film, R_{si} , becomes small, the transmission line can be simplified to the model in Fig. 11.1e, where $C_D = \Sigma C_{di}$ and $1/R_D = \Sigma 1/R_{di}$.

Fig. 11.1 Electrical equivalent circuits for an organic coating: (a) ideal coating, (b) real coating without corrosion, (c) adhering coating with the onset of corrosion in pinholes, (d) coating with disbonding, (e) coating with disbonding and small R_{si}

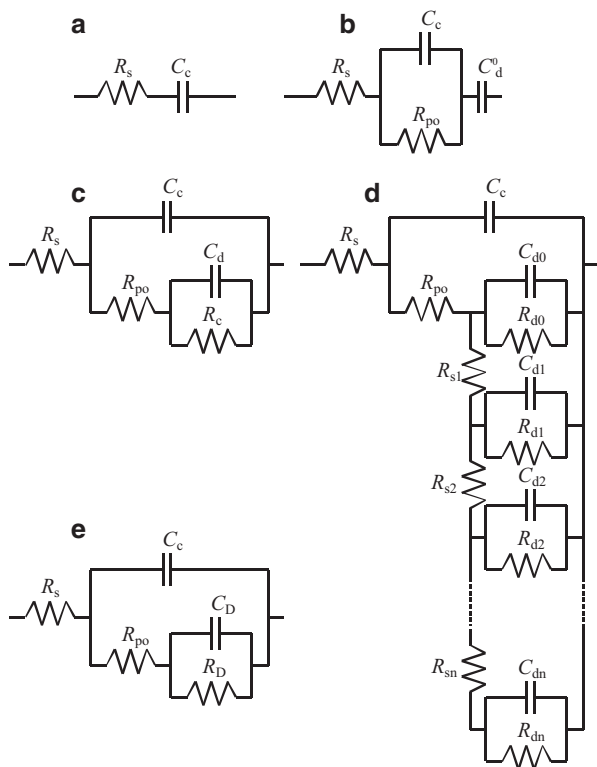
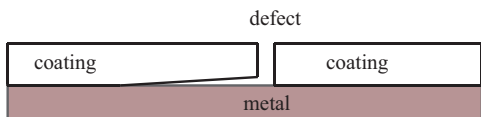


Fig. 11.2 Schematic of coating with defect and delamination under coating



11.2 Water Absorption in Organic Coating

The capacitance of a dielectric depends on its dielectric constant, ϵ , and thickness, d :

$$C_c = \frac{\epsilon \epsilon_0 A_0}{d}, \quad (11.1)$$

where ϵ_0 is the dielectric permittivity of vacuum and A_0 the geometric surface area. When the coating is in contact with an aqueous solution, water penetrates into the coating, changing its initial dielectric constant from 3–8 to larger values because the dielectric constant of water is $\epsilon_w = 78.5$ at 25 °C. The most widely used model to estimate the water content in a coating was put forward by Brasher and

Kingsbury [476], who proposed the following equation for the determination of the volume fraction in a coating (see also Ref. [477]):

$$\phi = K \frac{\log[C_C(t)/C_C(0)]}{\log \epsilon_w}, \quad (11.2)$$

where the indices t and 0 indicate coating capacitances after time t and the initial capacitance at time zero, and K accounts for the increase in volume, and it should not exceed 1.25. Usually it is taken as $K = 1$, corresponding to a constant volume. It was found that this formula often (but not always) overestimates water content (in comparison with the gravimetric method) [476, 478]. Castela and Simões [477] proposed a different model, applicable to homogeneous coatings, that does not suffer swelling:

$$\phi = \frac{C_C(t) - C_C(0)}{C_{\text{sol}} - C_{\text{air}}}, \quad (11.3)$$

where C_{sol} and C_{air} are the capacitances of the solution and air determined using Eq. (11.1). Equation (11.3) also usually overestimates water absorption.

In practical measurements, pure capacitances are rarely observed, and the CPE should be used to approximate the experimental data. However, capacitances may be easily obtained using the theory discussed in Sect. 8.1.

It should be kept in mind that organic coatings are characterized by low capacitances and very high resistances, demanding work at high frequencies, and it must be assured that the measuring equipment is able to measure such objects (Sects. 16.1 and 16.2 and Refs. [675–681]).

11.3 Analysis of Impedances of Organic Coatings

The parameters appearing in electrical equivalent models depend on the surface area [473, 474, 479–481]. There are two principal parameters: A_0 , the geometric surface area of the sample, and A_d , the disbonded surface area under the coating. Initially, only pinhole pores perpendicular to the electrode surface are formed without delamination (Fig. 11.1b), C_c is as defined in Eq. (11.1), and

$$R_{\text{po}} = R_{\text{po}}^0 / A_d = \rho d / A_d, \quad (11.4)$$

where ρ is the specific resistivity of the pinhole, and C_d^0 is calculated with respect to the geometric surface area. At this stage, $A_d \ll A_0$. With the increasing delamination of the coating, the parameters must be recalculated with respect to the real surface areas:

Fig. 11.3 Bode magnitude plots resulting from capacitive behavior of coatings corresponding to circuits in Fig. 11.1 a – continuous line, b – dashed line. Parameters:

$$\begin{aligned} R_s &= 100 \, \Omega, \\ C_d^0 &= 5 \times 10^{-8} \, \text{F}, \\ C_c &= 1.1 \times 10^{-10} \, \text{F}, \\ R_{po} &= 10^6 \, \Omega \end{aligned}$$

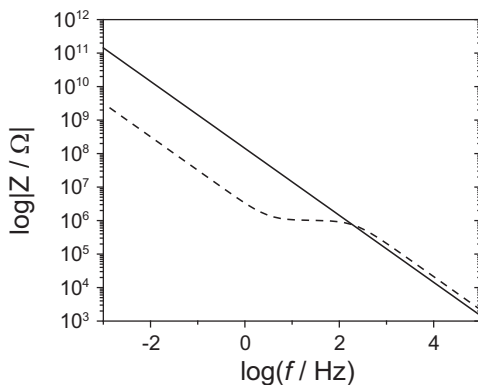
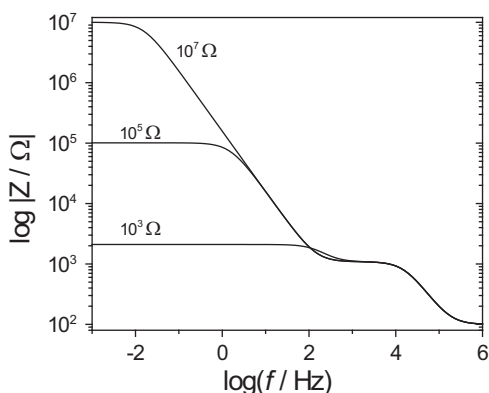


Fig. 11.4 Bode magnitude plots corresponding to disbonding coating (Fig. 11.1e). Parameters:

$$\begin{aligned} R_s &= 100 \, \Omega, C_c = 10^{-8} \, \text{F}, \\ R_{po} &= 10^3 \, \Omega, C_D = 10^{-6} \, \text{F}; \\ R_D &\text{ is indicated in graph} \end{aligned}$$



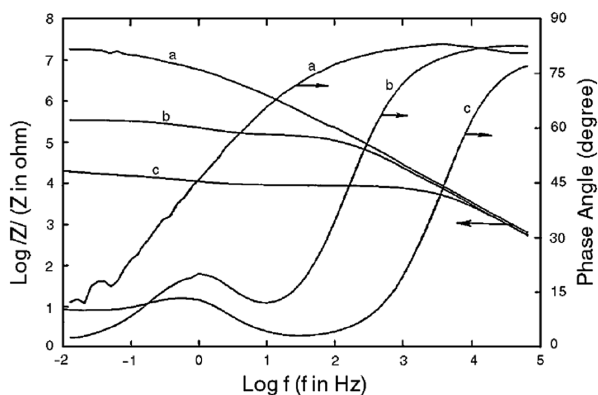
$$\begin{aligned} R_c &= R_c^0 / A_d, \\ C_d &= C_d^0 A_d, \\ C_c &= C_c^0 (A_0 - A_d), \end{aligned} \tag{11.5}$$

where R_c^0 is the specific corrosion resistance of the metal and the value of R_{po} decreases as damage to the coating increases, leading to the solution penetration.

The complex plane plots of the circuits in Fig. 11.1a, b are as those in Figs. 2.32 and 2.35, respectively. In the analysis of coating, usually Bode plots are studied. Bode magnitude plots for circuits in Fig. 11.1a, b are displayed in Fig. 11.3.

The complex plane plots corresponding to the circuits in Fig. 11.1c–e display two semicircles, as in Fig. 2.39. The corresponding Bode plots are shown in Fig. 11.4.

Fig. 11.5 Bode plots of steel coated with alkyd enamel after exposure to 0.5 M NaCl for (a) 43 days, (b) 90 days, and (c) 162 days (Reproduced with permission from NACE International, Houston, TX. All rights reserved; from Ref. [481] © NACE International 1993)



With a decrease in the corrosion resistance, low-frequency impedance decreases, displaying poorer coating protection. A practical example of the accelerated corrosion of coated steel following exposure to concentrated NaCl solution is displayed in Fig. 11.5, where a decrease in the low-frequency resistance from over 10^7 to $10^4 \Omega$ is observed after 162 days.

11.4 Conclusions

EIS has proven to be highly successful in studies of the quality of organic coatings, leading to publication of ISO norms. The alternative electrochemical methods based on corrosion current measurements are not sensitive enough, and methods based on peeling off the coating and inspection of the corrosion are destructive and cannot be applied to the initial stages of degradation. However, care must be taken to assure that the measurements are carried out correctly and the measuring equipment is able to measure very high resistances and low capacitances. Specialized equipment, such as the Solartron 1296 Dielectric Interface, is available commercially.

Chapter 12

Self-Assembled Monolayers, Biological Membranes, and Biosensors

Adsorbed organic layers on surfaces are models for biological bilayers, lipid membranes, and biosensors. EIS is an important tool in the study of these materials. In this chapter, the study of self-assembled monolayers, bilayers, and biosensors will be presented.

12.1 Self-Assembled Monolayers

Self-assembled monolayers (SAMs) [482–484] are usually formed by a spontaneous reaction of alkanethiols with solid metal surfaces (e.g., Au, Ag, Cu). They can also be prepared using the Langmuir-Blodgett method. They form well-ordered, close-packed monolayers and may be applied in the control of wetting and adhesion, chemical resistance, photosensitization, molecular recognition for sensor applications, in fundamental studies of electron transfer, and other applications. The chains might be easily functionalized with various groups, e.g., hydrophilic or redox groups, or become biocompatible. SAMs form a single hydrophobic layer of hydrocarbon chains, usually strongly linked to the metallic support; however, multiple layers might also be deposited. Thiols form chemically bonded monolayers Me-S-R (Fig. 12.1) where metal, Me, is gold.

Usually, quite compact layers are obtained. The simplest electrical equivalent model represents the solution resistance in series with the capacitance of a SAM, R_s , C_{SAM} (Fig. 12.2a). More detailed analysis reveals that the layers are rarely purely capacitive and their capacitance is in parallel with their resistance, R_{SAM} , leading to a circuit: $R_s(C_{\text{SAM}} R_{\text{SAM}})$. Moreover, a diffuse double layer exists at the SAM/solution interface [485, 486]. In such a case, the electrical equivalent circuit contains a diffuse-layer capacitance, C_{dl} , in parallel with the resistance, R_{dl} (Fig. 12.2b).

Fig. 12.1 Schematic representation of SAM at gold substrate

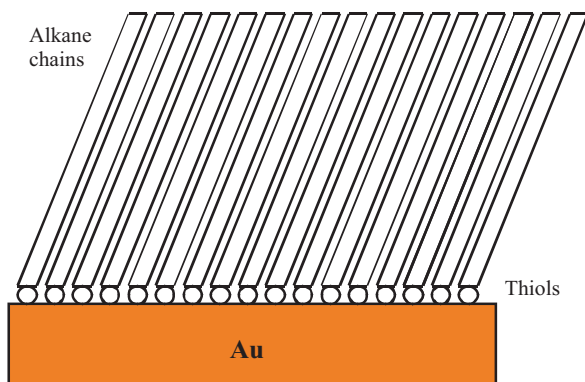


Fig. 12.2 Electrical equivalent circuits of SAMs: (a) simplified model, (b) model including diffuse double layer at SAM/solution interface, (c) SAM in presence of pinholes

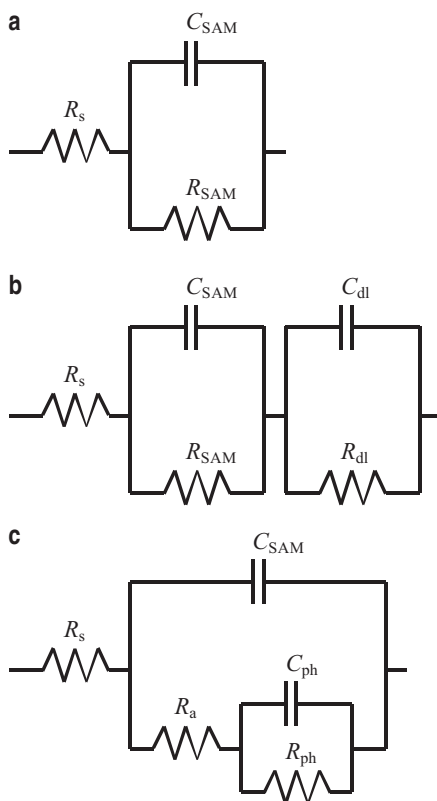
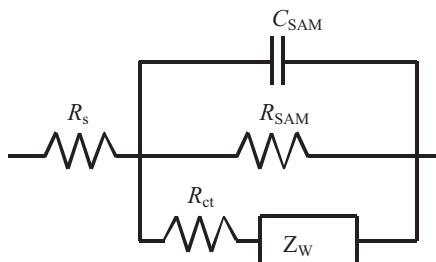


Fig. 12.3 Electrical equivalent system for SAMs with pinholes in presence of redox process



However, double-layer capacitance is usually neglected because it is much larger than that of the SAM (the dielectric constant of the organic layer is much lower than that of water), $C_{dl} \gg C_{SAM}$. In a series connection of capacitances, the resulting capacitance, $1/C_{eq} = 1/C_{dl} + 1/C_{SAM}$, and only a small capacitance, becomes important. In this case, the model reduces to that in Fig. 12.2a. This effect could be more important when ionized groups are attached to alkyl chains [485]. It is interesting to add that the reciprocal of the interfacial capacitance is linear with the number carbon atoms for longer chains, confirming that the capacitance is inversely proportional to the layer thickness [483, 487].

However, the SAMs formed are rarely ideal and they contain small defects called pinholes, e.g., bare metal sites or other defects. In such cases, an additional branch must be added in parallel (Fig. 12.2c) consisting of the resistance, R_a , in series with the parallel connection of the pinhole resistance, R_{ph} , and its capacitance, C_{ph} [488, 489]. The surface coverage of the pinholes is usually very small and does not influence very much the electrode capacitance. The presence of such pinholes can be easily detected using cyclic voltammetry or EIS [483, 490, 491]. The simplified electrical equivalent model of the redox reaction in the presence of pinholes is displayed in Fig. 12.3 [490, 492].

The resistance of SAMs is rarely observed [490]. The faradaic impedance of pinholes represented as charge transfer resistance, R_{ct} , in series with the Warburg mass transfer impedance, Z_W , should be modified to account for the diffusion layer overlap. In fact, an electrode covered with pinholes resembles a microarray electrode [493], and the corresponding impedance developed for microarray electrodes should be used [490, 494, 495]. On well-prepared SAMs a linear relationship between the logarithm of the heterogeneous rate constant, $\ln k_0$ and the number of CH_2 groups exists for thicker layers. Protsailo and Fawcett [492] found such a relationship for SAMs consisting of thiols $\text{C}_9\text{--C}_{18}$ at monocrystalline gold electrodes using $[\text{Ru}(\text{NH}_3)_6]^{3+/2+}$ as a redox species. However, a better model to study electron tunneling through SAMs are SAMs with attached redox centers [483, 496, 497]. Redox processes at SAMs were recently reviewed [498].

EIS allows for a good characterization of SAMs in the absence and presence of redox species in solution and attached to alkyl chains. These studies allowed for testing the theory of electron tunneling. SAMs are also used in biosensors (see below).

12.2 Lipid Bilayers

A lipid bilayer is a thin, polar membrane made of two layers of lipid molecules. These molecules contain one polar group attached to a nonpolar hydrophobic chain and typically contain phospholipids. A schematic diagram of such a bilayer is displayed in Fig. 12.4. In polar solvents, the polar groups are directed toward the solution and hydrophobic tails toward the core of the bilayer. The cell membranes of almost all living organisms and many viruses, as well as the membranes surrounding cell nuclei and other subcellular structures, are made of lipid bilayers [499]. However, most biological membranes are extremely complex structures consisting of hundreds or thousands of different molecules. Bilayer lipid membranes (BLMs) prepared *in vitro* resemble biomembranes and are used as models to understand their functioning. Studies of a planar BLM model system led to their applications in the fields of, for example, specific electrodes, biosensors, biomolecular electronic devices, and solar energy transducers [500, 501].

BLMs may be prepared as supported or freestanding membranes. Membranes deposited on solid supports are easier to prepare and more stable and have been studied extensively [502–508]; however, the use of an unsupported bilayer membrane separating two solutions is more important [509–517]. The resistances of the membranes are large and the capacitances are on the order of approximately $1 \mu\text{F cm}^{-2}$.

The impedance of freestanding membranes may be studied using the system displayed in Fig. 12.5. It uses a homemade differential amplifier. Similar possibilities occur with the use of two potentiostats, allowing for the grounding of the working electrodes (e.g., from Bank Elektronik [518]) or using a Solartron dielectric interface [519, 520].

For a simple planar bilayer membrane the impedance studies produce one semicircle on the complex plane plots according to the model $R_s(R_mC_m)$, from which the resistance, R_m , and capacitance, C_m , of the membrane can be simply determined.

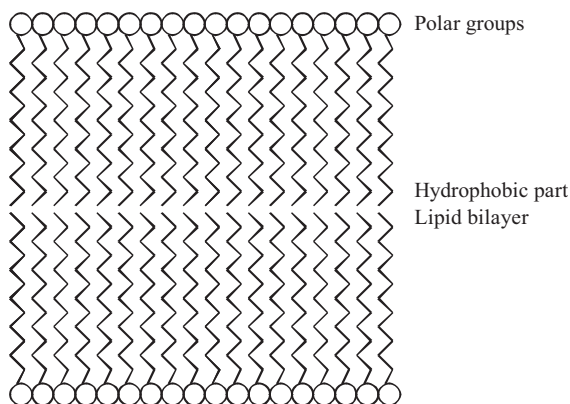


Fig. 12.4 Schematic representation of bilayer lipid membrane

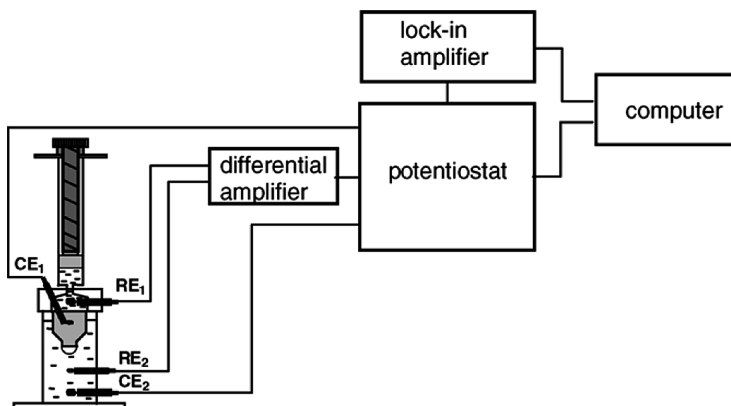


Fig. 12.5 System allowing measurements of membrane impedance containing differential amplifiers (From Ref. [512], copyright (2005), with permission from Elsevier)

Interesting studies were performed on membranes composed of two components, where the formation of complexes or domains was possible [510, 511, 514–516, 521–525].

Let us look at the example of interactions between phosphatidylethanolamine and α -tocopherol in bilayer membranes [515]. In this case, the formation of lipid domains consisting of phosphatidylethanolamine, 1, and phosphatidylethanolamine- α -tocopherol, 3, of a certain composition is observed. Assuming that only these two domains exist in the membrane and that the electrical parameters are additive, one can write an equation for the capacitance and resistance of the membrane:

$$C_m = C_1 c_1^S S_1 + C_3 c_3^S S_3; \quad \frac{1}{R_m} = \frac{1}{R_1} c_1^S S_1 + \frac{1}{R_3} c_3^S S_3, \quad (12.1)$$

where C_1 and C_3 are the capacitance of the membrane composed of pure components 1 and 3 (in F cm^{-2}), R_1 and R_3 are the specific resistances of these components ($\Omega \text{ cm}^2$), c_i^S are the surface concentrations of these components (mol cm^{-2}), and S_i are the surface areas occupied by 1 mol of pure components ($\text{cm}^2 \text{ mol}^{-1}$). Introducing the molar fraction of the components and the relation between surface concentrations,

$$x_1 = \frac{c_1^S}{c_1^S + c_3^S}; \quad x_3 = \frac{c_3^S}{c_1^S + c_3^S}; \quad c_1^S S_1 + c_3^S S_3 = 1, \quad (12.2)$$

and eliminating c_i^S it is possible to obtain relations for the membrane capacitance and conductance:

$$C_m = \frac{C_1 S_1 + (C_3 S_3 - C_1 S_1) x_3}{S_1 + (S_3 - S_1) x_3}; \quad \frac{1}{R_m} = \frac{R_1^{-1} S_1 + (R_3^{-1} S_3 - R_1^{-1} S_1)}{S_1 + (S_3 - S_1) x_3}. \quad (12.3)$$

These equations can be simplified for small values of x_3 to

$$\frac{C_m}{x_3} = \frac{C_1}{x_3} + \frac{(C_3 - C_1) S_3}{S_1}; \quad \frac{1}{R_m x_3} = \frac{1}{R_1 x_3} + \frac{\left(\frac{1}{R_3} - \frac{1}{R_1} \right) S_3}{S_1}. \quad (12.4)$$

These equations represent linear plots versus x_3^{-1} . It was found that these plots were linear, from which the surface area of the domain $S_3 = 320 \text{ \AA}^2$ was determined indicating that a stoichiometry of the phosphatidylethanolamine- α -tocopherol domain of 4:1 was obtained [515]. A similar formalism was used for systems containing three components when 1:1 complexes were formed in the membrane.

Ionic transport across membranes is of fundamental importance in physiology. To model such processes, lipid bilayers without [526] and with the addition of complexing compounds, such as crown ethers [527, 528], valinomycin [508, 513], or gramicidin [502, 504, 529–531], were also studied.

12.3 Biosensors

Biosensors are analytical devices that are able to detect biological components. SAMs and lipid bilayers are often used as platforms for the immobilization of biosensors [532–534], but other supports, such as Si–SiO₂ [535–537], TiO₂ [538], and polymers [539, 540], can also be used. Electrochemical biosensors [541, 542] might use potentiometric, field-effect transistor, amperometric, or impedimetric transducers.

Impedimetric [535, 543–547] biosensors monitor biointeractions using impedance. Biomaterials that can interact with electronic transducers include proteins such as, for example, enzymes, antibodies or antigens, and oligonucleotides or DNA fragments. This is a relatively new domain, and a Scopus search for *impedimetric biosensor* shows less than 200 citations.

Although they have been successfully applied at the academic level, commercial devices are being developed [548, 549]. Impedimetric immunosensors could potentially be used for qualitative purposes, such as, for example, in the detection of bacteria, pregnancy tests, allergy screening tests, etc [546].

Impidimetric biosensors can be:

- a. Capacitive (nonfaradaic), measuring changes in the electrode capacitance in the absence of redox reactions; for example, antibody-antigen interactions cause adsorption and a decrease in the electrode capacitance.

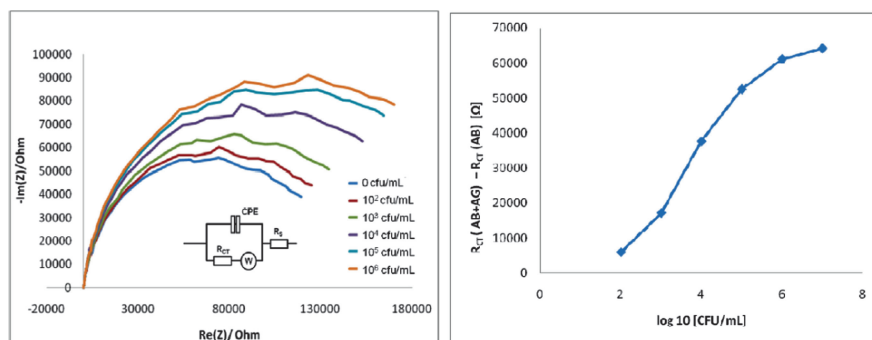


Fig. 12.6 *Left*: Complex plane plots obtained for a sensor with antibodies immobilized by covalent bonding as function of *E. coli* DNA. *Right*: Increase in R_{ct} versus logarithm of concentration. Concentrations are in colony-forming units per milliliter (From Ref. [552], copyright (2009), with permission from Elsevier)

b. Faradaic, in the presence of redox reactions measuring changes in the charge transfer resistance. These changes occur during adsorption/desorption of biomaterials.

In what follows, examples of the application of these methods will be presented. It should be added that these methods might be used in solutions or in microfluidic conditions [547].

An example of a capacitive biosensor is detection nucleic acids. SHARP Laboratories [548, 549] developed low-cost, selective, and multiuse sensors based on gold interdigitated microelectrodes with a microfluidic chamber. Gold electrodes were functionalized with DNA oligonucleotide (complementary to the targets) bound to the surface with thiol groups. They were applied to detect genes from *Escherichia coli* bacteria. An increase in impedance (measured at one frequency) with time was observed as the selective adsorption proceeded. After measurements the chambers were washed and regenerated. The response was nonlinear, and the slopes $\Delta Z/\Delta t$ versus log concentration were analyzed. The detection limit was 5–10 nM for DNA targets.

An inverse process of enzyme-catalyzed dissolution of a polymer coating [550, 551] leads to an easily detected increase in electrode capacitance. Such a process was studied for urea and immunoglobulin G (IgG) [550] and urea and creatinine in serum [551].

An example of redox sensors is a bacteria biosensor [552]. Gold working electrodes were covered with SAMs of mercaptohexadecanoic acid, and antibodies were attached covalently to the surface. $K_3[Fe(CN)_6]$ was used as the redox probe. Bacteria attached to the surface receptor, causing an increase in the charge transfer resistance. The increase in R_{ct} was plotted versus the logarithm of bacteria concentration (Fig. 12.6), and it presented a nonlinear calibration curve with a detection limit of 10–100 colony-forming units/mL.

The use of nanomaterials [545] such as gold nanoparticles and carbon nanotubes increases the sensor surface and enhances analytical detection. The use of PEGylated arginine functionalized magnetic nanoparticles for early detection of cervical cancer has been reported [553]. This sensor displayed good selectivity and sensitively down to 10 cells mL^{-1} .

Impedimetric biosensors represent a new and rapidly developing research area that permit the fast detection of biomaterials. Commercialization of such sensors is only beginning. More applications may be found in recent reviews [535, 543, 544, 546].

12.4 Conclusions

The area of impedance studies of self-assembled monolayers, bilayers, and biosensors is among the recent applications of EIS. They represent an area under development that has interesting fundamental and possibly practical applications. Research in this area falls somewhere between electrochemistry and biology and requires a sound knowledge of both domains. Apparently, knowledge of EIS is often insufficient.

Chapter 13

Conditions for Obtaining Good Impedances

EIS has a great advantage in comparison with other electrochemical techniques because it permits one to validate experimental data, that is, to determine whether obtained data are good [1]. This property arises from Cauchy's integral theorem [3, 554] implying a relation between the real and imaginary components of a complex function. Kramers [555, 556] and Kronig [557] introduced transformations allowing one to calculate the imaginary part from the real part and the real part from the imaginary impedance component. They applied it first to optics. In experimental impedance measurements, if the results obtained from the transformations agree with the experimental data, then one can state that the data are formally correct and are Kramers-Kronig compliant.

13.1 Kramers-Kronig Relations

The Kramers-Kronig relations allow one to calculate the real part of a complex function from the imaginary part and the imaginary part from the real part only. They were initially applied to electrical impedances by Bode [558] and further discussed and applied to EIS [559–568]. To satisfy Kramers-Kronig relations, the complex function must satisfy four criteria, as follows [223, 559–561]:

1. *Linearity*: a system is linear when its response to a sum of individual input signals is equal to the sum of the individual responses: $L(af_1 + bf_2) = aL(f_1) + bL(f_2)$. This condition implies that the system is described by a system of linear differential equations. Electrochemical systems are usually highly nonlinear, and the impedance is obtained by linearization of equations using small amplitudes of the applied perturbation. In addition, for linear systems responses are independent of the amplitude. This condition can be easily verified experimentally: one should decrease the applied amplitude twice and compare the results. If the obtained impedance is the same, the system is linear.

2. *Causality*: the response of a system must be entirely determined by the applied perturbation, that is, the output depends only on the present and past input values. A causal system cannot predict its future because its future is determined by the past events. This also means that the system does not generate noise independently of the applied signal for $t \geq 0$. Causal systems are called physically realizable systems. If a system is at rest and a perturbation is applied at $t = 0$, then the response must be constrained for $\omega \rightarrow 0$. In addition, the response must be zero at $\omega \rightarrow \infty$. However, in electrochemical systems, a weaker condition can be applied requiring that the transfer function be bounded.
3. *Stability*: the stability of a system is determined by its response to inputs. A stable system remains stable until excited by an external source, and it should return to its original state once the perturbation is removed, that is, the system cannot supply power to the output irrespective of the input. In other words, the total energy generated by the system cannot exceed the total input energy. A consequence of this condition is that the transfer function is bounded, i.e., $|Z(\omega)|^2 < A$, where A is a constant. A system is stable if its response to the impulse excitation approaches zero after a long time or when every bounded input produces a bounded output. The impedance $Z(s)$ must satisfy the following conditions: $Z(s)$ is real when s is real (that is, when $\omega \rightarrow 0$) and $\text{Re}[Z(s)] \geq 0$ when $\nu \geq 0$ (where $s = \nu + j\omega$). This last condition ensures that there are no negative resistances in the system. Impedance measurements must also be stationary, that is, the measured impedance must not be time dependent. This condition may be easily checked by repetitive recording of the impedance spectra and comparison of the obtained results, which should be identical.
4. *Finiteness*: this condition was already implied earlier. It means that the real and imaginary components of the impedance must be finite-valued over the entire frequency range $0 < \omega < \infty$. In particular, the impedance must tend to a constant real value for $\omega \rightarrow 0$ and $\omega \rightarrow \infty$.

Although these relations will be written below for impedances they also hold for admittances and other complex transfer functions. Assuming that all the aforementioned conditions are met, the Kramers-Kronig relations are obtained allowing the calculation of the imaginary impedance from the real part:

$$Z''(\omega) = -\left(\frac{2\omega}{\pi}\right) \int_0^{\infty} \frac{Z'(x) - Z'(\omega)}{x^2 - \omega^2} dx \quad (13.1)$$

and the real from the imaginary:

$$Z'(\omega) = Z'(\infty) + \frac{2}{\pi} \int_0^{\infty} \frac{xZ''(x) - \omega Z''(\omega)}{x^2 - \omega^2} dx, \quad (13.2)$$

$$Z'(\omega) = Z'(0) + \int_0^{\infty} \frac{\left(\frac{\omega}{x}\right) Z''(x) - Z''(\omega)}{x^2 - \omega^2} dx. \quad (13.3)$$

There are also similar relations for the phase angle and modulus [3]:

$$\varphi(\omega) = \left(\frac{2\omega}{\pi}\right) \int_0^{\infty} \frac{\ln|Z(x)|}{x^2 - \omega^2} dx, \quad (13.4)$$

$$\ln|Z(\omega)| = \frac{2}{\pi} \int_0^{\infty} \frac{\varphi(x)}{x - \omega} dx. \quad (13.5)$$

Several other forms of these relations can be found in the literature [3]. Although the preceding equations were written for impedances, *they are valid for any complex transfer function*. Kramers-Kronig relations are very restrictive, and in EIS some of them might be slightly relaxed, and instead of the impedances, the admittances can be used. This will be discussed in what follows.

Kramers-Kronig relations demand integration in a wide frequency range from zero to infinity, which is experimentally impossible. They are also sensitive to stochastic errors, ε , and the average value of the errors of the real, ε' , and imaginary, ε'' , parts must be equal to zero as well as the average value of the integral [273]:

$$E \left\{ \frac{2\omega}{\pi} \int_0^{\infty} \frac{\varepsilon'(x)}{x^2 - \omega^2} dx \right\} = 0. \quad (13.6)$$

Various methods have been proposed to carry out Kramers-Kronig transformations in practice; they are described in what follows.

13.1.1 Polynomial Approximation

One method is to approximate real and imaginary impedances as functions of the frequency by polynomials in ω [560, 561, 568, 569],

$$Z(\omega) = a_0 + a_1\omega + a_2\omega^2 + a_3\omega^3 + \dots = \sum_{i=0}^n a_i\omega^i, \quad (13.7)$$

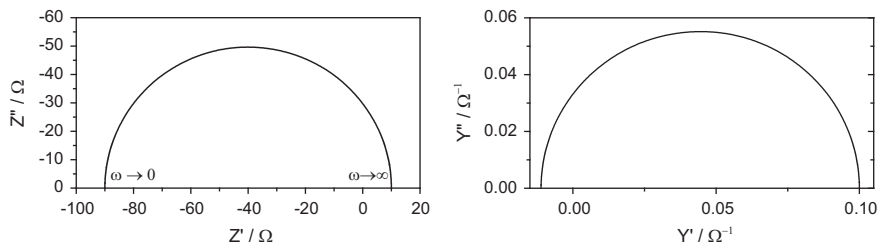


Fig. 13.1 Complex plane impedance and admittance plots for circuit in Fig. 2.34 with $R_s = 10 \Omega$, $C = 10^{-5} \text{ F}$, and $R = -100 \Omega$

or $\log \omega$ [564],

$$Z(\omega) = a_0 + a_1 \log \omega + a_2 (\log \omega)^2 + a_3 (\log \omega)^3 + \dots = \sum_{i=0}^n a_i (\log \omega)^i, \quad (13.8)$$

and subsequent integration of the polynomials using Eqs. (13.1), (13.2), and (13.3). Approximation by splines can also be used. However, there are two problems with this integration. First of all, integrations should be carried out in a frequency range from zero to infinity. Because experimental data are acquired in a limited frequency range, extrapolation must be carried out outside the experimental limits. In certain cases (e.g., one or two semicircles), one knows these limits and the extrapolation is easier. However, in some cases one does not know how the impedance should behave outside the experimental range, and the extrapolation might be doubtful. Integration in a more narrow frequency range could lead to significant errors [570]. Approximation by splines is not well suited for extrapolation outside the experimental frequency range.

Another problem is related to the discontinuity of the integrated function at $x = \omega$. Several authors have proposed a distribution of $1/(x^2 - \omega^2)$ in series around the point $x = \omega$ and an integration of the sum of the elements [560, 561, 563, 570].

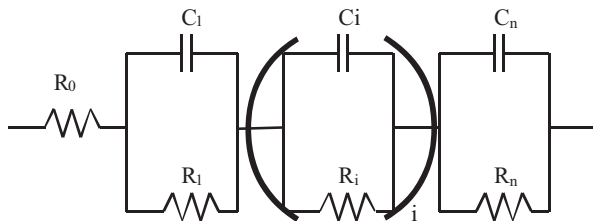
Although in principle Kramers-Kronig relations demand that the impedance have a finite value at $\omega = 0$ and $\omega \rightarrow \infty$, it has been shown that the CPE

$$\hat{Z} = \frac{1}{(j\omega)^\phi T} \quad (13.9)$$

transforms correctly for $-1 \leq \phi \leq 1$, including the Warburg impedance ($\phi = 0.5$) [561, 563, 571].

System with negative resistance cannot be represented by a passive circuit with positive R, L, and C elements. The stability criterion demands that there be no negative impedances in the system (rule 3 of Kramers-Kronig conditions). For example, the system shown in Fig. 13.1 contains negative resistance, and its impedance is not transformable. However, Kramer-Kronig transforms can also be applied to admittances. Admittance calculated for this case is also shown in Fig. 13.1, and it is perfectly Kramers-Kronig transformable. Moreover, infinite impedance corresponds to zero admittance which is transformable. This topic will be further discussed in Sect. 13.3.4.

Fig. 13.2 Voigt circuit consisting of $n(RC)$ elements



13.1.2 Checking Kramers-Kronig Compliance by Approximations

It is possible to replace the Kramers-Kronig integration by approximation. If the system can be well approximated by a linear circuit, then it must be Kramers-Kronig transformable. Orazem and coworkers [572, 573] proposed using the Voigt circuit displayed in Fig. 13.2.

Each element of this circuit consists of the connection of R and C in parallel, and it is, of course, transformable; therefore, their sum is also transformable. The impedance of the Voigt circuit is described by the following equation:

$$\hat{Z} = R_0 + \sum_{i=1}^n \frac{R_i}{1 + j\omega\tau_i} \quad (13.10)$$

where $\tau_i = R_i C_i$ is the time constant of element i of the circuit. Using a sufficient number of such elements the CPE or Warburg elements can also be approximated [572]. To approximate circuits containing inductances, negative values of R_i may be used keeping the time constants positive [572]. The number of Voigt elements necessary for a correct approximation depends on the system random errors: the greater the errors, the smaller the number of necessary elements.

Boukamp and Macdonald [574] and Boukamp [575] proposed fitting impedances to a Voigt circuit with a fixed distribution of time constants, taking six to seven time constants per decade or simply the time constant equal to the inverse of the experimental frequency ω_i , $\tau_i = 1/\omega_i$; in the latter case, a perfect approximation is obtained even in the presence of the experimental noise, which should, in principle, be avoided. By fixing the values of τ_i , the only unknown parameters in Eq. (13.10) are R_i . The CNLS approximation becomes linear and no initial guess of parameters R_i is necessary (Chap. 14). The approximating function becomes

$$\begin{aligned} \hat{Z}(\omega_k) &= R_0 + \sum_{i=1}^n \frac{R_i}{1 + j\omega_k\tau_i} = \\ &= R_0 + \sum_{i=1}^n \frac{R_i}{1 + (\omega_k\tau_i)^2} - j \sum_{i=1}^n \frac{\omega_k\tau_i R_i}{1 + (\omega_k\tau_i)^2}. \end{aligned} \quad (13.11)$$

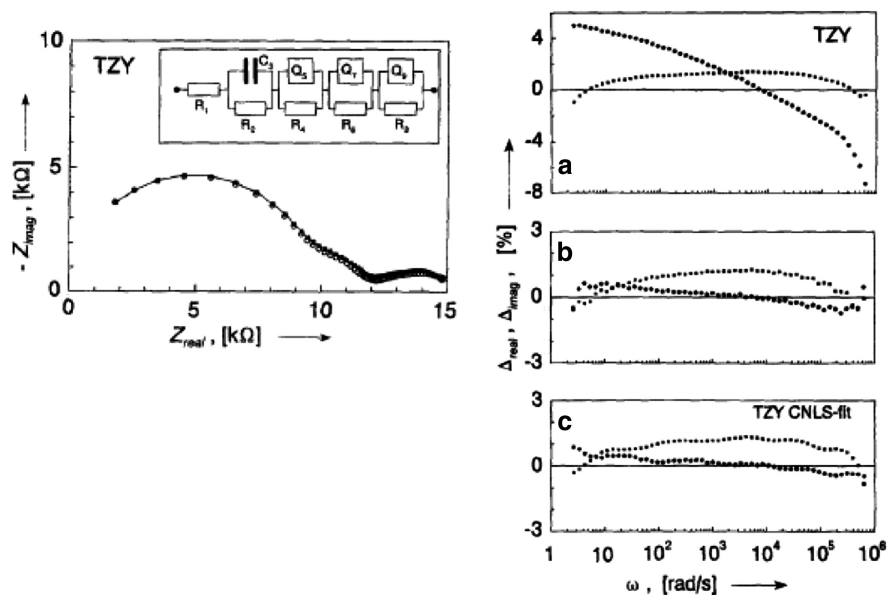
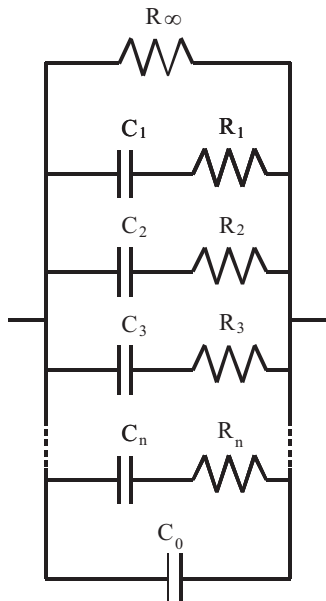


Fig. 13.3 Example of experimental data for solid electrolyte that are not Kramers-Kronig transformable, *left*, and residual plots: (a) real to imaginary and imaginary to real, (b) relative errors of complex transformation, and (c) errors of CNLS fit to model in (a); *circles*: real-to-imaginary; *squares*: imaginary-to-real transformations (From Ref. [575] Reproduced with permission of Electrochemical Society)

In the approximation, Boukamp suggested using modulus weighting. Moreover, in some cases it might be necessary to add inductance or capacitance in series with R_0 . Boukamp [575] presented an example of non-Kramers-Kronig-transformable data analyzed by CNLS fit (Fig. 13.3), where the symbol Q_i denotes a CPE. It is not evident from the complex plane plot if the impedance data are really transformable. To answer this question, the residual plots of the real and imaginary impedances, $\Delta = Z_{\text{exp}} - Z_{\text{transformed}}$, should be inspected. They are also presented in Fig. 13.3. It is evident that the differences are systematic, not random, and cannot be ascribed to random errors. This means that the impedance in Fig. 13.3a is not Kramers-Kronig transformable. In fact, it was found that steady state was not reached in the experiment, and the material properties changed with time.

In the case of blocking electrodes, the impedance increases to infinity as the frequency approaches zero. In such cases, approximation with the Voigt circuit is not appropriate. When a high-frequency impedance is finite, the easiest way to verify the Kramers-Kronig compliancy is to fit the impedances to the admittance representation of the circuit containing a ladder of (RC) element series (Fig. 13.4) [575]. In addition, capacitance, C_0 , or inductance can be added in parallel.

Fig. 13.4 Circuit proposed for fitting admittance of blocking electrodes



The admittance of this circuit at a frequency ω_k is

$$\begin{aligned} \hat{Y}(\omega_k) &= \frac{1}{R_\infty} + \sum_{i=1}^n \frac{1}{R_i + \frac{1}{j\omega_k C_i}} + j\omega_k C_0 = \\ &= \frac{1}{R_\infty} + \sum_{i=1}^n \frac{\omega_k^2 \tau_i C_i}{1 + (\omega_k \tau_i)^2} + j \left(\sum_{i=1}^n \frac{\omega_k C_i}{1 + (\omega_k \tau_i)^2} + \omega_k C_0 \right), \end{aligned} \quad (13.12)$$

where the values of ω_k are predefined (six to seven per decade). An example of such a test is shown in Fig. 13.5. Fewer than seven time constants per decade are necessary to approximate well the experimental admittances.

The conditions necessary for the Kramers-Kronig transform demand that the resistances be all positive. The values of R_i might be negative, but the corresponding C_i must also be negative to produce positive values of time constants [304]. However, in experimental work, negative dynamic impedances may appear, although they might lead to a stable dynamic response (see subsequent discussion on the Nyquist criterion of stability). Boukamp [575] suggested that to avoid this problem, one could add computationally a parallel resistance to the dispersion data so that the negative resistance is removed completely. An example of such an operation is displayed in Fig. 13.6. It is evident from plot b that the computational addition of the parallel resistor of 400 Ω eliminates negative resistance. However, such a procedure is not necessary, as shown in Sect. 13.3.4.

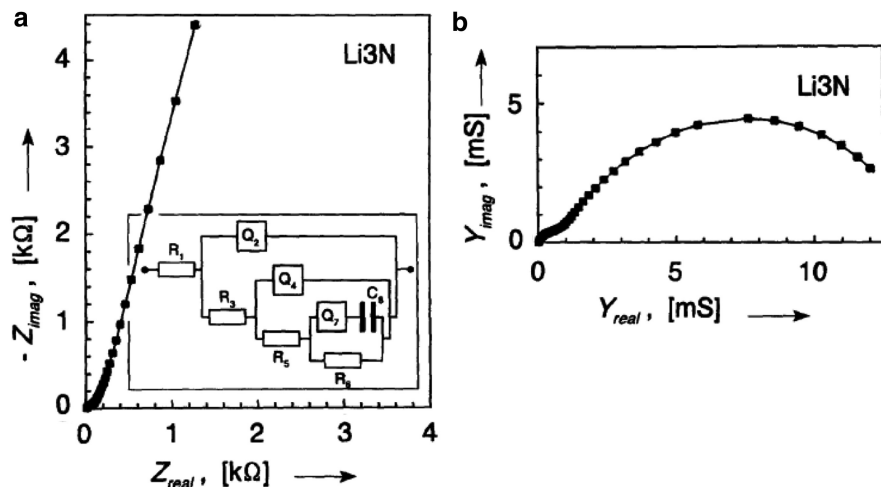


Fig. 13.5 Complex plane impedance and admittance plots for hydrogen-doped Li_3N monocrystals; (a) impedance plot and fit to model indicated in *inset*; (b) admittance plot and fit to Eq. (13.12); points experimental, line fits (From Ref. [575] Reproduced with permission of Electrochemical Society)

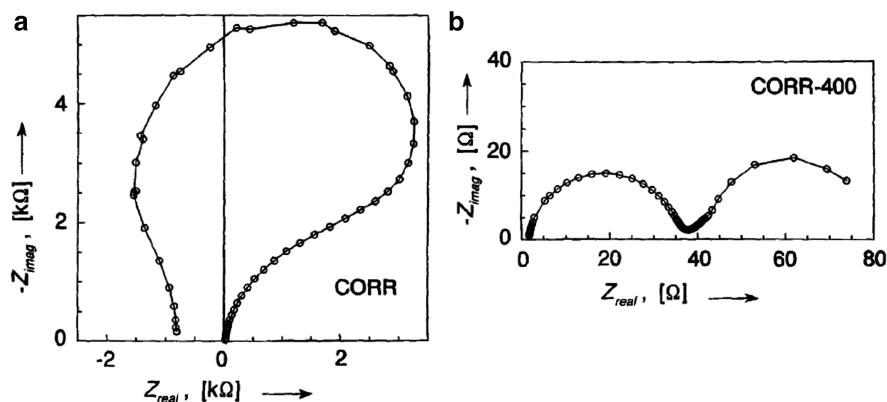


Fig. 13.6 Impedance of corroding Cr electrode; (a) experimental data, (b) experimental data with computational addition of parallel resistance of 400 Ω (From Ref. [575] Reproduced with permission of The Electrochemical Society)

Analysis of the plot in Fig. 13.6b using linear approximation, Eq. (13.11), is displayed in Fig. 13.7. Note that important deviations appear at $\omega > 10^3 \text{ rad s}^{-1}$. In further analysis, these data points were eliminated without any important loss of information in the high-frequency zone in Fig. 13.6a [575].

It should be stressed that approximations by Eq. (13.11) or Eq. (13.12) are used only for testing the compliance with the Kramers-Kronig transforms, and the parameters found have no physical meaning.

Fig. 13.7 Relative residuals for complex linear fit of data in Fig. 13.6b using 7.6 time constants per decade (From Ref. [575] Reproduced with permission of Electrochemical Society)

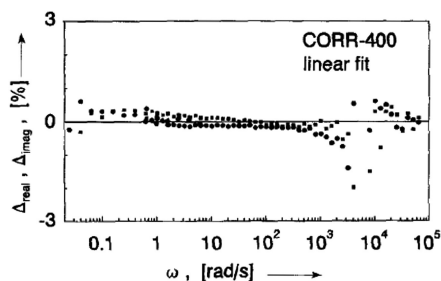
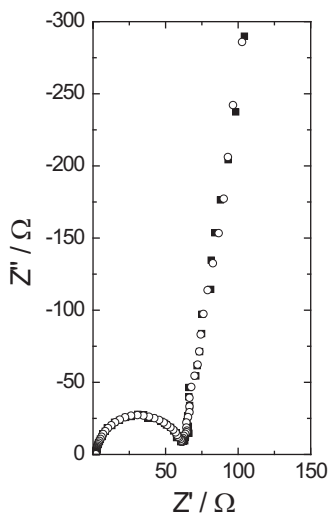


Fig. 13.8 Original (*squares*) and transformed (*open circles*) data in noise data file

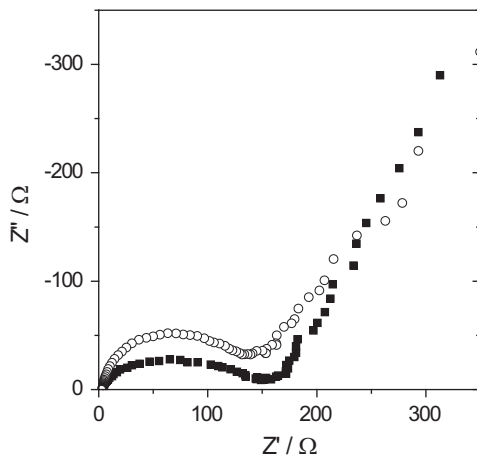


Boukamp has prepared a simple and easy-to-use program, KKtest, which uses Eq. (13.11) or Eq. (13.12) to check the validity of data. It is available on the Internet [576] and presented in Example 13.1 (see also Exercise 13.2 and 13.3).

Example 13.1 Check the Kramers-Kronig compliance of the data including noise and including drift using KKtest. A comparison of the original data with added random noise and KK transformed data is displayed in Fig. 13.8. Transformed data display no systematic differences from the original data, and one can say that the data are Kramers-Kronig compliant. The same may also be observed on the differences graph also displayed in the KKtest program.

Next the data drift should be analyzed. A comparison of the original and transformed data is shown in Fig. 13.9. It is evident that the original and transformed data are very different, which means that the original data are not Kramers-Kronig compliant and cannot be used for further analysis. Such systematic deviations are also observed on the difference graphs, see Exercises 13.2 and 13.3.

Fig. 13.9 Original (*squares*) and transformed (*open circles*) data in drift data file



13.2 Linearity

The linearity of the observed impedance is directly related to the amplitude of the ac signal applied to the system. Electrochemical systems are intrinsically nonlinear, and a sufficiently small amplitude is necessary to linearize such systems. Smith [29] suggested using an amplitude of $\leq 8/n$ mV peak to peak. A more detailed analysis was performed by Hirschorn et al. [577] and Hirschorn and Orazem [578] taking into account differences in the transfer coefficients and solution resistance. Assuming a simple model of the redox system without diffusion (Fig. 4.2) that is with negligible mass transfer impedance Z_W , the maximum ac voltage amplitude causing an error of $\leq 0.5\%$ is [577]

$$\Delta E = 0.2 \sqrt{\frac{k_f b_f + k_b b_b}{k_b b_f^3 + k_b b_b^3} \left(1 + \frac{R_s}{R_{t,obs}}\right)}, \quad (13.13)$$

where $b_i = \alpha_i n f$, α_i is the transfer coefficient, n is the number of electrons exchanged, $f = F/RT$, the indices f and b indicate forward and backward reactions, respectively, R_s is the solution resistance, and $R_{t,obs}$ is the charge transfer resistance. Because of the solution resistance, the actual potential applied to the electrode is lower than that used by the instrument, and this value depends on the frequency. For a case where the transfer coefficient $\alpha_f = 0.5$ and assuming $R_s \ll R_{t,obs}$ and $k_f = k_b$, the maximum amplitude for $n = 1$, ΔE , is 10 mV, while for $\alpha_f = 0.2$ it is 7.1 mV and depends on the slope of the current-potential curve. At high frequencies, the circuit reduces to a simpler ($R_s C_{dl}$) model, and a characteristic frequency for the transition from low- to high-frequency behavior is [578]

$$f_t = \frac{1}{2\pi R_{t,obs} C_{dl}} \left(1 + \frac{R_{t,obs}}{R_s} \right). \quad (13.14)$$

Application of Kramers-Kronig transforms reveals that they are not very sensitive to system nonlinearities [561]. Experimentally, nonlinearity affects the charge transfer resistances, which decrease with increases in the amplitude [561, 578–580]. However, it has been shown that when the experimental frequency passes through the transition frequency, Eq. (13.14), the Kramers-Kronig transforms will be affected by the nonlinearity of the system.

It seems that the simplest way to check for nonlinearity is to take measurements at different amplitudes and compare the obtained impedances, which should be identical for linear systems. In general, a 5 mV amplitude is recommended; however, in certain conditions, it might be different; Eq. (13.13) gives a good indication in simple conditions, but more information about the system kinetics is necessary.

13.3 Stability

13.3.1 Drift

One of the biggest problems in impedance measurements is related to changes in a system with time. This effect appears when surface conditions or electrode contamination evolves with time. An example of a corroding system in which a slow potential sweep was applied during the experiment is displayed in Fig. 13.10. This potential sweep simulates changes in the surface conditions of the corroding electrode. A Kramers-Kronig transform easily detects such changes. Transforms of

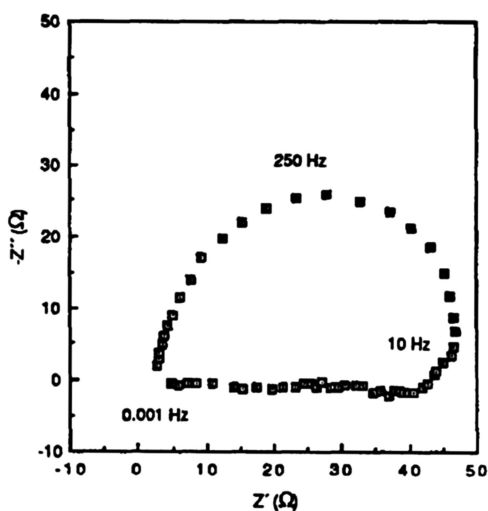
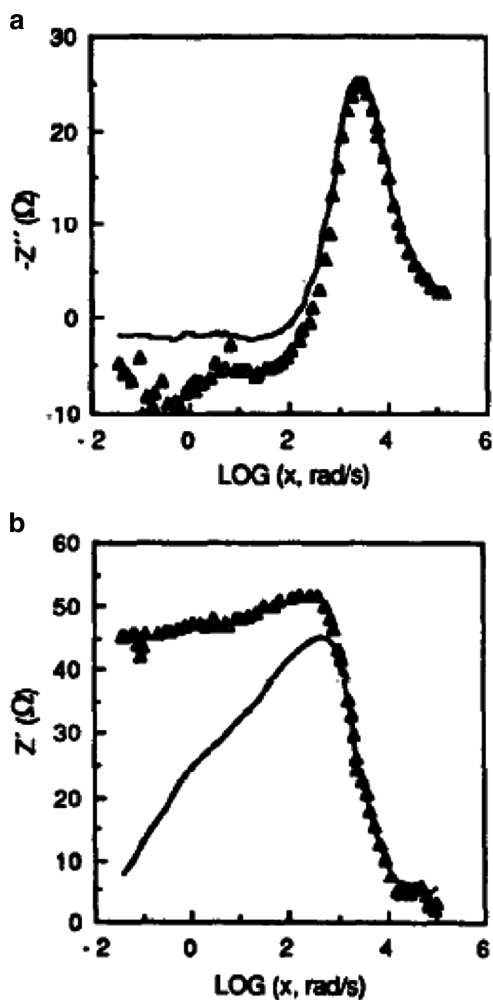


Fig. 13.10 Impedance of corroding iron electrode with superimposed potential sweep of 0.133 mV s^{-1} (From Ref. [561], copyright (1990), with permission from Elsevier)

Fig. 13.11 Kramers-Kronig transforms, (a) real to imaginary and (b) imaginary to real, of data in Fig. 13.10 (From Ref. [561], copyright (1990) with permission from Elsevier)



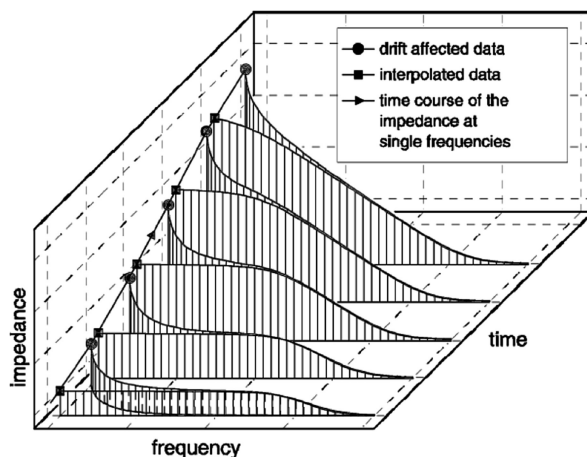
the experimental data in Fig. 13.10 are shown in Fig. 13.11. At low frequencies, which take much more time during measurements, strong deviations are observed. The influence of drift was recently simulated and discussed [579].

An odd harmonic test [125, 580] was also proposed in the literature to check system linearity.

13.3.2 Dealing with Nonstationary Impedances

In practice, there are often cases where impedance changes continuously with time. Such changes are observed in, for example, cases of active corrosion, fuel cell poisoning, and surface changes. In these cases, during the frequency sweep, each

Fig. 13.12 Experimental impedance data (*circles*) and method of obtaining time-invariant impedances (*squares*) (From Ref. [585] with permission of Royal Society of Chemistry)

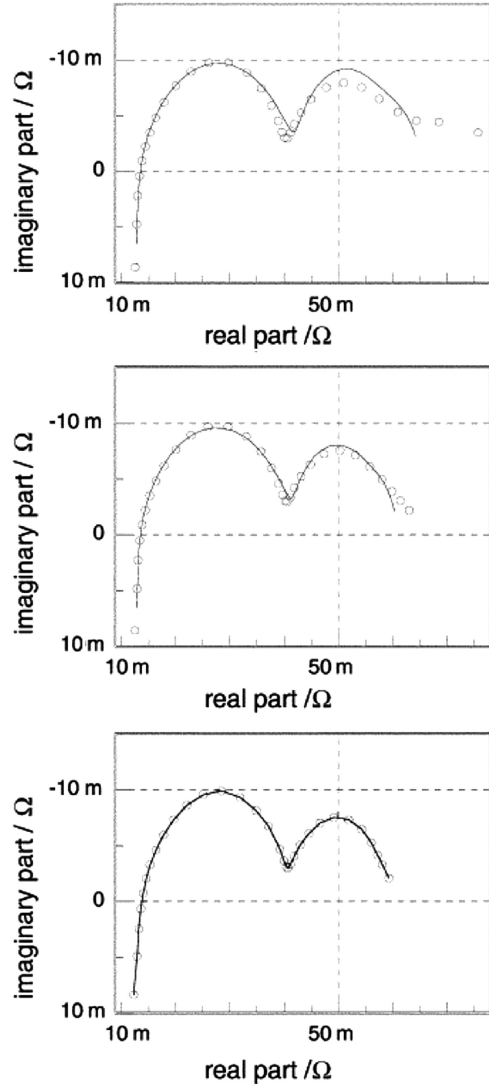


measurement corresponds to a new electrode state. The theoretical foundations of nonstationary systems were established by Stoykov and coworkers [581–584]; however, they were applied to simulated data only. Wagner and coworkers [585, 586] proposed a relatively simple interpolation method dealing with such systems. They recorded a series of impedance measurements at distinct time intervals, i.e., the time of each measurement at one frequency was assumed to be short and known. Then three-dimensional plots of impedance versus frequency and time were constructed (Fig. 13.12). The experimental impedances (circles) were first plotted as a function of frequency and time. Then data at each frequency were interpolated versus time (see an example of one line at the lowest frequency in Fig. 13.12), and impedances were found at a given time. This interpolation could supply impedances at various times. Such interpolation should be repeated at all frequencies. It is obvious that data at the lowest frequencies are most affected by drift because they take longer to be recorded. Such a procedure should be repeated for real/imaginary or magnitude/phase angle data. Although in general a smoothing function could be used for data interpolation at one frequency, the authors found that in their case a linear interpolation was sufficient. To further refine the obtained data, a Z-HIT transform (see Sect. 3.14) was applied, and the results from this transformation were used for analysis. An example of the results is displayed in Fig. 13.13.

13.3.3 Stability of Electrochemical Systems

In this section we will look in more detail at system stability [587]. In control system theory, a stable system is one that produces a bounded response to a bounded input. In general, system stability depends on the properties of the transfer function, in this case of the impedance or the admittance [588]. Impedance and

Fig. 13.13 Complex plane plots illustrating compensation of time drift for fuel cell under galvanostatic control, *top* – directly measured impedance, *middle* – after extrapolation procedure, *bottom* – after additional Z-HIT refinement; *continuous lines* – approximations (From Ref. [585] with permission of Royal Society of Chemistry)



admittance are defined as a ratio of the Laplace transforms of the potential and current:

$$\hat{Z}(s) = \frac{1}{\hat{Y}(s)} = \frac{\overline{E}(s)}{\overline{i}(s)}, \quad (13.15)$$

where the parameter $s = \sigma + j\omega$ is a complex number. Let us suppose that the potential is applied and the current is measured. Moreover, let us assume that the potential is simply Dirac's delta function, $\delta(t)$, applied at $t = 0$. Its Laplace transform is

$$L[\delta(t)] = 1 \text{ V/s}, \quad (13.16)$$

and the current in the Laplace domain is

$$\bar{i}(s) = \frac{1}{\hat{Z}(s)} = \hat{Y}(s) = \frac{K \prod_{m=1}^M (s - \mu_m) \prod_{n=1}^N [s^2 - 2v_n s + (v_n^2 + \beta_n^2)]}{\prod_{q=1}^Q (s - \lambda_q) \prod_{r=1}^R [s^2 - 2\rho_r s + (\rho_r^2 + \omega_r^2)]}, \quad (13.17)$$

where the admittance is represented as a ratio of two polynomials factored in linear and quadratic terms. Quadratic terms having real zeros (the delta of the quadratic equation is larger than zero) can always be presented in the form $s - \lambda_q$; however, when delta is negative, complex roots appear. The admittance has $M + N$ zeros and $Q + R$ poles, while the impedance has $M + N$ poles and $Q + R$ zeros. The parameters μ_m , v_n , β_n , λ_q , ρ_r , and ω_r are constants. The zeros of the admittance are

$$s = \mu_m \quad \text{and} \quad s = v_n \pm j\beta_n, \quad (13.18)$$

and the poles are

$$s = \lambda_q \quad \text{and} \quad s = \rho_r \pm j\omega_r. \quad (13.19)$$

Therefore, there are real and complex conjugated zeros and roots. Examples of such polynomials representing the impedance of a system were presented, for example, in Eq. (2.91) for an R - C connection, Eq. (2.94) for an R - L connection, and Eq. (2.97) for an R - L - C connection in series. This expression can be simplified into partial fractions:

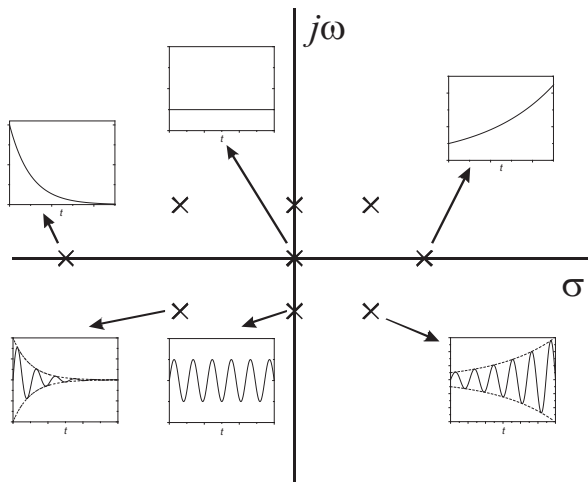
$$\bar{i}(s) = \hat{Y}(s) = \frac{1}{\hat{Z}(s)} = K \left[\sum_{q=1}^Q \frac{A_q}{s - \lambda_q} + \sum_{r=1}^R \frac{B_r}{s^2 - 2\rho_r s + (\rho_r^2 + \omega_r^2)} \right], \quad (13.20)$$

where A_q and B_r are called residues. The inverse Laplace transform gives the dependence of the current as a function of the potential:

$$i(t) = K \left[\sum_{q=1}^Q A_q \exp(\lambda_q t) + \sum_{r=1}^R B_r \frac{1}{\omega_r} \exp(\rho_r t) \sin(\omega_r t) \right]. \quad (13.21)$$

When the poles λ_q are negative, the current relaxes to zero and the system is stable. In the case of complex poles, Eq. (13.19), ρ_r must be negative or zero, that is, the real part of the root cannot be negative to assure stability. Solutions for different values of λ_q and ρ_r are presented in Fig. 13.14. Stable systems are obtained only when these values are negative or zero. When $\lambda_q = 0$, a time-independent constant

Fig. 13.14 Transients obtained for different positions and nature of poles at s -plane



signal is obtained, and when $p_r = 0$, a steady-state oscillation is produced. The poles and zeros of Eq. (13.17) are presented on the s -plane, where the x -axis is real (σ) and y -axis imaginary ($j\omega$). System theory [587] holds that a necessary and sufficient condition for a system to be stable is that all poles of the transfer function must have negative real parts. If some roots are positive, then the system becomes unstable as its response becomes unbounded. The preceding conditions apply to the system transfer function, which in Eq. (13.17) is written as the admittance. However, in electrochemistry, the impedance is usually studied. Therefore, the admittance transfer function should have all poles negative, which indicates that all zeros of the impedance should be negative. The admittance/impedance transfer function is usually written in the form

$$\hat{Z}(s) = K \frac{\prod_{i=1}^{N_z} (s - z_i)}{\prod_{k=1}^{N_p} (s - p_i)}, \quad (13.22)$$

where there are N_z zeros z_i and N_p poles p_i . A few examples are given in what follows.

Let us consider a simple circuit $R_0(R_1C_1)$, shown in Fig. 2.26. Its impedance is described by Eq. (2.128), which can be rearranged into the following form, Eq. (13.22):

$$\hat{Z}(s) = R_0 + \frac{1}{sC_1 + \frac{1}{R_1}} = \frac{R_0 \left[s + \frac{1}{C_1} \left(\frac{1}{R_0} + \frac{1}{R_1} \right) \right]}{s + \frac{1}{R_1C_1}}. \quad (13.23)$$

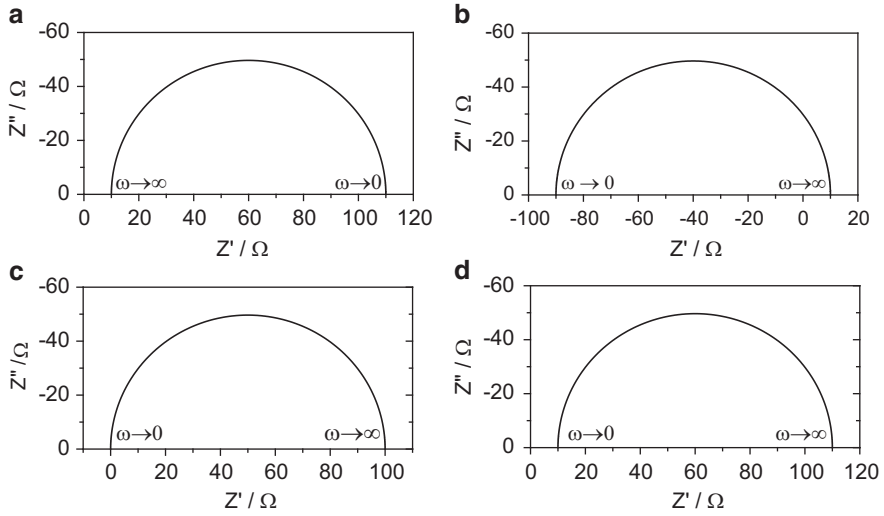


Fig. 13.15 Complex plane plots for a simple circuit $R_0(R_1C_1)$ consisting of resistance R_0 in series with parallel connection of capacitance C_1 and resistance R_1 , Eq. (13.23); parameters: $C_1 = 2 \times 10^{-5}$ F, (a) $R_0 = 10 \Omega$, $R_1 = 100 \Omega$, (b) $R_0 = 10 \Omega$, $R_1 = -100 \Omega$, (c) $R_0 = 100 \Omega$, $R_1 = -100 \Omega$, (d) $R_0 = 110 \Omega$, $R_1 = -100 \Omega$

This function has one pole,

$$p = -\frac{1}{R_1C_1}, \quad (13.24)$$

and one zero,

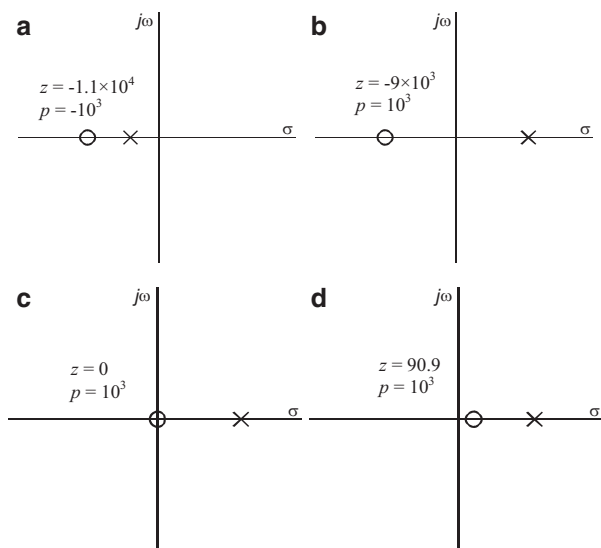
$$z = -\frac{1}{C_1} \left(\frac{1}{R_0} + \frac{1}{R_1} \right). \quad (13.25)$$

If all circuit parameters are positive, then the pole and zero are negative and the system is stable. For the impedances in Fig. 13.15 the poles and zeros are displayed on the s -plane in Fig. 13.16. When all the circuit parameters are positive, the poles and zeros are always negative. The complex plane plot in this case, which displays well known behavior, is shown in Fig. 13.15a.

Let us now assume that $R_{ct} < 0$. There are a few different cases, depending on the relative values of R_0 and R_1 .

When $R_0 < -R_1$, the zero-frequency impedance is negative, $R(\omega = 0) = R_0 + R_1 < 0$, the complex plane plot is shown in Fig. 13.15b, and the zero and pole are shown in Fig. 13.16b. The impedance zero is negative, the pole is positive, and therefore the system is stable.

Fig. 13.16 Representation of poles (X) and zeros (O) of impedance on s -plane; parameters as in Fig. 13.15; poles, p , and zeros, z , are in units s^{-1}



When $R_0 = -R_1$, the low-frequency resistance is zero, $R(\omega = 0) = 0$ (Fig. 13.15c). This means that the steady-state current does not perceive any resistance. This leads to a so-called saddle-node bifurcation [588–592]. Such a situation can be obtained for the system in Fig. 13.15b after adding an external resistor in the working electrode connection. A saddle-node bifurcation indicates that there are at least two stationary states and a hysteresis on current-potential characteristics due to nonlinearities in the system exists [590]. Such a behavior is observed, for example, in ethanol oxidation where negative resistances are detected [593, 594]. By adding an external resistance, a sharp peak appears in the reverse sweep of the cyclic voltammograms [595]. The position and shape of this peak are very sensitive to the value of the resistance in the working electrode circuit. At some point, the external resistance compensates the negative low-frequency resistance and the current starts to increase rapidly (Fig. 13.17) [595]. Although at some point the impedance at zero frequency becomes zero, surface conditions change and the current cannot reach infinity.

When $R_0 > -R_1$, both $R(\omega = 0)$ and $R(\omega = \infty)$ are positive, but the direction of the frequencies is opposite to that in Fig. 13.15a. Both the zero and the pole are positive, and the system is unstable.

Let us look at some other examples of a circuit containing a series connection of two (RC) elements in parallel and displaying two semicircles, as in Fig. 2.37, left. Let us assume that one resistance related to the low-frequency loop is negative, similar to that shown earlier in Fig. 5.3d for a system with one adsorbed species. An example of the complex plane plots obtained at different values of the resistance R_0 are displayed in Fig. 13.18. The impedance of this circuit is described as

Fig. 13.17 Cyclic voltammograms at Pt in 1 M EtOH and 0.5 M H₂SO₄ measured directly and after adding various resistances to working electrode connection; sweep rate 50 mV s⁻¹ (From Ref. [595], copyright (2012), with permission from Elsevier)

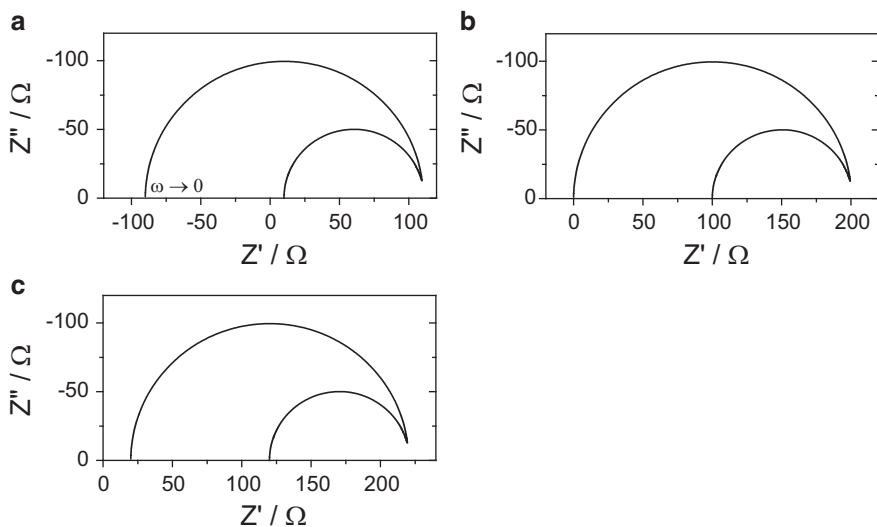
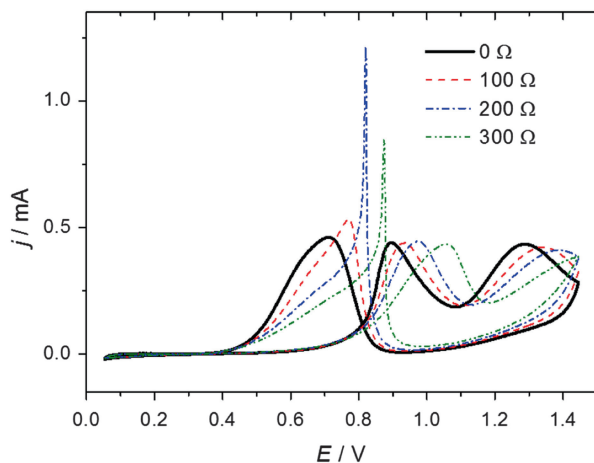


Fig. 13.18 Complex plane plots for circuit $R_0(R_1C_1)(R_2C_2)$ in Fig. 2.37 *left*. Parameters: $R_1 = 100 \, \Omega$, $C_1 = 2 \times 10^{-5} \, \text{F}$, $R_2 = -200 \, \Omega$, $C_2 = 0.01 \, \text{F}$; resistance in series R_0 : (a) $10 \, \Omega$, (b) $100 \, \Omega$, (c) $120 \, \Omega$

$$\begin{aligned}
 \hat{Z} &= R_0 + \frac{1}{\frac{1}{R_1} + sC_1} + \frac{1}{\frac{1}{R_2} + sC_2} = \\
 &= \frac{R_0 \left[s^2 + s \left[\frac{1}{R_1 C_1} + \frac{1}{R_2 C_2} + \frac{1}{R_0} \left(\frac{1}{C_1} + \frac{1}{C_2} \right) \right] + \frac{1}{C_1 C_2} \left(\frac{1}{R_1 R_2} + \frac{1}{R_0 R_1} + \frac{1}{R_0 R_2} \right) \right]}{\left(s + \frac{1}{R_1 C_1} \right) \left(s + \frac{1}{R_2 C_2} \right)}
 \end{aligned}
 \tag{13.26}$$

Table 13.1 Zeros and poles of impedances presented in Fig. 13.18

R_0/Ω	z_1/s^{-1}	z_2/s^{-1}	p_1/s^{-1}	p_2/s^{-1}
10	-5,509	-0.408	-500	0.5
100	-1,000	0	-500	0.5
120	-917	0.0454	-500	0.5

Fig. 13.19 Complex plane plots for circuit in Fig. 2.37

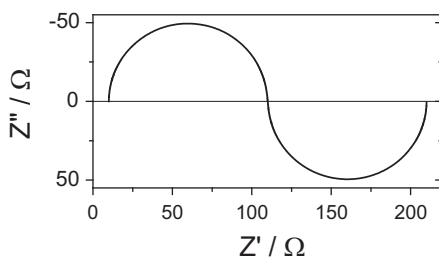
left. Parameters:

$$R_1 = 100 \Omega,$$

$$C_1 = 2 \times 10^{-5} \text{ F},$$

$$R_2 = 100 \Omega,$$

$$C_2 = -0.01 \text{ F}, R_0 = 10 \Omega$$



with zeros and poles

$$z_{1,2} = \frac{\frac{1}{R_1 C_1} + \frac{1}{R_2 C_2} + \frac{1}{R_0 C_1} + \frac{1}{R_0 C_2}}{2} \left[-1 \pm \sqrt{1 - \frac{\frac{4}{C_1 C_2} \left(\frac{1}{R_1 R_2} + \frac{1}{R_0 R_1} + \frac{1}{R_0 R_2} \right)}{\left(\frac{1}{R_1 C_1} + \frac{1}{R_2 C_2} + \frac{1}{R_1 C_1} + \frac{1}{R_0 C_2} \right)^2}} \right],$$

$$p_1 = -\frac{1}{R_1 C_1} \quad p_2 = -\frac{1}{R_2 C_2}. \quad (13.27)$$

Figure 13.18 presents complex plane plots for this model for different values of R_0 and the values of the poles and zeros presented in Table 13.1.

There is always one negative and one positive pole, which are independent of the value of R_0 . For the resistance $R_0 = 10 \Omega$ (Fig. 13.18a) there are two negative zeros, and the system is stable. For $R_0 = 100 \Omega$ one zero equals zero. In this case, the low-frequency impedance becomes zero, which indicates a saddle-node bifurcation. At $R_0 > 100 \Omega$, a positive zero appears, and the system is no longer stable.

The last example is of the same model as the preceding one, but with negative capacitance C_2 . Its complex plane plot is shown in Fig. 13.19. This system has two zeros: $z_1 = -5.491 \text{ s}^{-1}$ and $z_2 = 2.91 \text{ s}^{-1}$. Since one zero is positive, this system is always unstable.

Example 13.2 Using the electrical equivalent model $R_0(C_1(R_1(R_2 C_2)))$ in Fig. 2.27, check its stability assuming the following parameters: $R_0 = 10 \Omega$, $C_1 = 10^{-5} \text{ F}$, $C_2 = -0.001 \text{ F}$; and R_2 : (a) -150Ω , (b) -110Ω , (c) -80Ω .

Table 13.2 Zeros and poles of impedance in Eq. (13.28) for different values of parameter R_2

R_2/Ω	z_1/s^{-1}	z_2/s^{-1}	p_1/s^{-1}	p_2/s^{-1}
-150	-10,999	2.42	$1.66 - j 81.6$	$1.66 - j 81.6$
-110	-10,999	0	$0.449 - j 95.3$	$0.449 + j 95.3$
-80	-10,999	-3.41	$-1.25 - j 112$	$-1.25 + j 112$

First, the system impedance must be written in the form of Eq. (13.22):

$$Z = R_0 + \frac{1}{sC_1 + \frac{1}{R_1 + \frac{1}{sC_2 + \frac{1}{R_2}}}}$$

$$= R_0 \frac{s^2 + s \left[\frac{1}{C_2} \left(\frac{1}{R_1} + \frac{1}{R_2} \right) + \frac{1}{C_1} \left(\frac{1}{R_1} + \frac{1}{R_0} \right) \right] + \frac{1}{C_1 C_2} \left(\frac{1}{R_1 R_2} + \frac{1}{R_0 R_1} + \frac{1}{R_0 R_2} \right)}{\left[s^2 + s \left(\frac{1}{C_2} \left(\frac{1}{R_1} + \frac{1}{R_2} \right) + \frac{1}{R_1 C_1} \right) + \frac{1}{R_1 R_2 C_1 C_2} \right]} \quad (13.28)$$

Its zeros and poles were already presented in Eq. (2.160). The results are presented in Table 13.2 and the impedance plots in Fig. 13.20.

From the results presented it is evident that in case (a), the impedance displays one positive zero, which indicates that this system is unstable; in case (b), the low-frequency zero is equal to zero, which indicates a saddle-node bifurcation; and in case (c), both zeros are negative and poles are complex with negative real part; therefore, the system is stable.

The method presented here allows for the determination of system stability following determination of the system zeros and poles.

13.3.4 Nyquist Stability Criterion

Sometimes we would like to resolve system stability without modeling impedances or determining the zeros and poles of the impedance. This can be done using the Nyquist stability criterion [587, 588, 596] developed from the theory of complex functions and Cauchy's integral theorem, which can be stated as follows: an electrochemical system is stable if and only if the number of clockwise encirclements ($\#N$) of the origin of the $Z' - (-Z'')$ plane, going from low to high frequencies, equals the number of positive poles ($\#P$), i.e., in the right-hand s -plane. Therefore, the number of instabilities, that is, positive zeros, equals $\#Z = \#P - \#N$.

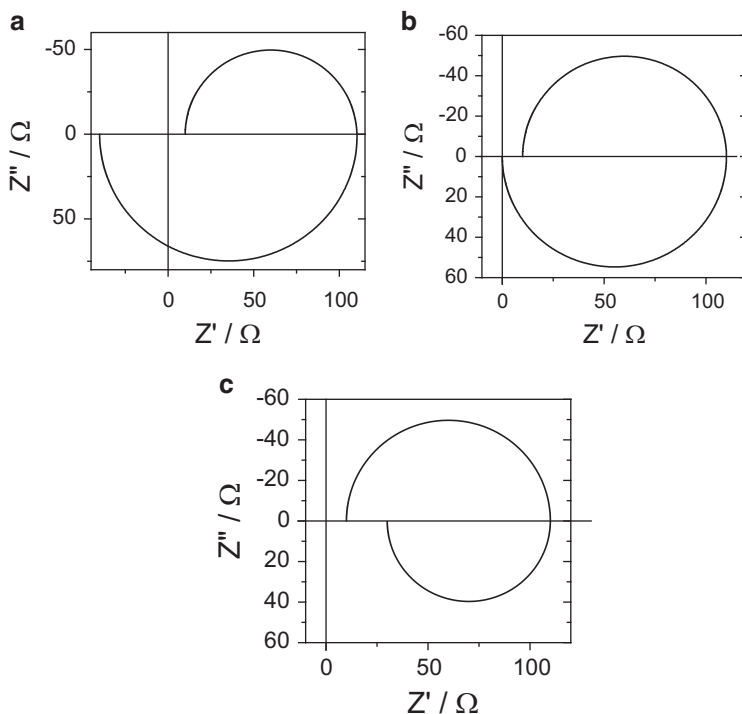


Fig. 13.20 Complex plane plots for model and data in Example 13.2

Let us look at the impedances in Fig. 13.15b–d. They all have a negative resistance and one positive pole, $\#P = 1$, Eq. (13.24). In Fig. 13.15b, going from $\omega = 0$ to $\omega \rightarrow \infty$ (that is, from left to right), the origin is circled once, which means that $\#N = 1$ and the number of instabilities $\#Z = \#P - \#N = 1 - 1 = 0$, and the system is stable. In Fig. 13.15c, the impedance at $\omega = 0$ is $Z = 0$, and a saddle-node bifurcation occurs. In Fig. 13.15d, R_1 is still negative; therefore, $\#P = 1$. The impedance does not encircle the origin, and $\#N = 0$; therefore, the number of instabilities is $\#Z = \#P - \#N = 1 - 0 = 1$, and this system is unstable.

Let us consider a system containing two parallel (RC) elements in series and displaying two semicircles ($R_0(R_1C_1)(R_2C_2)$, Fig. 2.37, left). Let us assume that the two resistances are negative, and the higher capacitance is negative given different solution resistances R_0 . The complex plane plots corresponding to this circuit for negative $R_1 = R_2$, negative C_2 , and different values of the serial resistance R_0 are displayed in Fig. 13.21. They will be used for the illustration of the stability criterion. The values of the zeros and poles of the impedances, calculated using Eq. (13.27), are shown in Table 13.3. There is always one positive and one negative pole. For $R_0 < 100 \, \Omega$ the impedance zeros are both negative. Going from low to high frequencies there is one clockwise encirclement of the origin, and as there is only one positive pole, there are no instabilities, $\#Z = \#P - \#N = 1 - 1 = 0$.

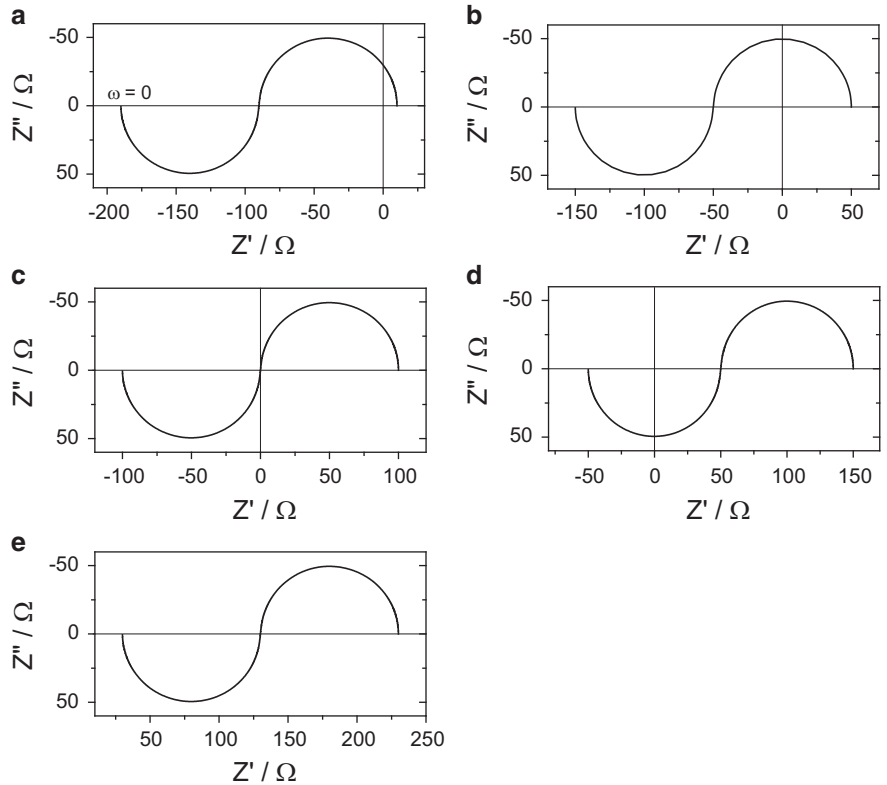


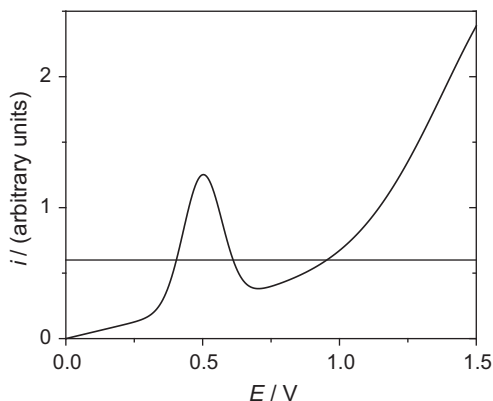
Fig. 13.21 Influence of serial resistance on complex plane plots for circuit in Fig. 2.37 left. Parameters: $R_1 = R_2 = -100\ \Omega$, $C_1 = 2 \times 10^{-5}\ \text{F}$, $C_2 = -0.01\ \text{F}$, $R_0 =$ (a) $10\ \Omega$, (b) $50\ \Omega$, (c) $100\ \Omega$, (d) $150\ \Omega$, (e) $230\ \Omega$

Table 13.3 Zeros and poles of impedance defined in Eq. (13.27) for parameters in Fig. 13.21

R_0/Ω	z_1/s^{-1}	z_2/s^{-1}	p_1/s^{-1}	p_2/s^{-1}
10	-4,489	-2.12	500	-1
50	-496	-3.02	500	-1
100	$0 - j\ 22.4$	$0 + j\ 22.4$	500	-1
150	$83.2 - j\ 82.2$	$83.2 + j\ 82.2$	500	-1
230	$141 - j\ 141$	$141 + j\ 141$	500	-1

When $R_0 = -R_2$, there are two complex conjugate zeros with real part equal to zero. On the complex plane plot, for one value of the frequency $\omega_H \neq 0$ the impedance becomes zero. This is a so-called Hopf bifurcation, and the frequency is called a Hopf frequency. At $R_0 > -R_2$, the zeros are complex with positive real part, which indicates instability (Fig. 13.14). In fact, in Fig. 13.21d, there is only a counterclockwise encirclement of the origin, and in case e, there are no encirclements; therefore, on the basis of the Nyquist theorem, the system is unstable.

Fig. 13.22 Example of current-potential curve; negative resistance may appear when $di/dE < 0$; parallel line indicates that multiple states are possible for one value of current



Applying the Nyquist theorem to the impedances in Fig. 13.18 it is evident that in case a, there is a negative low-frequency resistance and one pole is positive. However, the impedance encircles the origin once in the clockwise direction (going from low to high frequencies) and the number of instabilities is $\#Z = \#P - \#N = 1 - 1 = 0$; therefore, the system is stable. Other cases can be considered in a similar way.

13.3.5 Negative Dynamic Resistances and Their Origin

Negative impedance cannot be read from the steady-state polarization curve. However, in dynamic systems, for example, during a voltamperometric potential sweep, such effects can appear. These phenomena are often observed in corrosion in cases of active-passive transitions or transpassivity [588–600]. An example of the i – E curve where negative charge transfer resistances are observed is displayed in Fig. 13.22 (see also Refs. [599, 600]); they appear after the peak where the current is decreasing with increasing potential, $di/dE < 0$. It should also be noted that during potentiostatic experiments, one current value corresponds to one potential, whereas for one applied current (galvanostatic conditions) (horizontal line) three values of the current are possible because of multiple steady states.

Koper [597], Koper and Sluyters [598], and Krischer and Varela [601] discussed the conditions under which negative faradaic impedance can be observed. In general, current is described as

$$i_f = nFAk_f C(0), \quad (13.29)$$

where A is the electrode surface area, $C(0)$ is the surface concentration of the electroactive species, and other parameters have their usual meaning. Faradaic admittance is defined as

$$\hat{Y}_f = \frac{1}{\hat{Z}_f} = \frac{di_f}{dE} = nF \left[AC(0) \frac{dk_f}{dE} = Ak_f \frac{dC(0)}{dE} + k_f C(0) \frac{dA}{dE} \right]. \quad (13.30)$$

To obtain a negative faradaic impedance, the expression in parentheses in Eq. (13.30) must be negative. This can happen in one of three cases [597, 598]:

i. $dk_f/dE < 0$: this condition may occur in the following situations:

- (a) During potential-dependent adsorption of an inhibitor, which decreases the available free surface area. For example, one can assume that the heterogeneous rate constant changes according to

$$k_f(\theta, E) = [1 - \theta(E)]k_f(\theta = 0, E) + \theta(E)k_f(\theta = 1, E), \quad (13.31)$$

where θ is the surface coverage with the inhibitor and $k_f(\theta = 0, E) \gg k_f(\theta = 1, E)$.

- (b) During potential-dependent desorption of a catalyst in whose presence a reaction can proceed at a high rate. When the catalyst is desorbed, the reaction rate decreases with the potential.

ii. $dC(0)/dE < 0$: this condition occurs during strong electrostatic repulsion of ions in the double layer due to the Frumkin effect [17]. This effect is especially strong at low supporting electrolyte concentrations as the value of the potential in the outer Helmholtz plane becomes large (positive or negative for cations and anions, respectively).

iii. $dA/dE < 0$: this effect can appear when the available electrode surface decreases with increasing polarization due to the formation of a passivating or strongly inhibiting film (potential-dependent processes).

As we saw earlier, systems with a negative faradaic resistance, such as in Fig. 13.15, may be stable, depending on the value of the solution resistance. However, such impedance is not Kramers-Kronig-transform compliant. This is related to the general characteristics of transfer functions. However, there are two types of impedance experiments: potentiostatic or galvanostatic. When an ac voltage is applied and ac current measured, the corresponding transfer function (Laplace transform of the output to the Laplace transform of the input) is admittance,

$$\hat{Y}(\omega) = \frac{L[\text{output}]}{L[\text{input}]} = \frac{L[i(t)]}{L[E(t)]}, \quad (13.32)$$

and when ac current is used as a perturbation, the transfer function is impedance,

$$\hat{Z}(\omega) = \frac{L[E(t)]}{L[i(t)]}. \quad (13.33)$$

This means that *if the data were acquired under a potentiostatic perturbation, then one should use the admittance as the transfer function* for the Kramers-Kronig

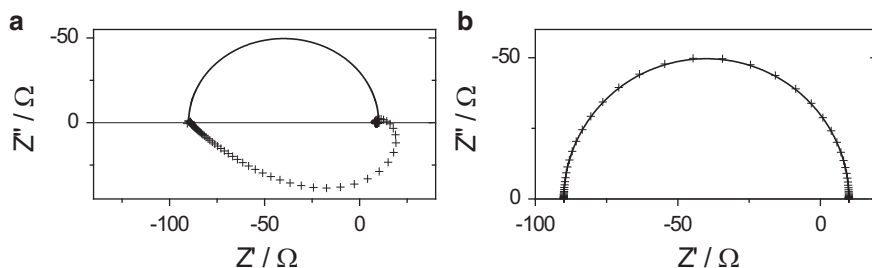


Fig. 13.23 Complex plane impedance data (continuous lines) and their Kramers-Kronig transformations (symbol +) for simple model with negative resistance; (a) transformation of impedance, (b) transformation of admittance (displayed here as impedance); data as in Fig. 13.15b

transformations, but *if the data were acquired under a galvanostatic perturbation, then one should use impedance* [561]. This fact is related to system stability. Although it is possible to acquire data using potentiostatic control, during galvanostatic control multiple states are possible for one value of current (Fig. 13.22), and oscillations might be observed [588, 599, 600]. In fact, for a system displaying negative resistance, as in Fig. 13.15b, impedances are not Kramers-Kronig compliant, but admittances are transformable. This result is displayed in Fig. 13.23.

These properties are understandable from the point of view of the stability of transfer functions. As was mentioned earlier, a stable transfer function cannot have any positive poles. In the foregoing case, the poles and zeros of the impedance are shown in Fig. 13.16b, and there is one positive pole and one negative zero, which means that the system is unstable. On the other hand, the admittance (inverse of impedance) has one negative pole and one positive zero, indicating that it is stable. Of course, systems containing only positive R , C , and L elements always have negative poles and zeros, and they are always stable and transformable in the admittance and impedance forms.

Example 13.3 Determine the current and impedance of a system displaying negative impedance (described below). It represents the irreversible metal dissolution and electrosorption of a species A on the surface, which block metal dissolution:



Use the following parameters: $k_1^0 = k_2^0 = 10^{-7} \text{ mol cm}^{-2} \text{ s}^{-1}$, $\alpha_1 = \alpha_2 = 0.5$, $\sigma_1 = 210 \mu\text{C cm}^{-2}$, $E = 0.1 \text{ V}$; neglect the diffusion of A^- .

Reactions (13.34) and (13.35) are described by the following equations:

$$v_1 = k_{1f}(1 - \theta), \quad (13.36)$$

$$v_2 = k_{2f}(1 - \theta) - k_{2b}\theta, \quad (13.37)$$

where the rate constants are potential dependent:

$$k_{1f} = k_1^0 \exp(\alpha_1 fE); \quad k_{2f} = k_2^0 \exp(\alpha_2 fE); \quad k_{2b} = k_2^0 \exp[-(1 - \alpha_2)fE]. \quad (13.38)$$

First, the steady-state conditions must be described. At a steady state, adsorption of species A is in equilibrium and $v_2 = 0$ and the surface coverage is

$$\theta = \frac{k_{2f}}{k_{2f} + k_{2b}}, \quad (13.39)$$

and the steady-state current is

$$i = Fv = F(v_1 + v_2) = F \frac{k_{1f}k_{2b}}{k_{2f} + k_{2b}}. \quad (13.40)$$

Next, the dynamic conditions must be solved. In general, the total ac current is written as

$$\Delta i = \left(\frac{\partial v}{\partial E} \right) \Delta E + \left(\frac{\partial v}{\partial \theta} \right) \Delta \theta, \quad (13.41)$$

where for each parameter a , $\Delta a = \tilde{a} \exp(j\omega t)$. This can be simplified to

$$\tilde{i} = F \left[\left(\frac{\partial v}{\partial E} \right) \tilde{E} + \left(\frac{\partial v}{\partial \theta} \right) \tilde{\theta} \right]. \quad (13.42)$$

The adsorption reaction for reaction (13.35) is

$$\Gamma_\infty \frac{d\theta}{dt} = v_2 = k_{2f}(1 - \theta) - k_{2b}\theta, \quad (13.43)$$

where Γ_∞ is the maximum surface concentration of the adsorbed species and can be expressed in terms of the maximal charge density necessary for full surface coverage, $\Gamma_\infty = \sigma_1/F$. The linearized form is

$$\Gamma_\infty j\omega \tilde{\theta} = \left(\frac{\partial v_2}{\partial E} \right) \tilde{E} + \left(\frac{\partial v_2}{\partial \theta} \right) \tilde{\theta}. \quad (13.44)$$

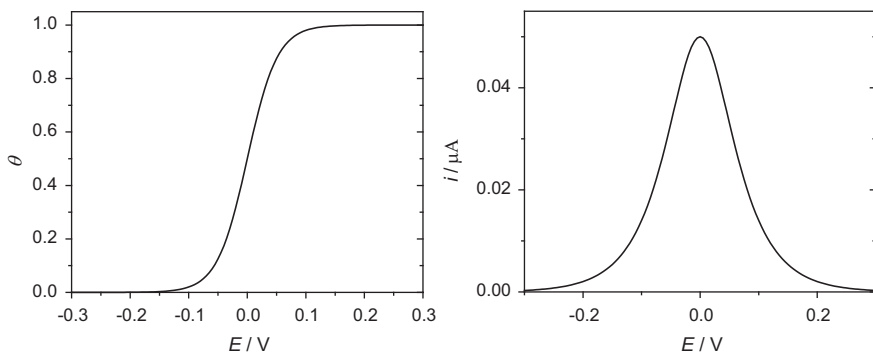


Fig. 13.24 Dependence of surface coverage and current on potential

Equations (13.42) and (13.44) may be written in matrix form:

$$\begin{bmatrix} -\left(\frac{\partial v}{\partial E}\right) \\ -\left(\frac{\partial v_2}{\partial E}\right) \end{bmatrix} = \begin{bmatrix} -\frac{1}{F} & \left(\frac{\partial v}{\partial \theta}\right) \\ 0 & \left(\frac{\partial v_2}{\partial \theta} - j\omega \frac{\sigma_1}{F}\right) \end{bmatrix} \begin{bmatrix} \tilde{i} \\ \tilde{\theta} \\ \tilde{E} \end{bmatrix}. \quad (13.45)$$

One notices the analogy to cases involving one adsorbed species. The system faradaic admittance is easily obtained from Eq. (13.45):

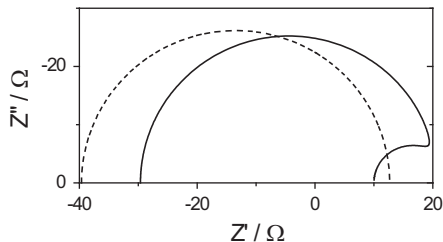
$$\begin{aligned} \tilde{Y}_f &= F \left[\left(\frac{\partial v}{\partial E}\right) + \frac{\left(\frac{\partial v}{\partial \theta}\right) \left(\frac{\partial v_2}{\partial E}\right)}{\left(\frac{\partial v_2}{\partial \theta}\right) - j\omega \frac{\sigma_1}{F}} \right] = F \left(\frac{\partial v}{\partial E}\right) + \frac{\frac{-F^2}{\sigma_1} \left(\frac{\partial v}{\partial \theta}\right) \left(\frac{\partial v_2}{\partial E}\right)}{j\omega - \frac{F^2}{\sigma_1} \left(\frac{\partial v_2}{\partial \theta}\right)} \\ &= A + \frac{B}{j\omega + C}. \end{aligned} \quad (13.46)$$

This equation is similar to that used for one adsorbed species, Eq. (5.51), and $A = 1/R_{ct}$. The total impedance must include a solution resistance and double-layer capacitance,

$$\hat{Z} = R_s + \frac{1}{j\omega C_{dl} + \frac{1}{Z_f}}, \quad (13.47)$$

and it displays two semicircles on the complex plane plot. Results of the calculations might be easily obtained using Maple/Mathematica. The dependence of the surface coverage and current on the potential is displayed in Fig. 13.24 and the total

Fig. 13.25 Complex plane plots of total (*continuous line*) and faradaic (*pointed line*) impedances at $E = 0.1$ V



and faradaic impedances in Fig. 13.25. At negative potentials, two semicircles are observed on the complex plane plots, whereas at positive potentials, where the current is decreasing, negative resistance corresponding to a low-frequency loop appears. Such plots were predicted for the case with one adsorbed species (Fig. 5.3).

13.4 Z-HIT Transform

Kramers-Kronig transforms require integration over frequencies from zero to infinity, which, in practice, is difficult to carry out. There exists a Hilbert logarithmic transform [602, 603] that can be used to validate impedance data in a limited frequency range. It is known under the name Z-HIT transform [585] and is used in the Zahner software [604]. The logarithm of a transfer function known for frequencies between ω_s and ω_o may be written as a function of the phase angle:

$$\ln|H(\omega_0)| = \ln|H(0)| + \frac{2}{\pi} \int_{\omega_s}^{\omega_0} \varphi(\omega) \, d \ln \omega + \sum_{k \geq 1, k \text{ odd}} \gamma_k \frac{d^k \varphi(\omega_0)}{(d \ln \omega)^k},$$

$$\gamma_k = -\frac{2}{\pi} \zeta(k+1) 2^{-k} \quad \text{for odd } k, k \geq 1; \quad \zeta(s) = \sum_{n=1}^{\infty} n^{-s}. \quad (13.48)$$

This series may be simplified to

$$\ln|H(\omega_0)| \approx \text{const} + \frac{2}{\pi} \int_{\omega_s}^{\omega_0} \varphi(\omega) \, d \ln \omega + \gamma \frac{d \varphi(\omega_0)}{d \ln \omega}, \quad (13.49)$$

where $\gamma = -\pi/6$. Equation (13.49) indicates that the logarithm of the transfer function may be calculated from the integral and the derivative of the phase angle [585] and presents an alternative to the Kramers-Kronig transform.

Application of the coherence function instead of the classical Kramers-Kronig transforms has also been proposed in the literature [37, 605] but is rarely used in practice.

13.5 Summary

Experimental impedance data should be validated before further analysis. Raw data might be verified using Kramers-Kronig or Z-Hit transforms. It should be kept in mind that these transforms are not very sensitive to system nonlinearities, and an additional test with different amplitudes could be carried out. An alternative to the aforementioned transforms is the approximation to linear circuits (Figs. 13.2 and 13.4).

If approximation by the transfer function in the form of Eq. (13.17) is possible, then poles of the transfer function can be analyzed because the stable transfer function cannot have positive poles. When such an analysis is not possible, one can use the Nyquist stability criterion. Only validated data can be used for analysis.

13.6 Exercises

Exercise 13.1 Carry out a K-K transform of the data in the file 1.z.

Exercise 13.2 Carry out a K-K transform of the data in the file 2.z.

Exercise 13.3 Carry out a K-K transform of the data in the file 3.z.

Exercise 13.4 Perform a K-K transform of the data in the file 4.z.

Exercise 13.5 Perform a K-K transform of the data in the file 5.z.

Chapter 14

Modeling of Experimental Data

14.1 Acquisition of “Good” Data

The purpose of analyzing EIS data is to determine the nature of the electrode process and its characteristic parameters. As was mentioned earlier, EIS is a very sensitive technique, but it does not provide a direct measure of physical phenomena. Other electrochemical experiments (dc, transients) should also be carried out, assuming good physical knowledge of the system (e.g., solution and surface composition, electrode geometry, dimensions, porosity, presence of various layers, hydrodynamic conditions). The interpretation of impedance data requires the use of an appropriate model. This is a rather difficult and sensitive task that must be carried out very carefully.

Initially, the experimental data must be acquired in a wide frequency range; usually ten points per frequency decade are registered. The lowest frequency is determined by the system stationarity. Usually, one should wait until the current following application of the steady-state potential (or potential in the galvanostatic mode) becomes stationary. It is also advisable to repeat the measurements at each potential twice and compare complex plane and Bode plots to check whether or not they are the same. Other tests may involve running measurements from low to high and then from high to low frequencies. When experiments are carried out at different potentials, they should be repeated from high to low and from low to high potentials and compared. Only stationary, i.e., repeatable, results should be used in the analysis.

For species in solution undergoing diffusion (without forced convection) the lowest frequency that can be used depends also on the hydrodynamic conditions. It is well known that the chronoamperometric curves in solutions might be measured up to 60 s, after which natural convection affects the linearity of diffusion. This means that measurements of the mass transport impedance are limited to approximately 0.1 Hz (or slightly lower). However, measuring diffusion in solid materials (e.g., hydrogen absorption in metals and alloys, lithium intercalation) is not influenced by convection, and the measurements might be carried out to the

millihertz range or lower. One should keep in mind that one ac cycle at 1 mHz takes 16.7 min and taking only one cycle might not always be sufficient because of system noise. Data are usually registered sequentially from high to low (or vice versa) frequencies, so the experimental time is longer than that of one cycle of the lowest frequency. To decrease the experimental time, the EG&G software uses single frequency scans at higher frequencies and applies the sum of frequencies at lower frequencies, followed by Fourier transform analysis. A sum of all odd frequencies might be used, although the experimental noise for individual frequencies is often larger as the individual amplitudes must be reduced to assure system linearity (Sect. 13.2).

If differences are detected, they indicate that the system is not stationary and further modifications must be made to assure data reproducibility. This might involve waiting longer at each potential or shortening the time of the experiment by abandoning lower frequencies (which require longer measurement times). Some systems evolve with time, e.g., during corrosion measurements, and each experiment is carried out in a different surface state. In such cases, one must be sure that during one experiment there are no important surface modifications and that reproducible data can be obtained by repetition of the experiment with a new sample.

Then the acquired data must be validated using Kramers-Kronig transforms. Such validated data can be used in subsequent analysis and modeling.

14.2 Types of Modeling

Modeling of experimental data may be divided into two types, as follows.

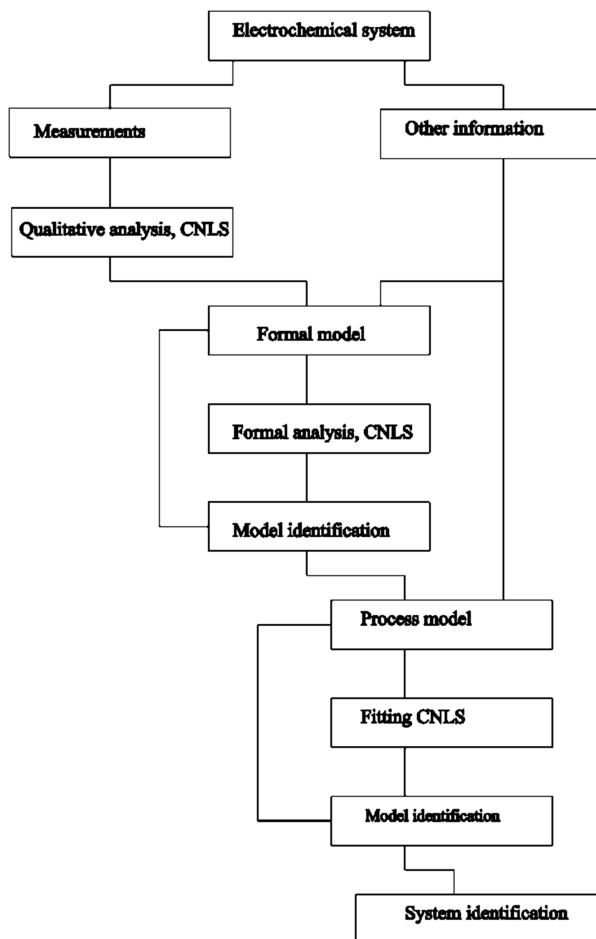
Measurement [606, 607], formal [27], or mathematical [608, 609] modeling explains experimental impedances in terms of mathematical functions or equivalent electrical circuits to obtain a good fit between the calculated and experimental impedances with a minimum number of parameters.

Physicochemical, process [566, 572, 606, 607], or structural [27, 610–612] modeling links measured impedances with physicochemical parameters of the electrochemical process (e.g., kinetic parameters, concentrations, diffusion coefficients, sample geometry, hydrodynamic conditions).

It is clear that in the measurement modeling, the parameters obtained often do not have a clear physicochemical significance. It should be stressed that proper modeling is the most difficult part of analysis and is often misunderstood and wrongly interpreted.

Zoltowski [608, 609] proposed that one should first use measurement modeling to determine the number and nature of the circuit elements and parameters describing the studied system. One could use equivalent circuits containing simple R , C , and L parameters, or one could use more complex distributed elements such as the CPE and other analytically described elements such as, for example, mass transfer impedance and a porous model.

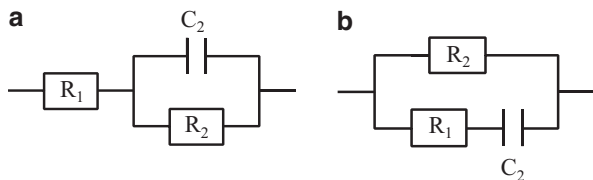
Fig. 14.1 Steps in modeling process as suggested by Zoltowski [608, 609]



The next step would be to construct a physicochemical model for a given process. As was shown in earlier chapters, one can write faradaic impedance equations for any mechanism. The problem is that complex mechanisms produce equations (models) containing more parameters than really are observed in the experimental data (determined by measurement modeling). It must be stressed that a physicochemical model cannot contain more adjustable parameters than the corresponding measurement model. More complex physicochemical models must be correctly simplified. Several additional experiments are usually necessary to determine the origin of certain elements, for example, by changing the concentration, hydrodynamic conditions, adding poisons, or changing the temperature.

The modeling process proposed by Zoltowski is schematically displayed in Fig. 14.1. To characterize an electrochemical system, one performs impedance measurements and the results are qualitatively analyzed. This analysis allows the construction of a formal model and determination of the nature and number of the

Fig. 14.2 Two electrical equivalent circuits producing one semicircle on complex plane plot and characterized by one time constant



parameters describing such a system. With information from other electrochemical and physicochemical methods, the process model is constructed leading to model identification and determination of the physicochemical parameters. The process is interactive, and repetitions/corrections might be necessary to finally describe the electrochemical system.

It must be added that such a process is not always possible. Certain phenomena cannot be described by analytical equations, for example, porous electrodes in the presence of a faradaic current and potential gradient, nonhomogeneous porous materials, diffusion to disk electrodes, and nonuniform diffusion. However, such phenomena might often be approximated by simpler analytical equations, although the obtained parameters might not have a clear meaning. For example, a semi-infinite porous model in the presence of a potential gradient may be approximated using a CPE, but the obtained parameters do not directly correspond to the electrode capacitance [435] (Fig. 9.29).

The main problem with equivalent circuit modeling is related to the fact that the same data may be exactly represented by different equivalent models. This problem will be illustrated in the following examples.

Example 14.1 A complex plane plot displaying one semicircle (Fig. 2.34) may be exactly described by two equivalent circuits (Fig. 14.2). The impedances of these circuits are

$$\hat{Z}_a = R_1 + \frac{1}{\frac{1}{R_2} + j\omega C_2} = \frac{(R_1 + R_2) + j\omega(R_1 R_2 C_2)}{1 + j\omega(R_2 C_2)}, \quad (14.1)$$

$$\hat{Z}_b = \frac{1}{\frac{1}{R_2} + \frac{1}{R_1 + \frac{1}{j\omega C_2}}} = \frac{R_1 + j\omega(R_1 R_2 C_2)}{1 + j\omega C_2(R_1 + R_2)}. \quad (14.2)$$

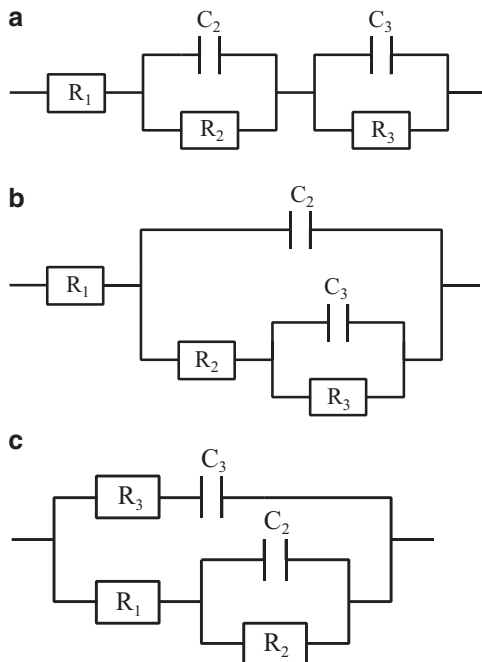
These two equations may be written in a unified form:

$$\hat{Z} = \frac{a_0 + a_1 j\omega}{b_0 + b_1 j\omega} = \frac{a_0 + a_1 j\omega}{1 + b_1 j\omega}, \quad (14.3)$$

where the parameters a_i and b_i are different for these two circuits:

$a_0 = R_1 + R_2$, $a_1 = R_1 R_2 C_2$, $b_0 = 1$, and $b_1 = R_2 C_2$ for circuit (a) and
 $a_0 = R_1$, $a_1 = R_1 R_2 C_2$, $b_0 = 1$, and $b_1 = C_2(R_1 + R_2)$ for circuit (b).

Fig. 14.3 Three circuits representing a system characterized by two time constants: (a) Voigt, (b) ladder, and (c) mixed



It is evident that these two forms are indistinguishable and produce exactly the same impedances and impedance complex plane and Bode plots for these two circuits. All the equations have three adjustable parameters. However, additional information is necessary to decide which circuit has a physical meaning in the given case. For example, when studying a redox process on an electrode in solution, circuit (a) is more probable because R_1 and C_2 have a meaning of solution resistance in series, with the electrode impedance consisting of a parallel connection of the double-layer capacitance, C_2 , and the charge transfer resistance, R_2 (Sect. 4.1 and Fig. 4.1).

Example 14.2 Let us consider now a circuit characterized by two time constants producing two semicircles on complex plane plots. Three possible circuits explaining the impedances are shown in Fig. 14.3. Circuit (a) represents so-called a Voigt circuit consisting of the resistance in series with two (RC) circuits in parallel; circuit (b) is a so-called ladder or nested circuit, and circuit (c) is a mixed circuit. The impedance of each circuit can be written as

$$\begin{aligned}\hat{Z}_a &= R_1 + \frac{1}{\frac{1}{R_2} + j\omega C_2} + \frac{1}{\frac{1}{R_3} + j\omega C_3} \\ &= \frac{(R_1 + R_2 + R_3) + j\omega(R_1 R_2 C_2 + R_1 R_3 C_3 + R_2 R_3 C_3) + (j\omega)^2(R_1 R_2 R_3 C_2 C_3)}{1 + j\omega(R_2 C_2 + R_3 C_3) + (j\omega)^2(R_2 R_3 C_2 C_3)},\end{aligned}\quad (14.4)$$

$$\begin{aligned}
\hat{Z}_b &= R_1 + \frac{1}{j\omega C_2 + \frac{1}{R_2 + \frac{1}{\frac{1}{R_3} + j\omega C_3}}} \\
&= \frac{(R_1 + R_2 + R_3) + j\omega(R_1 R_2 C_2 + R_1 R_3 C_2 + R_1 R_3 C_3 + R_2 R_3 C_3) + (j\omega)^2(R_1 R_2 R_3 C_2 C_3)}{1 + j\omega(R_2 C_2 + R_3 C_3 + R_3 C_2) + (j\omega)^2(R_2 R_3 C_2 C_3)},
\end{aligned} \tag{14.5}$$

$$\begin{aligned}
\hat{Z}_c &= \frac{1}{\frac{1}{R_3 + \frac{1}{j\omega C_3}} + \frac{1}{R_1 + \frac{1}{\frac{1}{R_2} + j\omega C_2}}} \\
&= \frac{(R_1 + R_2) + j\omega(R_1 R_2 C_2 + R_1 R_3 C_3 + R_2 R_3 C_3) + (j\omega)^2(R_1 R_2 R_3 C_2 C_3)}{1 + (j\omega)(R_1 C_3 + R_2 C_2 + R_2 C_3 + R_3 C_3) + (j\omega)^2(R_1 R_2 C_2 C_3 + R_2 R_3 C_2 C_3)}.
\end{aligned} \tag{14.6}$$

All these equations can be written in one simpler form:

$$\hat{Z} = \frac{a_0 + a_1(j\omega) + a_2(j\omega)^2}{b_0 + b_1(j\omega) + b_2(j\omega)^2} = \frac{a_0 + a_1(j\omega) + a_2(j\omega)^2}{1 + b_1(j\omega) + b_2(j\omega)^2}, \tag{14.7}$$

which indicates that all three circuits will produce the same impedances at all frequencies after proper adjustments of the parameters. All the equations have five adjustable parameters (because $b_0 = 1$).

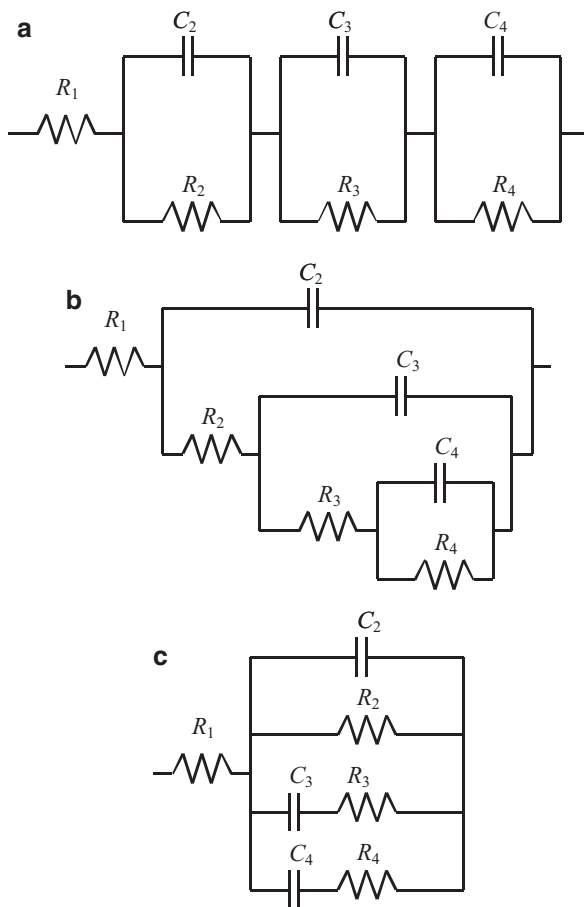
It should also be added that use of the equivalent circuits may introduce ambiguities. It is clear that in the Voigt circuit (a), permutation of the values of elements $R_2 - C_2$ and $R_3 - C_3$ does not change the impedance values and the attribution of values to one or another set is arbitrary, i.e. when fitting one can converge on either set. This fact is important when the system is studied as a function of the electrode potential (or other experimental parameter) to not exchange of these parameters (e.g. set of parameters 2 and 3). However, such an ambiguity does not appear in the ladder circuit (b).

Example 14.3 Compare systems with three time constants.

Three circuits characterized by three time constants are presented in Fig. 14.4: (a) Voigt, (b) ladder, and (c) Maxwell circuits. Their impedances might be written in one common form,

$$\hat{Z} = \frac{a_0 + a_1(j\omega) + a_2(j\omega)^2 + a_3(j\omega)^3}{b_0 + b_1(j\omega) + b_2(j\omega)^2 + b_3(j\omega)^3}, \tag{14.8}$$

Fig. 14.4 Three circuits representing systems with three time constants: (a) Voigt, (b) ladder, (c) Maxwell



with $b_0 = 1$ and they produce identical impedance characteristics. Only by using the additional mechanistic information can one decide which model should be used. For example, the ladder circuit might appear in systems with two adsorbed species (Sect. 5.3), while the Maxwell circuit appears in studies of dielectric phenomena [574].

Note that the same equivalent circuits can be presented in different forms; for example, the same ladder circuit is presented in Figs. 14.4b and 14.5, although at first glance they look different.

It should be added that sometimes CPEs must be used and the corresponding impedance adjusted to include such parameters [611]; however, using polynomial notation for impedances makes the model more complicated. For example, replacing C_2 in Fig. 14.3b by the CPE (T_2, ϕ_2) changes Eq. (14.5) into

Fig. 14.5 Another representation of ladder circuit presented in Fig. 14.4b

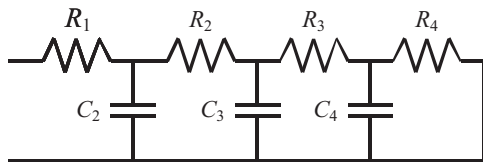
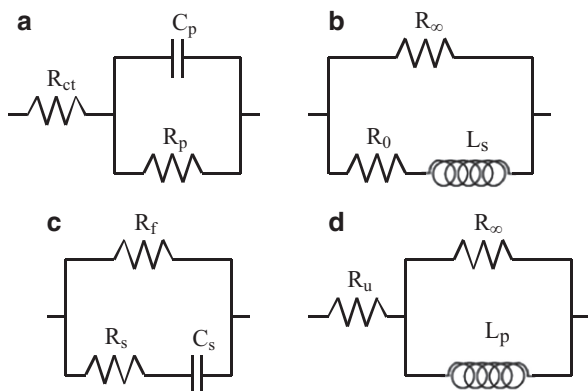


Fig. 14.6 Electrical equivalent circuits describing faradaic impedance of hydrogen evolution reaction



$$\begin{aligned}
 \hat{Z}_b &= R_1 + \frac{1}{(j\omega)^{\phi_2} T_2 + \frac{1}{R_2 + \frac{1}{\frac{1}{R_3} + j\omega C_3}}} \\
 &= \frac{(R_1 + R_2 + R_3) + (j\omega)^{\phi_2} (R_1 R_2 T_2 + R_1 R_3 T_2) + j\omega (R_1 R_3 C_3 + R_2 R_3 C_3) + (j\omega)^{1+\phi_2} (R_1 R_2 R_3 T_2 C_3)}{1 + (j\omega)^{\phi_2} (R_2 T_2 + R_3 T_2) + j\omega (R_3 C_3) + (j\omega)^{1+\phi_2} (R_2 R_3 T_2 C_3)}
 \end{aligned} \quad (14.9)$$

In such cases, it is simpler to use a direct fit to the equivalent circuit.

The same impedance behavior might be represented not only by permutation of R and C elements but also by replacing capacitance by inductance and using negative values of the parameters. This will be illustrated in Example 14.4.

Example 14.4 The faradaic impedance of a hydrogen evolution reaction can be represented by four different circuits displaying the same values of impedances and frequency dependence [211]. These circuits are displayed in Fig. 14.6. The faradaic impedances of circuits (a)–(d) are

$$\begin{aligned}
 (a) \hat{Z}_f &= R_{ct} + \frac{1}{\frac{1}{R_p} + j\omega C_p} = \frac{(R_{ct} + R_p) + j\omega(R_{ct}R_pC_p)}{1 + j\omega(R_pC_p)} \\
 &= (R_{ct} + R_p) \frac{\left(1 + j\omega \frac{R_{ct}R_pC_p}{R_{ct} + R_p}\right)}{1 + j\omega(R_pC_p)}, \quad (14.10)
 \end{aligned}$$

$$(b) \hat{Z}_f = \frac{1}{\frac{1}{R_\infty} + \frac{1}{R_0 + j\omega L_s}} = \frac{R_\infty R_0}{R_\infty + R_0} \frac{1 + j\omega \frac{L_s}{R_0}}{1 + j\omega \frac{L_s}{R_\infty + R_0}}, \quad (14.11)$$

$$(c) \hat{Z}_f = \frac{1}{\frac{1}{R_f} + \frac{1}{R_s + \frac{1}{j\omega C_s}}} = \frac{R_f + j\omega(R_f R_s C_s)}{1 + j\omega(R_f C_s + R_s C_s)}, \quad (14.12)$$

$$(d) \hat{Z}_f = R_u + \frac{1}{\frac{1}{R_L} + \frac{1}{j\omega L_p}} = \frac{R_u + j\omega\left(L_p + \frac{L_p R_u}{R_L}\right)}{1 + j\omega\left(\frac{L_p}{R_L}\right)}, \quad (14.13)$$

and the parameters of other circuits can be expressed in terms of the circuit (a) parameters:

$$\begin{aligned}
 (b) R_\infty &= R_{ct}; R_0 = -\frac{R_{ct}(R_{ct} + R_p)}{R_p}; L_s = -R_{ct}^2 C_p; \\
 (c) R_f &= R_{ct} + R_p; R_s = \frac{R_{ct}(R_{ct} + R_p)}{R_p}; C_p = \frac{R_p^2 C_p}{(R_{ct} + R_p)^2}; \\
 (d) R_u &= R_{ct} + R_p; R_L = -R_p; L_p = -R_p^2 C_p.
 \end{aligned} \quad (14.14)$$

That is, assuming the following values for the elements of circuit (a):

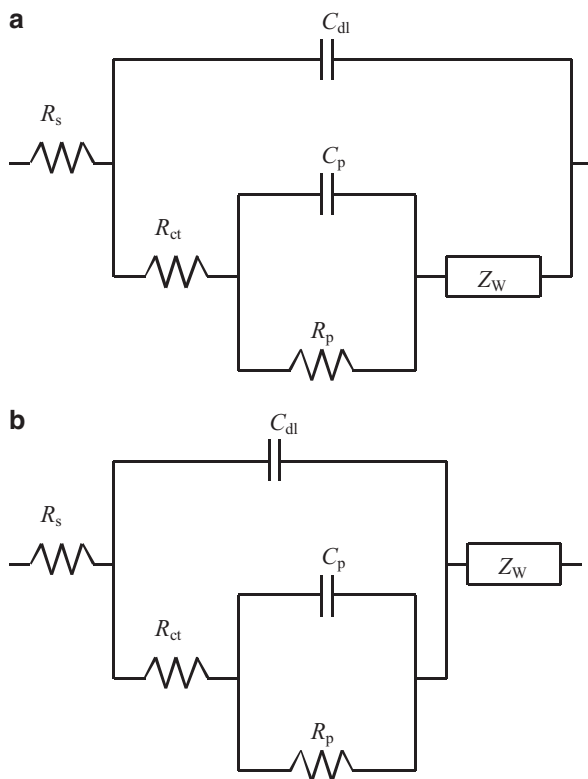
$$(a) R_{ct} = 70 \, \Omega; R_p = 100 \, \Omega; C_p = 0.01 \, \text{F} \quad (14.15)$$

the parameters of the other circuits are

$$\begin{aligned}
 (b) R_\infty &= 70 \, \Omega; R_0 = -119 \, \Omega; L_s = -49 \, \text{H}; \\
 (c) R_f &= 170 \, \Omega; R_s = 119 \, \Omega; C_s = 0.0346 \, \text{F}; \\
 (d) R_u &= 170 \, \Omega; R_L = -100 \, \Omega; L_p = -100 \, \text{H}.
 \end{aligned} \quad (14.16)$$

This means that a simple complex plot presenting one capacitive semicircle can be represented by other connections of R and C elements (as shown earlier) but also by circuits containing negative inductance and resistance. Of course, as has been proven in the literature, only the parameters of circuit (a) are more directly related

Fig. 14.7 Electrical equivalent model of mechanism involving one adsorbed species with diffusion (a) and a model with different position of Warburg element (b)



to the mechanism, although other circuits give exactly the same frequency-dependent impedances.

Example 14.5 Another example illustrates ambiguity in the position of the Warburg element. In Chap. 6, Eq. (6.28), and Fig. 6.1, a model was developed for the case of one adsorbed species with diffusion. However, the position of the Warburg impedance element (Fig. 14.7a) can be changed to 14.7b without practically affecting the quality of the fit that is both fits may be experimentally indistinguishable. Nevertheless, only the model in (a) has a physical meaning. Of course, the total impedance might be fitted to the model in Fig. 4.1b, expressing the faradaic impedance by Eq. (6.26).

14.3 Fitting the Experimental Data

The purpose of data fitting is to determine the values of the model parameters together with their standard deviations.

14.4 Error Classification

The observed impedance errors at each frequency, i , that is, the difference between the experimental, Z_i , and a fitted model impedance, $Z_{i,\text{calc}}$, arises from three major contributions [3]:

$$Z_i - Z_{i,\text{calc}} = \varepsilon_{i,\text{fit}} + \varepsilon_{i,\text{stoch}} + \varepsilon_{i,\text{bias}}, \quad (14.17)$$

where $\varepsilon_{i,\text{fit}}$ is the systematic error attributed to an incorrect model used in approximation, $\varepsilon_{i,\text{stoch}}$ is the stochastic (random) error intrinsic to each experiment with the average equal to zero, and $\varepsilon_{i,\text{bias}}$ is the systematic error in the experiment arising from drift and instrumental artifacts. The statistical methods of data analysis deal with the stochastic errors only, but other more complex methods allow one to deal with bias errors [613–615].

14.5 Methods for Finding the Best Parameters

The problem of fitting impedances is nonlinear, and the method usually used is the complex nonlinear least-squares (CNLS) method [3, 24, 25, 616–618]. In this method, a weighted sum of squares, S , of the differences between the experimental, Z'_i and Z''_i , and the model, $Z'_{i,\text{calc}}$ and $Z''_{i,\text{calc}}$ impedances is minimized by choosing the best values of the adjustable parameters and minimizing the weighted differences between the experimental and model (calculated) impedances:

$$S = \sum_{i=1}^N \left\{ w'_i \left[Z'_i - Z'_{i,\text{calc}} \right]^2 + w''_i \left[Z''_i - Z''_{i,\text{calc}} \right]^2 \right\}, \quad (14.18)$$

where w'_i and w''_i are the statistical weights of the data points and the summation runs over all the N frequencies. This minimization is usually carried out using the iterative Marquardt-Levenberg algorithm [619]. The initial estimation of the model parameters must be supplied. Because the method is iterative and nonlinear, the initial estimation of the parameters *must be relatively close to the experimental values*; otherwise, a divergence is obtained and a message, for example “singular matrix,” is obtained or the parameters are found with errors exceeding several times their values. The latter case may be related to a local flat minimum and a new set of initial parameters should be chosen. These problems are often observed for more complicated circuits characterized by many adjustable parameters and in the presence of distributed elements as in porous electrodes or those with semi-infinite-length or finite-length diffusion.

In more complicated cases, a part of the total circuit (usually the high-frequency part) might be fitted, the elements found fixed, and additional elements added as free parameters. Finally, all the parameters should be set as free and the final

approximation parameters found. Examples of this type of modeling will be shown in subsequent exercises.

Another method for finding the minimum is the so-called downhill simplex method [3, 619]. It requires only a function evaluation and does not use either function derivatives or matrix inversion. It may be relatively slow if one is trying to optimize many parameters and a shallow minimum, but it will always find a minimum (at least a local minimum). The problem with this technique is that it does not calculate the parameters' standard deviations directly. In such cases, it is advisable, after finding the minimum by the simplex method, to use these parameters in the CNLS approximation, which should converge quickly and provide standard deviations of the parameters.

Some new methods are based on the use of genetic algorithm optimization, but although they are very promising they are still rarely used [620]. They could be used in future to distinguish between some complex reaction mechanism, e.g. in corrosion.

14.6 Weighting Procedures

The proper choice of the statistical weighting in Eq. (14.18) is very important for the determination of the system parameters. There are several popular choices:

- a. Statistical weighting: $w'_i = 1/(\sigma'_i)^2$ and $w''_i = 1/(\sigma''_i)^2$
- b. Unit weighting: $w'_i = w''_i = 1$
- c. Modulus weighting [617, 622]: $w'_i = w''_i = 1/|Z|^2$
- d. Proportional weighting [24, 615, 623]: $w'_i = 1/(Z'_i)^2$ and $w''_i = 1/(Z''_i)^2$
- e. Weighting from measurement model [3, 613, 624, 625]:

$$\sigma'_i = \sigma''_i = \alpha |Z''_i| + \beta |Z'_i - R_s| + \gamma \frac{|Z_i|^2}{R_m}.$$

These weighting choices will be discussed below.

14.6.1 Statistical Weighting

Statistical weighting is the statistically most straightforward method. The impedance data should be acquired several (n) times and standard deviations calculated for the real and imaginary parts separately using the average impedance \bar{Z}_i at each frequency, i :

$$\sigma'_i = \sum_{k=1}^n \frac{(Z'_i(k) - \bar{Z}'_i)^2}{n-1} \text{ and } \sigma''_i = \sum_{k=1}^n \frac{(Z''_i(k) - \bar{Z}''_i)^2}{n-1}. \quad (14.19)$$

Then the statistical weight is calculated and used to calculate the sum of squares, S , Eq. (14.18). However, the biggest problem with this method is that, besides the fact that it is time consuming, the impedances may slowly change with time and the average will contain a systematic (drift) error. Because of this problem, it is rarely used. It could be replaced by weighting from the measurement model method.

The next three methods use information from one set of impedance measurements to estimate the weighted sum of squares. In these cases, assumptions about the weighting functions must be made.

14.6.2 Unit Weighting

Unit weighting is the simplest approach. It is assumed that each measured impedance is characterized by the same standard deviation, that is, each measured value has the same precision. This method might be useful for finding initial model parameters for relatively simple models. However, the biggest problem with this method is related to the fact that if the measured impedances change by orders of magnitude, the large values determine the sum of squares, S , and the small features may not be approximated at all. For example, for a model displaying one very small and one large semicircle on the complex plane plot, the smaller semicircle might be completely unnoticed by the approximating program. Of course, this deviation will be easily noticed on Bode phase angle plots.

14.6.3 Modulus Weighting

If impedance measurements are carried out at the same sensitivity scale for the real and imaginary components, the stochastic errors of the real and imaginary impedances will be similar, and one can use modulus weighting. Modulus weighting assumes the same statistical weights for real and imaginary parts, and they are proportional to the impedance modulus. This means that small and large impedances contribute in a similar way to the sum of squares and are equally important.

There are two possible choices for calculations of the modulus:

- a. Modulus of experimental impedances: $|Z_i| = \sqrt{Z_i'^2 + Z_i''^2}$
- b. Modulus of calculated impedances: $|Z_i| = \sqrt{Z_{i,\text{calc}}'^2 + Z_{i,\text{calc}}''^2}$

Because of the existence of random errors and the possibility of bias, it is recommended to use modulus weightings based on calculated impedances [626]. Macdonald [626] claims that modulus weighting introduces some bias to approximations.

14.6.4 Proportional Weighting

Proportional weighting was suggested by Macdonald [24, 615, 623, 626]. This method is especially important when the real and imaginary components have much different values. As in the case of modulus weighting, two choices are possible:

- a. Using experimental data: $w'_i = 1/(Z'_i)^2$ and $w''_i = 1/(Z''_i)^2$
- b. Using calculated data: $w'_i = 1/(Z'_{i,calc})^2$ and $w''_i = 1/(Z''_{i,calc})^2$

As before, it is recommended that calculated data be used [626]. Care must be taken in those cases where the imaginary impedances pass the real axes and become zero or very close to zero because their weight will go to infinity, exaggerating the importance of such points.

Modern approximation programs usually provide users with a choice of the weighting procedures and might contain other more advanced functions [626].

14.6.5 Weighting from Measurement Model

Orazem and coworkers [3, 624, 625] modified the method of statistical weighting in such a way that it could be used in cases of mildly nonstationary systems. Data should be acquired several times and fitted to the Voigt model, retaining a statistically significant number of circuit elements. From the differences between the experimental and model impedance values (each of which might be different for sequentially acquired impedances), the standard deviations might be determined at each frequency and then fitted to the model described earlier in (e). The calculated values are used in the calculation of the sum of squares, Eq. (14.18). The proposed procedure is detailed below:

- a. Impedance measurements should be repeated several times (six repetitions were used in Ref. [625]) in the same experimental conditions and at the same frequencies. The authors suggested that the standard deviations of the real and imaginary impedance components should be lower than 3 % of the impedance modulus at each frequency.
- b. A measurement series Voigt model, Figure 13.2, Eq. (13.10), should be fitted to each experimental data set, keeping the time constants positive and the resistances positive or negative. The number of Voigt elements should be increased until the confidence intervals 2σ (i.e., 95.4 %) for one of the parameters include zero. Then the number of the circuit elements should be decreased by one. If for one data set the number of Voigt elements is lower, then all other approximations should be recalculated with this reduced number of elements. This procedure satisfies the condition that the maximum number of parameters must be statistically important.
- c. The standard deviations of the residuals of the impedances, i.e., the differences between the experimental and corresponding model values, should be calculated

at each frequency. Such standard deviations should be bias free because they are calculated from the differences for all data sets, which were approximated separately.

- d. These standard deviations were fitted to the model for the data structure described earlier in point (e), p. 312.

The obtained standard deviations are used in the subsequent CNLS analysis of one of the impedance data files. Unfortunately, typical software programs, such as ZView, cannot perform this fitting. However, it can be easily done with Macdonald's LEVM program, although the experimental data should be prepared in a special format. An example of such an analysis is presented in Exercise 14.1. Several examples are discussed in the literature [613, 624, 627–632].

In practical approximations, modulus and proportional weighting procedures are usually used.

14.7 Statistical Tests

The purpose of modeling is to find an appropriate model described by an electrical circuit or equation by minimization of the sum of squares. Such model impedances should lie very close to the experimental ones without any systematic deviations. The first test is a visual comparison of the complex plane and Bode plots, which should agree. To assure that the approximating model is correct, several statistical tests might be used.

14.7.1 Chi-Square

The quality of fit may be verified by examining a χ^2 (chi-square) test. χ^2 is defined as

$$\chi^2 = \sum_{i=1}^N \left\{ \left[\frac{Z'_i - Z'_{i,\text{calc}}}{\sigma'_i} \right]^2 + \left[\frac{Z''_i - Z''_{i,\text{calc}}}{\sigma''_i} \right]^2 \right\}. \quad (14.20)$$

This parameter should be small. Because it depends on the number of points (i.e., frequencies), usually the reduced [617] value, which is χ^2 divided by the number of degrees of freedom, $\nu = 2N - m$, is calculated:

$$\chi^2_v = \frac{\chi^2}{\nu} = \frac{\chi^2}{2N - m}, \quad (14.21)$$

where N is the number of frequencies, i.e., there are $2N$ measured impedance values (N real and N imaginary), and m is the number of adjustable parameters used in the

model. If the estimates of σ_i are correct, this parameter should approach unity [619]. If the values of χ_v^2 are much larger than unity, the approximation or estimation of σ_i is incorrect. Values much lower than unity might indicate overestimation (too many parameters). The estimation of σ_i values might be accomplished by repeating the impedance measurements several times, as described earlier in Sects. 14.6.1 and 14.6.5. However, such data are not always available.

In CNLS approximations, modulus or proportional weightings are used. One can define the reduced sum of squares, for example, for proportional weighting:

$$S_v = \frac{S}{\nu} = \frac{1}{\nu} \sum_{i=1}^N \left\{ \left[\frac{Z'_i - Z'_{i,\text{calc}}}{Z'_{i,\text{calc}}} \right]^2 + \left[\frac{Z''_i - Z''_{i,\text{calc}}}{Z''_{i,\text{calc}}} \right]^2 \right\}. \quad (14.22)$$

If proportional or modulus errors are assumed, then the standard deviations of impedances are supposed to be proportional to the impedance values, $\sigma_i = \varepsilon Z_i$, where ε is the relative error of the measured impedances. A comparison of Eqs. (14.21) and (14.22) shows that

$$S_v = \varepsilon^2 \chi_v^2 \approx \varepsilon^2, \quad (14.23)$$

and the square root of the calculated reduced sum of squares is a measure of the relative error of the measured impedances.

In practice, the values of S_v are shown in commercial programs (however, the calculation details are rarely well documented). It should be stressed that for each weighting choices the values S_v are much different. This will be illustrated in the following example.

Example 14.6 Analysis of the experimental data are illustrated below. A numerical example is shown in Exercise 14.2. The impedance data are shown as symbols in Fig. 14.8. One should always start with the simplest possible model. The simplest model that can be used in this case is $R(RC)$; it contains three adjustable parameters. There are 67 data points, and $\nu = 2 \times 67 - 3 = 131$ degrees of freedom. In the same figure, the results of approximations using three weighting methods – (a) unity, (b) proportional, and (c) modulus – are presented. For these three models the following values of S and S_v were obtained: (a) $S = 205.4$, $S_v = 1.57$; (b) $S = 1.657$, $S_v = 0.0126$; (c) $S = 0.0524$, $S_v = 0.00040$. Of course, they cannot be simply compared between the models because different weighting procedures were used. Closer inspection of the results indicates that large differences were obtained for the proportional model, but for other models some systematic differences between the experimental and model data exist, which are visible on the Bode plots.

The differences can also be easily visualized by plotting the relative residuals, that is, the differences between the experimental and model impedances. If the model is correct, then the residuals should be randomly distributed around the zero line. An example of such a plot is shown in Fig. 14.9. It is evident that the residuals display systematic differences, which suggests that the model is not correct.

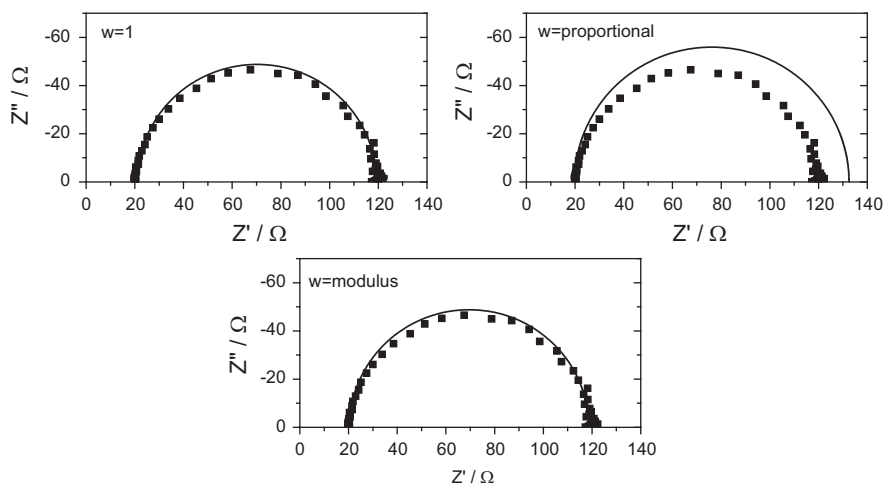


Fig. 14.8 Approximation of experimental data by model $R(RC)$ using unit, proportional, and modulus weighting

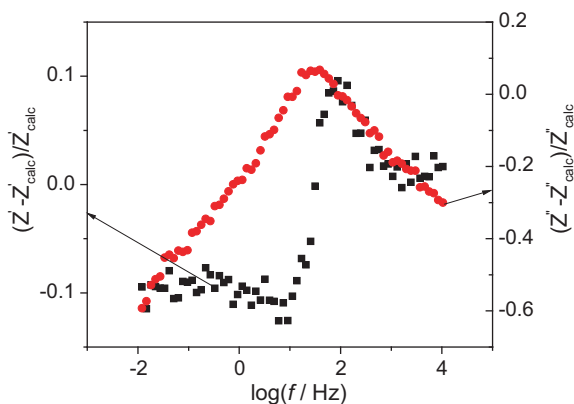


Fig. 14.9 Relative differences between experimental and calculated impedances for modulus weighting from Fig. 14.8

The next model one can use is one in which the capacitance is replaced by the CPE, that is, one more parameter is added. The results of the approximation to the model $R(QR)$ using different weighting methods are shown in Fig. 14.10. This time the approximation looks better. The values of the parameters S and S_v for the three weighting methods are as follows: (a) $S = 56.9$, $S_v = 0.434$; (b) $S = 0.0141$, $S_v = 0.00011$; (c) $S = 0.00708$, $S_v = 0.000054$. An important decrease in the sum of squares is observed after replacing the capacitance by the CPE. The plot of

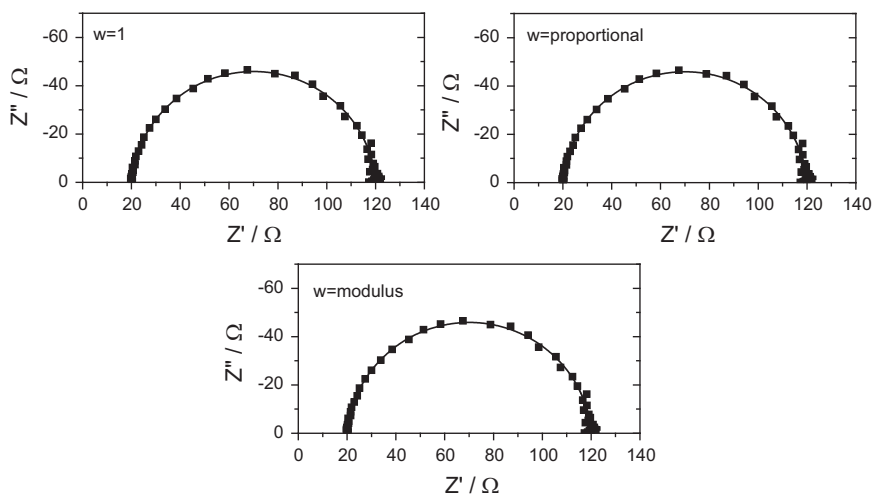


Fig. 14.10 Fit of experimental data to model containing CPE: $R(QR)$ for different weighting models

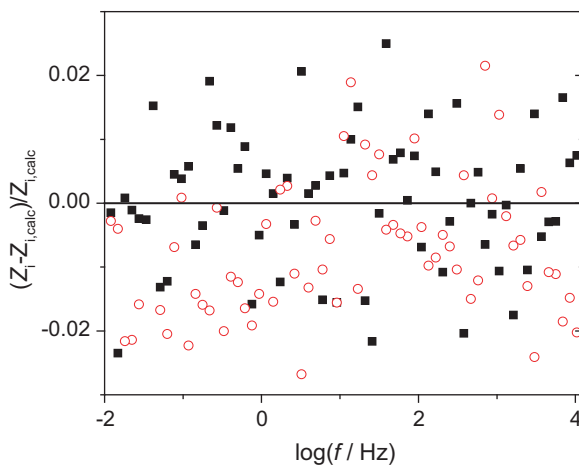


Fig. 14.11 Relative differences between experimental and calculated impedances for modulus weighting from Fig. 14.10

residuals is shown in Fig. 14.11. This time the residuals of the real and imaginary parts seem to be distributed randomly, and the fit is satisfactory.

In summary, analysis of the values of χ_v^2 or S_v is not sufficient to determine the goodness of fit. Additional analysis of the residuals and their randomness is also necessary.

14.7.2 Test F

The Fisher-Snedecor test F [633] is used to compare two different variances (square of standard deviations):

$$F = \frac{\sigma_1^2}{\sigma_2^2}. \quad (14.24)$$

This experimental value must be compared with $F(\alpha, \nu_1, \nu_2)$, where α is the confidence level, and ν_1 and ν_2 are the degrees of freedom of the numerator and denominator, respectively. The theoretical values $F(\alpha, \nu_1, \nu_2)$ are tabulated or might be calculated in Excel using the function F.INV.RT (former FINV). In practice, the most often used value for the confidence level are 0.05 and 0.01, corresponding to probabilities of 95 % and 99 %.

In the modeling of the impedance data one can use the F -test for the importance of the additional term [633]. One can add another parameter in the model only if this produces a statistically important decrease in the sum of squares. In general, if the sum of squares for the model containing m parameters is S_1 and after adding k parameters it is S_2 , the corresponding degrees of freedom are $2N - m$ and $2N - m - k$, respectively. Then one can write the following equation for the F -test:

$$F_{\text{exp}} = \frac{\frac{S_1 - S_2}{(2N - m) - (2N - m - k)}}{\frac{S_2}{2N - m - k}} = \frac{\frac{S_1 - S_2}{k}}{\frac{S_2}{2N - m - k}} = \frac{S_1^2}{S_2^2}. \quad (14.25)$$

This should be compared with the theoretical value of $F(\alpha, k, 2N - m - k)$. If $F_{\text{exp}} > F(\alpha, k, 2N - m - k)$, then the improvement is important and the new model may be accepted. If it is lower, then there is no reason to accept the new model and the simpler one should be retained. It is important to keep the number of new parameters as low as possible, that is, to add one parameter each time. In some cases, such as when a new (RC) parallel element is added to the Voigt circuit, one can use $k = 2$.

Example 14.7 Let us apply this test to the data in Example 14.6. In this case, $N = 67$, for the simpler model $R(CR)$ there are three parameters, and for the $R(QR)$ model there are four. Therefore, $\nu_1 = 1$ and $\nu_2 = 2 \times 67 - 4 = 130$. Let us apply this test to the unit weighting, where $S_1 = 205.4$ and $S_2 = 56.9$:

$$F_{\text{exp}} = \frac{\frac{205.4 - 56.9}{1}}{\frac{56.9}{130}} = 339.3. \quad (14.26)$$

The theoretical value is $F(0.05, 1, 130) = 3.91$; therefore, F_{exp} is much larger than the theoretical value and the addition of this one term is statistically justified at the confidence level assumed. Of course, this addition is justified for all three weighting procedures.

14.7.3 *t*-test for Importance of Regression Parameters

Another factor that should be considered is the standard deviation of the obtained parameters. When the standard deviation of a parameter is comparable to or larger than its value, such a parameter is unimportant in regression. This can be tested using a *t*-test:

$$t = \frac{p}{s_p}, \quad (14.27)$$

where p is the value of the parameter and s_p its standard deviation. The experimental value should be compared with that from the tables for $t(\alpha, 2N - m)$ for the confidence level of α and the number of degrees of freedom $2N - m$. If $t_{\text{exp}} > t(\alpha, 2N - m)$, this means that the parameter is much larger than its standard deviation and its presence is justified, but if it is lower, the parameter should be rejected.

Macdonald [634] proposed checking the precision of fitting parameters using Monte Carlo data simulations followed by CNLS approximations. This provides information about how accurately the parameters can be determined for an assumed amount of error in impedances and may be used in the design of experiments to extract such data precisely.

14.8 Conclusion

The experimental data that were checked by the Kramers-Kronig transforms may be used in modeling. First, usually, fit to an electrical equivalent model is carried out. It is important to use a proper weighting procedure and start with the simplest model. Then additional parameters can be added and their importance verified by the appropriate *F*- and *t*-tests. The number of adjustable parameters must be kept to a minimum. Additionally, comparison of the experimental and model impedances on complex plane and Bode plots should be carried out. Furthermore, plots of the residuals indicate the correctness of the model used. Next, on the basis of this fit, a physicochemical model might be constructed. One should check how the obtained parameters depend on the potential, concentration, gas pressure, hydrodynamic conditions, etc. If a strange or unusual dependence is obtained, one should check whether the assumed model is physically correct in the studied case. This is the most difficult part of modeling.

Exercises on impedance modeling are presented below.

14.9 Exercises

Exercise 14.1 Determine the error structure of the impedance in the files Z1.z, Z2.z, Z3.z, and Z4.z using Orazem's measurement model approach and determine the impedance parameters for Z1.z using the circuit $R_s(C_{dl}(R_{ct}Z_{FLW}))$, where Z_{FLW} is the finite-length transmissive mass transfer impedance.

Exercise 14.2 Find an electrical equivalent model describing data in the file 2.z. Try different weighting techniques. Calculate the sum of squares, S , and reduce the sum of squares, S_ν . Carry out an F -test.

Exercise 14.3 Fit data 3.z into the nested model $R_s(C_{dl}(R_{ct}(C_p R_p)))$. Check whether the use of CPEs instead of capacitances is statistically justified.

Exercise 14.4 Fit 4.z into the model $R_s(C_{dl}(R_{ct} C_p))$. Check whether the use of CPEs instead of capacitances is statistically justified.

Exercise 14.5 Fit the data in 5.z to the model $R(C(RW_s))$, where W_s is the transmissive mass transfer impedance. Check whether the use of the CPE is justified.

Chapter 15

Nonlinear Impedances (Higher Harmonics)

When linear electrical elements are used in circuits, the measured impedances are independent of the amplitude of the ac perturbation. However, in electrochemistry, the electrical equivalent parameters related to the kinetics, diffusion, and other aspects are nonlinear because the current is a nonlinear function of the applied potential. In such cases, as was already discussed in Sects. 4.2.1 and 13.2, a small perturbation amplitude must be used to avoid the formation of harmonics. Now let us look in more detail at the formation of nonlinearities and the applications of such methods.

Second and higher harmonic responses were studied at the very beginning of the development of impedance spectroscopy [15, 17, 29, 635, 636]. Let us look first at the simplest case of the Tafel equation.

15.1 Simple Electron Transfer Reaction Without Mass Transfer Effects

In the case of a simple one-electron transfer reaction in Tafel conditions (i.e., irreversible electrochemical process without mass transfer effects), the faradaic current is described as

$$i = i_{\text{ex}} \exp(\alpha f \eta), \quad (15.1)$$

where i_{ex} is the exchange current density, and η is the overpotential. Let us apply a sinusoidal potential perturbation $\Delta\eta$ on a dc potential η_{dc} :

$$\eta = \eta_{\text{dc}} + \Delta\eta = \eta_{\text{dc}} + E_0 \cos(\omega t), \quad (15.2)$$

where E_0 is the applied ac amplitude. The total current is

$$i = i_{\text{ex}} e^{\alpha f \eta_{\text{dc}}} e^{\alpha f E_0 \cos(\omega t)} = i_{\text{dc}} e^{\alpha f E_0 \cos(\omega t)}. \quad (15.3)$$

An oscillating current can be expressed as a Maclaurin series, see also Eq. (4.15) [15, 637, 638]:

$$i - i_{\text{dc}} = \Delta i = i_{\text{dc}} \left[1 + b \cos(\omega t) + \frac{1}{2!} b^2 \cos^2(\omega t) + \frac{1}{3!} b^3 \cos^3(\omega t) + \frac{1}{4!} b^4 \cos^4(\omega t) + \dots - 1 \right], \quad (15.4)$$

where $b = \alpha f E_0$. Using simple trigonometric identities [637, 639] this expression may be rearranged into harmonics:

$$\begin{aligned} \frac{\Delta i}{i_{\text{dc}}} &= i_0 + i_1 \cos(\omega t) + i_2 \cos(2\omega t) + i_3 \cos(3\omega t) + i_4 \cos(4\omega t) \\ &\quad + i_5 \cos(5\omega t) + \dots, \end{aligned} \quad (15.5)$$

where i_0 is the frequency-independent term and i_k are terms in front of $\cos(k\omega t)$:

$$\begin{aligned} i_0 &= \frac{1}{4} b^2 + \frac{1}{64} b^4 + \frac{1}{2304} b^6 + \dots, \\ i_1 &= b + \frac{1}{8} b^3 + \frac{1}{192} b^5 + \frac{1}{9216} b^7 + \dots = \sum_{k=1}^{\infty} \frac{b^k}{2^{2k} k! (k+1)!}, \\ i_2 &= \frac{1}{4} b^2 + \frac{1}{48} b^4 + \frac{1}{1536} b^6 + \dots, \\ i_3 &= \frac{1}{24} b^3 + \frac{1}{384} b^5 + \frac{1}{15360} b^7 + \dots, \\ i_4 &= \frac{1}{192} b^4 + \frac{1}{3840} b^6 + \dots, \\ i_5 &= \frac{1}{1920} b^5 + \frac{1}{46080} b^7 + \dots \end{aligned} \quad (15.6)$$

In these expressions, the influence of up to the seventh term is shown. Note that the frequency-independent term, i_0 , is not equal to zero; it is called a faradaic rectification current. It approaches zero for small amplitudes E_0 . Moreover, a current of odd frequencies contains only odd powers of b^k and that of even frequencies contains even powers. In addition, the importance of higher-order terms decreases, and when the amplitude E_0 is small, only the linear term is left out, $i_1 = b$, all the other terms become negligible, and a classical linearized

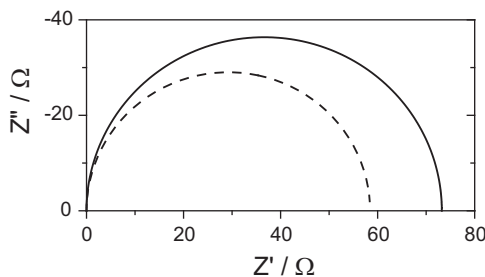


Fig. 15.1 Complex plane plots of fundamental harmonic impedances for simple redox reaction in Tafel zone; ac amplitudes: 5 mV rms – *continuous line*, 50 mV rms – *dashed line*; other parameters: $\alpha = 0.5$, $i_{\text{ex}} = 10^{-4}$ A, $\eta = 0.1$ V

impedance is obtained. It is evident that at larger amplitudes, all terms are influenced by higher-order terms.

The charge transfer resistance at the fundamental frequency, ω , may be obtained as [637]

$$R_{\text{ct}} = \lim_{E_0 \rightarrow 0} \left(\frac{E_0}{i_1 i_{\text{dc}}} \right) = \frac{1}{\alpha f i_{\text{dc}}}, \quad (15.7)$$

but the charge transfer resistance, including nonlinearities, \mathbb{R}_{ct} , is

$$\mathbb{R}_{\text{ct}} = \frac{E_0}{i_1 i_{\text{dc}}}, \quad (15.8)$$

that is, it is smaller than the R_{ct} value. This effect is presented in Fig. (15.1) for the fundamental harmonic impedance for two amplitudes of 5 and 50 mV rms. It is obvious that a larger amplitude causes lower charge transfer resistances because the higher harmonics influence the fundamental harmonic results.

Another approach to describing current nonlinearities is to use a Fourier series [640, 641]:

$$\frac{\Delta i}{i_{\text{dc}}} = I_0(b) - 1 + 2 \sum_{k=1}^{\infty} I_k(b) \cos(k\omega t), \quad (15.9)$$

where $I_k(b)$ are modified Bessel functions of b of order k . This implies that the currents in Eq. (15.6) converge to $i_0 = I_0(b) - 1$ and $i_k = I_k(b)$. In fact, they are series representations of the $I_n(b)$ Bessel functions. It should be mentioned that the Bessel functions $I_k(x)$ are available in Excel as BESSELI(x, k), and of course they might be computed easily in other programs such as Mathematica or Maple. The plot of the first few Bessel functions $I_k(b)$ is presented in Fig. 15.2 for different values of the ac impedance amplitude and $\alpha = 0.5$. These functions increase with increases of the parameter b . Only I_0 starts at one and all the other functions start at zero. Nevertheless, in Eq. (15.9) the frequency-independent term is $I_0(b) - 1$, which also starts at zero for $b \rightarrow 0$.

Fig. 15.2 Plot of Bessel $I_k(b)$ for different values of ac amplitude and $\alpha = 0.5$

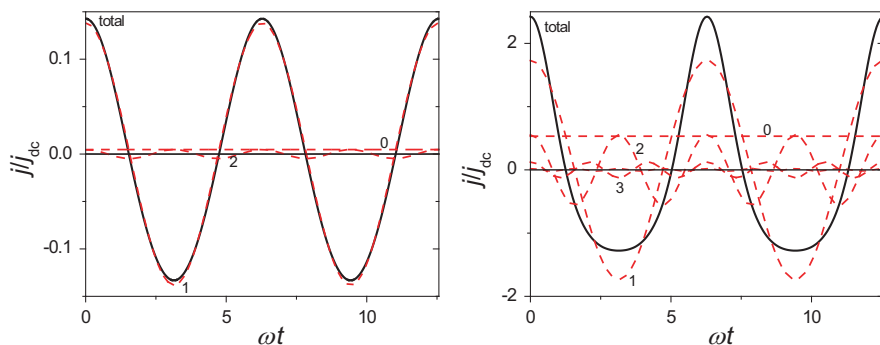
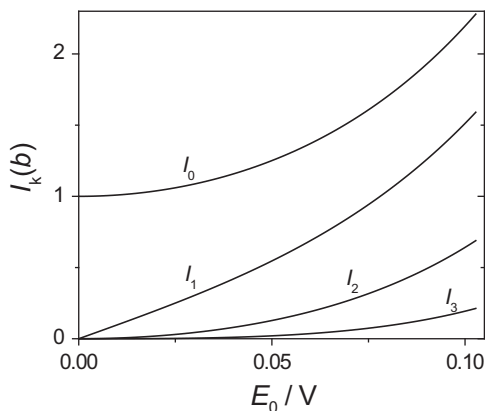


Fig. 15.3 Plots of total (*thick line*) and harmonics (*dotted lines*, harmonic number indicated) for faradaic impedance in one-electron Tafel conditions with $\alpha = 0.5$. Amplitudes: *left* – 5 mV rms, *right* – 50 mV rms

Let us look at the influence of nonlinearities on observed spectra for typical amplitudes of 5 and 50 mV rms, that is, amplitudes of $5\sqrt{2}$ and $50\sqrt{2}$ [641]. They are shown in Fig. 15.3. At small amplitudes, the nonlinear effects are negligible. However, for larger amplitudes the current observed in Tafel conditions is no longer sinusoidal and contains contributions from higher harmonics.

Harrington [641] noticed that measurements of the first harmonics at different amplitudes allow for the determination of the transfer coefficient. The ratio of the fundamental harmonic current using the amplitude E_0 and $2E_0$ equals

$$\frac{i(\omega, 2E_0)}{i(\omega, E_0)} = \frac{I_1(2b)}{I_1(b)} \quad (15.10)$$

and allows for the determination of the parameter b and, as a consequence, the transfer coefficient. Both amplitudes should be in the nonlinear zone, e.g., 30 and 60 mV.

One can proceed in a similar way when the current is described by the Butler-Volmer equation [637, 641, 642]

$$i = i_a \exp(b_a \eta) - i_c \exp(-b_c \eta), \quad (15.11)$$

where b_a and b_c contain anodic and cathodic transfer coefficients. This leads to

$$\begin{aligned} \Delta i &= i - i_{dc} = i_a \left(e^{b_a \cos(\omega t)} - 1 \right) - i_c \left(e^{-b_c \cos(\omega t)} - 1 \right) \\ &= i_a [I_0(b_a) - 1 + 2I_1(b_a) \cos(\omega t) + 2I_2(b_a) \cos(2\omega t) + 2I_3(b_a) \cos(3\omega t) + \dots] \\ &\quad - i_c [I_0(-b_c) - 1 + 2I_1(-b_c) \cos(\omega t) + 2I_2(-b_c) \cos(2\omega t) \\ &\quad + 2I_3(-b_c) \cos(3\omega t) + \dots]. \end{aligned} \quad (15.12)$$

Taking into account that $I_k(-b) = I_k(b)$ for k even and $I_k(-b) = -I_k(b)$ for k odd Eq. (15.12) becomes

$$\begin{aligned} \Delta i &= i_a [I_0(b_a) - 1] - i_c [I_0(b_c) - 1] \\ &\quad + 2 \sum_{k=1}^{\infty} \left[i_a I_k(b_a) - (-1)^k i_c I_k(b_c) \right] \cos(k\omega t). \end{aligned} \quad (15.13)$$

It simply contains the difference between two series. For small amplitudes the first frequency-independent term and harmonics for $k \geq 2$ become zero and a classical linear response ($k = 1$) is observed. Nonlinear effects are observed for larger ac amplitudes, generating larger values of b_a and b_c .

In the case of large applied amplitudes, the nonlinear effects depend on the solution resistance. In fact, ac voltage is attenuated by solution resistance, leading to the application of a lower amplitude. This effect was discussed in detail by Diard et al. [642–644].

It should be stressed that in the case of nonlinear effects, response at the fundamental frequency is perturbed.

15.2 Other Reaction Mechanism

Harmonic analysis was also applied to other reaction mechanisms. One of the simplest reactions is a reversible redox process with Red and Ox forms in the solution. When bulk concentrations and the diffusion coefficient of both forms are identical, the dc current may be described as [637, 642, 645]

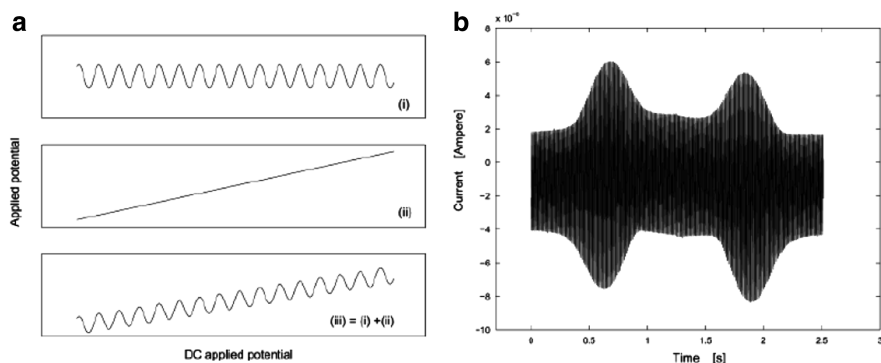


Fig. 15.4 (a) Signal applied in large-amplitude ac voltammetry: (i) ac signal, (ii) dc sweep, (iii) sum of two signals; (b) total current produced by application of signal (iii) in cyclic voltammetric conditions (Reprinted with permission from Ref. [649]. Copyright 2004 American Chemical Society)

$$i = \frac{nFDC^*}{\delta} \tanh \left[\frac{nf(E - E^0)}{2} \right]. \quad (15.14)$$

This equation can be written as an infinite series as was done previously. It converges for low ac amplitudes. A detailed analytical method of obtaining harmonic elements was described in Ref. [645]. Harmonic analysis was also applied to quasi-reversible reactions on a rotating disk electrode [642].

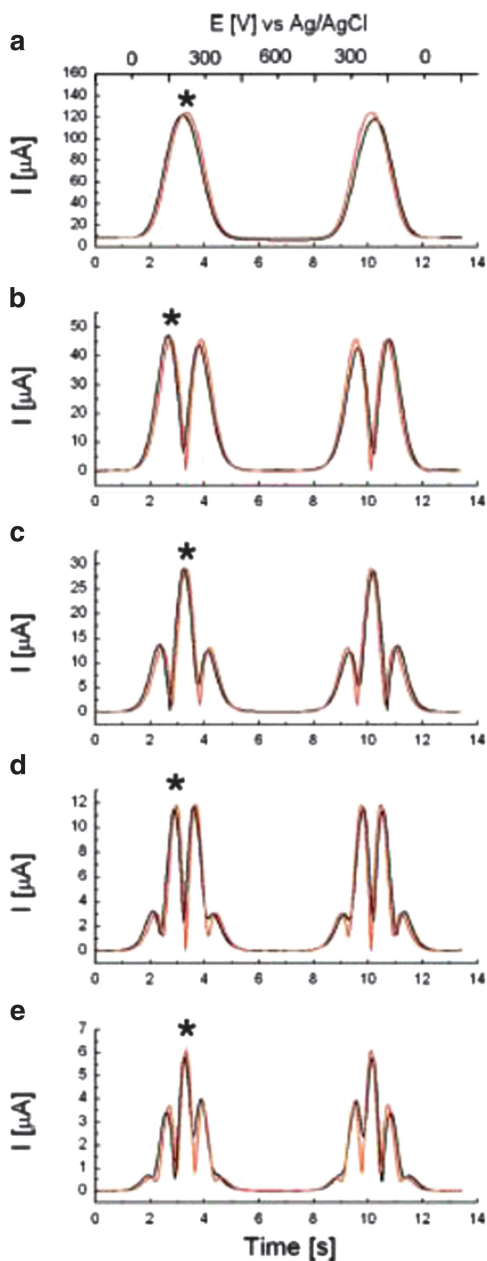
Other mechanisms studied include electrosorption with Langmuir isotherm [641] and a Volmer-Heyrovsky type of mechanism [641, 642]. The reader should consult these references for more details.

Bond and coworkers [646–657] have proposed use of the ac voltammetry with large ac signal superimposed on the linear sweep. The applied potential and measured current are presented in Fig. 15.4.

Then, to analyze the obtained current, a Fourier transform is applied and the responses at the fundamental, ω , and harmonic, 2ω , 3ω , 4ω , ..., frequencies are obtained. Next, the current responses at the fundamental and harmonic frequencies are extracted by an inverse Fourier transform. Harmonics up to the eighth order were obtained. Analysis of the kinetic parameters is carried out by comparison of the experimental and simulated data. Theoretical ac voltammograms were simulated using classical numerical simulations of the diffusion-kinetic process using an implicit finite-difference method [658, 659] with a subsequent Fourier analysis of the simulated data. An example of the comparison of the experimental and simulated data is shown in Fig. 15.5. In this case, oxidation of ferrocenemethanol appeared reversible, and a good agreement was found with the simulated data for the reversible process.

Fourier transform analysis of higher harmonic data is well suited to differentiate between the effects of the solution resistance and kinetics [649, 651]. It is well

Fig. 15.5 Large-amplitude fundamental to fifth (a–e) harmonic Fourier transformed ac cyclic voltammograms (*black*) obtained for reversible oxidation of 1 mM ferrocenemethanol, compared with simulations of reversible process (*red*). Conditions employed: $f = 21.46$ Hz, ac amplitude $E_0 = 100$ mV, sweep rate $\nu = 111.76$ mV s $^{-1}$ (Reprinted with permission from Ref. [652] (Fig. 15.2) Copyright 2008 American Chemical Society)



known that in cyclic voltammetry these two effects lead to an increase in the potential difference between anodic and cathodic peaks. A Fourier transform of higher harmonics can easily discriminate between these effects. An example is shown in Fig. 15.6, where the effects of the solution resistance and electron transfer

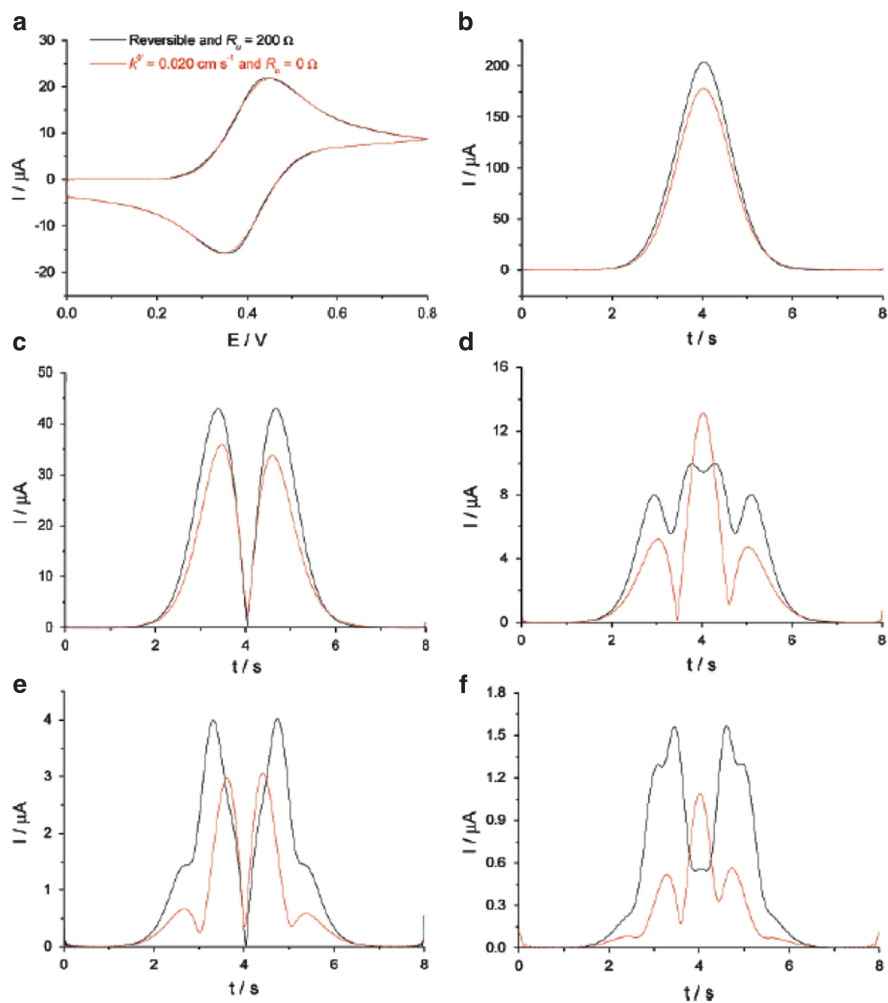


Fig. 15.6 Comparison of simulated FT large-amplitude ac voltammograms for a reversible process with solution resistance R_u of 200 Ω and a quasi-reversible process with $k^0 = 0.020 \text{ cm s}^{-1}$ and R_u of 0 Ω . (a) dc component, (b) fundamental, (c) second, (d) third, (e) fourth, and (f) fifth harmonics (Reprinted with permission from Ref. [651] (Fig. 15.2). Copyright 2007 American Chemical Society)

kinetics are completely different at higher harmonics. In general, linear elements such as solution resistance and double-layer capacitance should disappear at higher harmonics because they do not produce nonlinear effects. Bond and coworkers [649] stated that (a) the dc cyclic component provides an estimate of $E^{0'}$ (because the R_u and k^0 effects are minimized); (b) the fundamental harmonic provides an estimate of C_{dl} (because it has a high capacitance-to-faradaic current ratio); and (c) the second harmonic provides an estimate of R_u , k^0 , and α (because the C_{dl} effect

is minimized). They also studied the influence of noise on obtained results [650]. Fourier transform analysis of higher harmonic data was applied to study the kinetics of surface-bound molecules [647] and adsorbed films [653], chemical reactions coupled with electron transfer [652, 654], fast electron transfer processes [649, 655], and the low concentration of electroactive species [660, 652]. Its wider use is limited by a lack of commercial software to simulate and analyze data. The authors also discussed the use of square wave excitation to obtain similar information [661–665].

Another approach using nonlinear frequency response analysis with the help of the Volterra series expansion and generalized Fourier transform was also proposed and applied to the study of methanol or ferrocyanide oxidation [666–668].

15.3 Conclusions

The use of larger amplitudes generates harmonics and influences responses at the fundamental frequency. Analysis of higher harmonics may be carried out analytically in simpler cases or numerically in more complex cases of ac voltammetry. Careful analysis of higher harmonics allows for the discrimination of solution resistance and double-layer capacitance effects and of the kinetic parameters of electron transfer reactions and homogeneous chemical kinetics coupled with electrochemical reactions.

Chapter 16

Instrumental Limitations

Typical EIS measurements are usually carried out in a frequency range from 20 to 50 kHz to 0.1 Hz. However, in dielectric [669] or fast kinetic studies [670], high frequencies up to several megahertz are necessary. Such measurements cannot be carried out with a potentiostat, which is too slow and introduces additional phase shift. On the other hand, very slow frequencies in the millihertz or microhertz range are necessary in studies of intercalation (batteries [671, 672], hydride formation [673]). In addition, the measured impedance varies from several megaohms (or gigaohms) for paints and coatings, corrosion in concrete, or solid materials to milliohms or lower [674] for fuel cells or batteries. This puts high demands on the measurement equipment and can lead to errors and artifacts. This measuring equipment and cell problems will be described below.

16.1 Measurements of High Impedances

Measurements of high impedance, i.e., high-resistance and low-capacitance samples, are very demanding. Each potentiostat is characterized by a certain input impedance that limits its applications. One ISO norm, ISO 16773 (parts 1–4) [675], describes in detail equipment calibration and measurement procedures as well as application notes from Gamry [676] and Solarton [677–681].

As a first step, the potentiostat should be tested in an open circuit in a two-electrode setup. For this experiment the reference and auxiliary electrodes should be connected together with no connection between them and the working electrode (open circuit). Then the impedance measurements should be carried out in a frequency range of 10^5 –0.01 Hz. Although in typical electrochemical experiments the amplitude used is 3.5 mV rms (i.e., 5 mV amplitude, 10 mV peak to peak), in these measurements the amplitude might be larger, 20–30 mV rms. A higher amplitude is necessary when the sample impedance is very high and the current flow very low. The open-circuit impedance behaves as a parallel connection of the input resistance and capacitance (RC) (Fig. 2.33). The sample impedance $|Z|$ must

be much smaller than the potentiostat open-circuit impedance; otherwise, erroneous results will be obtained. If the potentiostat's input impedance is too small, one can use another piece of specialized equipment, such as the Solartron 1296 Dielectric Interface, which works with a frequency analyzer and is able to measure impedances up to 100 T Ω [677–681].

Accurate impedance measurements at high frequencies are affected by the input and cable capacitance. Approaches to dealing with this problem are discussed in Solartron Application Notes [679, 680].

Next, the equipment should be checked using a dummy cell, a simple (RC), $R_1(R_2C)$, or $(C_1(R_1(R_2C_2)))$ circuit, but with R_2 within a range of the measured sample resistances, on the order of gigaohms and a capacitance on the order of nanofarads [675]. This will give the accuracy of the measurements. One can also consult the accuracy contour map from the manual of a given potentiostat [676].

Finally, the sample should be measured. It should be kept in mind that an increase in the real surface area of a working electrode decreases its impedance. The counter electrode should be made of a noncorroding material, for example, a noble metal or other low-impedance electrode. Its surface area should be large, comparable to that of a sample, and placed in parallel to the working electrode. It might be necessary to place the measured cell in a Faraday cage.

Certain artifacts are also observed in studies in low-conductivity media [682]. In studies in pure 80 % and 100 % acetic acid a very important influence of the distance between the tip of a Luggin capillary and a working electrode made of stainless steel was observed (Fig. 16.1). These solutions were characterized by very large resistivities, 8–10 k Ω cm for 80 % and 8–12 M Ω for 100 % acetic acid. At short distances, high-frequency capacitive-inductive behavior is apparent. Similar behavior was also observed when a Pt pseudo-reference electrode was used. Such behavior was explained by the capacitive-resistive coupling between working and reference, working-auxiliary, and reference-auxiliary electrodes [682].

Similar artifacts were observed at high frequencies in highly conducting solutions [683] when the Luggin capillary was located too close to the electrode surface. In general, it should be experimentally checked whether the distance between the tip of a Luggin capillary and a reference electrode affects observed impedance spectra. The only effect of changing this distance should be a parallel displacement of the complex plane plot along the real axis, that is, the change in the uncompensated solution resistance. The conditions for the reference electrode will be discussed below.

16.2 Measurements at High Frequencies

The slow response of potentiostats limits studies at high frequencies. Although many manufacturers claim that their potentiostat can work at very high frequencies up to 1 MHz, in practice the upper limit is 50 to 100 kHz and in some cases as low as 20 kHz. This can be easily checked experimentally.

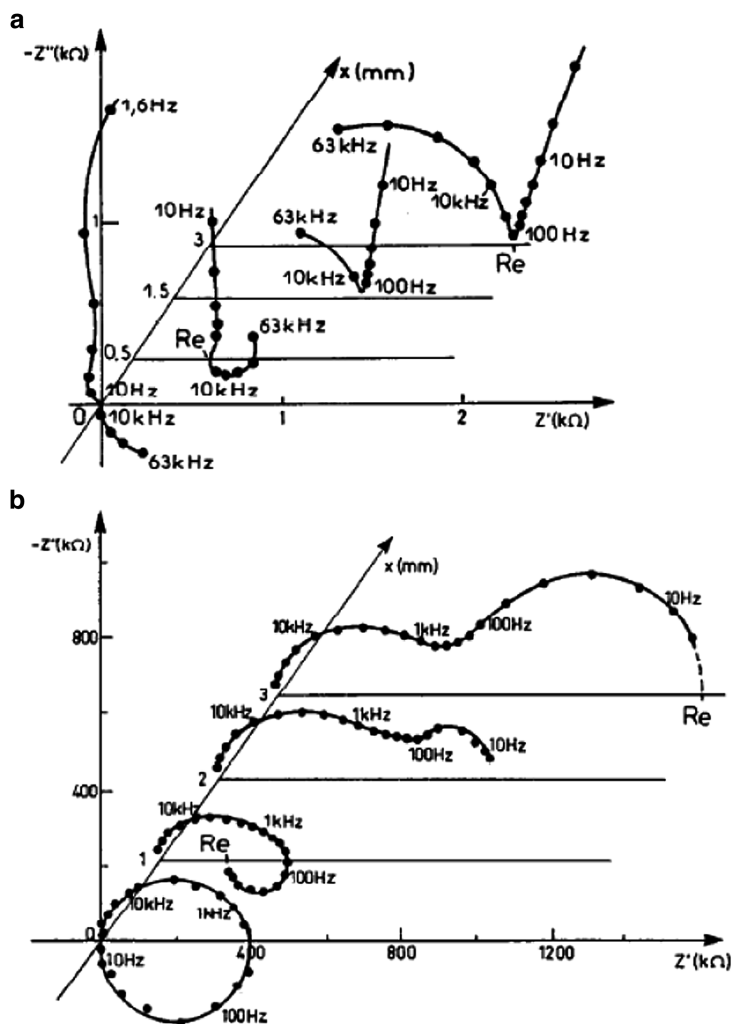


Fig. 16.1 Influence of distance between tip of Luggin capillary and working electrode in 80 % and 100 % acetic acid at stainless steel electrode (From Ref. [682], copyright (1990), with permission of Elsevier)

Schöne and Wiesbeck [684] proposed using two working electrodes (disk-ring) with electronic compensation of the solution resistance and frequency analyzer without a potentiostat. The potentiostat was used only for slow dc polarization of the working electrodes.

The use of two identical working electrodes was proposed by Sibert et al. [685]. The electrodes should be placed close to each other to minimize the solution resistance and be polarized by a small ac amplitude between them by a FRA. The current is measured as a potential drop on a small calibrated resistance

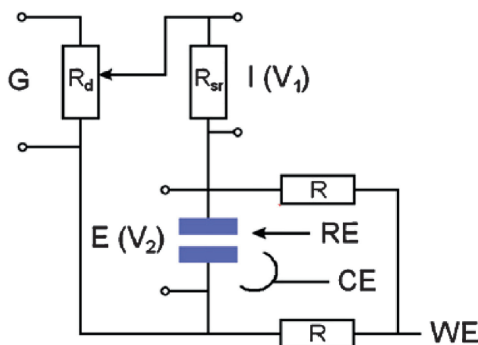


Fig. 16.2 Setup for high-frequency measurements using identical twin electrodes; ac generator G produces higher amplitude, which is divided by potentiometer R_d ; current is measured as potential drop (V_1) at R_{sr} ; potential is measured at electrodes (V_2), V_1 and V_2 are fed to FRA; both working electrodes are dc polarized through large resistance from potentiostat (From Ref. [686], copyright (2012), with permission from Elsevier)

and fed back to the frequency response analyzer. The dc polarization of these two electrodes at the same potential is assured by a potentiostat through large resistances. The electrical connections are shown in Fig. 16.2. This method was recently used to measure the fast reaction of HUPD at Pt [686]. The system worked well up to 1 MHz.

Fafilek [687] proposed another setup in which a potential is applied without a potentiostat to two electrodes, one working and another a very large-surface-area Pt electrode. In such an arrangement, the impedance of the large-surface-area Pt electrode might be neglected. This method was also used later to measure HUPD kinetics at a Pt electrode [686]. The connections are displayed in Fig. 16.3. This system allowed for measurements up to 1 MHz.

The systems shown previously make it possible to work at high frequencies without potentiostats, which have a limited response time, and to study fast electrochemical processes.

Some studies without a potentiostat or with a specially constructed fast potentiostat were carried out but with small currents at ultramicroelectrodes [688–690].

16.3 Measurements of Low Impedances

In the case of low sample impedances, large currents flow in the system. Large currents generate inductive effects in leads and measuring resistors at higher frequencies [691]. However, even larger inductive effects are generated by cells [692]. An example of such an effect is presented in Fig. 16.4. It appears at high frequencies and is similar to the effect of an inductance in series (compare with Fig. 2.41).

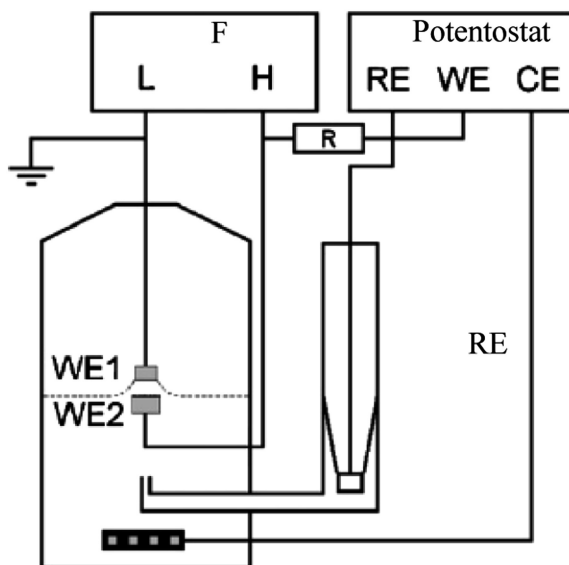


Fig. 16.3 Setup for high-frequency impedance measurements; WE1 working electrode, WE2 high-surface-area Pt electrode. Potential is applied and current measured by FRA; one electrode is polarized by potentiostat (From Ref. [686], copyright (2012), with permission from Elsevier)

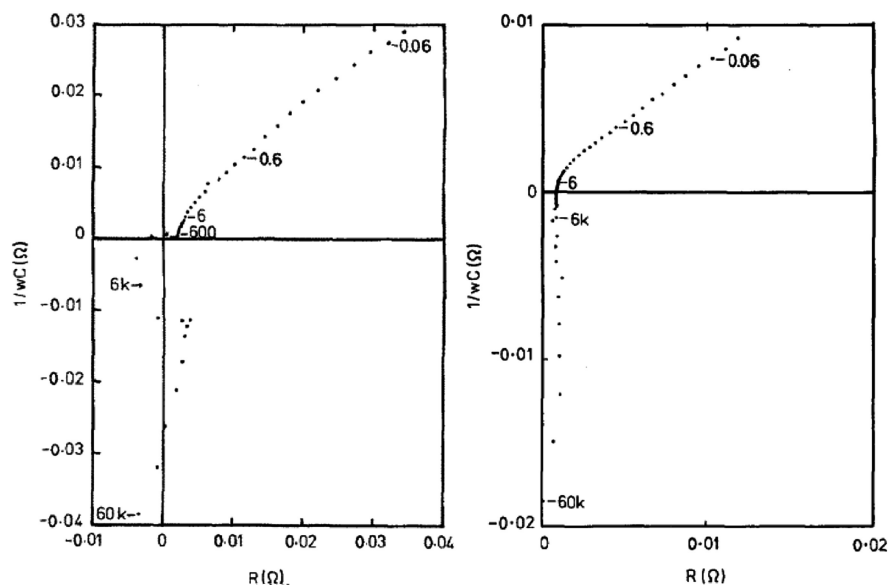


Fig. 16.4 Complex plane plots of impedance of lead acid battery using sense resistor of 10 Ω (left) and calibrated shortening bar (right) (From Ref. [691] with kind permission from Springer Science +Business Media)

This impedance was acquired using an internal resistance of commercial measuring equipment of $10\ \Omega$. As the cell impedance was less than $0.1\ \Omega$, a lower sense resistor was desirable. The authors used and calibrated a shortening bar as a $0.1245\ \Omega$ sensing resistor, determined its characteristics, and subtracted its impedance to obtain the pure impedance of the battery. The result is shown in Fig. 16.4 (right). In these measurements long commercial cables with crocodile clips were replaced by short cables bolted to the cell terminals. It is also recommended to use coaxial cables or twisted cable pairs in which currents flow in opposite directions, decreasing the inductive effect [693, 694].

Impedance measurements in such cases should be carried out in galvanostatic mode. In fact, applying a 5 mV amplitude to a sample having low resistance, e.g., $1\ \text{m}\Omega$, causes a current of 5 A and for lower impedances even more. Because it is technically difficult to apply amplitudes lower than 1 mV, the ac current is applied and the ac voltage measured [693, 694]. Potentiostats are usually slower in the galvanostatic than in the potentiostatic mode. However, they are faster in a two- than a three-electrode mode.

Ordinary potentiostats are limited to a highest current of approximately 1 A. To study higher currents, either booster potentiostats [695] or so-called load banks should be used [696, 697]. In load banks, the ac current may be modulated externally and the potential drop on a load resistor (proportional to current) and potential difference at the studied object are applied to the frequency response analyzer to measure the impedance. Analysis of the impedance of fuel cells with the separation of impedances of the anode, cathode, and load were presented by Diard et al. [698, 699]. A similar correction procedure was also described in Ref. [700].

In general, in studies of very low impedances, the ac current might be measured as a potential drop on a very small resistor and the ac voltage as a potential difference at the studied object; both ac voltages should be fed to the frequency response analyzer to measure the impedance. The impedance of the resistor and that of the cables/connections should be subtracted from the total measured impedance.

16.4 Reference Electrode

The quality of the reference electrode is primordial in all EIS studies. Its impedance must be low, below $1\ \text{k}\Omega$; therefore, some reference electrodes used in pH determination cannot be used (although they may work in dc experiments). Reference electrodes are usually equipped with a Luggin capillary probe to decrease the uncompensated solution resistance. The tip of the Luggin capillary is usually partially blocked with ceramic frits, Vycor glass frits, or asbestos threads to decrease the flow of the filling solution and possible contamination. Ideally, the inner reference electrode solution and the cell solution should be the same. This may be obtained using calomel or Ag|AgCl electrodes when working with chlorides, Hg| Hg_2SO_4 | SO_4^{2-} when working with sulfuric acid or sulfates, or Hg| OH^- when

working in alkaline solutions. The double junction reference electrodes is often used to avoid contamination, but the total impedance must be checked, especially in nonaqueous solutions.

It is simple to measure the impedance of the reference electrode. The reference electrode must be immersed in the electrolyte in a beaker, a large-surface-area inert electrode also immersed in this solution, and the impedance measured at the open-circuit potential [701].

The response time of the measuring circuit is also limited by the resistance of the electrolyte inside the Luggin capillary [702–704]. Strange impedances at high frequencies were also observed in highly conducting solutions [683] when the Luggin capillary was located too close to the electrode surface. To eliminate these problems, a Pt wire connected to the reference electrode through a small capacitor (100 pF to 10 nF) and immersed in the solution can be used [701, 702]. In such a configuration, the high-frequency signal flows through the capacitor and the dc signal through the reference electrode. It was also found that insertion of the Pt wire into the Luggin capillary (with no connections) also improved the response time of the reference electrode [704].

16.5 Conclusions

Modern impedance apparatus are capable of handling low or high impedances in a wide frequency range. However, care must be taken when working in more extreme conditions of high frequencies and very low or very high impedances. The measurement possibilities of the system must be well checked, usually using appropriate dummy cells.

One of the most often found artifacts is related to the reference electrode, its impedance, and the distance of the Luggin capillary from the electrode. Its impedance must be low, and if the distance from the working electrode is changed, only the solution resistance should change without affecting the shape of the impedances.

Chapter 17

Conclusions

Electrochemical impedance spectroscopy is a mature technique, and its fundamental mathematical problems are well understood. Impedances can be written for any electrochemical mechanism using standard procedures. Modern electrochemical equipment makes it possible to acquire data in a wide range of frequencies and with various impedance values. The validity of experimental data can be verified by standard procedures involving Kramers-Kronig transforms. Several programs either allow for the use of predefined simple and distributed elements in the construction of electrical equivalent circuits or directly fit data to equations (which should be defined by the user).

The biggest challenge is correctly interpreting the experimental data and assigning correct circuits/equations to the models. Formal fitting of the experimental impedances to electrical equivalent circuits is simple and represents the most widely used procedure; however, this procedure generally conveys little information about the electrochemical mechanism. The biggest problem in the analysis of impedances is correctly assigning a physical meaning to the observed features (physicochemical modeling). A casual perusal of the literature reveals that experimental data are often misinterpreted. It must be stressed that correct modeling is the most difficult part of analyzing impedance data. First, the steady-state current-potential characteristics must be well understood. Next, additional experiments with modifications to the concentration/partial pressure, temperature, hydrodynamic conditions, electrode surface, and morphology might be necessary.

Finally, once a correct physicochemical model is found and its parameters determined, then one may set about determining the kinetic parameters of the system. It should be emphasized that impedance parameters (e.g., resistances, capacitances, or other mechanism-related parameters) are derivatives of rates of electrochemical and chemical reactions and are complex functions of the rate constants and other parameters, for example, adsorption and concentration. Such analyses are carried out using nonlinear approximations of the impedance parameters as functions of the electrode potential and other experimental parameters, and these analyses are being performed on an increasingly frequent basis. Of course, one cannot neglect error analysis to check the reliability of the procedure.

Although most impedance spectra are relatively simple, in some cases – most often in corrosion – they are very complex. Macdonald [1] suggested doing analysis by pattern recognition using artificial neural networks coupled with extensive libraries of reaction mechanisms. However, although such tools are very promising they are still rarely used [620] and not yet commercially available.

Appendix: Laplace Transforms

L[f(t)] = F(s)

$f(t)$	$F(s)$
1	$\frac{1}{s}$
$\frac{1}{\sqrt{\pi t}}$	$\frac{1}{\sqrt{s}}$
$\sqrt{\frac{t}{\pi}}$	$\frac{1}{s^{3/2}}$
e^{at}	$\frac{1}{s-a}$
$\frac{1}{\sqrt{\pi t}} \exp\left(-\frac{k^2}{4t}\right)$	$\frac{1}{\sqrt{s}} \exp(-k\sqrt{s}) \quad k \geq 0$
$\operatorname{erfc}\left(\frac{y}{2\sqrt{t}}\right)$	$\frac{1}{s} \exp(-\sqrt{s}y)$
$\frac{1}{\sqrt{\pi(t-\tau)}}$	$\frac{\exp(-\tau s)}{\sqrt{s}}$
t	$\frac{1}{s^2}$
$\exp(a^2t) \operatorname{erfc}(at^{1/2})$	$\frac{1}{s^{1/2}(s^{1/2}+a)}$
$f^n(t)$	$s^n F(s) - s^{n-1}f(0) - s^{n-2}f'(0) - \dots - f^{n-1}(0)$
$\int_0^t f(t)dt$	$\frac{1}{s} F(s)$
$\int_0^t f(t-\tau)g(\tau)d\tau$	$F(s) \cdot G(s)$

(continued)

(continued)

$f(t)$	$F(s)$
$\sin(at)$	$\frac{a}{s^2 + a^2}$
$\cos(at)$	$\frac{s}{s^2 + a^2}$
$\frac{1}{a} \sinh(at)$	$\frac{1}{s^2 - a^2}$
$\cosh(at)$	$\frac{s}{s^2 - a^2}$

References

1. D.D. Macdonald, *Electrochim. Acta* **51**, 1376 (2006)
2. D.D. Macdonald, Reflections on the history of electrochemical impedance spectroscopy. Paper presented at 6th international symposium on electrochemical impedance spectroscopy Cocoa Beach, Florida, 17–21 May 2004
3. M.E. Orazem, B. Tribollet, *Electrochemical Impedance Spectroscopy* (Wiley, New York, 2008)
4. O. Heaviside, *Electrical Papers*, vols. 1–2 (MacMillan, New York, 1894)
5. W. Nernst, *Z. Elektrochem.* **14**, 622 (1894)
6. K.S. Cole, R.H. Cole, *J. Chem. Phys.* **9**, 341 (1941)
7. D.W. Davidson, R.H. Cole, *J. Chem. Phys.* **19**, 1484 (1951)
8. E. Warburg, *Ann. Phys. Chem.* **67**, 493 (1899)
9. P.I. Dolin, B.V. Ershler, *Acta Physicochem. URSS* **13**, 747 (1940)
10. J.E.B. Randles, *Trans. Farad. Soc.* **1**, 11 (1947); J.E.B. Randles, in *Transactions of the Symposium on Electrode Processes*, ed. by E. Yeager, (Wiley, New York, 1961), p. 209
11. C. Gabrielli, Identification of electrochemical processes by frequency response analysis, Technical Report Nr 004/83, Solartron Analytical, Issue 3, March 1998
12. P. Delahay, *New Instrumental Methods in Electrochemistry* (Interscience, New York, 1954)
13. B. Breyer, H.H. Bauer, *Alternating Current Polarography and Tensammetry*, ed. by P.J. Elving, I.M. Kolthoff (Wiley-Interscience, New York, 1963)
14. K.J. Vetter, *Electrochemical Kinetics* (Academic, New York, 1967)
15. D.D. Macdonald, *Transient Techniques in Electrochemistry* (Plenum Press, New York, 1977)
16. A.M. Bond, *Modern Polarographic Techniques in Analytical Chemistry* (Marcel Dekker, New York, 1980)
17. A.J. Bard, L.R. Faulkner, *Electrochemical Methods. Fundamentals and Applications* (Wiley, New York, 2001)
18. Southampton Electrochemistry Group (R. Greef, R. Peat, L.M. Peter, D. Pletcher, J. Roninson), *Instrumental Methods in Electrochemistry* (Ellis Horwood, New York, Chichester, 1985).
19. E. Gileadi, *Electrode Kinetics for Chemists, Engineers, and Material Scientists* (VCH, New York, 1993)
20. C.M.A. Brett, A.M. Oliveira Brett, *Electrochemistry, Principles, Methods, and Applications* (Oxford University Press, Oxford, 1993)
21. Z. Galus, *Fundamentals of Electrochemical Analysis* (Ellis Horwood, New York, 1994)
22. I. Rubinstein (ed.), *Physical Electrochemistry, Principles, Methods, and Applications* (Marcel Dekker, New York, 1995)
23. J.R. Macdonald (ed.), *Impedance Spectroscopy: Emphasizing Solid Materials and Systems*, 1st edn. (Wiley, New York, 2001)

24. E. Barsoukov, J.R. Macdonald (eds.), *Impedance Spectroscopy: Theory, Experiment, and Applications*, 2nd edn. (Wiley-Interscience, Hoboken, 2005)
25. V.F. Lvovich, *Impedance Spectroscopy, Applications to Electrochemical and Dielectric Phenomena* (Wiley, Hoboken, 2012)
26. X.-Z. Yuan, C. Song, H. Wang, J. Zhang, *Electrochemical Impedance Spectroscopy in PEM Fuel Cells* (Springer, London, 2010)
27. Z.B. Stoyanov, B.M. Grafov, B.S. Savova-Stoyanova, V.V. Elkin, V.V. Elkin, *Electrochemical Impedance* (Nauka, Moscow, 1991) (in Russian)
28. Z. Stoyanov, D. Vladikova, *Differential Impedance Analysis* (Marin Drinov Academic Publishing House, Sofia, 2005)
29. D.E. Smith, AC polarography and related techniques: theory and practice, in *Electroanalytical Chemistry: A Series of Advances*, ed. by A.J. Bard, vol. 1 (Marcel Dekker, New York, 1966), pp. 1–155
30. M. Sluyters-Rehbach, J.H. Sluyters, Sine wave methods in the study of electrode processes, in *Electroanalytical Chemistry: A Series of Advances*, ed. by A.J. Bard, vol. 4 (Marcel Dekker, New York, 1970), pp. 1–128
31. E.R. Brown, R.F. Large, Cyclic voltammetry, ac polarography, and related techniques, in *Physical Methods of Chemistry, Techniques of Chemistry*, ed. by A. Weissberger, W. Rossiter. Part IIA: Electrochemical Methods, vol. 1, 4th edn. (Wiley-Interscience, New York, 1971), pp. 423–530
32. D.E. Smith, Applications of on-line digital computers in ac polarography and related techniques, in *Electrochemistry: Calculations, Simulations, and Instrumentation*, ed. by J.S. Mattson, H.B. Mark, H.C. MacDonald (Marcel Dekker, New York, 1972), pp. 369–422
33. K.O. Hever, Solid state cells, impedance and polarization, in *Physics of Electrolytes*, vol. 2, Chap. 19, ed. by J. Hladik (Academic, New York, 1972), pp. 809–838
34. R.D. Armstrong, M.F. Bell, A.A. Metcalfe, The ac impedance of complex electrochemical reactions, in *Electrochemistry: A Specialist Periodical Report*, vol. 6, ed. by G.J. Hills, D. Pletcher, H.R. Thirsk (The Royal Society of Chemistry/The Chemical Society, Burlington House/London, 1978), p. 98127
35. W.I. Archer, R.D. Armstrong, The application of ac impedance methods to solid electrolytes, in *Electrochemistry: A Specialist Periodical Report*, ed. by G.J. Hills, D. Pletcher, H.R. Thirsk, vol. 7 (The Royal Society of Chemistry/The Chemical Society, Burlington House/London, 1980), pp. 157–202
36. I. Epelboin, C. Gabrielli, M. Keddam, H. Takenouti, The study of the passivation process by the electrode impedance analysis, in *Comprehensive Treatise of Electrochemistry*, vol. 4, (Plenum Press, New York, 1981) pp. 151–192
37. D.D. Macdonald, M.C.H. McCubre, Impedance measurements in electrochemical systems, in *Modern Aspects of Electrochemistry*, vol. 14, (Plenum Press, New York, 1982) pp. 61–150
38. C. Gabrielli, M. Keddam, H. Takenouti, The use of ac techniques in the study of corrosion and passivity, in *Corrosion: Aqueous Processes and Passive Films*, ed. by J.C. Scully. Treatise on Materials Science and Technology, vol. 23, treatise ed. H. Herman (Academic Press, New York, 1983), pp. 395–451
39. M. Sluyters-Rehbach, J. Sluyters, A.C. techniques (for electrode kinetics), in *Comprehensive Treatise of Electrochemistry*, ed. by J.O'M. Bockris, Yu.A. Chizmadzhev, B.E. Conway, S.U.M. Khan, S. Sarangapani, S. Srinivasan, R.E. White, E. Yeager, vol. 9 (Plenum Press, New York, 1984), pp. 177–292
40. E.R. Brown, J.R. Sandifer, Cyclic voltammetry, ac polarography, and related techniques, in *Physical Methods of Chemistry*, ed. by B.W. Rossiter, J.F. Hamilton. Electrochemical Methods, vol. 2, 2nd edn. (Wiley, New York, 1986), pp. 273–432
41. M. Sluyters-Rehbach, J.H. Sluyters, Alternating current and pulse methods, in *Comprehensive Chemical Kinetics*, ed. by C.H. Bamford, C.F.H. Tipper, R.G. Compton, A. Hamnett, G. Hancock, vol. 26 (Elsevier, New York, 1986), pp. 203–354

42. I.D. Raistrick, Application of impedance spectroscopy to materials science. *Ann. Rev. Mater. Res.* **16**, 343–370 (1986). Palo Alto, CA
43. N. Bonanos, B.C.H. Steele, E.P. Butler, W.B. Johnson, W.L. Worrell, D.D. Macdonald, M.C.H. McKubre, Applications of impedance spectroscopy: characterization of materials; solid state devices; corrosion of materials, in *Impedance Spectroscopy: Emphasizing Solid Materials and Systems*, 1st edn., ed. by J.R. Macdonald (Wiley, New York, 1987)
44. Z. Samec, V. Marecek, Study of the electrical double layer at the interface between two immiscible electrolyte solutions by impedance measurements, in *The Interface Structure and Electrochemical Processes at the Boundary Between Two Immiscible Liquids*, ed. by V.E. Kazarinov (Springer, New York, 1987), pp. 123–141
45. D.D. MacDonald, Applications of electrochemical impedance spectroscopy in electrochemistry and corrosion science, in *Techniques for Characterization of Electrodes and Electrochemical Processes*, ed. by R. Varma, J.R. Selman (Wiley, New York, 1991), pp. 515–580
46. F. Mansfeld, W.J. Lorenz, Electrochemical impedance spectroscopy (EIS): application in corrosion science and technology, in *Techniques for Characterization of Electrodes and Electrochemical Processes*, ed. by R. Varma, J.R. Selman (Wiley, New York, 1991), pp. 581–647
47. J.R. Scully, D.C. Silverman, M.W. Kendig (eds.), Electrochemical impedance: analysis and interpretation. Meeting of the American society for testing and materials, San Diego, ASTM Special technical publication No. 1188, ASTM, Philadelphia, 1993, 4–5 Nov 1991
48. J. Li, N.W. Downer, H.G. Smith, Evaluation of surface-bound membranes with electrochemical impedance spectroscopy, in *Biomembrane Electrochemistry (American Chemical Society Advances in Chemistry Series 235)*, ed. by M. Blank, I. Vodyanov (ACS, Washington, DC, 1994), pp. 491–510
49. C. Gabrielli, Electrochemical impedance spectroscopy: principles, instrumentation, and applications, in *Physical Electrochemistry: Principles, Methods, and Applications*, ed. by I. Rubinstein (Marcel Dekker, New York, 1995), pp. 243–292
50. L. Pospisil, Electrochemical impedance and related techniques (bioelectrochemistry), in *Bioelectrochemistry: Principles and Practice*, vol. 3 (Birkhauser Verlag, Basel, 1996), pp. 1–39
51. M. Rueda, Applications of the impedance method in organic electrode kinetics, in *Research in Chemical Kinetics*, ed. by R.G. Compton, G. Hancock, vol. 4 (Blackwell, Oxford, 1997), pp. 31–96
52. C. Gabrielli, *Use and Application of Electrochemical Impedance Techniques*, Solartron Technical Report Number 24, Issue B: April 1997
53. A.R. Mount, M.T. Robertson, AC impedance spectroscopy of polymer films – an overview, in *Comprehensive Chemical Kinetics*, ed. by C.H. Bamford, C.F.H. Tipper, R.G. Compton, A. Hamnett, G. Hancock, vol. 37 (Elsevier, New York, 1999), pp. 439–459
54. N.D. Cogger, N.J. Evans, *An Introduction to Electrochemical Impedance Measurement*, Solartron Technical Report No. 6, Part No.: BTR006 Issue: 05, (1999).
55. R. Cottis, S. Turgoose, *Corrosion Testing Made Easy: Electrochemical Impedance and Noise* (NACE International, Houston, 1999)
56. H.G.L. Coster, T.C. Chilcott, The characterization of membranes and membrane surfaces using impedance spectroscopy, in *Surface Chemistry and Electrochemistry of Membranes*, ed. by T.S. Sorensen (Marcel Dekker, New York, 1999), pp. 649–792
57. A. Lasia, Electrochemical impedance spectroscopy and its applications, in *Modern Aspects of Electrochemistry*, ed. by B.E. Conway, J.O.'M. Bockris, R.E. White, vol. 32 (Kluwer Academic/Plenum Press, New York, 1999), pp. 143–248
58. E.M. Zholtovskij, Impedance of multilayer membrane systems, in *Surface Chemistry and Electrochemistry of Membranes, Surfactant Science Series*, vol. 79, ed. by T.S. Sorensen (Marcel Dekker, New York, 1999) pp. 793–835
59. S. Hason, J. Dvorak, F. Jelen, V. Vetterl, Impedance analysis of DNA and DNA-drug interactions on thin mercury film electrodes, in *Critical Reviews in Analytical Chemistry*, vol. 32 (Taylor and Francis, Philadelphia, 2002), pp. 167–179

60. J. Janata, Electrochemical sensors and their impedances: a tutorial, in *Critical Reviews in Analytical Chemistry*, vol. 32 (Taylor and Francis, Philadelphia, 2002), pp. 109–120
61. A. Lasia, Applications of electrochemical impedance spectroscopy to hydrogen adsorption, evolution and absorption into metals, in *Modern Aspects of Electrochemistry*, vol. 35, ed. by B.E. Conway, R.E. White (Kluwer/Plenum, New York, 2002), p. 1
62. U. Retter, H. Lohse, Electrochemical impedance spectroscopy, in *Electroanalytical Methods: Guide to Experiments and Applications*, ed. by F. Scholz (Springer, Berlin, 2002) pp. 149–166
63. E. Ivers-Tiffée, A. Weber, H. Schichlein, Electrochemical impedance spectroscopy (methods in electrocatalysis for fuel cells), in *Handbook of Fuel Cells: Fundamentals, Technology, Applications*, ed. by W. Vielstich, A. Lamm, H. Gasteiger, vol. 2 (Wiley, Chichester, 2003), pp. 220–235
64. S. Krause, Impedance methods, in *Encyclopedia of Electrochemistry*, vol. 3, ed. by P.R. Unwin (Wiley-VCH, Weinheim, 2003) pp. 196–229
65. A.S. Bondarenko, G.A. Ragoisha, Inverse problem in potentiodynamic electrochemical impedance, in *Progress in Chemometrics Research*, ed. by A.L. Pomerantsev (Nova Science, New York, 2005), pp. 89–102
66. G. Garcia-Belmonte, Analysis of conducting polymer electrode morphology from ion diffusion impedance measurements, in *Progress in Electrochemistry Research*, ed. by M. Nunez (Nova Science, New York, 2005), pp. 123–143
67. G.A. Ragoisha, A.S. Bondarenko, Potentiodynamic electrochemical impedance spectroscopy, in *Electrochemistry: New Research*, ed. by M. Nunez (Nova Science, New York, 2005), pp. 51–75
68. H. Liu, X.-Z. Li, Application of electrochemical impedance spectroscopy to optimize photoelectrocatalytic oxidation in aqueous solution, in *New Trends in Electrochemistry Research*, ed. by M. Nunez (Nova Science, New York, 2007), pp. 119–143
69. G. Nagy, Z. Kerner, J. Balog, R. Schiller, *High Temperature Electrochemical Impedance Spectroscopy of Metals Related to Light Water Reactor Corrosion in Electrochemistry in Light Water Reactors: Reference Electrodes, Measurement, Corrosion and Tribocorrosion Issues* (European Federation of Corrosion Publ. No. 49), ed. by R.-W. Bosch, D. Feron, J.-P. Celis (CRC Press, Boca Raton/Woodhead/Cambridge, UK, 2007), pp. 122–133
70. M. Tupin, C. Bataillon, J.P. Gozlan, P. Bossis, High temperature corrosion of Zircaloy-4 followed by in-situ impedance spectroscopy and chrono- amperometry. Effect of an anodic polarization, in *Electrochemistry in Light Water Reactors: Reference Electrodes, Measurement, Corrosion and Tribocorrosion Issues* (European Federation of Corrosion Publ. No. 49), ed. by R.-W. Bosch, D. Feron, J.-P. Celis (CRC Press, Boca Raton/Woodhead/Cambridge, UK, 2007), pp. 134–155
71. J. Gimsa, *Characterization of Particles and Biological Cells by AC Electrokinetics in Interfacial Electrokinetics and Electrophoresis* (Surfactant Science Series 106), ed. by A.V. Delgado (Marcel Dekker, New York, 2002), p. 369400
72. A. Lasia, Modeling of impedances of porous electrodes, in *Modern Aspects of Electrochemistry*, ed. by M. Schlesinger, vol. 43 (Springer, New York, 2009), pp. 67–138
73. G.A. Korn, T.M. Korn, *Mathematical Handbook for Scientists and Engineers*, 2nd edn. (McGraw Hill, New York, 1968)
74. P.A. McCollum, B.F. Brown, *Laplace Transform and Theorems* (Holt, Reinhart and Winston, New York, 1965)
75. E.O. Brigham, *The Fast Fourier Transform* (Prentice-Hall, Englewood Cliffs, 1974)
76. J.W. Cooper, in *Transform Techniques in Chemistry*, ed. by P.R. Griffiths (Plenum Press, New York, 1978), p. 69
77. C.-T. Cheng, *One-Dimensional Digital Signal Processing* (Marcel Dekker, New York, 1979)
78. N.E. Hill, W.E. Vaughan, A.H. Price, M. Davies, *Dielectric Properties and Molecular Behaviour* (Van Nostrand Reinhold, London, 1969)

79. B.A. Boukamp, *Equivalent Circuit. User Manual*, 2nd edn. (University of Twente, The Netherlands, 1989)
80. G.J. Hills, R. Payne, *Trans. Farad. Soc.* **61**, 316 (1965)
81. P. Delahay, *Double Layer and Electrode Kinetics* (Interscience, New York, 1965)
82. D.M. Mohilner, in *Electroanalytical Chemistry*, vol. 1, Chap. 4, ed. by A. J. Bard (Marcel Dekker, New York, 1966), p. 241
83. *A Lock-In Primer*, EG&G, (Princeton Applied Research, Princeton, 1986)
84. P.E. Wellstead, *Frequency Response Analysis*, Technical Note No 10. (Solartron Instruments, 1999)
85. N.J. Evans, *Electrochem. Newslett.* **11** (1996)
86. D.A. Harrington, *J. Electroanal. Chemistry* **355**, 21 (1993)
87. F. Seland, R. Tunold, D.A. Harrington, *Electrochim. Acta* **51**, 3827 (2006)
88. F. Seland, R. Tunold, D.A. Harrington, *Electrochim. Acta* **53**, 6851 (2008)
89. H. Duncan, A. Lasia, *J. Electroanal. Chem.* **52**, 6195 (2007)
90. A.A. Pilla, *J. Electrochem. Soc.* **117**, 467 (1970)
91. A.A. Pilla, *J. Electrochem. Soc.* **118**, 1295 (1971)
92. K. Doblhofer, A.A. Pilla, *J. Electroanal. Chem.* **39**, 91 (1972)
93. A.A. Pilla, Laplace plane analysis of electrode reactions, in *Electrochemistry. Calculations, Simulations, and Instrumentations*, ed. J.S. Mattson, H.B. Mark, C. MacDonald, Jr., (Marcel Dekker, New York, 1972)
94. E. Barsoukov, S.H. Ryu, H. Lee, *J. Electroanal. Chem.* **536**, 109 (2002)
95. E.O. Birgham, *The Fast Fourier Transform* (Prentice-Hall, Englewood Cliffs, 1974)
96. G. Blanc, I. Epelboin, C. Gabrielli, M. Keddam, *Electrochim. Acta* **20**, 599 (1975)
97. C. Gabrielli, F. Huet, M. Keddam, J.F. Lizée, *J. Electroanal. Chem.* **138**, 201 (1982)
98. C. Gabrielli, M. Keddam, J.F. Lizée, *J. Electroanal. Chem.* **205**, 59 (1986)
99. S.C. Creason, J.W. Hayes, D.E. Smith, *J. Electroanal. Chem.* **47**, 9 (1973)
100. J.-S. Yoo, S.-M. Park, *Anal. Chem.* **72**, 2035 (2000)
101. S.-M. Park, J.-S. Yoo, *Anal. Chem.* **75**, 455A (2003)
102. S.E. Mochalov, V.S. Kolosnitsyn, *Instrum. Exp. Tech.* **43**, 53 (2000)
103. R. Jurczakowski, A. Lasia, *Anal. Chem.* **76**, 5033 (2004)
104. C. Gabrielli, F. Huet, M. Keddam, J.F. Lizée, *J. Electroanal. Chem.* **138**, 201 (1982)
105. G.S. Popkurov, R.N. Schindler, *Bulg. Chem. Commun.* **27**, 459 (1994)
106. G.S. Popkurov, R.N. Schindler, *Rev. Sci. Instr.* **64**, 3111 (1993)
107. M. Rosvall, M. Sharp, *Electrochem. Commun.* **2**, 338 (2000)
108. J.E. Garland, C.M. Pettit, D. Roy, *Electrochim. Acta* **49**, 2623 (2004)
109. G.A. Ragoisha, A.S. Bondarenko, *Electrochim. Acta* **50**, 1553 (2005)
110. J.P. Diard, B. LeGorrec, C. Montella, *J. Electroanal. Chem.* **377**, 61 (1994)
111. J. Hazi, D.M. Elton, W.A. Czerwinski, J. Schiewe, V.A. Vicente-Beckett, A.M. Bond, *J. Electroanal. Chem.* **437**, 1 (1997)
112. J.E. Garland, K.A. Assiongbon, C.M. Pettit, S.B. Emery, D. Roy, *Electrochim. Acta* **47**, 4113 (2002)
113. C.M. Pettit, J.E. Garland, M.J. Walters, D. Roy, *Electrochim. Acta* **49**, 3293 (2004)
114. J. Lu, J.E. Garland, C.M. Pettit, S.V. Babu, D. Roy, *J. Electrochem. Soc.* **151**, G717 (2004)
115. V.R.K. Gorantla, K.A. Assiongbon, S.V. Babu, D. Roy, *J. Electrochem. Soc.* **152**, G404 (2005)
116. S.B. Emery, J.L. Hubble, D. Roy, *Electrochim. Acta* **50**, 5659 (2005)
117. C.M. Pettit, P.C. Goonetilleke, D. Roy, *J. Electroanal. Chem.* **589**, 219 (2006)
118. C.M. Pettit, P.C. Goonetilleke, C.M. Sulyma, D. Roy, *Anal. Chem.* **78**, 3723 (2006)
119. G.A. Ragoisha, A.S. Bondarenko, *Electrochem. Commun.* **5**, 392 (2003)
120. G.A. Ragoisha, A.S. Bondarenko, N.P. Osipovich, E.A. Streltsov, *J. Electroanal. Chem.* **565**, 227 (2004)
121. G.A. Ragoisha, A.S. Bondarenko, N.P. Osipovich, S.M. Rabchynski, E.A. Streltsov, *Electrochim. Acta* **53**, 3879 (2008)

122. G.A. Ragoisha, N.P. Osipovich, A.S. Bondarenko, J. Zhang, S. Kocha, A. Iiyama, J. Solid State Electrochem. **14**, 531 (2010)
123. E. van Gheem, R. Pintelon, J. Vereecken, J. Schoukens, A. Hubin, P. Ver-boven, O. Blajiev, Electrochim. Acta **49**, 4753 (2004)
124. Y. Van Ingelgem, E. Trouvé, O. Blajiev, R. Pintelon, A. Hubin, Electroanalysis **21**, 730 (2009)
125. T. Breugelmans, E. Trouvé, J.-B. Jorcin, A. Alvarez-Pampliega, B. Geboes, H. Terryn, A. Hubin, Prog. Org. Coat. **69**, 215 (2010)
126. Y. Van Ingelgem, Implementation of multisine EIS in a toolbox for electrochemical studies, PhD Thesis, Vrije Universiteit Brussel, 2009
127. T. Breugelmans, E. Trouvé, Y. Van Ingelgem, J. Wielant, T. Hauffman, R. Hausbrand, R. Pintelon, A. Hubin, Electrochem. Commun. **12**, 2 (2010)
128. J. Zhang, S.X. Guo, A.M. Bond, F. Marken, Anal. Chem. **76**, 3619 (2004)
129. S.J.M. Rosvall, M. Sharp, A.M. Bond, J. Electroanal. Chem. **546**, 51 (2003)
130. S.J.M. Rosvall, M.J. Honeychurch, D.M. Elton, A.M. Bond, J. Electroanal. Chem. **515**, 8 (2001)
131. M.J. Honeychurch, A.M. Bond, J. Electroanal. Chem. **529**, 3 (2002)
132. D.J. Gavaghan, A.M. Bond, J. Electroanal. Chem. **480**, 133 (2000)
133. R.L. Sacci, D.A. Harrington, ECS Trans. **19**(20), 31 (2009)
134. M. Martin, Étude de l'adsorption et de l'absorption d'hydrogene dans le palladium en milieu alcalin, PhD Thesis, Université de Sherbrooke, 2010
135. T. Breugelmans, J. Lataire, T. Muselle, E. Tourwe, R. Pintelon, A. Hubin, Electrochim. Acta **76**, 375 (2012)
136. K. Darowicki, J. Orlikowski, G. Lentka, J. Electroanal. Chem. **486**, 106 (2000)
137. K. Darowicki, J. Electroanal. Chem. **486**, 101 (2000)
138. K. Darowicki, J. Kawula, Electrochim. Acta **49**, 4829 (2004)
139. K. Darowicki, P. Slepiski, Electrochim. Acta **49**, 763 (2004)
140. K. Darowicki, P. Slepiski, M. Szocinski, Prog. Org. Coat. **52**, 306 (2005)
141. P. Slepiski, K. Darowicki, K. Andrearczyk, J. Electroanal. Chem. **633**, 121 (2009)
142. S.J.M. Rosvall, M.J. Honeychurch, D.M. Elton, A.M. Bond, J. Electroanal. Chem. **515**, 8 (2001)
143. P. Slepiski, K. Darowicki, E. Janicka, G. Lentka, J. Solid State Electrochem. **16**, 3539 (2012)
144. J. Crank, *The Mathematics of Diffusion* (Oxford University Press, Glasgow, 1970)
145. S.R. Taylor, E. Gileadi, Corrosion **51**, 664 (1995)
146. J. Sluyters, Rec. Trav. Chim. Pays-Bas **79**, 1092 (1960)
147. T.J. VanderNoot, J. Electroanal. Chem. **300**, 199 (1991)
148. J. Sluyters, J.J.C. Oomen, Rec. Trav. Chim. Pays-Bas **79**, 1101 (1960)
149. J.R. Delmastro, D.E. Smith, J. Electroanal. Chem. **9**, 192 (1965)
150. G. Brisard, L'électroreduction du Cd²⁺ dans le DMSO en presence du perchlorate de tetraethylammonium, MSc Thesis, Université de Sherbrooke, 1986
151. W.R. Fawcett, A. Lasia, J. Phys. Chem. **82**, 1114 (1978)
152. R. de Levie, A.A. Husovsky, J. Electroanal. Chem. **22**, 29 (1969)
153. D.E. Smith, Anal. Chem. **35**, 610 (1963)
154. C. Gabrielli, P.P. Grand, A. Lasia, H. Perrot, J. Electrochem. Soc. **151**, A1943–A1949 (2004)
155. L. Birry, A. Lasia, Electrochim. Acta **51**, 3356 (2006)
156. M.H. Martin, A. Lasia, Electrochim. Acta **53**, 6317 (2008)
157. C. Gabrielli, P.P. Grand, A. Lasia, H. Perrot, J. Electrochem. Soc. **151**, A1943 (2004)
158. J.R. Macdonald, J. Phys. Chem. **60**, 343 (1974)
159. D.R. Franceschetti, J.R. Macdonald, R.P. Buck, J. Electrochem. Soc., **138**, 1368 (1991)
160. J.R. Macdonald, J. Phys. Condens. Matter **22**, 495101 (2010)
161. J.R. Macdonald, L.R. Evangelista, E. Kaminski Lenzi, G. Barbero, J. Phys. Chem. C **115**, 7648 (2011)
162. J.R. Macdonald, J. Phys. Chem. A **115**, 13370 (2011)

163. L.R. Evangelista, E.K. Lenzi, G. Barbero, J.R. Macdonald, *J. Phys. Condens. Matter* **23**, 485005 (2011)
164. J.R. Macdonald, *J. Phys. Condens. Matter* **24**, 175004 (2012)
165. M. Fleischmann, S. Pons, J. Daschbach, *J. Electroanal. Chem.* **317**, 1 (1991)
166. M. Fleischmann, S. Pons in *Ultramicroelectrodes*, ed. by M. Fleischmann, S. Pons, D.R. Rolison, P.P. Schmidt, (Datatech, Morganton, 1987), p. 52.
167. T. Jacobsen, K. West, *Electrochim. Acta* **40**, 255 (1995)
168. M. Fleischmann, S. Pons, *J. Electroanal. Chem.* **250**, 277 (1988)
169. R. Michel, C. Montella, C. Verdier, J.-P. Diard, *Electrochim. Acta* **55**, 6263 (2010)
170. V.G. Levich, *Physicochemical Hydrodynamics* (Prentice-Hall, Englewood Cliffs, 1962)
171. J.M. Coueignoux, D. Schuhmann, *J. Electroanal. Chem.* **17**, 245 (1968)
172. D.A. Scherson, J. Newman, *J. Electrochem. Soc.* **111**, 110 (1980)
173. B. Tribollet, J. Newman, *J. Electrochem. Soc.* **130** (1983) 823; 2016
174. C. Deslouis, C. Gabrielli, B. Tribollet, *J. Electrochem. Soc.* **130**, 2044 (1983)
175. E. Levart, D. Schuhmann, *J. Electroanal. Chem.* **53**, 77 (1974)
176. B. Tribollet, J. Newman, W.H. Smyrl, *J. Electrochem. Soc.* **135**, 134 (1988)
177. C. Deslouis, I. Epelboin, M. Keddam, J.C. Lestrade, *J. Electroanal. Chem.* **28**, 57 (1970)
178. M.E. Orazem, M. Durbha, C. Deslouis, H. Takenouti, B. Tribollet, *Electrochim. Acta* **44**, 4403 (1999)
179. M. Durbha, M.E. Orazem, B. Tribollet, *J. Electrochem. Soc.* **146**, 2199 (1999)
180. J. Barber, S. Morin, B.E. Conway, *J. Electroanal. Chem.* **446**, 125 (1998)
181. D.E. Smith, *Anal. Chem.* **35**, 602 (1963)
182. T.G. McCord, D.E. Smith, *Anal. Chem.* **41**, 116 (1969)
183. T.G. McCord, D.E. Smith, *J. Electroanal. Chem.* **26**, 61 (1970)
184. T.G. McCord, D.E. Smith, *Anal. Chem.* **41**, 1423 (1969)
185. T.G. McCord, H.L. Hung, D.E. Smith, *J. Electroanal. Chem.* **21**, 5 (1969)
186. A.M. Band, R.J. O'Halloran, I. Ruzic, D.E. Smith, *J. Electroanal. Chem.* **132**, 39 (1982)
187. J.W. Hayes, I. Ruzic, D.E. Smith, G.L. Booman, J.R. Delmastro, *J. Electroanal. Chem.* **51**, 269 (1974)
188. H.R. Sobel, D.E. Smith, *J. Electroanal. Chem.* **26**, 271 (1970)
189. I. Ruzic, H.R. Sobel, D.E. Smith, *J. Electroanal. Chem.* **65**, 21 (1975)
190. J. Hayes, I. Ruic, D.E. Smith, G.L. Booman, J.R. Delmastro, *J. Electroanal. Chem.* **51**, 245 (1974)
191. D.E. Smith, *Anal. Chem.* **35**, 610 (1963)
192. I. Ruzic, H.R. Sobel, D.E. Smith, *J. Electroanal. Chem.* **65**, 21 (1975)
193. R.J. Schwall, I. Ruzic, D.E. Smith, *J. Electroanal. Chem.* **60**, 117 (1975)
194. R.J. Schwall, D.E. Smith, *J. Electroanal. Chem.* **94**, 227 (1978)
195. T. Matusinovic, D.E. Smith, *J. Electroanal. Chem.* **98**, 133 (1979)
196. H. Gerischer, *Z. Physik. Chem.* **198**, 286 (1951)
197. B.A. Boukamp, H.J.M. Bouwmeester, *Solid State Ion.* **157**, 29 (2003)
198. B.A. Boukamp, *Solid State Ion.* **169**, 65 (2004)
199. B.A. Boukamp, M. Verbraeken, D.H.A. Blank, P. Holtappels, *Solid State Ion.* **177**, 2539 (2006)
200. S.B. Adler, J.A. Lane, B.C.H. Steele, *J. Electrochem. Soc.* **143**, 3554 (1996)
201. R.U. Atangulov, I.V. Murygin, *Solid State Ion.* **67**, 9 (1993)
202. S. Havriliak, S. Negami, *Polymer* **8**, 161 (1967)
203. F. Berthier, J.P. Diard, C. Montella, *J. Electroanal. Chem.* **460**, 226 (1999)
204. F. Berthier, J.P. Diard, B. Le Gorrec, C. Montella, *J. Electroanal. Chem.* **458**, 231 (1998)
205. E. Laviron, *J. Electroanal. Chem.* **97**, 135 (1979); **195**, 25 (1979); **105**, 35 (1979); **112**, 137 (1980); **117**, 17 (1981)
206. P. Los, E. Laviron, *J. Electroanal. Chem.* **432**, 85 (1997)
207. F. Prieto, M. Rueda, J. Hidalgo, E. Martinez, I. Navarro, *Electrochim. Acta* **56**, 7916 (2011)
208. M.E. Huerta Garrido, M.D. Pritzker, *J. Electroanal. Chem.* **594**, 118 (2006)

209. A. Lasia, J. Electroanal. Chem. **605**, 77 (2007)
210. J.M. Chapuzet, A. Lasia, J. Lessard, in *Electrocatalysis*, ed. by J. Lipkowski, P.N. Ross (Wiley VCH, New York, 1998)
211. D.A. Harrington, B.E. Conway, Electrochim. Acta **32**, 1703 (1987)
212. J.P. Diard, B. LeGorrec, C. Montella, Electrochim. Acta **42**, 1053 (1997)
213. A. Lasia, A. Rami, J. Electroanal. Chem. **294**, 123 (1990)
214. F. Berthier, J.P. Diard, R. Michel, J. Electroanal. Chem. **510**, 1 (2001)
215. F. Berthier, J.P. Diard, L. Pronzato, E. Walter, Automatica **32**, 973 (1996)
216. F. Berthier, J.P. Diard, P. Landaud, C. Montella, J. Electroanal. Chem. **362**, 13 (1993)
217. M.R.G. de Chialvo, A.C. Chialvo, J. Electrochem. Soc. **147**, 1619 (2000)
218. J.P. Diard, B. LeGorrec, C. Montella, J. Electroanal. Chem. **205**, 77 (1986)
219. J.P. Diard, P. Landaud, B. LeGorrec, C. Montella, J. Electroanal. Chem. **255**, 1 (1988)
220. J.P. Diard, B. LeGorrec, C. Montella, J. Electroanal. Chem. **326**, 13 (1992)
221. J.P. Diard, B. LeGorrec, C. Montella, C. Monteroocampo, J. Electroanal. Chem. **352**, 1 (1993)
222. F. Berthier, J.P. Diard, C. Montella, I. Volovik, J. Electroanal. Chem. **402**, 29 (1996)
223. J.J. DiStefano, III, A.R. Stubberud, I.J. Williams, *Theory and Problems of Feedback and Control Systems*, Schaum's Outline Series, 2nd edn. (McGraw-Hill, New York, 1990)
224. G. Doetsch, *Laplace Transformation* (Dover, New York, 1953)
225. C.-N. Cao, Electrochim. Acta **35**, 837 (1990)
226. L. Bai, B.E. Conway, J. Electrochem. Soc. **137**, 3737 (1990)
227. D.D. Macdonald, S. Real, S.I. Smedley, M. Urquidi-Macdonald, J. Electrochem. Soc. **135**, 2410 (1988)
228. U. Krewer, M. Christov, T. Vidakovic, K. Sundmacher, J. Electroanal. Chem. **589**, 148 (2006)
229. D.A. Harrington, J. Electroanal. Chem. **403**, 11 (1996)
230. D.A. Harrington, J. Electroanal. Chem. **449**, 9 (1998)
231. D.A. Harrington, J. Electroanal. Chem. **449**, 29 (1998)
232. D.A. Harrington, P. van den Driessche, Electrochim. Acta **44**, 4321 (1999)
233. J.D. Campbell, D.A. Harrington, P. van den Driessche, J. Watmough, J. Math. Chem. **32**, 281 (2002)
234. D.A. Harrington, P. van den Driessche, J. Electroanal. Chem. **567**, 153 (2004)
235. D.A. Harrington, P. van den Driessche, Electrochim. Acta **56**, 8005 (2011)
236. W.R. Smith, R.W. Missen, *Chemical Reaction Equilibrium Analysis: Theory and Algorithms* (Wiley, New York, 1982)
237. E. Leiva, Electrochim. Acta **41**, 2185 (1996)
238. A. Lasia, J. Electroanal. Chem. **562**, 23 (2004)
239. D.A. Harrington, B.E. Conway, J. Electroanal. Chem. **221**, 1 (1987)
240. M.R. Gennero de Chialvo, A.C. Chialvo, Electrochim. Acta **44**, 841 (1998)
241. A. Lasia, J. Electroanal. Chem. **562**, 23 (2004)
242. B. Losiewicz, R. Jurczakowski, A. Lasia, Electrochim. Acta **80**, 292 (2012)
243. B. Losiewicz, M. Martin, C. Lebouin, A. Lasia, J. Electroanal. Chem. **649**, 19 (2010)
244. C. Gabrielli, P.P. Grand, A. Lasia, H. Perrot, J. Electrochem. Soc. **151**, A1943 (2004)
245. H. Duncan, A. Lasia, Electrochim. Acta **52**, 6195 (2007)
246. B. Losiewicz, R. Jurczakowski, A. Lasia, Electrochim. Acta **56**, 5746 (2011)
247. R. Jurczakowski, B. Losiewicz, A. Lasia, Kinetics and thermodynamics of HUPD on iridium in perchloric and sulfuric acids. 59th Meeting of the International Society for Electrochemistry, Seville, September 2008
248. F. Dion, A. Lasia, J. Electroanal. Chem. **475**, 28 (1999)
249. S. Morin, H. Dumont, B.E. Conway, J. Electroanal. Chem. **412**(1999), 39 (1996)
250. A. Lasia, Curr. Top. Electrochem. **2**, 239 (1993)
251. E.R. Gonzalez, G. Tremiliosi-Filho, M.J. de Giz, Curr. Top. Electrochem. **2**, 167 (1993)
252. M.R.G. de Chialvo, A.C. Chialvo, Electrochem. Commun. **1**, 379 (1999)

253. P.M. Quaino, M.R.G. de Chialvo, A.C. Chialvo, *Electrochim. Acta* **52**, 7396 (2007)
254. C. Hitz, A. Lasia, *J. Electroanal. Chem.* **532**, 133 (2002)
255. L. Bai, D.A. Harrington, B.E. Conway, *J. Electroanal. Chem.* **32**, 1713 (1987)
256. P. Gu, L. Bai, L. Gao, R. Brousseau, B.E. Conway, *Electrochim. Acta* **37**, 2145 (1992)
257. D. Schonfuß, H.-J. Spitzer, L. Muller, *Russ. J. Electrochem.* **31**, 930 (1995)
258. J.H. Barber, B.E. Conway, *J. Electroanal. Chem.* **461**, 80 (1999)
259. M.J. de Giz, G. Tremiliosi-Filho, E.R. Gonzalez, *Electrochim. Acta* **39**, 1775 (1994)
260. M.J. de Giz, G. Tremiliosi-Filho, E.R. Gonzalez, S. Srinivasan, A.J. Appleby, *Int. J. Hydrog. Energy* **20**, 423 (1995)
261. R.K. Shervedani, A. Lasia, *J. Electrochem. Soc.* **144**, 511 (1997)
262. R.K. Shervedani, A. Lasia, *J. Electrochem. Soc.* **145**, 2219 (1998)
263. L.L. Chen, A. Lasia, *J. Electrochem. Soc.* **138**, 3321 (1991)
264. P. Los, A. Lasia, *J. Electroanal. Chem.* **333**, 115 (1992)
265. L.L. Chen, A. Lasia, *J. Electrochem. Soc.* **139**, 3214 (1992)
266. L.L. Chen, A. Lasia, *J. Electrochem. Soc.* **139**, 3458 (1992)
267. E.B. Castro, M.J. de Giz, E.R. Gonzalez, J.R. Vilche, *Electrochim. Acta* **42**, 951 (1997)
268. L.L. Chen, D. Guay, A. Lasia, *J. Electrochem. Soc.* **143**, 3576 (1996)
269. N.A. Assungao, M.J. de Giz, G. Tremiliosi-Filho, E.R. Gonzalez, *J. Electrochem. Soc.* **144**, 2794 (1997)
270. J.-P. Diard, B. Le Gorrec, C. Montella, *J. Electroanal. Chem.* **466**, 122 (1999)
271. J. Barber, B.E. Conway, *J. Electroanal. Chem.* **466**, 124 (1999)
272. A. Lasia, *J. Electroanal. Chem.* **593**, 159 (2006)
273. J.O.'M. Bockris, J. McBreen, L. Nanis, *J. Electrochem. Soc.* **112**, 1025 (1965)
274. C. Montella, *J. Electroanal. Chem.* **497**, 3 (2001)
275. S.Y. Qian, B.E. Conway, G. Jerkiewicz, *Int. J. Hydrog. Energy* **25**, 539 (2000)
276. A. Lasia, D. Gregoire, *J. Electrochem. Soc.* **142**, 3393 (1995)
277. C. Lim, S.-I. Pyun, *Electrochim. Acta* **38**, 2645 (1993)
278. C. Lim, S.-I. Pyun, *Electrochim. Acta* **39**, 363 (1994)
279. I.A. Bagotskaya, *Zh. Fiz. Khim.* **36**, 2667 (1962)
280. A.N. Frumkin, in *Advances in Electrochemistry and Electrochemical Engineering*, ed. by P. Delahay, vol. 3 (Interscience, New York, 1963), p. 287
281. J.S. Chen, J.P. Diard, R. Durand, C. Montella, *J. Electroanal. Chem.* **406**, 1 (1996)
282. M.H. Martin, A. Lasia, *Electrochim. Acta* **53**, 6317 (2008)
283. H. Duncan, A. Lasia, *Electrochim. Acta* **52**, 6195 (2007)
284. M.H. Martin, A. Lasia, *Electrochim. Acta* **54**, 5292 (2009)
285. H. Duncan, A. Lasia, *J. Electroanal. Chem.* **621**, 62 (2008)
286. L. Birry, Etude des reactions d'insertion d'hydrogene dans des electrodes de palladium, PhD Thesis, Universite de Sherbrooke, 2005
287. L.O. Valeen, S. Sunde, R. Tunold, *J. Alloy Comp.* **253–254**, 656 (1997)
288. B.S. Haran, B.N. Popov, R.E. White, *J. Power Sources* **75**, 56 (1998)
289. C. Wang, *J. Electrochem. Soc.* **145**, 1801 (1998)
290. L.O. Valeen, A. Lasia, J.O. Jensen, R. Tunold, *Electrochim. Acta* **47**, 2871 (2002)
291. P. Zoltowski, *Electrochim. Acta* **44**, 4415(1999); **51**, 1576 (2006); **55**, 6274 (2010)
292. P. Zoltowski, *J. Electroanal. Chem.* **501**, 89 (2001); **512**, 64 (2001); **536**, 55 (2002); **572**, 205 (2004); **600**, 54 (2007)
293. B. Legawiec, P. Zoltowski, *J. Phys. Chem. B* **106**, 4933 (2002)
294. P. Zoltowski, *Acta Mater.* **51**, 5489 (2003)
295. J.S. Chen, R. Durand, C. Montella, *J. Chim. Phys.* **91**, 383 (1994)
296. Y.-G. Yoon, S.I. Pyun, *Electrochim. Acta* **40**, 999 (1995)
297. K.S. Cole, R.H. Cole, *J. Chem. Phys.* **9**, 341 (1941)
298. D.W. Davidson, R.H. Cole, *J. Chem. Phys.* **19**, 1484 (1951)
299. P. Zoltowski, *J. Electroanal. Chem.* **443**, 149 (1998)
300. G. Lang, K.E. Heusler, *J. Electroanal. Chem.* **457**, 257 (1998)

301. A. Sadkowsky, J. Electroanal. Chem. **481**, 222 (2000); 232
302. A. Sadkowsky, Electrochim. Acta **38**, 2051 (1993)
303. M.E. Orazem, N. Pebere, B. Tribollet, J. Electrochem. Soc. **153**, B129 (2006)
304. B.A. Boukamp, Solid State Ion. **169**, 65 (2004)
305. G.J. Brug, A.L.G. van den Eeden, M. Sluyters-Rehbach, J.H. Sluyters, J. Electroanal. Chem. **176**, 275 (1984)
306. C.H. Hsu, F. Mansfeld, Corrosion **57**, 747 (2001)
307. S.P. Harrington, T.M. Devine, J. Electrochem. Soc. **155**, C381 (2008)
308. M.A. Rodriguez, R.M. Carranza, R.B. Rebak, J. Electrochem. Soc. **157**, C1 (2010)
309. M.A. Rodriguez, R.M. Carranza, J. Electrochem. Soc. **158**, C221 (2011)
310. V.M.W. Huang, V. Vivier, M.E. Orazem, N. Pebere, B. Tribollet, J. Electrochem. Soc. **154**, C99 (2007)
311. B. Hirschorn, M.E. Orazem, B. Tribollet, V. Vivier, I. Frateur, M. Musiani, Electrochim. Acta **55**, 6218 (2010)
312. M.H. Martin, A. Lasia, Electrochim. Acta **54**, 5292 (2009)
313. M.H. Martin, A. Lasia, Electrochim. Acta **56**, 8058 (2011)
314. B.B. Mandenbrot, *The Fractal Geometry of the Nature* (Freeman, San Francisco, 1982)
315. R. de Levie, J. Electroanal. Chem. **281**, 1 (1990)
316. F. Hausdorff, Math. Ann. **79**, 157 (1919)
317. L. Nyikos, T. Pajkossy, Electrochim. Acta **30**, 1533 (1985)
318. H. von Koch, Ark. Mat. Astron. Fys. **1**, 681 (1904)
319. A. Le Mehaute, G. Crepy, Solid State Ion. **9**(10), 17 (1983)
320. A. Le Mehaute, G. Crepy, A. Hurd, C. R. Acad. Sci. Paris **306**, 117 (1988)
321. L. Nyikos, T. Pajkossy, J. Electrochem. Soc. **133**, 2061 (1986)
322. L. Nyikos, T. Pajkossy, Electrochim. Acta **31**, 1347 (1986)
323. T. Pajkossy, L. Nyikos, Electrochim. Acta **34**, 171 (1989)
324. T. Pajkossy, J. Electroanal. Chem. **300**, 1 (1991)
325. L. Nyikos, T. Pajkossy, Electrochim. Acta **35**, 1567 (1990)
326. A.P. Borossy, L. Nyikos, T. Pajkossy, Electrochim. Acta **36**, 163 (1991)
327. A. Sakharova, L. Nyikos, T. Pajkossy, Electrochim. Acta **37**, 973 (1992)
328. T. Pajkossy, Heterog. Chem. Rev. **2**, 143 (1995)
329. A.P. Borossy, L. Nyikos, T. Pajkossy, Electrochim. Acta **36**, 163 (1991)
330. E. Chassaing, R. Sapoal, G. Daccord, R. Lenormand, J. Electroanal. Chem. **279**, 67 (1990)
331. M. Filoche, B. Sapoal, Electrochim. Acta **46**, 213 (2000)
332. T. Pajkossy, L. Nyikos, J. Electroanal. Chem. **332**, 55 (1992)
333. M. Keddad, H. Takenouti, Electrochim. Acta **33**, 445 (1988)
334. T. Pajkossy, J. Electroanal. Chem. **364**, 111 (1994)
335. S.H. Liu, Phys. Rev. Lett. **55**, 529 (1985)
336. T. Kaplan, L.J. Gray, Phys. Rev. **32**, 7360 (1985)
337. T. Kaplan, S.H. Liu, L.J. Gray, Phys. Rev. **34**, 4870 (1986)
338. T. Kaplan, L.J. Gray, S.H. Liu, Phys. Rev. B **35**, 5379 (1987)
339. B. Sapoal, Solid State Ion. **23**, 253 (1987)
340. B. Sapoal, J.-N. Chazalviel, J. Peyriere, Solid State Ion. **28–30**, 1441 (1988)
341. B. Sapoal, J.-N. Chazalviel, J. Peyriere, Phys. Rev. A **38**, 5867 (1988)
342. T. Pajkossy, L. Nyikos, Electrochim. Acta **34**, 181 (1989)
343. R. de Levie, A. Vogt, J. Electroanal. Chem. **278**, 25 (1990); **281**, 23 (1990)
344. J.-Y. Go, S.-I. Pyun, Fractal approach to rough surfaces and interfaces in electrochemistry. Mod. Asp. Electrochem. **39**, 167 (2005)
345. R. de Levie, J. Electroanal. Chem. **261**, 1 (1989)
346. W. Mulder, J. Electroanal. Chem. **326**, 231 (1992)
347. G.P. Lindsay, G.D. Patterson, J. Chem. Phys. **73**, 3348 (1980)
348. W. Schelder, J. Phys. Chem. **79**, 127 (1975)
349. A. Sakharova, L. Nyikos, Y. Pleskov, Electrochim. Acta **37**, 973 (1992)

350. A. Kerner, T. Pajkossy, J. Electroanal. Chem. **448**, 139 (1998)
351. M.L. Tremblay, M.H. Martin, C. Lebouin, A. Lasia, D. Guay, Electrochim. Acta **55**, 6283 (2010)
352. R. Jurczakowski, C. Hitz, A. Lasia, J. Electroanal. Chem. **572**, 355 (2004)
353. Z. Kerner, T. Pajkossy, Electrochim. Acta **46**, 207 (2000)
354. B. Emmanuel, J. Electroanal. Chem. **605**, 89 (2007)
355. J. Newman, J. Electrochem. Soc. **113**, 501 (1966)
356. J. Newman, J. Electrochem. Soc. **113**, 1235 (1966)
357. J. Newman, J. Electrochem. Soc. **117**, 198 (1970)
358. V.M.W. Huang, V. Vivier, M.E. Orazem, N. Pebere, B. Tribollet, J. Electrochem. Soc. **154**, C81 (2007)
359. V.M.W. Huang, V. Vivier, M.E. Orazem, N. Pebere, B. Tribollet, J. Electrochem. Soc. **154**, C89 (2007)
360. C. Blanc, M.E. Orazem, N. Pebere, B. Tribollet, V. Vivier, S. Wu, Electrochim. Acta **55**, 6313 (2010)
361. S.L. Wu, M.E. Orazem, B. Tribollet, V. Vivier, J. Electrochem. Soc. **156**, C28 (2009)
362. S.L. Wu, M.E. Orazem, B. Tribollet, V. Vivier, J. Electrochem. Soc. **156**, C214 (2006)
363. J.B. Jorcin, M.E. Orazem, N. Pebere, B. Tribollet, Electrochim. Acta **51**, 1473 (2006)
364. B. Hirschorn, M.E. Orazem, B. Tribollet, V. Vivier, I. Frateur, M. Musiani, J. Electrochem. Soc. **157**, 452 (2010)
365. B. Hirschorn, M.E. Orazem, B. Tribollet, V. Vivier, I. Frateur, M. Musiani, J. Electrochem. Soc. **157**, 458 (2010)
366. I. Frateur, V.M.W. Huang, M.E. Orazem, N. Pebere, B. Tribollet, V. Vivier, Electrochim. Acta **53**, 7386 (2008)
367. Z. Kerner, T. Pajkossy, Electrochim. Acta **47**, 2055 (2002)
368. T. Pajkossy, T. Wandlowski, D.M. Kolb, J. Electroanal. Chem. **414**, 209 (1997)
369. T. Pajkossy, Solid State Ion. **94**, 123 (1997)
370. T. Pajkossy, D.M. Kolb, Electrochim. Acta **46**, 3063 (2001)
371. Z. Kerner, T. Pajkossy, L.A. Kibler, D.M. Kolb, Electrochem. Commun. **4**, 787 (2002)
372. T. Pajkossy, L.A. Kibler, D.M. Kolb, J. Electroanal. Chem. **582**, 69 (2005)
373. T. Pajkossy, Solid State Ion. **176**, 1997 (2005)
374. T. Pajkossy, D.M. Kolb, Electrochem. Commun. **9**, 1171 (2007)
375. T. Pajkossy, L.A. Kibler, D.M. Kolb, J. Electroanal. Chem. **600**, 113 (2007)
376. A.N. Frumkin, V.I. Melik-Gaykazyan, Dokl. Akad. Nauk **5**, 855 (1951)
377. Z. Kerner, T. Pajkossy, Electrochim. Acta **47**, 2055 (2002)
378. E. Tuncer, J.R. Macdonald, J. Appl. Phys. **99**, 074106 (2006)
379. J.R. Macdonald, E. Tuncer, J. Electroanal. Chem. **602**, 255 (2007)
380. L.M. Delves, J. Walsh, *Numerical Solution of Integral Equations* (Clarendon, Oxford, 1974)
381. T.J. VanderNoot, J. Electroanal. Chem. **386**, 57 (1995)
382. F. Dion, A. Lasia, J. Electroanal. Chem. **475**, 28 (1999)
383. P.C. Hansen, Numer. Algorithm **6**, 1 (1994); **46**, 189 (2007)
384. H. Schichlein, A.C. Muller, M. Voigts, A. Krugel, E. Ivers-Tiffée, J. Appl. Electrochem. **32**, 875 (2002)
385. A. Leonide, V. Sonn, A. Weber, E. Ivers-Tiffée, J. Electrochem. Soc. **155**, B36 (2008)
386. V. Sonn, A. Leonide, E. Ivers-Tiffée, J. Electrochem. Soc. **155**, B675 (2008)
387. J.P. Schmidt, T. Chrobak, M. Ender, J. Illig, D. Klotz, E. Ivers-Tiffée, J. Power Sources **196**, 5342 (2011)
388. <http://jgrossmacdonald.com/levminfo.html>
389. E. Tuncer, S.M. Gubanski, IEEE Trans. Dielectr. Electr. Insul. **8**, 310 (2001)
390. Z. Stoyanov, Pol. J. Chem. **71**, 1204 (1997)
391. D. Vladikova, P. Zoltowski, E. Makowska, Z. Stoyanov, Electrochim. Acta **47**, 2943 (2002)
392. D. Vladikova, Z. Stoyanov, J. Electroanal. Chem. **572**, 377 (2004)
393. D. Vladikova, Z. Stoyanov, M. Viviani, J. Eur. Ceram. Soc. **24**, 1121 (2004)

394. D. Vladikova, G. Raikova, Z. Stoyanov, H. Takenouti, J. Kilner, S. Skinner, *Solid State Ion.* **176**, 2005 (2005)
395. D. Vladikova, J.A. Kilner, S.J. Skinner, G. Raikova, Z. Stoyanov, *Electrochim. Acta* **51**, 1611 (2006)
396. D.E. Vladikova, Z.B. Stoyanov, A. Barbucci, M. Viviani, P. Carpanese, J.A. Kilner, S.J. Skinner, R. Rudkin, *Electrochim. Acta* **53**, 7491 (2008)
397. M.Z. Krapchanska, D.E. Vladikova, G.S. Raikova, M.P. Slavova, Z.B. Stoyanov, *Bulg. Chem. Commun.* **43**, 120 (2011)
398. G. Raikova, D. Vladikova, Z. Stoyanov, *Bulg. Chem. Commun.* **43**, 133 (2011)
399. R. Jurczakowski, A. Lasia, Impedance studies of platinum electrode in acidic solutions, 219 ECS Meeting, Montreal, May 2011
400. I. Rousar, K. Micka, A. Kimla, *Electrochemical Engineering II* (Elsevier, Amsterdam, 1986)
401. A.N. Frumkin, *Zh. Fiz. Khim.* **23**, 1477 (1949)
402. O.S. Ksenzhek, V.V. Strender, *Dokl. Akad. Nauk SSSR* **106**, 487 (1956)
403. O.S. Ksenzhek, *Russ. J. Phys. Chem.* **36**, 331 (1962)
404. A. Winsel, *Z. Elektrochem.* **66**, 287 (1962)
405. F.A. Posey, *J. Electrochem. Soc.* **111**, 1173 (1964)
406. J.M. Bisang, K. Juttner, G. Kreysa, *Electrochim. Acta* **39**, 1297 (1994)
407. A. Lasia, in *Modern Aspects of Electrochemistry*, ed. by M. Schlesinger, vol. 43 (Springer, New York, 2009), p. 67
408. R. de Levie, in *Advances in Electrochemistry and Electrochemical Engineering*, ed. by P. Delahay, vol. 6 (Interscience, New York, 1967), p. 329
409. L.M. Gassa, J.R. Vilche, M. Ebert, K. Juttner, W.J. Lorenz, *J. Appl. Electrochem.* **20**, 677 (1990)
410. R. de Levie, *Electrochim. Acta* **8**, 751 (1963)
411. I.D. Raistrick, *Electrochim. Acta* **35**, 1579 (1990)
412. R. Jurczakowski, C. Hitz, A. Lasia, *J. Electroanal. Chem.* **582**, 85 (2005)
413. R. de Levie, *Electrochim. Acta* **10**, 113 (1965)
414. J. Gunning, *J. Electroanal. Chem.* **392**, 1 (1995)
415. H. Keiser, K.D. Beccu, M.A. Gutjahr, *Electrochim. Acta* **21**, 539 (1976)
416. C. Hitz, A. Lasia, *J. Electroanal. Chem.* **500**, 213 (2001)
417. K. Elout, F. Debuyck, M. Moors, A.P. Peteghem, *J. Appl. Electrochem.* **25**, 326 (1995)
418. K. Elout, F. Debuyck, M. Moors, A.P. Peteghem, *J. Appl. Electrochem.* **25**, 334 (1995)
419. L. Chen, A. Lasia, *J. Electrochem. Soc.* **139**, 3214 (1992)
420. L. Chen, A. Lasia, *J. Electrochem. Soc.* **140**, 2464 (1993)
421. A. Lasia, in *Current Topics in Electrochemistry*, vol. 3, (Research Trends, Trivandrum, 1993), p. 239
422. L. Birry, A. Lasia, *J. Appl. Electrochem.* **34**, 735 (2004)
423. Y. Goubeyre, B. Tribollet, C. Dagbert, L. Hyspecka, *J. Electrochem. Soc.* **153**, B162 (2006)
424. M. Itagaki, S. Suzuki, I. Shitanda, K. Watanabe, H. Nakazawa, *J. Power Sources* **164**, 415 (2007)
425. M. Itagaki, Y. Hatada, I. Shitanda, K. Watanabe, *Electrochim. Acta* **55**, 6255 (2010)
426. G. Paasch, K. Micka, P. Gersdorf, *Electrochim. Acta* **38**, 2653 (1993)
427. J. Bisquert, G. Garcia-Belmonte, F. Fabregat-Santiago, A. Compte, *Electrochem. Commun.* **1**, 429 (1999)
428. J. Bisquert, G. Garcia-Belmonte, F. Fabregat-Santiago, N.S. Ferriols, P. Bogdanoff, E.C. Pereira, *J. Phys. Chem. B* **104**, 2287 (2000)
429. J. Bisquert, *Phys. Chem. Chem. Phys.* **2**, 4185 (2000)
430. G. Lang, M. Ujvari, G. Inzelt, *Electrochim. Acta* **46**, 4159 (2001)
431. P. Los, A. Lasia, H. Menard, L. Brossard, *J. Electroanal. Chem.* **360**, 101 (1993)
432. I. Rousar, K. Micka, A. Kimla, *Electrochemical Engineering*, vol. II (Elsevier, Amsterdam, 1986), p. 133
433. K. Scott, *J. Appl. Electrochem.* **13**, 709 (1983)

434. S.I. Marshall, *J. Electrochem. Soc.* **138**, 1040 (1991)
435. A. Lasia, *J. Electroanal. Chem.* **397**, 27 (1995)
436. J.S. Newman, C.W. Tobias, *J. Electrochem. Soc.* **109**, 1183 (1962)
437. L.G. Austin, H. Lerner, *Electrochim. Acta* **9**, 1469 (1964)
438. S.K. Rangarajan, *J. Electroanal. Chem.* **22**, 89 (1969)
439. M. Keddarn, C. Rakomotavo, H. Takenouti, *J. Appl. Electrochem.* **14**, 437 (1984)
440. C. Cachet, R. Wiart, *J. Electroanal. Chem.* **195**, 21 (1985)
441. A. Lasia, *J. Electroanal. Chem.* **428**, 155 (1997)
442. A. Lasia, *J. Electroanal. Chem.* **454**, 115 (1998)
443. A. Lasia, *J. Electroanal. Chem.* **500**, 30 (2001)
444. H. Wendt, S. Rausch, T. Borucinski, in *Advances in Catalysis*, vol. 40 (Academic, New York, 1994), p. 87
445. S. Rausch, H. Wendt, *J. Appl. Electrochem.* **22**, 1025 (1992)
446. D.D. Macdonald, M. Urquidi-Macdonald, S.D. Bhaktam, B.G. Pound, *J. Electrochem. Soc.* **138**, 1359 (1991)
447. D.D. Macdonald, *Electrochim. Acta* **51**, 1376 (2006)
448. S.-I. Pyun, C.-H. Kim, S.-W. Kim, J.-H. Kim, *J. New Mat. Electrochem. Syst.* **5**, 289 (2002)
449. H.K. Song, Y.H. Jung, K.H. Lee, L.H. Dao, *Electrochim. Acta* **44**, 3513 (1999)
450. H.K. Song, H.Y. Hwang, K.H. Lee, L.H. Dao, *Electrochim. Acta* **45**, 2241 (2000)
451. H.K. Song, J.H. Sung, Y.H. Jung, K.H. Lee, L.H. Dao, M.H. Kim, H.N. Kim, *J. Electrochem. Soc.* **151**, E102 (2004)
452. H.K. Song, J.H. Jang, J.J. Kim, S.M. Oh, *Electrochem. Commun.* **8**, 1191 (2006)
453. M. Musiani, M. Orazem, B. Tribollet, V. Vivier, *Electrochim. Acta* **56**, 8014 (2011)
454. J.S. Newman, *Electrochemical Systems*, 2nd edn. (Prentice Hall, Englewood Cliffs, 1991)
455. S. Devan, V.R. Subramanian, R.E. White, *J. Electrochem. Soc.* **151**, A905 (2004)
456. M. Doyle, J.P. Meyers, J. Newman, *J. Electrochem. Soc.* **147**, 99 (2000)
457. J.P. Meyers, M. Doyle, R.M. Darling, J. Newman, *J. Electrochem. Soc.* **147**, 2930 (2000)
458. A.M. Svensson, L.O. Valeen, R. Tunold, *Electrochim. Acta* **50**, 2647 (2005)
459. T.E. Springer, T.A. Zawodzinski, M.S. Wilson, S. Gottesfeld, *J. Electrochem. Soc.* **143**, 587 (1996)
460. A.M. Svensson, H. Weydahl, S. Sunde, *Electrochim. Acta* **53**, 7483 (2008)
461. S. Sunde, I.A. Lervik, L.E. Owe, M. Tsyppkin, *J. Electrochem. Soc.* **156**, B927 (2009)
462. A.W. Bott, *Curr. Sep.* **17**, 98 (1998)
463. K. Rajeshwar, in *Encyclopedia of Electrochemistry*, vol. 6, ed. by A.J. Bard, M. Stratmann, S. Licht (Wiley-VCH, Weinheim, 2002), p. 1
464. W. Schottky, *Z. Phys.* **113**, 367 (1939); **118**, 539 (1942)
465. N.F. Mott, *Proc. R. Soc. Lond. Ser. A* **171**, 27 (1939)
466. K. Gelderman, L. Lee, S.W. Donne, *J. Chem. Educ.* **84**, 685 (2007)
467. R. Thapar, K. Rajeshwar, *Electrochim. Acta* **28**, 195 (1983)
468. S.P. Harrington, T.M. Devine, *J. Electrochem. Soc.* **155**, C381 (2008)
469. M.A. Rodriguez, R.M. Carranza, *J. Electrochem. Soc.* **158**, C221 (2011)
470. D. Vanmaekelbergh, *Electrochim. Acta* **42**, 1135 (1997)
471. Z. Hens, *J. Phys. Chem. B* **103**, 122 (1999)
472. M. Parthasarathy, N.S. Ramgir, B.R. Sathe, I.S. Mulla, V.K. Pillai, *J. Phys. Chem.* **111**, 13092 (2007)
473. J.D. Kellner, in *Electrochemical Techniques for Corrosion Engineering*, ed. by R. Baboian (National Association of Corrosion Engineers, Houston, TX, 1986), p. 161
474. M.W. Kendig, S. Jeanjaquet, J. Lumsden, in *Electrochemical Impedance: Analysis and Interpretation*, ASTM Special technical publication No. 1188, ed. by J.R. Scully, D.C. Silverman, M.W. Kendig (ASTM, Philadelphia, 1993), p. 407
475. R.G. Buchheit, in *Electrochemical Techniques in Corrosion Science and Engineering*, ed. by R.G. Kelly, J.R. Scully, D.W. Shoesmith, R.G. Buchheit (Marcel Dekker, New York, 2002), p. 257

476. D.M. Brasher, A.H. Kingsbury, *J. Appl. Chem.* **4**, 62 (1954)
477. A.S. Castela, A.M. Simoes, *Corr. Sci.* **45**, 1631 (2003); **45**, 1647 (2003)
478. F.S.A. Lindqvist, *Corrosion* **41**, 69 (1985)
479. M. Kendig, J. Scully, *Corrosion* **46**, 22 (1990)
480. F. Mansfeld, C.H. Tsai, *Corrosion* **47**, 958 (1991)
481. C.H. Tsai, F. Mansfeld, *Corrosion* **49**, 726 (1993)
482. H.O. Finklea, in *Electroanalytical Chemistry*, vol. 19, ed. by A.J. Bard, I. Rubinstein (Marcel Dekker, New York, 1996), pp. 109–335
483. H.O. Finklea, in *Encyclopedia of Analytical Chemistry*, ed. by R.A. Meyers, vol. 11 (Wiley, New York, 2000), p. 10090
484. D.K. Schwartz, *Annu. Rev. Phys. Chem.* **52**, 107 (2001)
485. R.P. Janek, W.R. Fawcett, A. Ulman, *J. Phys. Chem. B* **101**, 8550 (1997)
486. S. Zhang, N. Hugo, W. Li, T. Roland, L. Berguiga, J. Elezgaray, F. Argoul, *J. Electroanal. Chem.* **629**, 138 (2009)
487. M.D. Porter, T.B. Bright, D.L. Allara, C.E.D. Chidsey, *J. Am. Chem. Soc.* **109**, 3561 (1987)
488. M. Stelzle, G. Weissmuller, E. Sackmann, *J. Phys. Chem.* **97**, 2974 (1993)
489. M. Cohen-Atiya, A. Nelson, D. Mandler, *Electrochem. Commun.* **9**, 2827 (2007)
490. R.P. Janek, W.R. Fawcett, A. Ulman, *Langmuir* **14**, 3011 (1998)
491. L.V. Protsailo, W. Ronald Fawcett, D. Russell, R.L. Meyer, *Langmuir* **18**, 9342 (2002)
492. L.V. Protsailo, W.R. Fawcett, *Electrochim. Acta* **45**, 3497 (2000)
493. K. Tokuda, T. Gueshi, H. Matsuda, *J. Electroanal. Chem.* **102**, 41 (1979)
494. H.O. Finklea, D.A. Snider, J. Fedyk, E. Sabatani, Y. Gafni, I. Rubinstein, *Langmuir* **9**, 3660 (1993)
495. X. Lu, H. Yuan, G. Zuo, J. Yang, *Thin Solid Films* **516**, 6476 (2008)
496. H.O. Finklea, L. Liu, M.S. Ravenscroft, S. Punturi, *J. Phys. Chem.* **100**, 18852 (1996)
497. K. Weber, L. Hockett, S. Creager, *J. Phys. Chem.* **101**, 8286 (1997)
498. A.L. Eckermann, D.J. Feld, J.A. Shaw, T.J. Meade, *Coord. Chem. Rev.* **254**, 1769 (2010)
499. H.T. Tien, *Bilayer Lipid Membranes (BLM): Theory and Practice* (Marcel Dekker, New York, 1974)
500. *Advances in Planar Lipid Bilayers and Liposomes*, ed. by A. Iglic, Academic Press/Elsevier, book series, 16 volumes, 2005–2012
501. A.L. Ottova, H.T. Tien, *Bioelectrochem. Bioenerg.* **42**, 141 (1997)
502. S. Alonso-Romanowski, L.M. Gassa, J.R. Vilche, *Electrochim. Acta* **40**, 1561 (1995)
503. E. Sackmann, *Science* **271**, 43 (1996)
504. C. Steinem, A. Janshoff, H.-J. Galla, M. Siebert, *Bioelectrochem. Bioenerg.* **42**, 213 (1997)
505. C. Steinem, A. Janshoff, K. von dem Bruch, K. Reihs, J. Goossens, H.-J. Galla, *Bioelectrochem. Bioenerg.* **45**, 17 (1998)
506. A.E. Vallejo, C.A. Gervasi, L.M. Gassa, *Bioelectrochem. Bioenerg.* **47**, 343 (1998)
507. A.E. Vallejo, C.A. Gervasi, *Bioelectrochemistry* **57**, 1 (2002)
508. R. Naumann, D. Walz, S.M. Schiller, W. Knoll, *J. Electroanal. Chem.* **550**, 241 (2003)
509. P. Kramar, D. Miklavčič, M. Kotulska, A. Maček Lebar, in *Advances in Planar Lipid Bilayers and Liposomes*, vol. 11, ed. by A. Iglic (Elsevier, Amsterdam, 2010), p. 29
510. M. Naumowicz, Z. Figaszewski, *Bioelectrochemistry* **61**, 21 (2003)
511. M. Naumowicz, Z.A. Figaszewski, *J. Membr. Biol.* **205**, 29 (2005)
512. M. Naumowicz, A.D. Petelska, Z.A. Figaszewski, *Electrochim. Acta* **50**, 2155 (2005)
513. M. Naumowicz, J. Kotynska, A. Petelska, Z. Figaszewski, *Eur. Biophys. J.* **35**, 239 (2006)
514. M. Naumowicz, A.D. Petelska, Z.A. Figaszewski, *Electrochim. Acta* **51**, 5024 (2006)
515. M. Naumowicz, A.D. Petelska, Z.A. Figaszewski, *Electrochim. Acta* **54**, 1089 (2009)
516. M. Naumowicz, Z.A. Figaszewski, *J. Membr. Biol.* **227**, 67 (2009)
517. M. Naumowicz, A.D. Petelska, Z.A. Figaszewski, *Cell Biochem. Biophys.* **61**, 145 (2011)
518. http://www.bank-ic.de/encms/knowhow/1_differnzpotalmessen.html
519. A.J. Hinton, B. Sayers, <http://www.solartronanalytical.com/download/Advanced%20Instrumentation%20for%20Bio%20impedance%20Measurements.pdf> (1998)

520. R. Schmukler, in *Electrical Trauma*, ed. by R.E. Lee, E.G. Cravalho, J.F. Burke (Cambridge University Press, Cambridge, 1992), p. 239
521. M. Naumowicz, A.D. Petelska, Z.A. Figaszewski, *Cell. Mol. Biol. Lett.* **8**, 5 (2003)
522. M. Naumowicz, Z.A. Figaszewski, *Biophys. J.* **89**, 3174 (2005)
523. M. Naumowicz, A.D. Petelska, Z.A. Figaszewski, *Electrochim. Acta* **50**, 2155 (2005)
524. M. Naumowicz, A. D. Petelska, Z. A. Figaszewski, *Acta Biochim. Pol.* **55**, 721 (2008)
525. M. Naumowicz, Z.A. Figaszewski, *Bulg. Chem. Commun.* **41**, 185 (2009)
526. P. Diao, D. Jiang, X. Cui, D. Gu, R. Tong, B. Zhong, *Bioelectrochem. Bioenerg.* **45**, 173 (1998)
527. M. Naumowicz, A.D. Petelska, Z.A. Figaszewski, *Cell. Mol. Biol. Lett.* **8**, 383 (2009)
528. M. Naumowicz, Z.A. Figaszewski, *Bulg. Chem. Commun.* **41**, 167 (2009)
529. L.M. Gassa, A.E. Vallejo, S. Alonso-Romanowski, J.R. Vilche, *Bioelectrochem. Bioenerg.* **42**, 187 (1997)
530. A.E. Vallejo, C.A. Gervasi, *Bioelectrochemistry* **57**, 1 (2002)
531. C.A. Gervasi, A.E. Vallejo, *Electrochim. Acta* **47**, 2259 (2002)
532. S. Dong, J. Li, *Bioelectrochem. Bioenerg.* **42**, 7 (1997)
533. E.K. Sinner, W. Knoll, *Curr. Opin. Chem. Biol.* **5**, 705 (2001)
534. K.N. Chaki, K. Vijayamohan, *Biosens. Bioelectron.* **17**, 1 (2002)
535. E. Katz, I. Willner, *Electroanalysis* **15**, 913 (2003)
536. Y.H. Kim, J.S. Park, H.I. Jung, *Sens. Actuat. B* **138**, 270 (2009)
537. A.L. Ghindilis, K.R. Schwarzkopf, D.S. Messing, I. Sezan, P. Schuele, C. Zhan, M.W. Smith, H.M. Simon, D.R. Evans, *ECS Trans.* **33**(8), 59 (2010)
538. A.G. Mantzila, M.I. Prodromidis, *Electroanalysis* **17**, 1878 (2005)
539. F. Davis, M.A. Hughes, A.R. Cossins, S.P. Higson, *Anal. Chem.* **79**, 1153 (2007)
540. Y.S. Chen, C.C. Wu, J.J. Tsai, G.J. Wang, *Int. J. Nanomedicine* **7**, 133 (2012)
541. M. Pohanka, P. Skladal, *J. Appl. Biomed.* **6**, 57 (2008)
542. T.R.J. Holford, F. Davis, S.P.J. Higson, *Biosens. Bioelectron.* **34**, 12 (2012)
543. J.-G. Guan, Y.-Q. Miao, Q.-J. Zhang, *J. Biosci. Bioeng.* **97**, 219 (2004)
544. M.I. Prodromidis, *Pak. J. Anal. Environ. Chem.* **8**, 69 (2007)
545. I.I. Suni, *Trend Anal. Chem.* **27**, 604 (2008)
546. M.I. Prodromidis, *Electrochim. Acta* **55**, 4227 (2010)
547. Y. Wang, Z. Ye, Y. Ying, *Sensors* **12**, 3449 (2012)
548. A.L. Ghindilis, M.W. Smith, K.R. Schwarzkopf, C. Zhan, D.R. Evans, A.M. Baptista, H.M. Dimon, *Electroanalysis* **21**, 1459 (2009)
549. A.L. Ghindilis, M.W. Smith, D.S. Messing, V.N. Haynes, G.B. Middleton, K.R. Schwarzkopf, C.E. Campbell, C. Zhan, B. Ulrich, M.J. Frasier, P.J. Schuele, D.R. Evans, I. Sezan, J.W. Hartzell, H.M. Simon, *Biosens. Bioelectron.* **35**, 87 (2012)
550. C.J. McNeil, D. Athey, M. Ball, W.O. Ho, S. Krause, R.D. Armstrong, J. Des Wright, K. Rawson, *Anal. Chem.* **67**, 3928 (1995)
551. W.O. Ho, S. Krause, C.J. McNeil, J.A. Pritchard, R.D. Armstrong, D. Athey, K. Rawson, *Anal. Chem.* **71**, 1940 (1999)
552. M.B. dos Santos, C. Sporer, N. Sanvicens, N. Pascual, A. Errachid, E. Martinez, M.-P. Marco, V. Teixeira, J. Samiter, *Procedia Chem.* **1**, 1291 (2009)
553. S. Chandra, N. Barola, D. Bahadur, *Chem. Commun.* **47**, 11258 (2011)
554. R. Churchill, J. Brown, *Complex Variables and Applications*, 6th edn. (McGraw-Hill, New York, 1990)
555. H.A. Kramers, *Atti. Congr. Intern. Fisici. Como* **2**, 545 (1927)
556. H.A. Kramers, *Phys. Zeit.* **30**, 521 (1929)
557. R. de L. Kronig, *J. Opt. Soc. Am.* **12**, 547 (1926)
558. H.W. Bode, *Network Analysis and Feedback Amplifier Design* (Van Nostrand, New York, 1945)
559. D.D. Macdonald, M. Urquidi-Macdonald, *J. Electrochem. Soc.* **132**, 2316 (1985)
560. M. Urquidi-Macdonald, S. Real, D.D. Macdonald, *J. Electrochem. Soc.* **133**, 2018 (1986)
561. M. Urquidi-Macdonald, S. Real, D.D. Macdonald, *Electrochim. Acta* **35**, 1559 (1990)

562. D.D. Macdonald, M. Uurquidi-Macdonald, J. Electrochem. Soc. **137**, 515 (1990)
563. D. Townley, J. Electrochem. Soc. **137**, 3305 (1990)
564. J.M. Esteban, M.E. Orazem, J. Electrochem. Soc. **138**, 67 (1991)
565. M.E. Orazem, J.M. Esteban, O.C. Moghissi, Corrosion **47**, 248 (1991)
566. P. Agarwal, M.E. Orazem, L.H. Garcia-Rubio, in *Electrochemical Impedance: Analysis and Interpretation*, ASTM STP 1188, ed. by J.R. Scully, D.C. Silverman, M.W. Kendig (ASTM, Philadelphia, 1993), p. 115
567. C. Gabrielli, M. Keddam, H. Takenouti, in *Electrochemical Impedance: Analysis and Interpretation*, ASTM STP 1188, ed. by J.R. Scully, D.C. Silverman, M.W. Kendig (ASTM, Philadelphia, 1993), p. 140
568. B.J. Dougherty, S.I. Smedley, in *Electrochemical Impedance: Analysis and Interpretation*, ASTM STP 1188, ed. by J.R. Scully, D.C. Silverman, M.W. Kendig (ASTM, Philadelphia, 1993), p. 154
569. B.A. Boukamp, Solid State Ion. **62**, 131 (1993)
570. D.D. Macdonald, M. Urquidi-Macdonald, J. Electrochem. Soc. **137**, 3304 (1990)
571. M. Urquidi-Macdonald, D.D. Macdonald, J. Electrochem. Soc. **137**, 3306 (1990)
572. P. Agarwal, M.E. Orazem, L.H. Garcia-Rubio, J. Electrochem. Soc. **139**, 1917 (1992)
573. P. Agarwal, M.E. Orazem, L.H. Garcia-Rubio, J. Electrochem. Soc. **142**, 4159 (1995)
574. B.A. Boukamp, J.R. Macdonald, Solid State Ion. **74**, 85 (1994)
575. B.A. Boukamp, J. Electrochem. Soc. **142**, 1885 (1995)
576. <http://www.utwente.nl/tnw/ims/publication/downloads/>
577. B. Hirschorn, B. Tribollet, M.E. Orazem, Israel J. Chem. **48**, 133 (2008)
578. B. Hirschorn, M.E. Orazem, J. Electrochem. Soc. **156**, C345 (2009)
579. S. Noyel Victoria, S. Ramanathan, Electrochim. Acta **56**, 2602 (2011)
580. J.-P. Diard, B. Le Gorrec, C. Montella, J. Electroanal. Chem. **377**, 61 (1994)
581. Z.B. Stoyanov, B.S. Savova-Stoyanov, J. Electrochem. Soc. **133**, 133 (1985)
582. Z.B. Stoyanov, Electrochim. Acta **37**, 2357 (1992)
583. B. Savova-Stoyanov, Z.B. Stoyanov, Electrochim. Acta **37**, 2353 (1992)
584. Z. Stoyanov, Electrochim. Acta **38**, 1919 (1993)
585. C.A. Schiller, F. Richter, E. Gulzow, N. Wagner, Phys. Chem. Chem. Phys. **3**, 374 (2001)
586. C.A. Schiller, F. Richter, E. Gulzow, N. Wagner, Phys. Chem. Chem. Phys. **3**, 2113 (2001)
587. R.C. Dorf, R.H. Bishop, *Modern Control Systems* (Prentice Hall, Upper Saddle River, 2011)
588. M.T.M. Koper, in *Advances in Chemical Physics*, vol. 92, ed. by I. Prigogine, Stuart A. Rice (Wiley, New York, 1996), p. 161
589. P. Gray, S.K. Scott, *Chemical Oscillations and Instabilities. Non-linear Chemical Kinetics* (Clarendon, Oxford, 1994)
590. M.T.M. Koper, J. Electroanal. Chem. **409**, 175 (1996)
591. P. Strasser, M. Lubke, F. Raspel, M. Eiswirth, G. Ertl, J. Chem. Phys. **107**, 979 (1997)
592. P. Strasser, M. Eiswirth, G. Ertl, J. Chem. Phys. **107**, 991 (1997)
593. T. Iwasita, B. Rasch, E. Cattaneo, W. Vielstich, Electrochim. Acta **34**, 1073 (1989)
594. S.S. Mahapatra, A. Dutta, J. Datta, Electrochim. Acta **55**, 9097 (2010)
595. C. Desilets, A. Lasia, Electrochim. Acta **78**, 286 (2012)
596. H.W. Bode, *Network Analysis and Feedback Design* (Van Nostrand, New York, 1945)
597. M.T.M. Koper, Electrochim. Acta **37**, 1771 (1992)
598. M.T.M. Koper, J.H. Sluyters, J. Electroanal. Chem. **352**, 51 (1993)
599. A. Sadkowsky, M. Dolata, J.-P. Diard, J. Electrochem. Soc. **151**, E20 (2004)
600. A. Sadkowsky, J.-P. Diard, C. Montella, J. Electrochem. Soc. **156**, F7 (2009)
601. K. Krischer, H. Varela, Oscillations and other dynamic instabilities, in *Handbook of Fuel Cells*, ed. by W. Vielstich, J. Gataiger, A. Lamm, vol. 2, (Wiley, Chichester, 2003), p. 679
602. H. Gohr, unpublished results available from www.zahner.de
603. W. Ehms, unpublished results available from www.zahner.de
604. <http://www.zahner.de/thales.html#eis>

605. J.-P. Diard, P. Landaud, J.-M. Le Canut, B. Le Gorrec, C. Montella, *Electrochim. Acta* **39**, 2585 (1994)
606. M.E. Orazem, P. Agarwal, A.N. Jansen, P.T. Wojcik, L.H. Garcia-Rubio, *Electrochim. Acta* **38**, 1903 (1993)
607. M.E. Orazem, P. Agarwal, L.H. Garcia-Rubio, *J. Electroanal. Chem.* **378**, 51 (1994)
608. P. Zoltowski, *J. Electroanal. Chem.* **375**, 45 (1994)
609. P. Zoltowski, *Pol. J. Chem.* **68**, 1171 (1994)
610. Z.B. Stoyanov, B. Savova-Stoyanova, *J. Electroanal. Chem.* **209**, 11 (1986)
611. Z. Stoyanov, *Electrochim. Acta* **34**, 1187 (1989)
612. Z. Stoyanov, *Electrochim. Acta* **35**, 1493 (1990)
613. P. Agarwal, M.E. Orazem, L.H. Garcia-Rubio, *J. Electrochem. Soc.* **142**, 4159 (1995)
614. J.R. Macdonald, *Electrochim. Acta* **38**, 1883 (1993)
615. J.R. Macdonald, *Electrochim. Acta* **35**, 1483 (1990)
616. J.R. Macdonald, J. Schoonman, A.P. Lehn, *J. Electroanal. Chem.* **131**, 77 (1982)
617. B.A. Boukamp, *Solid State Ion.* **20**, 31 (1986)
618. R.H. Milocco, *J. Electroanal. Chem.* **273**, 243 (1989)
619. W.H. Press, S.A. Teukolsky, W.V. Vetterling, B.P. Flannery, *Numerical Recipes. The Art of Scientific Computing* (Cambridge University Press, Cambridge, 1992)
620. T.J. VanderNoot, I. Abrahams, *J. Electroanal. Chem.* **448**, 17 (1998)
621. J. Yu, H. Cao, Y. He, *Chemometr. Intell. Lab. Syst.* **85**, 27 (2007)
622. P. Zoltowski, *J. Electroanal. Chem.* **179**, 11 (1984)
623. J.R. Macdonald, J. Potter, *Solid State Ion.* **24**, 61 (1987)
624. M.E. Orazem, T. El Moustafid, C. Deslouis, B. Tribollet, *J. Electrochem. Soc.* **143**, 3880 (1996)
625. M.E. Orazem, P. Agarwal, C. Deslouis, B. Tribollet, *J. Electrochem. Soc.* **143**, 948 (1996)
626. J.R. Macdonald, *CNLS, LEVM / LEVMW Manual*, version 8.09, November 2009. <http://www.jrossmacdonald.com/levminfo.html>
627. P. Agarwal, M.E. Orazem, L.H. Garcia-Rubio, *J. Electrochem. Soc.* **139**, 1917 (1992)
628. P. Agarwal, M.E. Orazem, L.H. Garcia-Rubio, *Electrochim. Acta* **41**, 1017 (1996)
629. M. Durbha, M.E. Orazem, L.H. Garcia-Rubio, *J. Electrochem. Soc.* **144**, 48 (1997)
630. S.L. Carson, M.E. Orazem, O.D. Crisalle, L. Garcia-Rubio, *J. Electrochem. Soc.* **150**, E491 (2003)
631. S.K. Roy, M.E. Orazem, *J. Electrochem. Soc.* **154**, B883 (2007)
632. M.E. Orazem, B. Tribollet, *Electrochim. Acta* **53**, 7360 (2008)
633. P.R. Bevington, *Data Reduction and Error Analysis for the Physical Sciences* (McGraw-Hill, New York, 1969)
634. J.R. Macdonald, *J. Electroanal. Chem.* **307**, 1 (1991)
635. D.E. Smith, W.H. Reinmuth, *Anal. Chem.* **33**, 482 (1961)
636. J. Paynter, W.H. Reinmuth, *Anal. Chem.* **34**, 1335 (1962)
637. J.-P. Diard, B. Le Gorrec, C. Montella, *Electrochim. Acta* **39**, 539 (1994)
638. J.-P. Diard, B. Le Gorrec, C. Montella, *J. Electroanal. Chem.* **432**, 27 (1997)
639. D.E. Smith, *Anal. Chem.* **35**, 1011 (1963)
640. L. Mészáros, G. Mészáros, B. Lengyel, *J. Electrochem. Soc.* **141**, 2068 (1994)
641. D.A. Harrington, *Can. J. Chem.* **75**, 1508 (1997)
642. J.-P. Diard, B. Le Gorrec, C. Montella, *J. Electroanal. Chem.* **432**, 41 (1997)
643. J.-P. Diard, B. Le Gorrec, C. Montella, *J. Electroanal. Chem.* **432**, 53 (1997)
644. J.-P. Diard, B. Le Gorrec, C. Montella, *Corros. Sci.* **40**, 495 (1998)
645. S.O. Engblom, J.C. Myland, K.B. Oldham, *J. Electroanal. Chem.* **480**, 120 (2000)
646. A.M. Bond, N.W. Duffy, S.-X. Guo, J. Zhang, D. Elton, *Anal. Chem.* **77**, 186A (2005)
647. M.J. Honeychurch, A.M. Bond, *J. Electroanal. Chem.* **529**, 3 (2002)
648. J. Zhang, S.X. Guo, A.M. Bond, F. Marken, *Anal. Chem.* **76**, 3619 (2004)
649. A.A. Sher, A.M. Bond, D.J. Gavaghan, K. Harriman, S.W. Feldberg, N.W. Duffy, S.X. Guo, J. Zhang, *Anal. Chem.* **76**, 6214 (2004)

650. D.J. Gavaghan, A.M. Bond, *Electroanalysis* **18**, 333 (2006)
651. J. Zhang, S.X. Guo, A.M. Bond, *Anal. Chem.* **79**, 2276 (2007)
652. A.P. O'Mullane, J. Zhang, A. Brajter-Toth, A.M. Bond, *Anal. Chem.* **80**, 4614 (2011)
653. C.Y. Lee, A.M. Bond, *Langmuir* **26**, 5243 (2010)
654. C.Y. Lee, J.P. Bullock, G.F. Kennedy, A.M. Bond, *J. Phys. Chem. A* **114**, 10122 (2011)
655. E. Mashkina, A.M. Bond, *Anal. Chem.* **83**, 1791 (2011)
656. K. Bano, A. Nafady, J. Zhang, A.M. Bond, U.H. Inam, *J. Phys. Chem. C* **115**, 24153 (2011)
657. S.M. Matthews, M.J.A. Shiddiky, K. Yunus, D.M. Elton, N.W. Duffy, Y. Gu, A.C. Fisher, A.M. Bond, *Anal. Chem.* **84**, 6686 (2012)
658. D. Britz, *Digital Simulation in Electrochemistry*, 2nd edn. (Springer, Heidelberg, 1988)
659. M. Rudolph, in *Physical Electrochemistry: Principles, Methods, and Applications*, ed. by I. Rubinstein (Marcel Dekker, New York, 1995), p. 81
660. J. Schiewe, J. Hazi, V.A. Vicente-Beckett, A.M. Bond, *J. Electroanal. Chem.* **451**, 129 (1998)
661. D.J. Gavaghan, D. Elton, K.B. Oldham, A.M. Bond, *J. Electroanal. Chem.* **512**, 1 (2001)
662. D.J. Gavaghan, D. Elton, A.M. Bond, *J. Electroanal. Chem.* **513**, 73 (2001)
663. S.J.M. Rosvall, M. Sharp, A. Bond, *J. Electroanal. Chem.* **536**, 161 (2002)
664. J. Zhang, S.X. Guo, A.M. Bond, M.J. Honeychurch, K.B. Oldham, *J. Phys. Chem. B* **109**, 8935 (2005)
665. A.A. Sher, A.M. Bond, D.J. Gavaghan, K. Gillow, N.W. Duffy, S.X. Guo, J. Zhang, *Electroanalysis* **17**, 1450 (2005)
666. B. Bensmann, M. Petkovska, T. Vidakovic-Koch, R. Hanke-Rauschenbach, K. Sundmacher, *J. Electrochem. Soc.* **157**, B1279 (2010)
667. T.R. Vidakovic-Koch, V.V. Panic, M. Andric, M. Petkovska, K. Sundmacher, *J. Phys. Chem. C* **115**, 17341 (2011)
668. V.V. Panic, T.R. Vidakovic-Koch, M. Andric, M. Petkovska, K. Sundmacher, *J. Phys. Chem. C* **115**, 17352 (2011)
669. H. Duncan, A. Lasia, *Solid State Ion.* **176**, 1429 (2005)
670. B. Losiewicz, R. Jurczakowski, A. Lasia, *Electrochim. Acta* **80**, 292 (2012)
671. E. Barsoukov, J.H. Kim, C.O. Yoon, H. Lee, *J. Power Sources* **83**, 61 (2007)
672. E. Karden, S. Buller, R.W. De Doncker, *J. Power Sources* **85**, 72 (2000)
673. F. Vigier, R. Jurczakowski, A. Lasia, *J. Electroanal. Chem.* **602**, 145 (2007)
674. O.J. Kwon, M.S. Kang, S.H. Ahn, I. Choi, K.U. Lee, J.H. Jeong, I.-S. Han, J.C. Yang, J.J. Kim, *Int. J. Hydrog. Energy* **36**, 9799 (2011)
675. International Standard ISO 16773-1:2007(E), 16773-2:2007(E), 16773-3:2009(E), 16773-4:2009(E), Switzerland
676. (2013), <http://www.gamry.com/application-notes/eis-of-organic-coatings-and-paints/>, registration required
677. A.J. Hinton, B. Sayers, Advanced instrumentation for solid state applications. (2004), <http://www.solartronanalytical.com/download/Advanced-Instrumentation-for-Solid-State-Applications.pdf>, registration necessary.
678. A.J. Hinton, B. Sayers, Beyond the limits: 1296 dielectric interface. (1998), <http://www.solartronanalytical.com/download/Beyond-the-Limits-The-1296-Dielectric-Interface.pdf>
679. A.J. Hinton, B. Sayers, Advanced instrumentation for civil engineering applications. (1998), <http://www.solartronanalytical.com/download/Advanced-Instrumentation-for-Civil-Engineering-Applications.pdf>
680. A.J. Hinton, B. Sayers, Advanced instrumentation for bioimpedance measurements. (1998), <http://www.solartronanalytical.com/download/Advanced-Instrumentation-for-Bioimpedance-Measurements.pdf>
681. A.J. Hinton, Determination of coating adhesion using electrochemical impedance spectroscopy. <http://www.solartronanalytical.com/download/Coatings-Tech-Determination-of-Coating-Adhesion-Using-Electrochemical-Impedance-Spectroscopy.pdf>
682. S. Chechirlian, P. Eichner, M. Keddah, H. Takenouti, H. Mazille, *Electrochim. Acta* **35**, 1125 (1990)

683. A. Lasia, P. Los, unpublished data (1991)
684. G. Schone, W. Wiesbeck, J. Electroanal. Chem. **229**, 407 (1987)
685. E. Sibert, R. Faure, R. Durand, J. Electroanal. Chem. **515**, 71 (2001)
686. B. Losiewicz, R. Jurczakowski, A. Lasia, Electrochim. Acta **80**, 292 (2012)
687. G. Fafilek, Monats. Chem. **140**, 1121 (2009)
688. A.S. Baranski, A. Szulborska, Electrochim. Acta **41**, 985 (1996)
689. A.S. Baranski, A. Moyana, Langmuir **12**, 3295 (1996)
690. A.S. Baranski, L.J. Nelson, P. Norouzi, Anal. Chem. **70**, 2895 (1998)
691. S.A.G.R. Karunathilaka, R. Barton, M. Hughes, N.A. Hampson, J. Appl. Electrochem. **15**, 251 (1985)
692. H. Gohr, M. Mirnik, C.A. Schiller, J. Electroanal. Chem. **180**, 273 (1984)
693. Gamry Application notes, <http://www.gamry.com/application-notes/eis-measurement-of-a-very-low-impedance-lithium-ion-battery/>; <http://www.gamry.com/application-notes/low-impedance-eis-using-a-1-mohm-resistor/>; <http://www.gamry.com/application-notes/testing-electrochemical-capacitors-part-3-electrochemical-impedance-spectroscopy/>
694. J. Harper, M. Rust, B. Sayers, A. Savage, Solartron application note. (2004), <http://www.solartronanalytical.com/download/TB-ANALYTICAL-001-High-frequency-high-current-impedance-spectroscopy-Experimental-protocols-enabling-measurement-up-to-1-MHz-at-high-current-densities.pdf>
695. Gamry Application Note, (2013) <http://www.gamry.com/application-notes/low-impedance-eis-using-a-1-mohm-resistor/>; <http://www.gamry.com/application-notes/low-impedance-limits-with-the-gamry-reference-30k-booster/>
696. J.M. Le Canut, R.M. Abouatallah, D.A. Harrington, J. Electrochem. Soc. **153**, A857 (2006)
697. J.M. Le Canut, R. Latham, W. Merida, D.A. Harrington, J. Power Sources **192**, 457 (2009)
698. J.P. Diard, N. Glandut, P. Landaud, B. Le Gorrec, C. Montella, Electrochim. Acta **48**, 555 (2003)
699. J.P. Diard, N. Glandut, B. Le Gorrec, C. Montella, J. Electrochem. Soc. **151**, A2193 (2004)
700. D.E. Vladikova, Z.B. Stoykov, G.S. Raikova, Inductance correction in impedance studies of energy sources, in *Portable and Emergency Energy Sources*, ed. by Z. Stoykov, D. Vladikova (Prof. Marin Drinov Publishing House, Sofia, 2006), p. 383
701. Gamry Application Notes, (2013) <http://www.gamry.com/application-notes/reference-electrodes/>; <http://www.gamry.com/application-notes/measuring-the-impedance-of-your-reference-electrode/>
702. W. Botter Jr., D.M. Soares, O. Teschke, J. Electroanal. Chem. **267**, 279 (1989)
703. M.C. Wiles, D.J. Schiffrin, T.J. VanderNoot, A.F. Silva, J. Electroanal. Chem. **278**, 151 (1990)
704. S. Fletcher, M.D. Horne, J. Electroanal. Chem. **297**, 297 (1991)

Index

A

Ac bridges, 67–68
Ac voltammetry, 72–73
Admittance plots, 49

B

Biosensors, 268–270
 capacitive biosensors, 268
 faradaic sensors, 269
Bode plots, 49

C

Charge transfer resistance, 91, 94
Circuit description code, 47–48
Coatings and paints, 257–261
 analysis of impedances, 259–261
 delamination, 258
 electrical equivalent models, 257–258
 water absorption, 258–259
Complex numbers, 18–20
Complex plane plots, 49
Constant phase element (CPE). *See* Dispersion
 of impedances at solid electrodes

D

Determination of time constant distribution
 function, 196–201
 differential impedance analysis, 198–200
 least-squares deconvolution methods, 198
 regularization methods, 196–197
Dispersion of impedances at solid electrodes,
 177–201

 constant phase element, CPE, 158, 177–183
 CPE, Brug et al. model, 180, 254–255
 CPE, Hsu and Mansfeld model, 183
 2D distribution, 189
 3D distribution, 189
 differential impedance analysis, 198–200
 dispersion due to surface adsorption/
 diffusion processes, 192–195
 dispersion of time constants, 188–192
 fractal model, 183–187
 least-squares deconvolution methods, 198
 origin of CPE dispersion, 187–195
 regularization methods, 196–197
Distinguishability of kinetic parameters,
 140–141
Dynamic EIS (DEIS), 79–83

E

Electrocatalytic reactions involving hydrogen,
 155–175
 hydrogen absorption into metals, 166–175
 hydrogen evolution reaction, 159–162
 hydrogen underpotential deposition,
 155–158
 influence of hydrogen mass transfer on
 HER, 163–165

F

Fourier transform, 20–31, 75–83
 aliasing, 30–31
 fast Fourier transform, 23
 leakage, 28–30
Frequency response analyzers (FRA), 70–72

G

- General method of obtaining impedance of complex reactions, 147–153
- Gerischer impedance, 121–124

I**Impedance**

- admittance, 45
- adsorption (*see* Impedance of faradaic reactions in presence of adsorption)
- definition of ac impedance, 42
- definition of impedance, 44–47
- definition of operational impedance, 33–41
- determination, 67–84
- drift, 281–282
- dynamic EIS, 79–83
- electrical circuits, 32–47, 49, 51, 52, 55, 58, 62, 63
- history, 3–4
- ideally polarizable electrode, 85–86
- immittance, 45
- impedance plots, 48–64
- linearity, 280–281
- linearization, 89
- negative dynamic resistance, 294–299
- noise perturbation, 77
- non-stationary impedances, 282–283
- Nyquist criterion of stability, 291–294
- operator and ac impedance-table, 46
- poles and zeros, 286
- publications, 5
- pulse or step excitation, 75–77
- stability, 281–299
- stability of electrochemical systems, 283–291
- sum of sine waves excitation, 77–79
- Volmer–Heyrovsky reaction, 132, 140–141
- Z-HIT transform (*see* Z-HIT transform)
- Impedance of faradaic reactions in presence of mass transfer
 - analysis of $\cot \phi$, 100–101
 - CNLS analysis, 102
 - cylindrical diffusion, 113–116
 - De Levie-Husovsky analysis, 99–100
 - disk electrode, 116–117
 - finite length internal spherical diffusion, 112–113
 - finite length linear diffusion, 102–107
 - generalized Warburg element, 107–109
 - Gerischer impedance, 121–124
 - homogeneous reaction, 121–124
 - mass transfer coefficient, 92
 - Randles analysis, 97–99

- reflective boundary, 106–107
- rotating disk electrode, 117–120
- semi-infinite external spherical diffusion, 109–111
- semi-infinite linear diffusion, 86–97
- spherical diffusion, 109–113
- transmissive boundary, 103–106
- Warburg impedance, 92–94

Impedance of porous electrodes, 203–250

- ac signal penetration length, 208
- continuous porous model, 245–249
- de Levie model, 217
- distribution of pores, 244–245
- double or triple pore structure, 214
- electrodes of arbitrary shape, 211
- impedance of ideally polarizable porous electrodes, 203–217
- ohmic drop in solution and in electrode material, 214–217
- redox reactions, 217–244
 - in absence of dc current, 217–221
 - concentration gradient only, 230–241
 - potential and concentration gradient, 241–244
 - potential gradient only, 222–230
- transmission line, ideally polarizable electrode, 208, 215
- transmission line in presence of redox reaction, 218, 221
- V-grooved pore, 210

Impedance of faradaic reactions in presence of mass transfer

- impedance plots, 137–140
- inductive loops, 139
- one adsorbed species
 - no desorption, 127–131
 - with subsequent desorption, 131–141
- two adsorbed species, 141–145

Impedance of faradaic reactions in presence of mass transfer, 85–124**Instrumental limitations, 333–339**

- high frequencies, 334–336
- high impedances, 334–336
- low impedances, 336–338
- reference electrode, 338–339

K

- Kirchhoff laws, 8
- Kramers–Kronig relations, 271–280
 - by approximations, 275–280
 - impedance and admittance, 296
 - polynomial approximation, 273–275

L

Laplace transform, 13, 32, 73–75
Lipid bilayers, 266–268
 measurements, 267
Lissajous curves, 68–69
Lock-in amplifiers, 69–70

M

Modeling of experimental data, 301–320
 Chi-square test, 315–318
 errors, 311
 fitting experimental data, 310
 indistinguishable circuits, 305–309
 proportional weighting, 314
 statistical weighting, 312–313
 test-F, 319
 t-test, 320
 types of modeling, 302–310
 unit weighting, 313
 weighting from measurement model,
 314–315
 weighting procedures, 312–315

N

Nonlinear impedances, 323–331
 analytical models, 323–327
 numerical models, 328

O

Ohm's law, 7–8

P

Phase sensitive detection (PSD), 69–70
Phasors, 41, 88

R

Randles circuit, 94

S

Self-assembled monolayers, 263–270
 electrical equivalent circuits, 263
 pinholes, 264
Semiconductors and Mott-Schottky plots,
 251–255
 determination of flat band potential,
 253–255

W

Warburg impedance, 91

Z

Z-HIT transform, 299

